Investigations of the Cavitation and Damage Thresholds of Histotripsy and Applications in Targeted Tissue Ablation

by

Eli Vlaisavljevich

A dissertation submitted in partial fulfillment
of the requirements for the degree of
Doctor of Philosophy
(Biomedical Engineering)
in the University of Michigan
2015

Doctoral Committee:

Assistant Professor Zhen Xu, Chair
Professor Charles A. Cain
Associate Professor Mohamed E.H. El-Sayed
Professor J. Brian Fowlkes
Associate Professor William W. Roberts

Science is a way of thinking much more than it is a body of knowledge.

-CARL SAGAN

Dedication

For the Peer Reviewer

Acknowledgements

First and foremost, I would like to express my gratitude for my advisor, Dr. Zhen Xu. I am immensely grateful for Zhen's continuous support and guidance, and I appreciate her willingness to put up with me for as long as she has. I have been extremely fortunate to work in such a positive environment and learn from such a great role model. I admire Zhen both as a colleague and a friend, and I will forever benefit from the lessons she has taught me. I would also like to thank my dissertation committee members: Drs. Charles Cain, William Roberts, Brian Fowlkes, and Mohamed El-Sayed. It has been an honor to work with such an amazing group of people who have provided vital guidance and support throughout my graduate experience. I have learned so much about histotripsy from Charles, and I am continually inspired by his passion for research and vision for the future of therapeutic ultrasound. Will has given me a perspective into the clinical aspects of histotripsy that has shaped my research approach and kept me focused on developing histotripsy to address specific clinical needs. Brian has been an irreplaceable resource for my questions about the physics of histotripsy and nanodroplet-mediated histotripsy, and I am constantly inspired by the breadth of his expertise. Finally, I would like to thank Mohamed for all of his hard work developing nanodroplet-mediated histotripsy. This work could only have been accomplished through a complete collaboration, and I appreciate both Mohamed's expertise as well as his passion for the project.

In addition to my committee members, I would also like to thank the many current and former members of the Histotripsy Lab who have made significant contributions to both my

research and my overall experience at the University of Michigan. First off, none of my work would have been possible if it weren't for the transducers and electronics developed by Dr. Tim Hall, who has made my life much easier in the laboratory and much more enjoyable around the office. I would also like to thank the graduate students and post docs who have shared these past few years with me including Adam Maxwell, Yohan Kim, Ryan Miller, Xi Zhang, Kuang-Wei Lin, Alex Duryea, Steven Allen, Jonathan Sukovich, Jonathan Lundt, Tzu-Yin Wang, Simone Park, Hedieh Tamaddoni, and Yige Li. It has been a pleasure working in such a positive and collaborative environment. I am specifically indebted to Adam, the Nick Carter of therapeutic ultrasound, for teaching me so much about the physics of histotripsy and for providing an example for which I can aspire to strive towards. I also owe a special thanks to Yohan, Kuang-Wei, Ryan, Xi, Alex, and Jonathan for their help setting up experiments, calibrating transducers, fixing amplifiers, wrestling pigs and sheep, and the countless other ways in which they have made my work possible. I would also like to thank Dr. Gabe Owens for his hard work and valuable advice on our *in vivo* projects. In addition, I am immensely indebted to Dr. Kimberly Ives for all of her work overseeing our animal studies and for making the lab such a fun environment for research. Additionally, I would like to thank Steven Allen and Joan Greve for providing MRI imaging that has been a valuable component of our *in vivo* studies. I would like to thank Dr. Theodore Welling for his guidance on developing histotripsy for the treatment of liver cancer, and Dr. Xu Cheng for his help on our rat experiments. Finally, I would like to thank the undergraduate students and visiting scholars who have worked with me over these past few years especially Robert Rickel, Alexa Arvidson, Thai-Son Nguyen, Yu Ding, and Lifang Jin.

I would also like to thank my many collaborators outside of the Histotripsy Lab for their valuable contributions to our research. First, I would like to thank Dr. Yasemin Yuksel Durmaz

and Omer Aydin for their work on nanodroplet-mediated histotripsy, the development of which was only possible due to their tireless dedication. It was an honor to work with such knowledgeable and hardworking collaborators whose positive attitudes made this project both successful and enjoyable. I would also like to thank Dr. Eric Johnsen, Matthew Warnez, and Lauren Mancia for their theoretical work that has vastly improved our understanding of histotripsy. In addition, I would like to thank Drs. Andrew Putnam and Rahul Singh for their help characterizing tissue phantom mechanical properties and their input on the effects of tissue properties on histotripsy. Finally, I am grateful to all of our administrative staff, especially to Maria Steele, Kathleen McCrumb, and Therese Kummer, for keeping things running smoothly and for providing a positive environment to visit whenever I needed a distraction from the lab.

I would also like to thank our funding sources that have made this work possible. First, I would like to thank the National Science Foundation for awarding me a Graduate Research Fellowship. I am also thankful for the funding we received from the American Cancer Society, the National Institutes of Health, the Department of Defense, the Hartwell Foundation, and the Focused Ultrasound Foundation. Finally, I would like to thank the National Security Agency for continuously monitoring our work and backing up all of our data.

In addition to these people at the University of Michigan, I would also like to thank Dr. Rupak Rajachar for getting me started in research as an undergraduate at Michigan Tech. I was very lucky to have crossed paths with Dr. R, and there is no question that I am only in this position today because of him. Not only has Dr. R been an amazing mentor and role model who taught me how to properly conduct experiments and approach the research process, but he has also been an amazing friend whose positive influence on my life has extended well beyond my professional development. I would also like to thank my many friends who continue to add

excitement to my life, especially John Vadnais, Mike VanWagner, Derek Kitti, and Dillon Duncan. We have gone through some hard times together, and, while the tragedy of those murders will forever remain a part of our story, it means the world to me that these men remain such an important part of my life. Finally, I would like to thank the staff at ToWriteaWrong.com for all of their hard work keeping things afloat during these past few years while I have dedicated the majority of my time towards research.

I would like to end by expressing my love and gratitude to my girlfriend and solemate, Piyumi, for bringing so much happiness to my life. The past two years have been an absolute cliché, and I have enjoyed every day we have shared together. I am thankful to have this amazing woman in my life, and I appreciate how supportive she has been of both my work as a graduate student and as an author. I am fully aware of the sacrifices she has made for us, and I will never take her presence in my life for granted. Finally, I would like to thank my family for all of their support. It is impossible to describe how lucky I am to have such an amazing family, and I know it would take a document much longer than this dissertation in order to adequately express my gratitude for these people who have made my life possible. My dissertation was written for the peer reviewers, but my life will always be dedicated to the people I love. No one has done more for me or meant more to me than my Father, and I cannot begin to express how proud I am to have my Dad as my best friend. My Dad was the one who first taught me to question why, and everything that I have achieved in my life has been a direct result of His love and belief in me. He is truly the best man I know, and I hope to one day be worthy of walking in the Walker's footsteps. I have also been blessed with two amazing mothers who have given me love from both heaven and earth, and I will forever be indebted to them for shaping me into the person I am today through a wonderful combination of love, discipline, and apple pie. My two sisters, Bess

and Rose, have left no doubt that I will forever live in their shadows. I am proud to have two such strong and loving women as my sisters, and I am thankful both for their presence in my life as well as their sacrifices that have made our country a better place. I would also like to thank the rest of the V's for being such a wonderful part of my life. Nothing has brought me more joy than our time together at the cabin and our epic backyard boot hockey battles. I am thankful to have such amazing role models in Dan and Molly, and I can't begin to describe how much joy Ryan and Anna have brought to my life. I am so proud of these two kids who have grown into amazing young adults, and I can't wait to see where their lives take them in the years to come. I am also thankful for Lala and Gerry, who have supported me on every step of my journey while providing a perfect example of how to work hard to take care of the people you love. Finally, I would like to thank the rest of my extended family and friends who I am so fortunate to have in my life.

Eli Vlaisavljevich

June, 2015

Table of Contents

Dedication ..... **ii**

Acknowledgments ..... **iii**

List of Figures ..... **xix**

List of Tables ..... **xxxii**

Abstract ..... **xxxiv**

Chapter 1: Introduction **1**

1.1 Background: Focal Ablation 1

1.2 Histotripsy Therapy 2

1.3 Outline of this dissertation 5

1.4 References 7

Chapter 2: Histotripsy-induced Cavitation Cloud Initiation Thresholds in Tissue of Different Mechanical Properties **11**

2.1 Introduction 11

2.2 Methods 13

2.2.1 Therapeutic Ultrasound 13

2.2.2 Tissue Phantom Preparation 14

2.2.3 Tissue Phantom Mechanical Properties 15

2.2.4 Porcine Tissue Preparation 16

2.2.5 Tissue Mechanical Properties 16

2.2.6 Cavitation Cloud Initiation Detection 16
2.2.7 Bubble Expansion Simulation 19
2.2.8 Bubble Behavior 21
2.3 Results 22
2.3.1 Cavitation cloud initiation threshold in agarose tissue phantom 22
2.3.2 Cavitation cloud initiation threshold in porcine tissue 24
2.3.3 Bubble Expansion Simulation 26
2.3.4 Bubble Behavior 27
2.4 Discussion 28
2.5 Conclusion 33
2.6 References 34
Chapter 3: Effects of Ultrasound Frequency and Tissue Stiffness on the Histotripsy Intrinsic Threshold for Cavitation 37
3.1 Introduction 37
3.2 Methods 40
3.2.1 Sample Preparation 40
3.2.2 Histotripsy Pulse Generation 43
3.2.3 Cavitation Detection using Optical Imaging 45
3.2.4 Passive Cavitation Detection (PCD) 47
3.2.5 Intrinsic Threshold Measurement and Comparison 48
3.2.6 Threshold Simulation: Stabilized Nuclei 49
3.2.7 Threshold Simulation: Spontaneous Nucleation 52
3.3 Results 53
3.3.1 Intrinsic Threshold in Water 53

3.3.2 Intrinsic Threshold in Tissue Phantoms 56
3.3.3 Intrinsic Threshold in Bovine Tissue 59
3.3.4 Intrinsic Threshold Comparison 60
3.3.5 Threshold Simulation: Stabilized nuclei 62
3.3.6 Threshold Simulation: Spontaneous Nucleation 64
3.4 Discussion 65
3.5 Conclusion 69
3.6 References 70
Chapter 4: Effects of Temperature on the Histotripsy Intrinsic Threshold for Cavitation .74
4.1 Introduction 74
4.2 Methods 77
4.2.1 Experimental Setup 77
4.2.2 Histotripsy Pulse Generation 78
4.2.3 Cavitation Detection using Optical Imaging 80
4.2.4 Passive Cavitation Detection (PCD) 82
4.2.5 Intrinsic Threshold Calculation and Comparison 82
4.2.6 Threshold Simulation: Stabilized nuclei 83
4.2.7 Threshold Simulation: Spontaneous Nucleation 86
4.3 Results 87
4.3.1 Intrinsic Threshold vs. Temperature 87
4.3.2 Optical images of Cavitation Bubble Cloud 89
4.3.3 Passive Cavitation Detection (PCD) 90
4.3.4 Threshold Simulation: Stabilized nuclei 92

4.3.5 Threshold Simulation: Spontaneous Nucleation 95
4.4 Discussion 96
4.5 Conclusion 100
4.6 References 102
Chapter 5: Effects of Tissue Mechanical Properties on Susceptibility to Histotripsy-induced Tissue Damage....107
5.1 Introduction 107
5.2 Methods....109
5.2.1 Therapeutic Ultrasound Treatment....109
5.2.2 Histotripsy Tissue Phantom Treatment 110
5.2.3 Histotripsy *ex vivo* Porcine Tissue Treatment....111
5.2.4 *In vivo* Vessel-sparing Ablation 113
5.3 Results....116
5.3.1 Histotripsy in Agarose Tissue Phantoms....116
5.3.2 Histotripsy in *ex vivo* Porcine Tissues....117
5.3.3 *In vivo* Vessel-sparing Ablation 122
5.4 Discussion 126
5.5 Conclusion 130
5.6 References 131
Chapter 6: Effects of Thermal Preconditioning on Tissue Susceptibility to Histotripsy....135
6.1 Introduction....135
6.2 Methods....138
6.2.1 Bovine Tissue Processing....138

6.2.2 Constant Temperature Heating 138
6.2.3 Measurement of Tissue Stiffness 139
6.2.4 Histological Analysis 140
6.2.5 Histotripsy Treatment 141
6.2.6 HIFU Heating 142
6.3 Results 143
6.3.1 Controlled Preheating at 58°C 143
6.3.2 Controlled Preheating at 90°C 150
6.3.3 HIFU Heating 154
6.4 Discussion 158
6.5 Conclusion 164
6.6 References 165
Chapter 7: Effects of Tissue Stiffness, Ultrasound Frequency, and Pressure on Histotripsy-induced Cavitation Bubble Behavior 168
7.1 Introduction 168
7.2 Methods 171
7.2.1 Bubble Behavior Simulation 171
7.2.2 Tissue Phantom with Mechanically Tunable Properties 173
7.2.3 Histotripsy Pulse Generation 174
7.2.4 Optical Imaging 176
7.2.5 Experimental Design 178
7.2.6 Stress-Strain Estimation 179
7.2.7 Supra-threshold Bubble Behavior 179
7.3 Results 180

7.3.1 Bubble Behavior Simulation 180
7.3.2 Effects of Tissue Stiffness on Bubble Behavior 182
7.3.3 Effects of Ultrasound Frequency on Bubble Behavior 186
7.3.4 Estimated Stress-Strain 187
7.3.5 Bubble Behavior Generated using Dual-Frequency Beam 188
7.3.6 Supra-threshold Bubble Behavior 190
7.4 Discussion 193
7.5 Conclusion 197
7.6 References 199
Chapter 8: Visualizing the Histotripsy Process: Bubble Cloud-Cancer Cell Interactions .202
8.1 Introduction 202
8.2 Methods 203
8.2.1 Miniature Transducer-tank Setup 203
8.2.2 Ultrasound Generation 204
8.2.3 Cancer Cell Tissue Phantom Preparation 205
8.2.4 Single Pulse Cell-bubble Interaction 207
8.2.5 Multiple Pulse Cell-bubble Interaction 207
8.3 Results 208
8.3.1 Single Pulse Cell-bubble Interaction 208
8.3.2 Multiple Pulse Cell-bubble Interaction 209
8.4 Discussion 212
8.5 Conclusion 215
8.6 References 216

Chapter 9: Image-Guided Non-Invasive Ultrasound Liver Ablation using Histotripsy: Feasibility Study in an *in vivo* Porcine Model 219

9.1 Introduction 219

9.2 Methods 223

9.2.1 Porcine Surgical Procedures 223

9.2.2 Lesion Generation through Ribs and Overlying Tissue 224

9.2.3 Larger Lesion Ablation 226

9.2.4 Tissue-selective Liver Ablation 227

9.2.5 Liver MRI 227

9.2.6 Histological Evaluation 228

9.3 Results 229

9.3.1 Lesion Generation through Ribs and Other Overlying Tissue 229

9.3.2 Larger Lesion Ablation 232

9.3.3 Tissue-selective Liver Ablation 234

9.4 Discussion 237

9.5 Conclusion 241

9.6 References 243

Chapter 10: Non-Invasive Ultrasound Liver Ablation using Histotripsy: Chronic Study in an *in vivo* Rodent Model 248

10.1 Introduction 248

10.2 Methods 250

10.2.1 Animal Preparation 250

10.2.2 Histotripsy Lesion Generation 252

10.2.3 Magnetic Resonance Imaging (MRI) 253

10.2.4 Morphological and Histological Evaluation....255
10.3 Results....255
10.3.1 Histotripsy Liver Lesion Formation....255
10.3.2 Histotripsy Chronic Lesion Progression....257
10.3.3 MRI Liver Lesion Monitoring....260
10.3.4 Lung Histological Analysis....262
10.4 Discussion....263
10.5 Conclusion....268
10.6 References....269
Chapter 11: Nanodroplet-Mediated Histotripsy for Image-guided Targeted Ultrasound Cell Ablation....273
11.1 Introduction....273
11.2 Methods....276
11.2.1 Formulation and Characterization of Nanodroplets....276
11.2.2 Biocompatibility of Nanodroplets....278
11.2.3 Threshold Simulation for Nanodroplet-Mediated Cavitation....279
11.2.4 Ultrasound Setup....281
11.2.5 Preparation of Tissue Phantoms....283
11.2.6 Measurement of Histotripsy Threshold in Agarose Tissue Phantoms....284
11.2.7 Selective Cavitation in Composite Agarose Phantom....286
11.2.8 Bubble Behavior....287
11.2.9 Ablation of Red Blood Cells in Tissue Phantom....288
11.3 Results....289

11.3.1 Nanodroplets Formulation and Biocompatibility 289
11.3.2 Threshold Simulation for Nanodroplet-Mediated Cavitation 291
11.3.3 Measurement of Histotripsy Threshold in Agarose Tissue Phantoms 293
11.3.4 Selective Cavitation in Composite Agarose Phantom 295
11.3.5 Bubble Behavior 296
11.3.6 Ablation of Red Blood Cells in Tissue Phantom 298
11.4 Discussion 300
11.5 Conclusion 302
11.6 References 304
Chapter 12: Effects of Ultrasound Frequency on Nanodroplet-Mediated Histotripsy 308
12.1 Introduction 308
12.2 Methods 311
12.2.1 Formulation and Characterization of Nanodroplets 311
12.2.2 Preparation of Tissue Phantoms 313
12.2.3 Histotripsy Pulse Generation 314
12.2.4 Optical Imaging and Image Processing 316
12.2.5 Passive Cavitation Detection (PCD) 317
12.2.6 NMH Cavitation Threshold 318
12.2.7 NMH Bubble Size 319
12.2.8 NMH Multi-pulse Sustainability 320
12.3 Results 321
12.3.1 NMH Cavitation Threshold 321
12.3.2 NMH Bubble Size 324

12.3.3 NMH Multi-pulse Sustainability 326
12.4 Discussion 328
12.5 Conclusion 332
12.6 References 333
Chapter 13: Effects of Droplet Composition on Nanodroplet-Mediated Histotripsy 336
13.1 Introduction 336
13.2 Methods 339
13.2.1 Materials 339
13.2.2 Nanodroplet Formulation and Characterization 340
13.2.3 Preparation of Tissue Phantoms 342
13.2.4 Histotripsy Pulse Generation 343
13.2.5 Optical Imaging and Image Processing 344
13.2.6 Passive Cavitation Detection (PCD) 345
13.2.7 NMH Cavitation Threshold 347
13.2.8 NMH Multi-pulse Sustainability 348
13.3 Results 349
13.3.1 Nanodroplet Characterization 349
13.3.2 NMH Cavitation Threshold 351
13.3.3 NMH Multi-pulse Sustainability 354
13.4 Discussion 356
13.5 Conclusion 359
13.6 References 361
Chapter 14: The Role of Positive and Negative Pressure on Cavitation Nucleation in Nanodroplet-Mediated Histotripsy 364

14.1 Introduction 364
14.2 Methods 367
14.2.1 Nanodroplet Formulation and Characterization 367
14.2.2 Preparation of Tissue Phantoms 368
14.2.3 Histotripsy Pulse Generation 369
14.2.4 Optical Imaging and Image Processing 371
14.2.5 NMH Cavitation Threshold 373
14.3 Results 375
14.3.1 NMH Cavitation Threshold: Negative-Polarity Pulse 375
14.3.2 NMH Cavitation Threshold: Positive-Polarity Pulse 377
14.4 Discussion 380
14.5 Conclusion 383
14.6 References 385
Chapter 15: Summary and Future Work 389
15.1 Summary 389
15.2 Future Work 392
15.2.1 Investigation of Cavitation Nuclei in tissue 392
15.2.2 Intrinsic Threshold *In Vivo* 394
15.2.3 Effects of Temperature on the Shock Scattering Threshold 394
15.2.4 *In Vivo* Tumor Ablation 395
15.2.5 Dual-modality Therapy Approaches 395
15.2.6 Nanodroplet-mediated Histotripsy *In Vivo* Validation 396
15.3 References 397

List of Figures

Figure 1.1 Shock scattering mechanism. An initial bubble is first formed and expanded during the first cycles of the pulse, and the positive shockwaves of the following cycles are scattered from the individual bubbles. The scattered shockwaves constructively interfere with the incident negative pressure, forming a cavitation cloud propagating opposite the ultrasound propagation direction.. 4

Figure 1.2 Intrinsic threshold mechanism. Cavitation is generated directly along the ultrasound propagation direction using a single pulse with peak negative pressure exceeding a threshold intrinsic to the tissue. 5

Figure 2.1 Bubble cloud formation by shock scattering. During the initial cycles, individual bubbles are expanded in the focus due to the incident negative pressure (1). Shockwaves from subsequent cycles are scattered off initially expanded bubbles (2), which inverts the shock and constructively interferes with the negative phase of the next incident wave (3). Previous work has demonstrated a histotripsy bubble cloud is only formed when initial bubbles expand to a large enough size for shock scattering to result in sufficiently large reflected negative pressures (A). If expansion of initial bubbles is of insufficient size to cause significant scattering, the negative pressures produced will be insufficient to initiate a histotripsy bubble cloud (B).. 13

Figure 2.2 Example histotripsy pressure waveform 15

Figure 2.3 Experimental setup. A 1 MHz therapy transducer focus was aligned inside samples for cavitation initiation experiments. Bubble cloud formation was monitored using a low frequency marine hydrophone and verified with high speed optical imaging..... 19

Figure 2.4 Example waveforms collected by marine hydrophone with corresponding optical images of bubble cloud. Examples shown are of 2.5% agarose tissue phantoms treated at 10 Hz right below and above the cavitation cloud threshold with peak negative pressures of (A) 24.2 MPa and (B) 25.1 MPa. 23

Figure 2.5 Cavitation cloud initiation threshold in phantoms with varied agarose concentration. Threshold results show significant increase in the peak negative pressure required to initiate cavitation inside higher concentration tissue phantoms. All increases in threshold between gel concentrations were considered significant (p-values<0.05)..... 24

Figure 2.6 The initiation threshold of cavitation clouds induced by histotripsy in *ex vivo* porcine tissues plotted as a function of tissue Young's modulus. 26

Figure 2.7 Simulation of initial bubble expansion in tissues of varied Young's modulus. Plot shows the bubble radius for a 10 nm bubble subjected to the first cycle of a histotripsy pulse at a peak negative pressure of 15 MPa with Young's moduli varied from 1 kPa to 10 MPa..... 27

Figure 2.8 Bubble expansion in agarose tissue phantoms of varied concentrationResults show a significant decrease in (A) maximum bubble expansion and (B) bubble collapse time with increasing agarose concentration. All decreases in bubble diameter and collapse time between gel concentrations were considered significant (p-values<0.05). 28

Figure 3.1 Histotripsy waveforms. Plots showing example histotripsy waveforms produced by 345 kHz, 500 kHz, 1.5 MHz, and 3 MHz histotripsy transducers.. 44

Figure 3.2 Experimental setup. Histotripsy pulses were applied to the inside of water, mechanically tunable tissue phantoms, and various *ex vivo* bovine tissues. Cavitation was monitored using high speed optical imaging for transparent samples. Additionally, cavitation was monitored using one of the therapy transducer elements as passive cavitation detection for all samples. 47

Figure 3.3 Cavitation Detection. Sample PCD temporal (left) and frequency (center) signals were used for cavitation detection. Results showed agreement with high speed optical images of cavitation (right). Representative images shown are from 1.5 MHz histotripsy pulses applied to degassed water (ultrasound propagating top to bottom). 54

Figure 3.4 Example of Integrated Power Spectrum (SPCD) Bimodal distribution. Results show the SPCD for 100 histotripsy pulses applied by the 1.5 MHz transducer at a peak negative pressure of 25.3 MPa. A bimodal distribution is evident, with the lower, more consistent values indicating the absence of cavitation, and the larger, more variable values indicating the presence of one or more bubbles 55

Figure 3.5 Cavitation threshold in water. Example probability curves for water samples. Results showed a significant decrease the cavitation threshold for 90% O_2 water at 345 kHz and 500 kHz compared to degassed 15% O_2 water. No significant difference was observed between 90% O2 and 15% O2 water at 1.5 MHz or 3 MHz 56

Figure 3.6 Cavitation threshold in tissue phantoms. Example probability curves for mechanically tunable agarose tissue phantoms. Results showed no significant difference in the intrinsic threshold with increasing stiffness. A small increase of ~2-3 MPa was observed in the threshold as the frequency was increased from 345 kHz to 3 MHz 57

Figure 3.7 Cavitation detection in tissue phantoms. Example PCD signals (left) and corresponding optical images (right) of cavitation in agarose tissue phantoms of increasing Young's moduli. The PCD signal was observed to remain sensitive to cavitation in stiffer phantoms despite the observe decrease in bubble size. 59

Figure 3.8 Cavitation threshold in *ex vivo* bovine tissue. Example probability curves for *ex vivo* bovine liver, tongue, and tendon. A small increase of ~2-3 MPa was observed in the threshold as the frequency was increased from 345 kHz to 3 MHz..... 60

Figure 3.9 Intrinsic threshold comparison. (A) Bar plot shows the pint measured for all samples and frequencies studied in this work. The threshold for all samples remained between 24.7-30.6 MPa with the exception of 90% O_2 water at 345 kHz and 500 kHz, which was signficantly lower. Results showed no trend in the intrinsic threshold with increasing stiffness for E<1 MPa, but a small increase of ~2-3 MPa was observed for tendon (E=380 MPa). (B) Linear regression analysis demonstrated that the change in pint with increasing Young's modulus (tendon not included) was not significant via the Pearson correlation (r=-0.173, R2=0.030, p>0.05). (C) Linear regression analysis further showed that the ~2-3 MPa increase in pint with increasing frequency was significant via the Pearson correlation (r=0.57, R2=0.32, p<0.05). 61

Figure 3.10 Stabilized Nuclei Simulation. Simulated maximum bubble radius for a 2.5 nm initial bubble subjected to a single cycle histotripsy peak negative pressure waveform demonstrated a distinct threshold of ~28 MPa that was independent of (A) ultrasound frequency (E=1kPa) and (B) tissue stiffness for Young's moduli <1 MPa (f=1.5MHz). (C) Simulations demonstrated that the cavitation threshold measured experimentally (24.7-30.6 MPa) corresponded to initial bubble sizes between 2.3-2.85 nm (E=1kPa, f=500kHz). (D) Increasing the initial bubble size from 1-100 nm resulted in a decrease in the cavitation threshold with a larger decrease observed at lower frequency (E=1kPa). 63

Figure 3.11 CNT Simulation. Classical nucleation theory was used to predict the effects of frequency on the cavitation threshold using equation E7. Results demonstrated an increase in pt_CNT of 2.7 MPa as the frequency was increased from 345 kHz to 3 MHz (o). Comparisons to the average experimental results for pint in agarose tissue phantoms (♦) demonstrate close agreement between theory and experiments. 65

Figure 4.1 Experimental Set-up. Histotripsy pulses were applied to the inside of distilled, degassed water heated to 10°C, 20°C, 40°C, 60°C, 80°C, and 90°C. Heated water was circulated into a 150-mL custom-built cavitation chamber using a roller pump, and the temperature inside the chamber was monitored using a type T hypodermic needle thermocouple. Cavitation was monitored using high speed optical imaging and passive cavitation detection using one of the therapy transducer elements. 80

Figure 4.2 Acoustic waveform. Plots shows example acoustic waveform produced by the 1 MHz histotripsy transducer 81

Figure 4.3 Example probability curves (n=3) for samples heated to 10°C-90°C. Results show a significant decrease in the intrinsic threshold, p_{int}, with increasing temperature. 88

Figure 4.4 Scatter plot shows the p_{int} measured for all samples in this work as a function of temperature. Linear regression analysis demonstrated that the change in p_{int} with increasing temperature was significant via the Pearson correlation (r=0.99, R^2=0.98, p<0.05) 89

Figure 4.5 Cavitation Detection: 20°C. Images show sample PCD and optical images for pulses applied to distilled, degassed water heated to 20°C. PCD temporal (top) and frequency (middle) signals showed good agreement with high speed optical images of cavitation (bottom) 91

Figure 4.6 Cavitation Detection: 80°C. Images show sample PCD and optical images results for pulses applied to distilled, degassed water heated to 80°C. PCD temporal (top) and frequency

(middle) signals showed good agreement with high speed optical images of cavitation (bottom) 92

Figure 4.7 Stabilized Nuclei Simulation: Maximum Radius vs. Pressure. Simulated maximum bubble radius for a 2.16 nm initial bubble subjected to a single cycle negative pressure waveform exposed to water at 10°C-90°C using the values for surface tension and viscosity shown in Table 4.1. Results demonstrated a significant decrease in the cavitation threshold, p_{t_sim}, with increasing temperature 94

Figure 4.8 Stabilized Nuclei Simulations. Simulations independently changing (**A**) ambient temperature, (**B**) viscosity, and (**C**) surface tension demonstrated the decrease in threshold at higher temperatures was primarily due to changes in surface tension. (**D**) A further simulation demonstrated that the experimentally measured intrinsic thresholds corresponded to initial bubble sizes ranging from ~2 nm at 10°C to ~4 nm at 90°C..... 95

Figure 4.9 CNT Simulation. (A) Classical nucleation theory was used to predict the effects of temperature on the cavitation threshold, with results demonstrating p_{t_CNT} decreased from ~25.3 MPa at 10˚C to ~16.5 MPa at 90˚C. Simulations independently modulating temperature (B) and surface energy (C) demonstrated the decrease in threshold predicted by CNT were primarily due to changes in surface tension with increasing temperature..... 96

Figure 5.1 (A) A 1 MHz transducer was attached to a 3D positioning system controlled using a PC console. The therapy focus was aligned at the surface of the agarose tissue phantoms and *ex vivo* porcine tissue. (B) For the selective ablation *in vivo* porcine experiment, an ultrasound imaging probe was coaxially mounted with the therapy transducer and the unit was attached to a motorized positioning system and coupled to the pig with a degassed water bolus..... 113

Figure 5.2 Tissue phantom erosion results show lesion maximum diameter (A) and depth (B) for 0.3%, 1%, 2.5%, and 5% agarose gels treated with 5,000 histotripsy pulses at 10, 100, and 1000 Hz PRF. Results show a statistically significant decrease in lesion diameter and depth with increasing agarose concentration. All observed decreases in lesion depth and diameter were considered significant ($p<0.05$) except between 0.3% and 1% agarose at 100 Hz PRF (depth: 9.52 mm, 9.1 mm, $p=0.08$; diameter: 3.52 mm, 3.41 mm, $p=0.12$). Additionally, results show a statistically significant decrease in lesion size for increased PRF..... 117

Figure 5.3 Histotripsy tissue erosion is capable of perforating the majority of soft tissues. Results show select images of porcine tissues treated for 10 minutes with a 1 MHz therapy transducer (1 kHz PRF, 5 cycles). Histotripsy was demonstrated to be capable of completely eroding through the majority of the soft tissues tested in this study. A complete list of *ex vivo* tissue erosion results is shown in Table 5.1..... 120

Figure 5.4 Histotripsy tissue erosion is less effective in tissues with increased mechanical strength. Results show selected images of porcine tissues treated for 10 minutes with a 1 MHz transducer (1 kHz PRF, 5 cycles). Histotripsy treatment was demonstrated to be less effective in stronger tissues with only partial erosion or no visible damage observed. Partial erosion was most pronounced in composite tissues in which stronger layers were preserved while the weaker

tissue was completely eroded (i.e. adventitial layer of vessels or cartilage layer of trachea preserved). The complete list of *ex vivo* tissue erosion results is shown in Table 5.1..... 120

Figure 5.5 Comparison of selected tissue properties for histotripsy treated porcine tissues. Graphs show the average density (A), water content (B), tensile stress (C), and ultimate fractional strain (D) for perforated tissues compared to tissues with partial or no damage. Undamaged tissues demonstrated statistically significantly increased density, decreased water content, increased ultimate stress, and decreased ultimate strain compared to perforated group. No statistically significant difference was observed between perforated and partial ablation groups. P-values <0.05 were considered significant 122

Figure 5.6 Histotripsy selective ablation results demonstrated large hepatic vessels remained intact and functional inside histotripsy treated porcine liver *in vivo*. Results show (A) MRI image of a large *in vivo* porcine liver histotripsy lesion with major hepatic vessels remaining structurally intact inside the completely fractionated liver tissue. Doppler ultrasound images before (B) and after (C) histotripsy treatment demonstrated large blood vessels within the treated region remained functional after histotripsy 123

Figure 5.7 Histotripsy selective ablation results showed hepatic vessels remained intact within fractionated porcine liver *in vivo*. Results show select images of hepatic blood vessels (BV) inside untreated (A) and completely fractionated (B-F) liver tissue. A large number of smaller vessels and bile ducts (BD) were observed in the regions containing connective tissue surrounding hepatic vessels 124

Figure 5.8 Histotripsy selective ablation showed preservation of hepatic vessels was highly dependent on vessel type. (A) Plot shows the percentage of vessels remaining inside an *in vivo* porcine liver lesion formed by histotripsy organized by vessel type (B). *Results showed a statistically significant decrease in small veins, arterioles, venules, and capillaries inside the histotripsy lesion compared to untreated controls ($p<0.05$). 125

Figure 6.1 Experimental setup. (A) After heating, tissue Young's modulus (compression) was measured using a tissue elastometer. (B) Susceptibility to histotripsy was tested using a 750 kHz therapy transducer with the focused aligned to the tissue surface. Histotripsy was applied for five minutes using 5 cycle pulses, a pulse repetition frequency of 500 Hz, and pressure of 19/60 MPa (P-/P+)..... 140

Figure 6.2 Elastometer measurements for tissues heated at 58ºC demonstrated a significant decrease in the Young's modulus of tongue, artery, kidney medulla, and tendon (A:C, E), no significantly change for liver (D), and a significant increased for urethra (F). Heating at 90ºC significantly increased the Young's modulus of tongue, artery, kidney medulla, liver, and urethra (A:D, F) and significantly decreased the Young's modulus of tendon (E) 145

Figure 6.3 Representative Force vs. Strain Curves. Plots show representative Force vs. Strain curves measured by the elastometer for tissues samples comparing unheated control samples with samples that were heated for 4 hours at 58°C and 90°C, respectively 146

Figure 6.4 Images show histology slides stained with a trichrome blue staining for samples heated at 58°C for 4, 8, and 12 hours. Tongue, artery, and tendon showed a decrease in collagen

(blue) density with heating. Hydrolysis into gelatin (red) was observed in tendon after 8 and 12 hours. Urethra showed an increase in collagen density after heating compared to control..... 147

Figure 6.5 Histotripsy Treatment Pictures: 58°C Samples. Morphological analysis of bovine tissues after histotripsy demonstrated that tongue, artery, liver, kidney, and tendon were more susceptible to histotripsy-induced tissue damage after heating at 58°C. Urethra was observed to be less susceptible to histotripsy after heating at 58°C..... 149

Figure 6.6 Images show histology slides stained with a trichrome blue staining for samples heated at 90°C for 4, 8, and 12 hours. Results for tongue, artery, and urethra demonstrated an increase in collagen (blue) density with heating. In tendon, collagen hydrolyzed into gelatin (red) with heating. Some hydrolysis was also observed in the urethra after 12 hour heating..... 152

Figure 6.7 Histotripsy Treatment Pictures: 90°C Samples. Morphological analysis of bovine tissues after histotripsy demonstrated tongue, artery, liver, kidney, and urethra were less susceptible to histotripsy-induced tissue damage after heating at 90°C for 4 hours while tendon was more susceptible to histotripsy after heating. All tissues became more susceptible to histotripsy after heating was continued for 8 and 12 hours (compared to 4 hour samples) 153

Figure 6.8 HIFU Thermal Treatment. Plots show example temperature vs. time curves for HIFU heating of tendon measured using hypodermic needle thermocouples. For all experiments, 3 thermocouples were placed near the focal region, and HIFU was applied to rapidly increase the temperature to (A) ~60°C or (B) ~90°C. Once the desired temperature was reached, the PRF was lowered to stabilize the temperature at a near constant level for the duration of the heating. (B) For the higher temperature HIFU treatments, the temperature measured by the thermal couples did not remain above 90°C due to thermocouple movement caused by tissue contraction. Similar curves were obtained for HIFU treatments in all tissue types.. 155

Figure 6.9 Results showed an increase in susceptibility to histotripsy for tongue, liver, and tendon heated with ultrasound at a peak temperature of ~60°C. Tongue and liver samples heated with ultrasound at a peak temperature of ~90°C were less susceptible to histotripsy while tendon became more susceptible after heating 157

Figure 7.1 Representative free-field focal waveforms from four histotripsy transducers used to compare the effects of frequency on histotripsy bubble expansion. Bubbles were generated by histotripsy pulses at 345 kHz, 500 kHz, 1.5 MHz, and 3 MHz. 176

Figure 7.2 The focus of histotripsy transducers were aligned inside tissue phantoms of varied stiffness. Bubble expansion and collapse was monitored using high speed optical imaging. Note: different frequency transducers had different geometry and schematic is not drawn to scale ... 177

Figure 7.3 Bubble behavior simulation. Plots show simulated bubble R-T curves for a 2.5 nm initial bubble subjected to histripsy pulses with varied Young'g modulus (E), frequency (f), and peak negative pressure (p-). (A) Young's modulus was varied between 0kPa-1MPa (p-=30 MPa, f=345 kHz). (B) Frequency was compared for 345 kHz, 500 kHz, 1.5 MHz, and 3 MHz (p-=30 MPa, E=1 kPa). (C) p- was varied between 30MPa-60MPa (f=500 kHz, E=1 kPa). Results show an increase in bubble expansion with decreasing Young's modulus (A), decreasing ultrasound frequency (B), and increasing pressure (C) 181

Figure 7.4 Optical images of bubbles produced by 345 kHz, 500 kHz, 1.5 MHz, and 3 MHz histotripsy pulses inside agarose tissue phantoms of increasing Young's modulus taken at tmax. Results demonstrated a decrease in bubble size with increasing frequency and increasing tissue phantom stiffness. 183

Figure 7.5 Plots show the R-T curves for bubbles produced by 345 kHz, 500 kHz, 1.5 MHz, and 3 MHZ histotripsy pulses inside agarose tissue phantoms of increasing Young's modulus. Results demonstrated a decrease in bubble expansion and collapse time for stiffer tissue phantoms at all frequencies..... 184

Figure 7.6 Graphs show the relative changes in R_{max} for all tissue phantom and frequency combinations. Results demonstrated a significant decrease in R_{max} ($p<0.05$) with both increasing tissue stiffness (A) and increasing frequency (B). Statistical comparisons were made using a Student's t-test with a Bonferroni correction..... 185

Figure 7.7 Effects of ultrasound frequency on bubble behavior. Plots show the R-T curves for bubbles produced inside tissue phantoms using 345 kHz, 500 kHz, 1.5 MHz, and 3 MHZ histotripsy pulses. Results demonstrated that increasing frequency resulted in decreased bubble expansion and collapse time in all samples 187

Figure 7.8 (A) Strain calculation results demonstrated a decrease in strain with both increasing Young's modulus and frequency. (B) Stress analysis demonstrated a decrease in stress with increasing frequency, and an increase in stress at higher Young's modulus..... 188

Figure 7.9 Effects of using a dual-frequency waveform on bubble behavior. The ability to tailor bubble expansion using a previously developed dual-frequency approach was demonstrated using a 500 kHz and 3 MHz dual frequency transducer (Lin et al., 2014a). Images show example waveforms and the corresponding optical images of bubbles produced in degassed water using the 500 kHz (top), dual frequency (middle), and 3 MHz (bottom) transducers. Results demonstrated that the dual frequency bubbles grew to an intermediate size of 165.6±19.8 µm compared to 387.9±43.9 µm and 64.8±7.9 µm at 500 kHz and 3 MHz, respectively..... 189

Figure 7.10 Effects of modulating relative amplitude of each frequency on bubble expansion using dual-frequency histotripsy. Optical images of bubbles produced by the 500 kHz and 3 MHz dual frequency transducer with varied relative amplitude for the 500 kHz and 3 MHz components. Results demonstrated an increase in bubble size as the percentage of amplitude applied by the 500 kHz elements was increased..... 190

Figure 7.11 Effects of increasing $P(-)_{LS}$ on bubble cloud behavior. Optical images show bubble clouds formed from the 500 kHz transducer at $P(-)_{LS}$ values between 25.4-40.5 MPa in tissue phantoms with Young's moduli of 1.13 kPa (top) and 570 kPa (bottom). Results demonstrated an increase in the size of the bubble cloud with increasing pressure. However, no significant change in the size of individual bubbles within the clouds was observed with increasing $P(-)_{LS}$ 192

Figure 7.12 Plot shows R_{max} for bubbles formed by the 500 kHz transducer in the 570 kPa phantom at $P(-)_{LS}$ values ranging from 25.4 MPa to 58.9 MPa. No significant change in R_{max} was observed for individual bubbles within the clouds with increasing $P(-)_{LS}$ ($p>0.05$) 192

Figure 8.1 (A) Experimental set-up showing custom-built microscope transducer-tank. (B) Example acoustic waveform. (C) Schematic of tissue phantom containing a layer of breast cancer cells inside a fibrin gel. 205

Figure 8.2 Cancer cells exposed to a single histotripsy pulse were significantly deformed during both bubble expansion and collapse, with the largest deformations observed during collapse (between 46 μs and 74.75 μs). Arrows indicate regions containing bubbles (B) and the deformed cells (DC) 209

Figure 8.3 Cancer cells exposed to 1000 pulses were repeatedly deformed by bubbles (B) until cell rupture/removal was achieved, forming a well-defined lesion (L) at the focus..... 211

Figure 8.4 Cancer cells at the boundary of the histotripsy lesion were repeatedly deformed (pulled towards bubble) and often bisected multiple times before complete removal. Arrow indicates a breast cancer cell bisected over multiple pulses 211

Figure 9.1 Histotripsy *in vivo* porcine liver ablation experimental setup. (A) A 1 MHz histotripsy therapy transducer with coaxially aligned ultrasound imaging probe (insert) was attached to a motorized 3D positioning system controlled using a PC console and coupled to the pig with a degassed water bolus. (B) Histotripsy was applied transcutaneous through ribs and overlying tissue with treatments targeted to all positions within the liver. Specific treatment information is listed in Table 9.1..... 224

Figure 9.2 Liver ablation was guided by ultrasound imaging in real-time. Images show the histotripsy liver treatment monitored by ultrasound imaging before (A), during (B), and after (C) treatment. Prior to each treatment, the bubble cloud was generated in free water with the free-field focal location marked as an "x" on the ultrasound image (A). The histotripsy bubble cloud appears as a dynamically changing hyperechoic region on ultrasound imaging (B) while the resulting lesion appears hypoechoic (C) resulting from fractionation of liver parenchyma..... 230

Figure 9.3 Histotripsy treatment caused complete removal of liver parenchyma. Histotripsy liver lesions appear hyper-intense on MRI imaging (A) corresponding to the fractionated liver tissue. Histological evaluation (B) demonstrates histotripsy completely fractionated liver parenchyma into acellular debris (F) without damaging surrounding liver tissue (E). Histotripsy lesions contained sharp boundaries of approximately a few hundred micrometers between homogenized and intact liver tissue (C, D) 232

Figure 9.4 Results show histotripsy-generated fractionation of large volumes in the liver. MRI multi-slice analysis demonstrated liver volume of approximately 5x4x3 cm (60 cm^3) (A) was ablated. Histology (B) demonstrated histotripsy caused complete ablation throughout the large focal regions (D) without causing damage to surrounding tissue (C) 233

Figure 9.5 Gallbladder and hepatic vessels remained intact and functional within histotripsy treated region. MRI images demonstrate blood vessels (A) and gallbladder (D) remain structurally intact within the histotripsy focal volume while surrounding liver parenchyma was completely ablated. Doppler ultrasound images before (B) and after (C) histotripsy indicated that large vessels remained functional after treatment. Morphological observation of histotripsy lesions bordering the gallbladder (E, F) showed no signs of damage to the gallbladder itself .. 234

Figure 9.6 Histological evaluation of histotripsy lesions surrounding hepatic blood vessels. Results show that the tissue surrounding blood vessels was completely fractionated while blood vessels remained intact (A-D). All large and medium sized arteries (A) and veins (B) were observed to remain intact with no observed perforations. Multiple smaller blood vessels (B, C, D) and bile ducts (D) were also observed inside the histotripsy lesion. The smallest vessels observed to remain intact were approximately 50-100 μm in diameter. Localized hemorrhage within lesion resulted from rupture of capillaries and small vessels <100 μm in diameter 236

Figure 9.7 The number of vessels between 50-1000 μm were counted within a 100 mm2 region (n=4) within the histotripsy lesion and intact liver tissue. Results indicate a significant decrease in blood vessels between 50-100 μm ($p<0.01$). A decrease was observed for 100-200 μm and 200-300 μm vessels but was not significant ($p>0.1$) as a result of the high variability between samples. No significant differences in vessel count were observed between the histotripsy lesion and intact liver tissue for 300-400 μm and 400-1000 μm vessels. No blood vessels <50 μm were observed to remain within the histotripsy lesion after treatment 237

Figure 10.1 Histotripsy *in vivo* rat liver ablation experimental setup. (A,B) A 1 MHz histotripsy therapy transducer with coaxially aligned ultrasound imaging probe was attached to a motorized 3D positioning system controlled using a PC console. (C,D) The transducer was placed inside a tank of degassed water with the anesthetized rat placed above the transducer during the histotripsy liver treatments..... 252

Figure 10.2 (A) Histotripsy treatments were applied to the rat liver guided by real-time ultrasound imaging. After treatment, liver lesions were assessed using (B) MRI, (C) gross morphology, and (D) histology. In addition to the liver, the inferior lobes of the lungs were harvested after treatment and assessed using (E) gross morphology and (F) histology 256

Figure 10.3 Histotripsy liver lesions were assessed for gross morphology after animals were sacrificed on days 0, 3, 7, 14, 28 (A-E). Darkly colored hematomas seen on day 0 were replaced with fibrous tissue on days 3 and 7. The fibrous tissue was resolved on days 14 and 28, leaving a contracted tissue with virtually no fibrotic material remaining 259

Figure 10.4 Liver lesions for animals sacrificed after day 0, 3, 7, 14, 28 (A-E). Histology images of the lesion boundary (F-J) and a central portion of the lesion (K-O) after day 0, 3, 7, 14, 28 were analyzed to characterize chronic response of the liver to histotripsy therapy..... 259

Figure 10.5 Plot shows the average maximum cross-sectional area of the histotripsy liver lesions measured over the course of the experiment. The area of the hematoma and fibrous components of the lesion, as well as the total lesion cross-sectional area, were compared for rats euthanized after day 0, 3, 7, 14, and 28. Following an increase in maximum cross-sectional area between day 0 and 3, there was a rapid reduction in lesion size over the remainder of the study. All differences in lesion size were significant ($p<0.05$) 260

Figure 10.6 Representative MRI images for one rat acquired on days 0, 3, 7, 14, and 28 (A-E) (Lu=lungs, Li=liver, St=stomach, GI=gastrointestinal tract). (F) For a qualitative comparison of signal intensity, pilot data of an HCC tumor implanted in the rat liver is shown in Panel F 261

Figure 10.7 Plot shows the lesion volume measured by MRI for rats euthanized after day 28 (n=4). No significant difference in lesion size was observed between day 0 and day 3 ($p>0.05$). After day 3, there was a significant decrease in lesion volume over the remainder of the study ($p<0.05$) with no quantifiable lesions observed after day 28 262

Figure 10.8 Histology images of the inferior lobes of the lung after days 0, 3, 7, 14, 28 using 4x (A-E) and 40x magnification (F-J). Results showed localized lung hemorrhage on day 0, with the number of red blood cells inside the alveolar space decreasing at later time points and minimal hemorrhage remaining after 28 days 263

Figure 11.1 Formulation of PFP-loaded nanodroplets by self-assembly of amphiphilic triblock PEG45-b-PAA10-b-P(HDFMA8-co-MMA21) copolymer around the PFP core followed by shell cross-linkage via EDC/HNS coupling reactions. 278

Figure 11.2 Acoustic waveform and experimental setup. (A) The focus of one of the 500 kHz transducers was aligned inside tissue phantoms containing nanodroplets. Cavitation was monitored using high speed optical imaging. Example of a 2-cycle histotripsy pulse generated by the (B) 32 element and (C) 7 element transducers 282

Figure 11.3 (A) A representative image showing the size distribution of PFP-loaded nanodroplets. Results show an average nanodroplet size of approximately 200 nm with the peak of the size distribution at 128.5 ± 9.1 nm and 138.5 ± 8.0 nm at 22°C and 37°C, respectively. (B) MTT results show no significant change in the viability of PC-3 cells incubated with 0.3, 1. 5, 15, 30 and 75 μg/mL of the triblock copolymer used to formulate the PFP-loaded nanodroplets compared to PC-3 cells incubated with blank culture medium 291

Figure 11.4 A plot showing the simulated peak negative pressure (P-) threshold to expand a bubble from an initial diameter of 5–500 nm to 50 μm in tissue 292

Figure 11.5 Plot showing the histotripsy threshold in phantoms with and without nanodroplets. Results demonstrated a significant decrease in the pressure threshold to generate cavitation bubbles >50 μm with nanodroplets compared to control conditions (histotripsy only) 294

Figure 11.6 Images of nanodroplet-mediated cavitation in agarose tissue phantoms at increasing acoustic pressures. Images of cavitating bubble clouds (dark) generated using agarose phantoms containing nanodroplets at the pressure of 8.2–20.7 MPa (A–E). With increasing pressure, the area of the bubble cloud increased. In comparison, cavitation wasn't observed in control samples in this pressure range MPa (F) 294

Figure 11.7 Selective cavitation in a composite agarose tissue phantom. Optical images (middle) of agarose phantoms with hexagon shaped inclusions containing nanodroplets (top) showed cavitation within the focal area only occurred in locations containing nanodroplets while no cavitation was observed in regions without nanodroplets. Ultrasound imaging (bottom) demonstrated nanodroplet guided cavitation treatment can be monitored in real-time with bubbles appearing as dynamically changing hyperechoic regions 296

Figure 11.8 A plot of bubble behavior in agarose tissue phantoms. The diameter of bubble generated using a 2-cycle 500kHz pulse at 15MPa as a function of time. At each time point, the average bubble diameter and standard deviation are plotted. 297

Figure 11.9 Optical images of nanodroplet-mediated cell fractionation. Images of cavitation bubble cloud (dark) and lesions (white) generated in the RBC agarose gel (grey) using nanodroplet-mediated histotripsy at different pressure levels. A total of 2000 2-cycle pulses at 10 Hz PRF were used for each treatment..... 299

Figure 11.10 Nanodroplet-mediated lesion formation. The lesion area formed in the RBC agarose gel as a function of pulse number for treatments at 11.0, 15.9, and 20.7 MPa. No damage was formed for treatments at 6.2 MPa 299

Figure 12.1 Size distribution results show an average nanodroplet size of 177.9±1.9 nm..... 313

Figure 12.2 Acoustic waveforms. Example of a 2-cycle histotripsy pulses generated by the 345 kHz, 500 kHz, 1.5 MHz, and 3 MHz histotripsy transducers 315

Figure 12.3 Experimental set-up. The focus of the histotripsy transducer was aligned inside tissue phantoms with and without nanodroplets. Cavitation was monitored using high speed optical imaging and passive cavitation detection using one of the therapy elements..... 317

Figure 12.4 Cavitation detection. Sample passive cavitation detection (PCD) signals (top) and high speed optical images (bottom) used for cavitation detection. Results showed good agreement between the two methods. Representative images shown above are from 345 kHz histotripsy pulses applied to tissue phantoms containing nanodroplets..... 322

Figure 12.5 Cavitation threshold curves. Probability curves for tissue phantoms with and without nanodroplets. Results showed a significant decrease in the cavitation threshold with nanodroplets compared to controls. Results also showed a significant increase in the nanodroplet cavitation threshold with increasing frequency 323

Figure 12.6 Cavitation threshold results. Bar plots show the cavitation threshold results for tissue phantoms with and without perfluoropentane (PFP) nanodroplets at all frequencies studied in this work 323

Figure 12.7 Optical imaging results show a decrease in NMH bubble size compared with control bubbles produced at the same frequency at higher pressure. Results further show a significant decrease in bubble size with increasing frequency. Note: Different image magnifications were used for the above images to better image the bubbles at each frequency 325

Figure 12.8 Plot shows a comparison of the maximum bubble radius produced in tissue phantoms with and without nanodroplets by 345 kHz, 500 kHz, 1.5 MHz, and 3 MHz histotripsy pulses. The peak negative pressures (p-) applied for each condition are listed in Table 12.1.... 325

Figure 12.9 Optical images show NMH bubbles produced by 345 kHz (p-=10.8 MPa) and 3 MHz (p-=14.7 MPa) at a single focal point in tissue phantoms containing nanodroplets at a pulse

repetition frequency (PRF) of 1 Hz. Results showed a decrease in the number of bubbles observed at the focus with increasing pulse number 327

Figure 12.10 Plot shows a significant decrease ($p<0.05$) in P#Ext with increasing frequency. A sample size of 6 tissue phantoms was used for each experimental condition 328

Figure 13.1 Formulation of the triblock amphiphilic copolymer and nanodroplet preparation. **(A)** Chemical structure of each block in the triblock copolymer. **(B)** One-pot "click" reaction forms P(HDFMA-*co*-MMA)-*b*-P*t*BA-*b*-PEG. **(C)** Hydrolysis of the copolymer gives P(HDFMA-*co*-MMA)-*b*-PAA-*b*-PEG. **(D)** The process of PFC encapsulation into nanodroplets 341

Figure 13.2 (A) Example waveforms for 2-cycle histotripsy pulses generated by custom-built 345 kHz, 500 kHz, 1.5 MHz, and 3 MHz transducers. (B) Experimental set-up showing the focus of the histotripsy transducers aligned inside tissue phantoms containing PFP, PFH, or no nanodroplets. Cavitation was monitored using high speed optical imaging and passive cavitation detection using one of the therapy elements 346

Figure 13.3 Nanoparticle Tracking Analysis (left) demonstrated similar characteristics for (A) PFP and (B) PFH nanodroplets. Size distribution plots (right) show the average size of the droplets was 177.9±1.9 nm and 233.9±3.9 nm for PFP and PFH, respectively 350

Figure 13.4 Sample PCD signals (top) and high speed optical imaging (bottom) were used for cavitation detection for cavitation threshold experiments. Results showed good agreement between the two methods. Representative images shown above are from 1.5 MHz histotripsy pulses applied to tissue phantoms containing PFH nanodroplets. 352

Figure 13.5 Plots show sample probability curves for tissue phantoms containing PFP nanodroplets, PFH nanodroplets, and no nanodroplets at 345 kHz, 500 kHz, 1.5 MHz, and 3 MHz. At all frequencies, results showed a significant decrease in the cavitation threshold with both PFP and PFH nanodroplets compared to controls. Results also showed a slight increase in the nanodroplet cavitation threshold for PFH nanodroplets compared to PFP nanodroplets 352

Figure 13.6 Bar plots show the complete cavitation threshold results for tissue phantoms containing PFP nanodroplets, PFH nanodroplets, and no nanodroplets. All differences in the cavitation threshold between samples were statistically significant ($p<0.05$) 353

Figure 13.7 Optical images of NMH bubbles produced by 500 kHz (p-=12.6 MPa) pulses at a single focal point in phantoms containing PFP and PFH nanodroplets at a PRF of 1 Hz 355

Figure 13.8 Optical images of NMH bubbles produced by 3 MHz (p-=15.6 MPa) pulses at a single focal point in phantoms containing PFP and PFH nanodroplets at a PRF of 1 Hz 355

Figure 14.1 Nanoparticle Tracking Analysis demonstrated PFH nanodroplets had an average size of 233.9±3.9 nm 369

Figure 14.2 Example of (A) negative-polarity and (B) positive-polarity pulses produced by the frequency compounding transducer compared with a (C) dual-polarity pulse (500 kHz) commonly used in NMH therapy 372

Figure 14.3 2D spatial pressure fields were measured by the FOPH for a positive-polarity pulse. (A) Results demonstrated the location corresponding to the highest positive pressure was near the geometric focus. (B) The location corresponding to the highest negative pressure was ~0.5 mm away from the geometric focus in the axial direction..... 372

Figure 14.4 Tissue phantoms with and without PFH nanodroplets were placed at the focus of the frequency-compounding transducer for cavitation threshold experiments. Cavitation was monitored using high-speed optical imaging through the transducer's optical windows..... 373

Figure 14.5 Optical Images of cavitation bubbles generated from negative-polarity pulses inside (A) control phantoms and (B) PFH phantoms 376

Figure 14.6 Plots show the cavitation probability as a function of negative pressure for (A,C) control and (B,D) PFH phantoms exposed to (A,B) negative-polarity pulses and (C,D) positive-polarity pulses. Cavitation couldn't be generated in control phantoms exposed to positive-polarity pulses (Max P–=18.4 MPa) 377

Figure 14.7 Plots show the cavitation probability as a function of positive pressure for (A,C) control and (B,D) PFH phantoms exposed to (A,B) negative-polarity pulses and (C,D) positive-polarity pulses. A significant increase in the P+ threshold was observed for both control and PFH phantoms exposed to the positive-positive polarity pulses..... 378

Figure 14.8 Optical Images of cavitation bubbles generated from positive-polarity pulses inside (A) control phantoms and (B) PFH phantoms. Arrows on the plot indicate the locations in the focal region corresponding to the highest positive (P+) and negative (P–) pressures as measured by the FOPH [Fig. 14.3] 379

Figure 14.9 Plot compares the P– and P+ thresholds measured for PFH phantoms in this study (negative-polarity and positive-polarity pulses) with the thresholds previously measured using dual-polarity pulses (f=345kHz, 500kHz, 1.5MHz, 3 MHz). Results suggest NMH cavitation is generated directly from the *p*-of the incident wave 380

List of Tables

Table 2.1 Cavitation cloud initiation threshold in tissue phantoms. Table shows cavitation initiation threshold for agarose phantoms treated at PRFs of 10, 100, and 1000 Hz with corresponding Young's moduli values (tension, compression) 23

Table 2.2 Cavitation cloud initiation threshold in *ex vivo* porcine tissue. Table shows cavitation initiation threshold for porcine tissue treated at PRFs of 100 and 1000 Hz with corresponding Young's modulus (tension) values from literature 25

Table 3.1 Sample mechanical properties. Table shows the Young's modulus, density, and water content values for all samples tested in this study. The Young's modulus of agarose tissue phantoms was measured using shear rheology (E=3G). *Ex vivo* bovine liver, tongue, and tendon were used to cover a large range of tissue Young's modulus as measured in the literature..... 42

Table 3.2 Threshold results: All samples. Table shows the values for the intrinsic threshold, pint, calculated by the fitted curves for each sample, the mean values for pint, and σ. All values are pressure in MPa. Statistical analysis demonstrated that, for all sample types, a pair of samples existed within one sample type with a statistically significant difference ($p<0.05$). Additionally, there existed at least one pair in any two sample types with a significant difference 58

Table 4.1 Table shows the viscosity and surface tension values of water as a function of temperature from literature 87

Table 4.2 Table shows the values for the intrinsic threshold, p_{int}, calculated by the fitted curves for each sample, as well as the mean values for p_{int} and σ. All values are pressure in MPa 89

Table 5.1. Complete erosion results of *ex vivo* porcine tissues treated for 10 minutes at a PRF of 1000 Hz and 5 cycles showing extent of the observed erosion 119

Table 5.2. The table shows select results of *ex vivo* erosion in porcine tissue along with corresponding density, water content, ultimate stress, and ultimate strain values 121

Table 6.1 Histotripsy treatment results demonstrated that tongue, artery, liver, kidney, and tendon were more susceptible to histotripsy-induced tissue damage after heating at 58°C. Urethra was observed to be less susceptible to histotripsy after heating at 58°C..... 148

Table 6.2 Histotripsy treatment results showed that tongue, artery, liver, kidney, and urethra were less susceptible to histotripsy-induced tissue damage after heating at 90°C for 4 hours while tendon was more susceptible to histotripsy after heating. All tissues became more susceptible to histotripsy after heating was continued for 8 and 12 hours (compared to 4 hours)..... 154

Table 6.3 Histotripsy treatment results demonstrated an increase in susceptibility to histotripsy-induced tissue damage for tongue, liver, and tendon heated with ultrasound at a peak temperature of ~60°C. Tongue and liver samples heated with ultrasound at a peak temperature of ~90°C were less susceptible to histotripsy while tendon became more susceptible after heating at ~90°C .. 157

Table 7.1 Tissue phantom properties. Table shows the shear modulus, Young's modulus, density, and water content for the agarose tissue phantoms. The shear modulus (G) was measured at 20ºC using shear rheology. The Young's modulus was estimated from the shear modulus (E=3G).. 174

Table 7.2 R_{max}, t_{max}, and t_c values for all tissue phantom and frequency combinations. Results show a trend of decreasing R_{max}, t_{max}, and t_c with increase Young's modulus and increasing frequency..... 185

Table 9.1 Histotripsy lesion generation through ribs and overlying tissue parameters. Table shows an overview of the ribcage coverage (including intercostal space), overlying tissue depth, and liver location for 12 histotripsy lesions. Treatments covered all regions of the liver and were further targeted to areas containing critical anatomical structures such as the gallbladder (GB) or major hepatic blood vessels (BV). Bubble cloud initiation was achieved for all treatments resulting in histotripsy lesions with a maximum diameter between 1 cm and 2.2 cm 229

Table 12.1 Table shows the maximum bubble radius produced in tissue phantoms with and without nanodroplets, along with the peak negative pressure (*p*-) applied for each condition. The *p*- for each condition was chosen to be slightly above the nanodroplet-mediated histotripsy (NMH) and intrinsic cavitation thresholds of the sample at each frequency..... 326

Table 13.1 Table shows the values for the peak negative pressure, p_t, at which the fit curve set $P_{cav} = 0.5$ for each sample as well as the mean values for p_t and σ. A Student's t-test showed all differences in p_{t_mean} between samples were statistically significant ($p<0.05$) 353

Table 14.1 Table shows the values for the P– and P+ thresholds measured for control and PFH phantoms exposed to the negative-polarity and positive-polarity pulses along with previously measured thresholds using dual-polarity pulses 376

Abstract

Histotripsy is a noninvasive, cavitation-based ultrasound therapy that controls acoustic cavitation to mechanically fractionate soft tissue. In histotripsy, high pressure (>10 MPa) short duration (<15 cycles) ultrasound pulses are used to generate microbubbles that act as "micro-scalpels" that mechanically fractionate tissue into an acellular liquid homogenate. Histotripsy is currently being studied for many clinical applications where non-invasive tissue removal is desired including tissue debulking to treat benign prostatic hyperplasia, clot breakdown to treat deep vein thrombosis, perforation of the atrial septum in the treatment of congenital heart disease, cancer ablation, kidney stone removal, and fetal interventions.

This dissertation investigates the physical thresholds to initiate cavitation and produce tissue damage in histotripsy and factors affecting these thresholds in order to develop novel strategies for targeted tissue ablation. In the first part of this dissertation, the effects of tissue properties on histotripsy cavitation thresholds (shockscattering vs. intrinsic threshold mechanism) and damage thresholds were investigated. Results demonstrated that the histotripsy shock scattering threshold using multi-cycle pulses increases in stiffer tissues, while the histotripsy intrinsic threshold using single-cycle pulses is independent of tissue stiffness. Further, the intrinsic threshold slightly decreases with lower frequencies and significantly decreases with increasing temperature. The effects of tissue properties on the susceptibility to histotripsy-induced tissue damage were also investigated, demonstrating that stiffer tissue is more resistant to histotripsy. Based on these results, two strategies were investigated for increasing the

effectiveness of using histotripsy for the treatment of stiffer tissues. First, the effects of thermal preconditioning on tissue susceptibility to histotripsy was investigated, with results showing that prolonged heating of tissues at ~60°C caused tissue softening via collagen denaturing, thereby increasing tissue susceptibility to histotripsy, while prolonged heating of tissues at ~90°C caused tissue stiffening via collagen contraction which decreased tissue susceptibility to histotripsy. In addition, investigations of pulsing parameters suggested that using lower frequency may increase the efficiency of histotripsy tissue ablation by increasing bubble expansion. These results were supported by high-speed observations of cell-bubble interactions which demonstrated that histotripsy tissue ablation is due to the stress and strain directly applied to tissue structures by the rapid expansion and collapse of the histotripsy cavitation bubbles.

In the second part of this dissertation, the feasibility of using histotripsy for targeted liver ablation was investigated in two *in vivo* studies. First, the feasibility of applying histotripsy *in vivo* for non-invasive liver ablation was demonstrated in a porcine model, with results demonstrating that histotripsy was capable of non-invasively creating precise lesions throughout the entire liver. Additionally, the hypothesis that differences in tissue stiffness could be utilized to develop a tissue selective ablation approach was tested *in vivo*, with results showing that histotripsy was capable of completely fractionating the liver tissue surrounding the major hepatic vessels and the gallbladder while the fractionation was self-limited at the boundaries of these critical structures. In addition to this initial feasibility study, the long-term effects of histotripsy liver ablation were investigated in an *in vivo* rodent model, with results demonstrating that the liver homogenate resulting from histotripsy-induced tissue fractionation was completely resorbed over the course of 28 days.

In the final part of this dissertation, a novel ablation method combining histotripsy with acoustically sensitive nanodroplets was developed for targeted cancer cell ablation, demonstrating the potential of using nanodroplet-mediated histotripsy (NMH) for targeted, multi-focal ablation. Studies demonstrated that lower frequency and higher boiling point perfluorocarbon droplets can improve NMH therapy. The role of positive and negative pressure on cavitation nucleation in NMH was also investigated, showing that NMH cavitation nucleation is caused directly from the peak negative pressure of the incident wave, similar to histotripsy bubbles generated above the intrinsic threshold.

Overall, the results of this dissertation provide significant insight into the physical mechanisms underlying histotripsy tissue ablation and will help to guide the future development of histotripsy therapy for clinical applications such as the treatment of liver cancer. Future work will aim to build upon the studies detailed in this dissertation in order to further our understanding of the physical processes involved in histotripsy tissue ablation and to promote the clinical translation of histotripsy.

Chapter 1
Introduction

This dissertation investigates the effects of tissue properties on histotripsy, an ultrasound ablation technology based on acoustic cavitation, in order to develop optimal strategies for targeted tumor ablation using histotripsy. The research is separated into three categories: 1) investigations of the effects of tissue properties (i.e. tissue stiffness, temperature) on the thresholds to initiate a cavitation bubble cloud, the cavitation bubble behavior, and the damage thresholds in histotripsy, 2) *in vivo* studies of histotripsy liver ablation, and 3) nanodroplet-mediated histotripsy for targeted cancer cell ablation. This chapter will give a brief background of currently available tissue ablation methods followed by an introduction to histotripsy therapy. The chapter will then be concluded with an outline of the dissertation, which provides an overview of each chapter.

1.1 Background: Focal Ablation

Currently available minimally invasive tumor ablation methods are mostly thermal based, including RFA, microwave therapy, cryoablation, and laser ablation [1-4]. While these minimally invasive therapies have shown some success, these methods share inherent limitations due to the heat sink effect originating from blood flow [5-8]. Thermal ablation is inconsistent in tissue with non-uniform heat dissipation patterns, which is common in hypervascular tumors [9]. In particular, for tissue near major vessels, thermal ablation often results in incomplete tumor

necrosis [10, 11]. In addition, these methods are unsuitable for treating large tumors due to the excessive treatment time [5-8]. Another limitation facing these methods is the lack of imaging feedback during treatment. The treatment is evaluated before and after by computer tomography (CT) or magnetic resonance imaging (MRI) while no real-time imaging provides monitoring during treatment [2, 5, 6]. As such, there remains an unmet clinical need for a local ablation method capable of overcoming these limitations.

High intensity focused ultrasound (HIFU) is a non-invasive thermal ablation technique [12, 13]. The current HIFU systems use MRI thermometry to provide real-time monitoring of the thermal dose during treatment [14-17]. With its non-invasiveness, real-time MRI feedback, the ability to scan the focal zone over a large tumor volume, HIFU has the promise to improve upon the current ablation methods [18-20]. However, as a thermal-based method, HIFU is still affected by the heat sink effect, resulting in the reduced effectiveness in ablating tissue near major blood vessels, extended treatment time for larger hypervascular liver volumes, and a lack of treatment precision [17, 21]. As a result, there remains an unmet clinical need for an ablation method capable of overcoming these limitations.

1.2 Histotripsy Therapy

Histotripsy is a non-invasive non-thermal ultrasonic ablation method that fractionates tissue through the precise control of acoustic cavitation generated by high pressure (>10 MPa), short duration (<20μs) ultrasound pulses at low duty cycles (<1 %) [22-26]. Using microsecond, high-pressure pulses applied by an ultrasound transducer outside the body and focused to the target tissue, a cluster of microbubbles are generated and the energetic expansion and collapse of the microbubbles fractionates cells at the target [24, 27]. With sufficiently high pressure and dose,

histotripsy can completely fractionate soft tissue into an acellular liquid homogenate, with no recognizable cellular structures [24, 28]. Histotripsy can be used to create controlled tissue erosion at a fluid-tissue interface [26, 29, 30] or generate localized well-demarcated tissue fractionation inside bulk tissue [22, 31-35]. Since histotripsy is non-thermal, it is not affected by the heat sink effect from blood vessels and does not have the limitations associated with thermal ablation methods. Histotripsy can produce consistent and fast fractionation of tissue with different heat dissipation patterns, even when the tissue is in proximity to major vessels [36-39]. As a non-invasive ablation method, the therapy focus can be scanned to treat a large tumor volume (>3cm) and multiple nodules in a reasonably short period of time. Further, the histotripsy cavitation cloud can be visualized with ultrasound imaging, allowing precise targeting [37, 38, 40, 41]. The change in tissue during treatment can be also be directly monitored using standard imaging modalities such as ultrasound and MRI, which allows histotripsy to be guided in real time [41-43].

Previous work has demonstrated two mechanisms in which a histotripsy cavitation cloud can be generated. In the first, termed the "shock scattering mechanism," a dense lesion-forming cavitation bubble cloud is formed from a single multi-cycle histotripsy pulse (e.g., 3–20 cycles) using shock scattering from sparse initial bubbles formed and expanded during the initial cycles of the pulse [Fig 1.1] [44]. In this process of cloud initiation, these initial bubbles act as a pressure release surface wherein the following positive pressure half cycles, usually very high peak pressure shock fronts, are inverted and superimposed on the incident negative pressure phase to form extremely high negative pressures that produce a dense cavitation cloud growing back towards the transducer [44]. The dense bubble clouds thus formed are necessary to achieve histotripsy tissue fractionation. The process of shock scattering initiates a histotripsy bubble

cloud at negative pressure magnitudes weaker than what is required to directly generate dense bubble clouds without shock scattering [45]. Because of the complexity of the shock scattering process, multiple factors determine whether a cloud is initiated, including the distribution of heterogeneous nuclei in the focal region, the size and shape of initial single bubbles, the number of cycles, the shock rise time, and the positive pressure amplitudes [44-47].

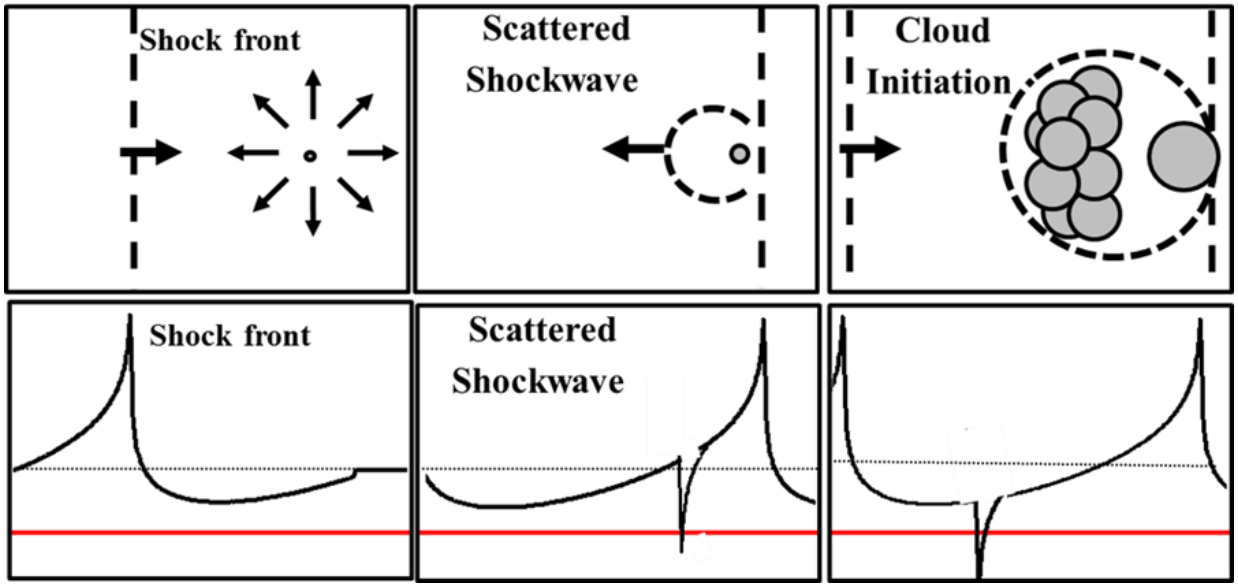

Figure 1.1 Shock scattering mechanism. An initial bubble is first formed and expanded during the first cycles of the pulse, and the positive shockwaves of the following cycles are scattered from the individual bubbles. The scattered shockwaves constructively interfere with the incident negative pressure, forming a cavitation cloud propagating opposite the ultrasound propagation direction. The red line represents the histotripsy intrinsic threshold (i.e. P- required to generate cavitation).

In addition to the shock scattering mechanism that uses a multi-cycle ultrasound pulse, there is another mechanism for histotripsy cloud formation termed the "intrinsic threshold mechanism," in which a 1-2 cycle pulse with a single dominant negative pressure phase is used to generate a bubble cloud directly from the negative pressure of the incident wave [Fig. 1.2] [48, 49]. With these short pulses, cavitation initiation depends solely on the negative pressure when it exceeds a distinct threshold intrinsic to the medium, without the contributions from shock scattering, resulting in a bubble cloud matching the portion of the focal region above the intrinsic

threshold [48, 49]. In contrast to shock scattering, the intrinsic threshold mechanism of cloud initiation does not rely on the expansion of initial bubbles in order to initiate a dense bubble cloud. A previous study by Maxwell *et al* using a 1.1 MHz histotripsy transducer demonstrated that the intrinsic threshold for water based soft tissues and tissue phantoms was approximately 26-30 MPa [49].

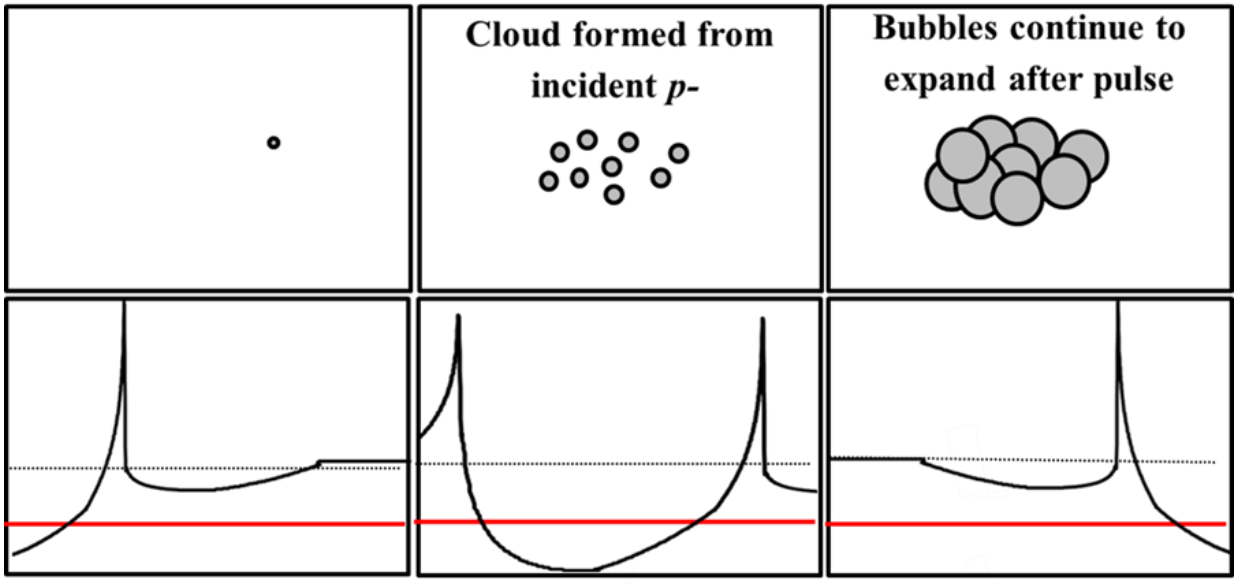

Figure 1.2 Intrinsic threshold mechanism. Cavitation is generated directly along the ultrasound propagation direction using a single pulse with peak negative pressure exceeding a threshold intrinsic to the tissue. The red line represents the histotripsy intrinsic threshold (i.e. P- required to generate cavitation).

1.3 Outline of this dissertation

This dissertation is separated into three categories. The first part of this dissertation (Chapters 2-8) investigates the effects of tissue properties on histotripsy therapy. Chapter 2 investigates the effects of tissue mechanical properties on the pressure threshold required to generate a histotripsy bubble cloud using the shock scattering method of cloud initiation. Chapter 3 investigates the effects of tissue mechanical properties and ultrasound frequency on the

pressure required to generate a histotripsy bubble cloud using the intrinsic threshold method of cloud initiation. Chapter 4 investigates the effects of temperature on the pressure required to generate a bubble cloud using the intrinsic threshold method of cloud initiation. Chapter 5 investigates the effects of tissue mechanical properties on susceptibility to histotripsy-induced tissue damage. Chapter 6 investigates the effects of thermal preconditioning on tissue susceptibility to histotripsy. Chapter 7 investigates the effects of tissue mechanical properties, ultrasound frequency, and pressure on histotripsy-induced cavitation bubble behavior. In Chapter 8, the process of histotripsy fractionation is investigated using a custom-built histotripsy transducer coupled to a microscope allowing for the histotripsy bubble interactions with cancer cells to be visualized on the cellular level.

The second part of this dissertation (Chapters 9-10) investigates the *in vivo* feasibility of using histotripsy for targeted liver ablation. In Chapter 9, the feasibility of applying histotripsy *in vivo* for non-invasive liver ablation was investigated using a porcine model with similar size and anatomic similarities to its human counterpart. In Chapter 10, the long-term effects of histotripsy liver ablation were investigated in a rodent model.

In the final part of this dissertation (Chapters 11-14), a novel ablation method combining histotripsy with acoustically sensitive nanodroplets is developed for targeted cancer cell ablation. Chapter 11 investigates the development of nanodroplet-mediated histotripsy (NMH) for targeted cancer cell ablation. Chapter 12 investigates the effects of ultrasound frequency on NMH therapy. Chapter 13 investigates the effects of droplet composition on NMH therapy. Chapter 14 investigates the role of positive and negative pressure on cavitation nucleation in NMH therapy. Finally, Chapter 15 summarizes the findings and contributions of this dissertation, and provides suggestions for future research into histotripsy tissue ablation.

1.4 References

[1] R. M. Charnley, *et al.*, "Cryotherapy for liver metastases: a new approach," *Br J Surg*, vol. 76, pp. 1040-1, Oct 1989.

[2] C. Erce and R. W. Parks, "Interstitial ablative techniques for hepatic tumours," *Br J Surg*, vol. 90, pp. 272-89, Mar 2003.

[3] H. W. Head and G. D. Dodd, 3rd, "Thermal ablation for hepatocellular carcinoma," *Gastroenterology*, vol. 127, pp. S167-78, Nov 2004.

[4] E. Liapi and J. F. Geschwind, "Transcatheter and ablative therapeutic approaches for solid malignancies," *J Clin Oncol*, vol. 25, pp. 978-86, Mar 10 2007.

[5] S. A. Curley, "Radiofrequency ablation of malignant liver tumors," *Oncologist*, vol. 6, pp. 14-23, 2001.

[6] D. S. Lu, *et al.*, "Influence of large peritumoral vessels on outcome of radiofrequency ablation of liver tumors," *J Vasc Interv Radiol*, vol. 14, pp. 1267-74, Oct 2003.

[7] J. A. Marrero and S. Pelletier, "Hepatocellular carcinoma," *Clin Liver Dis*, vol. 10, pp. 339-51, ix, May 2006.

[8] E. J. Patterson, *et al.*, "Radiofrequency ablation of porcine liver in vivo: effects of blood flow and treatment time on lesion size," *Ann Surg*, vol. 227, pp. 559-65, Apr 1998.

[9] T. Livraghi, *et al.*, "Treatment of focal liver tumors with percutaneous radio-frequency ablation: complications encountered in a multicenter study," *Radiology*, vol. 226, pp. 441-51, Feb 2003.

[10] A. J. Aschoff, *et al.*, "How does alteration of hepatic blood flow affect liver perfusion and radiofrequency-induced thermal lesion size in rabbit liver?," *J Magn Reson Imaging*, vol. 13, pp. 57-63, Jan 2001.

[11] M. Kudo, "Radiofrequency ablation for hepatocellular carcinoma: updated review in 2010," *Oncology*, vol. 78 Suppl 1, pp. 113-24, Jul 2010.

[12] T. A. Leslie and J. E. Kennedy, "High-intensity focused ultrasound principles, current uses, and potential for the future," *Ultrasound Q*, vol. 22, pp. 263-72, Dec 2006.

[13] G. ter Haar, "High intensity ultrasound," *Semin Laparosc Surg*, vol. 8, pp. 77-89, Mar 2001.

[14] S. Bobkova, *et al.*, "Focusing of High-Intensity Ultrasound through the Rib Cage Using a Therapeutic Random Phased Array," *Ultrasound in Medicine and Biology*, vol. 36, pp. 888-906, Jun 2010.

[15] E. Cochard, *et al.*, "Ultrasonic focusing through the ribs using the DORT method," *Med Phys,* vol. 36, pp. 3495-503, Aug 2009.

[16] V. A. Khokhlova, *et al.*, "Focus Splitting Associated with Propagation of Focused Ultrasound through the Rib Cage," *Acoust Phys,* vol. 56, pp. 665-674, Sep 2010.

[17] A. Okada, *et al.*, "A case of hepatocellular carcinoma treated by MR-guided focused ultrasound ablation with respiratory gating," *Magn Reson Med Sci,* vol. 5, pp. 167-71, Oct 2006.

[18] C. X. Li, *et al.*, "[High intensity focused ultrasound for liver cancer]," *Zhonghua Zhong Liu Za Zhi,* vol. 25, pp. 94-6, Jan 2003.

[19] J. P. McWilliams, *et al.*, "Percutaneous ablation of hepatocellular carcinoma: current status," *J Vasc Interv Radiol,* vol. 21, pp. S204-13, Aug 2010.

[20] L. Zhang, *et al.*, "High-intensity focused ultrasound (HIFU): effective and safe therapy for hepatocellular carcinoma adjacent to major hepatic veins," *Eur Radiol,* vol. 19, pp. 437-45, Feb 2009.

[21] T. A. Leslie, *et al.*, "High-intensity focused ultrasound ablation of liver tumours: can radiological assessment predict the histological response?," *Br J Radiol,* vol. 81, pp. 564-71, Jul 2008.

[22] J. E. Parsons, *et al.*, "Pulsed cavitational ultrasound therapy for controlled tissue homogenization," *Ultrasound Med Biol,* vol. 32, pp. 115-29, Jan 2006.

[23] W. W. Roberts, *et al.*, "Pulsed cavitational ultrasound: a noninvasive technology for controlled tissue ablation (histotripsy) in the rabbit kidney," *J Urol,* vol. 175, pp. 734-8, Feb 2006.

[24] Z. Xu, *et al.*, "Investigation of intensity thresholds for ultrasound tissue erosion," *Ultrasound Med Biol,* vol. 31, pp. 1673-82, Dec 2005.

[25] J. E. Parsons, *et al.*, "Pulsed cavitational ultrasound therapy for controlled tissue homogenization," *Ultrasound in Medicine and Biology,* vol. 32, pp. 115-29, Jan 2006.

[26] Z. Xu, *et al.*, "Controlled ultrasound tissue erosion," *IEEE Trans Ultrason Ferroelectr Freq Control,* vol. 51, pp. 726-36, Jun 2004.

[27] J. E. Parsons, *et al.*, "Spatial variability in acoustic backscatter as an indicator of tissue homogenate production in pulsed cavitational ultrasound therapy," *IEEE Trans Ultrason Ferroelectr Freq Control,* vol. 54, pp. 576-90, Mar 2007.

[28] T. L. Hall, *et al.*, "Histotripsy of rabbit renal tissue in vivo: temporal histologic trends," *J Endourol,* vol. 21, pp. 1159-66, Oct 2007.

[29] Z. Xu, *et al.*, "Noninvasive creation of an atrial septal defect by histotripsy in a canine model," *Circulation,* vol. 121, pp. 742-9, Feb 16 2010.

[30] G. E. Owens, *et al.*, "Therapeutic ultrasound to noninvasively create intracardiac communications in an intact animal model," *Catheterization and Cardiovascular Interventions,* vol. 77, pp. 580-588, 2011.

[31] W. W. Roberts, "Focused ultrasound ablation of renal and prostate cancer: current technology and future directions," *Urol Oncol,* vol. 23, pp. 367-71, Sep-Oct 2005.

[32] A. M. Lake, *et al.*, "Histotripsy: Minimally Invasive Technology for Prostatic Tissue Ablation in an In Vivo Canine Model," *Urology,* vol. 72, pp. 682-686, 2008.

[33] C. R. Hempel, *et al.*, "Histotripsy Fractionation of Prostate Tissue: Local Effects and Systemic Response in a Canine Model," *The Journal of Urology,* vol. 185, pp. 1484-1489, 2011.

[34] G. R. Schade, *et al.*, "Urethral-sparing Histotripsy of the Prostate in a Canine Model," *Urology,* vol. 80, pp. 730-735, 2012.

[35] E. Vlaisavljevich, *et al.*, "Image-Guided Non-Invasive Ultrasound Liver Ablation Using Histotripsy: Feasibility Study in an In Vivo Porcine Model," *Ultrasound in medicine & biology,* vol. 39, pp. 1398-1409, 2013.

[36] T. L. Hall, *et al.*, "Histotripsy of the prostate: dose effects in a chronic canine model," *Urology,* vol. 74, pp. 932-7, Oct 2009.

[37] Y. Kim, *et al.*, "Non-invasive pulsed cavitational ultrasound for fetal tissue ablation: feasibility study in a fetal sheep model," *Ultrasound Obstet Gynecol,* vol. 37, pp. 450-7, Apr 2011.

[38] A. D. Maxwell, *et al.*, "Noninvasive treatment of deep venous thrombosis using pulsed ultrasound cavitation therapy (histotripsy) in a porcine model," *J Vasc Interv Radiol,* vol. 22, pp. 369-77, Mar 2011.

[39] N. R. Styn, *et al.*, "Histotripsy of VX-2 tumor implanted in a renal rabbit model," *J Endourol,* vol. 24, pp. 1145-50, Jul 2010.

[40] G. E. Owens, *et al.*, "Therapeutic ultrasound to noninvasively create intracardiac communications in an intact animal model," *Catheter Cardiovasc Interv,* vol. 77, pp. 580-8, Mar 1 2011.

[41] R. M. Miller, *et al.*, "Real-time elastography-based monitoring of histotripsy tissue fractionation using color Doppler," in *Ultrasonics Symposium (IUS), 2012 IEEE International*, 2012, pp. 196-199.

[42] T. L. Hall, *et al.*, "Relaxation Properties of Cavitation Induced Tissue Lesions," presented at the Joint Annual Meeting of the International Society for Magnetic Resonance in Medicine. , 2007.

[43] T. Y. Wang, *et al.*, "Quantitative ultrasound backscatter for pulsed cavitational ultrasound therapy- histotripsy," *IEEE Trans Ultrason Ferroelectr Freq Control,* vol. 56, pp. 995-1005, May 2009.

[44] A. D. Maxwell, *et al.*, "Cavitation clouds created by shock scattering from bubbles during histotripsy," *J Acoust Soc Am,* vol. 130, pp. 1888-98, Oct 2011.

[45] A. D. Maxwell, *et al.*, "Inception of Cavitation Clouds by Scattered Shockwaves," *IEEE Ultrasonics Symposium,* pp. 3B-2, 2010.

[46] E. Vlaisavljevich, *et al.*, "Histotripsy-induced cavitation cloud initiation thresholds in tissues of different mechanical properties," *IEEE Trans Ultrason Ferroelectr Freq Control,* vol. 61, pp. 341-52, Feb 2014.

[47] Z. Xu, *et al.*, "High speed imaging of bubble clouds generated in pulsed ultrasound cavitational therapy--histotripsy," *IEEE Trans Ultrason Ferroelectr Freq Control,* vol. 54, pp. 2091-101, Oct 2007.

[48] K. W. Lin, *et al.*, "Histotripsy beyond the intrinsic cavitation threshold using very short ultrasound pulses: microtripsy," *IEEE Trans Ultrason Ferroelectr Freq Control,* vol. 61, pp. 251-65, Feb 2014.

[49] A. D. Maxwell, *et al.*, "Probability of cavitation for single ultrasound pulses applied to tissues and tissue-mimicking materials," *Ultrasound Med Biol,* vol. 39, pp. 449-65, Mar 2013.

Chapter 2
Histotripsy-induced Cavitation Cloud Initiation Thresholds in Tissue of Different Mechanical Properties

A majority component of this chapter has been published in *IEEE Transactions on Ultrasonics, Ferroelectric, and Frequency Control* © 2014 IEEE. Reprinted, with permission, from [1].

2.1 Introduction

Histotripsy is a non-invasive tissue ablation method that controls cavitation to fractionate soft tissue through high pressure (>10 MPa), short duration (<20 μsec) ultrasound pulses at low duty cycles (<1%) [2-5]. Histotripsy depends on the initiation and maintenance of a dense cavitation bubble cloud to produce mechanical tissue fractionation [4, 6]. With sufficiently high pressure (>10 MPa peak negative pressures) and adequate number of pulses (>500 pulses), histotripsy can completely fractionate soft tissue into a liquid-appearing homogenate resulting in effective tissue removal [5, 7]. The histotripsy process is often self-limited at anatomical boundaries such as blood vessels, the capsule of an organ (e.g. the prostate) or fibrous structures (e.g. the collecting system in the kidney) [8, 9]. These structures have a higher Young's modulus than surrounding tissue.

In histotripsy, the dense lesion-forming cavitation bubble cloud has a higher threshold to initiate than the thresholds for inertial cavitation of individual microbubbles reported in the literature [10-19]. A dense bubble cloud can be formed during one multi-cycle histotripsy pulse

using shock scattering from single bubbles formed and expanded from the initial cycles of the pulse [Fig. 2.1(A)] [20]. In this process of cloud initiation, these initial bubbles act as a pressure release surface wherein the following positive pressure half cycles, usually very high peak pressure shock fronts, are inverted and superimposed on the incident negative pressure phase to form extremely high negative pressures that produce a dense cavitation cloud growing back towards the transducer [20]. The dense bubble clouds thus formed are necessary to achieve histotripsy tissue fractionation. The process of shock scattering initiates a histotripsy bubble cloud at negative pressure magnitudes weaker than what is required to directly generate dense bubble clouds without shock scattering [16]. Sufficient expansion of initial bubbles coupled with a shock thickness that is very small compared to the bubble diameter (~100 nm vs. 100 μm) results in strong scattering of the shock and bubble cloud formation [16]. If the sparsely distributed initial bubbles are too small, they cannot effectively reflect and invert the subsequent shock front to initiate dense lesion-forming bubble clouds [Fig. 2.1] [16].

Tissue mechanical properties have been proposed to affect cavitation threshold and bubble expansion in elastic media similar to soft tissue [21-26]. We hypothesize that the expansion of initial bubbles during the histotripsy pulse is impeded in tissue of increased mechanical stiffness (i.e. Young's modulus), which reduces shock scattering and increases the pressure threshold (of incident wave) necessary to initiate a cavitation bubble cloud [Fig. 2.1(B)]. In this chapter, we investigate the threshold to initiate a dense cavitation cloud in mechanically tunable tissue mimicking agarose phantoms and various *ex vivo* porcine tissues covering a wide range of mechanical properties.

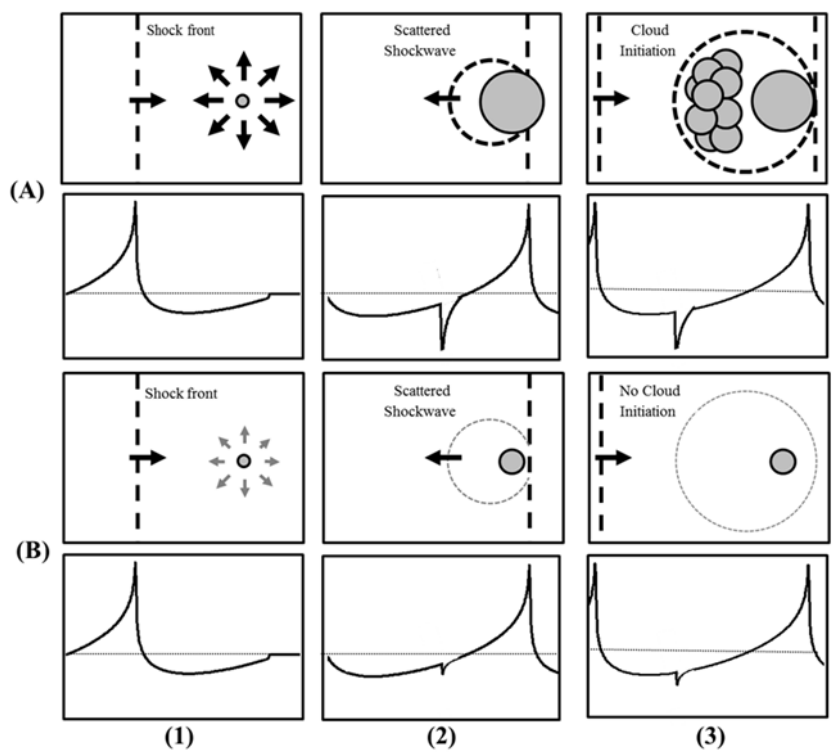

Figure 2.1. Bubble cloud formation by shock scattering. During the initial cycles, individual bubbles are expanded in the focus due to the incident negative pressure (1). Shockwaves from subsequent cycles are scattered off initially expanded bubbles (2), which inverts the shock and constructively interferes with the negative phase of the next incident wave (3). Previous work has demonstrated a histotripsy bubble cloud is only formed when initial bubbles expand to a large enough size for shock scattering to result in sufficiently large reflected negative pressures (A). If expansion of initial bubbles is of insufficient size to cause significant scattering, the negative pressures produced will be insufficient to initiate a histotripsy bubble cloud (B).

2.2 Methods

2.2.1 Therapeutic Ultrasound

Histotripsy pulses were generated by a 1 MHz focused ultrasonic transducer (Imasonic, Besançon, France) with an aperture of 100 mm, focal length of 90 mm, and a 50 mm-diameter concentric hole. The transducer was driven by a custom-designed class D amplifier with appropriate electrical matching circuits built in our laboratory. Input signals were provided by a custom built Field-Programmable Gate Array (FPGA) board (Altera Corporation, San Jose, CA,

USA) that functioned as a signal generator. Acoustic waveforms produced by the 1 MHz therapeutic transducer were obtained using a fiber optic probe hydrophone built in house [27]. Pressure wave measurements were recorded in free-field in both degassed water and degassed 1,3-Butanediol (Sigma-Aldrich) at room temperature. Measurements were made in 1,3-Butanediol to prevent cavitation at the fiber tip at high pressures. Butanediol was chosen because it has almost identical acoustic impedance to water, so no correction due to mismatch was needed for the peak negative pressure measurements. The effects of attenuation were minimized by submerging the hydrophone in only a small volume of butanediol with sound propagating approximately 1 mm in butanediol. The hydrophone sensitivity in butanediol was calibrated by comparison with known measurements in water. Both fluids were used because water is needed for reference and butanediol allowed higher peak negative pressure amplitudes to be measured directly. While the positive pressures measured in butanediol were suppressed due to the higher attenuation, the negative pressures which were used as metrics for the cavitation threshold were shown to match those measured in water. The peak negative pressures used in this work were 10-27.9 MPa. Positive pressures were measured up to >80 MPa corresponding to a peak negative pressure of 15 MPa. At higher pressure, peak positive pressure could not be accurately measured due to instantaneous cavitation at the fiber tip in water and attenuation or saturation effects in Butanediol. The peak positive pressures corresponding to negative pressures > 15 MPa used in some of the experiments are expected to be higher than 80 MPa.

2.2.2 Tissue Phantom Preparation

Agarose phantoms were used to provide a well-controlled elastic medium for this study. Agarose phantoms of 0.3%, 1%, 2.5%, and 5% w/v were prepared by slowly mixing agarose

powder (Agarose Type VII, Sigma-Aldrich) into saline solution (0.9% sodium chloride, Hospira) heated above 70°C. The solution was stirred on a hot plate until the gel turned completely transparent. Agarose solutions were degassed under a partial vacuum of 20.5 psi for 30 minutes. After removing agarose mixtures from the vacuum, the solution was poured into 15×5×5 cm rectangular polycarbonate tissue phantom holders. Tissue phantom holders were placed in a refrigerator at 4°C to allow the agarose solution to solidify prior to use.

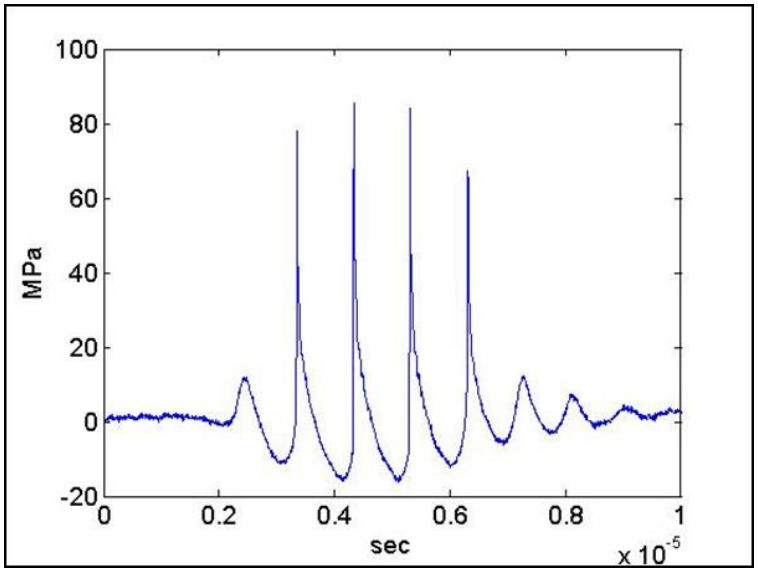

Figure 2.2. Example histotripsy pressure waveform.

2.2.3 Tissue Phantom Mechanical Properties

The mechanical properties of agarose phantoms can be varied over a physiologically-relevant range by changing agarose concentration [28]. The agarose phantoms were made following the protocol previously described by Normand et al. in which the Young's modulus was characterized for agarose phantoms of varying concentration [28]. Agarose phantoms were selected to cover the mechanical stiffness of tissues found in the body from non-load bearing

tissues such as lung, fat, and kidney (Young's moduli ranging from 1-10 kPa) to strong load bearing tissues such as cartilage (Young's moduli of ~1 MPa).

2.2.4 Porcine Tissue Preparation

Fresh porcine lung, fat, kidney, liver, heart, skeletal muscle, skin, tongue, tendon, cartilage, and bone were excised and immediately placed into degassed 0.9% saline solution and stored at 4°C until experiments. Tissue samples were sectioned (minimum size of 5 cm3) and warmed to room temperature in degassed saline under a partial vacuum of 20.5 psi for 4 hours prior to experiments. All tissues were used within 48 hours of harvesting.

2.2.5 Tissue Mechanical Properties

Tissue mechanical properties have been characterized using numerous metrics in the literature including elastic modulus, bulk modulus, ultimate stress, and ultimate fractional strain [28-37]. Mechanical strength has also been shown to correlate to tissue composition including tissue density, water content, and protein concentration [28, 38-41]. In order to compare cloud initiation threshold results with tissue stiffness, Young's modulus values from literature were chosen as a tissue mechanical property metric for this study. Tissues investigated in this work covered the large range of Young's moduli seen in the body from <5 kPa to >100 MPa.

2.2.6 Cavitation Cloud Initiation Detection

To measure the threshold to initiate a cavitation bubble cloud, histotripsy pulses were targeted inside agarose tissue phantoms or porcine tissue placed in a water tank [Fig. 2.3]. Five cycle pulses at pulse repetition frequencies (PRF) of 10 Hz, 100 Hz, or 1000 Hz were applied by

the 1MHz transducer. The acoustic backscatter of the therapy pulse from the bubble cloud was received by a low frequency, unfocused marine hydrophone (Aquarian Audio Products, H1a) with a sensitivity of -220dB re 1V/μPa at 100 kHz. Hydrophone was placed directly above the therapy transducer facing the therapy focus to receive the acoustic backscatter signal at an approximately 30° angle. The significantly increased amplitude of the acoustic backscatter signal was used to detect the initiation of dense cavitation clouds. Example waveforms from the low frequency hydrophone with and without cavitation are shown in Figure 2.3.4. The frequency spectrum of the hydrophone signal showed local frequency peaks at 100 kHz, 300 kHz, and 500 kHz with the largest peak at 100 kHz. Experimental results and analysis demonstrate that these low frequency components are due to the therapy pulse envelop and system response of the low frequency hydrophone. These low frequency peaks change with the duration (i.e. envelope) of the therapy pulse.

A three-step method has been developed to process the acoustic backscatter signals to detect the cavitation cloud initiation threshold. First, the energy of the acoustic backscatter signal from each pulse was calculated by integrating the square of the voltage signal received from the hydrophone. Second, the threshold for detecting cloud initiation was defined as the mean plus three standard deviations of the uninitiated acoustic backscatter energy (no cavitation cloud), which was calculated at a very low therapy pulse pressure (<5 MPa) for 30 trials of 1000 pulses each. The acoustic backscatter energy was normalized to the spatial peak pulse average intensity (I_{SPPA}) of the corresponding therapy pulses [12]. Third, the initiation of the bubble cloud was determined when the normalized acoustic backscatter energy exceeded the defined threshold within the first 10 histotripsy pulses and was maintained above the threshold for the duration of the 1000 pulses at a given pressure. A similar method using acoustic backscatter has previously

been used to detect cavitation cloud initiation in histotripsy which correlates with tissue fractionation generation at >97% success rate [4]. Initiation within the first 10 pulses and maintenance over the 1000 pulses were chosen as part of the initiation criteria here as rapid initiation of the bubble cloud and maintenance for over 1000 pulses are needed to produce effective and efficient tissue fractionation based on previous studies. A sample size of 6 tissue phantoms or tissue samples was used for each agarose concentration and porcine tissue type. In each sample, 60 pressure levels ranging from 8-28 MPa were tested with 1000 pulses applied for each individual pressure. Each pressure level was tested in a different location (1 cm spacing) to avoid the influence of the previous exposure on the threshold measurement. The lowest pressure level when initiation was detected was recorded as the cloud initiation threshold in that sample.

Bubble cloud initiation detected using acoustic backscatter was verified through optical images of the bubble cloud generation in the agarose phantom using a high-speed, 1 megapixel CCD camera (Phantom V210, Vision Research) capable of a maximum frame rate of 2000 fps. The camera was focused with a macro-bellows lens (Tominon, Kyocera) and backlit by a continuous light source. The camera was triggered to record one image for each applied pulse, 10 μs after the beginning of the pulse reached the focus. The camera exposure time was 2-5 μs. Bubbles were indicated as black regions > 5 pixels in the shadowgraphic images and a bubble cloud was considered initiated when more than 10 bubbles were visible within the image within the first 10 histotripsy pulses and throughout the remaining 1000 pulses as previously described for the backscatter detection method. The minimum resolvable diameter of a bubble was about 10-20 μm as a result of the magnification and the minimum 5 pixel area and 2μm/pixel resolution. A sample size of 6 tissue phantoms or tissue samples (cut into sections with a minimum size of 5 cm^3) was used for each agarose concentration and porcine tissue type. Cloud

initiation threshold results in different tissue phantoms and porcine tissues (n=6) were compared using a Student's t-test. P-values<0.05 were considered statistically significant.

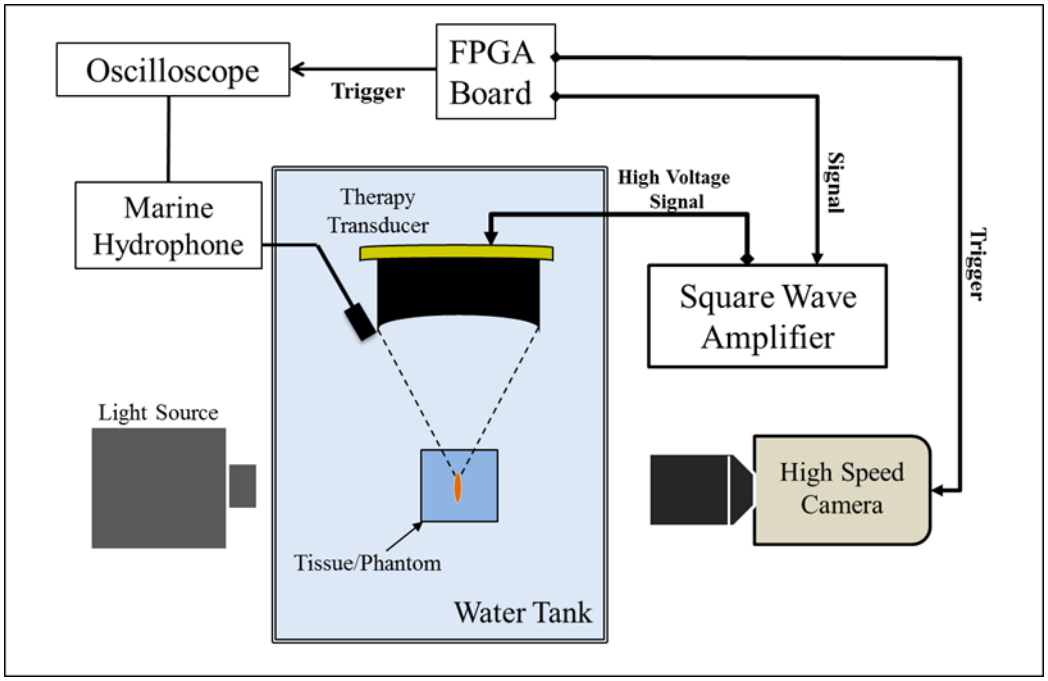

Figure 2.3. Experimental setup. A 1 MHz therapy transducer focus was aligned inside samples for cavitation initiation experiments. Bubble cloud formation was monitored using a low frequency marine hydrophone and verified with high speed optical imaging.

2.2.7 Bubble Expansion Simulation

To investigate the effects of tissue Young's modulus on the growth of initial bubbles, a numerical simulation based on a linear Kelvin-Voigt model was developed. We hypothesize that the first significant tension experienced by a nucleus will cause it to grow explosively, and that the behavior will be affected by the tissue elasticity. To test this hypothesis, simulations exposed a 10 nm initial bubble to a single cycle of 15 MPa peak negative pressure and 70 MPa peak positive pressure. For this proof of principle, we assume the surrounding medium to have homogeneous properties, and that the bubble contains air and remains spherical. These assumptions allow us to use a numerical model developed in-house [29] for simulating spherical

bubble dynamics in a viscoelastic medium with viscous, elastic, relaxation and retardation effects, including liquid compressibility and heat transfer.

Since the present focus is on growth, we neglect heat transfer and consider the simplest viscoelastic model (linear Kelvin-Voigt) that includes viscosity and elasticity [25]. In the Kelvin-Voigt model, the stress tensor τ is related to the deformation tensor γ and the rate of deformation tensor $\dot{\gamma}$ through

$$\tau = 2G\gamma + 2\mu\dot{\gamma} \quad (\mathbf{E2.1})$$

where G is the shear modulus (elasticity) and μ is the viscosity. The stress tensor is related to the bubble radius R through the Keller-Miksis equation

$$\left(1-\frac{\dot{R}}{c}\right)R\ddot{R}+\frac{3}{2}\left(1-\frac{\dot{R}}{3c}\right)\dot{R}^2=\frac{1}{\rho}\left(1+\frac{\dot{R}}{c}+\frac{R}{c}\frac{d}{dt}\right)\left(p_g-\frac{2S}{R}-p_\infty(t)+3\int_R^\infty\frac{\tau_{rr}}{r}dr\right) \quad (\mathbf{E2.2})$$

which depends on the medium's sound speed c, density ρ, and surface tension against air S. Here $p_\infty(t)$ is the absolute forcing pressure, r is the radial coordinate, and overdots ($\dot{}$) denote derivatives with respect to time, t. The air within the bubble is assumed to have spatially uniform pressure given by the polytropic relationship

$$p_g = p_0\left(\frac{R_0}{R}\right)^{3\kappa} \quad (\mathbf{E2.3})$$

where $\kappa = 1.4$ is the ratio of specific heats for air, R_0 is the initial bubble radius, and $p_0 = p_\infty(0) + 2S/R_0$ is the initial bubble pressure. By conservation of mass, the radial velocity of the surrounding medium is $u(r,t) = R^2\dot{R}/r^2$, and hence

$$\dot{\gamma}_{rr} = -\frac{\partial u}{\partial r} = -\frac{2R^2\dot{R}}{r^3} \quad (\mathbf{E2.4}), \quad \gamma_{rr} = -\frac{2}{3r^3}(R^3 - R_0^3) \quad (\mathbf{E2.5}),$$

from which it follows that

$$3\int_R^\infty\frac{\tau_{rr}}{r}dr = -\frac{4G}{3}\left(1-\frac{R_0^3}{R^3}\right)-\frac{4\mu\dot{R}}{R} \quad (\mathbf{E2.6}).$$

These substitutions allow the Keller-Miksis equation to be solved for the bubble wall acceleration $\ddot{R}$ and integrated in time. The properties $\rho = 1060\ \mathrm{kg/m^3}$, $c = 1430\ \mathrm{m/s^2}$, and $S = 0.056$ (blood-air surface tension) were used to describe the surrounding medium. The medium's viscosity was assumed to be that of blood viscosity ($\mu = 3.0$ cP) while the Young's modulus ($E = 3G$) was varied in decades from 1 kPa to 10 MPa in order to match the range of tissues studied in this work. The bubble radius was graphed as a function of time over this range of Young's moduli to provide insight into the effects of tissue elasticity on the expansion of small bubbles at the focus of histotripsy pulses.

2.2.8 Bubble Behavior

To study the effects of mechanical properties on bubble expansion and collapse, optical images of the growth and collapse of individual bubbles and the cloud were recorded by the high-speed camera. A bubble cloud was generated by 5-cycle histotripsy pulses at 25.9 MPa peak negative pressure applied by 1MHz transducer with a PRF of 100 Hz. Due to the limited frame rate of the camera, we could not image the bubble expansion and collapse during and after a single histotripsy pulse. Therefore, a series of time-delayed images of bubble clouds generated by 200 identical pulses with delay increased 2 μs per pulse were taken to reconstruct a sequence of bubble images covering the entire period of bubble expansion and collapse. Shadowgraph images were converted from grayscale to binary by an intensity threshold determined by the background intensity using image processing software (MATLAB, The Mathworks). The size of single bubbles visible within the bubble cloud was measured for each pulse to determine the maximum bubble expansion diameter as well as the time until bubble collapse. The time until bubble collapse measured in this work was measured as the time from the pulse arriving at the

focus until a bubble was no longer visible on optical imaging using the same 5 pixel (10 μm) qualification as outlined in the previous section. A sample size of 6 tissue phantoms was used for each agarose concentration.

2.3 Results

2.3.1 Cavitation cloud initiation threshold in agarose tissue phantom

To test the effects of tissue mechanical properties on the pressure threshold required to generate a bubble cloud, histotripsy pulses [Fig 2.2] were applied to the centers of mechanically tunable agarose tissue phantoms. Bubble cloud initiation results from the acoustic backscatter energy received with the low frequency hydrophone were shown to correlate with the optical images [Fig 2.4]. All bubble clouds generated in this work contained 10 or more bubbles and resulted in a hydrophone signal above the defined threshold of the mean plus three standard deviations of the normalized uninitiated acoustic backscatter energy. Acoustic hydrophone measurements of histotripsy applied to tissue phantoms at different acoustic pressures demonstrated a statistically significant increase in the cavitation cloud initiation threshold with increasing agarose phantom concentration. Tissue phantoms with higher agarose concentration have a Young's modulus [Table 2.1] ranging from a Young's modulus (compression) of 1.5 kPa in the 0.3% agarose phantoms to 929 kPa for the 5% agarose phantoms. Results in Figure 5 showed that the bubble cloud initiation threshold significantly increased as agarose concentration was increased from 0.3% to 1%, 2.5%, and 5% [Fig 2.5]. For example, for 5 cycle pulses at a PRF of 100 Hz, the cloud initiation peak negative pressure threshold increased from 14.0 MPa to 24.7 MPa as the phantom agarose concentration was changed from 0.3% to 5%, corresponding to a change in Young's modulus of nearly 10^3. The trend of increasing cavitation cloud initiation

pressure with increasing agarose concentration was seen for all PRFs tested. Additionally, cavitation cloud initiation thresholds were observed to be significantly lower at higher PRF.

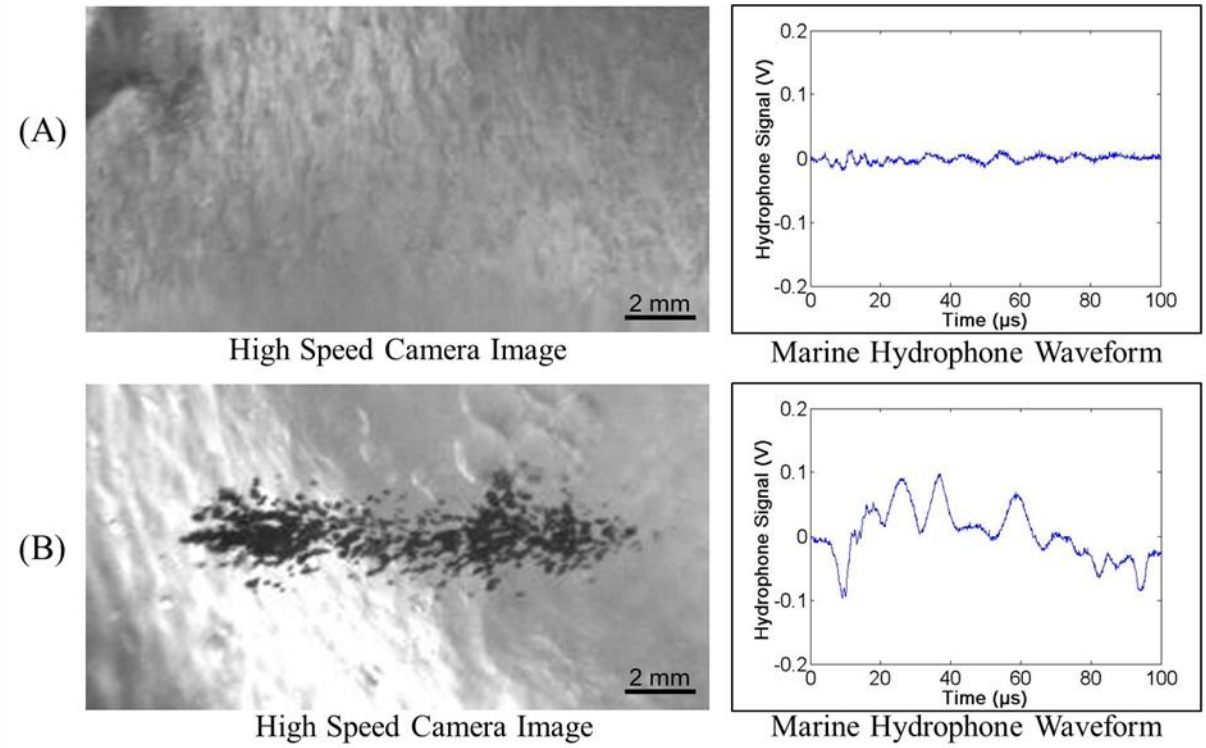

Figure 2.4. Example waveforms collected by marine hydrophone with corresponding optical images of bubble cloud. Examples shown are of 2.5% agarose tissue phantoms treated at 10 Hz right below and above the cavitation cloud threshold with peak negative pressures of (A) 24.2 MPa and (B) 25.1 MPa.

Table 2.1 Cavitation cloud initiation threshold in tissue phantoms. Table shows cavitation initiation threshold for agarose phantoms treated at PRFs of 10, 100, and 1000 Hz with corresponding Young's moduli values (tension, compression) [28].

% Agarose	Threshold (MPa) PRF 10	Threshold (MPa) PRF 100	Threshold (MPa) PRF 1000	Young's Modulus (MPa) Compression, Tension
0.30%	15.94±0.88	14.0±0.80	11.54±0.49	0.0015, N/A
1%	19.34±0.77	18.34±0.79	12.94±0.58	0.038, N/A
2.50%	24.75±0.52	21.77±0.65	18.98±0.82	0.25, 0.44
5%	25.98±0.42	24.66±0.33	20.65±1.44	0.93, 1.34

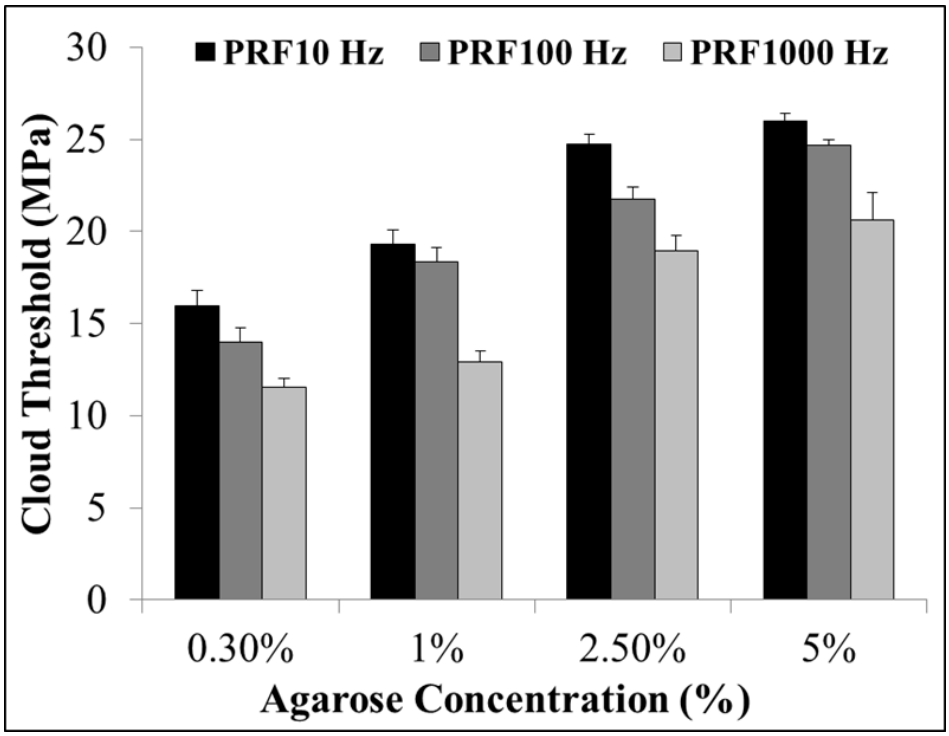

Figure 2.5. Cavitation cloud initiation threshold in phantoms with varied agarose concentration. Threshold results show significant increase in the peak negative pressure required to initiate cavitation inside higher concentration tissue phantoms. All increases in threshold between gel concentrations were considered significant (p-values<0.05).

2.3.2 Cavitation cloud initiation threshold in porcine tissue

Cavitation cloud initiation threshold was investigated in *ex vivo* porcine tissues covering a range of different mechanical properties at PRFs of 100 and 1000 Hz [Table 2.2]. The cloud initiation thresholds for porcine skin, tongue, tendon, and cartilage (high Young's modulus) were significantly higher than other tissues such as skeletal muscle, cardiac muscle, and liver (intermediate Young's modulus) while lung, fat, and kidney (low Young's modulus) were significantly lower. All differences in cloud initiation threshold between types of porcine tissue were significant ($p<0.05$) except the differences between fat and kidney; skin and tongue; and tongue and tendon ($p>0.05$). These three tissue combinations that didn't show a significant difference in threshold had similar mechanical properties (elastic modulus). Cavitation cloud

initiation was unattainable in bone for both 100 and 1000 Hz PRFs and in cartilage at 100 Hz PRF. A complete list of initiation threshold results in *ex vivo* porcine tissues are summarized in Table 2.2 along with the corresponding Young's moduli. Further analysis showed a trend of increasing cavitation cloud initiation threshold with increased Young's modulus [Fig 2.6]. Logarithmic regression analysis demonstrated a high correlation between the cloud initiation threshold and Young's modulus for tissues with Young's moduli below 0.1 MPa , with R^2 values of 0.85 and 0.76 at 100 Hz and 1000 Hz PRF, respectively. The cavitation cloud initiation threshold plateaued at an upper limit between 25-30 MPa for tissues with Young's moduli above 0.1 MPa (cartilage and tendon), for both PRFs of 100 Hz and 1000 Hz [Fig 2.6].

Table 2.2 Cavitation cloud initiation threshold in ex vivo porcine tissue. Table shows cavitation initiation threshold for porcine tissue treated at PRFs of 100 and 1000 Hz with corresponding Young's modulus (tension) values from literature [30-39].

Tissue	Threshold (MPa) PRF 100	Threshold (MPa) PRF 1000	Young's Modulus (MPa)
Lung	15.78±0.89	13.42±1.08	0.0026
Fat	17.13±1.41	13.26±1.85	0.0032
Kidney	17.84±1.48	14.56±0.95	0.0061
Liver	19.97±0.77	17.75±1.07	0.0087
Heart	20.03±0.36	17.06±1.28	0.0042
Muscle	21.01±0.48	19.12±0.57	0.0062
Skin	25.10±0.69	23.21±1.01	0.014
Tongue	26.54±0.88	24.27±0.44	0.025
Tendon	26.41±0.52	24.47±0.49	380
Cartilage	no cloud	27.28±0.85	0.90
Bone	no cloud	no cloud	18600

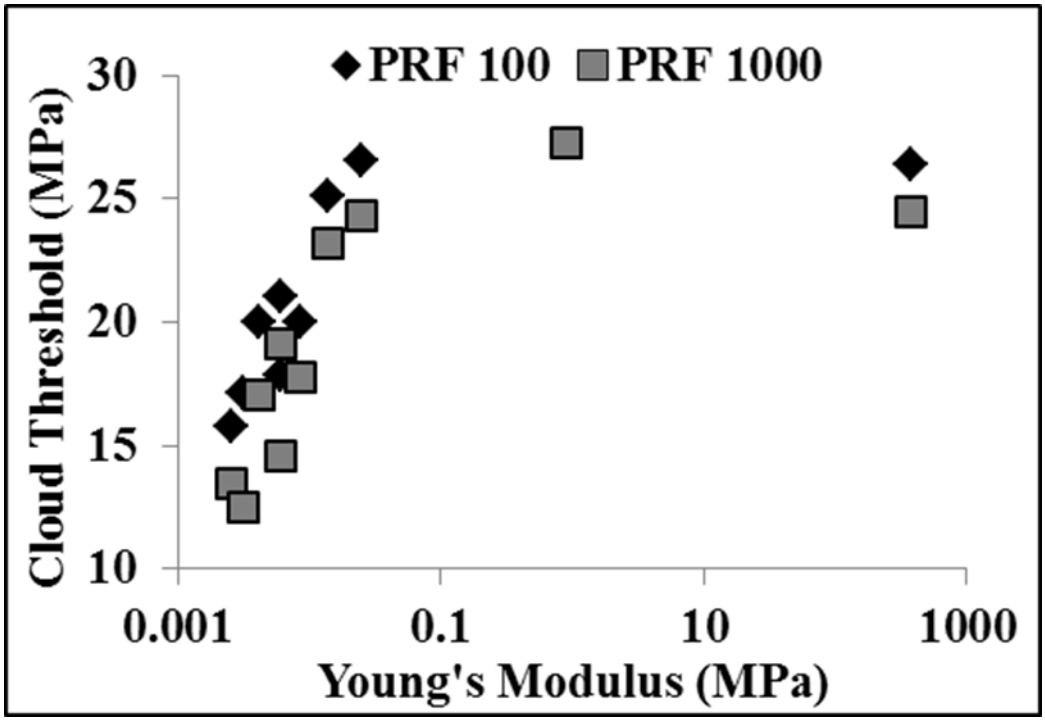

Figure 2.6. The initiation threshold of cavitation clouds induced by histotripsy in ex vivo porcine tissues plotted as a function of tissue Young's modulus.

2.3.3 Bubble Expansion Simulation

The effects of tissue Young's modulus on the growth of initial bubbles during histotripsy was investigated using a numerical simulation based on a linear Kelvin-Voigt model. Simulation results supported the hypothesis that increases in Young's modulus cause a reduction in bubble expansion [Fig. 2.7]. A plot showing the history of the bubble radius for a 10 nm initial bubble subjected to the first cycle of a histotripsy pulse at a peak negative pressure of 15 MPa demonstrated a decrease in bubble expansion as Young's moduli was varied from 1 kPa to 10 MPa. Following the passage of the pulse, the bubble rapidly expands, slows down as it reaches a maximum radius, and collapses violently. Increases in Young's modulus were shown to inhibit bubble growth as predicted as this elastic property ("spring-like" behavior) increases the isotropic stress on the bubble as the departure from the original configuration becomes larger

[40]. Results further showed that only a small reduction in bubble expansion was observed between Young's moduli of 1 kPa to 10 kPa while larger decreases in bubble expansion were observed as Young's moduli was increased to 100 kPa, 1 MPa, and 10 MPa. For instance, for a Young's modulus of 10 kPa, the growth was reduced by about 2% compared to 1 kPa, while the growth was reduced by ~12% at Young's modulus of 0.1 MPa, nearly a factor of 2 at Young's modulus of 1 MPa, and factor of 4 at a Young's modulus of 10 MPa. These decreases in expansion of initial bubbles have previously been shown to result in a decrease in shock scattering [16], which supports our hypothesis and helps explain why higher pressures are required for cloud initiation in tissues with higher Young's moduli.

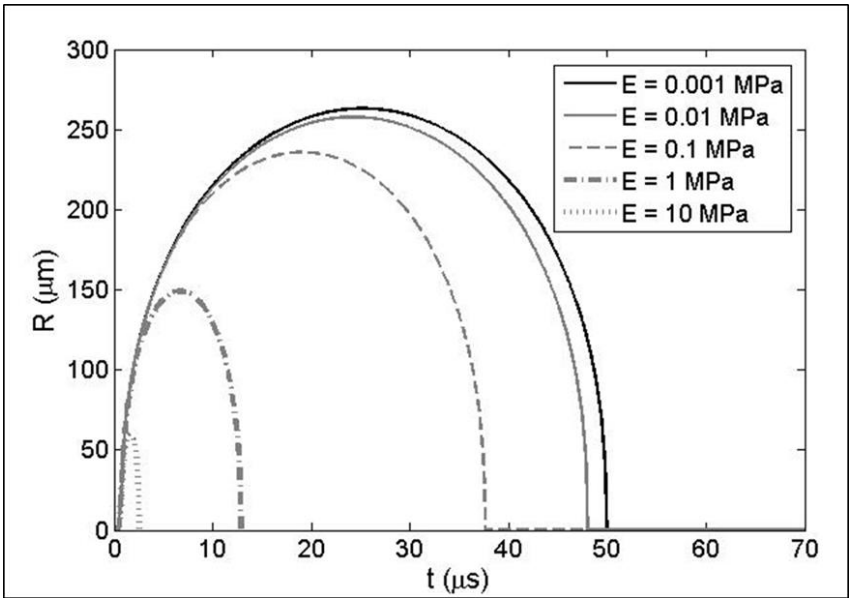

Figure 2.7. Simulation of initial bubble expansion in tissues of varied Young's modulus. Plot shows the bubble radius for a 10 nm initial bubble subjected to the first cycle of a histotripsy pulse at a peak negative pressure of 15 MPa with Young's moduli varied from 1 kPa to 10 MPa.

2.3.4 Bubble Behavior

The results from the bubble behavior experiments showed a significant decrease in both maximum bubble expansion and bubble cloud collapse time in tissue phantoms of increased mechanical stiffness [Fig.2.8] supporting our hypothesis and validating numerical simulation

results. The maximum bubble diameter was significantly higher in the 0.3% agarose compared to the higher concentration gels with the average maximum bubble diameter decreasing from 373.8±38.2 μm for the 0.3% phantom to 268.7±44.8 μm, 140.2±38.2 μm, and 58.4±23.4 μm for the 1%, 2.5%, and 5% phantoms, respectively. The bubble cloud collapse time followed a similar trend with a significantly shorter bubble cloud lifespan observed in the higher concentration phantoms. The average bubble cloud collapse time decreased from 98.5±12.0 μs for the 0.3% phantom to 86.5±7.5 μs, 53.5±2.5 μs, and 37.5±5.7 μs for the 1%, 2.5%, and 5% phantoms, respectively. All differences in maximum diameter and bubble collapse time were statistically significant ($p<0.05$). Control treatments in which bubble clouds generated by 200 identical pulses without the 2 μs delay increased demonstrated the average bubble size within the cloud remained consistent with no significant difference in bubble size over 200 pulses.

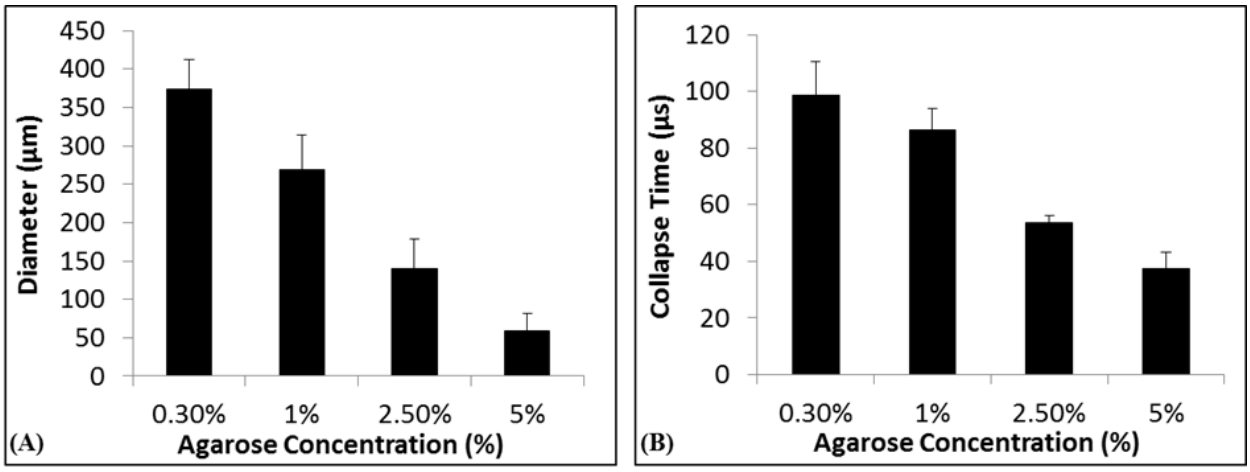

Figure 2.8. Bubble expansion in agarose tissue phantoms of varied concentration. Results show a significant decrease in (A) maximum bubble expansion and (B) bubble collapse time with increasing agarose concentration. All decreases in bubble diameter and collapse time between gel concentrations were considered significant (p-values<0.05).

2.4 Discussion

In this chapter, the effects of tissue mechanical properties on histotripsy bubble cloud initiation threshold were studied. The results of this work support our hypothesis that increases in

tissue mechanical stiffness lead to higher cloud initiation thresholds when the shock scattering mechanism is the mode of dense bubble cloud formation. This increase in initiation threshold for stronger tissues with higher Young's moduli was demonstrated in a mechanically tunable agarose tissue phantom as well as excised porcine tissue. The mechanism responsible for this increase in cavitation cloud threshold is hypothesized to be the result of decreased bubble expansion in tissue with higher mechanical stiffness, which leads to reduced shock scattering. Results further support this hypothesis as maximum bubble diameter was decreased in higher agarose concentration tissue phantoms.

The first part of this work investigated the effects of increased tissue mechanical stiffness on the pressure threshold to initiate a dense bubble cloud in histotripsy. Controlled increases in the stiffness of tissue phantoms consistently resulted in significant increases in the cavitation cloud initiation threshold. This trend of increasing threshold for tissues with higher Young's moduli was verified in *ex vivo* tissue. Results demonstrated a high correlation between the cavitation initiation threshold and tissue Young's modulus. Among the tissues tested, cavitation could not be generated in cartilage at 100 Hz PRF and bone at both 100 and 1000 Hz PRF. The finding that cloud initiation threshold is dependent on tissue properties explains previous observations where bubble cloud initiation was difficult to achieve within certain tissues such as cartilage and highly calcified aged plaque.

In addition to the shock scattering mechanism using multi-cycle ultrasound pulses, there is another mechanism for cloud formation by using shorter pulses (≤3 cycles). In a separate study [41], histotripsy bubbles have been generated in tissue phantoms and *ex vivo* tissues using a single 1-2 cycle pulse when the peak negative pressure exceeds a distinct threshold that seems to be intrinsic to the media, which is referred to as the "intrinsic threshold" of the tissue. The

intrinsic threshold is at the peak negative pressure of ~26-30 MPa in soft tissue containing mostly water and appears independent of tissue type with the exception of fat. With the extremely short pulse, bubble cloud initiation depends solely on the negative pressure, without contribution from shock scattering, resulting in bubble cloud formation matching the region of the focal region above the intrinsic threshold of ~26-30 MPa. This intrinsic threshold range is close to the peak negative pressure thresholds in tissues with high Young's moduli (tongue, tendon, cartilage) observed in this work (25-28 MPa) as well in the higher concentration 5% agarose tissue phantoms. This suggests that bubble cloud formation in tissues with higher Young's moduli was primarily driven by the negative pressure of the incident wave while the contributions of shock scattering were significantly decreased in tissues with higher Young's moduli probably due to suppressed bubble expansion, which was also observed. This finding further explains why the trend of increasing threshold with increasing Young's modulus was only observed to hold up to approximately 0.1 MPa. When the Young's modulus reached 0.1 MPa, the threshold saturated to near the intrinsic threshold for cloud initiation, and further increases in Young's modulus did not further increase the pressure threshold.

In order to initiate the dense lesion-forming bubble cloud observed in histotripsy using the shock scattering mechanism, single bubbles must expand during the initial cycles of the pulse in order for the shockwave to be effectively scattered. If these initial bubbles do not expand to sufficient size, a dense bubble cloud will not be initiated using shockwave scatter from these bubbles. For example, a previous study using a 1 MHz therapeutic transducer demonstrated that initial bubbles must expand to >80 μm in order to effectively scatter the shock wave and initiate a dense bubble cloud [16]. Simulations in this previous study further showed that, using an incident wave of 20 MPa peak negative pressure and 90 MPa peak positive pressure, increasing

initial bubble size from 100 μm to 200 μm resulted in a peak negative pressure increase from <30 MPa to >60 MPa. Our work shows that the expansion of initial bubbles was significantly decreased for higher Young's moduli, which would result in decreased shock scattering. The simulation shows that three orders of magnitude increase in the Young's modulus (from 1 kPa to 1MPa) results in 2-fold decrease in the maximum radius of the initial bubble. Correspondingly, the experimental results demonstrated a factor of 2 increase was observed in the threshold with a 10^3 increase in tissue Young's modulus. These results support our hypothesis that the increases in cloud initiation threshold are a result of impeded expansion of initial bubbles due to increases in tissue Young's modulus. As the Young's modulus provides only the simplest description of the elastic response of the material, future work will aim to develop a full model of the shock scattering process to predict the scattered pressure field in tissues with different microstructural mechanics and viscoelastic properties in order to better understand the results of this study.

The numerical simulation results were further supported by experiments showing decreased bubble expansion in tissue phantoms with higher Young's modulus. It is worth noting that the bubbles measured were within a cavitation cloud rather than the single bubbles formed during initial cycles of the pulse that were referred to in our hypothesis and modeled in the simulation. The initial bubbles were difficult to capture especially in higher agarose concentration phantoms due to the precise timing and ultrafast frame rate necessary to image them. The elastic properties of the media is expected to impact the expansion of bubbles within the cloud in a similar manner to the initial single bubbles essential to shock scattering and cloud initiation, which is suggested by the similar trend seen in both simulations and experiments. As a result of impeded bubble expansion in stiffer tissues, larger negative pressures are needed to expand initial bubbles to sufficient size for shock scattering. Additionally, an increase in the

positive pressure shock amplitude also probably contributes by increasing the amplitude of the reflected inverted shockwaves, which then interact with the incident negative pressure of the subsequent cycle to produce tensile pressures exceeding the intrinsic threshold of the tissue.

Understanding the dependence of bubble cloud initiation threshold on tissue mechanical properties will help guide future histotripsy treatments. For example, treatments in softer tissues such as kidney and fat can be initiated at lower acoustic pressures than those in firmer tissues such as heart and liver. Although results suggest histotripsy treatments may not be feasible in very stiff tissues such as tendon and cartilage, the observation that the cavitation cloud threshold is lower at higher PRFs may be utilized to decrease the acoustic pressure needed to initiate cavitation by increasing PRF if desired for these applications. The mechanism responsible for the decreased threshold at higher PRF is not completely understood. We hypothesize that the higher PRF pulses facilitate the growth of pre-existing nuclei in the focus to form the initial bubbles and achieve shock scattering. Future work is needed to investigate this hypothesis to determine the specific mechanism.

The suppression of bubble expansion and the decrease in the time until bubble collapse was observed in stiffer tissue phantoms. As the energetic bubble expansion and collapse is believed to cause tissue fractionation, this reduced bubble expansion will likely also result in a decrease in the rate and extent of tissue fractionation even in cases when a bubble cloud has been initiated. This finding further suggests that treating well above the intrinsic threshold may be necessary in order to achieve the bubble expansion needed for effective fractionation in stiffer tissues. Future work will investigate the bubble cloud dynamics and tissue fractionation in stiffer tissues of increasing mechanical strength and aim to develop strategies to increase bubble expansion and fractionation efficiency in stiffer tissues when needed.

The findings in this chapter may guide the development of a self-limiting tissue-selective fractionation technique using histotripsy. The mechanical strength and stiffness is higher for many vital tissues such as blood vessels and renal connecting system in comparison to other tissues such as liver and kidney. The differential threshold offers the ability to create a self-limiting tissue-selective ablation strategy which would spare stiffer tissues with higher mechanical strength while ablating other surrounding tissues, for example, ablating liver metastases while preserving the hepatic portal vein and artery or fractionating kidney tumors while protecting the collecting system.

2.5 Conclusion

In this chapter, the effects of tissue properties on histotripsy cavitation cloud initiation threshold were investigated. The results demonstrate a significant increase in cavitation initiation threshold for tissues of increased mechanical stiffness. Cavitation cloud initiation threshold increased in agarose tissue phantoms and porcine tissues with higher Young's modulus. The results further suggest that these increases in cavitation cloud initiation threshold are the result of decreased bubble expansion and reduced shock scattering in stiffer tissues. This work improves our understanding of how tissue mechanical properties affect histotripsy and provide a rational basis to tailor acoustic parameters for treatment of the specific tissues of interest.

2.6 References

[1] E. Vlaisavljevich, *et al.*, "Histotripsy-induced cavitation cloud initiation thresholds in tissues of different mechanical properties," *IEEE Trans Ultrason Ferroelectr Freq Control*, vol. 61, pp. 341-52, Feb 2014.

[2] J. E. Parsons, *et al.*, "Pulsed cavitational ultrasound therapy for controlled tissue homogenization," *Ultrasound Med Biol*, vol. 32, pp. 115-29, Jan 2006.

[3] W. W. Roberts, *et al.*, "Pulsed cavitational ultrasound: a noninvasive technology for controlled tissue ablation (histotripsy) in the rabbit kidney," *J Urol*, vol. 175, pp. 734-8, Feb 2006.

[4] Z. Xu, *et al.*, "Investigation of intensity thresholds for ultrasound tissue erosion," *Ultrasound in Medicine & Biology*, vol. 31, pp. 1673-1682, 2005.

[5] Z. Xu, *et al.*, "Controlled ultrasound tissue erosion," *IEEE Trans Ultrason Ferroelectr Freq Control*, vol. 51, pp. 726-36, Jun 2004.

[6] J. E. Parsons, *et al.*, "Spatial variability in acoustic backscatter as an indicator of tissue homogenate production in pulsed cavitational ultrasound therapy," *IEEE Trans Ultrason Ferroelectr Freq Control*, vol. 54, pp. 576-90, Mar 2007.

[7] T. L. Hall, *et al.*, "Histotripsy of rabbit renal tissue in vivo: temporal histologic trends," *J Endourol*, vol. 21, pp. 1159-66, Oct 2007.

[8] A. M. Lake, *et al.*, "Renal ablation by histotripsy--does it spare the collecting system?," *J Urol*, vol. 179, pp. 1150-4, Mar 2008.

[9] E. Vlaisavljevich, *et al.*, "Image-Guided Non-invasive Ultrasound Liver Ablation Using Histotripsy: Feasibility Study in an In Vivo Porcine Model," *Ultrasound Med Biol*, May 14 2013.

[10] J. B. Fowlkes and L. A. Crum, "Cavitation threshold measurements for microsecond length pulses of ultrasound," *J Acoust Soc Am*, vol. 83, pp. 2190-201, Jun 1988.

[11] C. K. Holland and R. E. Apfel, "Thresholds for transient cavitation produced by pulsed ultrasound in a controlled nuclei environment," *J Acoust Soc Am*, vol. 88, pp. 2059-69, Nov 1990.

[12] Z. Xu, *et al.*, "Investigation of intensity thresholds for ultrasound tissue erosion," *Ultrasound Med Biol*, vol. 31, pp. 1673-82, Dec 2005.

[13] A. J. Coleman, *et al.*, "The cavitation threshold of human tissue exposed to 0.2-MHz pulsed ultrasound: preliminary measurements based on a study of clinical lithotripsy," *Ultrasound Med Biol*, vol. 21, pp. 405-17, 1995.

[14] J. B. Fowlkes, *et al.*, "Acoustic generation of bubbles in excised canine urinary bladders," *J Acoust Soc Am,* vol. 89, pp. 2740-4, Jun 1991.

[15] F. J. Fry, *et al.*, "Threshold ultrasonic dosages for structural changes in the mammalian brain," *J Acoust Soc Am,* vol. 48, p. Suppl 2:1413+, Dec 1970.

[16] A. D. Maxwell, *et al.*, "Inception of Cavitation Clouds by Scattered Shockwaves," *IEEE Ultrasonics Symposium,* pp. 3B-2, 2010.

[17] G. R. Ter Harr, *et al.*, "Evidence for Acoustic Cavitation In Vivo: Thresholds for Bubble Formation with 0.75-MHz Continuous Wave and Pulsed Beams," *IEEE Trans Ultrason Ferroelectr Freq Control,* vol. 33, pp. 162-4, 1986.

[18] J. Gateau, *et al.*, "In vivo bubble nucleation probability in sheep brain tissue," *Phys Med Biol,* vol. 56, pp. 7001-15, Nov 21 2011.

[19] J. Gateau, *et al.*, "Statistics of acoustically induced bubble-nucleation events in in vitro blood: a feasibility study," *Ultrasound Med Biol,* vol. 39, pp. 1812-25, Oct 2013.

[20] A. D. Maxwell, *et al.*, "Cavitation clouds created by shock scattering from bubbles during histotripsy," *J Acoust Soc Am,* vol. 130, pp. 1888-98, Oct 2011.

[21] J. S. Allen and R. A. Roy, "Dynamics of gas bubbles in viscoelastic fluids. II. Nonlinear viscoelasticity," *J Acoust Soc Am,* vol. 108, pp. 1640-50, Oct 2000.

[22] J. S. Allen and R. A. Roy, "Dynamics of gas bubbles in viscoelastic fluids. I. Linear viscoelasticity," *J Acoust Soc Am,* vol. 107, pp. 3167-78, Jun 2000.

[23] J. B. Freund, "Suppression of shocked-bubble expansion due to tissue confinement with application to shock-wave lithotripsy," *J Acoust Soc Am,* vol. 123, pp. 2867-74, May 2008.

[24] J. Jimenez-Fernandez and A. Crespo, "Bubble oscillation and inertial cavitation in viscoelastic fluids," *Ultrasonics,* vol. 43, pp. 643-51, Aug 2005.

[25] X. Yang and C. C. Church, "A model for the dynamics of gas bubbles in soft tissue," *J Acoust Soc Am,* vol. 118, pp. 3595-606, Dec 2005.

[26] E. A. Zabolotskaya, *et al.*, "Modifications of the equation for gas bubble dynamics in a soft elastic medium," *J Acoust Soc Am,* vol. 118, pp. 2173-81, Oct 2005.

[27] J. E. Parsons, *et al.*, "Cost-effective assembly of a basic fiber-optic hydrophone for measurement of high-amplitude therapeutic ultrasound fields," *J Acoust Soc Am,* vol. 119, pp. 1432-40, Mar 2006.

[28] V. Normand, *et al.*, "New insight into agarose gel mechanical properties," *Biomacromolecules,* vol. 1, pp. 730-8, Winter 2000.

[29] M. Warnez and E. Johnsen, "Numerical investigations of inertial cavitation in viscoelastic media.," *In Preparation,* 2013.

[30] F. A. Duck, *Physical properties of tissue: a comprehensive reference book.* : Academic Press, 1990.

[31] V. Egorov, *et al.*, "Soft tissue elastometer," *Med Eng Phys,* vol. 30, pp. 206-12, Mar 2008.

[32] M. Geerligs, *et al.*, "Linear viscoelastic behavior of subcutaneous adipose tissue," *Biorheology,* vol. 45, pp. 677-88, 2008.

[33] R. L. Kane, *et al.*, "Ventricular elastic modulus as a function of age in the Syrian golden hamster," *Circ Res,* vol. 38, pp. 74-80, Feb 1976.

[34] T. A. Krouskop, *et al.*, "A pulsed Doppler ultrasonic system for making noninvasive measurements of the mechanical properties of soft tissue," *J Rehabil Res Dev,* vol. 24, pp. 1-8, Spring 1987.

[35] S. J. Lai-Fook and R. E. Hyatt, "Effects of age on elastic moduli of human lungs," *J Appl Physiol,* vol. 89, pp. 163-8, Jul 2000.

[36] J. Y. Rho, *et al.*, "Young's modulus of trabecular and cortical bone material: ultrasonic and microtensile measurements," *J Biomech,* vol. 26, pp. 111-9, Feb 1993.

[37] H. U. Staubli, *et al.*, "Mechanical tensile properties of the quadriceps tendon and patellar ligament in young adults," *Am J Sports Med,* vol. 27, pp. 27-34, Jan-Feb 1999.

[38] H. Yamada, *Strength of biologic materials.* . New York: Robert E. Kreiger, 1973.

[39] Y. Zheng and A. F. Mak, "Effective elastic properties for lower limb soft tissues from manual indentation experiment," *IEEE Trans Rehabil Eng,* vol. 7, pp. 257-67, Sep 1999.

[40] C. Y. Hua and E. Johnsen, "Nonlinear oscillations following the Rayleigh collapse of a gas bubble in a linear viscoelastic (tissue-like) medium," *Physics of Fluids,* vol. 25, Aug 2013.

[41] A. D. Maxwell, *et al.*, "Probability of cavitation for single ultrasound pulses applied to tissues and tissue-mimicking materials," *Ultrasound Med Biol,* vol. 39, pp. 449-65, Mar 2013.

Chapter 3

Effects of Ultrasound Frequency and Tissue Stiffness on the Histotripsy Intrinsic Threshold for Cavitation

A majority component of this chapter has been published in *Ultrasound in Medicine and Biology*

3.1 Introduction

Histotripsy is a noninvasive tissue ablation method that controllably fractionates soft tissue through cavitation generated by high pressure (>10 MPa), short duration (<20μs) ultrasound pulses at low duty cycles (<1 %) [2-4]. Histotripsy depends on the initiation and maintenance of a dense cavitation bubble cloud to produce mechanical tissue fractionation [4, 5]. With sufficiently high pressure and dose, histotripsy can completely fractionate soft tissue into an acellular liquid homogenate, resulting in effective tissue disintegration [4, 6].

Previous work has demonstrated two mechanisms in which a histotripsy cavitation cloud can be generated. In the first, termed the "shock scattering mechanism," a dense bubble cloud is formed from a single multi-cycle histotripsy pulse (e.g., 3–20 cycles) using shock scattering from sparse initial bubbles formed and expanded during the initial cycles of the pulse [7]. In this process, single or sparse initial bubbles, which for the purpose of this study will be termed "incidental bubbles," are formed from large heterogeneous nuclei in the focus or due to the growing of cavitation nuclei over multiple cycles [8, 9]. These incidental bubbles are formed

significantly below the intrinsic threshold, which is termed as the threshold to generate cavitation directly from the incident negative pressure phase of a single cycle pulse. These incidental bubbles act as pressure release surfaces wherein the following positive pressure shock fronts are inverted and superimposed on the incident negative pressure phase to form negative pressures that produce a dense cavitation cloud growing back toward the transducer [7]. Using the shock scattering mechanism, bubble clouds are initiated at negative pressures ranging from 10-28 MPa. Because of the complexity of the shock scattering process, multiple factors determine whether a cloud is initiated, including the distribution of heterogeneous nuclei in the focal region, the size and shape of initial single bubbles, the number of cycles, the shock rise time, and the positive pressure amplitudes [7, 8, 10, 11]. Additionally, our previous study demonstrated that increases in tissue stiffness result in higher cloud initiation thresholds when using the shock scattering mechanism of bubble cloud formation [10]. The mechanism responsible for this increase was hypothesized to be decreased bubble expansion in tissues with higher Young's modulus, which leads to reduced shock scattering [10]. Results of that study suggested that bubble cloud formation in tissues with Young's moduli >100 kPa was primarily driven by the negative pressure of the incident wave while the contributions of shock scattering were significantly decreased due to suppressed bubble expansion [10].

In addition to the shock scattering mechanism that uses a multi-cycle ultrasound pulse, there is another mechanism for histotripsy cloud formation termed the "intrinsic threshold mechanism," in which a 1-2 cycle pulse with a single dominant negative pressure phase is used to generate a bubble cloud directly from the negative pressure of the incident wave [12, 13]. With these short pulses, cavitation initiation depends solely on the negative pressure when it exceeds a distinct threshold intrinsic to the medium, without the contributions from shock

scattering, resulting in a bubble cloud matching the portion of the focal region above the intrinsic threshold [12, 13]. In contrast to shock scattering, it is possible that the histotripsy intrinsic threshold will not be affected by changes in tissue stiffness, since the intrinsic threshold mechanism of cloud initiation does not rely on the expansion of initial incidental bubbles in order to initiate a dense bubble cloud. In the previous study by Maxwell *et al*, an intrinsic threshold of approximately 26-30 MPa was observed for water based soft tissues and tissue phantoms using a 1.1 MHz histotripsy transducer, while the threshold for tissue composed primarily of lipids was significantly lower (15.4 MPa for adipose tissue) [13]. However, Maxwell *et al* was limited to the measurement of the cavitation probability at a single ultrasound frequency (1.1 MHz) and in tissue phantoms and soft tissues with a limited range of Young's moduli ($\leq$ 36 kPa) [13].

In this chapter, we investigate the effects of tissue stiffness and ultrasound frequency on the histotripsy intrinsic threshold in tissues with a wide range of Young's moduli using multiple frequencies. To accomplish this goal, the probability of inertial cavitation was measured by subjecting water, mechanically tunable agarose tissue phantoms, and various *ex vivo* tissues covering a wide range of stiffness (Young's moduli=1.13 kPa–380 MPa) to histotripsy pulses produced by 345 kHz, 500 kHz, 1.5 MHz, and 3 MHz histotripsy transducers. The intrinsic threshold was defined as the peak negative pressure at which the probability of generating cavitation, p_{cav}, from a single histotripsy pulse was p_{cav}=0.5. As previous studies show that there is a significant difference in the intrinsic threshold between water-based tissues and lipid-based tissues, and, since the former type covers most soft tissues, we focused on water-based tissues in this study. The results of this chapter will help explain the role of ultrasound frequency and tissue stiffness in generating a histotripsy bubble cloud using the intrinsic threshold method.

In the final part of this chapter, two numerical models are used to investigate the potential characteristics of the "intrinsic nuclei" in tissue. Previous work by Maxwell *et al*. suggested that the histotripsy intrinsic threshold relies upon cavitation nuclei that are intrinsic to the tissue [13]. By intrinsic, we mean that the nuclei appear to be associated with the properties of the medium itself rather than impurities. Although it is possible that these nuclei too are related to impurities, it seems unlikely, as several groups using different sample processing methods have measured approximately the same threshold for inertial cavitation associated with these nuclei in the range of 24 to 33 MPa in distilled water [13-17]. Various theoretical studies suggest that the intrinsic nuclei can be modelled as semi-permanent stabilized gas nuclei caused by impurities in the liquid [16, 18-20] or spontaneous nuclei that form bubbles in a medium by energy-density fluctuations described by classical nucleation theory [21-24]. In the previous study by Maxwell *et al*., a theoretical simulation using a 2.5 nm stabilized nuclei resulted in a cavitation threshold closely matching experiments [13]. However, it remains unclear if the intrinsic nuclei are small, stabilized gas nuclei or spontaneous nuclei. Therefore, in this chapter, two separate simulations were performed to investigate the pressure thresholds predicted by spontaneous and nanometer-sized stable nuclei, with the intention to provide a theoretical explanation for the intrinsic thresholds measured experimentally.

3.2 Methods

3.2.1 Sample Preparation

The intrinsic cavitation threshold was tested for distilled water, mechanically tunable agarose tissue phantoms, and *ex vivo* bovine tissues (liver, tongue, and tendon). The agarose

tissue phantoms and *ex vivo* tissues selected are all water-based, as this paper focuses on water-based tissue. Cavitation probability versus pressure was measured in three samples of each type.

First, the effect of ultrasound frequency on the cavitation threshold was tested in distilled, degassed water (15% O_2). Water was degassed prior to experiments in order to minimize any stable gas bubbles in the sample. Water samples were degassed by repeated boiling and then placing the sample to cool under a partial vacuum (~20 kPa, absolute) for 30 minutes. For comparison, the threshold in minimally degassed water (90% O_2), was also investigated. Gas saturation was measured using an O_2 meter (DO200; YSI, Yellow Springs, OH, USA).

To compare the effects of tissue stiffness on the cavitation threshold, mechanically tunable agarose tissue phantoms were used to provide a well-controlled elastic medium for this study. Agarose phantoms were selected to cover the mechanical stiffness of tissues found in the body from non-load bearing tissues such as lung, liver, and kidney (Young's moduli ranging from 1-10 kPa) to strong load bearing tissues such as cartilage (Young's moduli of ~1 MPa). Agarose phantoms of 0.3%, 1%, 2.5%, and 5% w/v were prepared by slowly mixing agarose powder (Agarose Type VII; Sigma-Aldrich, St. Louis, MO, USA) into saline solution (0.9% sodium chloride; Hospira, Lake Forest, Illinois, USA) heated to boiling temperature. The solution was stirred on a hot plate until the gel turned completely transparent and then allowed to boil for ten minutes. After boiling, solutions were allowed to cool and were degassed under a partial vacuum (~20 kPa, absolute) for 30 minutes. After degassing, the solution was poured into tissue phantom holders and placed in a refrigerator at 4°C to allow the agarose solution to solidify prior to use. The mechanical properties of the agarose phantoms were measured using a parallel-pate AR-G2 rheometer (TA Instruments, New Castle, DE, USA) on a Peltier stage, similar to previous studies [25, 26]. The stage was initially heated to 90°C, and samples were

allowed to melt for 1 minute before the top plate was lowered to create a gap of 1000 μm. The stage was cooled to 60°C and excess solution was wiped off and the gap was sealed with mineral oil (Sigma, St. Louis, MO, USA) to prevent evaporation. Samples were held at 60°C for two minutes to ensure a uniform starting temperature, and then cured at 4°C for 20 minutes. The samples were then heated to 20°C for 10 minutes and the mechanical properties were measured. The shear modulus (G) was measured at a frequency of 0.1 radian per second with 0.05% strain for 5% and 2.5% tissue phantoms and 0.1% strain for 1% and 0.3% tissue phantoms. Three independent samples were measured for each weight percent, with the results reported as the mean ± a 95% confidence interval. The Young's modulus (E) was estimated from the shear modulus as E=3G [Table 3.1].

Table 3.1 Sample mechanical properties. Table shows the Young's modulus, density, and water content values for all samples tested in this study. The Young's modulus of agarose tissue phantoms was measured using shear rheology (E=3G). Ex vivo bovine liver, tongue, and tendon were used to cover a large range of tissue Young's modulus as measured in the literature [27-33].

	Young's Modulus (kPa)	Density (kg/m³)	Water Content (%)
Water	-	998	100
0.3% Agarose	1.13±.047	1003.0	98.8
1% Agarose	21.7±1.0	1010.0	98.1
2.5% Agarose	242±27	1025.0	96.7
5% Agarose	570±46	1050.0	94.3
Liver	8.7	1060	74.2
Tongue	25	-	66
Tendon	380,000	1165	63

For *ex vivo* tissue experiments, fresh bovine liver, tongue, and tendon were excised at a local slaughter house and immediately placed into degassed 0.9% saline solution and stored at 4°C until experiments. Tissue samples were sectioned and warmed to room temperature in degassed saline under a partial vacuum (~20 kPa, absolute) for 4 hours prior to experiments. Each sample was embedded in a 1% agarose tissue phantom, which was prepared as described above. The samples were embedded in agarose to fix the position of the tissue and displace any

remaining air. All tissue samples were several cm in the dimension transverse to the acoustic axis and at least 1 cm in dimension along the acoustic axis as positioned during testing. All tissues were used within 48 hours of harvesting. In order to compare the cavitation threshold results with tissue stiffness, Young's modulus values from literature were chosen as a tissue mechanical property metric for this study and are provided in [Table 3.1] [27-33].

3.2.2 Histotripsy Pulse Generation

Histotripsy pulses were generated at four ultrasound frequencies (345 kHz, 500 kHz, 1.5 MHz, and 3 MHz) using three custom-built histotripsy transducers. The 345 kHz pulses were generated by a twenty element array transducer with a geometric focus of 150 mm, an aperture size of 272 mm, and an f-number of 0.55. The 1.5 MHz pulses were generated by a six element array transducer with a geometric focus of 55mm, an aperture of 79 mm in the elevational direction and 69 mm in the lateral direction, and effective f-numbers of 0.7 and 0.8 in the elevational and lateral directions, respectively. The 500 kHz and 3 MHz pulses were generated by a dual frequency array transducer that consisted of twelve 500-kHz elements and seven 3-MHz elements. For the 500 kHz elements, the geometric focus was 40 mm, the aperture size was 71 mm, and the f-number was 0.56. For the 3 MHz elements, the geometric focus was 40 mm, the aperture size was 80 mm, and the f-number was 0.5. The design of this dual frequency transducer has been described in detail in a previous study [34].

To measure the intrinsic threshold in each sample, short pulses with a single dominant negative pressure phase were applied to the sample [Fig. 3.1]. We expect that the differences in the f-numbers of the transducers do not impact the intrinsic threshold measurements, as the intrinsic threshold depends primarily on the negative pressure phase of the pulse and is not

affected by the positive pressure phase or nonlinear propagation, although it may be affected by differences in the beam dimensions [12, 13]. To generate a short therapy pulse, a custom high-voltage pulser developed in-house was used to drive the transducers. The pulser was connected to a field-programmable gate array (FPGA) development board (Altera DE1 Terasic Technology, Dover, DE, USA) specifically programmed for histotripsy therapy pulsing. This setup allowed the transducers to output short pulses consisting of less than two cycles. A fiber-optic probe hydrophone (FOPH) built in-house [35] was used to measure the acoustic output pressure of the transducers. At higher pressure levels, the acoustic output could not be directly measured due to cavitation at the fiber tip. These pressures were estimated by a summation of the output focal *p*-values from individual transducer elements. This approximation assumes minimal nonlinear distortion of the waveform occurs within the focal region. In a previous study [13], this estimated *p*- was found to be accurate within 15% compared to direct focal pressure measurements in water and in a medium with a higher cavitation threshold, 1,3 butanediol.

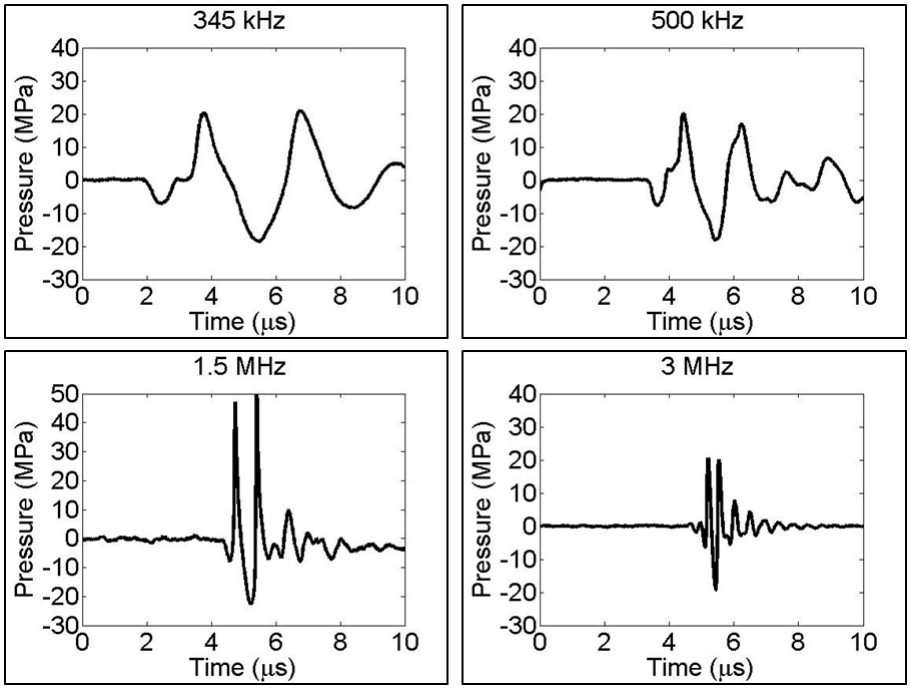

Figure 3.1. Histotripsy waveforms. Plots showing example histotripsy waveforms produced by 345 kHz, 500 kHz, 1.5 MHz, and 3 MHz histotripsy transducers.

For threshold experiments, histotripsy pulses were applied inside different samples at a pulse repetition frequency (PRF) of 0.5 Hz. The PRF was kept very low to minimize the possibility that cavitation from one pulse would change the probability of cavitation on a subsequent pulse. In a previous study [13], it was demonstrated that for PRFs > 1 Hz, cavitation during a pulse increased the likelihood of cavitation on a following pulse, but this effect was not observed for PRFs below 1 Hz, since the residual nuclei from a histotripsy pulse dissolve within ~1 second after the histotripsy pulse. In solid samples, the focus was translated for each pulse by 1 mm transverse to the acoustic propagation direction in a 10 × 10 grid for each pressure level in order to minimize the effects of cavitation damage to the solid sample altering the probability of cavitation. Although each focal volume only received a single pulse for solid samples, the PRF was kept at a low rate of 0.5 Hz for consistency. Translating the volume and using a low PRF were both done to prevent the effects of the previous pulse from affecting the results on a subsequent pulse. At each pressure level tested, 100 pulses were applied to the sample.

3.2.3 Cavitation Detection using Optical Imaging

High speed optical imaging was used as a method to detect cavitation for water and agarose tissue phantoms using two high speed cameras [Fig. 3.2]. The cameras were triggered to record one image for each applied pulse at a time point approximately corresponding to the maximum bubble expansion for each sample and frequency combination. These time points were determined prior to experiments in a separate study by changing the delay time on the camera to reconstruct representative radius vs. time curves of the bubbles and identify the time corresponding to maximum bubble expansion [36]. For experiments with the 345 kHz and 1.5 MHz transducers, a high-speed, 1 megapixel CCD camera (Phantom V210, Vision Research,

Wayne, NJ, USA) was aligned with the transducer and backlit by a continuous white-light source. The camera was focused using a macro-bellows lens (Tominon 1:4.5, F=105 mm; Kyocera, Kyoto, Japan), giving the captured images a resolution of approximately 5.9 μm per pixel and 3.4 μm per pixel for 345 kHz and 1.5 MHz, respectively. For experiments with the 500 kHz and 3 MHz dual frequency transducer, a digital, 1.3-megapixel CCD camera (PN: FL3-U3-13Y3M-C, Flea® 3; PointGrey, Richmond, BC, Canada) was positioned perpendicularly to the dual-frequency array transducer facing one of its optical windows. A Nikon 4X objective (MRP70040; Nikon, Chiyoda, Tokyo, Japan) was attached to the camera with extension tubes to magnify the image plane, giving the captured images a resolution of approximately 2.5 μm per pixel. A pulsed white-light LED was placed on the diametrically-opposed optical window of the dual-frequency array transducer, which provided back-lit illumination. The camera exposure time was 2 μs for all images. After acquisition, shadowgraph images were converted from grayscale to binary by an intensity threshold determined by the background intensity using image processing software (MATLAB; The Mathworks, Natick, MA, USA). Bubbles were indicated as any black regions >5 pixels in diameter. By this criterion, the minimum resolvable bubble radius was 14.75 μm, 6.25 μm, 8.5 μm, and 6.25 μm for the 345 kHz, 500 kHz, 1.5 MHz, and 3 MHz transducers, respectively. The number of frames that contained cavitation bubbles was recorded, and the fraction of total frames (out of 100) for which any cavitation was detected was determined as the cavitation probability.

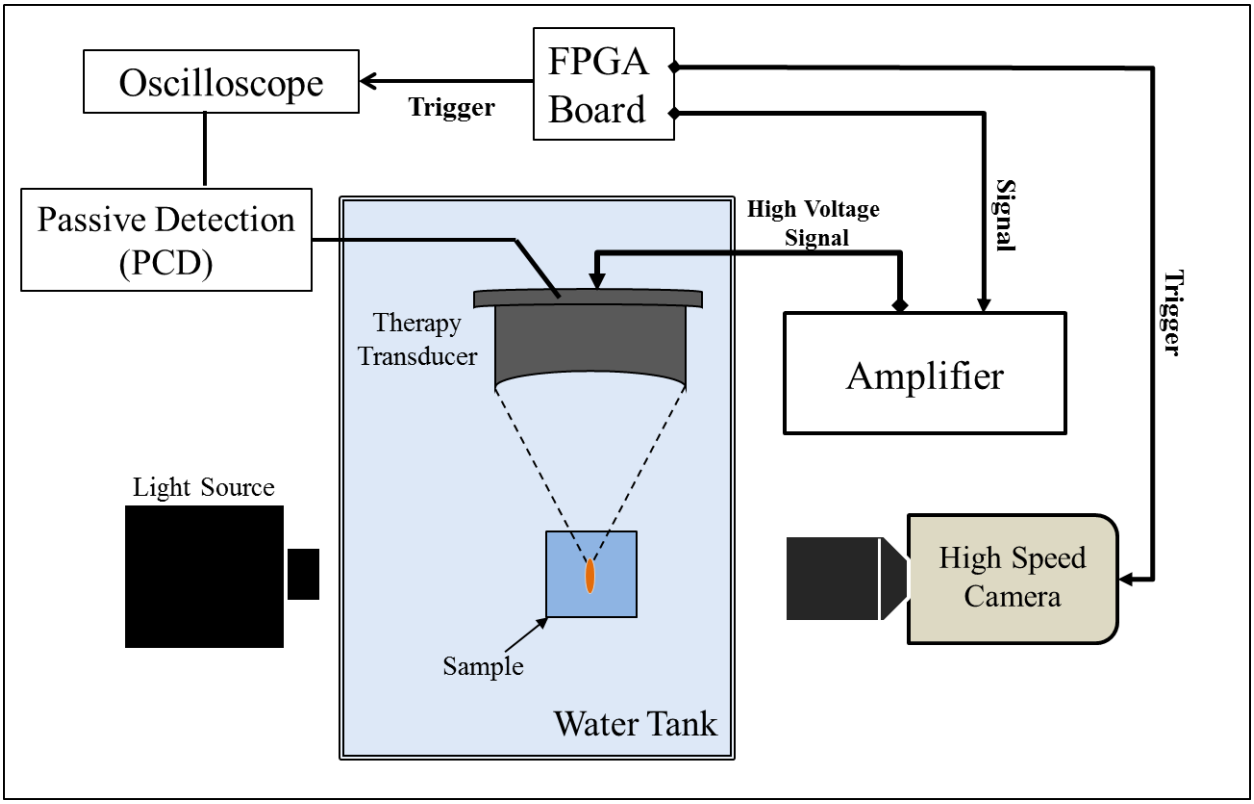

Figure 3.2. Experimental setup. Histotripsy pulses were applied to the inside of water, mechanically tunable tissue phantoms, and various ex vivo bovine tissues. Cavitation was monitored using high speed optical imaging for transparent samples. Additionally, cavitation was monitored using one of the therapy transducer elements as passive cavitation detection for all samples.

3.2.4 Passive Cavitation Detection (PCD)

High speed imaging simplifies the detection of cavitation in transparent media but could not be used with tissue samples. As a result, an acoustic method was also used to identify cavitation in the focal zone in all media. Additionally, since relying upon an image of the bubbles taken at a single time point is a potential limitation, the PCD method allowed cavitation to be monitored over a much longer time period following the passage of the pulse. For each experiment, one of the transducer's therapy elements was also used for PCD to detect the presence of cavitation in the focal region [Fig 3.2]. The PCD signal was connected to an oscilloscope (LT372; Lecroy, Chestnut Ridge, NY, USA) with the time window selected to

record the backscattering of the therapy pulse from cavitation bubbles [13, 17, 37]. To determine whether cavitation occurred during a pulse, the signal generated by backscattering of the incident pulse from the focus was analyzed following the method used in the previous study by Maxwell *et al* [13]. In this process, a bubble is generated by the negative pressure phase of the pulse, and the following positive pressure is then scattered off the bubble and detected by the PCD. It should be noted, however, that subsequent bubbles aren't formed from shock scattering in this case since the pulse contains a single dominant negative phase. Previous work has demonstrated that generating a bubble cloud from shock scattering requires both the scattering of the positive pressure and the constructive interference with the subsequent negative cycles to generate bubbles [7, 8, 10]. Although some positive pressure is scattered here, there are no (or very small) following negative pressure cycles to constructively interfere with the scattered shockwave. The exception to this would be if the reflected shock directly exceeds the intrinsic threshold which would not be expected (and wasn't observed) under the conditions used in this study. The backscattered pressure amplitude was received by the PCD at the time point corresponding to two times the time of flight for the focal length of the respective transducers. The integrated frequency power spectrum (S_{PCD}) of the backscatter signal was used as a measure of whether cavitation occurred according to the method previously described by Maxwell *et al* [13].

3.2.5 Intrinsic Threshold Measurement and Comparison

The probability of observing cavitation followed a sigmoid function, given by

$$P(p_-) = \frac{1}{2} + erf\left(\frac{p_- - p_{int}}{\sqrt{2\sigma^2}}\right) \quad (\mathbf{E3.1})$$

where *erf* is the error function, p_{int} is the negative pressure at which the probability p_{cav}=0.5, σ is a variable related to the width of the transition between p_{cav}=0 and p_{cav}=1, with ± σ giving the

difference in pressure from about p_{cav}=0.15 to p_{cav}=0.85 for the fit [13]. The intrinsic threshold for each sample, p_{int}, is defined as the p- corresponding to p_{cav}=0.5 as calculated by the curve fit. Curve fitting for all data sets was performed using an OriginLab curve fitting program (OriginPro 9.1; OriginLab Corporation, Northampton, MA, USA). The fit curves for all samples were analyzed statistically to determine whether the differences in the values of p_{int} were significantly different from each other. The standard errors for p_{int} were estimated by a covariance matrix using the delta method [38]. The curves were compared using a two-sample t-test with statistic $t\left(p_{int1}-p_{int2},\sqrt{SE_1^2+SE_2^2}\right)$ at a 95% confidence interval. Results were considered statistically significant for $p<0.05$. Note that the standard error does not include the uncertainty in absolute pressure from the hydrophone measurement, only the uncertainty in the fit, because the values p_{int} are relative.

3.2.6 Threshold Simulation: Stabilized Nuclei

To provide a theoretical explanation to the experimental results, a numerical model based on a linear Kelvin-Voigt model was used to investigate the effects of tissue stiffness and ultrasound frequency on the pressure threshold, assuming that the intrinsic threshold is due to nanometer-sized stabilized cavitation nuclei in the tissue. In a previous study, a similar model showed a pressure threshold matching the histotripsy intrinsic threshold at 1.1 MHz when an initial bubble radius of 2.5 nm was used, corresponding with a threshold for inertial cavitation of 28.1 MPa [13]. For nuclei of this size, surface tension dominates the cavitation threshold, similar to the Blake threshold [13, 39, 40]. To test the effects of tissue stiffness and ultrasound frequency on the threshold for generating inertial cavitation, simulations exposed a 2.5 nm initial bubble to a single peak negative pressure

$$p_a(t) = \begin{cases} p_A \left(\frac{1+\cos[\omega(t-\delta)]}{2} \right)^n, & |t-\delta| \leq \frac{\pi}{\omega} \\ 0, & |t-\delta| > \frac{\pi}{\omega} \end{cases} \quad (\mathbf{E3.2})$$

where p_A is the peak negative pressure, ω is the angular frequency of the experimental ultrasound wave, δ is a time delay, and *n* is a curve-fitting parameter which was set to 3.7 so that the shape of the simulated waveform *p*- closely matched the shape and duration of the *p*- from the histotripsy waveforms used experimentally. It should be noted that these theoretical waveforms were used for simulations instead of the experimentally measured waveforms [Fig 3.1]. The positive pressure of the experimentally measured waveforms caused rapid collapse of the bubbles that did not match experiments. One explanation for the mismatch is that the bubble scattered the positive portion of the waveform without shrinking. While this is a limitation of the current model, it is likely an appropriate assumption considering previous work showing that the bubbles formed using the intrinsic threshold method are generated directly from the negative pressure of the incident wave and do not depend on the positive pressure [12, 13].

For this study, we assume the surrounding medium to have homogeneous properties, and that the bubble contains air and remains spherical. These assumptions allow us to use a numerical model developed in-house for simulating spherical bubble dynamics in a viscoelastic medium with viscous, elastic, relaxation and retardation effects, including liquid compressibility and heat transfer. Since the present focus is on the initial threshold behavior and the resulting growth, we neglect heat transfer and consider a simple viscoelastic model (linear Kelvin-Voigt) that includes viscosity and elasticity [41]. In the Kelvin-Voigt model, the stress tensor τ is related to the deformation tensor γ and the rate of deformation tensor $\dot{\gamma}$ through

$$\tau = 2G\gamma + 2\mu\dot{\gamma} \quad (\mathbf{E3.3})$$

where G is the shear modulus (elasticity) and μ is the viscosity. The stress tensor is related to the bubble radius R through the Keller-Miksis equation [42]

$$\left(1-\frac{\dot{R}}{c}\right)R\ddot{R}+\frac{3}{2}\left(1-\frac{\dot{R}}{3c}\right)\dot{R}^2=\frac{1}{\rho}\left(1+\frac{\dot{R}}{c}+\frac{R}{c}\frac{d}{dt}\right)\left(p_g-\frac{2S}{R}-p_\infty(t)+3\int_R^\infty\frac{\tau_{rr}}{r}dr\right) \quad (\mathbf{E3.4})$$

which depends on the medium's sound speed c, density ρ, and surface tension against air S. Here $p_\infty(t)$ is the absolute forcing pressure, r is the radial coordinate, and overdots ($\dot{}$) denote derivatives with respect to time, t. The air within the bubble is assumed to have spatially uniform pressure given by the polytropic relationship

$$p_g=p_0\left(\frac{R_0}{R}\right)^{3\kappa} \quad (\mathbf{E3.5})$$

where κ=1.4 is the ratio of specific heats for air, R_0 is the initial bubble radius, and $p_0=p_\infty(0)+2S/R_0$ is the initial bubble pressure. Using the Yang and Church model,

$$3\int_R^\infty\frac{\tau_{rr}}{r}dr=-\frac{4G}{3}\left(1-\frac{R_0^3}{R^3}\right)-\frac{4\mu\dot{R}}{R} \quad (\mathbf{E3.6})$$

the Keller-Miksis equation can be solved for the bubble wall acceleration $\ddot{R}$ and integrated in time [41]. The properties ρ=1000 kg/m^3, c=1497 m/s^2, μ=1.00 mPa-s (viscosity of water), and S=72 mN-m (water-air surface tension) were used to approximate the surrounding medium. The Young's modulus (approximated for soft tissue as E = 3G) was varied in decades from 1 kPa to 10 MPa to compare the effects of Young's modulus on the cavitation threshold. Ultrasound frequencies were 345 kHz, 500 kHz, 1.5 MHz, and 3 MHz for comparison with experimental results. The maximum bubble radius was plotted as a function of the peak negative pressure using different ultrasound frequencies and tissue Young's moduli for initial bubble nuclei of 2.5 nm. A further simulation was conducted to investigate the threshold as a function of initial nuclei size in order to determine the range of nuclei corresponding the experimentally measured

thresholds. The pressure threshold for this simulation was defined as the pressure required to expand an initial bubble to >15 μm in radius, to be consistent with the minimum resolution for optical images recorded experimentally. This criteria is more reasonable for histotripsy therapy than the commonly used criteria for inertial cavitation of R_{max}>2 $R_{0,}$ since previous work has shown that histotripsy bubbles must be sufficiently expanded to sizes much greater than $2R_0$, often >50 μm, in order to fractionate tissue [2, 11, 36, 43] .

3.2.7 Threshold Simulation: Spontaneous Nucleation

High To investigate the effects of ultrasound frequency on the cavitation threshold predicted for spontaneous nucleation, a theoretical analysis was performed based on classical nucleation theory (CNT) [17, 21, 24]. Previous studies using CNT suggest that the cavitation threshold decreases at lower frequency due to the larger focal volume and increased duration of the applied *p*- [21, 24]. The threshold predicted by CNT, p_{t_CNT}, was calculated as

$$p_{t\_CNT} = \left(\frac{16\pi\alpha^3}{3k_bT * \ln\frac{\Gamma_0 V_f \tau_f}{\ln 2}} \right)^{0.5} \quad (\mathbf{E3.7})$$

where α is the surface energy, k_b is the Boltzmann's constant, T is temperature in Kelvin, Γ_0 is a prefactor, V_f is the focal volume for a given frequency, and τ_f is the time the focal volume is above a given pressure [17, 21-24]. Γ_0 was set to Γ_0=10^{33} similar to previous work [24] and T was set to 293K to match experiments. V_f and τ_f were modified for each frequency with τ_f set to one fourth of the acoustic period and V_f representing the focal volume of each transducer. The values of V_f were calculated from the -6 dB FWHM beam profiles of the transducers used in this study assuming an ellipsoidal focus, and were 47.07 mm^3, 7.89 mm^3, 2.30 mm^3, and 0.072 mm^3, for 345 kHz, 500 kHz, 1.5 MHz, and 3 MHz, respectively. The surface energy, α, was set to 18.8

mN/m, ~25% of the macroscopic surface tension of water. This value for surface energy was chosen such that results matched the experimental threshold at 500 kHz. Previous work has suggested that, since the cavitation nucleus has a nanoscopic size, it is not accurate to use the bulk, macroscopic surface tension value for surface energy [17, 22]. The surface energy value used in this study closely matches the value calculated in a previous study by Herbert et al., and resulted in more reasonable results for p_{t_CNT} than those calculated using the macroscopic values of surface tension [17].

3.3 Results

3.3.1 Intrinsic Threshold in Water

To investigate the effects of ultrasound frequency on the intrinsic threshold, histotripsy pulses were first applied to distilled, degassed water using the 345 kHz, 500 kHz, 1.5 MHz, and 3 MHz histotripsy transducers. Optical imaging results show that the intrinsic threshold, p_{int}, in water was found to be between p_{int} = 24.9−27.7 MPa, with σ_{mean} = 1.6 MPa for 345 kHz; p_{int} = 25.8−26.7 MPa, with σ_{mean} = 2 MPa for 500 kHz; p_{int} = 26.2−27.8 MPa, with σ_{mean} = 1.2 MPa for 1.5 MHz; and p_{int} = 26.1−27.9 MPa, with σ_{mean} = 1.1 MPa for 3 MHz. Figure 3.3 shows example images taken using the 1.5 MHz transducer at peak negative pressure levels from below to above the intrinsic threshold. In the experimental data for all frequencies, cavitation was observed with p_{cav} = 1 for p_- higher than 30 MPa. As pressure was increased above the intrinsic threshold, the bubbles were visualized in an increasingly larger area with a greater number of bubbles present in this focal region as has been previously observed [12, 13]. Although the bubbles covered a larger area at higher pressure, the diameter of bubbles that could be individually identified appeared to be consistent between pressure levels for the same frequency at the time point

captured by the camera, potentially due to bubble-bubble interactions suppressing the growth of adjacent bubbles or bubble-induced pressure saturation caused by energy loss into each bubble as it forms, which has previously been observed in shock wave lithotripsy [44, 45]. When varying frequency, differences in bubble size were noticed with lower frequency producing larger bubbles.

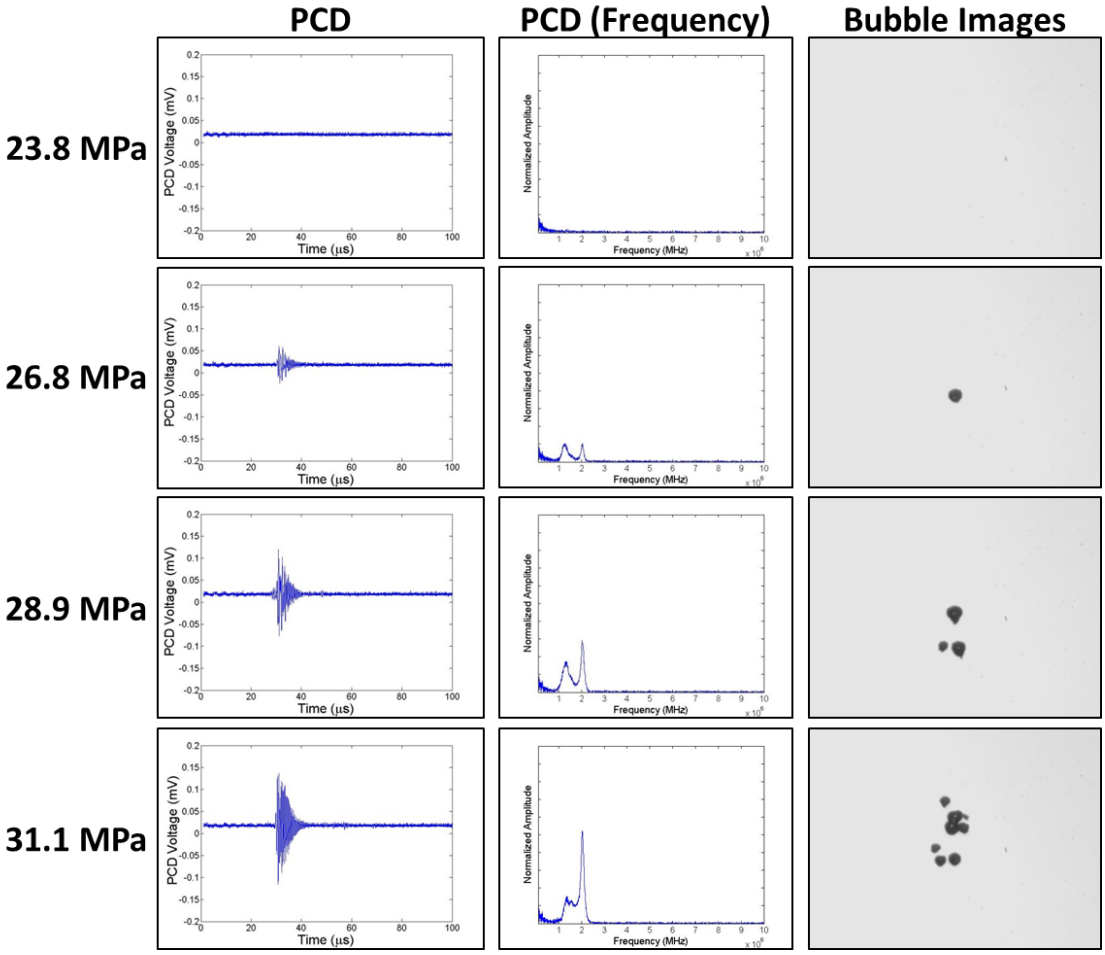

Figure 3.3. Cavitation Detection. Sample PCD temporal (left) and frequency (center) signals were used for cavitation detection. Results showed agreement with high speed optical images of cavitation (right). Representative images shown are from 1.5 MHz histotripsy pulses applied to degassed water (ultrasound propagating top to bottom).

In addition to high speed imaging, cavitation was monitored using one of the therapy transducer elements for PCD following a previously established method [13]. The cavitation detection results from PCD and optical imaging methods matched well in water [Fig. 3.3]. When

cavitation occurred on high-speed images, the PCD signal was a multi-cycle burst of significantly increased amplitude with a center frequency near the therapy transducer frequency. When no cavitation was observed on the camera, the PCD signal amplitude was small. Figure 3.4 shows an example of the relative values of S_{PCD} versus pulse number for 100 pulses near the intrinsic threshold in degassed water using the 1.5 MHz transducer.

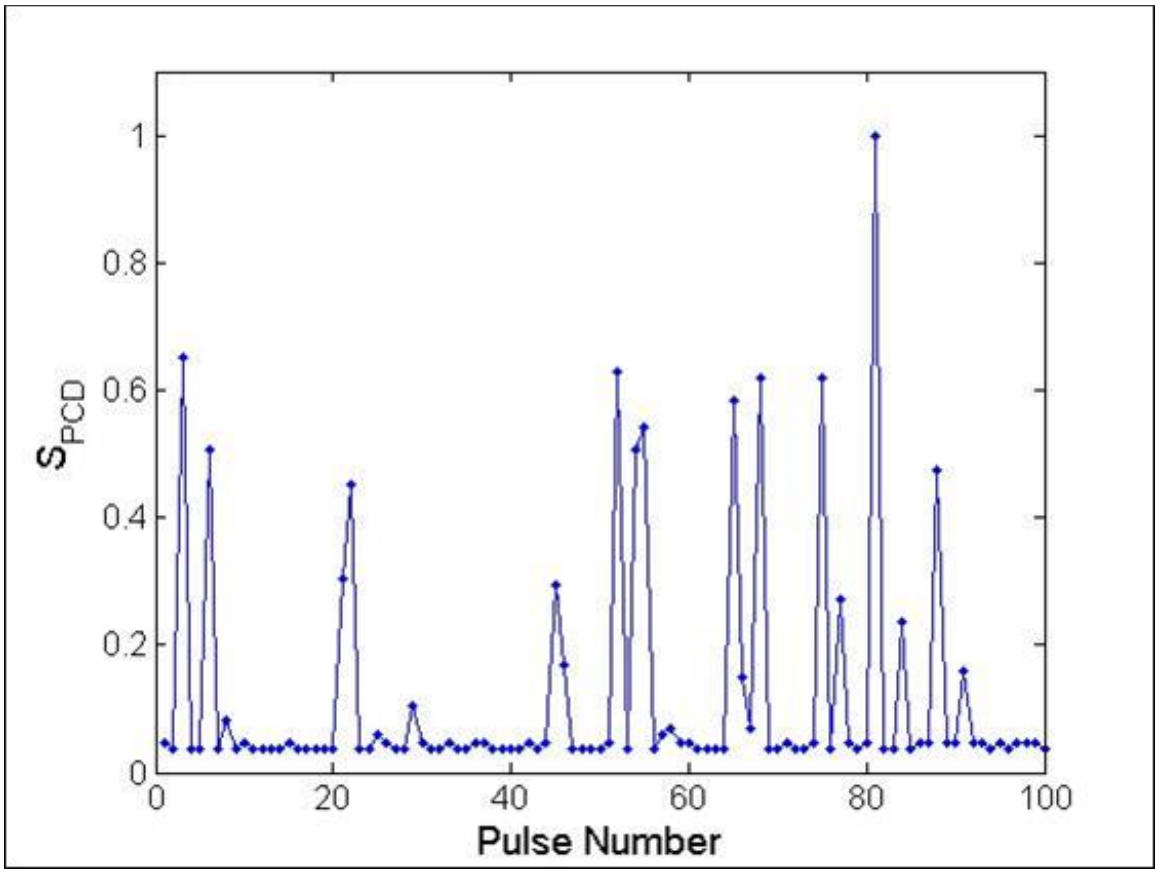

Figure 3.4. Example of Integrated Power Spectrum (SPCD) Bimodal distribution. Results show the SPCD for 100 histotripsy pulses applied by the 1.5 MHz transducer at a peak negative pressure of 25.3 MPa. A bimodal distribution is evident, with the lower, more consistent values indicating the absence of cavitation, and the larger, more variable values indicating the presence of one or more bubbles.

The gas concentration of the water sample had a small effect on the cavitation probability curve at 1.5 MHz and 3 MHz, but showed a large difference at 345 kHz and 500 kHz [Fig.3.5]. For example, the cavitation threshold in both degassed (15% O_2) and gassy water (90% O_2) was between 26.3-27.4 MPa for all samples at 1.5 MHz and 3 MHz. In contrast, the cavitation

threshold in gassy water (90% O_2) was observed to decrease by 6.5 MPa at 500 kHz and 13.6 MPa at 345 kHz compared to the intrinsic threshold in degassed water (15% O_2) [Fig.3.5].

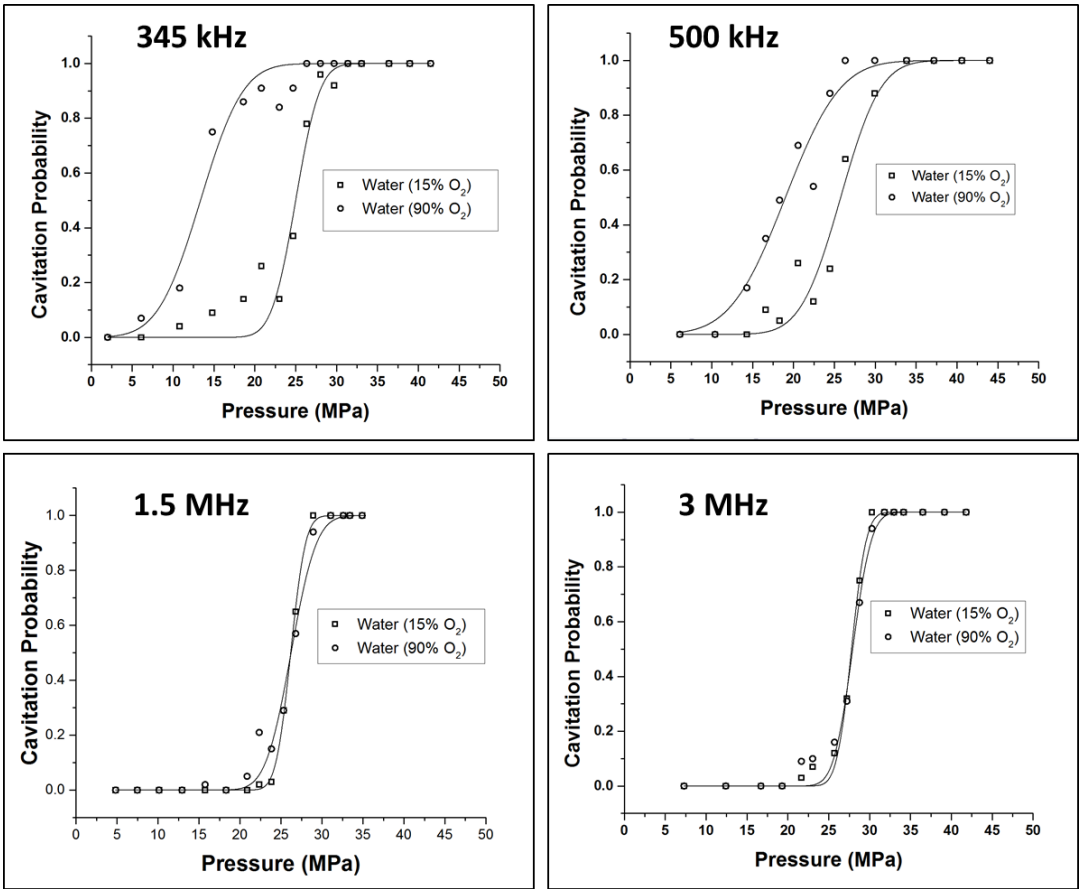

Figure 3.5. Cavitation threshold in water. Example probability curves for water samples. Results showed a significant decrease the cavitation threshold for 90% O_2 water at 345 kHz and 500 kHz compared to degassed 15% O_2 water. No significant difference was observed between 90% O2 and 15% O2 water at 1.5 MHz or 3 MHz.

3.3.2 Intrinsic Threshold in Tissue Phantoms

To investigate the effects of tissue stiffness on the intrinsic threshold, experiments were repeated inside mechanically tunable tissue phantoms. Four types of tissue phantoms were tested at each frequency, with the Young's moduli ranging from 1.13-570 kPa. Results demonstrated a similar function of cavitation probability versus pressure in all tissue phantoms [Fig. 3.6]. Furthermore, the intrinsic threshold was observed to be similar in tissue phantoms of all Young's

moduli. For example, at 1.5 MHz, the intrinsic threshold for the four types of tissue phantoms ranged from 24.8-26.7 MPa [Table 3.2]. The region over which cavitation occurred in each sample was similar at similar pressure levels. One difference between tissue phantoms was the bubbles observed in stiffer tissue phantoms were smaller in size at the time point captured by the camera [Fig 3.**7]**. The PCD was shown to remain sensitive to the cavitation bubbles formed in all tissue phantoms despite the differences in bubble size [Fig 3.**7]**. Comparing the effect of frequency on the threshold in tissue phantoms showed a small difference of ~2-3 MPa in the intrinsic threshold when the frequency was increased from 345 kHz to 3 MHz. The average intrinsic threshold for all phantom and frequency combinations ranged from 24.7-27.8 MPa.

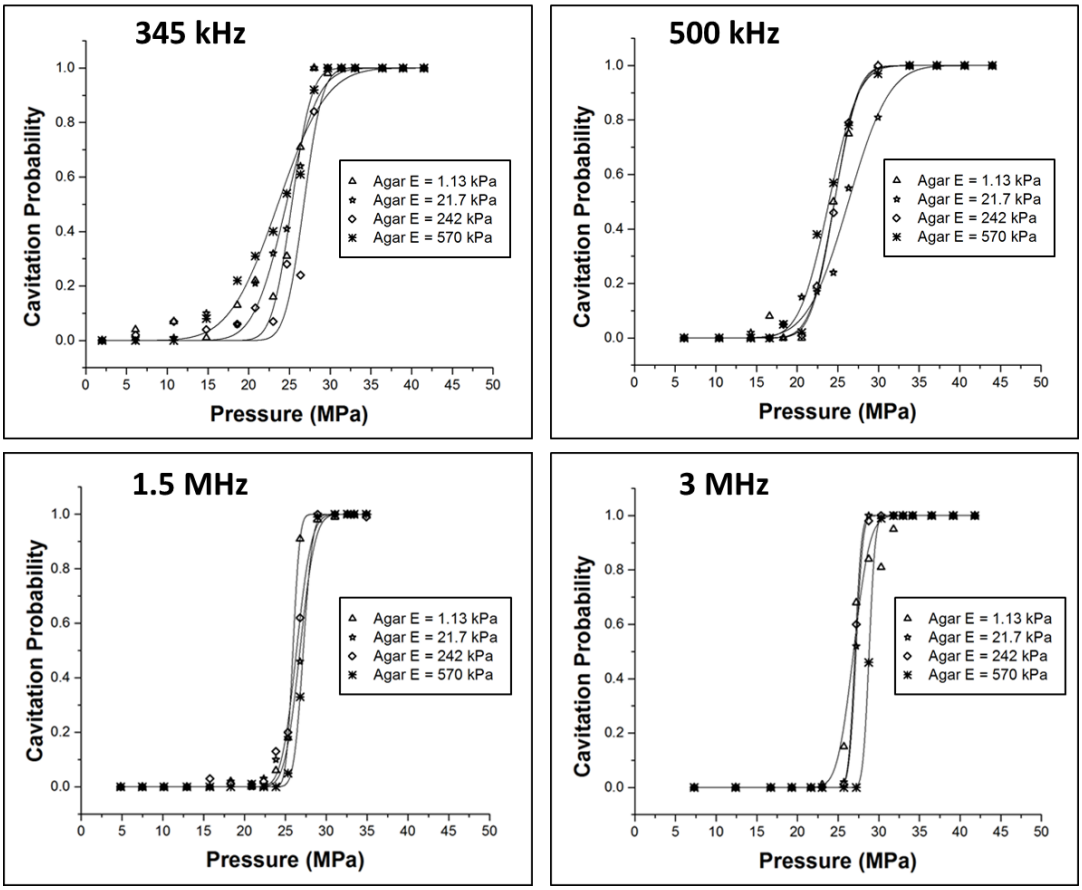

Figure 3.6. Cavitation threshold in tissue phantoms. Example probability curves for mechanically tunable agarose tissue phantoms. Results showed no significant difference in the intrinsic threshold with increasing stiffness. A small increase of ~2-3 MPa was observed in the threshold as the frequency was increased from 345 kHz to 3 MHz.

Table 3.2 Table shows the values for the intrinsic threshold, p_{int}, calculated by the fitted curves for each sample, the mean values for p_{int} and σ. All values are pressure in MPa.

Frequency	Material	P_{int} (1)	P_{int} (2)	P_{int} (3)	P_{int} (Mean)	σ (mean)
345 kHz						
	Water (15% O_2)	27.7	24.9	25.0	25.9	1.6
	Water (90% O_2)	10.7	13.3	12.8	12.3	3.8
	Agar E = 1.13 kPa	25.8	23.7	24.6	24.7	2.0
	Agar E = 21.7 kPa	25.9	23.7	24.7	24.8	2.0
	Agar E = 242 kPa	26.8	24.8	25.0	25.5	1.9
	Agar E = 570 kPa	25.9	24.9	23.6	24.8	2.2
	Liver	24.9	25.5	24.0	24.8	1.9
	Tongue	25.0	25.6	26.5	25.7	1.4
	Tendon	27.8	27.7	27.4	27.6	1.4
500 kHz						
	Water (15% O_2)	25.9	25.8	26.7	26.1	2.0
	Water (90% O_2)	20.3	19.0	19.6	19.6	3.6
	Agar E = 1.13 kPa	24.6	23.5	27.6	25.2	1.8
	Agar E = 21.7 kPa	23.5	26.3	26.7	25.5	1.8
	Agar E = 242 kPa	24.6	26.9	24.9	25.5	2.0
	Agar E = 570 kPa	24.7	26.3	23.9	25.0	1.8
	Liver	25.1	26.5	24.3	25.3	2.0
	Tongue	25.0	25.6	25.0	25.2	2.2
	Tendon	28.1	28.9	27.7	28.2	2.8
1.5 MHz						
	Water (15% O_2)	27.6	27.8	26.2	27.2	1.2
	Water (90% O_2)	26.2	26.9	25.7	26.3	1.6
	Agar E = 1.13 kPa	25.9	25.5	27.9	26.4	0.7
	Agar E = 21.7 kPa	26.8	27.0	26.3	26.7	1.0
	Agar E = 242 kPa	27.2	25.9	26.7	26.6	0.7
	Agar E = 570 kPa	25.7	23.8	24.9	24.8	0.7
	Liver	27.0	26.7	28.8	27.5	1.5
	Tongue	28.2	26.8	28.1	27.7	1.4
	Tendon	28.8	29.9	28.6	29.1	1.6
3 MHz						
	Water (15% O_2)	27.8	27.9	26.1	27.3	1.1
	Water (90% O_2)	27.1	27.2	27.9	27.4	1.1
	Agar E = 1.13 kPa	28.4	26.9	27.1	27.5	1.3
	Agar E = 21.7 kPa	26.9	27.2	26.3	26.8	0.9
	Agar E = 242 kPa	27.1	26.6	27.0	26.9	0.8
	Agar E = 570 kPa	27.4	28.8	27.2	27.8	0.7
	Liver	27.4	26.5	27.6	27.2	1.1
	Tongue	28.5	28.1	28.7	28.5	1.2
	Tendon	30.3	31.5	30.1	30.6	0.8

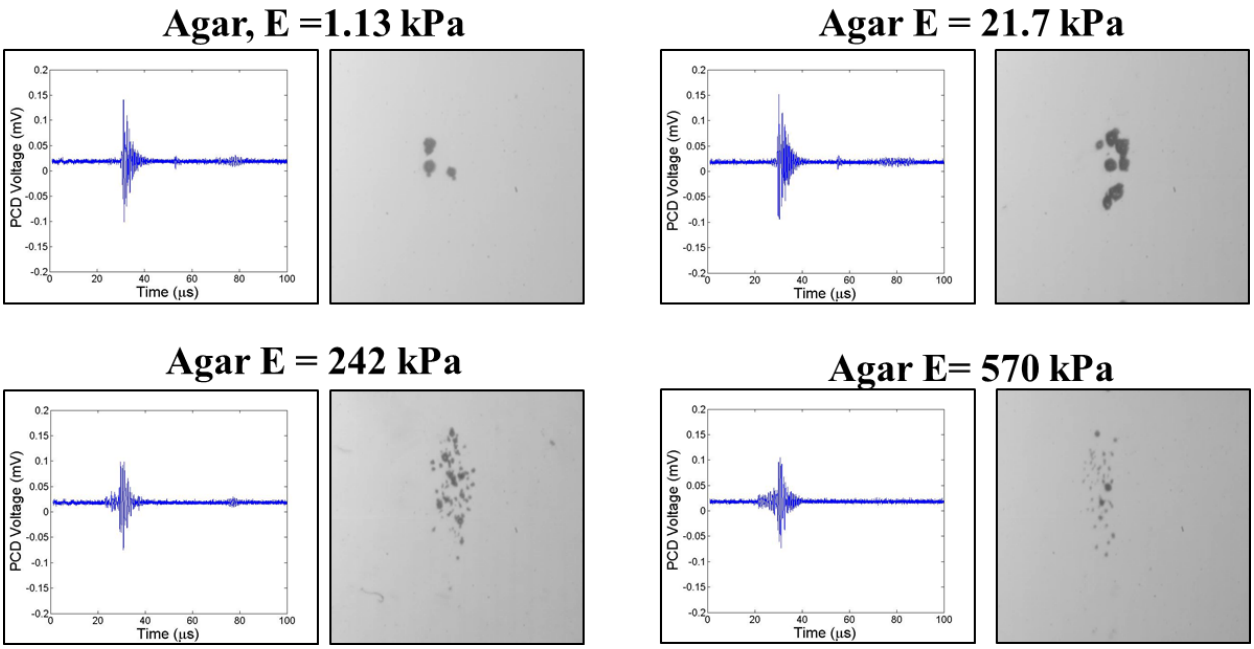

Figure 3.7. Cavitation detection in tissue phantoms. Example PCD signals (left) and corresponding optical images (right) of cavitation in agarose tissue phantoms of increasing Young's moduli. The PCD signal was observed to remain sensitive to cavitation in stiffer phantoms despite the observe decrease in bubble size.

3.3.3 Intrinsic Threshold in Bovine Tissue

To validate the results from water and tissue phantom experiments, the intrinsic threshold was investigated in select *ex vivo* bovine tissues. Bovine liver (E=8.7 kPa), tongue (E=25 kPa), and tendon (E=380 MPa) were chosen to cover a wide range of tissue strength. In these tissues, PCD detection demonstrated a similar function of cavitation probability versus pressure in tissues as those in tissue phantoms and degassed water [Fig. 3.8]. The intrinsic threshold was observed to be similar in all tissues with only a small increase observed for tendon [Fig. 3.8]. For example, at 1.5 MHz, the average intrinsic threshold for the three types of tissue ranged from 27.5 MPa (liver) to 29.1 MPa (tendon). Comparing the effect of frequency on the intrinsic threshold showed a small increase with increasing frequency. For example, in liver samples, the

intrinsic threshold ranged from 24.8 MPa at 345 kHz to 27.2 MPa at 3 MHz. The intrinsic threshold for all tissues and frequency combinations ranged from 24.8-30.6 MPa.

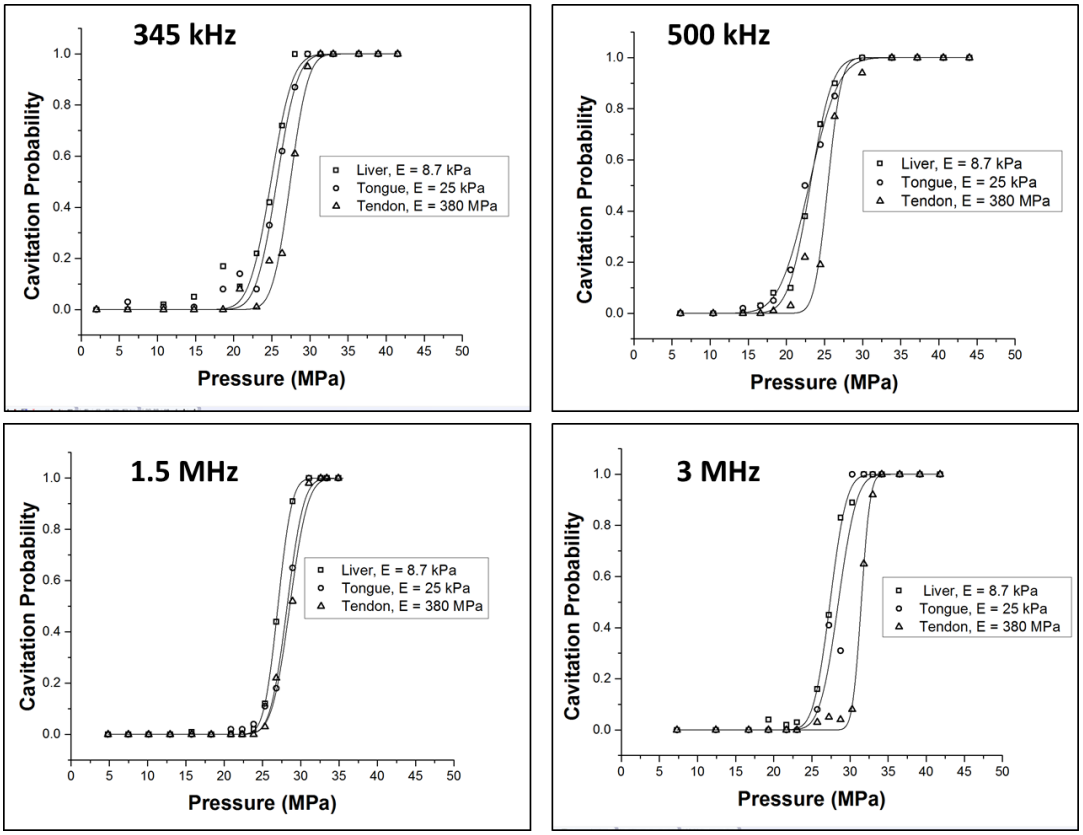

Figure 3.8. Cavitation threshold in ex vivo bovine tissue. Example probability curves for *ex vivo* bovine liver, tongue, and tendon. A small increase of ~2-3 MPa was observed in the threshold as the frequency was increased from 345 kHz to 3 MHz.

3.3.4 Intrinsic Threshold Comparison

The intrinsic threshold for all samples was compared using the curve fitting method and statistical analysis described above. In general, the standard errors in the estimate of the intrinsic threshold, p_{int}, were small compared to the variance between samples of the same type. Excluding the gassy water (90% O_2), p_{int} for all samples and frequencies was observed to be between 24.8-30.6 MPa, and the σ_{mean} between 0.7-2.8 MPa. The full cavitation threshold results for all samples are listed in Table 3.2. Overall, results showed no noticeable trend in the intrinsic

threshold between samples with Young's moduli <1 MPa. However, a small increase of ~2-3 MPa was observed for tendon (E=380 MPa) compared to other samples (E=1.13-570 kPa). Additionally, results demonstrated a small but consistent increase in the intrinsic threshold of ~2-3 MPa when the frequency was increased from 345 kHz to 3 MHz [Fig. 3.9(A)]. It should be noted that, in addition to the small changes in threshold observed with changes in frequency, larger σ_{mean} values were observed at 345 kHz and 500 kHz compared to 1.5 MHz and 3 MHz [Table 3.2].

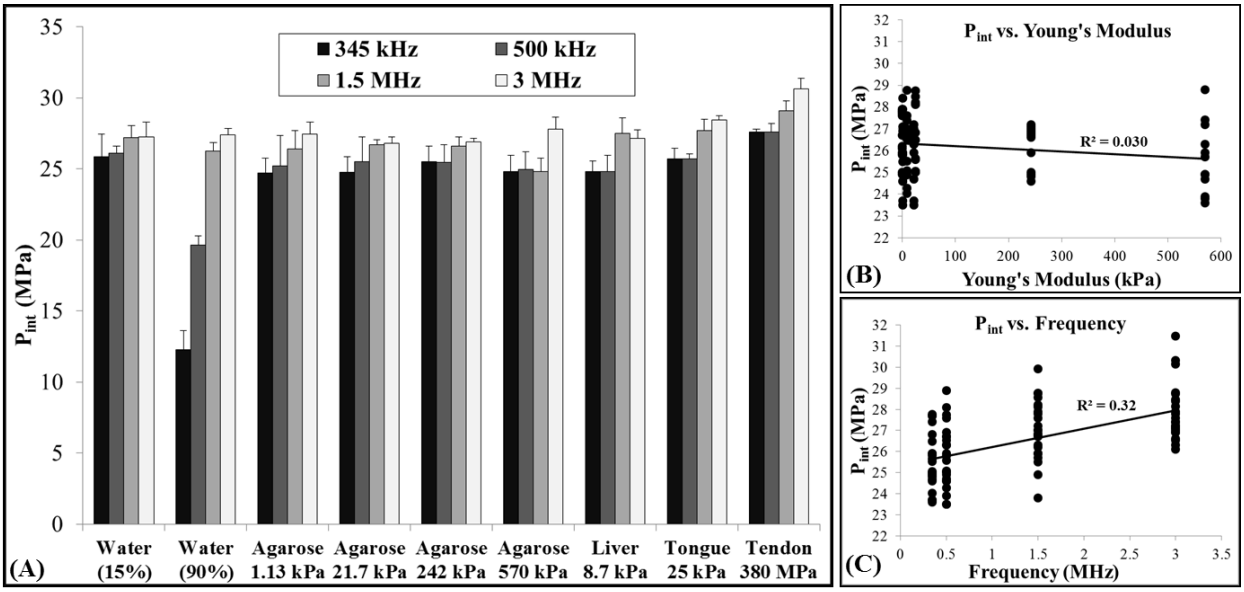

Figure 3.9. (A) Bar plot shows the p_{int} measured for all samples and frequencies. The p_{int} for all samples remained between 24.7-30.6 MPa with the exception of 90% O_2 water at 345 kHz and 500 kHz, which was significantly lower. (B) Linear regression analysis demonstrated that the change in p_{int} with increasing Young's modulus (tendon not included) was not significant via the Pearson correlation (r=-0.173, R2=0.030, p>0.05). (C) Linear regression analysis further showed that the ~2-3 MPa increase in p_{int} with increasing frequency was significant via the Pearson correlation (r=0.57, R2=0.32, p<0.05).

A two-way ANOVA was also performed on the data shown in Figure 3.9(A), demonstrating no significant difference in the threshold between samples at a given frequency, with the exception of the threshold in tendon which was observed to be significantly increased

($p<0.05$). The ANOVA also showed a significant increase in the threshold between 345 kHz and 3 MHz for all samples. However, only some of the differences between intermediate frequencies were significant. The effects of Young's modulus and ultrasound frequency were also analyzed by plotting p_{int} for all samples except 90% O_2 water [Table 3.2] as a function of Young's modulus and frequency [Fig. 3.9]. Linear regression analysis demonstrated that the change in p_{int} with increasing Young's modulus (tendon not included) was not significant via the Pearson correlation ($r=-0.173$, $R^2=0.03$, $p>0.05$) [Fig. 3.9(B)], but the change in p_{int} with increasing frequency was significant via the Pearson correlation ($r=0.57$, $R^2=0.32$, $p<0.05$) [Fig. 3.9(C)].

3.3.5 Threshold Simulation: Stabilized nuclei

To provide a theoretical explanation to the experimental results, the effects of tissue stiffness and ultrasound frequency on the cavitation threshold were investigated using a single bubble numerical simulation assuming a nanometer sized stable nucleus. When the peak negative pressure, p_A, was less than some threshold value, p_{t_sim}, bubble expansion was minimal ($R_{max}<2$ R_0). As p_A was increased above p_{t_sim}, great bubble growth and collapse were observed ($R_{max}>10^4$ R_0). The peak negative pressure corresponding to this transition was defined as the inertial cavitation threshold, p_{t_sim}. Using a 2.5 nm initial bubble, p_{t_sim} was observed to be ~28 MPa for all frequencies tested [Fig. 3.10(A)]. Similarly, p_{t_sim} was observed to be independent of tissue elastic modulus from 1 kPa to ~1 MPa, due to the threshold being dominated by surface tension rather than the macroscopic properties of the media such as the Young's modulus [Fig. 3.10(B)]. However, when the Young's modulus was increased to 10 MPa, cavitation threshold was no longer determined solely by surface tension and p_{t_sim} increased to ~32 MPa [Fig. 3.10(B)]. It should be noted that the simulation could not accurately predict the intrinsic threshold in tendon

(E=380 MPa). In contrast to the ~2-3 MPa increase in threshold observed experimentally, the model predicted a threshold of >315 MPa when the Young's modulus was 380 MPa.

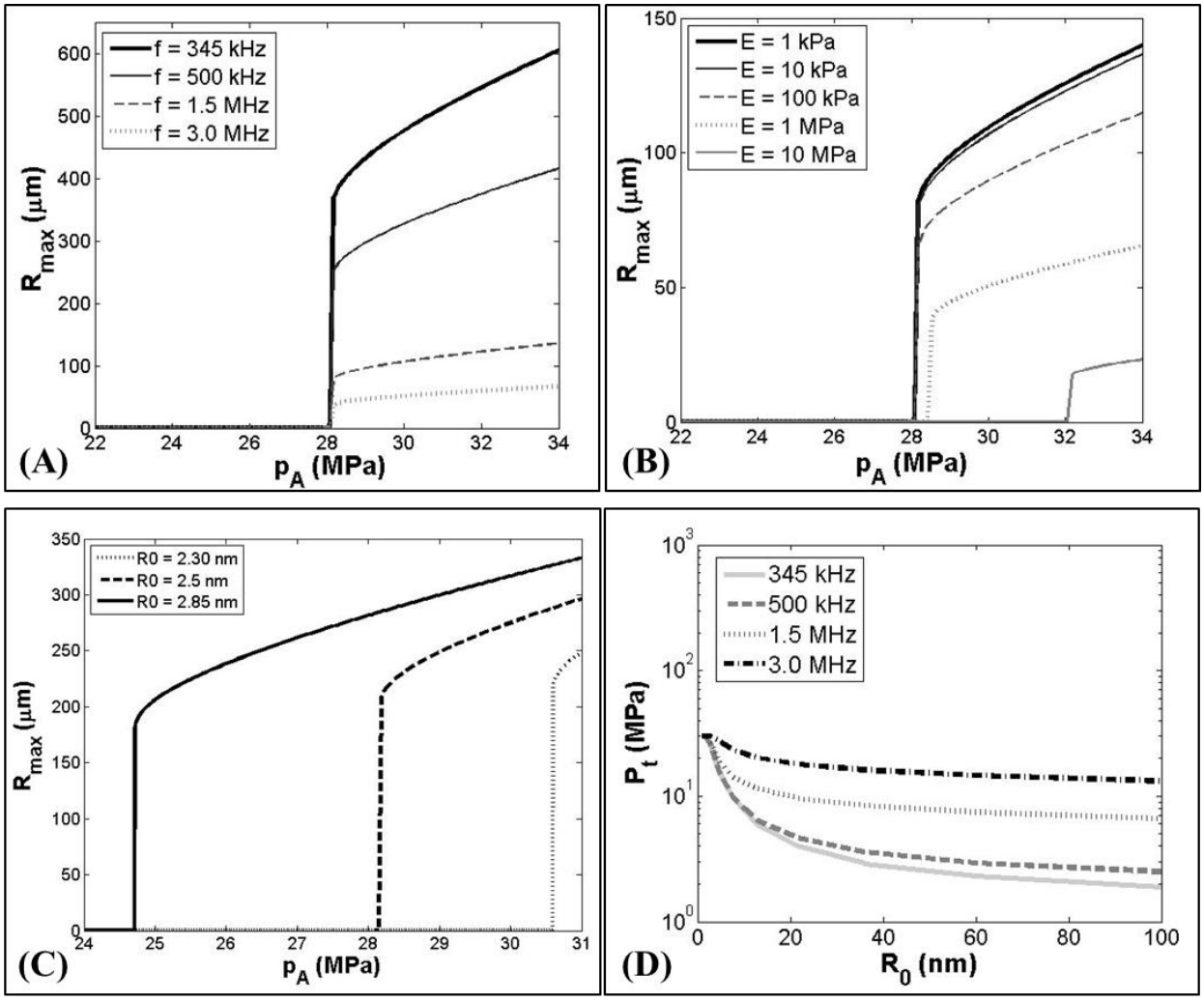

Figure 3.10. Simulated maximum bubble radius for a 2.5 nm initial bubble subjected to a single cycle histotripsy peak negative pressure waveform demonstrated a distinct threshold of ~28 MPa that was independent of (A) ultrasound frequency (E=1kPa) and (B) tissue stiffness for Young's moduli <1 MPa (f=1.5MHz). (C) Simulations demonstrated that the cavitation threshold measured experimentally (24.7-30.6 MPa) corresponded to initial bubble sizes between 2.3-2.85 nm (E=1kPa, f=500kHz). (D) Increasing the initial bubble size from 1-100 nm resulted in a decrease in the cavitation threshold with a larger decrease observed at lower frequency (E=1kPa).

The effects of initial nuclei size on the inertial cavitation threshold were also investigated, demonstrating a significant drop in the inertial cavitation threshold with increasing initial bubble radius [Fig. 3.10]. Simulations showed that the experimentally observed thresholds corresponded

to an initial bubble size between 2.3 nm (p_{t_sim} = 30.6 MPa) and 2.85 nm (p_{t_sim} = 24.7 MPa) [Fig. 3.10(C)]. Simulations comparing a larger range of initial nuclei size demonstrated a significant reduction in p_{t_sim} as the nuclei size was increased from 2 nm to ~40-60 nm, at which point the threshold appeared to plateau [Fig. 3.10(D)]. In the case of nuclei above ~40-60 nm, the final bubble size was dictated through several competing terms including the applied pressure and the tissue elasticity rather than being dominated by surface tension as is the case for smaller initial bubbles, which led to bubbles expanding to approximately the same size with the same p_{t_sim} regardless of initial radius. This effect has similarly been observed in previous studies on shock wave lithotripsy [46]. The finding that the threshold decreased with increasing bubble radius, especially at lower frequency [Fig. 3.10(D)], helps to explain the significant decrease in the cavitation for 90% O_2 water at 345 kHz and 500 kHz [Fig. 3.5]. However, it should also be noted that the likelihood of getting a large bubble in the field is much greater at low frequency than high frequency due to the larger focal volume (>2 orders of magnitude difference between 345 kHz and 3 MHz), which wasn't accounted for in the single bubble simulation and likely contributed to the experimental results.

3.3.6 Threshold Simulation: Spontaneous Nucleation

The effects of ultrasound frequency on the cavitation threshold predicted by classical nucleation theory (CNT) were also investigated with a simulation as described in the Methods (E3.7). CNT results predicted that the cavitation threshold would increase by ~2.3 MPa when the frequency was increased from 345 kHz to 3 MHz. These results closely matched experiments, with the value of p_{t_CNT} increasing from 24.9 MPa to 27.2 MPa when the frequency was increased from 345 kHz to 3 MHz [Fig. 3.5]. Figure 3.11 shows p_{t_CNT} compared with the

average p_{int} measured for all agarose tissue phantoms at each frequency. These results suggest that the increase in threshold at higher frequency measured experimentally is due to the smaller focal zone and shorter duration of the applied *p-*. In fact, since bubbles are generated directly from the single *p- phase* of the incident wave, it may be more appropriate to use the duration of the applied *p-* as a metric instead of frequency which may incorrectly imply periodic forcing.

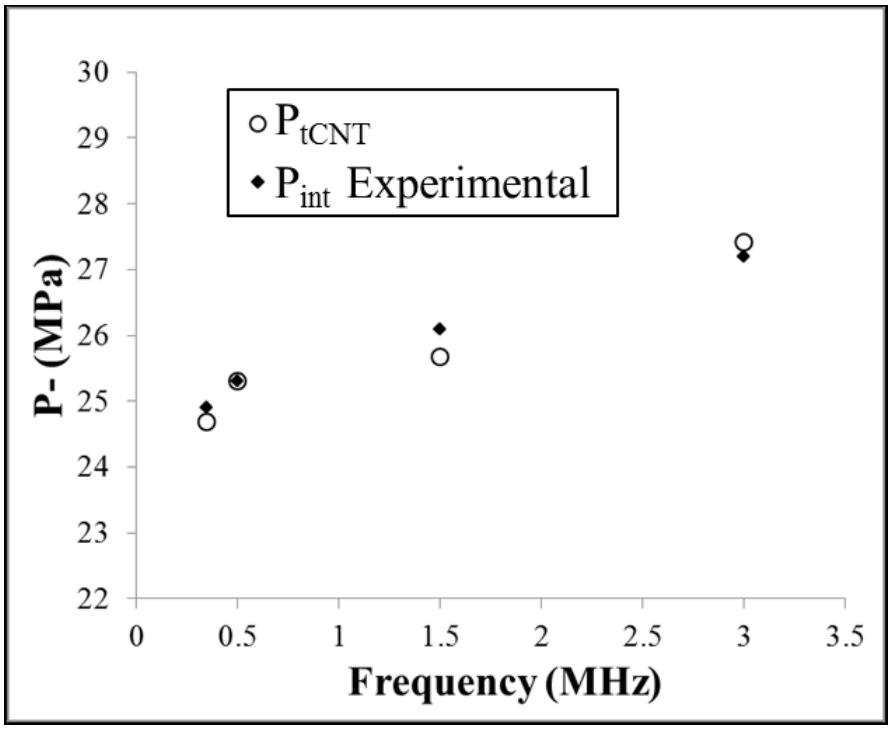

Figure 3.11. CNT Simulation. Classical nucleation theory was used to predict the effects of frequency on the cavitation threshold using equation E3.7. Results demonstrated an increase in pt_CNT of 2.7 MPa as the frequency was increased from 345 kHz to 3 MHz (o). Comparisons to the average experimental results for pint in agarose tissue phantoms (♦) demonstrate close agreement between theory and experiments.

3.4 Discussion

In previous studies, stiffer tissues had increased resistance to histotripsy fractionation and required a higher pressure threshold to generate a cavitation cloud via the shock scattering method [10, 47]. In this chapter, the effects of tissue stiffness on the histotripsy intrinsic threshold were investigated, with results supporting our hypothesis that the intrinsic threshold is

independent of tissue stiffness. At all frequencies tested, no noticeable trend of increasing threshold was observed for phantoms and tissues with Young's moduli <1 MPa, and only a small increase was observed for tendon (E=380 MPa). The observed increase for tendon was also small (~2-3 MPa) in comparison to previously measured differences between water-based and non-water based media such as 1,3 butanediol or adipose tissue, which resulted in a ~5-10 MPa change in the intrinsic threshold [13].

The finding that the intrinsic threshold is independent of tissue stiffness is of significant importance to the development of histotripsy therapy. As suggested by Maxwell *et al*, the intrinsic threshold approach has the potential to create a more predictive and reliable histotripsy therapy [12, 13]. In this study, we show that, using the intrinsic threshold method, histotripsy bubbles can be reliably generated at the same pressure in many tissue types. As a result, initiating cavitation above the intrinsic threshold appears to be much more predictable than using shock scattering, which has been shown to require higher pressure to generate a bubble cloud in stiffer tissues [10]. For the same reasons, the intrinsic threshold approach is also more predictable and reproducible than cavitation initiation using longer pulses or adding contrast agents, even though these methods can lower cavitation threshold [48-52]. It should be noted, however, that stiffer tissues may remain resistant to histotripsy fractionation even in cases when a bubble cloud has been generated due to impeded bubble expansion as well as the higher ultimate stress and ultimate strain of these tissues [36, 47, 53]. It is likely that the decrease in bubble expansion in stiffer tissues, which were observed in this study, will result in a decrease in the rate and extent of tissue fractionation even in cases when a bubble cloud has been initiated. As a result, using lower frequency may be necessary to facilitate bubble expansion for the treatment of stiffer tissues.

In addition to tissue stiffness, this work investigated the effects of frequency on the intrinsic threshold, with the results showing a small increase of ~2-3 MPa when the frequency was increased from 345 kHz to 3 MHz, which covers the range frequently used for histotripsy therapy. Since the intrinsic threshold was observed to be nearly independent of frequency for the histotripsy therapy range, treatment optimization strategies can instead focus on other considerations such as the desired bubble expansion, the optimal focal zone, or the available acoustic window required for the treatment of specific tissues. For example, the larger focal zone at lower frequency may be utilized in instances when large volume ablation is desired, such as the removal of large tumors in the liver [53]. On the other hand, higher frequency may provide a smaller focal zone for treatments in which high precision is required such as the removal of blood clots in deep vein thrombosis or stroke [54].

Another observation that may help guide histotripsy parameter optimization is the finding that "incidental cavitation bubbles" formed below the intrinsic threshold are more likely to be generated at lower frequency, which was observed in 90% O_2 water at 345 kHz and 500 kHz [Fig. 3.5]. This finding suggests that using higher frequency will reduce the risk of collateral damage outside the treatment region by minimizing "incidental bubbles" formed in these external locations, which was previously observed in a study comparing histotripsy fractionation at 500 kHz and 3 MHz [34]. Additionally, this finding suggests that lower frequency may enhance the shock scattering process which relies on cavitation generation from incidental bubbles and the expansion of these initial bubbles, both of which were enhanced at lower frequency in this study.

In the final part of this chapter, two models were used to provide some insight into the "intrinsic nuclei" population. First, a stable bubble model was used, predicting a threshold that

was independent of tissue stiffness for Young's moduli <1 MPa. However, the model was inaccurate for Young's moduli >1 MPa and couldn't accurately predict the threshold in tendon. This result, along with the experimental observation that the intrinsic threshold in tissue is similar to the intrinsic threshold of water, suggests that nucleation actually occurs in the water inside tissue where the Young's modulus is negligible. If this is true, the Young's modulus would only affect macroscopic bubble motion but would not impact the initial bubble behavior. This would explain why the model is inaccurate for large Young's moduli since it models homogeneous bulk tissue properties down to very small sizes that do not reflect actual tissue conditions at the nanoscopic scale (i.e. porosity, anisotropy). The stable bubble model further showed that the cavitation threshold was independent of frequency for the range tested for a 2.5 nm initial bubble and predicted that the thresholds measured in experiments (24.7-30.6 MPa) corresponded to initial bubble sizes between 2.3-2.85 nm. While this analysis may shed some light on the possible size range of stable nuclei in tissue, it is unlikely that the changes in threshold with frequency are due to changes in nuclei size since the same samples were exposed for all frequencies. It is more likely that the decrease in threshold at lower frequency is due to the larger focal volume and increased duration of the applied pressure, as predicted by the CNT model. The change in threshold predicted by CNT closely matched experimental results in the present study, as well as in Arvengas *et al* (Arvengas et al. 2011a), who measured the cavitation probability between 1-2 MHz. Comparing the effects of frequency predicted by CNT and the stable bubble model suggests that the intrinsic threshold generates bubbles from spontaneous nuclei within the water inside tissue. However, while these results provide some insight into the potential intrinsic nuclei population, future work is still needed to conclusively determine whether the intrinsic nuclei are actually spontaneous nuclei described by classical nucleation

theory, nanometer sized stabilized gas nuclei, or if a more advanced microscopic model is needed in order to describe these nuclei.

3.5 Conclusion

In this chapter, the effects of tissue stiffness and ultrasound frequency on the histotripsy intrinsic threshold were investigated by applying 1-2 cycle histotripsy pulses to mechanically tunable tissue phantoms and *ex vivo* bovine tissues using 345 kHz, 500 kHz, 1.5 MHz, and 3 MHz histotripsy transducers. Results demonstrated that the histotripsy intrinsic threshold is independent of stiffness for tissue phantoms and soft tissues with Young's moduli <1 MPa, with only a small increase in the intrinsic threshold observed for tendon (E=380 MPa). Results further showed only a small increase in the intrinsic threshold of ~2-3 MPa when the frequency was increased from 345 kHz to 3 MHz. Overall, the results of this chapter suggest that the intrinsic threshold approach is predictable and reproducible in initiating cavitation, regardless of the tissue types and frequency used.

3.6 References

[1] E. Vlaisavljevich, *et al.*, "Effects of Ultrasound Frequency and Tissue Stiffness on the Histotripsy Intrinsic Threshold for Cavitation," *Ultrasound Med Biol*, 2015.

[2] J. E. Parsons, *et al.*, "Pulsed cavitational ultrasound therapy for controlled tissue homogenization," *Ultrasound Med Biol*, vol. 32, pp. 115-29, Jan 2006.

[3] W. W. Roberts, *et al.*, "Pulsed cavitational ultrasound: a noninvasive technology for controlled tissue ablation (histotripsy) in the rabbit kidney," *J Urol*, vol. 175, pp. 734-8, Feb 2006.

[4] Z. Xu, *et al.*, "Investigation of intensity thresholds for ultrasound tissue erosion," *Ultrasound Med Biol*, vol. 31, pp. 1673-82, Dec 2005.

[5] J. E. Parsons, *et al.*, "Spatial variability in acoustic backscatter as an indicator of tissue homogenate production in pulsed cavitational ultrasound therapy," *IEEE Trans Ultrason Ferroelectr Freq Control*, vol. 54, pp. 576-90, Mar 2007.

[6] T. L. Hall, *et al.*, "Histotripsy of rabbit renal tissue in vivo: temporal histologic trends," *J Endourol*, vol. 21, pp. 1159-66, Oct 2007.

[7] A. D. Maxwell, *et al.*, "Cavitation clouds created by shock scattering from bubbles during histotripsy," *J Acoust Soc Am*, vol. 130, pp. 1888-98, Oct 2011.

[8] A. D. Maxwell, *et al.*, "Inception of Cavitation Clouds by Scattered Shockwaves," *IEEE Ultrasonics Symposium*, pp. 3B-2, 2010.

[9] A. D. Maxwell, *et al.*, "Cavitation clouds created by shock scattering from bubbles during histotripsy," *Journal of the Acoustical Society of America*, vol. 130, pp. 1888-98, Oct 2011.

[10] E. Vlaisavljevich, *et al.*, "Histotripsy-induced cavitation cloud initiation thresholds in tissues of different mechanical properties," *IEEE Trans Ultrason Ferroelectr Freq Control*, vol. 61, pp. 341-52, Feb 2014.

[11] Z. Xu, *et al.*, "High speed imaging of bubble clouds generated in pulsed ultrasound cavitational therapy--histotripsy," *IEEE Trans Ultrason Ferroelectr Freq Control*, vol. 54, pp. 2091-101, Oct 2007.

[12] K. W. Lin, *et al.*, "Histotripsy beyond the intrinsic cavitation threshold using very short ultrasound pulses: microtripsy," *IEEE Trans Ultrason Ferroelectr Freq Control*, vol. 61, pp. 251-65, Feb 2014.

[13] A. D. Maxwell, *et al.*, "Probability of cavitation for single ultrasound pulses applied to tissues and tissue-mimicking materials," *Ultrasound Med Biol*, vol. 39, pp. 449-65, Mar 2013.

[14] L. J. Briggs, "The Limiting Negative Pressure of Water between 0-Degrees-C and 50-Degrees-C," *Science,* vol. 111, pp. 461-461, 1950.

[15] M. Greenspan and C. E. Tschiegg, "Radiation-Induced Acoustic Cavitation - Threshold Versus Temperature for Some Liquids," *Journal of the Acoustical Society of America,* vol. 72, pp. 1327-1331, 1982.

[16] G. N. Sankin and V. S. Teslenko, "Two-threshold cavitation regime," *Doklady Physics,* vol. 48, pp. 665-668, Dec 2003.

[17] E. Herbert, *et al.*, "Cavitation pressure in water," *Physical Review E,* vol. 74, Oct 2006.

[18] E. N. Harvey, *et al.*, "Bubble formation in animals I. Physical factors," *Journal of Cellular and Comparative Physiology,* vol. 24, pp. 1-22, Aug 1944.

[19] D. E. Yount, "Skins of Varying Permeability - Stabilization Mechanism for Gas Cavitation Nuclei," *Journal of the Acoustical Society of America,* vol. 65, pp. 1429-1439, 1979.

[20] N. F. Bunkin, *et al.*, "Cluster structure of stable dissolved gas nanobubbles in highly purified water," *Journal of Experimental and Theoretical Physics,* vol. 108, pp. 800-816, May 2009.

[21] A. Arvengas, *et al.*, "Fiber optic probe hydrophone for the study of acoustic cavitation in water," *Rev Sci Instrum,* vol. 82, p. 034904, Mar 2011.

[22] A. Arvengas, *et al.*, "Cavitation in heavy water and other liquids," *J Phys Chem B,* vol. 115, pp. 14240-5, Dec 8 2011.

[23] J. C. Fisher, "The Fracture of Liquids," *Journal of Applied Physics,* vol. 19, pp. 1062-1067, 1948.

[24] M. S. Pettersen, *et al.*, "Experimental investigation of cavitation in superfluid 4He," *Phys Rev B Condens Matter,* vol. 49, pp. 12062-12070, May 1 1994.

[25] A. P. Balgude, *et al.*, "Agarose gel stiffness determines rate of DRG neurite extension in 3D cultures," *Biomaterials,* vol. 22, pp. 1077-1084, May 2001.

[26] T. A. Ulrich, *et al.*, "Probing cellular mechanobiology in three-dimensional culture with collagen-agarose matrices," *Biomaterials,* vol. 31, pp. 1875-1884, Mar 2010.

[27] L. C. Diem K., *Documenta Geigy scientific tables, 7th Edition.* : Macclesfield, 1970.

[28] F. A. Duck, *Physical properties of tissue: a comprehensive reference book.* : Academic Press, 1990.

[29] ICRP, *Report of the Task Group on Reference Man : a report.* Oxford, New York: Pergamon Press, 1975.

[30] ICRU, *Tissue Substitutes in Radiation Dosimetry and Measurement.* : Intl Commission on Radiation, 1989.

[31] H. U. Staubli, *et al.*, "Mechanical tensile properties of the quadriceps tendon and patellar ligament in young adults," *Am J Sports Med,* vol. 27, pp. 27-34, Jan-Feb 1999.

[32] H. Q. Woodard and D. R. White, "The composition of body tissues," *Br J Radiol,* vol. 59, pp. 1209-18, Dec 1986.

[33] H. Yamada, *Strength of biologic materials.* . New York: Robert E. Kreiger, 1973.

[34] K. W. Lin, *et al.*, "Dual-beam histotripsy: a low-frequency pump enabling a high-frequency probe for precise lesion formation," *IEEE Trans Ultrason Ferroelectr Freq Control,* vol. 61, pp. 325-40, Feb 2014.

[35] J. E. Parsons, *et al.*, "Cost-effective assembly of a basic fiber-optic hydrophone for measurement of high-amplitude therapeutic ultrasound fields," *J Acoust Soc Am,* vol. 119, pp. 1432-40, Mar 2006.

[36] E. Vlaisavljevich, *et al.*, "Investigation of the role of tissue stiffness and ultrasound frequency in histotripsy-induced cavitation. ," presented at the Symposium on Therapeutic Ultrasound, Las Vegas, NV, 2014.

[37] R. A. Roy, *et al.*, "An Acoustic Backscattering Technique for the Detection of Transient Cavitation Produced by Microsecond Pulses of Ultrasound," *Journal of the Acoustical Society of America,* vol. 87, pp. 2451-2458, Jun 1990.

[38] D. W. Hosmer and S. Lemeshow, "Confidence interval estimation of interaction," *Epidemiology,* vol. 3, pp. 452-6, Sep 1992.

[39] T. G. Leighton, *The acoustic bubble*: Academic Press, San Diego, 1994.

[40] F. G. Blake, "Gas Bubbles as Cavitation Nuclei," *Physical Review,* vol. 75, pp. 1313-1313, 1949.

[41] X. Yang and C. C. Church, "A model for the dynamics of gas bubbles in soft tissue," *J Acoust Soc Am,* vol. 118, pp. 3595-606, Dec 2005.

[42] J. B. Keller and M. Miksis, "Bubble Oscillations of Large-Amplitude," *Journal of the Acoustical Society of America,* vol. 68, pp. 628-633, 1980.

[43] E. Vlaisavljevich, *et al.*, "Nanodroplet-mediated histotripsy for image-guided targeted ultrasound cell ablation," *Theranostics,* vol. 3, pp. 851-64, 2013.

[44] J. B. Freund, "Suppression of shocked-bubble expansion due to tissue confinement with application to shock-wave lithotripsy," *J Acoust Soc Am,* vol. 123, pp. 2867-74, May 2008.

[45] Y. A. Pishchalnikov, *et al.*, "Effect of firing rate on the performance of shock wave lithotriptors," *BJU Int,* vol. 102, pp. 1681-6, Dec 2008.

[46] P. Zhong, *et al.*, "Effects of tissue constraint on shock wave-induced bubble expansion in vivo," *Journal of the Acoustical Society of America,* vol. 104, pp. 3126-3129, Nov 1998.

[47] E. Vlaisavljevich, *et al.*, "Effects of tissue mechanical properties on susceptibility to histotripsy-induced tissue damage," *Phys Med Biol,* vol. 59, pp. 253-70, Jan 20 2014.

[48] E. L. Carstensen, *et al.*, "The search for cavitation in vivo," *Ultrasound Med Biol,* vol. 26, pp. 1377-85, Nov 2000.

[49] J. B. Fowlkes and L. A. Crum, "Cavitation threshold measurements for microsecond length pulses of ultrasound," *J Acoust Soc Am,* vol. 83, pp. 2190-201, Jun 1988.

[50] C. K. Holland and R. E. Apfel, "Thresholds for transient cavitation produced by pulsed ultrasound in a controlled nuclei environment," *J Acoust Soc Am,* vol. 88, pp. 2059-69, Nov 1990.

[51] Z. Kyriakou, *et al.*, "HIFU-induced cavitation and heating in ex vivo porcine subcutaneous fat," *Ultrasound Med Biol,* vol. 37, pp. 568-79, Apr 2011.

[52] D. L. Miller and R. M. Thomas, "Ultrasound Contrast Agents Nucleate Inertial Cavitation in-Vitro," *Ultrasound in Medicine and Biology,* vol. 21, pp. 1059-1065, 1995.

[53] E. Vlaisavljevich, *et al.*, "Image-guided non-invasive ultrasound liver ablation using histotripsy: feasibility study in an in vivo porcine model," *Ultrasound Med Biol,* vol. 39, pp. 1398-409, Aug 2013.

[54] A. D. Maxwell, *et al.*, "Noninvasive thrombolysis using pulsed ultrasound cavitation therapy - histotripsy," *Ultrasound Med Biol,* vol. 35, pp. 1982-94, Dec 2009.

Chapter 4
Effects of Temperature on the Histotripsy Intrinsic Threshold for Cavitation

A majority component of this chapter is excerpted from a manuscript in preparation for submission to *Physics in Medicine and Biology*.

4.1 Introduction

Histotripsy is a noninvasive tissue ablation method that controllably fractionates soft tissue through cavitation generated by high pressure (>10 MPa), short duration (<20μs) ultrasound pulses at low duty cycles (<1 %) [1-3]. Histotripsy depends on the initiation and maintenance of a dense cavitation bubble cloud to produce mechanical tissue fractionation [3, 4]. With sufficiently high pressure and dose, histotripsy can completely fractionate soft tissues into an acellular liquid homogenate, resulting in effective tissue disintegration [5-7]. Histotripsy is currently being studied for many clinical applications where non-invasive tissue removal is desired including benign prostatic hyperplasia [8], kidney stones [9], deep vein thrombosis [10], congenital heart disease [11, 12], and cancer [13, 14].

Previous work has demonstrated three mechanisms with which a histotripsy cavitation cloud can be generated. The three methods are boiling histotripsy, shock scattering histotripsy, and intrinsic threshold histotripsy, using increasingly higher pressure and shorter pulse duration. In boiling histotripsy, millisecond long pulses at moderate pressure (>5,000 cycles, P– = 8-14

MPa) are used to generate a histotripsy bubble cloud through shockwave boiling [15, 16]. In shock scattering histotripsy, a multi-cycle histotripsy pulse at high pressure (~3–20 cycles, P– = 10-28 MPa) is used to form a dense bubble cloud through shock scattering from single or sparse initial bubbles expanded during the initial cycles of the pulse [17, 18]. In intrinsic threshold histotripsy, a single pulse with a single dominant negative pressure phase at very high pressure (<2 cycles, P– = 24-30 MPa) is used to form a dense bubble cloud directly the negative pressure of the incident wave [19-22]. The intrinsic threshold is defined as the peak negative pressure at which the probability of generating cavitation, p_{cav}, from a single histotripsy pulse with a single dominant negative pressure phase is p_{cav}=0.5. Using these short pulses, cavitation initiation depends primarily on the negative pressure phase of the waveform as well as the properties the media. When the pressure exceeds a distinct threshold intrinsic to the medium, without the contributions from shock scattering, it results in a bubble cloud matching the portion of the focal region above the intrinsic threshold [19-22].

Previous work studying intrinsic threshold histotripsy has demonstrated that cavitation can be predictably and reliably generated when the peak negative pressure, *p*-, is raised above the intrinsic threshold of a given media. Maxwell *et al* showed measured an intrinsic threshold of ~26-30 MPa for soft tissues and tissue phantoms that are water-based using a 1.1 MHz histotripsy transducer, while the threshold for tissue composed primarily of lipids was significantly lower (15.4 MPa for adipose tissue) [20]. The intrinsic threshold measured for water-based soft tissues and tissue phantoms closely matched the intrinsic threshold of water, suggesting that cavitation nucleation occurs in the water inside of tissue. This hypothesis was further supported by recent work demonstrating that the intrinsic threshold of various water-

based soft tissues and tissue phantoms was independent of tissue stiffness and closely matched the intrinsic threshold of water at ultrasound frequencies ranging from 345 kHz to 3 MHz [21].

Although previous work in our lab has provided significant insight into the process of generating cavitation using the intrinsic threshold method, these studies have been limited to experiments performed at room temperature (~20°C). Understanding the effects of temperature on the intrinsic threshold is essential to the development of histotripsy therapy approaches using the intrinsic threshold method in order to accurately predict the intrinsic thresholds expected at body temperature *in vivo*. In addition, understanding the effects of temperature on the intrinsic threshold may provide insight into the thresholds for generating cavitation in boiling histotripsy or high intensity focused ultrasound (HIFU) thermal ablation, where the tissue temperature is elevated by long ultrasound pulses. This study investigates the effects of temperature on the histotripsy intrinsic threshold using a one-cycle pulse to eliminate shock scattering. Based on previous studies showing that the surface tension of water decreases with increasing temperatures [23], we hypothesize that the intrinsic threshold, which is highly dependent upon surface tension of the medium, will decrease with increasing temperature. This hypothesis is further supported by a prior study by Herbert *et al* which measured a cavitation threshold that decreased from 26 MPa at 0.1°C to 17 MPa at 80°C using pulsing parameters close to those used in intrinsic threshold histotripsy (single pulses of 4-6 acoustic cycles) [24].

To test the hypothesis that the intrinsic threshold decreases at higher temperatures, the probability of generating inertial cavitation was measured for 1 MHz histotripsy pulses applied to distilled, degassed water heated to temperatures ranging from 10°C-90°C, with the intrinsic threshold compared as a function of ambient temperature. To investigate the theoretical explanation for the intrinsic thresholds measured experimentally, two numerical models were

used to simulate the effect of temperature on the intrinsic threshold. Previous work has suggested that the histotripsy intrinsic threshold relies upon cavitation nuclei that are intrinsic to the media [20, 21]. By intrinsic, we mean that the nuclei appear to be associated with the properties of the medium itself rather than impurities. Although it is possible that these nuclei too are related to impurities, it seems unlikely, as several groups using different sample processing methods have measured approximately the same threshold for inertial cavitation associated with these nuclei in the range of 24 to 33 MPa in distilled water [20, 21, 24-27]. These negative pressure thresholds are significantly higher than the pressure required to generate "incidental cavitation bubbles" using long duration pulses, high PRF, or constant exposures, as these approaches likely rely on nuclei that are not intrinsic to the media and do not show the same distinct threshold behavior [28-33]. Previous work has suggested that the "intrinsic nuclei" may consist of either semi-permanent stabilized gas nuclei [27, 34-36] or spontaneous nuclei that form bubbles in a medium by energy-density fluctuations described by classical nucleation theory (CNT) [37-40]. Therefore, in this study we investigate the effects of temperature on the thresholds predicted by both stable bubble and CNT models, with the results compared to the experimentally measured thresholds.

4.2 Methods

4.2.1 Experimental Setup

The effects of temperature on the histotripsy intrinsic cavitation threshold were investigated by exposing 1 MHz histotripsy pulses to distilled, degassed water heated to 10°C, 20°C, 40°C, 60°C, 80°C, and 90°C. Water was degassed to 15% O_2 prior to experiments in order to minimize any stable gas bubbles in the sample. Gas saturation was measured using an O_2

meter (DO200; YSI, Yellow Springs, OH, USA) for each sample prior to testing to ensure consistency throughout all experiments. Water was heated inside a constant temperature water bath, consisting of a slow cooker (Crock-Pot, SCCPVL610-S, Manchester, UK) connected to a sous-vide temperature controller (Dorkfood, DSV, Pensacola, Florida, USA). A roller pump (Masterflex, Cole-Parmer, Vernon Hills, IL, USA) was used to circulate heated water into a cavitation chamber [Fig.4.1]. The 150-mL cavitation chamber, which has been described in detail in a previous study [20], was used to allow sonication of the sample and simultaneous visualization of the region of interest. The chamber components were made from polytetrafluoroethylene, glass, and 316 stainless steel to operate over a wide temperature range. Two glass windows were inserted into the walls of the chamber to facilitate high-speed photography of the cavitation activity. Acoustic windows in the front and back, made from 12 μm thick, low-density polyethylene membranes, were added to contain water in the chamber and allow ultrasound propagation into the sample. Fluid inlet and outlet ports were integrated into the top and bottom of the chamber for circulation. The temperature inside the water tank, slow cooker, and cavitation chamber was monitored using 3 type T hypodermic needle thermocouples (Physitemp Instruments Inc., Clifton, NJ, USA). For experiments, the temperature inside the cavitation chamber was maintained within ±1°C of the reported value, as measured outside the acoustic focus by a thermocouple inserted at the outlet port of chamber.

4.2.2 Histotripsy Pulse Generation

Histotripsy pulses were generated by an 18-element 1 MHz histotripsy transducer. The transducer has an effective 9.8 cm (lateral) x 8 cm (elevational) aperture and a 7 cm focal distance. The focal beam volume (−6 dB) of the transducer was measured to be 6.5 mm (axial) x

1.3 mm (lateral) x 1.5 mm (elevational) using a fiber-optic probe hydrophone (FOPH) built in-house [41]. To measure the intrinsic threshold in each sample, short pulses (<2 cycles) with a single dominant negative pressure phase were applied to the sample [Fig.4.2]. To generate a short pulse, a custom high-voltage pulser developed in-house was used to drive the transducers. The pulser was connected to a field-programmable gate array (FPGA) development board (Altera DE1 Terasic Technology, Dover, DE, USA) specifically programmed for histotripsy therapy pulsing. This setup allowed the transducers to output short pulses consisting of less than two cycles. The acoustic output pressure of the transducers was measured using the FOPH at 20°C [41]. At higher pressure levels, the acoustic output could not be directly measured due to cavitation at the fiber tip. These pressures were estimated by a summation of the output focal *p*-values from individual transducer elements. This approximation assumes minimal nonlinear distortion of the waveform occurs within the focal region. In a previous study [20], this estimated *p*- was found to be accurate within 15% compared to direct focal pressure measurements in water and in a medium with a higher cavitation threshold, 1,3 butanediol.

For threshold experiments, histotripsy pulses were applied at a pulse repetition frequency (PRF) of 0.5 Hz. The PRF was kept very low to minimize the possibility that cavitation from one pulse would change the probability of cavitation on a subsequent pulse. In a previous study [20], it was demonstrated that for PRFs > 1 Hz, cavitation during a pulse increased the likelihood of cavitation on a following pulse, but this effect was not observed for PRFs below 1 Hz, since the residual nuclei from the ultrasound pulse dissolve within ~1 second after the pulse. At each pressure level tested, 100 pulses were applied to the sample for each set of experiments. For 90°C samples, pulses were applied in four subsets of 25 pulses in order to ensure the temperature was maintained within the ±1°C criteria.

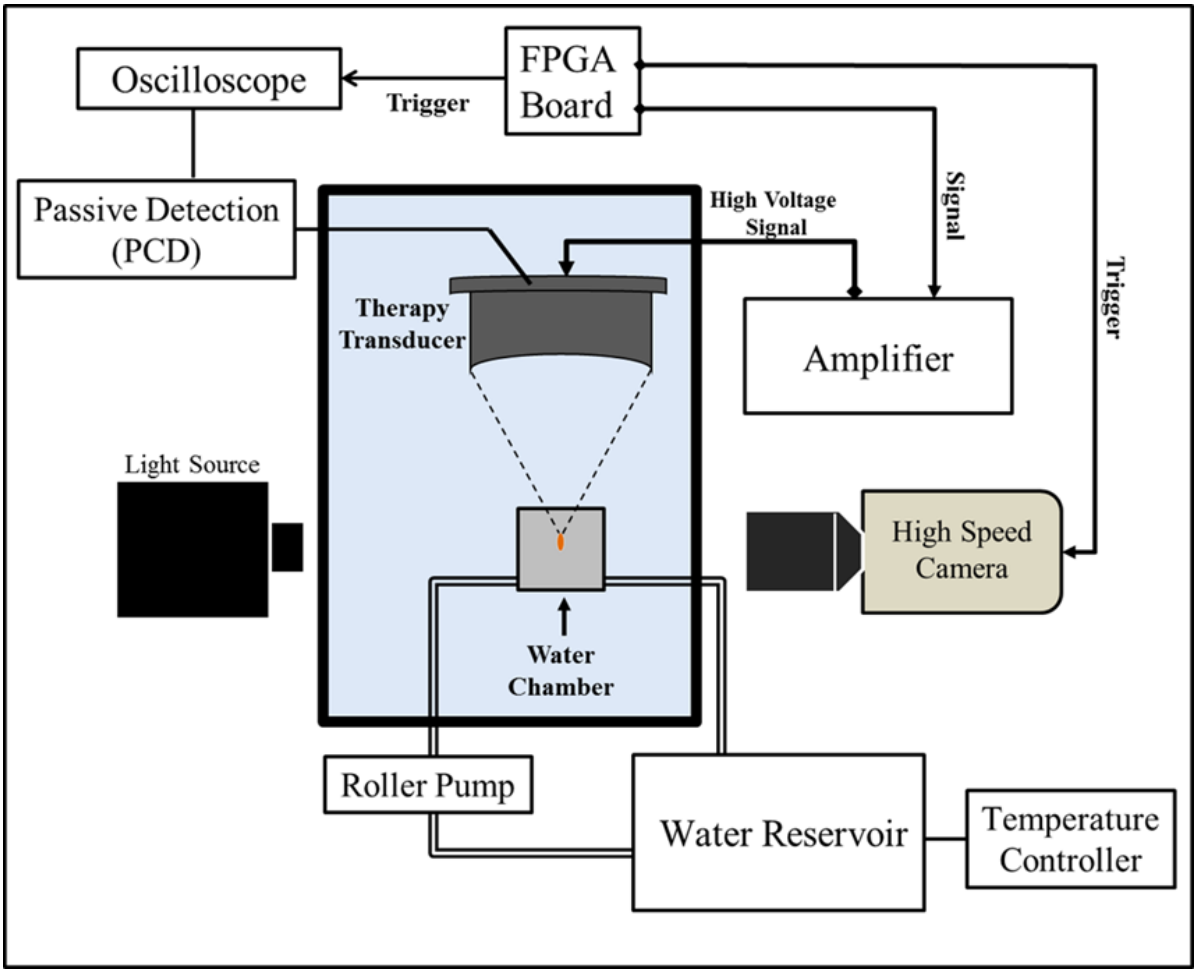

Figure 4.1. Histotripsy pulses were applied to the inside of distilled, degassed water heated to 10°C, 20°C, 40°C, 60°C, 80°C, and 90°C. Heated water was circulated into a 150-mL cavitation chamber using a roller pump, and the temperature inside the chamber was monitored using a type T hypodermic needle thermocouple. Cavitation was monitored using high speed optical imaging and passive cavitation detection using one of the therapy transducer elements.

4.2.3 Cavitation Detection using Optical Imaging

High speed optical imaging was used as a method to detect cavitation [Fig.4.1]. A high-speed, 1 megapixel CCD camera (Phantom V210, Vision Research, Wayne, NJ, USA) was aligned with the transducer focus through the optical window of the chamber. The camera was backlit by a continuous white-light source. The camera was focused using a macro-bellows lens (Tominon 1:4.5, F=105 mm; Kyocera, Kyoto, Japan), giving the captured images a resolution of

approximately 4.8 μm per pixel. The camera was triggered to record one image for each applied pulse at a time point approximately corresponding to the maximum bubble expansion, which was determined prior to experiments by changing the delay time on the camera to reconstruct representative radius vs. time curves of the bubbles and identify the time corresponding to maximum bubble expansion. The camera exposure time was 2 μs for all images. After acquisition, shadowgraph images were converted from grayscale to binary by an intensity threshold determined by the background intensity using image processing software (MATLAB; The Mathworks, Natick, MA, USA). Bubbles were indicated as any black regions >5 pixels in diameter. By this criterion, the minimum resolvable bubble radius was 12 μm. The number of frames that contained cavitation bubbles was recorded, and the fraction of total frames (out of 100) for which any cavitation was detected was determined as the cavitation probability.

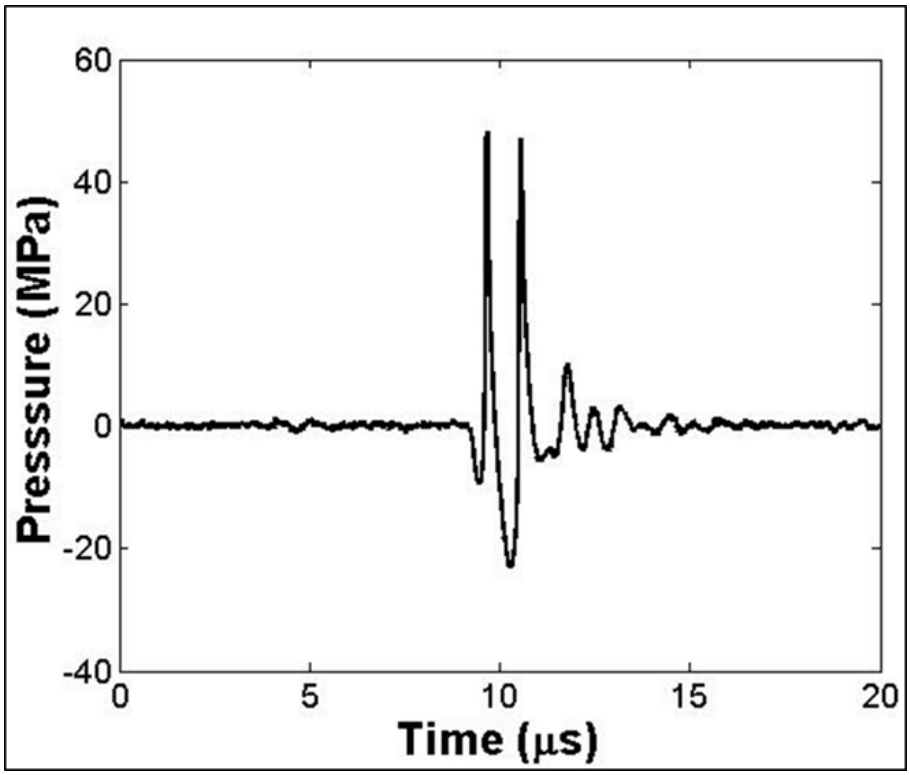

Figure 4.2. Plot shows an example acoustic waveform produced by the 1 MHz histotripsy transducer.

4.2.4 Passive Cavitation Detection (PCD)

In addition to high-speed imaging, an acoustic method was also used to identify cavitation in the focal zone in all media, following a previously established method [20, 21, 42]. Since relying upon an image of the bubbles taken at a single time point is a potential limitation, the PCD method allowed cavitation to be monitored over a much longer time period following the passage of the pulse. For each experiment, one of the transducer's therapy elements was also used to receive acoustic emission signals for PCD to detect the presence of cavitation in the focal region [Fig.4.1]. The PCD signal was connected to an oscilloscope (LT372; Lecroy, Chestnut Ridge, NY, USA) with the time window selected to record the backscattering of the therapy pulse from cavitation bubbles [20, 21, 24, 43]. To determine whether cavitation occurred during a pulse, the signal generated by backscattering of the incident pulse from the focus was analyzed following the method used in a previous study. The backscattered pressure amplitude was received by the PCD at the time point corresponding to two times the time of flight for the focal length of the respective transducers. The integrated frequency power spectrum (S_{PCD}) of the backscatter signal was used as a measure of whether cavitation occurred, following the method previously described by Maxwell *et al* [20].

4.2.5 Intrinsic Threshold Calculation and Comparison

The probability of observing cavitation followed a sigmoid function, given by

$$P(p_-) = \frac{1}{2} + erf\left(\frac{p_- - p_{int}}{\sqrt{2\sigma^2}}\right) \quad (\mathbf{E4.1})$$

where *erf* is the error function, p_{int} is the negative pressure at which the probability p_{cav}=0.5, σ is a variable related to the width of the transition between p_{cav}=0 and p_{cav}=1, with ± σ giving the difference in pressure from about p_{cav}=0.15 to p_{cav}=0.85 for the fit. The intrinsic threshold for

each sample, p_{int}, is defined as the p- corresponding to p_{cav}=0.5 as calculated by the curve fit. Curve fitting for all data sets was performed using an OriginLab curve fitting program (OriginPro 9.1; OriginLab Corporation, Northampton, MA, USA). The fit curves for all samples were analyzed statistically to determine whether the differences in the values of p_{int} were significantly different from each other. The standard errors for p_{int} were estimated by a covariance matrix using the delta method [44]. The curves were compared using a two-sample t-test with statistic $t\left(p_{int1}-p_{int2},\sqrt{SE_1^2+SE_2^2}\right)$ at a 95% confidence interval. Results were considered statistically significant for $p<0.05$. Note that the standard error does not include the uncertainty in absolute pressure from the hydrophone measurement, only the uncertainty in the fit, because the values of p_{int} are relative.

4.2.6 Threshold Simulation: Stabilized Nuclei

To provide a theoretical explanation for the experimental results, a numerical model treating water as a compressible Newtonian fluid with heat transfer was used to investigate the effects of temperature on the pressure threshold, assuming that the intrinsic threshold is due to nanometer-sized stabilized cavitation nuclei. In previous studies, a Kelvin-Voigt viscoelastic model neglecting heat transfer showed a pressure threshold matching the histotripsy intrinsic threshold at various frequencies when an initial bubble radius of ~2-3 nm was used [20, 21]. For nuclei of this size, the pressure due to surface tension is the primary factor that determines the cavitation threshold, similar to the Blake threshold [20, 21, 45, 46]. In this study, the effects of temperature on the threshold for generating inertial cavitation were first investigated using a 2.16 nm initial bubble, which was chosen to match the experimentally observed cavitation threshold

at 20˚C. To test the effects of temperature on the cavitation threshold for a 1 MHz histotripsy pulse, simulations exposed a 2.16 nm initial bubble to a single peak negative pressure

$$p_a(t) = \begin{cases} p_A \left(\frac{1+\cos[\omega(t-\delta)]}{2}\right)^n, & |t-\delta| \le \frac{\pi}{\omega} \\ 0, & |t-\delta| > \frac{\pi}{\omega} \end{cases} \quad \textbf{(E4.2)}$$

where p_A is the peak negative pressure, ω is the angular frequency of the sound wave, δ is a time delay, and n is a curve-fitting parameter which was set to 3.7 so that the shape of the simulated waveform p- closely matched the shape and duration of the p- from the histotripsy waveform used experimentally. For this study, we assume the surrounding medium to have homogeneous properties, and that the bubble contains air and remains spherical. These assumptions allow us to use a numerical model developed in-house for simulating spherical bubble dynamics in general viscoelastic media. To model water in this study, we assume a viscous medium of zero elasticity that includes a compressibility and heat transfer. We consider bubble dynamics governed by the Keller-Miksis equation [47]:

$$\left(1-\frac{\dot{R}}{c}\right)R\ddot{R} + \frac{3}{2}\left(1-\frac{\dot{R}}{3c}\right)\dot{R}^2 = \frac{1}{\rho}\left(1+\frac{\dot{R}}{c}+\frac{R}{c}\frac{d}{dt}\right)\left(p_B - p_\infty(t) - \frac{2S}{R} - \frac{4\mu\dot{R}}{R}\right) \quad (\mathbf{E4.3})$$

which depends on the medium's sound speed c, density ρ, and surface tension against air S. Here $p_\infty(t)$ is the absolute forcing pressure, r is the radial coordinate, and overdots ($\dot{}$) denote derivatives with respect to time, t. It is commonly assumed that the air within the bubble has a spatially uniform pressure given by the polytropic relationship $p_B = p_0(R_0/R)^{3\kappa}$ where κ=1.4 is the ratio of specific heats for air, R_0 is the initial bubble radius, and $p_0 = p_\infty(0) + 2S/R_0$ is the initial bubble pressure. For the purposes of this study, however, we employ a full thermal model that solves the partial differential equations for temperature fields inside and outside of the

bubble [48, 49]. The Keller-Miksis equation is coupled to the energy equation inside the bubble (**E5**) through the internal bubble pressure, p_B:

$$\dot{p_B} = \frac{3}{R}\left((\kappa - 1)K\frac{\partial T}{\partial r}\Big|_R - \kappa p_B \dot{R}\right) \quad (\mathbf{E4.4})$$

$$\frac{\kappa - 1}{\kappa}\frac{p_B}{T}\left[\frac{\partial T}{\partial t} + \frac{1}{\kappa p_B}\left((\kappa - 1)K\frac{\partial T}{\partial r} - \frac{r\dot{p_B}}{3}\right)\frac{\partial T}{\partial r}\right] - \dot{p}_B = \nabla \cdot (K\nabla T) \quad (\mathbf{E4.5})$$

where T is the radially varying temperature of the air inside the bubble, which has ratio of specific heats κ. The thermal conductivity of air inside the bubble is given by $K = K_A T + K_B$, where K_A and K_B are empirical constants. Prescribed conditions at the bubble-liquid interface relate the temperature inside the bubble to the temperature of the liquid medium outside of the bubble, T_M: $T|_{r=R} = T_M|_{r=R}$ and $K|_{r=R}\frac{\partial T}{\partial r}_{r=R} = K_M\frac{\partial T_M}{\partial r}\Big|_{r=R}$. This medium is assumed to have constant thermal conductivity (K_M), thermal diffusivity (D_M), specific heat (C_p), and density (ρ_∞). The energy equation outside of the bubble

$$\frac{\partial T_M}{\partial t} + \frac{R^2\dot{R}}{r^2}\frac{\partial T_M}{\partial r} = D_M\nabla^2 T_M + \frac{12\mu}{\rho_\infty C_p}\left(\frac{R^2\dot{R}}{r^3}\right)^2 \quad (\mathbf{E4.6})$$

includes a viscous dissipation term: $\frac{12\mu}{\rho_\infty C_p}\left(\frac{R^2\dot{R}}{r^3}\right)^2$, where μ is the viscosity of water. Two final boundary conditions complete the system: The temperature of the medium is assumed to approach an ambient temperature, T_∞ as $r \to \infty$ and, due to bubble symmetry, the internal temperature has a gradient of zero at the bubble center. A more detailed discussion of the numerical implementation of this model has been outlined in previous studies [48, 50].

To compare the effects of temperature (10˚C to 90˚C) on the cavitation threshold, the ambient temperature (T_∞), viscosity (μ), and surface tension (S) of water were varied. The values

of viscosity and surface tension as a function of temperature were taken from the literature [23, 51] and are listed in Table 4.1. The maximum bubble radius was plotted as a function of the peak negative pressure for an initial bubble of 2.16 nm, which was chosen to match the experimental data at 20°C. Additionally, separate simulations were conducted to compare the effects of ambient temperature, viscosity, and surface tension on the cavitation threshold independently. Finally, a further simulation was conducted to investigate the range of nuclei corresponding to the experimentally measured thresholds using the values of viscosity and surface tension listed in Table 4.1.

4.2.7 Threshold Simulation: Spontaneous Nuclei

To investigate the effects of temperature on the cavitation threshold predicted for spontaneous nucleation, a theoretical analysis was performed based on classical nucleation theory (CNT) [24, 37, 39, 40, 52]. CNT predicts that the cavitation threshold decreases at higher temperatures and the corresponding decrease in the surface energy of the medium [37, 40]. The threshold predicted by CNT, p_{t_CNT}, was calculated as

$$p_{t\_CNT} = \left(\frac{16\pi\alpha^3}{3k_bT * \ln\frac{\Gamma_0 V_f \tau_f}{\ln 2}} \right)^{0.5} \quad (\mathbf{E4.7})$$

where α is the surface energy, k_b is the Boltzmann's constant, T is temperature in Kelvin, Γ_0 is a prefactor, V_f is the focal volume for a given frequency, and τ_f is the time the focal volume is above a given pressure [24, 37-40]. Γ_0 was set to $\Gamma_0=10^{33}$ and τ_f set to one fourth of the acoustic period, similar to previous work [21, 40]. V_f was set to 6.64 mm^3, as calculated from the -6 dB FWHM beam profiles of the 1 MHz transducer used in this study assuming an ellipsoidal focus. For comparison with experiments, T was varied from 283K to 363K (10˚C to 90˚C) and the

surface energy, α, was set to 25% of the macroscopic surface tension of water, as calculated as a function of temperature [Table 4.1]. These values for surface energy were chosen based on previous work which suggesting that it is not accurate to use the bulk, macroscopic surface tension value for surface energy [21, 24, 38]. A surface energy value of ~25% of the macroscopic surface tension of water at 20˚C has been used in two previous studies in order to provide a more reasonable agreement with experimentally observed cavitation thresholds [21, 24].

Table 4.1. Table shows the viscosity and surface tension values of water as a function of temperature from literature [23, 51].

Temperature (°C)	Viscosity (mPa-s)	Surface Tension (mN-m)
0.1	1.79	75.64
10	1.31	74.23
20	1.00	72.75
30	0.80	71.20
40	0.65	69.60
50	0.55	67.94
60	0.47	66.24
70	0.40	64.47
80	0.35	62.67
90	0.31	60.82
100	0.28	58.91

4.3 Results

4.3.1 Intrinsic Threshold vs. Temperature

The intrinsic threshold for all samples was compared using the curve fitting method and statistical analysis described above. Comparing the effect of temperature on the histotripsy intrinsic threshold demonstrated a similar function of cavitation probability versus pressure at all

temperatures, with p_{int} decreasing as the temperature increased [Fig.4.3]. The p_{int} was observed to decrease from 28.4±1.3 MPa at 10˚C to 11.7±1.2 MPa at 90˚C [Table 4.2]. In general, the standard errors in the estimate of the intrinsic threshold, p_{int}, were small compared to the variance between samples at a given temperature. Additionally, results showed an increase in σ_{mean} with increasing temperature, with σ_{mean} ranging from 1.1 MPa at 10˚C to 3.3 MPa at 90˚C [Table 4.2]. The effect of temperature on the intinsic threshold was further analyzed by plotting p_{int} as a function of temperature, with linear regression analysis demonstrating that the change in p_{int} with temperature was significant via the Pearson correlation ($r=0.99$, $R^2=0.98$, $p<0.05$) [Fig.4.4].

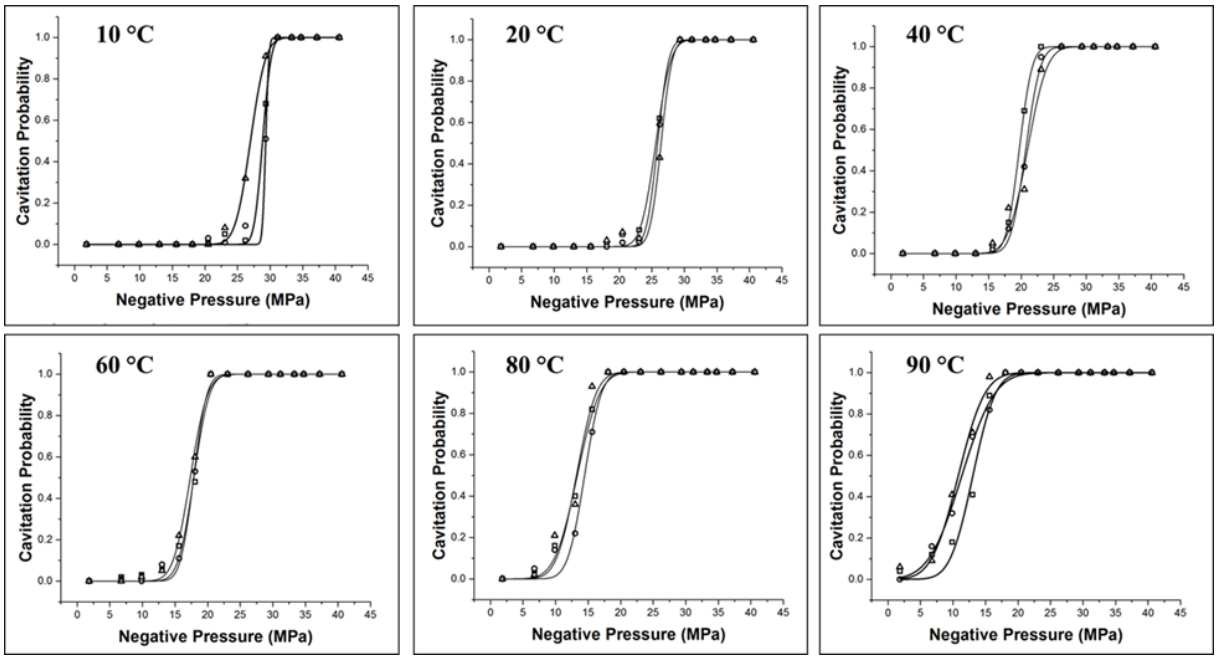

Figure 4.3. Example probability curves (n=3) for samples heated to 10°C-90°C. Results show a significant decrease in the intrinsic threshold, p_{int}, with increasing temperature.

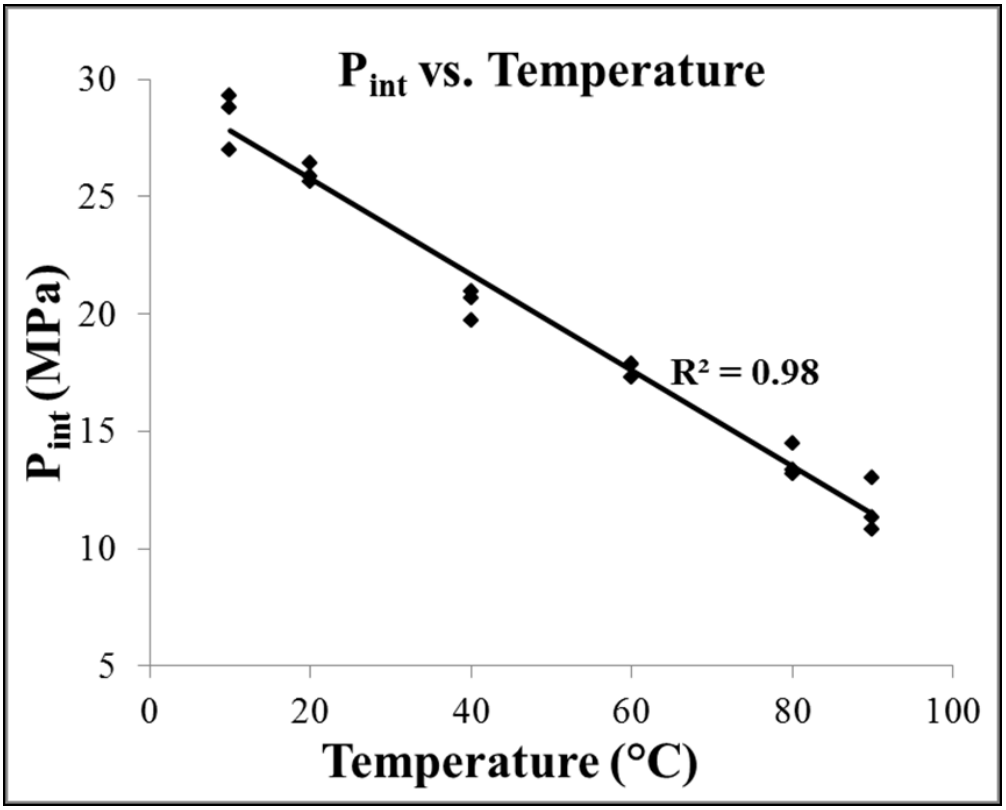

Figure 4.4. Scatter plot shows the p_{int} measured for all samples in this work as a function of temperature. Linear regression analysis demonstrated that the change in p_{int} with increasing temperature was significant via the Pearson correlation ($r=0.99$, $R^2=0.98$, $p<0.05$).

Table 4.2. Table shows the values for the intrinsic threshold, p_{int}, calculated by the fitted curves for each sample, as well as the mean values for p_{int} and σ. All values are pressure in MPa.

Temperature	P_{int} (1)	P_{int} (2)	P_{int} (3)	P_{int} (mean)	σ (mean)
10°C	28.84	29.31	26.98	28.4	1.1
20°C	25.62	25.88	26.41	26.0	1.5
40°C	19.70	20.69	20.95	20.4	1.9
60°C	17.88	17.85	17.30	17.7	1.9
80°C	13.33	14.46	13.21	13.7	2.4
90°C	13.05	10.80	11.34	11.7	3.3

4.3.2 Optical images of Cavitation Bubble Cloud

Cavitation bubbles were observed on the high-speed camera when a certain negative pressure was exceeded. For example, Figure 4.5 and Figure 4.6 show example optical images

and PCD signals taken for samples heated to 20˚C and 80˚C, respectively. As the pressure was further increased, the bubbles were visualized in an increasingly larger area with a greater number of bubbles present in the focal region [Fig.4.5, Fig.4.6], similar to the behavior of intrinsic threshold bubble clouds observed in previously studies [19-22, 42]. Although the bubbles covered a larger area at higher pressure, the diameter of the bubbles that could be individually identified appeared to be consistent between pressure levels at the time point captured by the camera, potentially due to bubble-bubble interactions suppressing the growth of adjacent bubbles or bubble-induced pressure saturation caused by energy loss into each bubble as it forms, as has previously been proposed [22]. When increasing the temperature, the pressure at which cavitation was observed was reduced [Fig.4.5, Fig.4.6]. However, no apparent differences in the appearance of the bubble clouds were observed for different temperatures [Fig.4.5, Fig.4.6]. For example, the cavitation bubble clouds formed at 20˚C ([Fig.4.5], appeared to show similar bubble cloud appearance (i.e. well-defined bubble clouds with similar sized bubbles throughout the cloud) to the bubble clouds formed at 80˚C [Fig.4.6]. Due to the decrease in threshold at higher temperatures, the size of the bubble cloud for a given pressure level increased at higher temperature.

4.3.3 Passive Cavitation Detection (PCD)

In addition to high speed imaging, cavitation was monitored using one of the therapy transducer elements for PCD following a previously established method [20, 21, 42], with results showing close agreement between optical imaging and PCD detection methods [Fig.4.5, Fig.4.6]. When cavitation occurred on high-speed images, the PCD signal was a multi-cycle burst of significantly increased amplitude with a center frequency near the therapy transducer frequency.

When no cavitation was observed on the camera, the PCD signal amplitude was small. At higher temperatures, the PCD signal arrived at the transducer sooner than at lower temperatures due to the reduced speed of sound in the warmer water. However, no noticeable differences in the frequency of the PCD signal were observed at different temperatures.

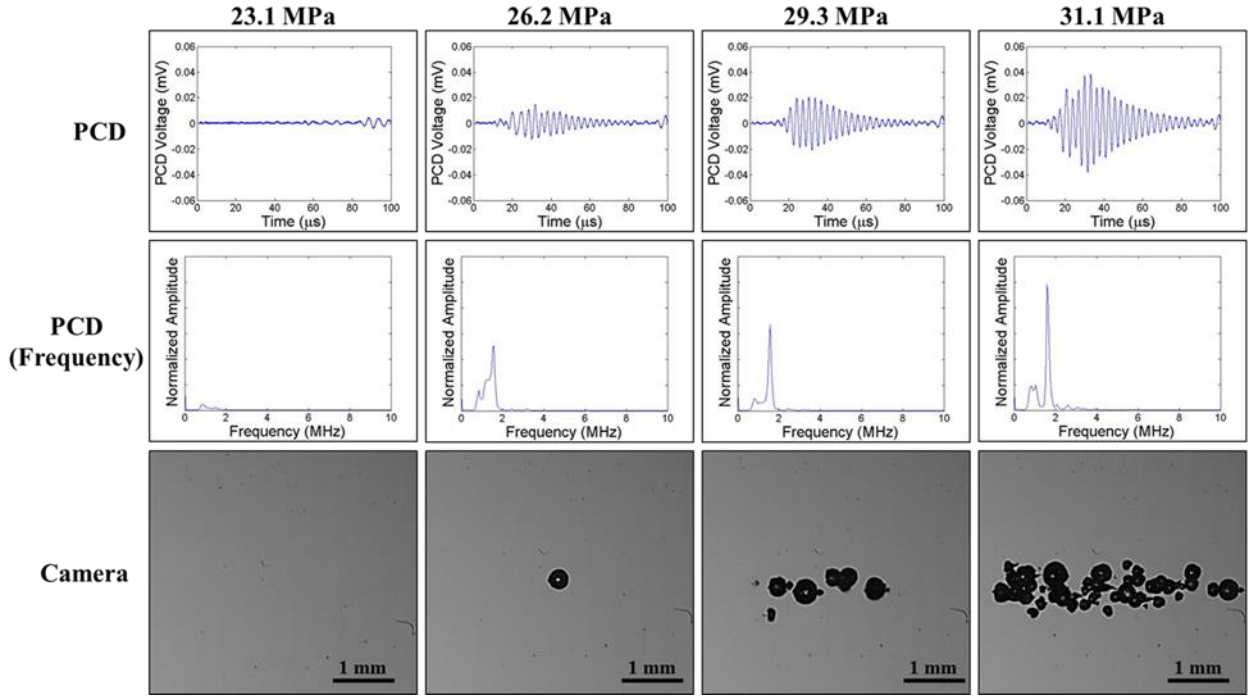

Figure 4.5. Cavitation Detection: 20°C. Images show sample PCD and optical imaging results for pulses applied to distilled, degassed water heated to 20°C. PCD temporal (top) and frequency (middle) signals showed good agreement with high speed optical images of cavitation (bottom).

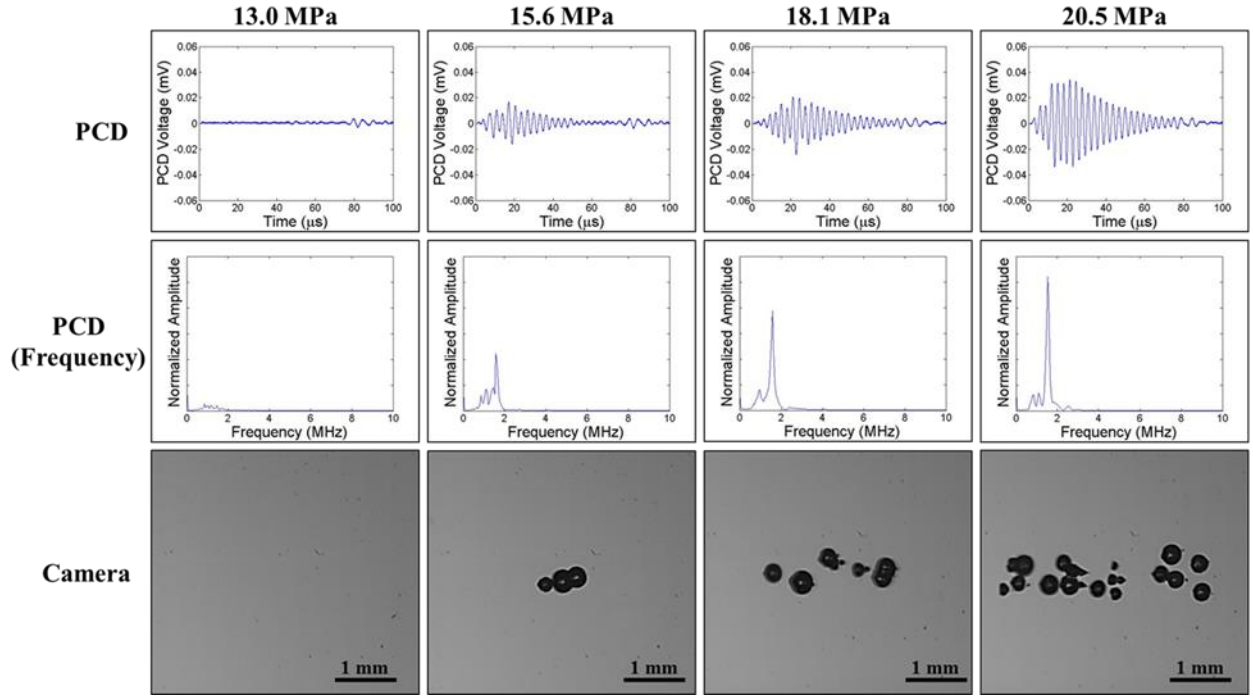

Figure 4.6. Cavitation Detection: 80°C. Images show sample PCD and optical imaging results for pulses applied to distilled, degassed water heated to 80°C. PCD temporal (top) and frequency (middle) signals showed good agreement with high speed optical images of cavitation (bottom).

4.3.4 Threshold Simulation: Stabilized Nuclei

To provide a theoretical explanation for the experimental results, the effects of ambient temperature and the corresponding changes in surface tension and viscosity on the cavitation threshold were investigated using a single bubble numerical simulation assuming a nanometer sized stable nucleus. When the peak negative pressure, p_A, was less than some threshold value, p_{t_sim}, bubble expansion was minimal ($R_{max}<2\ R_0$). As p_A was increased above p_{t_sim}, great bubble growth and collapse were observed ($R_{max}>10^4\ R_0$). The peak negative pressure corresponding to this transition was defined as the inertial cavitation threshold, p_{t_sim}. Using a 2.16 nm initial bubble, p_{t_sim} was observed to decrease with increasing temperature when using the values for surface tension and viscosity shown in Table 4.1. For example, Figure 4.7 shows p_{t_sim} decreased from ~26.5 MPa at 10˚C to ~21.75 MPa at 90˚C. Although p_{t_sim} significantly decreased with

increasing temperature, only negligible differences in the maximum bubble radius, R_{max}, were observed at different temperatures [Fig.4.7], similar to experimental observations [Fig.4.5, Fig.4.6]. For example, the R_{max} at the threshold for 10˚C (p_{t_sim}=~26.54 MPa) was ~110 µm compared to an R_{max} of ~100 µm at the threshold for 90˚C (p_{t_sim}=~21.75 MPa). The similar values for R_{max} for these different conditions is due to the fact that only the initial threshold behavior is dominated by surface tension, while the larger expansion behavior and final bubble size are dictated by several competing terms including the applied pressure and viscosity of the fluid.

Simulations independently modulating ambient temperature [Fig.4.8(A)], viscosity [Fig.4.8(B)], and surface tension [Fig.4.8(C)] were also conducted, demonstrating that the increase in p_{t_sim} was primarily due to the changes in surface tension at higher temperatures. No significant changes in p_{t_sim} were observed when the ambient temperature was changed from T_∞ =10˚C to T_∞ =90˚C for a constant surface tension of $S_{20^\circ C}$=72 mN-m [Fig.4.8(A)]. Simulations performed at 20˚C with viscosity varied from $\mu_{10^\circ C}$=1.31 mPa-s to $\mu_{90^\circ C}$=0.31 mPa-s demonstrated only a negligible decrease of ~0.02 MPa with decreasing values of viscosity [Fig.4.8(B)]. Simulations performed at 20˚C with surface tension varied from $S_{10^\circ C}$=74.21 mN-m to $S_{90^\circ C}$=60.8 mN-m demonstrated an increase in p_{t_sim} for increasing values of surface tension, ranging from p_{t_sim}=26.54 MPa at $S_{10^\circ C}$=74.21 mN-m to p_{t_sim}=21.76 MPa at $S_{90^\circ C}$=60.8 mN-m [Fig.4.8(C)].

In addition to investigating the changes in the cavitation threshold with changing temperature, the single bubble model was also used to estimate the potential nuclei sizes that would be predicted based on the experimentally observed cavitation thresholds. Using the viscosity and surface tension values in Table 4.1, simulations showed that the experimentally

observed thresholds shown in Table 4.2 corresponded to initial bubble sizes ranging from 2.02 nm at 10˚C to 4.02 nm at 90˚C [Fig.4.8(D)].

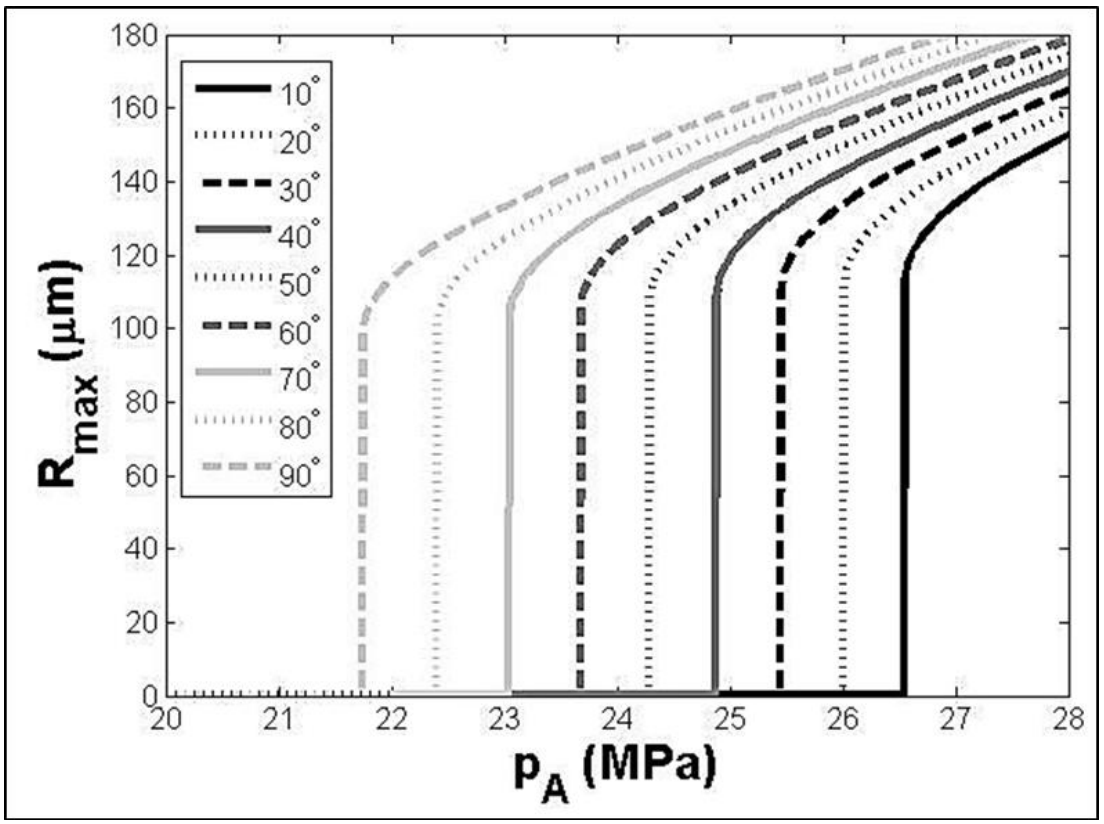

Figure 4.7. Stabilized Nuclei Simulation: Maximum Radius vs. Pressure. Simulated maximum bubble radius for a 2.16 nm initial bubble subjected to a single cycle negative pressure waveform exposed to water at 10°C-90°C using the values for surface tension and viscosity shown in Table 4.1. Results demonstrated a significant decrease in the cavitation threshold, p_{t_sim}, with increasing temperature.

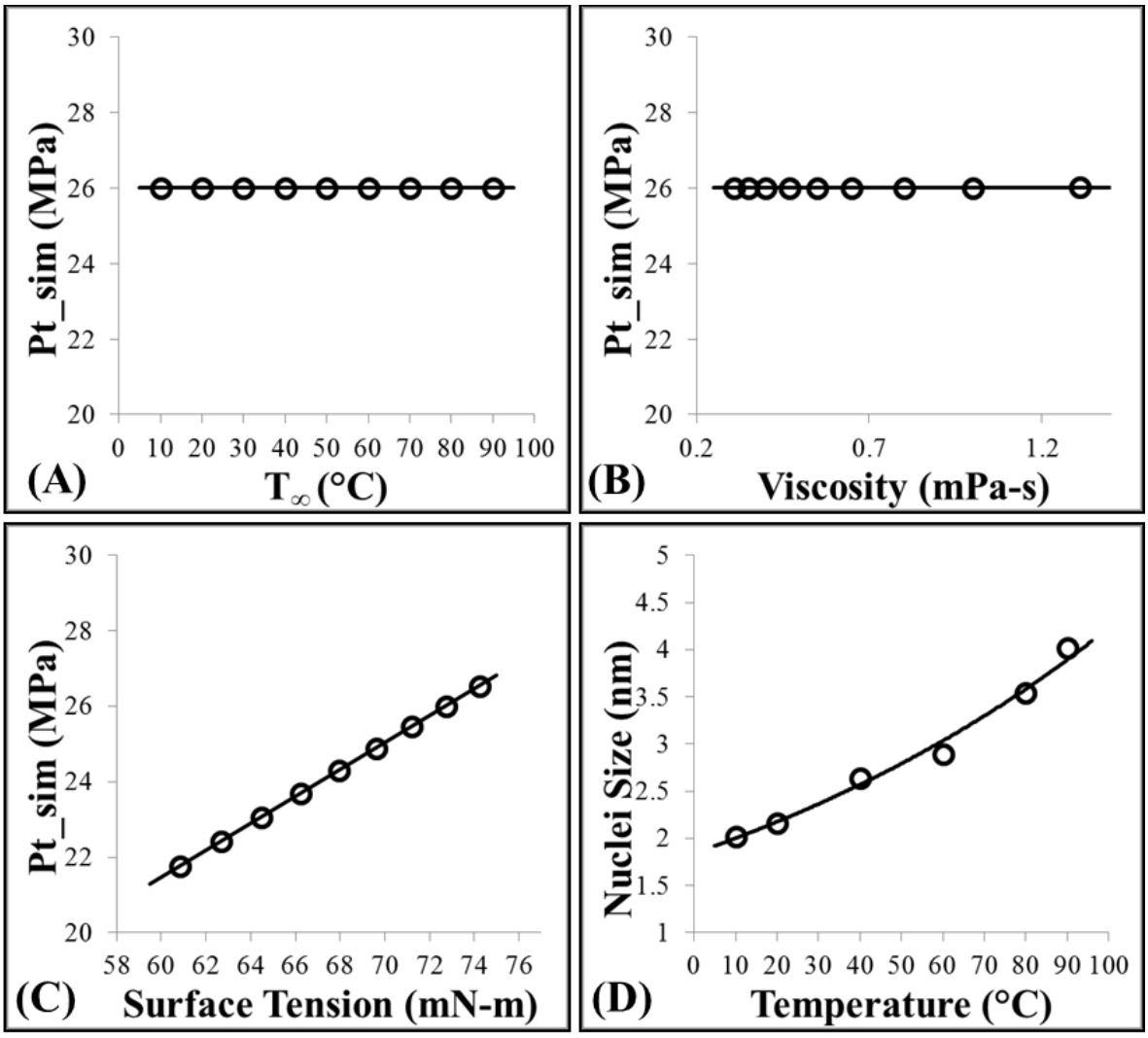

Figure 4.8. Stabilized Nuclei Simulations. Simulations independently changing (**A**) ambient temperature, (**B**) viscosity, and (**C**) surface tension demonstrated the decrease in threshold at higher temperatures was primarily due to changes in surface tension. (**D**) A further simulation demonstrated that the experimentally measured intrinsic thresholds corresponded to initial bubble sizes ranging from ~2 nm at 10ºC to ~4 nm at 90ºC.

4.3.5 Threshold Simulation: Spontaneous Nucleation

The effects of temperature on the cavitation threshold predicted by classical nucleation theory (CNT) were investigated with a simulation as described in the Methods (E4.7). CNT results predicted that the cavitation threshold would decrease with increasing temperature and the

corresponding decrease in surface energy, with the results ranging from p_{t_CNT}=25.3 MPa at 10˚C to p_{t_CNT}=16.5 MPa at 90˚C [Fig.4.9].

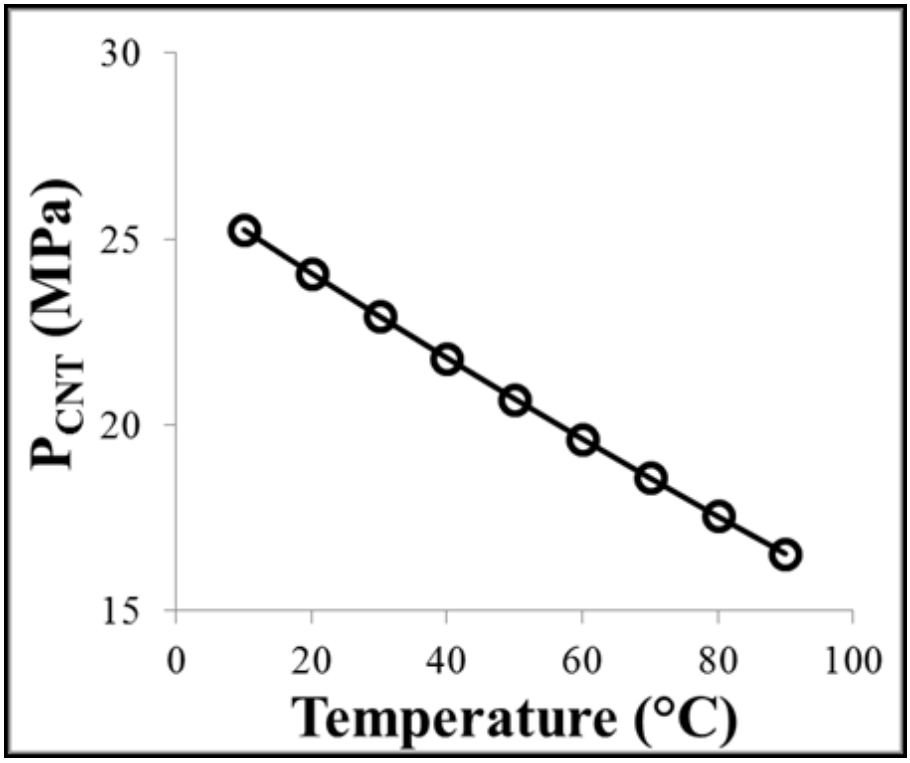

Figure 4.9. CNT Simulation. (A) Classical nucleation theory was used to predict the effects of temperature on the cavitation threshold, with results demonstrating p_{t_CNT} decreased from ~25.3 MPa at 10˚C to ~16.5 MPa at 90˚C.

4.4 Discussion

In this study, the effects of temperature on the histotripsy intrinsic threshold were investigated, with results supporting our hypothesis that increasing temperature decreases the intrinsic cavitation threshold. A nearly linear decrease in the intrinsic threshold was observed as the temperature was increased from 10˚C to 90˚C, ranging from ~28 MPa at 10˚C to ~12 MPa at 90˚C. At higher temperatures, the histotripsy bubble clouds were generated at significantly reduced pressure, but showed no significant changes in bubble cloud behavior. These findings are consistent with our hypothesis that the histotripsy intrinsic threshold decreases at higher

temperatures due to the lower surface tension, as the surface tension has previously been shown to dominate the initial threshold behavior [20, 21], while having only a minor influence on the resulting bubble expansion and collapse behavior [22].

The experimental results in this study were supported by theoretical analysis demonstrating that the changes in the intrinsic threshold at higher temperature are primarily due to the increased temperature and the corresponding decrease in the surface tension of the media. Results from the stable bubble model demonstrated that the cavitation threshold for nanometer-sized gas nuclei is highly dependent upon the temperature of the medium, with an ~5 MPa decrease in the threshold predicted when the temperature is increased from 10˚C to 90˚C for an initial bubble size of 2.16 nm. The stable bubble model further calculated that the experimentally observed intrinsic thresholds correlated to an initial bubble size ranging from ~2 nm at 10˚C to ~4 nm at 90˚C. While it is possible that this analysis might shed some light on the size range the "intrinsic nuclei" and potential changes in nuclei size with temperature, it remains unclear if these "intrinsic nuclei" are in fact nanometer-sized stable bubbles or spontaneous nuclei, as similar trends in the cavitation threshold with temperature were predicted by the CNT model which assumes spontaneous nucleation. The CNT results demonstrated a significant decrease of ~9 MPa in the threshold as the temperature was increased from 10˚C to 90˚C. While the results from the two models used in this study do not precisely match the experimentally measured thresholds which showed a larger decrease with temperature, they may provide some insight into the physical mechanisms responsible for the experimentally observed decrease in the intrinsic threshold, as both models supported the hypothesis that the decrease in the intrinsic threshold is primarily due to the decrease in surface tension at higher temperatures.

The finding that the intrinsic threshold decreases as temperature increases is of significant importance to the development of histotripsy therapy and suggests that the intrinsic threshold *in vivo* will be predictable based on the local tissue temperature and pulsing parameters. For example, the results of this study calculated that the intrinsic threshold near body temperature using a 1 MHz transducer was ~20.4 MPa (40˚C), compared to ~26 MPa at 20˚C. These results also suggest that the intrinsic threshold could be modulated by altering the focal temperature (i.e. using lower amplitude pulses for heating followed by a single large negative pressure cycle), which would allow the benefits of intrinsic threshold histotripsy to be taken advantage of at a reduced pressure level. These benefits of using the intrinsic threshold method include generating well-confined bubble clouds matching the portion of the beam profile above the intrinsic threshold as well as the ability to precisely modulate the bubble dynamics by altering the pulse parameters [19, 21, 22, 53]. In addition to modulating the intrinsic threshold by altering the focal temperature, the results of this study suggest that the intrinsic threshold could be altered using other approaches that change the surface tension of the media at the focus, as has previously been shown using perfluorocarbon nanodroplets for nanodroplet-mediated histotripsy [42, 54, 55].

In addition to intrinsic threshold histotripsy, the results of this study may also be relevant to cavitation generation using other methods of cloud initiation such as boiling histotripsy and shock scattering histotripsy. For example, the intrinsic threshold observed at higher temperatures (P– = ~12 MPa at 90°C) was within the pressure range commonly used for boiling histotripsy (P– = ~8-14 MPa). It is possible that the boiling bubble is generated at the point when the temperature at the focus is raised sufficiently high to lower the intrinsic threshold of the media to the level of the incident P–. However, it remains unclear if the same process is responsible for

boiling histotripsy and intrinsic threshold histotripsy, as the longer pulse durations using in boiling histotripsy suggest that the boiling bubble may also generated from larger heterogeneous cavitation nuclei in the focus, similar to the nucleation process in shock scattering histotripsy. If this latter process is responsible for nucleating the boiling bubble, then the differences between shock scatting and boiling histotripsy would primarily be differences in the bubble dynamics (i.e. dense bubble cloud vs. single large boiling bubble), which would occur once the temperature reaches the point where the vapor pressure inside the bubble is larger than the atmospheric pressure. This possibility seems to be supported by observations of smaller cavitation bubbles forming at the focus in boiling histotripsy prior to the formation of the large boiling bubble. Future work is needed to fully explain the nucleation process in boiling histotripsy. In addition to the nucleation of the boiling bubble, the results of this study may also be relevant to the phenomenon of cavitation shielding in boiling histotripsy, which occurs in the prefocal region at higher pressure amplitudes and prevents the formation of a boiling bubble [56]. Using the results of this study along with the spatial pressure and temperature distributions in the focal region of boiling histotripsy, it may be possible to predict the thresholds for generating prefocal bubbles, if in fact these bubbles are generated above the intrinsic threshold in these regions. Future work will further investigate this possibility.

The results of this study may also be relevant to generating bubble clouds using shock scattering histotripsy. Previous work studying the shock scatting method of bubble cloud initiation has suggested that shock scattering bubble clouds are likely initiated from larger, heterogeneous nuclei in the medium [17, 18]. The cavitation threshold for these larger bubbles is no longer dominated by the surface tension of the medium [17, 18, 21, 22, 45, 46, 54, 57, 58], suggesting that the initial threshold behavior in shock scattering histotripsy may not be

significantly affected by the temperature of the medium and the corresponding changes in surface tension (although the lower intrinsic threshold will likely decrease the total negative pressure required to generate a dense bubble cloud after shock scattering has occurred). In addition, this also suggests that changes in temperature may not significantly change the pressure required for "incidental cavitation bubbles" generated using longer duration pulses, high PRF, or constant exposures [28-33]. Previous work suggests that these "incidental bubbles" are generated from larger heterogeneous cavitation nuclei similar to shock scattering, which are less reliable for generating a bubble cloud compared to the intrinsic threshold and do not show the same distinct threshold behavior since the cavitation threshold is not dominated by the surface tension of the medium [28-33]. These "incidental bubbles" are minimized in intrinsic threshold histotripsy due to the very short pulses applied at low PRF (≤1Hz), but are likely responsible for the deviations from the intrinsic threshold curves at lower pressures observed in this and previous studies [20, 21]. Future work will investigate the effects of temperature on the shock scattering and "incidental bubble" thresholds.

4.5 Conclusion

In this chapter, the effects of temperature on the histotripsy intrinsic threshold were investigated by applying 1-2 cycle histotripsy pulses to distilled, degassed water heated between 10˚C to 90˚C using a 1 MHz histotripsy transducer. Results demonstrated that the histotripsy intrinsic threshold significantly decreased with increasing temperature, showing a nearly linear decrease from 28.4±1.3 MPa at 10˚C to 11.7±1.2 MPa at 90˚C. Theoretical analysis suggested that this decrease in the intrinsic threshold at higher temperatures is primarily due to the decreases in surface tension. Based on our previous work, the intrinsic thresholds in water are

expected to match closely with the intrinsic thresholds in tissue phantoms and soft tissues that are water-based. Overall, the results of this chapter indicate that the intrinsic threshold to initiate a histotripsy bubble cloud is highly dependent upon the temperature of the medium, which may allow for a better prediction of cavitation generation at body temperature or at the elevated temperatures commonly achieved in boiling histotripsy and ultrasound thermal therapies.

4.6 References

[1] J. E. Parsons, *et al.*, "Pulsed cavitational ultrasound therapy for controlled tissue homogenization," *Ultrasound Med Biol*, vol. 32, pp. 115-29, Jan 2006.

[2] W. W. Roberts, *et al.*, "Pulsed cavitational ultrasound: a noninvasive technology for controlled tissue ablation (histotripsy) in the rabbit kidney," *J Urol*, vol. 175, pp. 734-8, Feb 2006.

[3] Z. Xu, *et al.*, "Controlled ultrasound tissue erosion: the role of dynamic interaction between insonation and microbubble activity," *J Acoust Soc Am*, vol. 117, pp. 424-35, Jan 2005.

[4] J. E. Parsons, *et al.*, "Spatial variability in acoustic backscatter as an indicator of tissue homogenate production in pulsed cavitational ultrasound therapy," *IEEE Trans Ultrason Ferroelectr Freq Control*, vol. 54, pp. 576-90, Mar 2007.

[5] T. L. Hall, *et al.*, "Histotripsy of rabbit renal tissue in vivo: temporal histologic trends," *J Endourol*, vol. 21, pp. 1159-66, Oct 2007.

[6] E. Vlaisavljevich, *et al.*, "Effects of tissue mechanical properties on susceptibility to histotripsy-induced tissue damage," *Phys Med Biol*, vol. 59, pp. 253-70, Jan 20 2014.

[7] Z. Xu, *et al.*, "Investigation of intensity thresholds for ultrasound tissue erosion," *Ultrasound Med Biol*, vol. 31, pp. 1673-82, Dec 2005.

[8] C. R. Hempel, *et al.*, "Histotripsy fractionation of prostate tissue: local effects and systemic response in a canine model," *J Urol*, vol. 185, pp. 1484-9, Apr 2011.

[9] A. P. Duryea, *et al.*, "In vitro comminution of model renal calculi using histotripsy," *IEEE Trans Ultrason Ferroelectr Freq Control*, vol. 58, pp. 971-80, May 2011.

[10] A. D. Maxwell, *et al.*, "Noninvasive treatment of deep venous thrombosis using pulsed ultrasound cavitation therapy (histotripsy) in a porcine model," *J Vasc Interv Radiol*, vol. 22, pp. 369-77, Mar 2011.

[11] G. E. Owens, *et al.*, "Therapeutic ultrasound to noninvasively create intracardiac communications in an intact animal model," *Catheter Cardiovasc Interv*, vol. 77, pp. 580-8, Mar 1 2011.

[12] Z. Xu, *et al.*, "Noninvasive creation of an atrial septal defect by histotripsy in a canine model," *Circulation*, vol. 121, pp. 742-9, Feb 16 2010.

[13] N. R. Styn, *et al.*, "Histotripsy of VX-2 tumor implanted in a renal rabbit model," *J Endourol*, vol. 24, pp. 1145-50, Jul 2010.

[14] E. Vlaisavljevich, *et al.*, "Image-Guided Non-Invasive Ultrasound Liver Ablation Using Histotripsy: Feasibility Study in an In Vivo Porcine Model," *Ultrasound in medicine & biology,* vol. 39, pp. 1398-1409, 2013.

[15] J. C. Simon, *et al.*, "Ultrasonic atomization of tissue and its role in tissue fractionation by high intensity focused ultrasound," *Phys Med Biol,* vol. 57, pp. 8061-78, Dec 7 2012.

[16] Y. N. Wang, *et al.*, "Histological and biochemical analysis of mechanical and thermal bioeffects in boiling histotripsy lesions induced by high intensity focused ultrasound," *Ultrasound Med Biol,* vol. 39, pp. 424-38, Mar 2013.

[17] A. D. Maxwell, *et al.*, "Cavitation clouds created by shock scattering from bubbles during histotripsy," *J Acoust Soc Am,* vol. 130, pp. 1888-98, Oct 2011.

[18] E. Vlaisavljevich, *et al.*, "Histotripsy-induced cavitation cloud initiation thresholds in tissues of different mechanical properties," *IEEE Trans Ultrason Ferroelectr Freq Control,* vol. 61, pp. 341-52, Feb 2014.

[19] K. W. Lin, *et al.*, "Histotripsy beyond the intrinsic cavitation threshold using very short ultrasound pulses: microtripsy," *IEEE Trans Ultrason Ferroelectr Freq Control,* vol. 61, pp. 251-65, Feb 2014.

[20] A. D. Maxwell, *et al.*, "Probability of cavitation for single ultrasound pulses applied to tissues and tissue-mimicking materials," *Ultrasound Med Biol,* vol. 39, pp. 449-65, Mar 2013.

[21] E. Vlaisavljevich, *et al.*, "Effects of Ultrasound Frequency and Tissue Stiffness on the Histotripsy Intrinsic Threshold for Cavitation," *Ultrasound Med Biol,* 2015.

[22] E. Vlaisavljevich, *et al.*, "Effects of Tissue Stiffness, Ultrasound Frequency, and Pressure on Histotripsy-induced Cavitation Bubble Behavior," *Phys Med Biol,* 2015.

[23] N. B. Vargaftik, *et al.*, "International Tables of the Surface-Tension of Water," *Journal of Physical and Chemical Reference Data,* vol. 12, pp. 817-820, 1983.

[24] E. Herbert, *et al.*, "Cavitation pressure in water," *Physical Review E,* vol. 74, Oct 2006.

[25] L. J. Briggs, "The Limiting Negative Pressure of Water between 0-Degrees-C and 50-Degrees-C," *Science,* vol. 111, pp. 461-461, 1950.

[26] M. Greenspan and C. E. Tschiegg, "Radiation-Induced Acoustic Cavitation - Threshold Versus Temperature for Some Liquids," *Journal of the Acoustical Society of America,* vol. 72, pp. 1327-1331, 1982.

[27] G. N. Sankin and V. S. Teslenko, "Two-threshold cavitation regime," *Doklady Physics,* vol. 48, pp. 665-668, Dec 2003.

[28] E. L. Carstensen, *et al.*, "The search for cavitation in vivo," *Ultrasound Med Biol,* vol. 26, pp. 1377-85, Nov 2000.

[29] J. B. Fowlkes and L. A. Crum, "Cavitation threshold measurements for microsecond length pulses of ultrasound," *J Acoust Soc Am,* vol. 83, pp. 2190-201, Jun 1988.

[30] C. K. Holland and R. E. Apfel, "Thresholds for transient cavitation produced by pulsed ultrasound in a controlled nuclei environment," *J Acoust Soc Am,* vol. 88, pp. 2059-69, Nov 1990.

[31] Z. Kyriakou, *et al.*, "HIFU-induced cavitation and heating in ex vivo porcine subcutaneous fat," *Ultrasound Med Biol,* vol. 37, pp. 568-79, Apr 2011.

[32] J. Gateau, *et al.*, "In vivo bubble nucleation probability in sheep brain tissue," *Phys Med Biol,* vol. 56, pp. 7001-15, Nov 21 2011.

[33] J. Gateau, *et al.*, "Statistics of acoustically induced bubble-nucleation events in in vitro blood: a feasibility study," *Ultrasound Med Biol,* vol. 39, pp. 1812-25, Oct 2013.

[34] N. F. Bunkin, *et al.*, "Cluster structure of stable dissolved gas nanobubbles in highly purified water," *Journal of Experimental and Theoretical Physics,* vol. 108, pp. 800-816, May 2009.

[35] E. N. Harvey, *et al.*, "Bubble formation in animals I. Physical factors," *Journal of Cellular and Comparative Physiology,* vol. 24, pp. 1-22, Aug 1944.

[36] D. E. Yount, "Skins of Varying Permeability - Stabilization Mechanism for Gas Cavitation Nuclei," *Journal of the Acoustical Society of America,* vol. 65, pp. 1429-1439, 1979.

[37] A. Arvengas, *et al.*, "Fiber optic probe hydrophone for the study of acoustic cavitation in water," *Rev Sci Instrum,* vol. 82, p. 034904, Mar 2011.

[38] A. Arvengas, *et al.*, "Cavitation in heavy water and other liquids," *J Phys Chem B,* vol. 115, pp. 14240-5, Dec 8 2011.

[39] J. C. Fisher, "The Fracture of Liquids," *Journal of Applied Physics,* vol. 19, pp. 1062-1067, 1948.

[40] M. S. Pettersen, *et al.*, "Experimental investigation of cavitation in superfluid 4He," *Phys Rev B Condens Matter,* vol. 49, pp. 12062-12070, May 1 1994.

[41] J. E. Parsons, *et al.*, "Cost-effective assembly of a basic fiber-optic hydrophone for measurement of high-amplitude therapeutic ultrasound fields," *J Acoust Soc Am,* vol. 119, pp. 1432-40, Mar 2006.

[42] E. Vlaisavljevich, *et al.*, "Effects of Ultrasound Frequency on Nanodroplet-Mediated Histotripsy," *Ultrasound Med Biol,* May 7 2015.

[43] R. A. Roy, *et al.*, "An Acoustic Backscattering Technique for the Detection of Transient Cavitation Produced by Microsecond Pulses of Ultrasound," *Journal of the Acoustical Society of America,* vol. 87, pp. 2451-2458, Jun 1990.

[44] D. W. Hosmer and S. Lemeshow, "Confidence interval estimation of interaction," *Epidemiology,* vol. 3, pp. 452-6, Sep 1992.

[45] F. G. Blake, "Gas Bubbles as Cavitation Nuclei," *Physical Review,* vol. 75, pp. 1313-1313, 1949.

[46] T. G. Leighton, *The acoustic bubble*: Academic Press, San Diego, 1994.

[47] J. B. Keller and M. Miksis, "Bubble Oscillations of Large-Amplitude," *Journal of the Acoustical Society of America,* vol. 68, pp. 628-633, 1980.

[48] V. Kamath, *et al.*, "A Theoretical-Study of Sonoluminescence," *Journal of the Acoustical Society of America,* vol. 94, pp. 248-260, Jul 1993.

[49] A. Prosperetti, *et al.*, "Nonlinear Bubble Dynamics," *Journal of the Acoustical Society of America,* vol. 83, pp. 502-514, Feb 1988.

[50] M. Warnez and E. Johnsen, "The effect of relaxation time on cavitation dynamics in viscoelastic media: A numerical investigation of growth and forced oscillations," *[In Preparation],* 2014.

[51] L. Korson, *et al.*, "Viscosity of Water at Various Temperatures," *Journal of Physical Chemistry,* vol. 73, pp. 34-&, 1969.

[52] F. Caupin and E. Herbert, "Cavitation in water: a review," *Comptes Rendus Physique,* vol. 7, pp. 1000-1017, Nov-Dec 2006.

[53] K. W. Lin, *et al.*, "Dual-beam histotripsy: a low-frequency pump enabling a high-frequency probe for precise lesion formation," *IEEE Trans Ultrason Ferroelectr Freq Control,* vol. 61, pp. 325-40, Feb 2014.

[54] E. Vlaisavljevich, *et al.*, "Nanodroplet-mediated histotripsy for image-guided targeted ultrasound cell ablation," *Theranostics,* vol. 3, pp. 851-64, 2013.

[55] Y. Yuksel Durmaz, *et al.*, "Development of nanodroplets for histotripsy-mediated cell ablation," *Mol Pharm,* vol. 11, pp. 3684-95, Oct 6 2014.

[56] T. Khokhlova, *et al.*, "Comparison of Boiling Histotripsy Lesions Generated at Different Ultrasound Frequencies.," presented at the International Symposium for Therapeutic Ultrasound, Utrecht, Netherlands, 2015.

[57] X. Yang and C. C. Church, "A model for the dynamics of gas bubbles in soft tissue," *J Acoust Soc Am,* vol. 118, pp. 3595-606, Dec 2005.

[58] A. D. Maxwell, *et al.*, "Inception of Cavitation Clouds by Scattered Shockwaves," *IEEE Ultrasonics Symposium*, pp. 3B-2, 2010.

Chapter 5

Effects of Tissue Mechanical Properties on Susceptibility to Histotripsy-induced Tissue Damage

A majority component of this chapter has been published in *Physics in Medicine and Biology* © 2014 PMB. Reprinted, with permission, from [1].

5.1 Introduction

Histotripsy is a non-invasive tissue ablation method that controls acoustic cavitation to mechanically fractionate soft tissue through high pressure, microsecond-long ultrasound pulses at low duty cycles (<1%) [2-6]. Histotripsy depends on the initiation and maintenance of a cavitation bubble cloud to produce tissue fractionation [7, 8]. With sufficiently high pressure and an adequate number of pulses, histotripsy can completely fractionate soft tissues into a liquefied acellular homogenate resulting in effective tissue removal [6, 9]. Histotripsy is currently being studied for many clinical applications where non-invasive tissue removal is desired including tissue debulking to treat benign prostatic hyperplasia (BPH) [10], thrombolysis [11, 12], perforation of the atrial septum in the treatment of congenital heart diseases [13, 14], tumor ablation [15], kidney stone removal [16], and fetal interventions [17, 18].

Tissue mechanical properties have been observed to affect the histotripsy process. The damage caused by histotripsy is often self-limiting at anatomical boundaries such as blood vessels, the capsule of an organ (e.g., the prostate), or fibrous structures (e.g., the collecting

system in the kidney) [19-21]. The rate of histotripsy-induced tissue damage also seems to be affected by tissue mechanical properties, with a decreased efficiency for tissues with higher elastic modulus [22, 23]. Understanding the susceptibility of tissues with differing mechanical properties to histotripsy therapy will facilitate advancement of this technology. This knowledge will help improve parameter optimization strategies for current clinical applications and potentially identify new clinical targets.

In this chapter, we study how tissue mechanical properties impact the production and extent of damage caused by a histotripsy-induced bubble cloud. We hypothesize that increases in tissue mechanical strength will decrease the tissue's susceptibility to damage induced by histotripsy. To study the effect of mechanical properties on the tissue's susceptibility to histotripsy-induced damage without influences from changing bubble dynamics, a cavitating bubble cloud was generated in the same fluid (degassed water) at the tissue-fluid interface on tissue phantoms and *ex vivo* tissue. Erosion into the tissue surface was then analyzed. Mechanically tunable agarose tissue phantoms were used at varying mechanical properties. In addition, forty-three different types of *ex vivo* porcine tissues with a wide range of mechanical properties were also treated, and the production and extent of erosion were analyzed as a function of tissue properties including ultimate stress, ultimate fractional strain, density, and water content. These experiments will help determine the feasibility of using histotripsy as a method for non-invasive tissue removal in a wide range of potential clinical applications.

We also hypothesize that, based on the different susceptibilities of tissues to histotripsy, ablation of a target tissue can be self-limited at the boundaries of the vital anatomical structures if the vital structures are of higher mechanical strength (e.g. major blood vessels) than the target tissue volume (e.g. liver). The feasibility of a vessel-sparing ablation strategy was tested in

porcine liver containing major hepatic vessels and bile ducts *in vivo*. As current thermal-based ablation methods have difficulty effectively ablating the tissue surrounding large vessels while preserving the vessels [24-27], such a vessel-sparing ablation feature can help histotripsy to address an important clinical need.

5.2 Methods

5.2.1 Therapeutic Ultrasound Treatment

Histotripsy pulses were generated by a 1 MHz focused ultrasonic transducer (Imasonic, SAS, Voray sur l'Ognon, France) with an aperture of 100 mm and focal length of 90 mm. Elements were driven in phase through a custom-designed class D amplifier with appropriate electrical matching circuits built in our laboratory and associated low voltage (20V DC power supply; E3630A Hewlett Packard Company, Palo Alto, CA, USA) and high voltage (600V DC power supply; GEN 600, TDK Lambda Americas Inc., San Diego, CA, USA) power supplies. Input signals were provided by a custom built Field-Programmable Gate Array (FPGA) board (Altera Corporation, San Jose, CA, USA) that functioned as a signal generator. Acoustic pressure waveforms produced by the 1 MHz therapeutic transducer were obtained using a fiber optic probe hydrophone built in house [28]. Pressure wave measurements were recorded in free-field in both degassed water and degassed 1,3-Butanediol (Sigma-Aldrich) at room temperature. Measurements were made in 1,3-Butanediol to prevent cavitation at the fiber tip at high pressures. The peak positive pressures were measured up to >80 MPa corresponding to a peak negative pressure of 15 MPa. At higher pressure, peak positive pressure could not be accurately measured due to instantaneous cavitation at the fiber tip in water and attenuation or saturation

effects in Butanediol. The peak positive pressures corresponding to negative pressures >15 MPa that were used in these experiments are expected to be higher than 80 MPa.

5.2.2 Histotripsy Tissue Phantom Treatment

Agarose tissue phantoms with adjustable mechanical properties were used to provide a well-controlled environment for this study. The mechanical properties of agarose phantoms can be adjusted over a physiologically relevant range by changing agarose concentration. Agarose phantoms of 0.3%, 1%, 2.5%, and 5% w/v were selected to cover the mechanical strength of tissues found in the body from non-load bearing tissues such as fat, lung and brain to strong load bearing tissues such as tendon and cartilage [29]. For example, the ultimate stress of 5% agar gel is 214 kPa compared to 77.7 KPa for 2.5% gel while the compression moduli for 0.3%, 1%, 2.5%, and 5% agarose is 1.5 kPa, 38 kPa, 254 kPa, and 929 kPa, respectively [29]. These values cover the range of most soft tissues with moduli ranging from ~2-5 kPa (Lung, fat, heart) to ~900 kPa (cartilage). Agarose phantoms were prepared by slowly mixing agarose powder (Agarose Type VII, Sigma-Aldrich, St. Louis, MO, USA) into saline solution (0.9% sodium chloride, Hospira, Lake Forest, IL, USA) heated above 70°C. The solution was stirred on a hot plate until the gel became visually transparent. The agarose solution was then degassed under a partial vacuum of 20.5 psi for 30 minutes. After removing the agarose mixture from the vacuum, the solution was poured into rectangular polycarbonate tissue phantom holders and placed in a refrigerator at 4°C to allow gel to solidify prior to use.

A histotripsy bubble cloud was formed at the tissue phantom-water interface using 5-cycle long ultrasound pulses with peak negative pressure of 18 MPa and PRFs of 10, 100, and 1000 Hz [Fig. 5.1(A)]. These parameters were selected to ensure bubble cloud generation at the

gel-water interface. Histotripsy treatments were applied to the agarose phantom surface at 6 locations each for 5,000 pulses. Erosion damage for each parameter was assessed by sectioning the tissue phantoms samples and measuring the maximum lesion depth and diameter using a microscope (Nikon Eclipse 50i, Nikon Corp., Tokyo, Japan). Statistical comparisons were made using a Student's t-test. P-values<0.05 were considered significant. Error bars on graphs represent standard error of the mean (SEM).

5.2.3 Histotripsy *ex vivo* Porcine Tissue Treatment

Forty-three types of excised porcine tissue of various mechanical properties were tested to cover the entire range of mechanical strength found in tissue. The tested samples included brain, heart (ventricular myocardium), fat, skeletal muscle, liver, lung, gallbladder, pancreas, kidney (cortex), spleen, stomach, lymph node, adrenal glands, thyroid, trachea, esophagus, bladder, skin, eye, optic nerve, femoral nerve, aorta, vena cava, femoral artery, femoral vein, ureter, urethra, ovary, uterus, cervix, small intestine, large intestine, tongue, articular cartilage, elastic cartilage, meniscus, ligament, tendon, heart valve tendons, trabecular bone, cortical bone, and tooth. The tissue samples were excised and immediately placed into degassed 0.9% saline solution and stored at 4°C. Prior to the experiments, the tissue was warmed to room temperature in degassed saline under a partial vacuum of 20.5 psi for 4 hours. Tissues thicker than the 10 mm axial size of the bubble cloud (muscle, liver, kidney, fat, lung, heart) were cut into 5 mm thick sections for treatment in order to assess for tissue perforation. All samples were used within 48 hours of harvesting.

The 1 MHz therapeutic ultrasound transducer was positioned in the water tank with the focus of transducer aligned to the tissue surface [Fig. 5.1(A)]. A histotripsy bubble cloud was

formed at the tissue-water interface using 5-cycle long ultrasound pulses with peak negative pressure of 18 MPa and PRF of 1000 Hz. Bubble cloud formation and alignment were verified using high-speed optical and ultrasound imaging. Histotripsy treatments were applied to the tissue surface for 10 minutes (n=4). The longer treatment times for the *ex vivo* experiments were specifically chosen to demonstrate the resistance of stronger tissues wasn't merely a result of insufficient treatment time being required for stronger tissues, as the effects of histotripsy have been previously demonstrated to depend on the number of applied pulses. After treatment, the tissue samples were examined for damage (lesion formation) by gross morphology. Results were organized into tissues with complete erosion leading to perforation (large lesion through entire tissue), partial/little erosion (small observed lesions and/or some samples with no observed erosion), and no damage. Porcine tissue erosion results were further compared to tissue properties found in literature that have been correlated to tissue strength. In this work, ultimate stress, ultimate fractional strain, density, and water content values from literature were chosen as metrics for tissue properties. Ultimate stress and ultimate fractional strain were preferred to elastic modulus due to a more direct relevance to the investigation of tissue fractionation (properties at the point of rupture) as well as their wider availability and consistency within the literature. Density and water content values were used due to their high correlation to a wide range of mechanical properties [30-34]. The average values of these tissue properties for the three groups (perforation, partial erosion, and no damage) were plotted as an average ± the standard deviation. Differences between groups were compared using a Wilcoxon signed-rank t-test. P-values < 0.05 were considered significant.

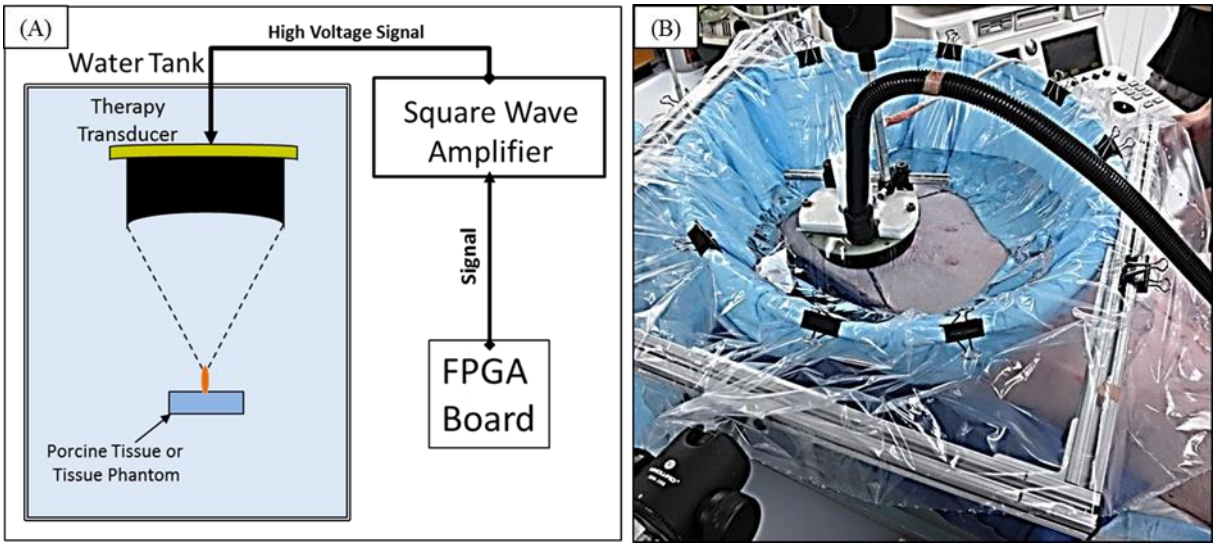

Figure 5.1. (A) A 1 MHz transducer was attached to a motorized 3D positioning system controlled using a PC console. The therapy focus was aligned at the surface of the agarose tissue phantoms and *ex vivo* porcine tissue. (B) For the selective ablation *in vivo* porcine experiment, an ultrasound imaging probe was coaxially mounted with the therapy transducer and the unit was attached to a motorized positioning system and coupled to the pig with a degassed water bolus.

5.2.4 *In vivo* Vessel-sparing Ablation

The feasibility of using histotripsy to selectively ablate porcine liver while preserving blood vessels of higher mechanical strength was investigated *in vivo*. The livers of two pigs (94 and 66 lbs.) were treated with histotripsy. Porcine liver was chosen due to the anatomical structures including hepatic blood vessels and bile ducts present within the organ. Liver vasculature covers a wide range of sizes and mechanical properties from large hepatic vessels, which reach 1.5 cm in diameter and ultimate stresses of 1-3 MPa down to small vessels and capillaries <10 μm in diameter with negligible mechanical strength [35-37]. In comparison, the ultimate stress of liver is 0.27 MPa [38]. Pigs were pre-medicated with Telazol (6 mg/kg) and Xylazine (2.2 mg/kg) and an intravenous catheter was placed in an auricular vein. Pigs underwent endotracheal intubation and were maintained under full anesthesia on isoflurane gas (1.5-2.0%) for the duration of the procedure. Anesthetized pigs were placed in a dorsal

recumbent position upon the surgical table and the skin over the targeted tissue was treated with a depilatory cream to remove hair to improve ultrasound coupling. To ensure ultrasound propagation to targeted tissue, a degassed water bolus was coupled to the skin with a thin plastic membrane and ultrasound coupling gel.

An 8 MHz phased array ultrasonic imaging probe (Model S8, Philips Electronics, Andover, MA) was aligned coaxially with the therapy transducer. An ultrasound imaging system (Sonos 7500, Philips Electronics, Andover, MA) was used to locate the liver target and histotripsy was applied transcutaneously through the ribs and overlying tissue [Fig 5.1(B)]. The cavitation cloud was initiated by slowly increasing the driving voltage until a bubble cloud was visualized in the liver on ultrasound imaging. Histotripsy (10 cycles, 500 Hz PRF, estimated *in situ* peak negative pressure ~17 MPa) was applied to liver and the therapy focus was mechanically scanned over 12 cm^3 (3×2×2 cm scan) and 18 cm^3 (3×3×2 cm scan) volumes, resulting in significantly larger actual treated regions due to the size of the bubble cloud and breathing motion. Each point within the block was treated for 4 seconds (2,000 pulses) and adjacent treatment spots were separated by 2 mm in the transverse plane and by 5 mm axially. The *in vivo* parameters were chosen based on previous experiments demonstrating that the liver can be completely fractionated within 2,000 pulses. The pulse duration of 10 cycles was used here to keep consistent with previous *in vivo* liver ablation experiments. Doppler images of large blood vessels within the treatment region were taken before and after treatment to determine whether vessels continued to have blood flow. After the procedure, the pigs were euthanized without recovery with an intravenous injection of sodium pentobarbital (140-160 mg/kg) and the liver was harvested and imaged with a 7T small animal MRI scanner (Varian, Inc., Palo Alto,

CA, USA). Both T1 and T2 weighted multi-slice spin-echo images of the liver were acquired along both coronal and axial planes.

After the MRI procedure, the liver was fixed in formalin and dissected, with samples stained with hematoxylin and eosin (H&E). The damage to the liver, vessels, and bile ducts within and surrounding the treatment region was examined histologically under a microscope (Nikon Eclipse 50i) using 4x, 10x, 20x, and 40x objective lenses. To quantitatively assess the distribution of blood vessels remaining after histotripsy, the number of vessels was counted using three H&E slides for each lesion (total n=6). Vessels were organized into seven groups based on the type of vessel and size (inner diameter): large arteries (>1 mm), large veins (>1 mm), small arteries (0.3-1 mm), small veins (0.1-1 mm), arterioles (20-300 μm), venules (20-100 μm), and capillaries (<10 μm). The thickness of the intima, media, and adventitia was included for each vessel type, as the mechanical strength of the blood vessels is dependent on the thickness of these layers [31, 35-37, 39, 40]. The media and adventitial layers are primarily responsible for vessel mechanical strength under normal physiologic conditions [35, 36, 39]. The loosely woven collagen fibers in the adventitial layer align under loading conditions to provide the vessel with a high ultimate stress necessary to prevent over-distension and vessel rupture [35, 36, 39]. Although quantitative values of mechanical strength could not be found for all the different vessel groups, increasing thickness of the media and adventitia indicates higher mechanical strength. For each H&E slide, the number of vessels of each type in one hundred 1 mm^2 regions of the lesion and surrounding liver (control) was counted. The mean and standard deviation of the number of vessels for the six slides were calculated with the lesion results plotted as a percentage of the control region. To compare the treatment and control regions, a two-sided Student's t-test was conducted for each vessel type (n=6). P-values <0.05 were considered

statistically significant. All procedures used in this work were reviewed and approved by the University Committee on Use and Care of Animals at the University of Michigan.

5.3 Results

5.3.1 Histotripsy in Agarose Tissue Phantoms

The diameter and depth of lesions decreased for tissue phantoms with higher agarose concentration, which also had higher mechanical strength [Fig. 5.2]. The compression moduli of the agarose gels increases with concentration from 1.5 kPa, 38 kPa, 254 kPa, and 929 kPa for 0.3%, 1%, 2.5%, and 5% agarose, respectively. A statistically significant decrease in the mean maximum diameter of the lesion was observed for tissue phantoms of increased strength treated at all PRFs with larger differences between the 1%, 2.5%, and 5% tissue phantoms and smaller decreases between the 0.3% and 1% samples [Fig. 5.2(A)]. For example, at a PRF of 10 Hz, the mean of the maximum diameter of the lesion decreased from 3.95 mm for the 0.3% gel to 3.56 mm for the 1% gel, 2.84 mm for the 2.5% gel, and 0.87 mm for the 5% gel. Similarly, a statistically significant decrease in the maximum lesion depth was observed for higher agarose concentration phantoms. Larger differences were again seen between the 1%, 2.5%, and 5% tissue phantoms [Fig. 5.2(B)]. For example, at a PRF of 10 Hz, the maximum depth decreased from 9.61 mm for the 0.3% gel to 9.47 mm for the 1% gel, 7.21 mm for the 2.5% gel, and 4.30 mm for the 5% gel. All decreases in lesion depth and diameter were statistically significant ($p<0.05$) except between the 0.3% and 1% gels at 100 Hz PRF (depth: 9.52 mm, 9.1 mm, $p=0.08$; diameter: 3.52 mm, 3.41 mm, $p=0.12$). The lesion size in the lower concentration agarose gels (0.3% and 1%) closely matched the bubble cloud size in free field of approximately 3.5 mm in the transversal plane and 10 mm in the axial plane. Additionally, the results show a decrease in

maximum diameter and depth with increasing PRF treatments [Fig. 5.2]. For example for the 2.5% agarose phantom, the maximum lesion diameters were 2.82±0.18 mm, 2.36±0.21 mm, and 1.26±0.10 mm, and the maximum lesion depths were 7.21±0.24 mm, 6.23±0.42 mm, and 5.11±0.19 mm for PRFs of 10, 100, and 1000 Hz, respectively.

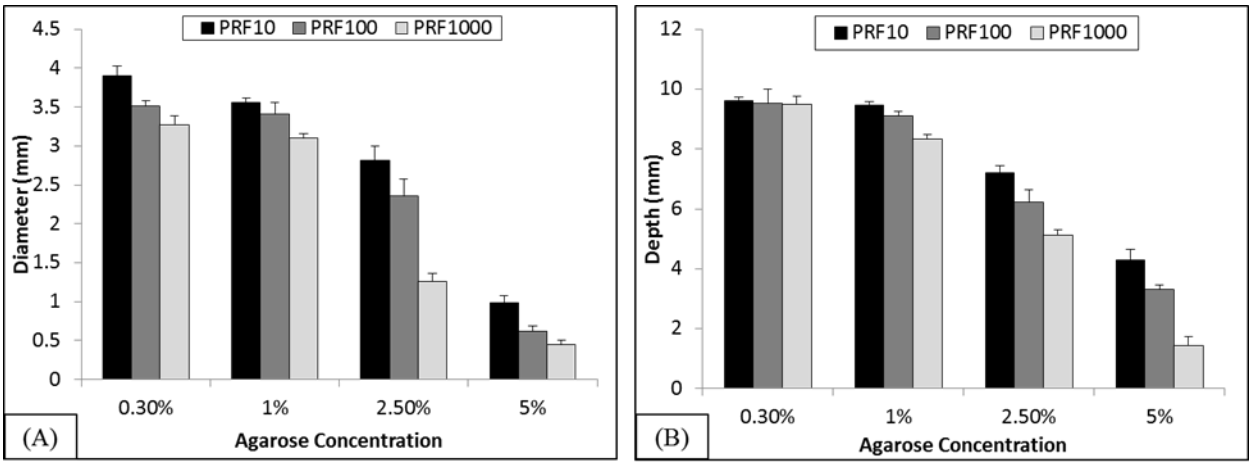

Figure 5.2. Tissue phantom erosion results show lesion maximum diameter (A) and depth (B) for 0.3%, 1%, 2.5%, and 5% agarose gels treated with 5,000 histotripsy pulses at 10, 100, and 1000 Hz PRF. Results show a statistically significant decrease in lesion diameter and depth with increasing agarose concentration. All observed decreases in lesion depth and diameter were considered significant ($p<0.05$) except between 0.3% and 1% agarose at 100 Hz PRF (depth: 9.52 mm, 9.1 mm, $p=0.08$; diameter: 3.52 mm, 3.41 mm, $p=0.12$). Additionally, results show a statistically significant decrease in lesion size for increased PRF.

5.3.2 Histotripsy in *ex vivo* Porcine Tissues

Histotripsy-induced erosion was examined using 43 types of harvested porcine tissues (n=4) from non-load bearing tissues such as fat, lung, and brain to strong load bearing tissues such as tendon and cartilage. Tissues were exposed to a histotripsy bubble cloud for 10 minutes generated using 5-cycle pulses at 18 MPa peak negative pressure and 1 kHz PRF. Gross morphology showed complete erosion (i.e. perforation) in the majority of tissues including brain, heart, fat, skeletal muscle, liver, lung, gallbladder, pancreas, kidney, spleen, stomach, lymph node, adrenal glands, thyroid, esophagus, eye, optic nerve, femoral nerve, ureter, urethra, ovary,

ovarian cyst, uterus, cervix, small intestine, large intestine, and ligament [Fig. 5.3]. A smaller group of tissues treated with histotripsy showed no sign of damage, including skin, cartilage (all types), tendon, heart valve tendons, trabecular bone, cortical bone, and tooth, demonstrating certain tissues are less susceptible to histotripsy induced damage [Fig. 5.3]. Additionally, partial erosion was observed in some tissues including tongue (small lesion), bladder (small lesion), urethra (damage to inner lining, no damage to outer layer), and blood vessels (damage to intima and media, no damage to adventitia) [Fig. 5.4]. The entire list of erosion results are recorded in [Table 5.1]. Edema at the therapy target was observed for intestines, pancreas, thyroid, and gallbladder [Table 5.1]. All tissues with observed edema also exhibited complete erosion.

Tissue erosion results were compared to tissue ultimate stress, ultimate fractional strain, density, and water content values [Table 5.1]. Results demonstrated a statistically significant difference in average tissue strength between perforated tissues compared to the undamaged group, with perforated tissues having a lower average density, higher average water content, lower ultimate stress, and higher ultimate fractional strain [Fig. 5.5]. The average density of perforated tissues of 1040.4±32.5 kg/m^3 was lower than the density of undamaged tissues of 1509.7±488.3 kg/m^3 ($p<0.05$) [Fig. 5.5]. The average water content for perforated tissues of 76.1±5.9% was higher ($p<0.05$) than the average water content in undamaged tissues of 43.7±27.2% [Fig. 5.5(B)]. The average ultimate tensile stress for perforated tissues was 0.3525±.26 MPa compared to an average of 40.44±55.80 MPa for undamaged tissues [Fig. 5.5(C)]. All tissues with ultimate stresses below 1 MPa were completely eroded with the only exception being the partial damage to the bladder which had an extremely high ultimate fractional strain [Table 5.2]. Ultimate fractional strain showed a statistically significant difference ($p<0.05$) between completely perforated tissues which had an average ultimate strain

of 0.8163±0.36 compared to 0.2348±0.26 for undamaged tissues [Fig. 5.5(D)]. No statistically significant differences were observed between perforated and partially damaged groups for any of the tissue properties compared. A list of erosion results with corresponding tissue properties are recorded in Table 5.2.

Table 5.1. Complete erosion results of *ex vivo* porcine tissues treated for 10 minutes at a PRF of 1000 Hz and 5 cycles showing extent of the observed erosion.

Tissue	Perforation	Partial	No Erosion	Fluid Uptake
Brain	x			
Heart	x			
Fat	x			
Skeletal Muscle	x			
Ligament	x			
Aorta (Outside), Media	x			
Aorta (Outside), intima	x			
Aorta (Inside), Media	x			
Aorta (Inside), intima	x			
Artery, Femoral (O), Media	x			
Artery, Femoral (O), Intima	x			
Artery, Femoral (I), Media	x			
Artery, Femoral (I), Intima	x			
Vena Cava (O), Media	x			
Vena Cava (O), Intima	x			
Vena Cava (I), Media	x			
Vena Cava (I), Intima	x			
Vein, Femoral (O), Media	x			
Vein, Femoral (O), Intima	x			
Vein, Femoral (O), Media	x			
Vein, Femoral (O), Intima	x			
Liver	x			
Eye (surface)	x			
Optic Nerve	x			
Nerve, Femoral	x			
Trachea, internal lining	x			
Lung	x			
Esophagus	x			
Stomach wall	x			
Kidney, Cortex	x			
Kidney, Medulla	x			
Adrenal Glands	x			
Spleen	x			
Lymph node	x			
Ureter	x			
Urethra (female), inner	x			
Ovary, wall	x			
Ovarian Cyst	x			
Uterus, wall	x			
Cervix	x			
Large Intestine	x			x
Small intestine	x			x
Thyroid	x			x
Gallbladder	x			x
Pancreas	x			x
Tongue		x		
Aorta (O), Adventitia		x		
Aorta (I), Adventitia		x		
Vena Cava (O), Adventitia		x		
Vena Cava (I), Adventitia		x		
Bladder		x		
Skin			x	
Cartilage, Articular			x	
Cartilage, Meniscus			x	
Cartilage, Elastic			x	
Tendon			x	
Artery, Femoral (O), Adventitia			x	
Artery, Femoral (I), Adventitia			x	
Vein, Femoral (O), Adventitia			x	
Vein, Femoral (O), Adventitia			x	
Heart Valve Tendons			x	
Trachea, Cartilage			x	
Urethra (female), outer			x	
Bone, cortical			x	
Bone, trabecular			x	
Tooth			x	

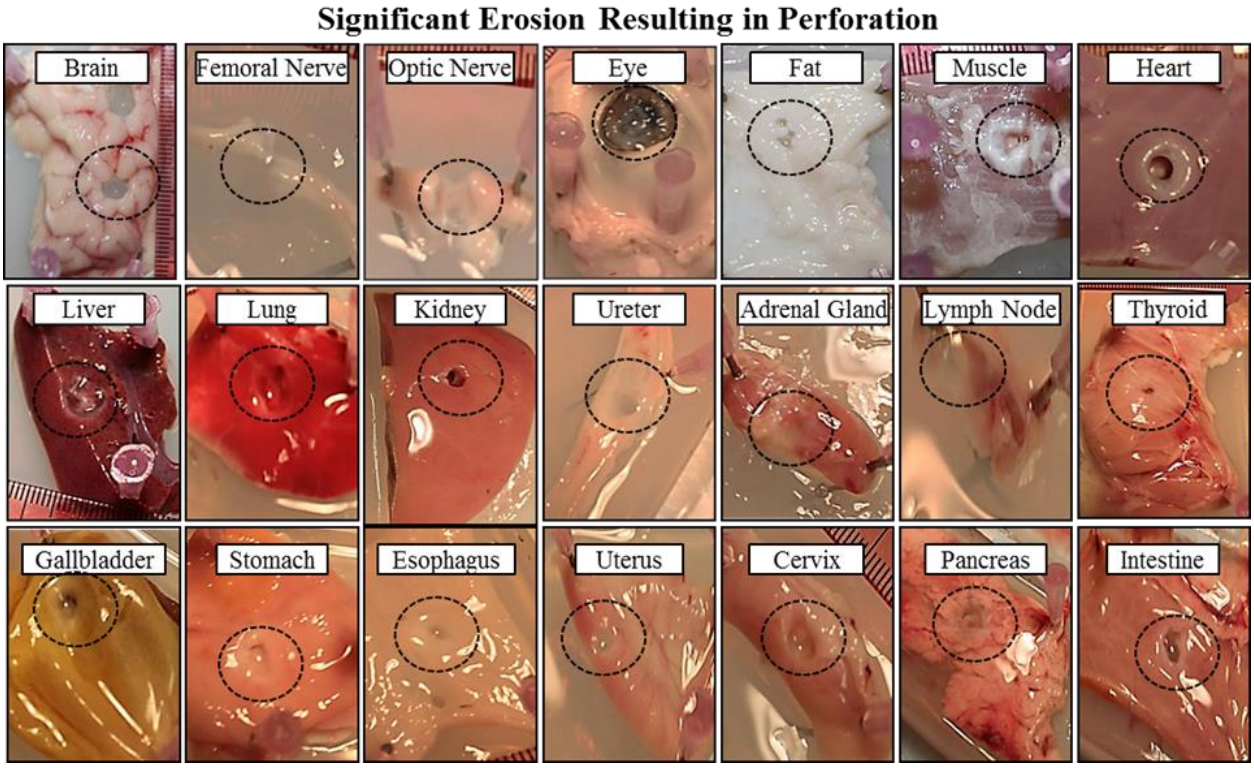

Figure 5.3. Histotripsy was demonstrated to be capable of completely eroding through the majority of the soft tissues tested in this study. A complete list of ex vivo tissue erosion results is shown in Table 5.1.

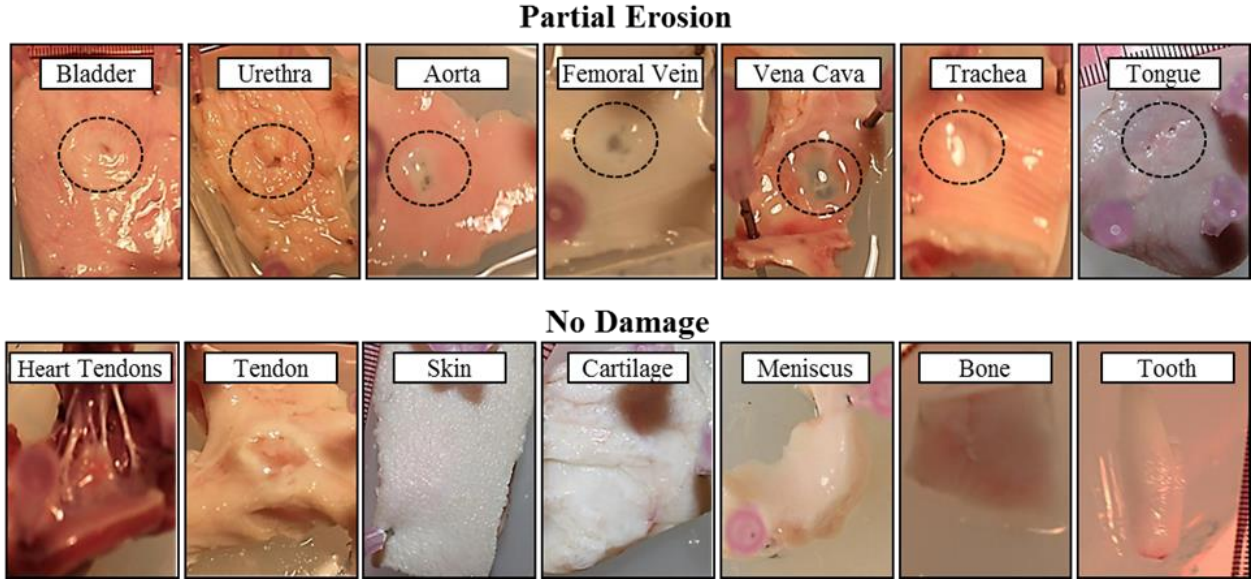

Figure 5.4. Histotripsy treatment was demonstrated to be less effective in stronger tissues with only partial erosion or no visible damage observed. Partial erosion was most pronounced in composite tissues in which stronger layers were preserved while the weaker tissue was completely eroded (i.e. adventitial layer of vessels or cartilage layer of trachea preserved). The complete list of ex vivo tissue erosion results is shown in Table 5.1.

Table 5.2. The table shows select results of *ex vivo* erosion in porcine tissue along with corresponding density, water content, ultimate stress, and ultimate strain values.

Tissue	Perforation	Partial	No Erosion	Fluid Uptake	Density, kg/m³	Water Content (%)	Average ultimate tensile stress, MPa	Ultimate fractional strain
Fat	x				916	21.2		
Adrenal Glands	x				1024.5	58.1		
Brain	x				1039	77.4		
Esophagus	x				1040	76	0.59	0.73
Bladder		x			1040	65	0.24	2.26
Large Intestine	x			x	1044	79	0.68	1.17
Small intestine	x			x	1044	79	0.55	0.43
Pancreas	x			x	1045	71		
Skeletal Muscle	x				1047	74.1	0.11	0.61
Ovary, wall	x				1048	83		
Kidney	x				1049	76.6	0.05	0.52
Stomach wall	x				1050	75	0.55	0.93
Thyroid	x			x	1051	85		
Uterus, wall	x				1052	79	0.18	1.5
Spleen	x				1054	77		
Vein, Femoral		x			1056	72.6	2.9	0.66
Heart	x				1060	75.9	0.11	0.64
Liver	x				1060	74.2	0.27	0.54
Artery, Femoral		x			1062.5	70	1.4	0.69
Lung	x				1066	77.9		
Trachea, Cartilage			x		1080	60	2.4	0.19
Cartilage			x		1098	72	2.8	0.18
Skin			x		1150	65.35	11	0.685
Tendon			x		1165	63	53	0.09
Bone, trabecular			x		1920	23		
Bone, cortical			x		1990	13.5	133	0.029
Tooth			x		2165	9.15		

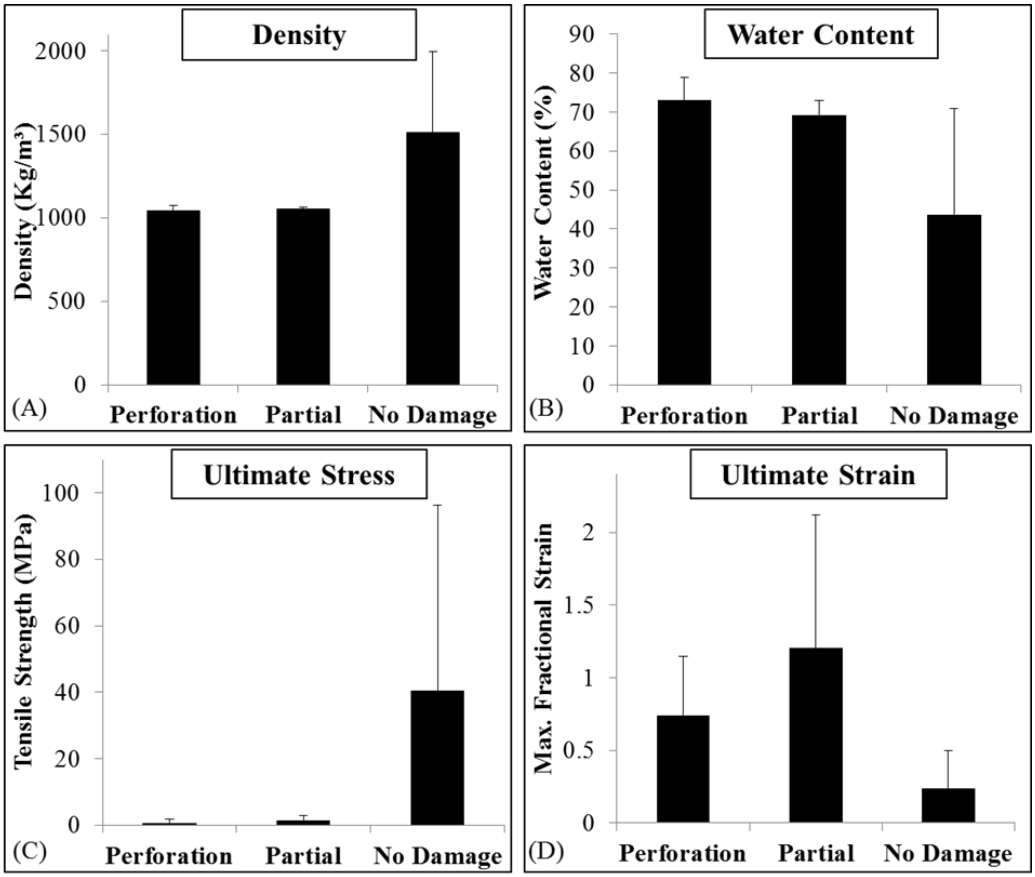

Figure 5.5. Comparison of selected tissue properties for histotripsy treated porcine tissues. Graphs show the average density (A), water content (B), tensile stress (C), and ultimate fractional strain (D) for perforated tissues compared to tissues with partial or no damage. Undamaged tissues demonstrated significantly increased density, decreased water content, increased ultimate stress, and decreased ultimate strain compared to perforated group. No statistically significant difference was observed between perforated and partial ablation groups. P-values <0.05 were considered significant.

5.3.3 *In vivo* Vessel-sparing Ablation

Two intact porcine livers containing a hierarchy of blood vessels were treated *in vivo* using histotripsy with a peak negative pressure right above the threshold to initiate a bubble cloud in the liver based on the ultrasound imaging feedback. Our *ex vivo* experiments showed a higher resistance of vessels to histotripsy-induced erosion in comparison to liver tissue. MRI multi-slice analysis of the *in vivo* lesions demonstrated lesion volumes of approximately 18 cm^3 and 60 cm^3 with multiple large vessels remaining within the fractionated liver volumes [Fig.

5.6(A)]. Large hepatic vessels visible within the lesion were shown to remain patent on ultrasound Doppler imaging [Fig. 5.6(B-C)]. Histological evaluation of the lesion indicated hepatic parenchyma was completely fractionated into acellular debris while large vessels (>1 mm diameter) remained intact within the treated region. No damage or perforation to any vessels larger than 1mm in diameter was observed. In the *ex vivo* study, partial damage was observed to the intima and media of large vessels while the adventitia remained intact. However, for those experiments, histotripsy was applied directly to a stretched open *ex vivo* vessel wall and treated for much longer treatment times (10,000 pulses). The extensive connective tissue observed to surround the large hepatic vessels in the adventitial layer *in vivo* likely enhanced the vessel resistance to histotripsy and prevented the bubbles from damaging the weaker media and intima layers. No damage to the endothelial layer was observed for vessels that remained completely intact within the treated volume. An extensive network of intermediate vessels (300-1000 μm diameter) and bile ducts was also found intact throughout the treated lesion [Fig. 5.7]. Localized hemorrhage was visible within the lesion due to the rupture of capillaries and small vessels.

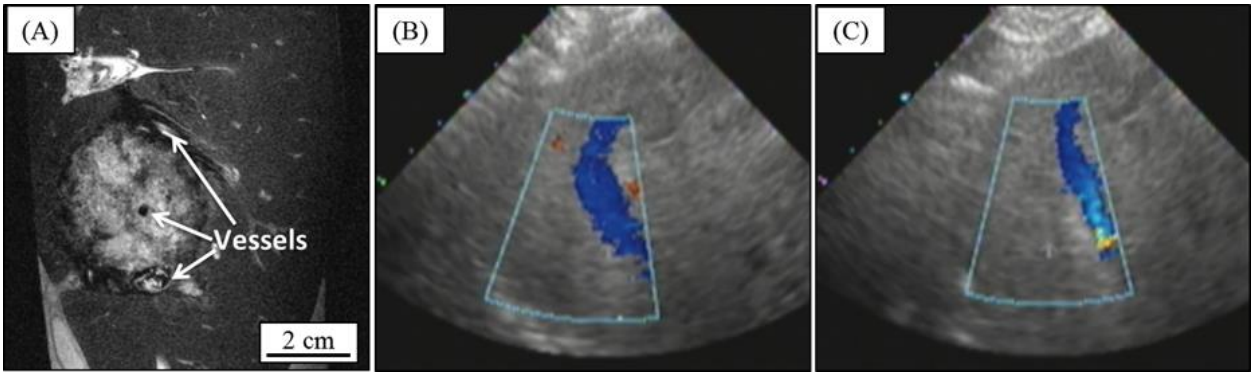

Figure 5.6. Histotripsy selective ablation results demonstrated large hepatic vessels remained intact and functional inside histotripsy treated porcine liver in vivo. Results show (A) MRI image of a large in vivo porcine liver histotripsy lesion with major hepatic vessels remaining structurally intact inside the completely fractionated liver tissue. Doppler ultrasound images before (B) and after (C) histotripsy treatment demonstrated large blood vessels within the treated region remained functional after histotripsy.

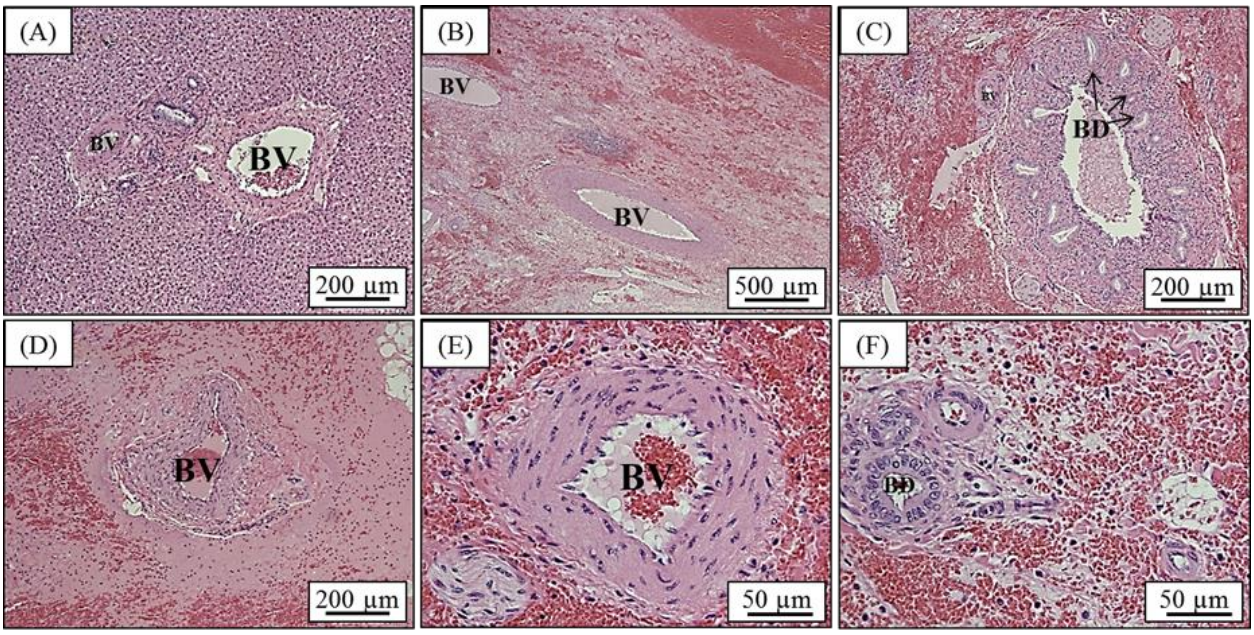

Figure 5.7. Histotripsy selective ablation results showed hepatic vessels remained intact within fractionated porcine liver *in vivo*. Results show select images of hepatic blood vessels (BV) inside untreated (A) and completely fractionated (B-F) liver tissue. A large number of smaller vessels and bile ducts (BD) were observed in the regions containing connective tissue surrounding hepatic vessels.

Quantitative analysis of vessels remaining inside the lesions showed a statistically significant decrease ($p<0.05$) in the number of capillaries, venules, arterioles, and small veins compared to intact liver controls [Fig. 5.8]. The lesions contained 64.9% of small veins, 13.9% of arterioles, and 3.9% of venules compared to controls while no capillaries were observed inside the lesion. No statistically significant difference ($p>0.05$) was found for large arteries, large veins, or small arteries with 105.5% of large arteries, 110% of large veins, and 78.5% of small arteries remaining compared to controls [Fig. 5.8]. The blood vessel types remaining inside the treated region had larger inner diameters and thicker walls with thicker media and adventitial layers than the vessel types ablated by histotripsy [Fig. 5.8] [31, 37, 40, 41]. For example, the thickness of the adventitial layer was between 200-400 µm for the larger arteries, 60-300 µm for larger veins, 20-200 µm for smaller arteries, 6-120 µm for smaller veins, and < 20 µm for arterioles and

venules. Thicker media and adventitial layers have previously been correlated with increases in vessel mechanical strength with adventitial layers of 200-400 μm associated with an ultimate tensile stress >1MPa for large vessels which is higher than the ultimate stress of liver (0.27 MPa) [31, 35-37, 39-41]. These results indicate that vessels with increased mechanical strength were preserved inside the histotripsy lesion while smaller, weaker vessels were ablated along with the liver.

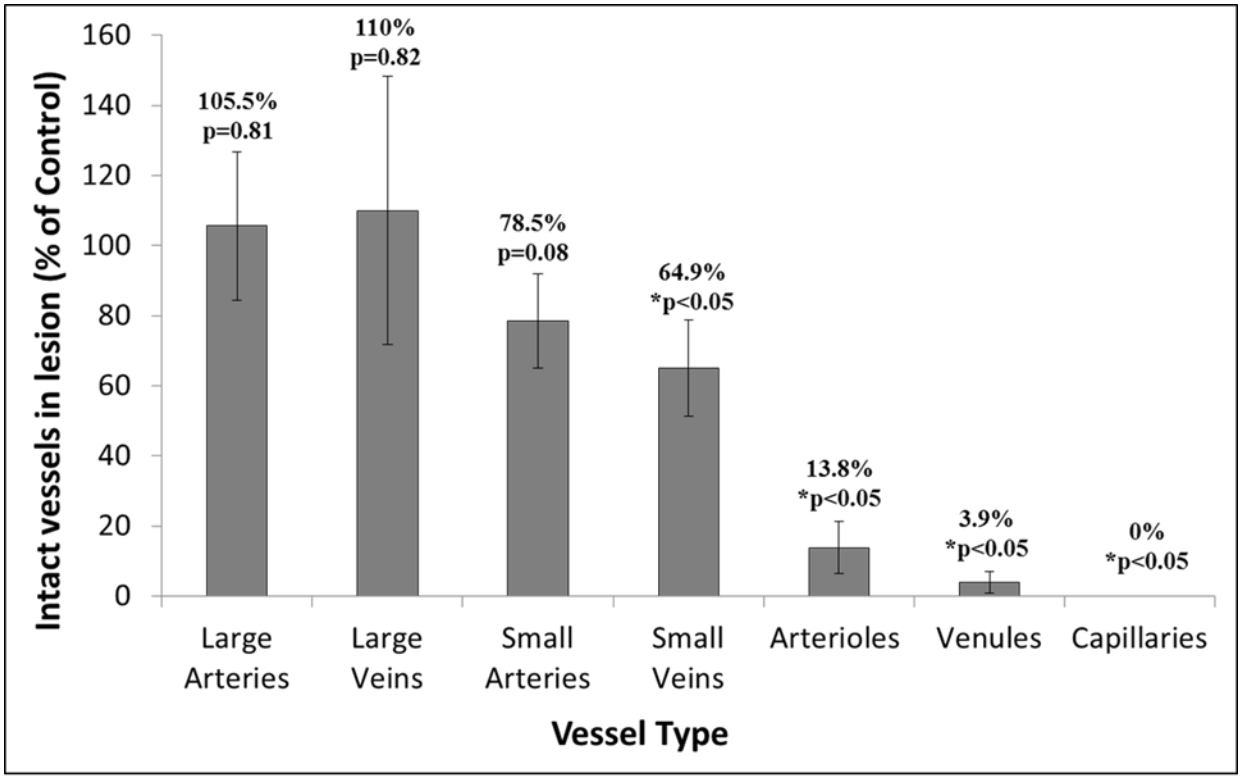

Vessel Type		Large Arteries	Large Veins	Small Arteries	Small Veins	Arterioles	Venules	Capillaries
Inner Diameter		>1 mm	>1 mm	0.3-1 mm	0.1-1 mm	20-300 μm	20-100 μm	<10 μm
Total Wall Thickness		500-1000 μm	100-500 μm	50-500 μm	10-200 μm	5-50 μm	1-20 μm	0.5 μm
Approximate Layer Thickness	Intima	0.5 μm	0.5 μm	0.5 μm	0.5 μm	0.5 μm	0.5 μm	0.5 μm
	Media	300-600 μm	40-200 μm	30-300 μm	4-80 μm	3-30 μm	0.5-8 μm	0 μm
	Adventitia	200-400 μm	60-300 μm	20-200 μm	6-120 μm	2-20 μm	0.5-12 μm	0 μm

Figure 5.8. Histotripsy selective ablation showed preservation of hepatic vessels was highly dependent on vessel type. (A) Plot shows the percentage of vessels remaining inside an in vivo porcine liver lesion formed by histotripsy organized by vessel type (B). *Results showed a statistically significant decrease in small veins, arterioles, venules, and capillaries inside the histotripsy lesion compared to untreated controls ($p<0.05$).

5.4 Discussion

In this chapter, the effectiveness of histotripsy in treating tissues of varied mechanical characteristics was investigated. Results show a decrease in susceptibility to histotripsy damage for tissues of increased mechanical strength. The wide range of tissues tested in this work provides a guide to the feasibility of using histotripsy to address a variety of clinical applications in which the removal of a specific tissue type is desired. Additionally, the *in vivo* feasibility of using histotripsy for vessel-sparing ablation was investigated, suggesting histotripsy has the potential to act as a self-limiting tissue-selective fractionation technique.

For both tissue phantom and *ex vivo* tissue experiments, the cavitating bubble cloud was generated at the tissue-fluid interface in the degassed water using the same acoustic pressure. Similar levels of bubble expansion and collapse were expected to be produced in the degassed water for treatment of different samples, but tissues with higher mechanical strength displayed higher resistance to the damage generation. These results suggest that stronger tissues can resist more of the mechanical loading from the cavitation activity before mechanical breakdown induced by histotripsy occurs. Results demonstrated that undamaged tissues had higher average densities, lower average water content, higher ultimate stress, and lower ultimate fractional strain than the tissues perforated by histotripsy. The finding that undamaged tissues had a higher ultimate stress makes sense intuitively as tissues with higher ultimate stress are by definition more resistant to fractionation. The finding that undamaged tissues had lower ultimate strains, however, suggests that tissue resistance to deformation (high ultimate stress) appears to play a more significant role in resisting histotripsy-induced damage than withstanding large deformations (high ultimate strain) for the majority of tissues. The only tissue with a low ultimate stress observed to resist erosion was the urinary bladder, which was only partially

eroded (very small lesion formed only partially through tissue). However, the bladder had a higher ultimate fractional strain (2.26) than all other tissues, which allows the bladder to undergo large mechanical strains without rupture. This finding suggests a different method of resisting histotripsy damage for the bladder compared to the other undamaged tissues.

This chapter showed that, given the same cavitation activity at a tissue-fluid interface, tissues with higher mechanical strength were more resistant to the damage induced by histotripsy. For bulk tissue fractionation, the bubble expansion is impeded in stiffer tissue resulting in less cavitation effects on the tissue in addition to the increased resistance of stronger tissues to histotripsy-induced damage. This impeded bubble expansion will likely result in an even higher damage threshold for bulk fractionation of stronger tissues. One way to potentially work around the impeded bubble expansion in stronger tissues may be to create a fluid-tissue interface in the bulk tissue by generating a fluid homogenate in the bulk tissue and erode outward from there (similar to the blood vessels in the *in vivo* situation in this study), which may be an effective approach to fractionation stiff bulk tissue. Future work will study the nonlinear viscoelastic response of tissues under the high strain rates induced by histotripsy to provide a more complete understanding of the results of this study in order to develop optimal strategies to fractionate tissues with different mechanical properties for both tissue erosion and bulk fractionation. Future studies will also investigate the specific mechanism with which histotripsy damages tissues and the process with which stronger tissues are capable of resisting histotripsy on the micro-scale (i.e. effects of extracellular matrix and cytoskeletal mechanics).

In addition to erosion, edema was observed in the pancreas, small and large intestines, thyroid, and gallbladder. This fluid uptake was observed for tissue adjacent to the eroded lesion with the extent of fluid uptake being most noticeable in the pancreas. Fluid uptake into tissue

during cavitation has been previously observed for uterine endometrium and is possibly due to the cavitation cloud pumping fluid across the tissue boundary via microjetting [42]. Edema was not observed in uterine tissue in this study, likely because treatment was applied to the external uterine perimetrium rather than the endometrium. The tissues in which edema was observed in this work have similar structure to uterine endometrium, i.e. membranous tissue structures with large surface area. This finding suggests that the fluid uptake phenomenon is most likely to occur in membranous tissues with high surface area commonly found in digestive system organs or glandular structures. In addition to asymmetric bubble collapse and microjetting, it is also possible that the observed fluid uptake into these tissues is a result of ultrasonic atomization and fountain formation which has been observed in studies of boiling histotripsy [43, 44], as well as possible fluid uptake caused by acoustic streaming from the histotripsy bubble cloud which has been shown to generate high velocity fluid flows [45]. Future work will be needed to investigate the specific mechanism causing fluid uptake.

The feasibility of using histotripsy as a vessel-sparing selective fractionation technique was shown *in vivo*. Based on the results of *ex vivo* experiments where the large vessels had a higher resistance to histotripsy-induced damage than liver, we hypothesized that by selecting an appropriate pressure and treatment time, fractionation of the liver could be self-limiting at the boundaries of large vessels. Results supported our hypothesis demonstrating no statistically significant difference in the number of large arteries and veins remaining inside the histotripsy treated lesion compared to intact liver. The vessel preservation is highly dependent on vessel size and structure. While large vessels were preserved, there was a statistically significant decrease in the number of smaller vessels remaining inside the lesion. The high ultimate stress or high ultimate strain of large vessels could both play a role in the preservation of these vessels, which

are highly compliant under normal physiologic conditions but also have a high ultimate stress under loading conditions due to the fibrous connective tissue in the adventitial layer. It is likely that the number and type of vessels remaining inside the histotripsy lesions would change based on treatment parameters. For example, increasing the pressure or number of pulses may result in fewer small arteries and veins remaining after treatment while very long treatment times could potentially rupture the major blood vessels.

An interesting observation from the *ex vivo* experiments performed in this work was that the femoral nerve was completely fractionated while a previous study demonstrated histotripsy spared nerves during treatment for BPH [21]. The mechanical properties of the femoral nerve are closely related to the other perforated tissues and are in agreement with our hypothesis that softer tissues are more susceptible to histotripsy damage. There are two possible explanations to account for the discrepancy with the previous study in the prostate. First, the *ex vivo* treatments performed in this work consisted of many more pulses than what was applied to the prostate in the paper by Styn et al. Second, it is likely that the nerve-sparing response previously observed is aided by the connective tissue surrounding nerves *in vivo* in a similar way in which the adventitial layer appears to protect the blood vessels from histotripsy induced damage. The nerves treated in this study were harvested without the surrounding connective tissue in order to see the effects of histotripsy on only the nerve tissue itself, which could explain why the nerve was perforated by histotripsy in this study while previously being preserved *in vivo*. Future work will further investigate the potential of nerve-sparing tissue fractionation and the role of the surrounding connective tissue in the process.

In addition to the increased resistance to histotripsy, separate work has demonstrated increases in the cavitation initiation threshold in stronger tissues, which likely plays a role in the

selective ablation technique [46]. The level of bubble expansion also decreased in tissue with higher mechanical strength [46]. These effects act complementary to one another and suggest the ability to further optimize this approach to utilize both the cavitation threshold gradient as well as the damage resistance gradient. Future work will aim to optimize this self-limiting vessel-sparing fractionation technique and expand it to other critical tissues with higher mechanical strength, such as major nerves or collecting systems. This approach can be beneficial for clinical applications where removal of a tissue surrounding important anatomical structures is desired, such as the removal of tumors near large vessels which is currently a major problem for surgery and thermal ablation therapies which have difficulty effectively ablating tissue surrounding large vessels while preserving the vessels [24-27].

5.5 Conclusion

In this chapter, the effects of tissue properties on histotripsy tissue damage were investigated. The results of this work demonstrate decreased or no fractionation for tissues of increased mechanical strength. Additionally, the feasibility of using histotripsy as a tissue selective ablation method was demonstrated in an *in vivo* porcine liver where large hepatic vessels with higher mechanical strength were preserved while surrounding hepatic parenchyma with lower mechanical strength was completely fractionated. These results improve our understanding of how tissue mechanical properties affect histotripsy and provide a rational basis to extend histotripsy to address additional clinical needs.

5.6 References

[1] E. Vlaisavljevich, *et al.*, "Effects of tissue mechanical properties on susceptibility to histotripsy-induced tissue damage," *Phys Med Biol,* vol. 59, pp. 253-70, Jan 20 2014.

[2] K. Kieran, *et al.*, "Refining histotripsy: defining the parameter space for the creation of nonthermal lesions with high intensity, pulsed focused ultrasound of the in vitro kidney," *J Urol,* vol. 178, pp. 672-6, Aug 2007.

[3] J. E. Parsons, *et al.*, "Pulsed cavitational ultrasound therapy for controlled tissue homogenization," *Ultrasound Med Biol,* vol. 32, pp. 115-29, Jan 2006.

[4] W. W. Roberts, *et al.*, "Pulsed cavitational ultrasound: a noninvasive technology for controlled tissue ablation (histotripsy) in the rabbit kidney," *J Urol,* vol. 175, pp. 734-8, Feb 2006.

[5] Z. Xu, *et al.*, "Investigation of intensity thresholds for ultrasound tissue erosion," *Ultrasound in Medicine & Biology,* vol. 31, pp. 1673-1682, 2005.

[6] Z. Xu, *et al.*, "Controlled ultrasound tissue erosion," *IEEE Trans Ultrason Ferroelectr Freq Control,* vol. 51, pp. 726-36, Jun 2004.

[7] J. E. Parsons, *et al.*, "Spatial variability in acoustic backscatter as an indicator of tissue homogenate production in pulsed cavitational ultrasound therapy," *IEEE Trans Ultrason Ferroelectr Freq Control,* vol. 54, pp. 576-90, Mar 2007.

[8] Z. Xu, *et al.*, "Investigation of intensity thresholds for ultrasound tissue erosion," *Ultrasound Med Biol,* vol. 31, pp. 1673-82, Dec 2005.

[9] T. L. Hall, *et al.*, "Histotripsy of rabbit renal tissue in vivo: temporal histologic trends," *J Endourol,* vol. 21, pp. 1159-66, Oct 2007.

[10] C. R. Hempel, *et al.*, "Histotripsy fractionation of prostate tissue: local effects and systemic response in a canine model," *J Urol,* vol. 185, pp. 1484-9, Apr 2011.

[11] A. D. Maxwell, *et al.*, "Noninvasive thrombolysis using pulsed ultrasound cavitation therapy - histotripsy," *Ultrasound Med Biol,* vol. 35, pp. 1982-94, Dec 2009.

[12] A. D. Maxwell, *et al.*, "Noninvasive treatment of deep venous thrombosis using pulsed ultrasound cavitation therapy (histotripsy) in a porcine model," *J Vasc Interv Radiol,* vol. 22, pp. 369-77, Mar 2011.

[13] G. E. Owens, *et al.*, "Therapeutic ultrasound to noninvasively create intracardiac communications in an intact animal model," *Catheter Cardiovasc Interv,* vol. 77, pp. 580-8, Mar 1 2011.

[14] Z. Xu, *et al.*, "Noninvasive creation of an atrial septal defect by histotripsy in a canine model," *Circulation,* vol. 121, pp. 742-9, Feb 16 2010.

[15] N. R. Styn, *et al.*, "Histotripsy of VX-2 tumor implanted in a renal rabbit model," *J Endourol,* vol. 24, pp. 1145-50, Jul 2010.

[16] A. P. Duryea, *et al.*, "Histotripsy erosion of model urinary calculi," *J Endourol,* vol. 25, pp. 341-4, Feb 2011.

[17] Y. Kim, *et al.*, "Non-invasive pulsed cavitational ultrasound for fetal tissue ablation: feasibility study in a fetal sheep model," *Ultrasound Obstet Gynecol,* vol. 37, pp. 450-7, Apr 2011.

[18] Y. Kim, *et al.*, "Developmental impact and lesion maturation of histotripsy-mediated non-invasive tissue ablation in a fetal sheep model," *Ultrasound Med Biol,* vol. 39, pp. 1047-55, Jun 2013.

[19] A. M. Lake, *et al.*, "Renal ablation by histotripsy--does it spare the collecting system?," *J Urol,* vol. 179, pp. 1150-4, Mar 2008.

[20] C. Allam, *et al.*, "Histotripsy Effects on the Bladder Trigone: Functional and Histologic Consequences in the Canine Model," *J Endourol,* Jun 3 2013.

[21] N. Styn, *et al.*, "Histotripsy homogenization of the prostate: thresholds for cavitation damage of periprostatic structures," *J Endourol,* vol. 25, pp. 1531-5, Sep 2011.

[22] M. Cooper, *et al.*, "Controlled Ultrasound Tissue Erosion: the Effects of Tissue Type, Exposure Parameters, and the Role of Dynamic Microbubble Activity.," presented at the IEEE International Ultrasonics, Ferroelectric, and Frequency Control Joint 50th Anniversary Conference, 2004.

[23] J. Xu and T. A. Bigelow, "Experimental investigation of the effect of stiffness, exposure time and scan direction on the dimension of ultrasound histotripsy lesions," *Ultrasound Med Biol,* vol. 37, pp. 1865-73, Nov 2011.

[24] S. A. Curley, "Radiofrequency ablation of malignant liver tumors," *Oncologist,* vol. 6, pp. 14-23, 2001.

[25] D. S. Lu, *et al.*, "Influence of large peritumoral vessels on outcome of radiofrequency ablation of liver tumors," *J Vasc Interv Radiol,* vol. 14, pp. 1267-74, Oct 2003.

[26] J. A. Marrero and S. Pelletier, "Hepatocellular carcinoma," *Clin Liver Dis,* vol. 10, pp. 339-51, ix, May 2006.

[27] E. J. Patterson, *et al.*, "Radiofrequency ablation of porcine liver in vivo: effects of blood flow and treatment time on lesion size," *Ann Surg,* vol. 227, pp. 559-65, Apr 1998.

[28] J. E. Parsons, *et al.*, "Cost-effective assembly of a basic fiber-optic hydrophone for measurement of high-amplitude therapeutic ultrasound fields," *J Acoust Soc Am,* vol. 119, pp. 1432-40, Mar 2006.

[29] V. Normand, *et al.*, "New insight into agarose gel mechanical properties," *Biomacromolecules,* vol. 1, pp. 730-8, Winter 2000.

[30] L. C. Diem K., *Documenta Geigy scientific tables, 7th Edition.* : Macclesfield, 1970.

[31] F. A. Duck, *Physical properties of tissue: a comprehensive reference book.* : Academic Press, 1990.

[32] ICRP, *Report of the Task Group on Reference Man : a report.* Oxford, New York: Pergamon Press, 1975.

[33] ICRU, *Tissue Substitutes in Radiation Dosimetry and Measurement.* : Intl Commission on Radiation, 1989.

[34] H. Q. Woodard and D. R. White, "The composition of body tissues," *Br J Radiol,* vol. 59, pp. 1209-18, Dec 1986.

[35] P. Fratzl, *Collagen: Structure and Mechanics*. New York, NY: Springer Science+Business Media, LLC, 2008.

[36] G. A. Holzapfel and R. W. Ogden, *Biomechanics of Soft Tissue in Cardiovascular Systems.* . New York, NY: Springer-Verlag, 2003.

[37] E. N. Marieb and K. Hoehn, *Human Anatomy and Physiology, 7th Edition*: Pearson Education, Inc., 2007.

[38] T. P. Moffitt, *et al.*, "Mechanical properties of coagulated albumin and failure mechanisms of liver repaired with the use of an argon-beam coagulator with albumin," *J Biomed Mater Res,* vol. 63, pp. 722-8, 2002.

[39] C. A. Schulze-Bauer, *et al.*, "Mechanics of the human femoral adventitia including the high-pressure response," *Am J Physiol Heart Circ Physiol,* vol. 282, pp. H2427-40, Jun 2002.

[40] H. Yamada, *Strength of biologic materials.* . New York: Robert E. Kreiger, 1973.

[41] R. K. Jain, "Determinants of tumor blood flow: a review," *Cancer Res,* vol. 48, pp. 2641-58, May 15 1988.

[42] K. W. Lin, *et al.*, "Ultrasound-induced fluid uptake phenomenon in porcine uterine tissue.," presented at the IEEE International Ultrasonics Symposium, San Diego, CA, 2010.

[43] J. C. Simon, *et al.*, "Ultrasonic atomization of tissue and its role in tissue fractionation by high intensity focused ultrasound," *Phys Med Biol,* vol. 57, pp. 8061-78, Dec 7 2012.

[44] Y. N. Wang, *et al.*, "Histological and biochemical analysis of mechanical and thermal bioeffects in boiling histotripsy lesions induced by high intensity focused ultrasound," *Ultrasound Med Biol,* vol. 39, pp. 424-38, Mar 2013.

[45] S. Park, *et al.*, "Non-invasive embolus trap using histotripsy-an acoustic parameter study," *Ultrasound Med Biol,* vol. 39, pp. 611-9, Apr 2013.

[46] E. Vlaisavljevich, *et al.*, "Effects of Tissue Mechanical Properties on Histotripsy," in *IEEE International Ultrasonics Symposium,* 2011.

Chapter 6
Effects of Thermal Preconditioning on Tissue Susceptibility to Histotripsy

6.1 Introduction

Histotripsy is a non-invasive tissue ablation method that controls acoustic cavitation to mechanically fractionate soft tissue [2-5]. With sufficiently high pressure and an adequate number of pulses, histotripsy can completely fractionate soft tissues into a liquefied acellular homogenate resulting in effective tissue removal [5, 6]. Histotripsy is currently being studied for many clinical applications where non-invasive tissue removal is desired including tissue debulking to treat benign prostatic hyperplasia [7], clot breakdown to treat deep vein thrombosis [8], perforation of the atrial septum in the treatment of congenital heart diseases [9, 10], cancer ablation [11, 12], kidney stone removal [13], and fetal interventions [14].

Tissue mechanical properties have been observed to affect the histotripsy process [15-17]. In a previous study, it was demonstrated that stiffer tissues are less susceptible to histotripsy-induced tissue damage [15]. In that study, histotripsy was shown capable of completely ablating

the majority of soft tissues, while producing no damage for stiffer tissues such as tendon and cartilage [15]. The finding that stiffer tissues are more resistant to histotripsy has been utilized to improve histotripsy therapy for specific clinical applications by developing a tissue selective ablation approach in which softer tissues (i.e. liver, kidney) are completely fractionated while stiffer tissues within the focal region (i.e. blood vessels, collecting system) are preserved [12, 15, 18]. However, the resistance of stiffer tissues to histotripsy may also be problematic in cases where the removal of a stiff tissue is desired, such as in the treatment of fibrous masses (i.e. fibroadenoma, uterine fibroids, or fibrous tumors) or the debulking of stiff tissues (i.e. tendon, ligament, or tongue). As such, a pretreatment strategy that could alter the susceptibility of tissues to histotripsy would be a valuable tool in developing histotripsy for clinical applications in which the removal of stiff tissues is desired.

In this chapter, we investigate the effects of thermal preconditioning on tissue susceptibility to histotripsy therapy. Previous work has shown that heating can alter tissue stiffness due to changes in the structure of intracellular and extracellular proteins such as actin, myosin, and collagen [19, 20]. Changes in tissue stiffness are dependent upon multiple factors including tissue composition, heating temperature, and heating duration [19, 20]. Since the stiffness of most tissues is largely dictated by collagen composition, we hypothesize that the effectiveness of a thermal pretreatment will be largely determined by the changes in collagen. Previous work has shown that the Young's modulus of isolated collagen fibers and selective collagenous tissues decreases when heated between 50°C-60°C due to collagen denaturing (unraveling of the collagen triple helix) and breakdown of chemical crosslinks between collagen fibers [19-23]. However, the Young's modulus of selective collagenous tissues has been shown to increase when heated at higher temperatures 65°C-90°C due to collagen contraction (shrinking

of individual collagen fibers) [19-23]. Additionally, collagen can also hydrolyze into gelatin (individual fibers cleaved into small pieces), significantly decreasing tissue stiffness [19, 20]. Based on these previous studies, we investigate two different heating temperatures for thermal preconditioning, 58°C and 90°C. We hypothesize that the majority of tissues will soften and become more susceptible to histotripsy after preheating at 58°C due to collagen denaturing, but that tissues will rapidly stiffen and become less susceptible to histotripsy after preheating at 90°C due to collagen contraction, unless collagen hydrolysis into gelatin occurs. Furthermore, in order to provide a more complete understanding of the effects of thermal preconditioning on tissues with different compositions and tissue stiffness's, we investigate the effects of heating on a variety of tissue types.

In the first part of this chapter, a constant temperature water bath (58°C and 90°C) was used to provide a controlled heating environment to study the effects of thermal preconditioning on tissue susceptibility to histotripsy for various *ex vivo* bovine tissues (tongue, artery, liver, kidney medulla, tendon, urethra). After heating, Young's modulus was measured using a microelastometer, and changes in collagen composition (i.e. collagen structure/density) were analyzed histologically. The effects of preheating on the susceptibility to histotripsy-induced tissue damage was then investigated by applying histotripsy to heated and unheated tissues using a 750 kHz histotripsy transducer. Based on these results, a final set of experiments was conducted to demonstrate the feasibility of using high intensity focused ultrasound (HIFU) to provide the thermal preconditioning treatment, as previous work has demonstrated that HIFU can significantly alter tissue stiffness [24]. Overall, the aim of this study is to investigate the feasibility of using thermal preconditioning to decrease tissue stiffness and increase the

susceptibility of tissues to histotripsy, which could be a valuable tool in developing histotripsy for clinical applications in which the removal of stiff tissues is desired.

6.2 Methods

6.2.1 Bovine Tissue Processing

To compare the effects of preheating on tissue stiffness and the susceptibility to histotripsy-induced tissue damage, a variety of *ex vivo* bovine tissues were used. Fresh bovine tongue, artery, liver, kidney, tendon, and urethra were excised at a local slaughterhouse and immediately placed into degassed 0.9% saline solution and stored at 4°C until experiments. Tissue samples were harvested from 5-12 animals for each set of tissue type and experimental conditions (i.e. external heating and HIFU heating at 58°C and 90°C). Tissue samples were sectioned and warmed to room temperature prior to heating experiments. After heating, tissues were either fixed for histology, tested for stiffness using a soft tissue elastometer, or degassed for histotripsy treatments. All samples were used within 48 hours of harvesting.

6.2.2 Constant Temperature Heating

In order to investigate the effects of preheating on tissue stiffness and susceptibility to histotripsy in a controlled environment, *ex vivo* tissues were heated in a constant temperature water bath, consisting of a slow cooker (Crock-Pot, SCCPVL610-S, Manchester, UK) connected to a sous-vide temperature controller (Dorkfood, DSV, Pensacola, Florida, USA). *Ex vivo* bovine tongue, artery, liver, kidney medulla, tendon, and urethra were submerged in the water bath and heated for 4, 8, and 12 hours at 58°C and 90°C, with the temperature controller set to maintain a constant water temperature within ±2°C. These temperatures (58°C and 90°C) were chosen

based on previous work showing that collagen denaturing (tissue softening) increases with temperature up to ~60°C, at which point the individual collagen fibers start to contract (tissue stiffening) with the majority of collagen fibers contracting rapidly at temperatures above ~85°C [19, 20]. In this study, we expand on this previous work to investigate the effects of thermal preconditioning on a variety of tissue types with different compositions and tissue stiffness's. Prior to heating, tissues were sectioned into thin pieces <1cm in thickness in order to ensure tissues were more uniformly heated. For each temperature and heating duration, separate tissue samples were heated for Young's modulus measurements (n=6), histological analysis (n=4), and histotripsy treatment experiments (n=6).

6.2.3 Measurement of Tissue Stiffness

In order to investigate the effects of heating on tissue stiffness, a soft tissue microelastometer (MicroElastometer Model 0301, Artann Laboratories, West Trenton, NJ, USA) was used to measure the Young's modulus (compression) of tissue samples. The Young's modulus was measured for tissue samples heated for 4, 8, and 12 hours at 58°C and 90°C as well as unheated controls. Tissues were sectioned into small samples just larger than the microelastometer piston, which was a rectangular stamp of 8.88 mm by 3.98 mm [Fig. 6.1(A)]. The microelastometer measures tissue stiffness under quasi-static deformation using a small piston that incrementally increases the force applied to the tissue which rests on a pressure sensitive stage. By measuring the vertical tissue displacement and applied force, the stress and strain (compression) can be measured and used to calculate the tissue Young's modulus. The Young's Modulus (E) was calculated as the stress divided by the strain. Although tissue is not linearly elastic, an average Young's modulus was estimated from the microelastometer software

as described in previous studies [25, 26], and the results were compared for all samples. Additionally, force vs. strain curves were generated for each sample to provide a more complete analysis of tissue viscoelasticity. For each sample, three measurements were conducted to ensure a consistent measurement was observed. For each experimental condition, 6 tissue samples were analyzed, with the results compared using a Student's t-test. P-values < 0.05 were considered significant. Tissue samples were kept hydrated in water until immediately prior to the Young's modulus measurements. As the Young's modulus measurements of each sample took less than 1 minute, no significant tissue dehydration was expected to occur.

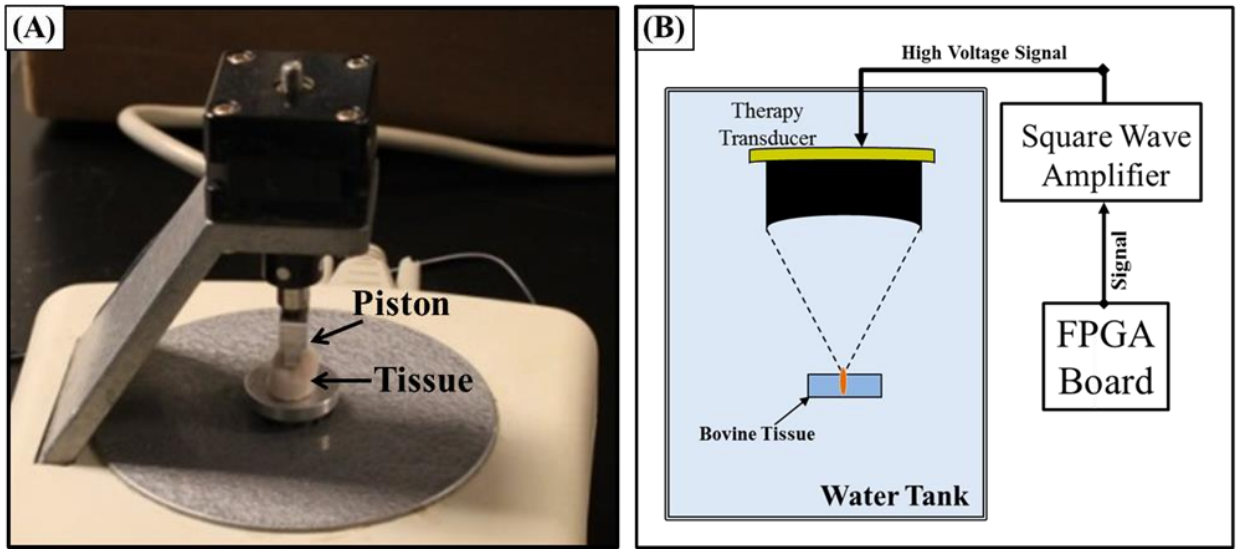

Figure 6.1. Experimental Setup. (A) After heating, tissue Young's modulus (compression) was measured using a tissue elastometer. (B) Susceptibility to histotripsy was tested using a 750 kHz therapy transducer with the focused aligned to the tissue surface. Histotripsy was applied for five minutes using 5 cycle pulses, a pulse repetition frequency of 500 Hz, and pressure of 19/60 MPa (P-/P+).

6.2.4 Histological Analysis

To investigate the changes in tissue composition (i.e. collagen structure/density) with heating, histological analysis of tissues was conducted using a Masson's trichrome stain, which uses three stains to visualized tissue collagen (blue), muscle/cytoplasm (red), and nuclei (black).

After heating, tissue samples were fixed in formalin, dissected, processed, and then stained. The changes in tissue composition were examined histologically under a microscope (Nikon Eclipse 50i) using 4x, 10x, 20x, and 40x objective lenses.

6.2.5 Histotripsy Treatment

To compare the susceptibility of tissues to histotripsy-induced damage, histotripsy therapy was applied to the surface of tissue samples using a 750 kHz therapy transducer (Imasonic, SAS, Voray sur l'Ognon, France) with an aperture of 15 cm and a geometric focal length of 12 cm. The transducer was driven by a custom-designed class D amplifier with appropriate electrical matching circuits built in our laboratory and associated low voltage (20V DC power supply; E3630A Hewlett Packard Company, Palo Alto, CA, USA) and high voltage (600V DC power supply; GEN 600, TDK Lambda Americas Inc., San Diego, CA, USA) power supplies. Input signals were provided by a custom built Field-Programmable Gate Array (FPGA) board (Altera Corporation, San Jose, CA, USA) that functioned as a signal generator.

For each set of heating parameters and tissue type, six tissue samples were treated with histotripsy using the experimental set up shown in Figure 6.1(B). The tested samples included tongue, artery, liver, kidney medulla, tendon, and urethra that were heated for 0, 4, 8, and 12 hours at 58°C and 90°C. Prior to histotripsy treatments, tissues were allowed to cool to room temperature under a partial vacuum (~20 kPa, absolute) for 30 minutes to remove any gas trapped within the tissue. Each sample was then embedded onto a 1% w/v agarose tissue phantom to hold tissues inside the water tank for histotripsy treatments. The focus of the 750 kHz transducer was aligned to the surface of the tissue, and a histotripsy bubble cloud was formed at the tissue-water interface using 5-cycle long ultrasound pulses, a pulse repetition

frequency (PRF) of 500 Hz, and peak pressures of 19/60 MPa (P-/P+) as measured by a fiber-optic probe hydrophone (FOPH) built in-house [27]. Bubble cloud formation and alignment were verified using optical and ultrasound imaging. Histotripsy treatments were applied to the tissue surface for 5 minutes (n=6). All samples of a given tissue type were treated in the same orientation as shown in the images in the results section. More specifically, artery and urethra samples were cut open and histotripsy was applied to the internal surface of the lumen (i.e. intima). Kidney samples were sectioned so that histotripsy could be applied to the kidney medulla tissue. Liver samples were not sectioned in any specific orientation. Tongue samples were sectioned transverse to the tongue, with histotripsy applied to the tongue muscle tissue (not the fibrous surface of the tongue). Histotripsy was applied to the side of the tendon samples in the transverse direction as shown. After treatment, tissue samples were examined for damage (lesion formation) by gross morphology. Results were organized into tissues with complete damage (large lesion through entire tissue, i.e. perforation), partial damage (lesion formed into, but not completely through, the tissue), surface damage (slight damage to the tissue surface), and no damage.

6.2.6 HIFU Heating

The feasibility of using thermal HIFU to precondition tissues prior to histotripsy was investigated using *ex vivo* tongue, liver, and tendon. HIFU was applied to tissues using the same 750 kHz therapy transducer for histotripsy treatments with the temperature at the focus measured using 3 type T hypodermic needle thermocouples (Physitemp Instruments Inc., Clifton, NJ, USA). Thermocouples were superficially inserted into the tissue at the transducer focus, and the temperature was monitored during treatments in real-time. HIFU was applied using 30-35 cycle

pulses at a pressure of 8/25 MPa (P-/P+) and a PRF varying from 1300-1750 Hz. During HIFU, the peak temperature measured by the thermocouples was allowed to increase to the desired maximum temperature (60°C or 90°C) and then the PRF was lowered to maintain a nearly constant temperature for the duration of the HIFU exposure. HIFU treatments were applied for 10 minutes in tongue and liver and for 30 minutes in tendon. These treatment durations (10-30 minutes) were chosen in order to investigate if the trends observed for controlled heating experiments could be replicated using HIFU heating in more reasonable treatments times compared to the much longer durations applied in the controlled heating experiments (4-12 hours).

6.3 Results

6.3.1 Controlled Preheating at 58°C

To test the hypothesis that heating at 58°C will soften tissues and increase their susceptibility to histotripsy due to collagen denaturing, bovine tongue, artery, kidney medulla, liver, tendon, and urethra were used. Results demonstrated that heating at 58°C decreased the Young's modulus of tongue, artery, kidney medulla, liver, and tendon [Fig. 6.2(A-E)], with the decrease in modulus significant ($p<0.05$) in all cases compared to controls except for tendon at 4 hours and liver at all-time points ($p>0.05$). Of all the tissues heated at 58°C, only urethra showed an increase in Young's modulus [Fig. 6.2(F)]. Analysis of the force vs. strain curves demonstrated that tendon showed a nearly linear elastic behavior, with a decrease in Young's modulus observed for heated samples [Fig. 6.3(E)]. Further analysis of the force vs. strain curves showed that tissue viscoelasticity was highly nonlinear in unheated samples of tongue, artery, kidney medulla, and liver. In these control samples, the tissues were initially highly compliant

(i.e. small load resulting in large strains), but stiffened with increasing strain [Fig. 6.3(A-D)]. The force vs. strain curves for these tissues demonstrated a decrease in initial compliance (i.e. stiffening of tissue under small strain loading) after heating at 58°C [Fig. 6.3(A-D)]. However, these tissues showed a reduction in the slope of the curve for the higher strain regions of heated tissues compared to control tissues (i.e. softening of tissue under large strain loading) [Fig. 6.3(A-D)]. Analysis of the force vs. strain curves for urethra showed nearly linear elastic behavior with an increase in Young's modulus for heated samples [Fig. 6.3(F)].

Histological analysis demonstrated a decrease in collagen density for all tissues heated at 58°C, except for urethra. Representative Masson's trichrome stain slides of the tongue and artery show a significant decrease in collagen (blue) density for heated samples compared to controls [Fig. 6.4]. The distance between muscle fibers (red) was observed to increase with heating in these tissues, with this effect most pronounced in the tongue [Fig. 6.4]. A similar decrease in collagen density was seen for tendon, where the collagen density decreased continuously as the tissue was heated for 4, 8, and 12 hours [Fig. 6.4]. Additionally, an increasing amount of hydrolysis of collagen (blue) into gelatin (dark red) was observed in tendon as the heating duration was increased [Fig. 6.4]. Of all the tissues heated at 58°C, only urethra showed an increase in collagen density with heating [Fig. 6.4], matching the Young's modulus results [Fig. 6.2(F)]. The increase in density and tissue stiffness for urethra was potentially caused by the contraction of elastic fibers inside the highly compliant urethra.

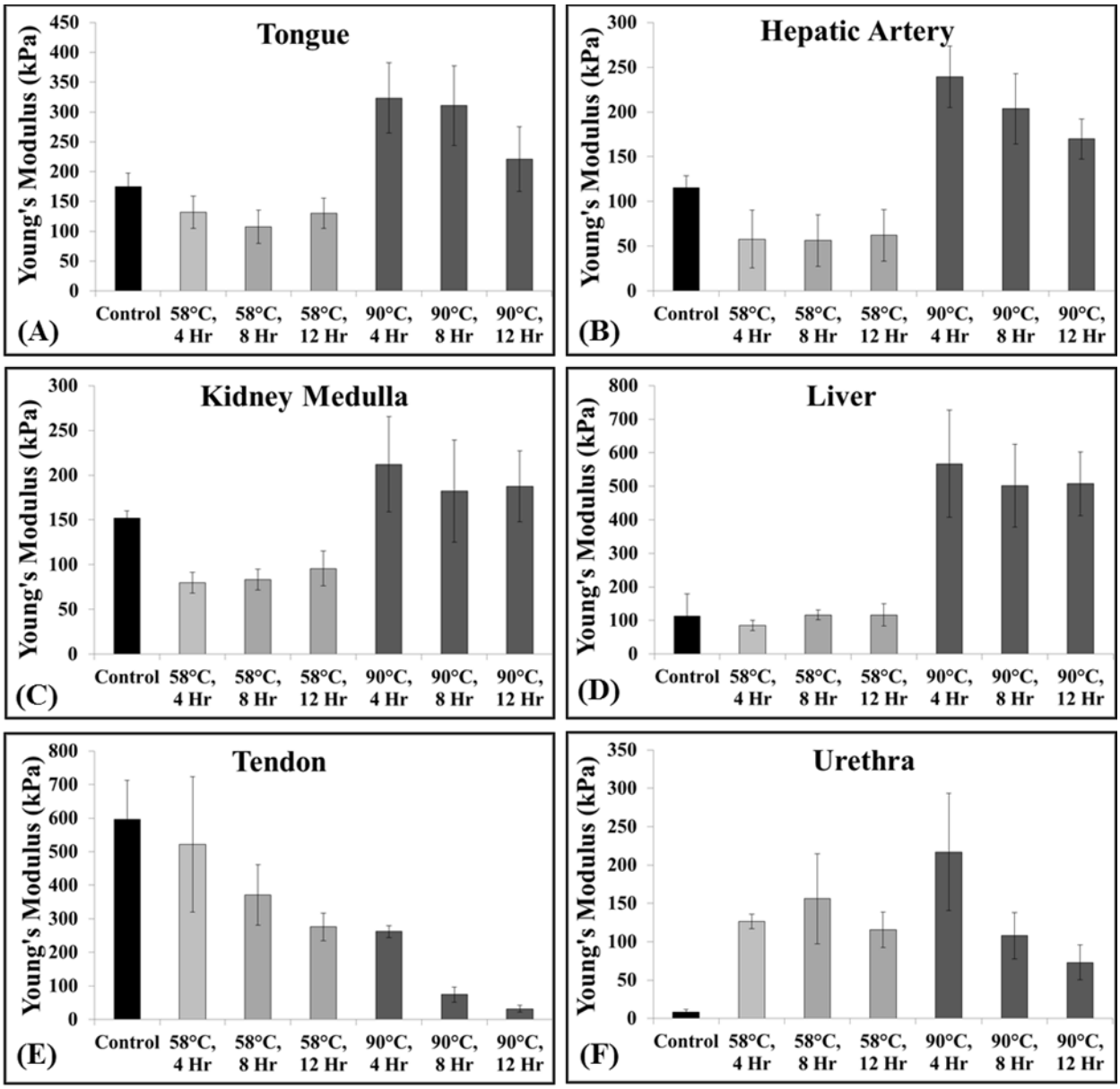

Figure 6.2. Elastometer measurements for tissues heated at 58ºC demonstrated a significant decrease in the Young's modulus of tongue, artery, kidney medulla, and tendon (A:C,E), no significantly change for liver (D), and a significant increased for urethra (F). Heating at 90ºC significantly increased the Young's modulus of tongue, artery, kidney medulla, liver, and urethra (A:D, F) and significantly decreased the Young's modulus of tendon (E).

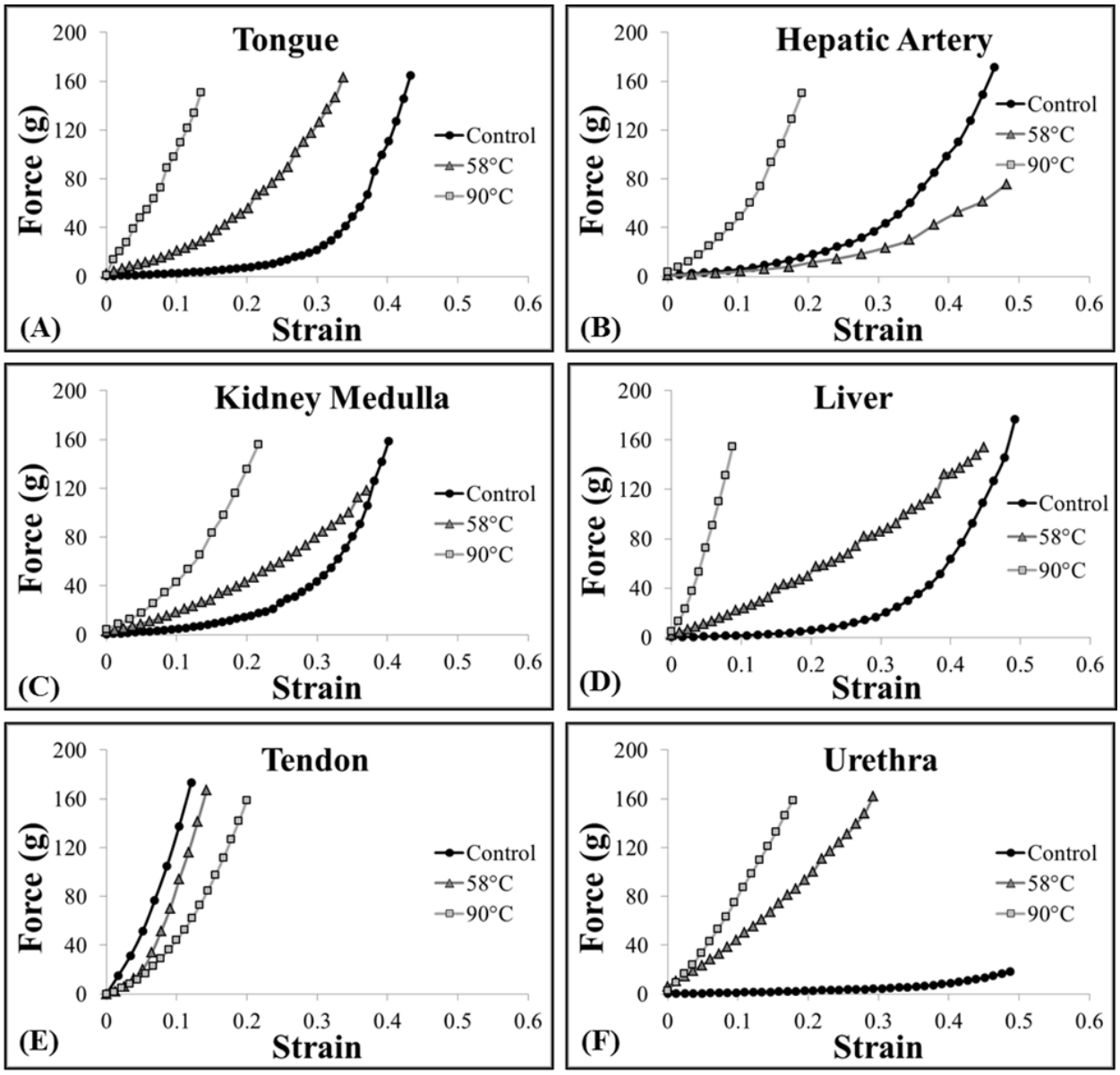

Figure 6.3. Representative Force vs. Strain Curves. Plots show representative Force vs. Strain curves measured by the elastometer for tissues samples comparing unheated control samples with samples that were heated for 4 hours at 58°C and 90°C, respectively.

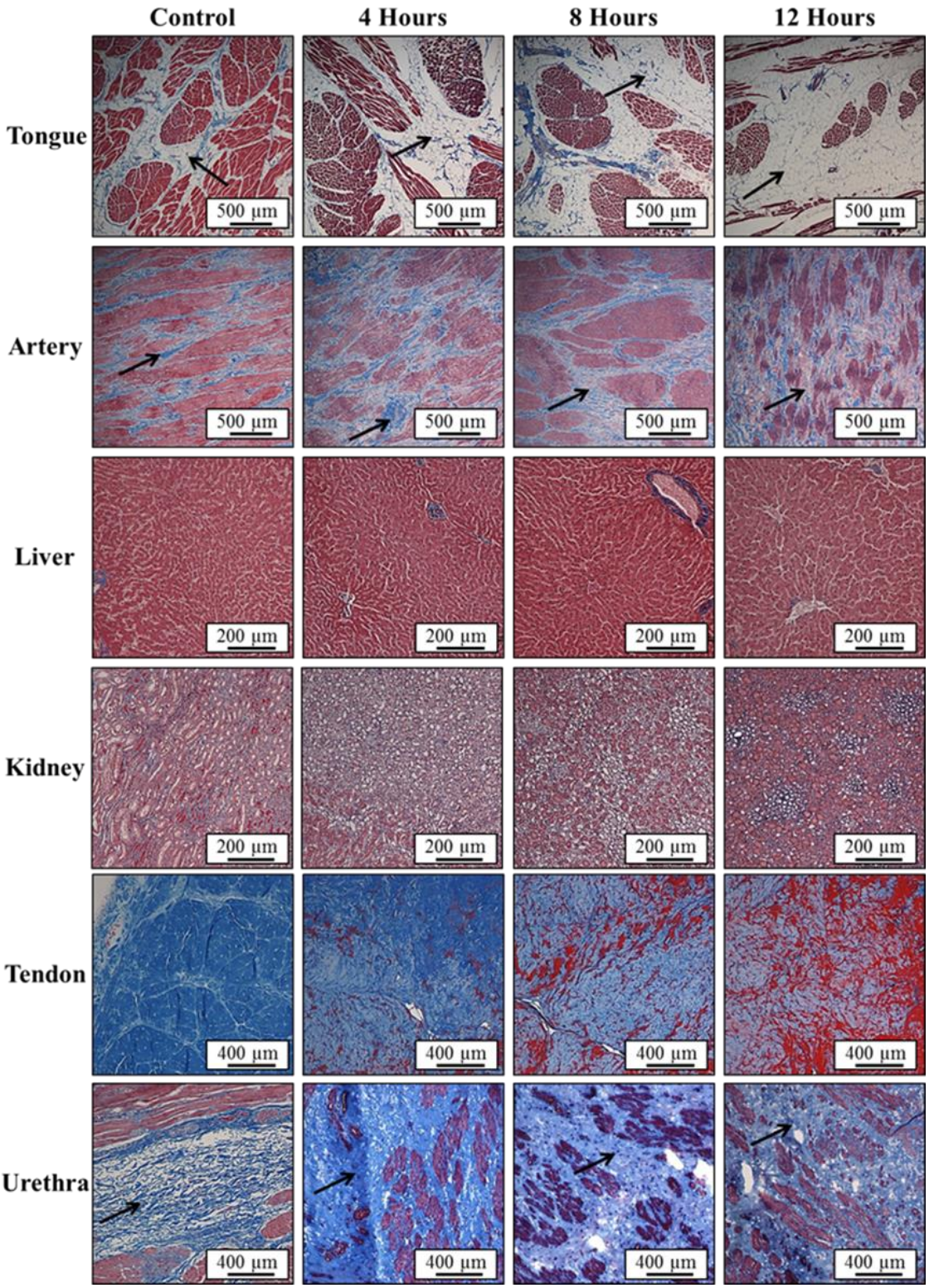

Figure 6.4. Images show histology slides stained with a trichrome blue staining for samples heated at 58°C for 4, 8, and 12 hours. Tongue, artery, and tendon showed a decrease in collagen (blue) density with heating. Hydrolysis into gelatin (red) was observed in tendon after 8 and 12 hours. Urethra showed an increase in collagen density after heating compared to control.

Histotripsy treatment results demonstrated that decreases in tissue stiffness with preheating resulted in an increased susceptibility to histotripsy [Fig. 6.5]. For example, histotripsy could only partially damage tongue, artery, and liver prior to heating but could form a lesion completely through the tissue after preheating for 4 hours at 58°C [Fig. 6.5]. A similar trend of increasing susceptibility with preheating was observed for kidney medulla and tendon samples. However, even after heating for 12 hours, only superficial damage to the surface of tendon was observed [Fig. 6.5]. In contrast to the other tissues, urethra was observed to be less susceptible to histotripsy after heating [Fig. 6.5], matching the tissue stiffness results [Fig. 6.2(F)]. Complete results from the treatments of tissues preheated at 58°C are shown in Table 6.1.

Table 6.1. Histotripsy treatment results for 58°C samples showed that tongue, artery, liver, kidney, and tendon were more susceptible to histotripsy while urethra was less susceptible.

Heated at 58°C		**Histotripsy Lesion** (# Samples/Total Samples)			
Tissue Type	**Heating Duration**	**No Visible Damage**	**Surface Damage Only**	**Partial Damage (No Perforation)**	**Complete Damage (Perforation)**
Tongue					
	Control	0/6	0/6	**6/6**	0/6
	4 Hours	0/6	0/6	0/6	**6/6**
	8 Hours	0/6	0/6	0/6	**6/6**
	12 Hours	0/6	0/6	0/6	**6/6**
Artery					
	Control	0/6	**3/6**	**3/6**	0/6
	4 Hours	0/6	0/6	0/6	**6/6**
	8 Hours	0/6	0/6	0/6	**6/6**
	12 Hours	0/6	0/6	0/6	**6/6**
Liver					
	Control	0/6	0/6	**6/6**	0/6
	4 Hours	0/6	0/6	0/6	**6/6**
	8 Hours	0/6	0/6	0/6	**6/6**
	12 Hours	0/6	0/6	0/6	**6/6**
Kidney					
	Control	**4/6**	**2/6**	0/6	0/6
	4 Hours	0/6	**1/6**	**5/6**	0/6
	8 Hours	0/6	0/6	0/6	**6/6**
	12 Hours	0/6	0/6	0/6	**6/6**
Tendon					
	Control	**6/6**	0/6	0/6	0/6
	4 Hours	**5/6**	**1/6**	0/6	0/6
	8 Hours	0/6	**6/6**	0/6	0/6
	12 Hours	0/6	**6/6**	0/6	0/6
Urethra					
	Control	0/6	**5/6**	**1/6**	0/6
	4 Hours	**6/6**	0/6	0/6	0/6
	8 Hours	**3/6**	**3/6**	0/6	0/6
	12 Hours	0/6	**6/6**	0/6	0/6

Figure 6.5. Morphological analysis of bovine tissues after histotripsy demonstrated that tongue, artery, liver, kidney, and tendon were more susceptible to histotripsy-induced tissue damage after heating at 58°C. Urethra was observed to be less susceptible to histotripsy after heating at 58°C.

6.3.2 Controlled Preheating at 90°C

The hypothesis that preheating tissues at 90°C will stiffen tissues and decrease susceptibility to histotripsy due to collagen contraction was tested using bovine tongue, artery, kidney medulla, liver, tendon, and urethra. Results demonstrated that preheating at 90°C for 4 hours significantly increased the Young's modulus of tongue, artery, kidney medulla, liver, and urethra compared to controls ($p<0.05$) [Fig. 6.2(A-D,F)]. After 8 and 12 hours of preheating at 90°C, the Young's modulus of these tissues decreased compared to the 4 hour samples, but remained significantly higher than the unheated controls ($p<0.05$) [Fig. 6.2(A-D,F)]. Of all the tissues preheated at 90°C, only tendon demonstrated a decrease in Young's modulus compared to the unheated controls [Fig. 6.2(E)]. The decreases in Young's modulus for tendon preheated at 90°C were much larger than the decreases observed at 58°C [Fig. 6.2(E)]. For example, heating tendon for 4 hours at 90°C resulted in a similar decrease in Young's modulus as seen in samples heated for 12 hours at 58°C [Fig. 6.2(E)]. Results further demonstrated that the Young's modulus of tendon continually decreased for samples heated for 4, 8, and 12 hours [Fig. 6.2(E)]. Analysis of the force vs. strain curves show tissue stiffening after 4 hours of heating at 90°C for all tissue types except tendon, which showed a decrease in stiffness [Fig. 6.3].

Prior to fixing tissue for histology, tissues were examined using gross morphology. In contrast to tissues preheated at 58°C which were observed to expand slightly, all tissues preheated at 90°C significantly shrunk after heating. Morphological analysis also showed that tongue, artery, kidney medulla, liver, and urethra appeared dried out and felt significantly tougher than tissues preheated at 58°C, likely due to increased density and decreased water content due to collagen contraction. Histological analysis of these tissues showed a significant increase in collagen density observed after 4 hours of preheating at 90°C [Fig. 6.6]. For longer

duration heating, collagen density was observed to decrease compared to the 4 hour samples, likely due to collagen dissolution or hydrolysis [Fig. 6.6]. The trends observed for tendon preheated at 90°C were different than those observed for other tissues. Although tendon was also observed to shrink after heating, morphological analysis demonstrated continual softening of the tendon, which also became more transparent and gel-like as the duration of heating was increased, likely due to collagen hydrolysis into gelatin. This trend was verified by histology which showed a continual decrease in collagen (blue) density as the heating duration was increased, as well as a corresponding increase in gelatin (dark red) with heating [Fig. 6.6]. Collagen hydrolysis into gelatin was also observed, albeit to a much lesser extent, in urethra samples heated for 12 hours at 90°C [Fig. 6.6]. For all samples, the morphology and trends histology matched the trends in tissue stiffness measured by the soft tissue elastometer.

Histotripsy treatment results demonstrated that increases in tissue stiffness, which were observed for all tissues except tendon, resulted in decreased susceptibility to histotripsy for samples preheated at 90°C for 4 hours [Fig. 6.7]. Samples preheated at 90°C for 8 and 12 hours were more susceptible to histotripsy than samples heated for 4 hours [Fig. 6.7]. For all 90°C heating durations, liver, tongue, artery, and kidney medulla samples were less susceptible to histotripsy than tissues heated for the same duration at 58°C. In contrast, tendon heated at 90°C was more susceptible to histotripsy than tendon heated at 58°C. As the duration of 90°C heating was increased, the susceptibility of tendon to histotripsy continually increased, with complete ablation through the tendon achieved for all 12 hour samples [Fig. 6.7]. A similar result was observed for the urethra after 12 hours of heating, with complete ablation in 4 out of 6 samples. Complete results from the histotripsy treatments of tissues heated at 90°C are shown in Table 6.2.

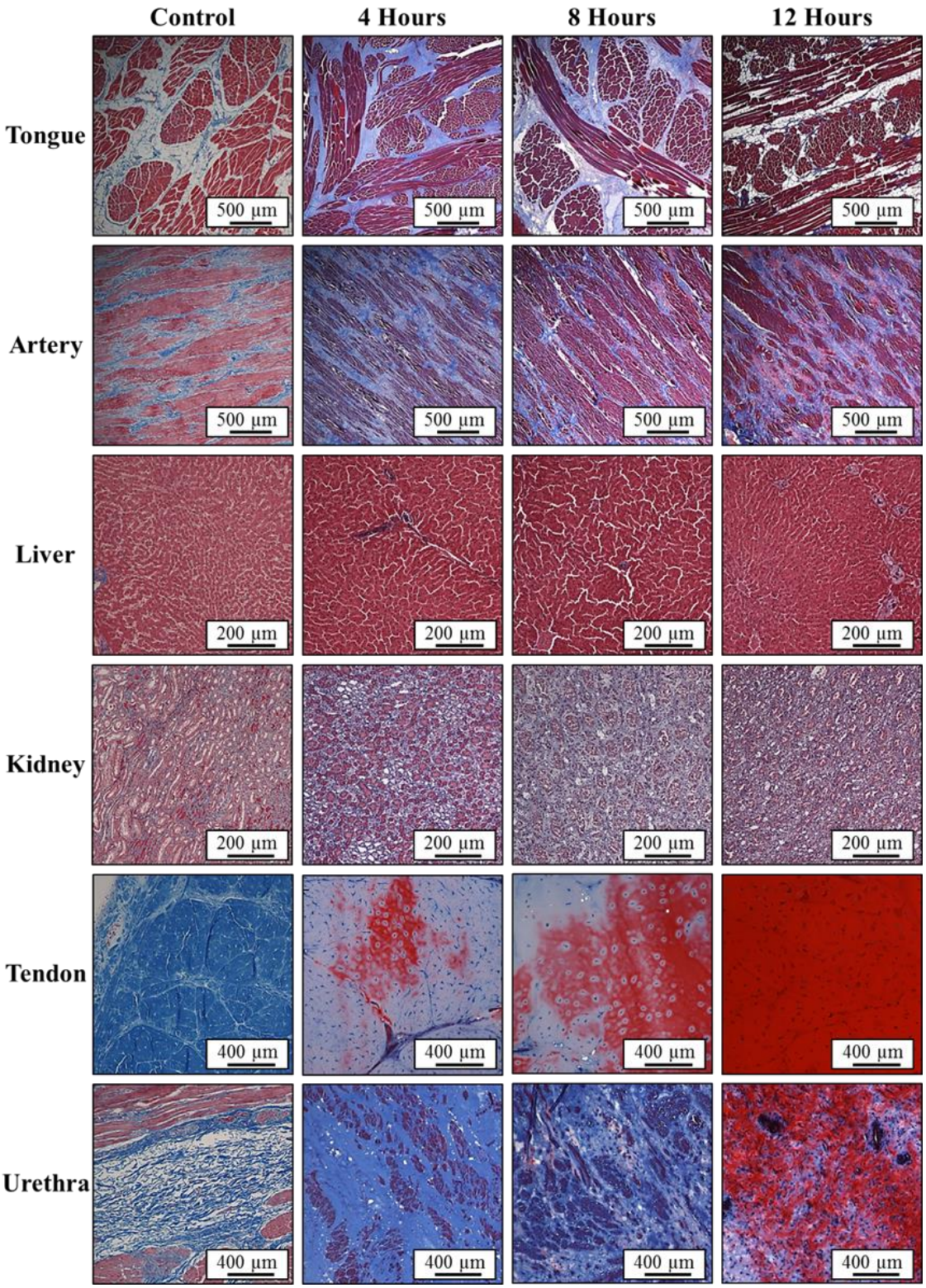

Figure 6.6. Images show histology slides stained with a trichrome blue staining for samples heated at 90°C for 4, 8, and 12 hours. Results for tongue, artery, and urethra demonstrated an increase in collagen (blue) density with heating. In tendon, collagen hydrolyzed into gelatin (red) with heating. Some hydrolysis was also observed in the urethra after 12 hour heating.

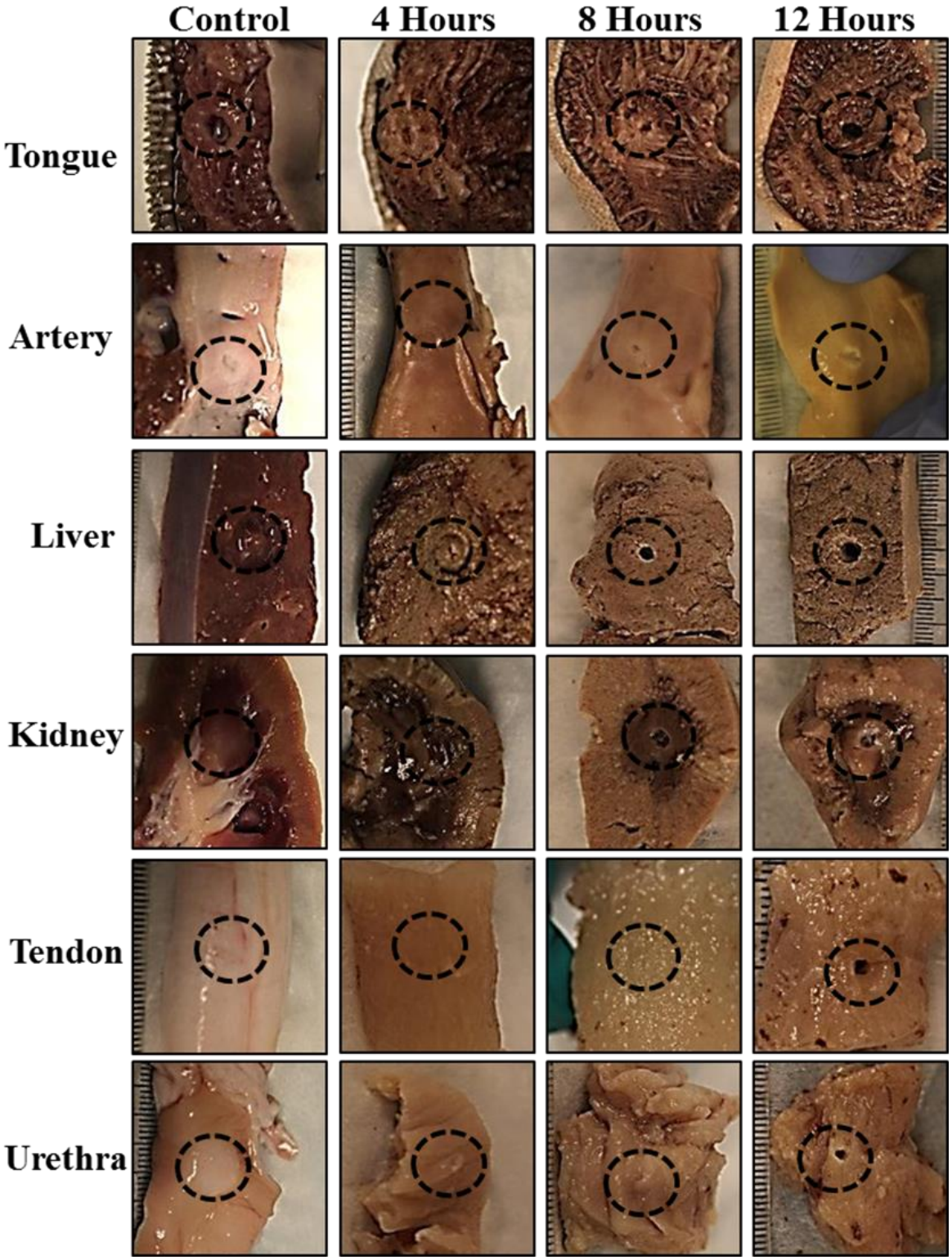

Figure 6.7. Morphological analysis of bovine tissues after histotripsy show tongue, artery, liver, kidney, and urethra were less susceptible to histotripsy after heating at 90°C for 4 hours while tendon was more susceptible to histotripsy after heating. All tissues became more susceptible to histotripsy after heating was continued for 8 and 12 hours (compared to 4 hour samples).

Table 6.2. Histotripsy treatment results demonstrated that tongue, artery, liver, kidney, and urethra were less susceptible to histotripsy-induced tissue damage after heating at 90°C for 4 hours while tendon was more susceptible to histotripsy after heating. All tissues became more susceptible to histotripsy after heating was continued for 8 and 12 hours (compared to 4 hours).

Heated at 90°C		**Histotripsy Lesion** (# Samples/Total Samples)			
Tissue Type	**Heating Duration**	**No Visible Damage**	**Surface Damage Only**	**Partial Damage (No Perforation)**	**Complete Damage (Perforation)**
Tongue					
	Control	0/6	0/6	**6/6**	0/6
	4 Hours	**2/6**	**4/6**	0/6	0/6
	8 Hours	0/6	**3/6**	**3/6**	0/6
	12 Hours	0/6	0/6	**2/6**	**4/6**
Artery					
	Control	0/6	**3/6**	**3/6**	0/6
	4 Hours	**6/6**	0/6	0/6	0/6
	8 Hours	**1/6**	**5/6**	0/6	0/6
	12 Hours	0/6	**3/6**	**3/6**	0/6
Liver					
	Control	0/6	0/6	**6/6**	0/6
	4 Hours	0/6	**6/6**	0/6	0/6
	8 Hours	0/6	0/6	**2/6**	**4/6**
	12 Hours	0/6	0/6	0/6	**6/6**
Kidney					
	Control	**4/6**	**2/6**	0/6	0/6
	4 Hours	**5/6**	**1/6**	0/6	0/6
	8 Hours	0/6	**4/6**	**2/6**	0/6
	12 Hours	0/6	0/6	**1/6**	**5/6**
Tendon					
	Control	**6/6**	0/6	0/6	0/6
	4 Hours	0/6	**6/6**	0/6	0/6
	8 Hours	0/6	**1/6**	**4/6**	**1/6**
	12 Hours	0/6	0/6	0/6	**6/6**
Urethra					
	Control	0/6	**5/6**	**1/6**	0/6
	4 Hours	**2/6**	**3/6**	**1/6**	0/6
	8 Hours	0/6	**4/6**	**2/6**	0/6
	12 Hours	0/6	0/6	**2/6**	**4/6**

6.3.3 HIFU Heating

Bovine liver, tongue, and tendon were exposed to thermal HIFU followed by histotripsy therapy to demonstrate the feasibility of using HIFU to alter tissue susceptibility to histotripsy. For HIFU treatments, the temperature at the focus was quickly increased to ~60°C or ~90°C and then the PRF was lowered to hold the temperature constant for the duration of heating [Fig. 6.8].

It should be noted that tissues heated to ~90°C significantly deformed during heating due to tissue contraction, causing the thermocouples to move out of the focus and making it difficult to measure a high temperature for the duration of heating. For example, the tendon was observed to bend in half within 30 seconds after the temperature reached ~90°C, resulting in movement of the thermocouples out of the focus and a decrease in the measured temperature [Fig. 6.8(B)]. Similar trends were observed for all tissue types heated to 90°C. The movement of the focus due to tissue contraction made it difficult to measure a sustained peak temperature in the targeted range, but it is expected that the actual peak temperature in the tissue remained near 90°C for the duration of heating. No tissue contraction was observed for the ~60°C HIFU treatments, resulting in a measured peak temperature that remained near ~60°C for the duration of the exposure [Fig. 6.8(A)]. The heating parameters (peak temperature, duration) applied for all samples are listed in Table 6.3.

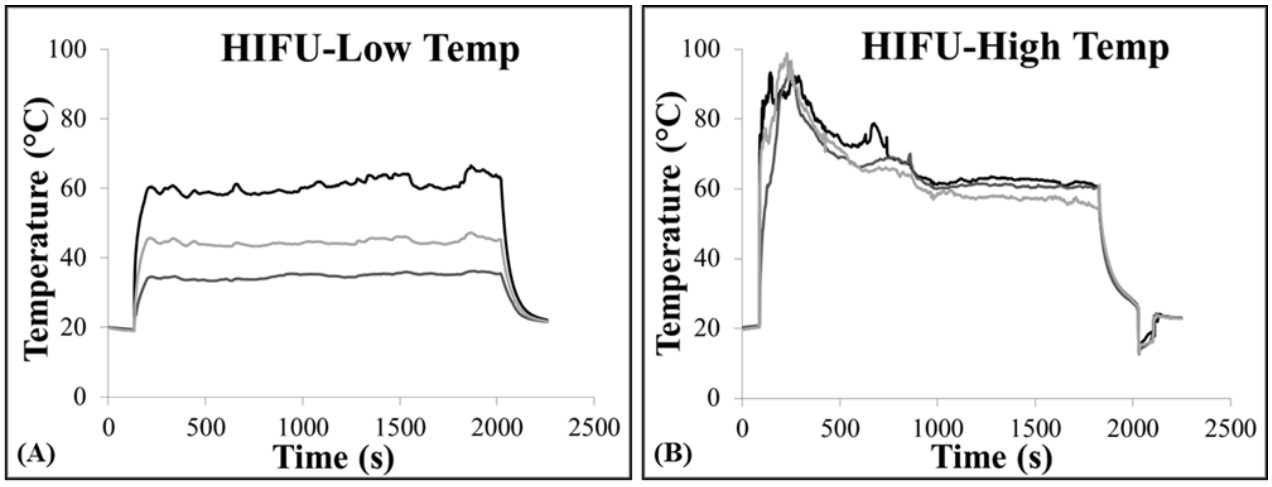

Figure 6.8. HIFU Thermal Treatment. Plots show example temperature vs. time curves for HIFU heating of tendon measured using hypodermic needle thermocouples. For all experiments, 3 thermocouples were placed near the focal region, and HIFU was applied to rapidly increase the temperature to (A) ~60°C or (B) ~90°C. Once the desired temperature was reached, the PRF was lowered to stabilize the temperature at a near constant level for the duration of the heating. (B) For the higher temperature HIFU treatments, the temperature measured by the thermal couples did not remain above 90°C due to thermocouple movement caused by tissue contraction. Similar curves were obtained for HIFU treatments in all tissue types.

After heating with HIFU, tissues were treated with histotripsy using the same parameters as in the controlled heating experiments, with results showing similar trends [Table 6.3]. All tissues were more susceptible to histotripsy after HIFU was applied at ~60°C [Fig. 6.9]. Histotripsy was capable of forming well defined lesions completely through all liver and tongue samples that were preheated with HIFU for 10 minutes at 60°C, whereas only partial damage was observed for control samples [Fig. 6.9]. Similarly, histotripsy treatments applied to tendon preheated with HIFU for 30 minutes at 60°C resulted in superficial lesions visible on the tendon surface, demonstrating a slight increase in susceptibility to histotripsy compared to control samples [Fig. 6.9].

For the 90°C HIFU treatments, liver and tongue samples were observed to increase in stiffness, with visible contraction and tissue dehydration observed after heating [Fig. 6.9]. Histotripsy results showed that tongue was less susceptibility to histotripsy after 90°C HIFU, with only superficial damage to the surface of the tongue compared to lesions formed partially into the tongue in control samples [Fig. 6.9, Table 6.3]. Partial damage through the tissue was observed in liver samples heated with HIFU at 90°C as well as in control samples [Table 6.3]. However, gross morphology revealed that the histotripsy lesions in these tissues stopped at the center of the focal region where the extent of tissue stiffening was most significant [Fig. 6.9]. Furthermore, in some samples, the lesions were observed to form around the dense tissue in the focal region, similar to previous work demonstrating that histotripsy can be self-limiting at the boundaries of stiffer tissues [12, 15, 18]. Results for tendon samples heated with HIFU at 90°C showed a significant increase in susceptibility to histotripsy, with well-defined lesions formed partially through the tendon in all heated samples compared to no damage in control samples [Fig. 6.9, Table 6.3].

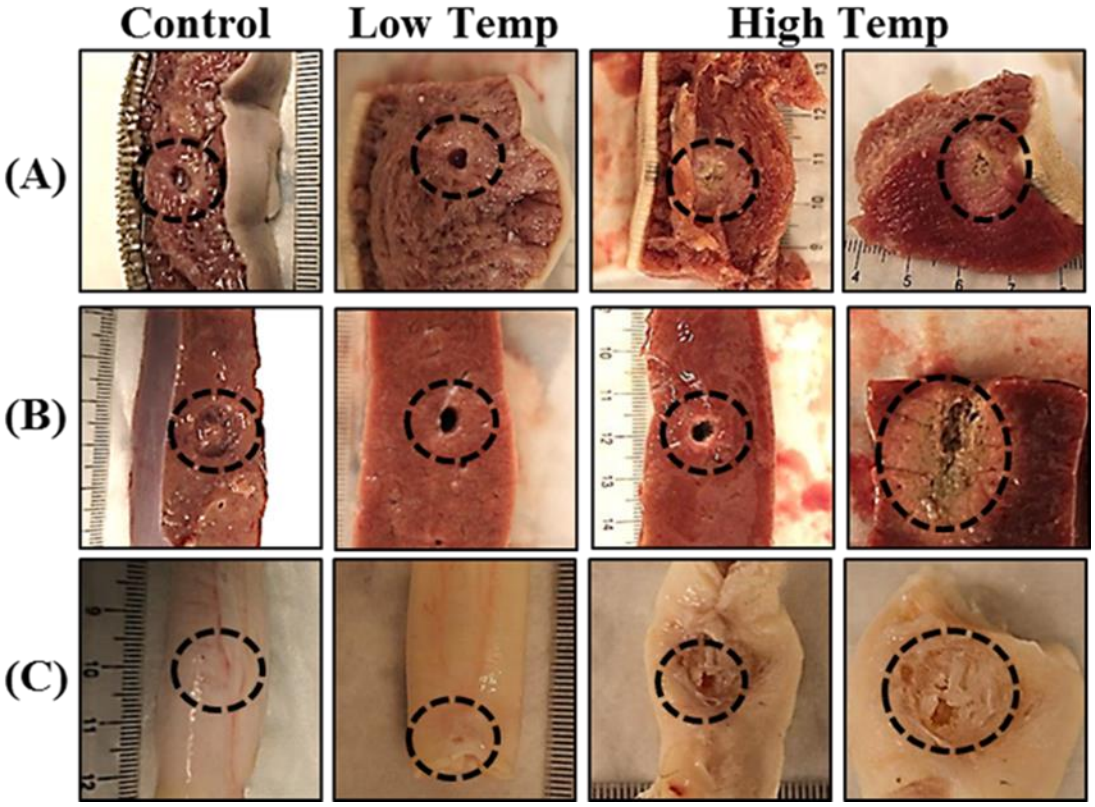

Figure 6.9. Results showed an increase in susceptibility to histotripsy for tongue, liver, and tendon heated with ultrasound at a peak temperature of ~60°C. Tongue and liver samples heated with ultrasound at a peak temperature of ~90°C were less susceptible to histotripsy while tendon became more susceptible after heating.

Table 6.3. Histotripsy treatment results demonstrated an increase in susceptibility to histotripsy-induced tissue damage for tongue, liver, and tendon heated with ultrasound at a peak temperature of ~60°C. Tongue and liver samples heated with ultrasound at a peak temperature of ~90°C were less susceptible to histotripsy while tendon became more susceptible after heating at ~90°C.

HIFU Heating			**Histotripsy Lesion** (# Samples/Total Samples)			
Tissue Type	**Peak Temp**	**Heating Duration**	**No Visible Damage**	**Surface Damage Only**	**Partial Damage (No Perforation)**	**Complete Damage (Perforation)**
Tongue	**Control**	**0**	0/6	0/6	**6/6**	0/6
	~60°C	**10 minutes**	0/6	0/6	0/6	**6/6**
	~90°C	**10 minutes**	0/6	**6/6**	0/6	0/6
Liver	**Control**	**0**	0/6	0/6	**6/6**	0/6
	~60°C	**10 minutes**	0/6	0/6	0/6	**6/6**
	~90°C	**10 minutes**	0/6	0/6	**6/6**	0/6
Tendon	**Control**	**0**	**6/6**	0/6	0/6	0/6
	~60°C	**30 minutes**	0/6	**6/6**	0/6	0/6
	~90°C	**30 minutes**	0/6	0/6	**6/6**	0/6

6.4 Discussion

Tissue mechanical properties play a significant role in the histotripsy process, with stiffer tissues being more resistant to histotripsy [15]. In this chapter, the effects of thermal preconditioning on tissues was investigated, with results demonstrating that increasing temperature can be used to modulate tissue stiffness and susceptibility to histotripsy. In the first part of this study, a constant temperature water bath was used to provide a controlled heating environment to study the effects of preheating (58°C and 90°C) on various *ex vivo* bovine tissues. Results of these experiments demonstrated that, with the exception of urethra, preheating tissues at 58°C decreased the tissue Young's modulus due to collagen denaturing and the breakdown of the chemical cross-links between collagen fibers. The decreases in tissue stiffness and initial tissue compliance after heating at 58°C resulted in an increase in susceptibility to histotripsy. In contrast, tissues preheated at 90°C had the opposite response to heating, with an increase in tissue stiffness observed due to collagen contraction. The exception to this was tendon preheated at 90°C, in which the Young's modulus decreased and the susceptibility to histotripsy increased due to collagen hydrolysis into gelatin.

The results of this chapter demonstrate that thermal preconditioning of tissues depends on multiple factors including heating temperature, heating duration, and tissue composition. For example, the results suggest that, in order to soften most tissues, heating should be applied at a temperature that can maximize collagen denaturing while minimizing collagen contraction. However, while tissue softening due to collagen denaturing is likely sufficient to improve histotripsy ablation in most tissues, very stiff tissues such as tendon may require substantial collagen hydrolysis into gelatin in order to sufficiently soften the tissue prior to histotripsy. It should be noted, however, that substantial collagen hydrolysis into gelatin was not directly

observed in the majority of tissues, likely due to tissue dehydration caused by collagen contraction [20]. While some degree of hydrolysis is likely responsible for the decrease in tissue stiffness and increased susceptibility to histotripsy in all tissues heated at 90°C for the longer durations, the degree of hydrolysis was significantly greater in tendon compared to the other tissue types. Since the hydrolysis process requires water [20], significant hydrolysis will likely only be achievable in tissues such as tendon or ligament which are composed primarily of collagen and water with minimal ground substance (proteoglycans, glycosaminoglycans, and glycoproteins) [28]. As observed in this study, the rate and extent of collagen hydrolysis is significantly reduced in tissues containing a larger amount of ground substance, since collagen contraction drives the free water out of the tissue, leaving collagen fibers surrounded by dehydrated ground substance that does not contain enough water to facilitate substantial hydrolysis [20, 29]. These results demonstrate the need for further work investigating the effects of heating on other tissue components that may counteract the changes in collagen (i.e. elastic fibers, ground substance), especially in tissues whose mechanical properties are significantly determined by these components. For example, unlike the other tissues, urethra was shown to increase in stiffness after heating at 58°C, potentially due to the contraction of elastic fibers. Similarly, the effects of heating on tissue stiffness in muscular tissues will also be highly dependent upon the changes in the structure (i.e. denaturation/contraction) of actin and myosin proteins in addition to the changes in collagen [19, 20]. In addition, the extent of chemical cross-linking between collagen fibers further complicates the process, as previous studies have shown that the rate and extent of collagen denaturation and hydrolysis are dependent upon the extent of chemical cross-linking (as well as the direct effects of collagen cross-linking on tissue stiffness)

[23, 29]. Future work will aim to optimize the thermal pretreatment parameters for specific tissues of interest.

In the final part of this chapter, the feasibility of using HIFU for tissue preconditioning was investigated, with the results supporting our hypothesis that HIFU can be used to alter tissue stiffness and susceptibility to histotripsy. For example, the susceptibility to histotripsy was shown to increase for liver and tongue samples heated with HIFU at ~60°C but decrease when heated at ~90°C. The results for tendon also matched the controlled heating experiments, with a slight increase in susceptibility to histotripsy observed after HIFU heating at ~60°C, and a more substantial increase in susceptibility observed at ~90°C. These results show the initial feasibility of using a purely ultrasonic pretreatment strategy. For example, in this study, the same 750 kHz transducer was used to apply both thermal HIFU and histotripsy to the tissue by modulating the pulse parameters.

The results of this chapter show the initial feasibility of using thermal HIFU as a pretreatment strategy for histotripsy. However, future work is needed to optimize this approach for specific clinical applications in order to determine if this strategy is practical *in vivo*. For example, the peak temperatures applied by HIFU in this study (60°C-90°C) may be difficult to sustain for long durations *in vivo* without causing unwanted damage to surrounding and overlying tissue. Furthermore, the thermal pretreatment strategy may not be a viable option for very large volumes, unless the heating duration can be significantly reduced to avoid causing profound consequences to the surrounding and overlying tissue. As such, future work is needed to optimize the thermal pretreatment approach in order to develop a practical treatment strategy for specific clinical applications. Nonetheless, the results of this initial study, which demonstrated that tissue susceptibility to histotripsy was significantly altered after 10-30 minutes

of HIFU heating, are promising. The changes to the tissue for HIFU heating were localized to the focal region of the transducer and seemed to occur much more rapidly than for the external heating experiments. For example, significant contraction of the tendon was observed within ~30 seconds after the temperature reached ~90°C in comparison to a much slower process for controlled heating experiments in which the tendon slowly contracted over the course of many minutes or hours. Furthermore, previous work has shown that small changes in heating temperature can substantially change the rate of tissue softening (<5°C change in temperature resulted in an order of magnitude increase in softening rate) [24], suggesting that our pretreatment approach may be optimized to alter tissue stiffness in much shorter durations than those used in this study.

Thermal pretreatment of tissues not only has the potential to improve the ablation of very stiff tissues, but it may also be used to increase the efficiency of ablation in softer tissues, such as the liver and tongue samples in this study. However, choosing optimal heating parameters will be essential in developing this approach in order to avoid tissue stiffening due to collagen contraction. This possibility should also be considered in ultrasound ablation applications that combine thermal and mechanical effects such as cavitation enhanced HIFU [30] or boiling histotripsy [31]. For example, the results of this study suggest that the high temperatures used in boiling histotripsy may either increase tissue stiffness (reducing the efficiency of tissue fractionation) or decrease tissue stiffness (increasing the efficiency of tissue fractionation), depending on the treatment parameters. This effect likely explains the results of a previous study investigating volume ablation using boiling histotripsy, which demonstrated that stiff tissues (i.e. blood vessels) inside the focal volume were more likely to remain intact as the extent of thermal damage was decreased [32].

In addition to the changes in tissue susceptibility to histotripsy, the thermal pretreatment approach may have other effects on histotripsy treatments applied inside bulk tissue, as previous work has shown that the histotripsy cavitation threshold and bubble dynamics are highly dependent upon tissue properties [15, 16, 33, 34]. Stiffer tissues have been shown to impede bubble expansion, thereby reducing the strain applied to the tissue [34]. These changes in bubble dynamics would be expected to further enhance the effects seen in this study (i.e. larger bubbles generated in softer tissue would increase fractionation efficiency while smaller bubbles in stiffer tissues would impede tissue fractionation). In addition to the changes in bubble dynamics, previous work has demonstrated that the pressure threshold for generating histotripsy bubble clouds using the shock scattering method of cloud initiation (multi-cycle pulses) increases in stiffer tissues [16], which would also enhance the effects seen in this study. In contrast, previous work studying the intrinsic threshold method of cloud initiation (single cycle pulses) has shown that the intrinsic threshold is independent of tissue stiffness [33]. However, the intrinsic threshold would likely be impacted by changes in focal temperature (i.e. decreased threshold at higher temperature). In addition, the cavitation threshold would likely decrease for tissues in which local dehydration occurs due to collagen contraction, as previous work suggests that histotripsy bubbles are generated in the water inside of the tissue [33]. Future work will investigate the effects of the thermal pretreatment strategy on the histotripsy cavitation thresholds and the resulting bubble behavior.

The thermal pretreatment strategy investigated in this chapter has clinically relevant implications for the development of histotripsy therapy. For example, this approach may allow histotripsy to be extended to clinical applications where the removal of very stiff tissues is desired, such as the treatment of tendons, ligaments, fibroadenomas, uterine fibroids, and fibrous

tumors. However, since the required time-temperature will likely be above the threshold for tissue necrosis [35], the thermal pretreatment strategy may be limited to applications where the desired clinical outcome is to potentiate tissue removal rather than simply inducing tissue death, such as in the treatment of benign masses such fibroadenomas or uterine fibroids. Using a combined thermal pretreatment and histotripsy approach may also be beneficial for improving the treatment of malignant tumors using thermal ablation, as previous work has shown that thermal ablation often leaves behind a permanent fibrous mass which is often associated with negative side effects such as pain or loss of organ function [36, 37]. In contrast to the permanent fibrous mass left after thermal ablation, the fractionated tissue homogenate produced in histotripsy is resorbed over time, which may be beneficial in certain clinical applications [6, 38]. Future work will aim to develop the thermal preconditioning strategy for clinical applications in which this approach would be both practical and beneficial to the patient.

Overall, the results of this chapter demonstrate that thermal preconditioning can alter tissue mechanical properties in order to increase tissue susceptibility to histotripsy. While this work focused on a thermal method, the general pretreatment approach introduced in this study could feasibly be extended to non-thermal methods. For example, the same effect may be achieved by locally administering a drug or enzyme that disrupts tissue collagen prior to histotripsy treatment. It is possible that this “tissue marinating” pretreatment approach may be more feasible than the “tissue cooking” approach in certain clinical applications in which thermal ablation is impractical, such as the treatment of large volumes or in regions containing large blood vessels [39, 40].

6.5 Conclusion

In this chapter, the effects of thermal preconditioning on tissue susceptibility to histotripsy were investigated. Results demonstrated that the effects of the thermal preconditioning depend on multiple factors including tissue composition, heating temperature, and heating duration. Controlled heating experiments demonstrated that the Young's modulus decreased in the majority of tissues when heated to 58°C due to collagen denaturing, resulting in an increase in susceptibility to histotripsy. In contrast, heating to 90°C increased the Young's modulus of the majority of soft tissues due to collagen contraction. The exception to this was seen in tendon, in which heating at 90°C caused significant softening due to collagen hydrolysis into gelatin, resulting in a significant increase in susceptibility to histotripsy. Based on these results, a final set of experiments was conducted using thermal HIFU to provide the preconditioning treatment, demonstrating that a thermal pretreatment strategy can be implemented non-invasively using a purely ultrasonic method. Overall, the results of this chapter demonstrate the proof of concept for using a thermal therapy approach to precondition tissue mechanical properties and alter the susceptibility of tissues to histotripsy.

6.6 References

[1] E. Vlaisavljevich, *et al.*, "The Effects of Thermal Preconditioning on Tissue Susceptibility to Histotripsy," *Ultrasound in medicine & biology,* 2015.

[2] J. E. Parsons, *et al.*, "Pulsed cavitational ultrasound therapy for controlled tissue homogenization," *Ultrasound Med Biol,* vol. 32, pp. 115-29, Jan 2006.

[3] W. W. Roberts, *et al.*, "Pulsed cavitational ultrasound: a noninvasive technology for controlled tissue ablation (histotripsy) in the rabbit kidney," *J Urol,* vol. 175, pp. 734-8, Feb 2006.

[4] Z. Xu, *et al.*, "Controlled ultrasound tissue erosion: the role of dynamic interaction between insonation and microbubble activity," *J Acoust Soc Am,* vol. 117, pp. 424-35, Jan 2005.

[5] Z. Xu, *et al.*, "Controlled ultrasound tissue erosion," *IEEE Trans Ultrason Ferroelectr Freq Control,* vol. 51, pp. 726-36, Jun 2004.

[6] T. L. Hall, *et al.*, "Histotripsy of rabbit renal tissue in vivo: temporal histologic trends," *J Endourol,* vol. 21, pp. 1159-66, Oct 2007.

[7] C. R. Hempel, *et al.*, "Histotripsy fractionation of prostate tissue: local effects and systemic response in a canine model," *J Urol,* vol. 185, pp. 1484-9, Apr 2011.

[8] A. D. Maxwell, *et al.*, "Noninvasive treatment of deep venous thrombosis using pulsed ultrasound cavitation therapy (histotripsy) in a porcine model," *J Vasc Interv Radiol,* vol. 22, pp. 369-77, Mar 2011.

[9] G. E. Owens, *et al.*, "Therapeutic ultrasound to noninvasively create intracardiac communications in an intact animal model," *Catheter Cardiovasc Interv,* vol. 77, pp. 580-8, Mar 1 2011.

[10] Z. Xu, *et al.*, "Noninvasive creation of an atrial septal defect by histotripsy in a canine model," *Circulation,* vol. 121, pp. 742-9, Feb 16 2010.

[11] N. R. Styn, *et al.*, "Histotripsy of VX-2 tumor implanted in a renal rabbit model," *J Endourol,* vol. 24, pp. 1145-50, Jul 2010.

[12] E. Vlaisavljevich, *et al.*, "Image-guided non-invasive ultrasound liver ablation using histotripsy: feasibility study in an in vivo porcine model," *Ultrasound Med Biol,* vol. 39, pp. 1398-409, Aug 2013.

[13] A. P. Duryea, *et al.*, "In vitro comminution of model renal calculi using histotripsy," *IEEE Trans Ultrason Ferroelectr Freq Control,* vol. 58, pp. 971-80, May 2011.

[14] Y. Kim, *et al.*, "Developmental impact and lesion maturation of histotripsy-mediated non-invasive tissue ablation in a fetal sheep model," *Ultrasound Med Biol*, vol. 39, pp. 1047-55, Jun 2013.

[15] E. Vlaisavljevich, *et al.*, "Effects of tissue mechanical properties on susceptibility to histotripsy-induced tissue damage," *Phys Med Biol*, vol. 59, pp. 253-70, Jan 20 2014.

[16] E. Vlaisavljevich, *et al.*, "Histotripsy-induced cavitation cloud initiation thresholds in tissues of different mechanical properties," *IEEE Trans Ultrason Ferroelectr Freq Control*, vol. 61, pp. 341-52, Feb 2014.

[17] E. Vlaisavljevich, *et al.*, "Investigation of the role of tissue stiffness and ultrasound frequency in histotripsy-induced cavitation," presented at the International Symposium on Therapeutic Ultrasound, Las Vegas, NV, 2014.

[18] A. M. Lake, *et al.*, "Renal ablation by histotripsy--does it spare the collecting system?," *J Urol*, vol. 179, pp. 1150-4, Mar 2008.

[19] D. Baldwin, "Sous vide cooking: A review," *International Journal of Gastronomy and Food Science*, vol. 1, pp. 15-30, 2012.

[20] E. Tornberg, "Effects of heat on meat proteins - Implications on structure and quality of meat products," *Meat Sci*, vol. 70, pp. 493-508, Jul 2005.

[21] H. Hoermann and H. Schlebusch, "Reversible and irreversible denaturation of collagen fibers," *Biochemistry*, vol. 10, pp. 932-937, 1971.

[22] M. S. Wall, *et al.*, "Thermal modification of collagen," *Journal of Shoulder and Elbow Surgery*, vol. 8, pp. 339-344, Jul-Aug 1999.

[23] N. T. Wright and J. D. Humphrey, "Denaturation of collagen via heating: an irreversible rate process," *Annu Rev Biomed Eng*, vol. 4, pp. 109-28, 2002.

[24] E. Sapin-de Brosses, *et al.*, "Temperature dependence of the shear modulus of soft tissues assessed by ultrasound," *Physics in Medicine and Biology*, vol. 55, pp. 1701-1718, Mar 21 2010.

[25] K. Kim, *et al.*, "Noninvasive ultrasound elasticity imaging (UEI) of Crohn's disease: animal model," *Ultrasound Med Biol*, vol. 34, pp. 902-12, Jun 2008.

[26] H. Xie, *et al.*, "Correspondence of ultrasound elasticity imaging to direct mechanical measurement in aging DVT in rats," *Ultrasound Med Biol*, vol. 31, pp. 1351-9, Oct 2005.

[27] J. E. Parsons, *et al.*, "Cost-effective assembly of a basic fiber-optic hydrophone for measurement of high-amplitude therapeutic ultrasound fields," *J Acoust Soc Am*, vol. 119, pp. 1432-40, Mar 2006.

[28] H. Q. Woodard and D. R. White, "The composition of body tissues," *Br J Radiol,* vol. 59, pp. 1209-18, Dec 1986.

[29] P. Fratzl, *Collagen: Structure and Mechanics*. New York, NY: Springer Science+Business Media, LLC, 2008.

[30] R. Takagi, *et al.*, "Enhancement of Localized Heating by Ultrasonically Induced Cavitation in High Intensity Focused Ultrasound Treatment," *Japanese Journal of Applied Physics,* vol. 49, 2010.

[31] Y. N. Wang, *et al.*, "Histological and Biochemical Analysis of Mechanical and Thermal Bioeffects in Boiling Histotripsy Lesions Induced by High Intensity Focused Ultrasound," *Ultrasound in Medicine and Biology,* vol. 39, pp. 424-438, Mar 2013.

[32] Y.-N. Wang, *et al.*, "Mechanical decellularization of tissue while sparing extracellular matrix using boiling histotripsy," presented at the International Symposium for Therapeutic Ultrasound, Las Vegas, NV, 2014.

[33] E. Vlaisavljevich, *et al.*, "Effects of Ultrasound Frequency and Tissue Stiffness on the Histotripsy Intrinsic Threshold for Cavitation," *Ultrasound Med Biol,* 2015.

[34] E. Vlaisavljevich, *et al.*, "Effects of Tissue Stiffness, Ultrasound Frequency, and Pressure on Histotripsy-induced Cavitation Bubble Behavior," *Phys Med Biol,* 2015.

[35] S. A. Sapareto and W. C. Dewey, "Thermal dose determination in cancer therapy," *Int J Radiat Oncol Biol Phys,* vol. 10, pp. 787-800, Jun 1984.

[36] J. E. Coad, *et al.*, "Radiofrequency ablation causes 'thermal fixation' of hepatocellular carcinoma: a post-liver transplant histopathologic study," *Clin Transplant,* vol. 17, pp. 377-84, Aug 2003.

[37] J. Ding, *et al.*, "Comparison of two different thermal techniques for the treatment of hepatocellular carcinoma," *Eur J Radiol,* vol. 82, pp. 1379-84, Sep 2013.

[38] T. L. Hall, *et al.*, "Histotripsy of the prostate: dose effects in a chronic canine model," *Urology,* vol. 74, pp. 932-7, Oct 2009.

[39] T. A. Leslie, *et al.*, "High-intensity focused ultrasound ablation of liver tumours: can radiological assessment predict the histological response?," *Br J Radiol,* vol. 81, pp. 564-71, Jul 2008.

[40] A. Okada, *et al.*, "A case of hepatocellular carcinoma treated by MR-guided focused ultrasound ablation with respiratory gating," *Magn Reson Med Sci,* vol. 5, pp. 167-71, Oct 2006.

Chapter 7

Effects of Tissue Stiffness, Ultrasound Frequency, and Pressure on Histotripsy-induced Cavitation Bubble Behavior

A majority component of this chapter has been published in *Physics in Medicine and Biology* © 2015 PMB. Reprinted, with permission, from [1].

7.1 Introduction

Histotripsy is a non-invasive tissue ablation method that controls cavitation to mechanically fractionate soft tissue through high pressure (>10 MPa), short duration (<20 μsec) ultrasound pulses at low duty cycles (<1%) [2-4] . Histotripsy depends on the initiation and maintenance of a cavitation bubble cloud to produce mechanical tissue fractionation [2, 4]. In order to effectively fractionate tissue into accelluar debris, histotripsy requires bubbles to rapidly expand from nanometer-sized initial nuclei into large cavitation bubbles greater than ~50μm in diameter [2, 5, 6]. Using a pressure high enough to initiate a bubble cloud and expand bubbles to a sufficient size, histotripsy has been shown capable of completely fractionating soft tissue into a liquid-appearing homogenate with no cellular structures remaining, resulting in effective tissue removal [3, 4, 7, 8]. Previous work has shown that the histotripsy process is affected by tissue mechanical properties with stiffer tissues showing increased resistance to histotripsy-induced fractionation [8-10]. One possible explanation for the increase in resistance for stiffer tissues is

that stiffer tissues impede bubble expansion, therefore reducing the strain applied to tissue structures [9-11].

There are two mechanisms in which a cavitation cloud can be generated using a single pulse in histotripsy. In the first mechanism, termed the “shock scattering mechanism” of cloud initiation, a dense bubble cloud can be formed from a multi-cycle histotripsy pulse using scattering of the positive shocks from individual bubbles formed and expanded from the initial cycles of the pulse [12]. Using the shock scattering mechanism, histotripsy bubble clouds are initiated at negative pressure magnitudes ranging from 10-28 MPa and are dependent upon multiple factors including the distribution of heterogeneous nuclei in the focal region, the size and shape of initial single bubbles, the strength of the shock front, and the positive pressure amplitudes [12-14]. Increases in tissue stiffness result in higher cloud initiation thresholds when using the shock scattering mechanism of bubble cloud formation [10]. The mechanism responsible for this increase in cavitation cloud threshold was hypothesized to be a decrease in the expansion of initial bubbles in tissues with higher Young’s modulus, which leads to reduced shock scattering [10] . Results of that study further suggested that bubble cloud formation in tissues with Young’s moduli >100 kPa was primarily driven by the negative pressure of the incident wave while the contributions of shock scattering were significantly decreased, likely due to suppressed bubble expansion [10].

The second mechanism for histotripsy cavitation cloud formation is termed the “intrinsic threshold mechanism”, in which a single pulse with only one high amplitude negative phase can be used to generate a bubble cloud when the peak negative pressure of the incident wave directly exceeds a threshold intrinsic to the medium, without the contributions from shock scattering [15, 16] . Using this intrinsic threshold mechanism, the volume of the bubble cloud formation

matches the portion of the focal region above the intrinsic threshold [10, 15, 16]. In contrast to the shock scattering threshold approach, as the intrinsic threshold mechanism of cloud initiation does not rely on the expansion of individual bubbles in order to initiate a bubble cloud, the histotripsy intrinsic threshold is independent of tissue stiffness [10]. However, since histotripsy lesions only form when the strain exceeds the ultimate strain of the tissue, it is possible that stiffer tissues may remain resistant to histotripsy fractionation even in cases when a bubble cloud has been generated through the intrinsic threshold mechanism due to impeded bubble expansion (decreased strain applied to tissue) as well as the higher ultimate stresses and strains of these tissues (ability to withstand higher stress and strain) [9, 10].

Cavitation bubble dynamics have been shown to be dependent on the viscoelastic properties of the media [11, 17-21]. More specifically, bubble expansion has been shown to be suppressed in media with increased Young's moduli and viscosity [18, 20, 21]. Similar observations have been made in previous histotripsy studies in which smaller bubbles were observed when histotripsy pulses were applied inside tissue phantoms of increasing stiffness [10, 16]. However, these observations have often relied upon images of bubbles at a single time point [16] or images of bubbles produced using the shock scattering mechanism of cloud initiation [10], making it difficult to determine the actual pressure experienced by the bubble.

In this chapter, we aim to investigate the effects of tissue stiffness and ultrasound frequency on the temporal behavior of individual bubbles produced by histotripsy pulses using the intrinsic threshold mechanism of cloud generation, as the acoustic field is complicated by the scattering of the positive pressure using the shock scattering approach. We hypothesize that increasing Young's modulus will suppress bubble expansion, helping to explain the increased damage resistance previously observed for stiffer tissues. Furthermore, we hypothesize that

lower frequency will enhance bubble expansion due to the longer rarefactional phase of the applied pulse. To test these hypotheses, histotripsy pulses produced by 345 kHz, 500 kHz, 1.5 MHz, and 3 MHz histotripsy transducers were applied to mechanically tunable agarose tissue phantoms, with the resulting radius vs. time (R-T) curves reconstructed using high speed optical imaging. The results of this work will provide a better understanding of the effects of tissue stiffness and ultrasound frequency on histotripsy which is essential to advance histotripsy and provide rationale to guide parameter optimization for treatment of specific tissues.

7.2 Methods

7.2.1 Bubble Behavior Simulation

To investigate the effects of tissue stiffness and ultrasound frequency on the growth of histotripsy bubbles, a numerical model based on a Kelvin-Voigt viscoelastic model was used. We hypothesize that the first significant tension experienced by a nucleus will cause it to grow explosively, and that the behavior will be affected by the tissue elasticity. To test this hypothesis, simulations exposed a 2.5 nm initial gas nucleus to a single peak negative pressure

$$p_a(t) = \begin{cases} p_A\left(\frac{1+\cos[\omega(t-\delta)]}{2}\right)^n, & |t-\delta| \le \frac{\pi}{\omega} \\ 0, & |t-\delta| > \frac{\pi}{\omega} \end{cases} \quad \textbf{(E7.1)}$$

where p_A is the peak negative pressure, ω is the angular frequency of the experimental ultrasound wave, δ is a time delay, and n is a curve-fitting parameter set to n=3.7 to closely match the shape of experimental waveforms. A 2.5 nm initial bubble was chosen to model the homogeneous nuclei that are used to generate bubbles in histotripsy using the intrinsic threshold mechanism of cloud initiation. In a previous study using this 2.5 nm initial bubble, the cavitation threshold behavior matched experimental results generated using a single 2-cycle pulse [16]. For

this proof of principle, we assume the surrounding medium to have homogeneous properties, and that the bubble contains air and remains spherical. In this study, we use an in-house code developed to simulate spherical bubble dynamics in general viscoelastic media, including compressibility and thermal effects [22]. To describe the bubble response to a far-field pressure variation, p_{inf} (t), we solve the the compressible Keller-Miksis equation

$$\left(1-\frac{\dot{R}}{c}\right)R\ddot{R}+\frac{3}{2}\left(1-\frac{\dot{R}}{3c}\right)\dot{R}^2=\left(1+\frac{\dot{R}}{c}\right)\left[\frac{p_B-p_\infty(t)}{\rho}-\frac{4\mu\dot{R}}{R}-\frac{2S}{\rho R}-E_{NT}\right]+\frac{R}{\rho c}\frac{d}{dt}(p_a-p_\infty) \quad (\mathbf{E7.2})$$

where ρ is the surrounding medium's density, c is the speed of sound, S is the surface tension, and μ is the viscosity. Here, the overdots ($\dot{}$) denote derivatives with respect to time, t. For simplicity, the air within the bubble behaves adiabatically, so that

$$p_g=p_0\left(\frac{R_0}{R}\right)^{3\kappa} \quad (\mathbf{E7.3})$$

where $\kappa=1.4$ is the ratio of specific heats for air, R_0 is the initial bubble radius, with

$$p_0=p_\infty(0)+\frac{2S}{R_0} \quad (\mathbf{E7.4})$$

The viscoelasticity of the medium is modeled using a Kelvin-Voigt approach, in which the stress consists of the sum of viscous and elastic contributions. Because of the large deformations during growth, a hyperelastic (Neo-Hookean) constitutive relation is used [23], to yield the following elastic term, E_{NT},

$$E_{NT}=\frac{G}{2}\left(5-4\left(\frac{R_0}{R}\right)-\left(\frac{R_0}{R}\right)^4\right) \quad (\mathbf{E7.5})$$

where G is the linear shear modulus. The equations are marched forward in time using explicit Runge-Kutta time marching with adaptive time stepping to compute the radius (and all relevant quantities) as a function of time. The properties $\rho=1000\ \mathrm{kg/m^3}$, $c=1497\ \mathrm{m/s^2}$, $\mu=1.00\ \mathrm{mPa\cdot s}$ (viscosity of water), and $S=72$ mN-m (water-air surface tension) were used to

approximate the surrounding medium. The Young's modulus (E = 3G) was varied in decades from 1 kPa to 1 MPa to compare the effects of Young's modulus on bubble expansion. Ultrasound frequencies included 345 kHz, 500 kHz, 1.5 MHz, and 3 MHz for comparison with experimental results. The bubble radius was graphed as a function of time to provide insight into the effects of tissue elasticity, ultrasound frequency, and peak negative pressure on the temporal expansion and collapse of cavitation bubbles during histotripsy. All numerical simulations were conducted using a single bubble model and did not account for potential bubble-bubble interactions that may occur within a histotripsy bubble cloud.

7.2.2 Tissue Phantom with Mechanically Tunable Properties

Agarose phantoms with mechanically tunable properties were used to provide a well-controlled elastic medium for this study. Agarose phantoms of 0.3%, 1%, 2.5%, and 5% w/v were prepared by slowly mixing agarose powder (Agarose Type VII; Sigma-Aldrich, St. Louis, MO, USA) into saline solution (0.9% sodium chloride; Hospira, Lake Forest, Illinois, USA) heated to boiling temperature. The solution was stirred on a hot plate until the gel turned completely transparent and then allowed to boil for ten minutes. After boiling, agarose solutions were allowed to cool and were degassed under a partial vacuum (~20 kPa, absolute) for 30 minutes. After removing agarose mixtures from the vacuum, the solution was poured into tissue phantom holders and placed in a refrigerator at 4°C to allow the agarose solution to solidify prior to use.

The mechanical properties of the 0.3%, 1%, 2.5%, and 5% w/v agarose phantoms were measured using a parallel-pate AR-G2 rheometer (TA Instruments, New Castle, DE, USA) on a Peltier stage, similar to previous studies [24, 25]. The stage was initially heated to 90°C, and

samples were allowed to melt for 1 minute before the top plate was lowered to create a gap of 1000 µm. The stage was cooled to 60°C and excess agarose solution was wiped off and the gap was sealed with mineral oil (Sigma, St. Louis, MO, USA) to prevent evaporation. Samples were held at 60°C for two minutes to ensure a uniform starting temperature within the fluid, and then cured at 4°C for 20 minutes. The samples were then heated to 20°C for 10 minutes and the mechanical properties were measured. The shear modulus (G) was measured at a frequency of 0.1 radian per second with 0.05% strain for 5% and 2.5% tissue phantoms and 0.1% strain for 1% and 0.3% tissue phantoms. Three independent samples were measured for each weight percent, with the results reported as the mean ± a 95% confidence interval [Table 7.1]. The Young's modulus (E) was estimated from the shear modulus as E=3G [Table 7.1].

Table 7.1. Tissue phantom properties. Table shows the shear modulus, Young's modulus, density, and water content for the agarose tissue phantoms. The shear modulus (G) was measured at 20ºC using shear rheology. The Young's modulus was estimated from the shear modulus (E=3G).

	Shear Modulus (kPa)	Young's Modulus (kPa)	Density (kg/m³)	Water Content (%)
Water	-	-	998.0	100.0
0.3% Agarose	0.38±0.16	1.13±.047	1003.0	98.8
1% Agarose	7.24±0.34	21.7±1.0	1010.0	98.1
2.5% Agarose	80.8±8.9	242±27	1025.0	96.7
5% Agarose	190±15	570±46	1050.0	94.3

7.2.3 Histotripsy Pulse Generation

Histotripsy pulses were generated at four different ultrasound frequencies (345 kHz, 500 kHz, 1.5 MHz, and 3 MHz) using three custom-built histotripsy transducers developed in house. The 345 kHz histotripsy pulses were generated by a twenty-element array transducer with a geometric focus of 150 mm, an aperture size of 272 mm, and an effective f-number of 0.55. The 1.5 MHz histotripsy pulses were generated using a six-element array transducer with a geometric focus of 55mm, an aperture of 79 mm in the elevational direction and 69 mm in the lateral direction, and effective f-numbers of 0.7 and 0.8 in the elevational and lateral directions,

respectively. The 500 kHz and 3 MHz pulses were generated by a dual frequency array transducer that consisted of twelve 500-kHz elements and seven 3-MHz elements. For the 500 kHz elements, the geometric focus was 40 mm, the aperture size was 71 mm, and the effective f-number was 0.56. For the 3 MHz elements, the geometric focus was 40 mm, the aperture size was 80 mm, and the effective f-number was 0.5. The design of this dual frequency transducer has been described in detail in a previous study [26].

To generate short therapy pulses, a custom high-voltage pulser developed in-house was used to drive the transducers. The pulser was connected to a field-programmable gate array (FPGA) development board (Altera DE1 Terasic Technology, Dover, DE, USA) specifically programmed for histotripsy therapy pulsing. This setup allowed the transducers to output short pulses consisting only one high peak negative phase. This very short pulse minimized the possibility of cavitation occurring through shock scattering, therefore cavitation would be generated only by the negative-pressure half cycle of the incident wave. A fiber-optic probe hydrophone (FOPH) built in-house [27] was used to measure the acoustic output pressure of the transducers. At peak negative pressure levels higher than 20 MPa, the acoustic output couldn't be directly measured due to cavitation generation at the fiber tip. The higher pressures were estimated by a summation of the pressure values from individual transducer elements. In a previous study [16], the estimated pressure from the linear summation, $P(-)_{LS}$, had a good agreement with the *p*- measured directly at peak negative pressure up to 30MPa in a higher cavitation threshold medium, 1,3 butanediol. Sample acoustic waveforms produced by the four frequency transducers are shown in Figure 7.1.

For the experiments to study the cavitation bubble behavior generated by a dual-frequency beam, a transducer consisting both 500 kHz and 3 MHz elements was used to produce

a combined 500 kHz and 3 MHz pulse as described in a previous study [26]. This pulse was generated by setting the arrival times for the 500 kHz and 3 MHz pulses to the point of maximal negative pressure overlap at the focus, with the combined peak negative pressure rising above the intrinsic threshold. Using this approach, bubble behavior was compared in samples treated with 500 kHz only, 3 MHz only, and a dual-frequency pulse with approximately equal half of the negative pressure generated from each frequency. Furthermore, the relative contribution of 500 kHz and 3 MHz was varied (while keeping the overall pressure constant) to demonstrate the ability to precisely control bubble expansion using this dual-frequency approach.

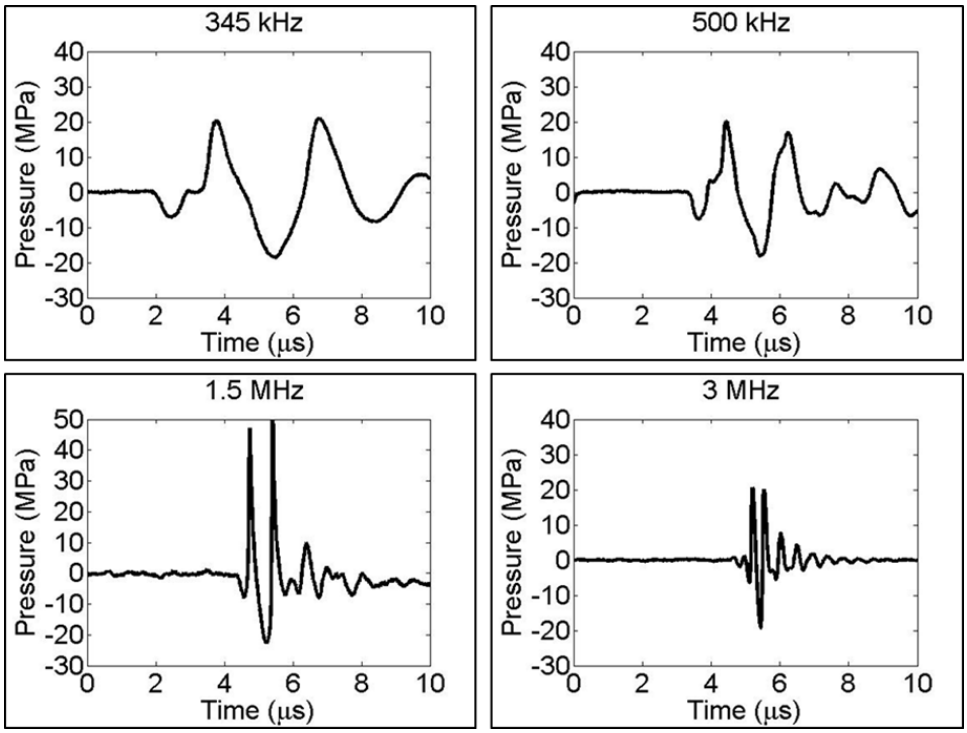

Figure 7.1. Representative free-field focal waveforms from four histotripsy transducers used to compare the effects of frequency on histotripsy bubble expansion. Bubbles were generated by histotripsy pulses at 345 kHz, 500 kHz, 1.5 MHz, and 3 MHz.

7.2.4 Optical Imaging

Optical images of the growth and collapse of individual bubbles were recorded by two high speed cameras [Fig. 7.2]. For experiments with the 345 kHz and 1.5 MHz transducers, a

high-speed, 1-megapixel CCD camera (Phantom V210, Vision Research, Wayne, NJ, USA) was aligned with the transducer and backlit by a continuous light source. The camera was focused using a macro-bellows lens (Tominon 1:4.5, F=105 mm; Kyocera, Kyoto, Japan), giving the captured images a resolution of approximately 5.9 µm and 3.4 µm per pixel for 345 kHz and 1.5 MHz, respectively. For experiments with the 500 kHz and 3 MHz dual frequency transducer, a digital, 1.3-megapixel CCD camera (PN: FL3-U3-13Y3M-C, Flea® 3, PointGrey, Richmond, BC, Canada) was positioned perpendicularly to the dual-frequency array transducer facing one of its optical windows. A Nikon 4X objective (MRP70040; Nikon, Chiyoda, Tokyo, Japan) was attached to the camera with extension tubes to magnify the image plane, giving the captured images a resolution of approximately 2.5 µm per pixel. A pulsed white-light LED (BXRA-50C9000-J-00, Bridgelux, Livermore, CA, USA) was placed on the diametrically-opposed optical window of the dual-frequency array transducer, which provided back-lit illumination.

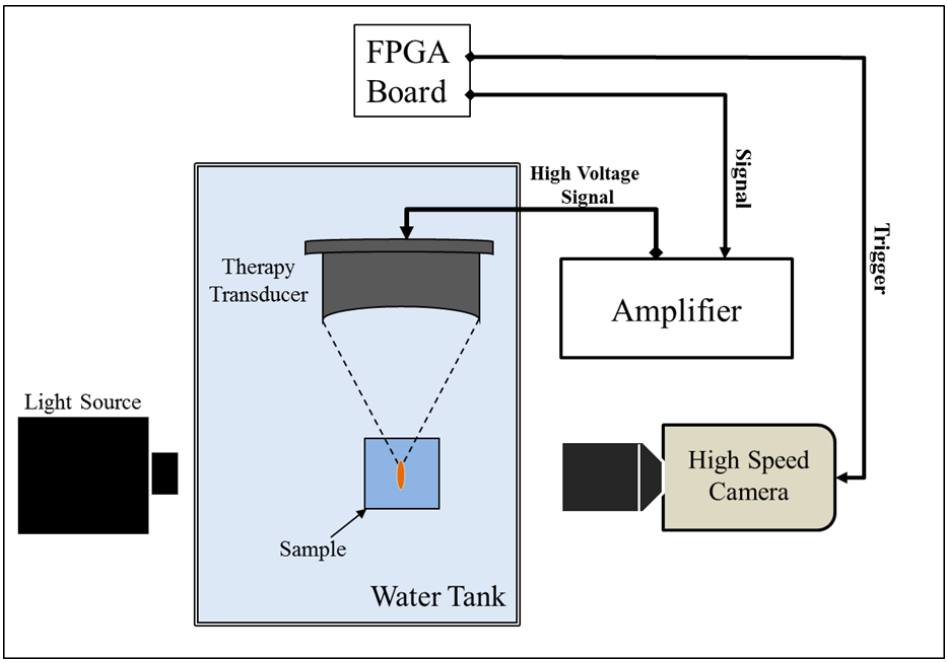

Figure 7.2. The focus of histotripsy transducers were aligned inside tissue phantoms of varied stiffness. Bubble expansion and collapse was monitored using high speed optical imaging. Note: different frequency transducers had different geometry and schematic is not drawn to scale.

7.2.5 Experimental Design

To study the effects of ultrasound frequency and tissue stiffness on histotripsy-induced bubble behavior, histotripsy bubbles were generated in degassed water (~20% O_2) and agarose tissue phantoms with varied stiffness using 1-2 cycle histotripsy pulses at 345 kHz, 500 kHz, 1.5 MHz, 3 MHz, and the dual-frequency waveform (500 kHz and 3 MHz). Waveforms used at all frequencies had one high negative pressure phase with a peak negative pressure slightly greater than the histotripsy intrinsic threshold [10]. More specifically, the peak negative pressure, $P(-)_{LS}$, used were 26.4 MPa (345 kHz), 26.3 MPa (500 kHz), 26.8 MPa (1.5 MHz), and 28.8 MPa (3 MHz). Due to the limited frame rate of the cameras, we could not image the bubble expansion and collapse during and after a single histotripsy pulse. Therefore, a series of time-delayed images of bubbles were used to reconstruct that average expansion and collapse behavior of the bubbles produced by identical histotripsy pulses. The specific delay times were varied based on the frequency and sample stiffness in order to reconstruct a sequence of bubble images covering the entire period of bubble expansion and collapse. For each sample at each time delay, the radius of bubbles produced by twenty identical histotripsy pulses was recorded. Each pulse was applied to a different point in the sample (2 mm spacing) to prevent the effects of cavitation damage from altering the tissue phantom mechanical properties. Shadowgraph images were converted from grayscale to binary by an intensity threshold determined by the background intensity using image processing software (MATLAB, The Mathworks, Natick, MA, USA). The size of single bubbles was measured for all twenty pulses to determine the bubble expansion radius, and the mean and standard deviation in bubble radius was calculated for each time delay. The calculated values for the bubble radius at each time delay were used to plot the average

bubble radius as a function of time for all frequency and sample combinations. A sample size of 6 tissue phantoms was used for each agarose concentration.

7.2.6 Stress-Strain Estimation

Finite strains and stresses applied by the cavitation bubbles to the surrounding media for the different tissue phantoms and frequency combinations tested in this study were computed. The Green-Lagrange strain tensor and the maximum deviatoric stress in the theta-theta direction applied to the tissue at the bubble wall were estimated as

$$\varepsilon_{\vartheta\vartheta} = \frac{\left(\left(\frac{R_{max}}{R_0}\right)^2\right)-1}{2} \quad (\mathbf{E7.6}) \quad \text{and} \quad \tau_{\vartheta\vartheta} = \frac{G}{3}\left[\left(\frac{R_{max}}{R_0}\right)^2 - \left(\frac{R_0}{R_{max}}\right)^4\right] \quad (\mathbf{E7.7}),$$

respectively, where R_0 was 2.5 nm and R_{max} was the maximum bubble radius measured for each condition experimentally [23, 28]. The estimated maximum strain and stress predicted from the measured bubble radius were plotted for each ultrasound frequency and tissue phantom stiffness.

7.2.7 Supra-threshold Bubble Behavior

To study the effects of increasing pressure on cavitation bubble behavior using pressure beyond the intrinsic threshold, bubbles were generated in degassed water (~20% O_2) and agarose tissue phantoms with varied stiffness using histotripsy pulses at 345 kHz, 500 kHz, 1.5 MHz, and 3 MHz. Pulses were applied to samples at increasing $P(-)_{LS}$ above the histotripsy intrinsic threshold, and the resulting bubble cloud behavior was observed using a series of time-delayed optical images using the same method described above. For each experimental condition, images were analyzed to compare the size of the bubble cloud as well as the size of individual bubbles within the cloud.

7.3 Results

7.3.1 Bubble Behavior Simulation

The effects of tissue stiffness and ultrasound frequency on histotripsy-induced bubble behavior were investigated using the numerical model described earlier. Results supported the hypothesis that increases in tissue stiffness cause a reduction in bubble expansion and collapse time. A plot showing the bubble radius vs. time (R-T) curve for a 2.5 nm initial bubble subjected to a 345 kHz pulse with peak negative pressure of 30 MPa (E7.1) demonstrated a decrease in bubble expansion as the Young's modulus was varied from 0 kPa to 1 MPa [Fig. 7.3(A)]. Following the passage of the pulse, the bubble rapidly expands, slows down as it reaches a maximum radius (R_{max}), and collapses violently. Bubble growth was decreased for higher Young's moduli as predicted due to this elastic property ("spring-like" behavior) increasing the isotropic stress on the bubble as it expands [29]. Results showed only a small reduction in bubble expansion between Young's moduli of 1 kPa to 10 kPa while larger decreases in bubble expansion were observed as Young's moduli was increased to 100 kPa and 1 MPa. For example, for the 345 kHz condition shown in Fig. 7.3(A), R_{max} at a Young's modulus of 10 kPa was reduced by <3% compared to 1 kPa, while R_{max} was reduced by ~18% at Young's modulus of 100 kPa, and by ~54% at a Young's modulus of 1 MPa. The time until maximum bubble expansion, t_{max}, and the time until bubble collapse, t_c, were also observed to decrease with increasing Young's modulus [Fig.7.3(A)]. For example, compared to 1 kPa, t_{max} decreased by ~6.5%, ~34%, and ~75% at 10kPa, 100kPa, and 1 MPa, respectively. Similarly, t_c decreased by ~5.5%, ~37%, and ~80% at 10kPa, 100kPa, and 1 MPa, respectively, compared to a Young's modulus of 1 kPa [Fig. 7.3(A)].

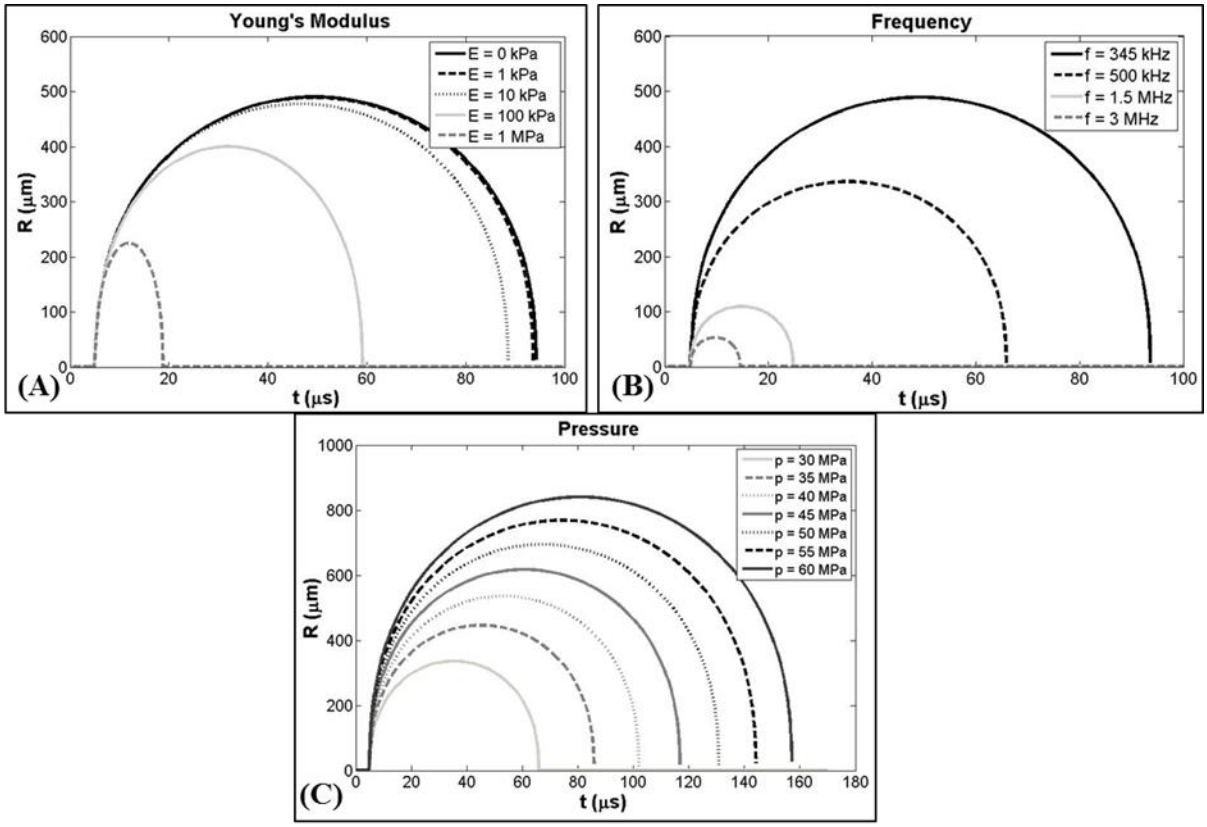

Figure 7.3. Bubble behavior simulation. Plots show simulated bubble R-T curves for a 2.5 nm initial bubble subjected to histotripsy pulses with varied Young's modulus (E), frequency (f), and peak negative pressure (p-). (A) Young's modulus was varied between 0kPa-1MPa (p-=30 MPa, f=345 kHz). (B) Frequency was compared for 345 kHz, 500 kHz, 1.5 MHz, and 3 MHz (p-=30 MPa, E=1 kPa). (C) p- was varied between 30MPa-60MPa (f=500 kHz, E=1 kPa). Results show an increase in bubble expansion with decreasing Young's modulus (A), decreasing ultrasound frequency (B), and increasing pressure (C).

Results of the frequency simulation supported the hypothesis that decreasing frequency facilitates larger bubble expansion. A plot showing R-T curve for a 2.5 nm initial bubble subjected to histotripsy pulses with peak negative pressure of 30 MPa demonstrated an increase in bubble expansion as the pulse frequency (E7.1) was decreased from 3 MHz to 345 kHz [Fig. 7.3(B)]. Decreases in frequency were shown to increase bubble expansion as the larger duration of the applied pressure at lower frequency increased the amount of energy imparted to the bubble and thus increased the resulting expansion. Results demonstrated that R_{max} changed by approximately an order of magnitude as the frequency was changed from 345 kHz to 3 MHz. For

example, compared to the R_{max} at 345 kHz, the R_{max} was reduced by ~31%, ~77%, and ~89% at 500kHz, 1.5 MHz, and 3 MHz, respectively [Fig. 7.3(B)]. Results also showed similar decreases in both t_{max} and t_c. For example, compared to 345 kHz, t_{max} decreased by ~30%, ~70%, and ~82% at 500kHz, 1.5 MHz, and 3 MHz, respectively. Similarly, t_c decreased by ~30%, ~74%, and ~87% at 500kHz, 1.5 MHz, and 3 MHz, respectively, compared to 345 kHz [Fig. 7.3(B)].

In addition to the effects of tissue stiffness and ultrasound frequency, a final simulation was conducted to investigate the effects of peak negative pressure on bubble expansion. A plot showing the R-T curve for a 2.5 nm initial bubble subjected to a 500 kHz histotripsy pulse demonstrated a consistent increase in bubble expansion as the peak negative pressure was increased from 30 MPa to 60 MPa [Fig. 7.3(C)]. Increases in the peak negative pressure resulted in larger bubbles due to the increased energy imparted into the bubble which acts to enhance bubble expansion. Results demonstrated a linear increase in R_{max} from 335.9 μm for the 30 MPa pulse to 840.4 μm for the 60 MPa pulse at 500 kHz [Fig. 7.3(C)]. Furthermore, results showed linear increases in both t_{max} and t_c with increasing pressure [Fig. 7.3(C)].

7.3.2 Effects of Tissue Stiffness on Bubble Behavior

Experimental analysis demonstrated a significant decrease in bubble expansion as the tissue phantom stiffness was increased from a Young's modulus of 1.13 kPa to a Young's modulus of 570 kPa, with the trend being consistent for all four histotripsy frequencies [Fig. 7.4]. For example, at 345 kHz, R_{max} decreased by ~34%, ~64%, and ~73% in the 21.7 kPa, 242 kPa, and 570 kPa phantoms, respectively compared to the R_{max} in the 1.13 kPa phantom [Fig. 7.5]. The trend of decreasing bubble size with increasing stiffness was consistent for all frequencies tested [Table 7.2]. To compare the effects of tissue stiffness independent of ultrasound frequency,

R_{max} in all tissue phantoms was normalized to R_{max} at each frequency in water, demonstrating a consistent trend of decreasing R_{max} with increasing stiffness [Fig. 7.6(A)]. These results demonstrated a negligible decrease in R_{max} for tissue phantoms with Young's moduli of 1.13 kPa (compared to water) while the R_{max} in the 21.7 kPa phantoms was decreased to 50-80% of the R_{max} in water. R_{max} was further reduced to <40% the size in water when the tissue phantom Young's modulus was increased to 242 kPa, and <25% of the R_{max} in water for 570 kPa phantoms.

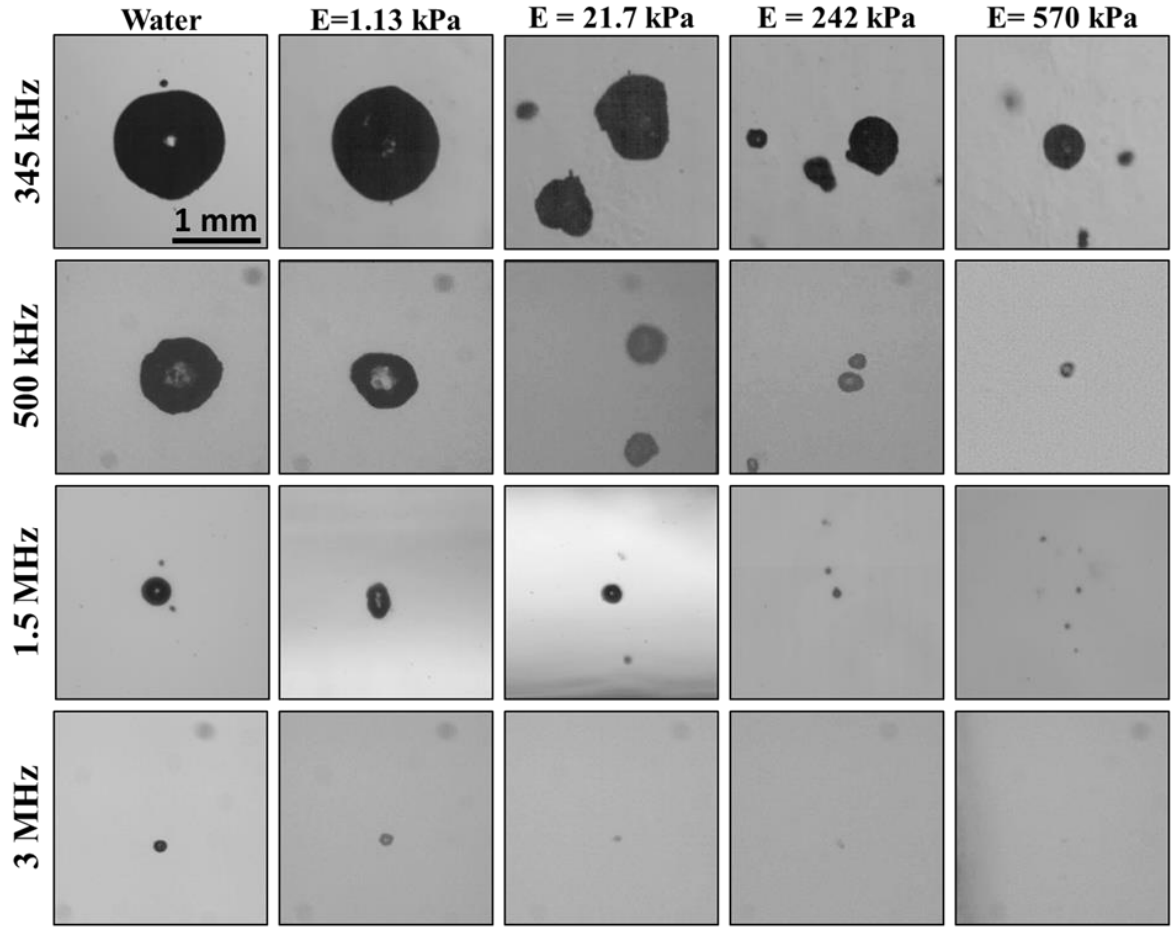

Figure 7.4. Optical images of bubbles produced by 345 kHz, 500 kHz, 1.5 MHz, and 3 MHz histotripsy pulses inside agarose tissue phantoms of increasing Young's modulus taken at t_{max}. Results demonstrated a decrease in bubble size with increasing frequency and increasing tissue phantom stiffness.

The bubble lifespan was also decreased in tissue phantoms with increased Young's modulus [Fig. 7.5]. Both the time until maximum bubble expansion, t_{max}, and the time until bubble collapse, t_c, were shown to decrease in tissue phantoms with increased Young's modulus [Table 7.2]. Due to the imaging resolution in this study, t_c was defined as the time point at which the average bubble size reduced to <10% of the maximum bubble radius. It should be noted that the accuracy of the reported t_{max} and t_c values was limited by the temporal resolution of these experiments and the method of averaging the behavior of many bubbles to reconstruct the R-T curves for each condition. The trends of decreasing t_{max} and t_c for phantoms with increased Young's modulus were observed for all frequencies tested [Fig. 7.5].

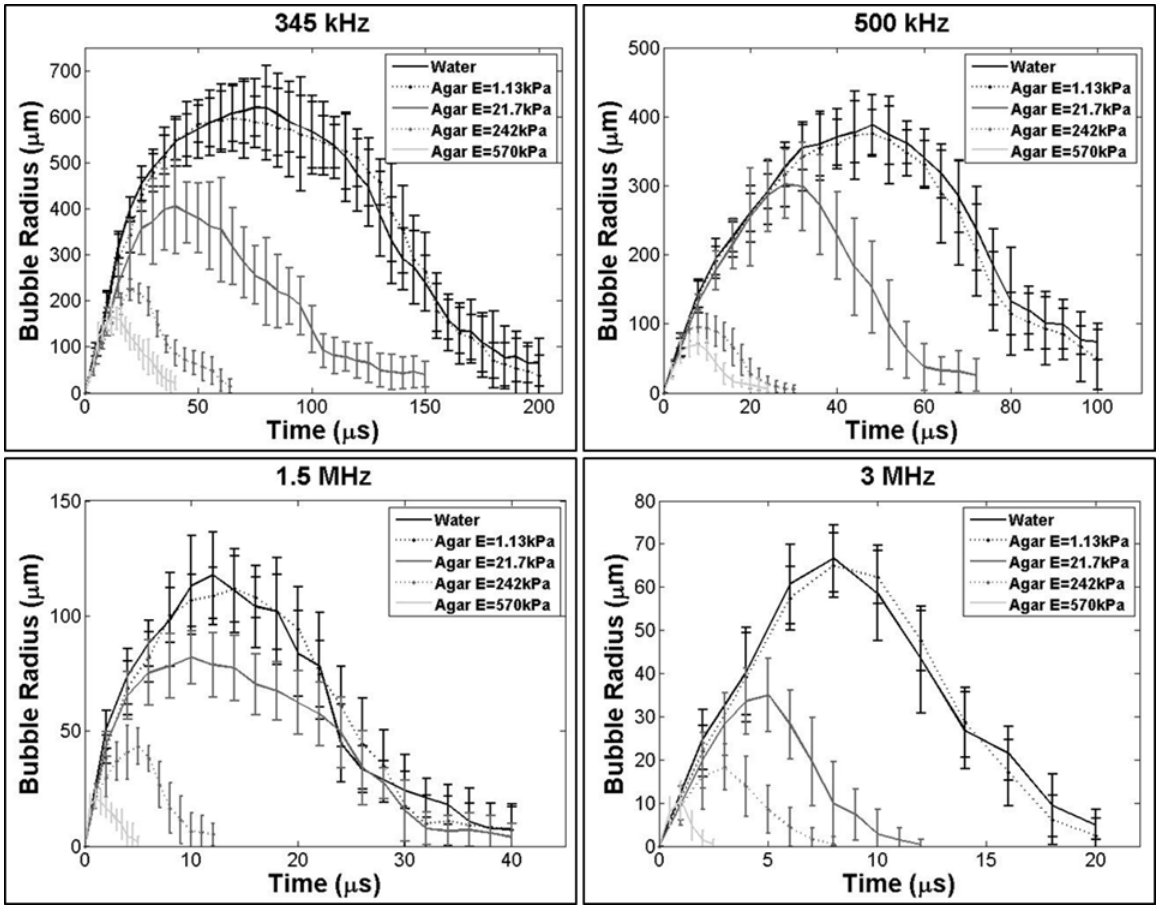

Figure 7.5. Plots show the R-T curves for bubbles produced by 345 kHz, 500 kHz, 1.5 MHz, and 3 MHZ histotripsy pulses inside agarose tissue phantoms of increasing Young's modulus. Results demonstrated a decrease in bubble expansion and collapse time for stiffer tissue phantoms at all frequencies.

Table 7.2. R_{max}, t_{max}, and t_c values for all tissue phantom and frequency combinations. Results show a trend of decreasing R_{max}, t_{max}, and t_c with increase Young's modulus and frequency.

Frequency	Material	R_{max} (μm)	t_{max} (μs)	t_c (μs)
345 kHz				
	Water	617.2±61.8	75	200
	E=1.13 kPa	600.1±70.9	65	190
	E=21.7 kPa	398.8±102.5	40	150
	E=242 kPa	216.1±22.3	20	64
	E=570 kPa	163.9±37.2	12	40
500 kHz				
	Water	387.9±43.9	48	100
	E=1.13 kPa	380.3±34.0	48	100
	E=21.7 kPa	297.4±50.5	28	72
	E=242 kPa	98.3±25.3	8.0	26
	E=570 kPa	71.8±15.1	8.0	24
1.5 MHz				
	Water	114.1±18.9	12.0	36.0
	E=1.13 kPa	111.5±14.5	14.0	32.0
	E=21.7 kPa	79.5±11.5	10.0	32.0
	E=242 kPa	42.1±7.9	5.0	12
	E=570 kPa	20.6±4.1	1.0	5.0
3 MHz				
	Water	64.8±7.9	8.0	20
	E=1.13 kPa	65.2±7.0	8.0	18
	E=21.7 kPa	34.3±8.5	5.0	10
	E=242 kPa	18.0±5.3	3.0	7.0
	E=570 kPa	11.0±4.4	1.0	2.5

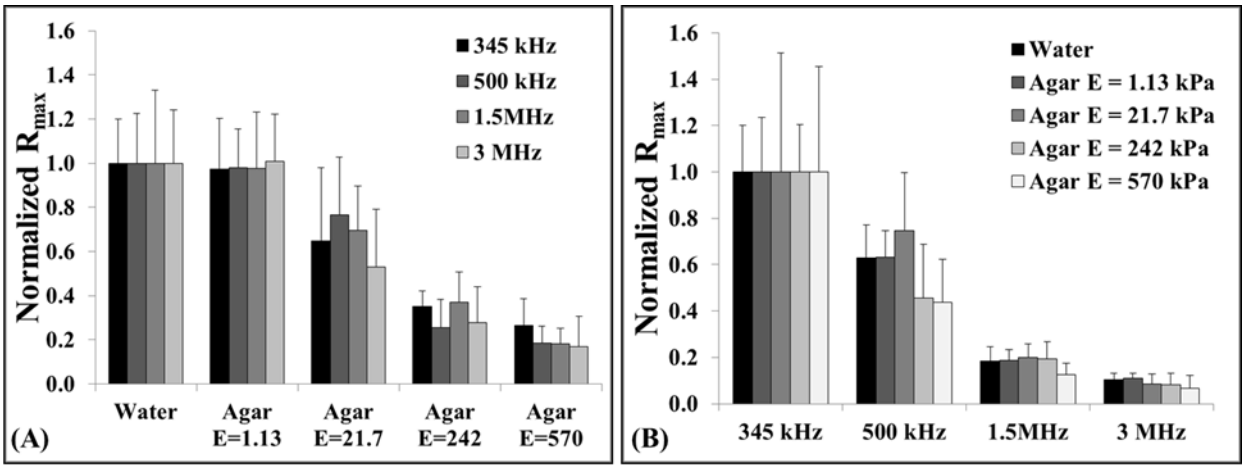

Figure 7.6. Graphs show the relative changes in R_{max} for all tissue phantom and frequency combinations. Results demonstrated a significant decrease in R_{max} ($p<0.05$) with both increasing tissue stiffness (A) and increasing frequency (B). Statistical comparisons were made using a Student's t-test with a Bonferroni correction.

7.3.3 Effects of Ultrasound Frequency on Bubble Behavior

A significant decrease in bubble expansion was observed as the ultrasound frequency was increased from 345 kHz to 3 MHz, with the trend being consistent over the range of tested tissue phantom stiffness [Fig. 7.7]. R_{max} was highest at 345 kHz and decreased by approximately an order of magnitude as the frequency was increased to 3 MHz [Table 7.2]. The trend of decreasing bubble size with increasing frequency was consistent for all tissue phantoms. To compare the effects of frequency independent of tissue stiffness, the R_{max} in all samples was normalized to the R_{max} at 345 kHz, demonstrating a consistent trend of decreasing bubble size with increasing frequency for the same tissue phantom elasticity [Fig. 7.6(B)]. These results demonstrated a significant decrease in bubble size at 500 kHz with bubbles ~40-60% those seen at 345 kHz. R_{max} was further reduced to ~20% and ~10% at frequencies of 1.5 MHz and 3 MHz, respectively.

The bubble lifespan was also decreased at higher frequency [Fig. 7.7]. Both the time until maximum bubble expansion, t_{max}, and the time until bubble collapse, t_c, were shown to decrease at higher frequency [Table 7.2]. Interestingly, the observed values for t_{max} were similar at different frequencies when normalized to the period (1/f) at each frequency. For example, in the 1.13 kPa phantom, t_{max} in terms of periods was 22.4 periods, 24.0 periods, 21.0 periods, and 24.0 periods at 345 kHz, 500 kHz, 1.5 MHz, and 3 MHz, respectively. In terms of periods, t_c was 69.0 periods, 50.0 periods, 48.0 periods, and 54.0 periods at 345 kHz, 500 kHz, 1.5 MHz, and 3 MHz, respectively, for the 1.13 kPa phantom. Similar trends of decreasing t_{max} and t_c with increasing frequency were observed for all tissue phantoms tested [Fig. 7.7].

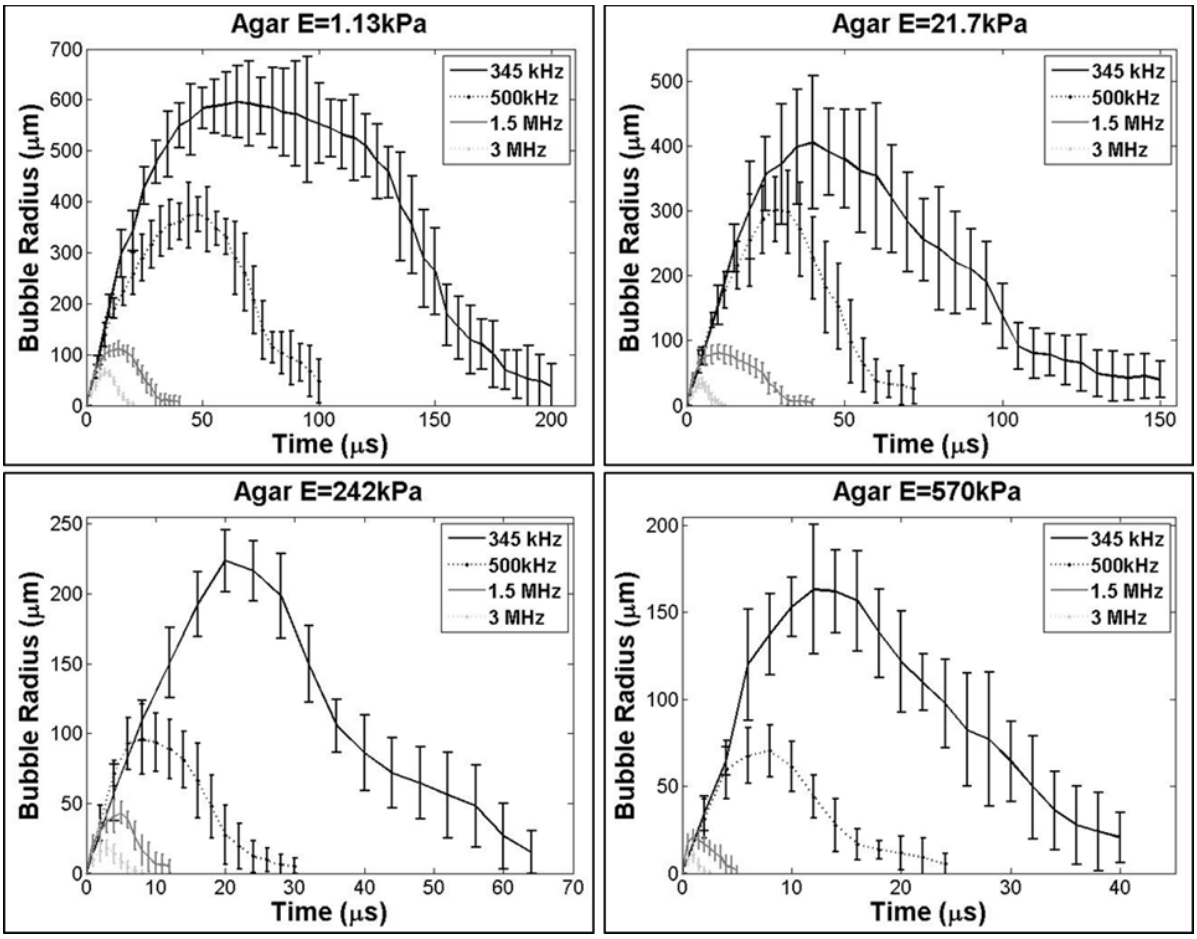

Figure 7.7. Effects of ultrasound frequency on bubble behavior. Plots show the R-T curves for bubbles produced inside tissue phantoms using 345 kHz, 500 kHz, 1.5 MHz, and 3 MHZ histotripsy pulses. Results demonstrated that increasing frequency resulted in decreased bubble expansion and collapse time in all samples.

7.3.4 Estimated Stress-Strain

An estimate of the maximum strain (E7.6) and stress (E7.7) applied to the surrounding media was calculated based on the R-T curves for the different ultrasound frequency and tissue phantom stiffness combinations. Results demonstrated a decrease in the estimated maximum strain applied to the surrounding medium with both increasing stiffness and increasing frequency [Fig. 7.8(A)]. For example, at 345 kHz, a change in Young's modulus from 1.13 kPa to 570 kPa resulted in a >90% reduction in the estimated strain applied to the surrounding medium. A similar reduction in strain was observed with increasing frequency with a >98% reduction in the

predicted strain applied to the 1.13 kPa phantom when the frequency was increased from 345 kHz to 3 MHz. Results for the estimated maximum stress showed a trend of decreasing stress with increasing frequency [Fig. 7.8(B)]. For example, the predicted stress applied to the 570 kPa phantom at 3 MHz was <0.4% of the estimated stress at 345 kHz. Additionally, results for the estimated maximum stress showed a trend of increasing stress with increasing stiffness [Fig. 7.8(B)]. For example, at 500 kHz the predicted stress applied to a 1.13 kPa phantom was <5% that applied to the 570 kPa phantom [Fig. 7.8(B)].

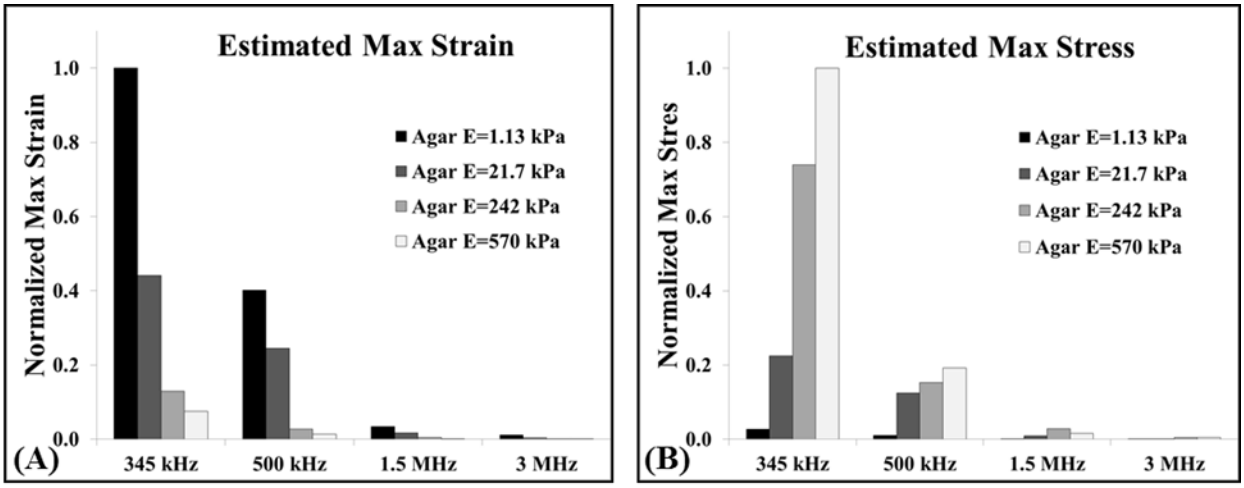

Figure 7.8. (A) Strain calculation results demonstrated a decrease in strain with both increasing Young's modulus and frequency. (B) Stress analysis demonstrated a decrease in stress with increasing frequency, and an increase in stress at higher Young's modulus.

7.3.5 Bubble Behavior Generated using Dual-Frequency Beam

The bubble behavior generated by histotripsy transducers at 500 kHz, 3 MHz, and a combined dual-frequency (500 kHz and 3 MHz) was investigated. Results demonstrated the R_{max} produced by a dual-frequency pulse with approximately 50% of the negative pressure from each frequency was between the R_{max} of bubbles produced by the single frequency components at a similar total peak negative pressure [Fig. 7.9]. The applied pressures for the individual frequencies of the combined waveform shown in Figure 7.9 were 14.3 MPa and 13.6 MPa for

500 kHz and 3 MHz, respectively, with a total $P(-)_{LS}$ of 27.9 MPa. The R_{max} in degassed water for the combined waveform was 165.6±19.8 µm compared to 387.9±43.9 µm and 64.8±7.9 µm at 500 kHz and 3 MHz, respectively. This trend was also observed in all tissue phantoms.

The ability to specifically tailor bubble size using this approach was demonstrated by varying the percentage of contribution from the respective frequencies [Fig. 7.10]. Results showed a continual increase bubble expansion as the percentage of the *p*- amplitude from 500 kHz was increased and the contribution from 3 MHz was decreased. For example, in degassed water, R_{max} was observed to decrease from 387.9±43.9 µm at 500 kHz only (500kHz:3MHz = 100:0) to 286.0±31.4 µm, 192.1±25.0 µm, 138.8±17.5 µm, 98.8±10.2 µm, and 64.8±7.9 when the ratio of 500kHz:3MHz was 74:26, 58:42, 42:58, 24:76, and 0:100, respectively [Fig. 7.10].

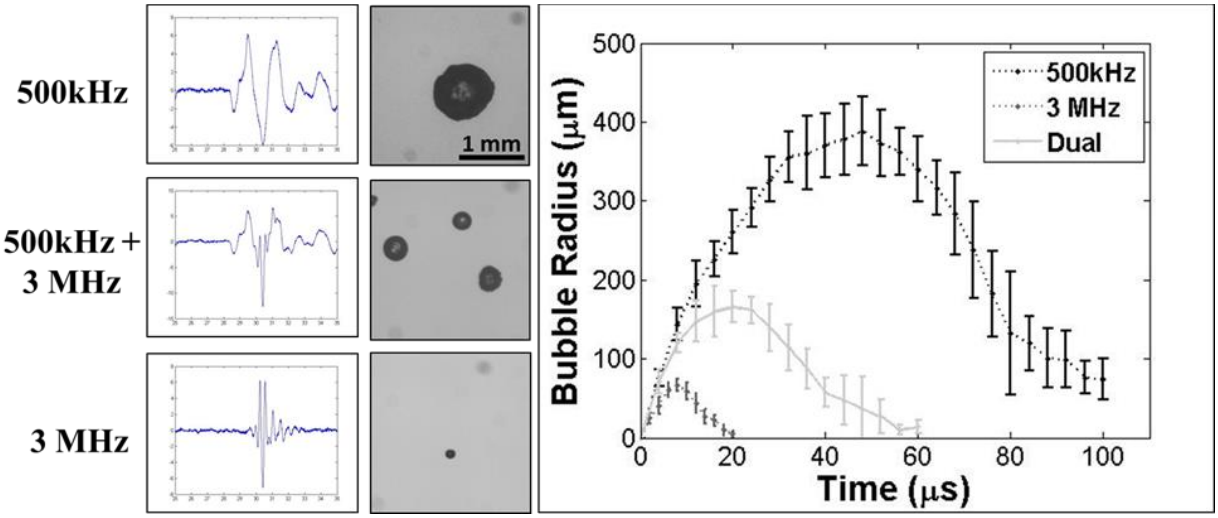

Figure 7.9. The ability to tailor bubble expansion using a previously developed dual-frequency approach was demonstrated using a 500 kHz and 3 MHz dual frequency transducer (Lin et al., 2014a). Images show example waveforms and the corresponding optical images of bubbles produced in degassed water using the 500 kHz (top), dual frequency (middle), and 3 MHz (bottom) transducers. Results demonstrated that the dual frequency bubbles grew to an intermediate size of 165.6±19.8 µm compared to 387.9±43.9 µm and 64.8±7.9 µm at 500 kHz and 3 MHz, respectively.

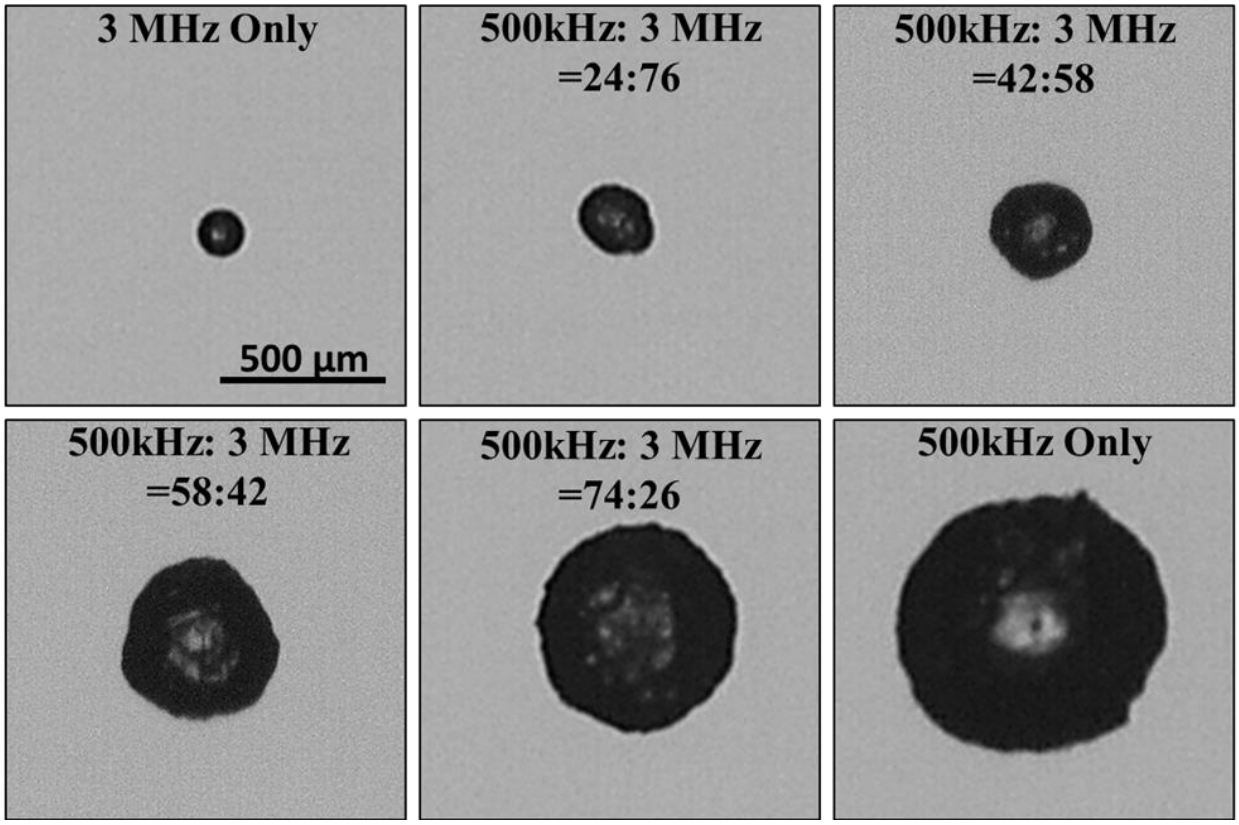

Figure 7.10. Effects of modulating relative amplitude of each frequency on bubble expansion using dual-frequency histotripsy. Optical images of bubbles produced by the 500 kHz and 3 MHz dual frequency transducer with varied relative amplitude for the 500 kHz and 3 MHz components. Results demonstrated an increase in bubble size as the percentage of amplitude applied by the 500 kHz elements was increased.

7.3.6 Supra-threshold Bubble Behavior

To test the effects of increasing pressure on bubble behavior, experiments were repeated for histotripsy pulses with $P(-)_{LS}$ increasing above the intrinsic threshold. As $P(-)_{LS}$ was increased, results demonstrated a consistent increase in the overall size of the bubble cloud matching the portion of the beam profile above the intrinsic threshold, as has been previously observed [15, 26] [Fig. 7.11]. However, although the size of the bubble cloud increased with increasing $P(-)_{LS}$, the R_{max} for individual bubbles within the cloud was not observed to significantly change [Fig. 7.11]. Furthermore, the size of individual bubbles was observed to be nearly uniform throughout the

bubble cloud, although some larger bubbles were observed at the edges of the cloud in the weaker phantoms, potentially due to bubble coalescence [Fig. 7.11]. For all frequencies and tissue phantom combinations tested, no significant difference in R_{max} was observed with increasing $P(-)_{LS}$ for individual bubbles that could be identified within the cloud. For example, Figure 7.11 shows images of bubble clouds produced in tissue phantoms with Young's moduli of 1.13 kPa and 570 kPa using the 500 kHz histotripsy transducer at increasing $P(-)_{LS}$. As $P(-)_{LS}$ was increased, the size of the bubble cloud increased while no significant difference in R_{max} was observed. It should be noted that only the bubbles that could be individually identified and were not overlapping with adjacent bubbles were included in this analysis. Reconstructing the R-T curves for individual bubbles within the cloud was more difficult at higher $P(-)_{LS}$ levels due to the density of bubbles within the cloud, especially in water and tissue phantoms with low Young's moduli, due to bubble overlapping or coalescence. However, the R_{max} of bubbles that could be individually identified within the cloud showed no significant difference compared to bubbles produced at $P(-)_{LS}$ directly above the intrinsic threshold. Due to the reduced bubble expansion for the higher stiffness phantoms and higher ultrasound frequencies, more bubbles remained separate from one another within the cloud, allowing the bubble R-T curves to be quantified for bubbles within the cloud. For example, Figure 7.12 shows the R_{max} for bubbles produced by the 500 kHz transducer in the 570 kPa tissue phantoms at $P(-)_{LS}$ values ranging from 25.4 MPa to 58.9 MPa. Despite the >30 MPa increase in $P(-)_{LS}$, no significant difference in R_{max} was observed ($p>0.05$) [Fig. 7.12].

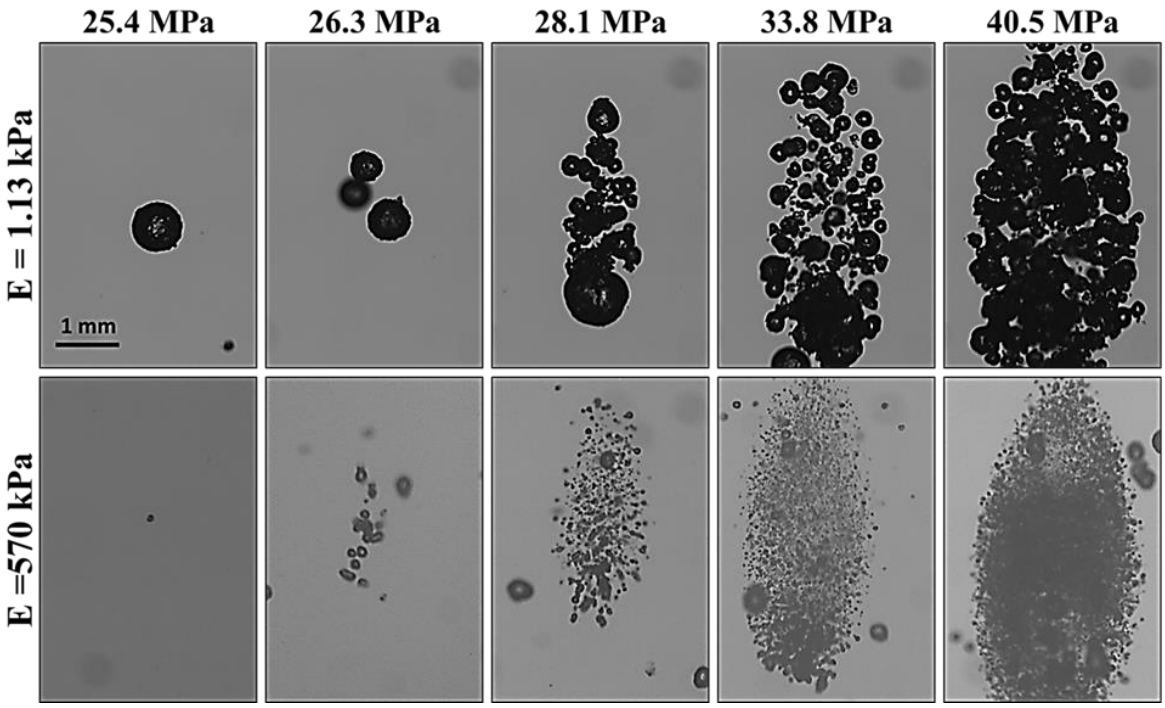

Figure 7.11. Effects of increasing $P(-)_{LS}$ on bubble cloud behavior. Optical images show bubble clouds formed from the 500 kHz transducer at $P(-)_{LS}$ values between 25.4-40.5 MPa in tissue phantoms with Young's moduli of 1.13 kPa (top) and 570 kPa (bottom). Results demonstrated an increase in the size of the bubble cloud with increasing pressure. However, no significant change in the size of individual bubbles within the clouds was observed with increasing $P(-)_{LS}$.

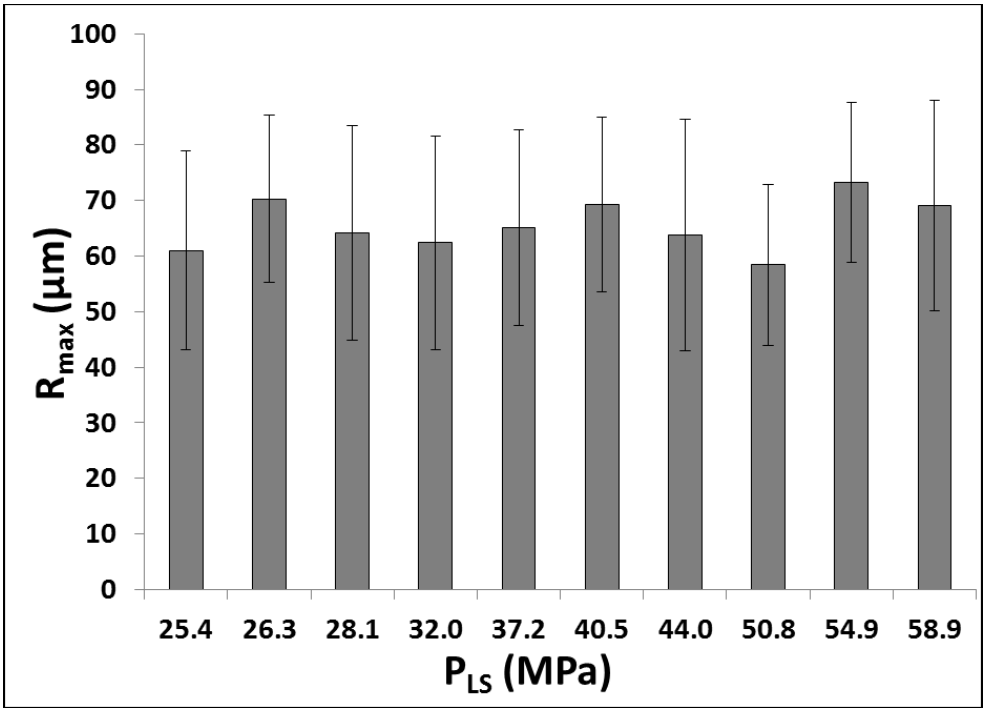

Figure 7.12. Plot shows R_{max} for bubbles formed by the 500 kHz histotripsy transducer in the 570 kPa phantom at $P(-)_{LS}$ values ranging from 25.4 MPa to 58.9 MPa. No significant change in R_{max} was observed for individual bubbles within the clouds with increasing $P(-)_{LS}$ ($p>0.05$).

7.4 Discussion

The first part of this chapter investigated the effects of increased stiffness on the behavior of histotripsy bubbles produced using the intrinsic threshold mechanism. In a separate study, the intrinsic threshold was shown to be independent of tissue stiffness and frequency due to the dominance of surface tension in determining the inertial cavitation threshold of the nanometer-sized cavitation nuclei [10]. In contrast, the numerical simulation in this study demonstrated that the subsequent expansion and collapse of the cavitation bubbles are affected by the elastic properties of the medium. Increases in Young's modulus resulted in a significant reduction in bubble expansion. Experimental results validated this trend with controlled increases in phantom stiffness consistently resulting in significant decreases in R_{max}. For all frequencies, the R_{max} in the stiffest tissue phantoms (E=570 kPa) was <25% the size of the R_{max} in the weakest phantoms (E=1.13 kPa). These results help explain the previous finding that stiffer tissues are more resistant to histotripsy-induced tissue damage, which was hypothesized to be due to reduced strain applied to tissues as a result of impeded bubble expansion [8, 10]. This hypothesis was further assessed by computing the predicted stresses and strains at the bubble wall at maximum expansion. These measurements demonstrated that the observed decreases in bubble expansion would result in a decrease in the strain applied to surrounding stiffer tissues. Despite the decreases in bubble expansion, higher stresses were predicted for stiffer tissues as a result of the higher Young's moduli. Previous work found that tissues resistant to histotripsy had higher ultimate stresses and Young's moduli, but similar (and often lower) ultimate strains, compared to tissues that could be completely fractionated [9]. This finding suggests that stiffer tissues are able to withstand the increased stress predicted in this study, while a likely limiting factor to

achieving tissue fractionation is the ability to expand bubbles to a sufficient size in which the applied strain rises above the ultimate strain of the tissue. Overall, the theoretical and experimental results support our hypothesis that increases in tissue stiffness lead to decreased bubble expansion and reduced strain to surrounding tissue, leading to increased damage resistance for stiffer tissues treated with histotripsy.

In addition to the effects of tissue stiffness, the role of ultrasound frequency was also investigated. Results from the numerical simulation demonstrated that bubble expansion was dependent upon the duration of the rarefactional phase, with lower frequency resulting in increased bubble expansion. These results were validated by experiments in tissue phantoms demonstrating an approximately order of magnitude decrease in R_{max} when the frequency was increased from 345 kHz to 3 MHz. At lower frequency, bubble expansion was increased due to more energy being imparted into the bubble as a result of the increased duration of the applied rarefactional pressure. It is interesting to note that the bubble lifespan, when normalized to the period (1/f) is almost constant across different frequencies. Overall, these findings suggest that, although bubble expansion is impeded in stiffer tissues, lower frequency may be used to enhance bubble expansion for the fractionation of stiffer tissues. This hypothesis was supported by the stress-strain calculations which predicted an increase in both the stress and strain applied to tissues at lower frequency.

In the final part of this chapter, the effects of pressure on bubble expansion were investigated. Results of the simulation predicted that increasing pressure would result in a corresponding increase in bubble expansion. However, the predicted increases in individual bubble size were not observed in experiments. Instead, as $P(-)_{LS}$ was increased, the size of individual bubbles within the focal region appeared to remain constant. Although the overall size

of the bubble cloud increased with increasing $P(-)_{LS}$, the bubbles within the cloud appeared to be of uniform size approximately matching the size of the individual bubbles measured at $P(-)_{LS}$ directly above the intrinsic threshold. This finding may suggest that the individual bubbles formed throughout the entire focal region actually experience the intrinsic threshold pressure rather than a higher pressure as predicted by the linear summation. This possibility is supported by the observation that bubbles in the center of the cloud did not grow larger than peripheral bubbles. We hypothesize that the propagating acoustic wave loses energy into the bubbles when cavitation is generated. This effect has been previously observed in shock wave lithotripsy where a decrease in peak negative pressure has been measured when cavitation bubbles are generated [28, 30]. In this process, the ultrasound beams constructively interfere with one another as they propagate towards the focal region until the peak negative pressure reaches the intrinsic threshold. Once the intrinsic threshold is reached, a cavitation bubble is generated, and the pressure drops below the intrinsic threshold for a short distance as the beams continue to propagate until intrinsic threshold is reached once again, with this process repeating through the entire focal volume. As a result of this process of transferring energy into the forming bubbles, the constructive interference needed to reach pressure beyond the intrinsic threshold at the focus does not occur.

In addition to explaining the bubble behavior observed in this study, the proposed process of bubble-induced pressure saturation also suggests that some caution should be taken when reporting the peak negative pressure levels achieved in histotripsy therapy. Although the pressure estimated from the linear summation of individual elements has shown good agreement up to 30 MPa with the *p*- measured directly in a higher cavitation threshold medium, 1,3 butanediol, in a previous study [16], the results of this work suggest that the actual pressure achieved at the focus

may be limited to the intrinsic threshold of the medium. In reality, pressures exceeding the intrinsic threshold may not occur when cavitation is generated. As such, it is perhaps better to report the applied pressure as a "potential peak negative pressure" measured from the linear summation. Another metric that may be useful to report may be the dimensions of the focal region that exceeds the intrinsic threshold, as this dimension consistently matches the size and location of the cavitation cloud that is generated as well as the resulting histotripsy lesion [15]. However, it is important to note that this process of bubble-induced pressure saturation is only one potential explanation for the observation that R_{max} did not increase at higher $P(-)_{LS}$. Another possible explanation is that bubble-bubble interactions within the cloud act to limit the expansion of adjacent bubbles, an effect which wasn't accounted for in the single bubble simulations used in the study. Future work will aim to investigate these different possibilities both experimentally and theoretically by developing relevant multi-bubble models.

Overall, the results of this chapter improve our understanding of the histotripsy process and will help to improve parameter optimization for histotripsy treatments of specific tissues. For example, the finding that increasing $P(-)_{LS}$ above the intrinsic threshold increases the size of the bubble cloud but does not change the size of individual bubbles inside the focus suggests that alternative strategies such as decreasing frequency will be required to enhance bubble expansion. The results of this study demonstrate that bubble size is dictated by the waveform characteristics at the intrinsic threshold. As a result, bubble size can be predictably manipulated by changing the waveform parameters. This ability to tailor bubble expansion was demonstrated in this study using a dual-frequency approached previously developed by Lin et al [26]. This approach allows for the size of bubbles produced by a single transducer to be quickly modulated by adjusting the relative proportion of the peak negative pressure produced by each of the two frequencies. Based

on a specific clinical application, this dual-frequency approach could be used to design optimal pulsing strategies. For example, there is a tradeoff between using higher frequency to increase precision due to the smaller focal zone compared to using lower frequency to enhance bubble expansion. The dual-frequency approach also has the potential to improve the effectiveness of a selective ablation strategy that has previously been developed in which softer tissues are fractionated while surrounding stiffer tissues such as vital blood vessels inside the focal volume remain intact [8, 9]. By optimizing the waveform so that bubble expansion is large enough to fractionate the softer tissue but not the stiffer tissue, the risk of fractionating the stiffer vital tissue will be further reduced.

7.5 Conclusion

In this chapter, the effects of tissue stiffness and ultrasound parameters on histotripsy-induced cavitation bubble behavior were investigated. The results demonstrate that increasing tissue phantom stiffness results in a significant decrease in bubble expansion and collapse time, helping to explain previous findings that stiffer tissues are more resistant to histotripsy-induced tissue damage. It was also shown that decreasing ultrasound frequency facilitates bubble expansion, suggesting that lower frequency may potentially be more effective at fractionating stiffer tissues using histotripsy. Experimental results further showed that increasing $P(-)_{LS}$ resulted in a larger bubble cloud, but did not increase the expansion of individual bubbles within the cloud, potentially due to bubble-induced pressure saturation at the intrinsic threshold or due to bubble-bubble interactions within the cloud.. Finally, this work demonstrated the potential of using a previously developed dual-frequency strategy to modulate the expansion of histotripsy bubbles. Overall, the results of this study improve our understanding of how tissue stiffness and

ultrasound parameters affect the histotripsy bubble cloud behavior and provide a rational basis to tailor acoustic parameters for treatment of the specific tissues of interest.

7.6 References

[1] E. Vlaisavljevich, *et al.*, "Effects of Tissue Stiffness, Ultrasound Frequency, and Pressure on Histotripsy-induced Cavitation Bubble Behavior," *Phys Med Biol,* 2015.

[2] J. E. Parsons, *et al.*, "Pulsed cavitational ultrasound therapy for controlled tissue homogenization," *Ultrasound Med Biol,* vol. 32, pp. 115-29, Jan 2006.

[3] W. W. Roberts, *et al.*, "Pulsed cavitational ultrasound: a noninvasive technology for controlled tissue ablation (histotripsy) in the rabbit kidney," *J Urol,* vol. 175, pp. 734-8, Feb 2006.

[4] Z. Xu, *et al.*, "Investigation of intensity thresholds for ultrasound tissue erosion," *Ultrasound Med Biol,* vol. 31, pp. 1673-82, Dec 2005.

[5] E. Vlaisavljevich, *et al.*, "Nanodroplet-mediated histotripsy for image-guided targeted ultrasound cell ablation," *Theranostics,* vol. 3, pp. 851-64, 2013.

[6] Z. Xu, *et al.*, "High speed imaging of bubble clouds generated in pulsed ultrasound cavitational therapy--histotripsy," *IEEE Trans Ultrason Ferroelectr Freq Control,* vol. 54, pp. 2091-101, Oct 2007.

[7] T. L. Hall, *et al.*, "Histotripsy of rabbit renal tissue in vivo: temporal histologic trends," *J Endourol,* vol. 21, pp. 1159-66, Oct 2007.

[8] E. Vlaisavljevich, *et al.*, "Image-guided non-invasive ultrasound liver ablation using histotripsy: feasibility study in an in vivo porcine model," *Ultrasound Med Biol,* vol. 39, pp. 1398-409, Aug 2013.

[9] E. Vlaisavljevich, *et al.*, "Effects of tissue mechanical properties on susceptibility to histotripsy-induced tissue damage," *Phys Med Biol,* vol. 59, pp. 253-70, Jan 20 2014.

[10] E. Vlaisavljevich, *et al.*, "Effects of Ultrasound Frequency and Tissue Stiffness on the Histotripsy Intrinsic Threshold for Cavitation," *In Submission,* 2014.

[11] J. S. Allen and R. A. Roy, "Dynamics of gas bubbles in viscoelastic fluids. II. Nonlinear viscoelasticity," *J Acoust Soc Am,* vol. 108, pp. 1640-50, Oct 2000.

[12] A. P. Duryea, *et al.*, "Histotripsy erosion of model urinary calculi," *J Endourol,* vol. 25, pp. 341-4, Feb 2011.

[13] A. D. Maxwell, *et al.*, "Inception of Cavitation Clouds by Scattered Shockwaves," *IEEE Ultrasonics Symposium,* pp. 3B-2, 2010.

[14] E. Vlaisavljevich, *et al.*, "Histotripsy-induced cavitation cloud initiation thresholds in tissues of different mechanical properties," *IEEE Trans Ultrason Ferroelectr Freq Control,* vol. 61, pp. 341-52, Feb 2014.

[15] K. W. Lin, *et al.*, "Histotripsy beyond the intrinsic cavitation threshold using very short ultrasound pulses: microtripsy," *IEEE Trans Ultrason Ferroelectr Freq Control,* vol. 61, pp. 251-65, Feb 2014.

[16] A. D. Maxwell, *et al.*, "Probability of cavitation for single ultrasound pulses applied to tissues and tissue-mimicking materials," *Ultrasound Med Biol,* vol. 39, pp. 449-65, Mar 2013.

[17] J. S. Allen and R. A. Roy, "Dynamics of gas bubbles in viscoelastic fluids. I. Linear viscoelasticity," *J Acoust Soc Am,* vol. 107, pp. 3167-78, Jun 2000.

[18] J. B. Freund, "Suppression of shocked-bubble expansion due to tissue confinement with application to shock-wave lithotripsy," *J Acoust Soc Am,* vol. 123, pp. 2867-74, May 2008.

[19] J. Jimenez-Fernandez and A. Crespo, "Bubble oscillation and inertial cavitation in viscoelastic fluids," *Ultrasonics,* vol. 43, pp. 643-51, Aug 2005.

[20] X. Yang and C. C. Church, "A model for the dynamics of gas bubbles in soft tissue," *J Acoust Soc Am,* vol. 118, pp. 3595-606, Dec 2005.

[21] E. A. Zabolotskaya, *et al.*, "Modifications of the equation for gas bubble dynamics in a soft elastic medium," *J Acoust Soc Am,* vol. 118, pp. 2173-81, Oct 2005.

[22] M. Warnez and E. Johnsen, "The effect of relaxation time on cavitation dynamics in viscoelastic media: A numerical investigation of growth and forced oscillations," *[In Preparation],* 2014.

[23] R. Gaudron, *et al.*, "Bubble dynamics in a viscoelastic medium with nonlinear elasticity, submitted (2014)." vol. [submitted], 2014.

[24] A. P. Balgude, *et al.*, "Agarose gel stiffness determines rate of DRG neurite extension in 3D cultures," *Biomaterials,* vol. 22, pp. 1077-1084, May 2001.

[25] T. A. Ulrich, *et al.*, "Probing cellular mechanobiology in three-dimensional culture with collagen-agarose matrices," *Biomaterials,* vol. 31, pp. 1875-1884, Mar 2010.

[26] K. W. Lin, *et al.*, "Dual-beam histotripsy: a low-frequency pump enabling a high-frequency probe for precise lesion formation," *IEEE Trans Ultrason Ferroelectr Freq Control,* vol. 61, pp. 325-40, Feb 2014.

[27] J. E. Parsons, *et al.*, "Cost-effective assembly of a basic fiber-optic hydrophone for measurement of high-amplitude therapeutic ultrasound fields," *J Acoust Soc Am,* vol. 119, pp. 1432-40, Mar 2006.

[28] Y. C. Fung, *Foundations of solid mechanics*. Englewood Cliffs, N.J.: Prentice-Hall, 1965.

[29] C. Y. Hua and E. Johnsen, "Nonlinear oscillations following the Rayleigh collapse of a gas bubble in a linear viscoelastic (tissue-like) medium," *Physics of Fluids,* vol. 25, Aug 2013.

[30] Y. A. Pishchalnikov, *et al.*, "Effect of firing rate on the performance of shock wave lithotriptors," *BJU Int,* vol. 102, pp. 1681-6, Dec 2008.

Chapter 8

Visualizing the Histotripsy Process: Bubble Cloud-Cancer Cell Interactions

A majority component of this chapter is excerpted from a manuscript in preparation for submission to *Ultrasound in Medicine and Biology*.

8.1 Introduction

Histotripsy is a non-invasive ablation method that controls cavitation to mechanically fractionate soft tissue through high pressure (>10 MPa), short duration (<20 μsec) ultrasound pulses at low duty cycles (<1%) [1-5]. Histotripsy depends on the initiation and maintenance of a cavitation bubble cloud to produce mechanical tissue fractionation [6, 7]. With a sufficient number of pulses, histotripsy can completely fractionate tissue into a liquid-appearing homogenate with no cellular structures remaining [6-10]. Previous work has shown that histotripsy can produce precise lesions with bisected cells often observed at the sharply demarcated lesion boundary [6-10]. Histotripsy is currently being studied for many clinical applications where non-invasive tissue removal is desired including tissue debulking to treat benign prostatic hyperplasia [11], clot breakdown to treat deep vein thrombosis [12], perforation of the atrial septum in the treatment of congenital heart diseases [13, 14], cancer ablation [10, 15], and fetal interventions [16].

Some effort has been made towards understanding histotripsy process. Experiments in agarose tissue phantoms containing a layer of red blood cells (RBCs) have demonstrated lesion

morphology correlating to bubble cloud area [17-19]. Furthermore, single bubbles on the cloud periphery have been observed to cause localized damage similar to the maximum expanded diameter of individual bubbles. These studies have led to the hypothesis that the rapid expansion and collapse of histotripsy bubbles fractionates tissue by inducing large stress and strain on the adjacent tissue structures. However, the process of histotripsy tissue fractionation has not yet been visualized on a cellular level or on the time scales at which the damage is achieved. Additionally, while RBC phantoms are a good model to visualize the area ablated by histotripsy, the model is limited to suspended RBCs that fractionate at significantly smaller deformations than adherent cells attached to an extracellular matrix (ECM) [20-23]. Therefore, the question remains as to how histotripsy fractionates adherent cells within an ECM that can undergo much larger deformations before rupture [20-23].

In this chapter, the histotripsy process was visualized at the cellular level for the first time using a custom-built histotripsy transducer incorporated into the stage of an inverted microscope, which was coupled to high-speed imaging. Optically transparent tissue phantoms with cancer cells embedded inside fibrin-based gels were used to mimic real tissue with cells adherent to a three dimensional matrix, and the bubble-cell interactions produced by a single histotripsy pulse as well as over multiple histotripsy pulses were imaged.

8.2 Methods

8.2.1 Miniature Transducer-tank Setup

A custom-built miniature transducer tank [Fig.8.1(A)] was designed to generate and image a histotripsy bubble cloud-cell interaction using an inverted microscope (Nikon Eclipse Ti, 10X magnification), which was coupled to a high-speed camera. The miniature transducer-tank

was designed to achieve short, high-pressure histotripsy pulses and fit into a 16x11cm microscope stage with an optical window at the bottom of tank for the microscope objective. Four, 2-cm diameter piezoceramic elements (Elements; Steiner & Martins) were positioned 3 cm apart on the semicircular side of the tank wall. The transducer had center frequency of 2 MHz and geometric focal length of 3 cm. The transducer tank was filled with degassed water at room temperature (~20°C) with elements completely submerged. A two axis micro-positioning system was built support the tissue phantom and to adjust the position of the phantom with respect to the transducer focus.

8.2.2 Ultrasound Generation

Histotripsy pulses were generated by the 4 element, 2 MHz microscope transducer. Input signals were provided by a custom built field-programmable gate array (FPGA) board (Altera Corporation, San Jose, CA, USA) that functioned as a signal generator. The transducer was calibrated using a fiber optic probe hydrophone built in house [24] and the focal pressure waveforms were recorded in free-field in degassed water at 20°C [Fig.8.1(B)]. Bubble clouds were produced with peak negative pressure of ~11 MPa and a pulse length of 10 cycles.

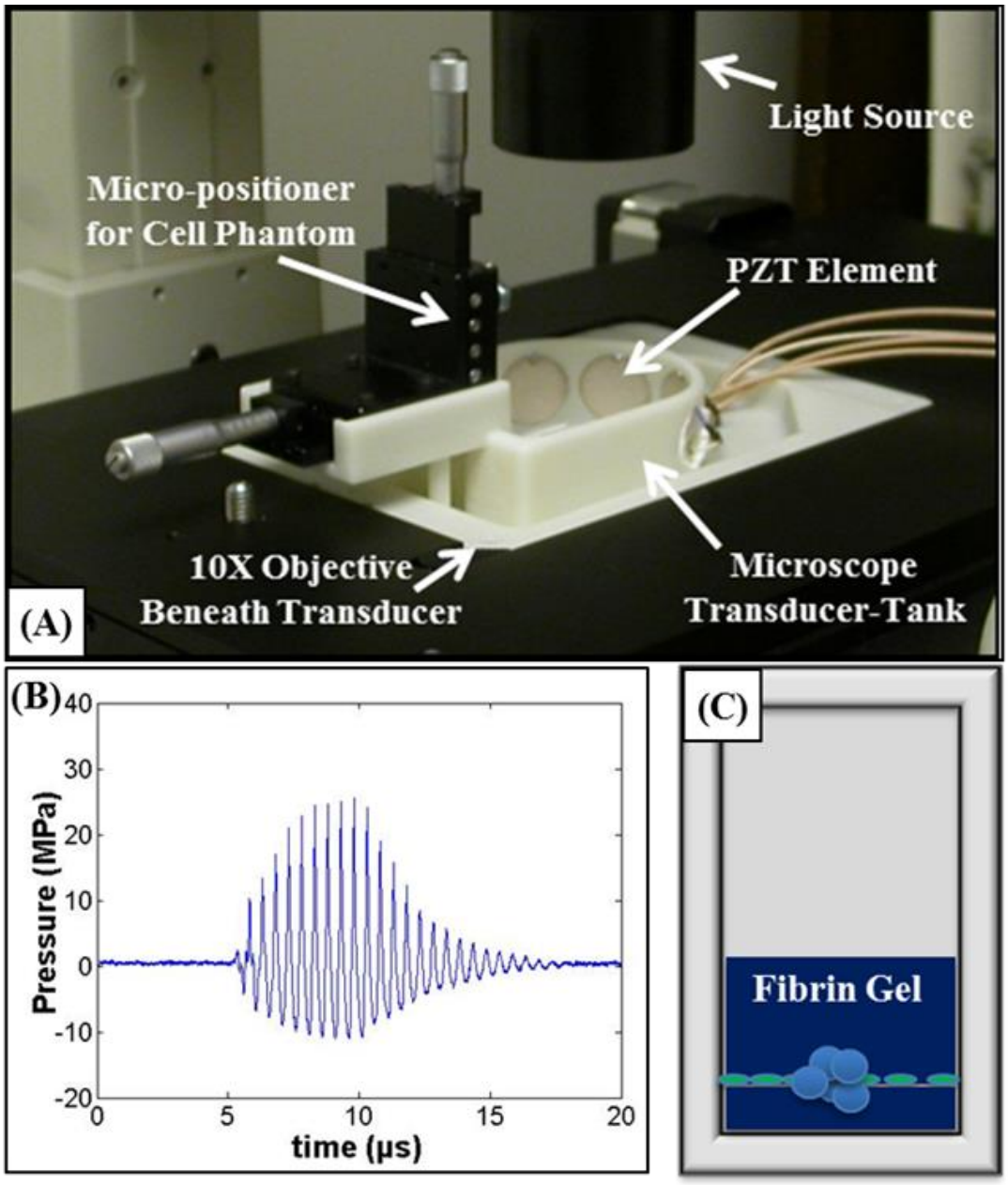

Figure 8.1. (A) Experimental set-up showing custom-built microscope transducer-tank. (B) Example acoustic waveform. (C) Schematic of tissue phantom containing a layer of breast cancer cells inside a fibrin gel.

8.2.3 Cancer Cell Tissue Phantom Preparation

Since previous work has demonstrated that tissue mechanical properties significantly impact histotripsy [3, 4, 25, 26], an optically transparent fibrin-based tissue phantom with an embedded layer of human breast cancer cells (BCCs, MDAMB231) was used to mimic adherent

cells inside a tissue-like ECM environment. Cell culture work was performed under ThermoForma Class II A1 Biological Safety Cabinet and cells were incubated at 37°C and 5% CO_2. BCCs were cultured in Dulbecco's Modified Eagle's Medium (DMEM; Gibco) supplemented with 10% fetal bovine serum (FBS; Media Tech) and 1% penicillin/streptomycin (P/S; Media Tech). BCCs were passaged every six days with media change every third day. Cell washes were performed with sterile phosphate buffered saline (PBS; Gibco). BCCs were detached for experimental seeding with 0.05% Trypsin/0.53mM EDTA in HBSS without sodium bicarbonate, calcium, and magnesium (Trypsin-EDTA; Cellgro). BCCs were used prior to passage 15 and were seeded ($2x10^4$ cells/cm^2) onto a fibrin gel inside cell culture boxes made of acoustically transparent, 0.1 mm thick polycarbonate (Polycarbonate; McMaster). Cell boxes (20mm x 20mm x 40mm) were washed 3 times in 95% ethanol and sterilized 20 minutes under ultra violet light prior to use. Cells were seeded onto 4 mm thick fibrin gel to mimic extracellular matrix within tissue (fibrin gel was chosen for similar acoustic and mechanical properties to soft tissue). To make the fibrin gel, a fibrinogen solution (Fibrinogen from bovine plasma; Sigma Aldrich) of 10 mg/ml was prepared in the culture medium and split into cell boxes. Thrombin (Thrombin; Sigma Aldrich) was then added (20 µl/ml) along with 5% FBS, and the solution was incubated at 37°C for 1 hour prior to seeding to ensure solidification of fibrin. The shear modulus of the fibrin gel (10 mg/ml) used in this study has previously been measured to be ~377 Pa [27]. BCCs were cultured on fibrin for three days before histotripsy treatment. An additional 8 mm thick fibrin gel was added over cells 1 day prior to treatment to mimic behavior inside a tissue ECM environment [Fig.8.1(C)].

8.2.4 Single Pulse Cell-bubble Interaction

To study the bubble-cell interaction induced by a single histotripsy pulse, an ultra-fast digital camera (SIM 802, Optronis) was aligned to the inverted microscope left optical port. The camera was externally triggered to synchronize recorded images with the histotripsy pulse at specific delay intervals. A flash lamp was also triggered and positioned over cells to illuminate images with an exposure time of 2μs. A single 10-cycle histotripsy pulse was applied to tissue phantoms containing an embedded BCC monolayer, and the camera was triggered to record 16 images with the first image taken 20 μs before the pulse and 15 images taken after the arrival of the pulse with inter-frame durations between 4-6 μs. Recorded images spanned the entirety of expansion and collapse of a bubble cloud after arrival of a single pulse and the subsequent cell response following collapse. Since images during the pulse were blurred due to the ultrasound wave interfering with imaging, the cell response during bubble expansion and collapse after the pulse was investigated.

8.2.5 Multiple Pulse Cell-bubble Interaction

To study bubble-cell interactions over multiple pulses, a high-speed, 1 megapixel CCD camera (Phantom V210, Vision Research) with frame rate of 2000 fps was aligned to the inverted microscope left optical port as it allows up to 4000 image storage for each acquisition in comparison to the 16 frame storage for the ultra-fast SIM camera. The camera was externally triggered to synchronize recorded images with the histotripsy pulse at specific delay intervals. An exposure time of 20 μs was used for each recorded frame. 1000 histotripsy pulses (10-cycles, 50 Hz PRF) were applied to tissue phantoms containing an embedded BCC monolayer, and the camera was triggered to record images 24 μs after the arrival of each pulse.

8.3 Results

8.3.1 Single Pulse Cell-bubble Interaction

Experiments exposing tissue phantoms containing a layer of embedded breast cancer cells to a single histotripsy pulse demonstrated that the histotripsy bubbles induced significant cell displacement and deformation during both expansion and collapse, as well as after bubble collapse due to the tissue inertial response. The largest cell deformations were observed for cells immediately adjacent to the bubble wall during bubble collapse. Figure 8.2 shows a representative video of the cellular response to a single histotripsy pulse. During expansion (first five frames), the cells were displaced in the direction of the radial bubble wall expansion, with the rate of cell displacement decreasing as the bubble reached its maximum size [Fig.8.2]. During collapse, much larger cell displacements were observed, with the cells immediately surrounding the bubble translated toward the collapsing bubble. After collapse, significantly fewer cells remained in the bubble exposed regions, with these cells irreversibly ruptured or detached from the fibrin matrix <100 μs after the pulse arrived at the focus. For example, the cells surrounding large bubble shown in Figure 8.2 were observed to move more than 200 μm during bubble collapse, with ~half of the cells exposed to the bubble (top right corner) remaining after the treatment. For cells further away from the bubble, only very small displacements were observed with cells returning to their initial positions and remaining intact after the treatment. Cell displacement was consistently observed for all experiments, with larger bubbles inducing greater cell displacement during both expansion and collapse. For example, in Figure 8.2, much larger displacements were observed around the large bubble (top right) compared to the smaller bubble (left), with cell removal only occurring in the region exposed to the larger bubble.

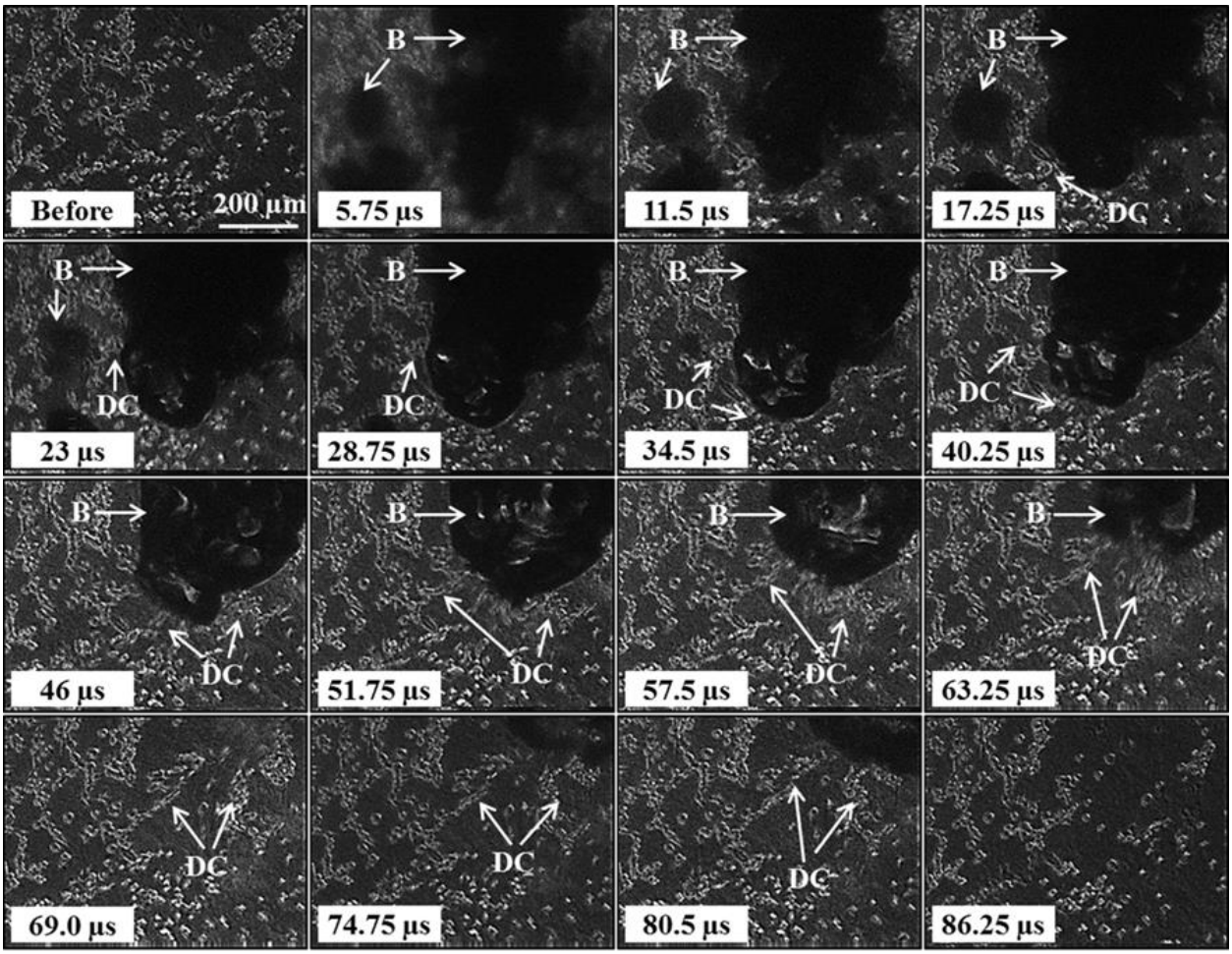

Figure 8.2. Cancer cells exposed to a single histotripsy pulse were significantly deformed during both bubble expansion and collapse, with the largest deformations observed during collapse (between 46 µs and 74.75 µs). Arrows indicate regions containing bubbles (B) and the deformed cells (DC).

8.3.2 Multiple Pulse Cell-bubble Interaction

Experiments exposing tissue phantoms containing a layer of embedded breast cancer cells to multiple histotripsy pulses demonstrated histotripsy completely fractionated all cell at the focus into acellular debris. Cells adjacent to the histotripsy bubbles underwent large deformations after each pulse, with cells at the boundary of the expanding lesion often remaining intact for many pulses before rupture [Fig.8.3]. Over multiple pulses, cell bisection and complete removal occurred for all cells within the region exposed to the bubble cloud, with many cells

experiencing multiple large deformations prior to rupture [Fig.8.3]. A significant increase in both bubble cloud size and lesion area was observed with increasing number of pulses, with a clearly defined lesion containing no cells remaining after 1000 pulses. As tissue fractionation progressed, cells (or parts of cells) were observed to be pulled towards the bubble cloud, similar to what was observed in single pulse experiments after bubble collapse. Cells at the boundary of the expanding lesion underwent large tensile strains (pulled towards the bubble cloud) and were often bisected multiple times over many pulses before complete removal [Fig.8.4]. For example, the cell indicated by the arrow in Figure 8.4 was pulled towards the bubble cloud and underwent at least three significant deformations (~150%-250% of original length) over approximately 40 pulses, resulting in the cell being bisected twice before complete removal. Since only one time point was visualized per pulse, it is likely that the cell underwent additional significant deformations during this period that were not directly observed. After cell bisection, the remaining portions of the cell continued to be deformed, demonstrating the interconnected nature of the intracellular and extracellular matrix in the tissue phantom. In some cases, cell deformation appeared to be induced directly from bubble-cell interactions. However, in many other cases, cell deformation was observed for cells a short distance away from the bubble, likely due to the strain induced by the bubbles on the ECM, similar to what was observed in the single pulse experiments.

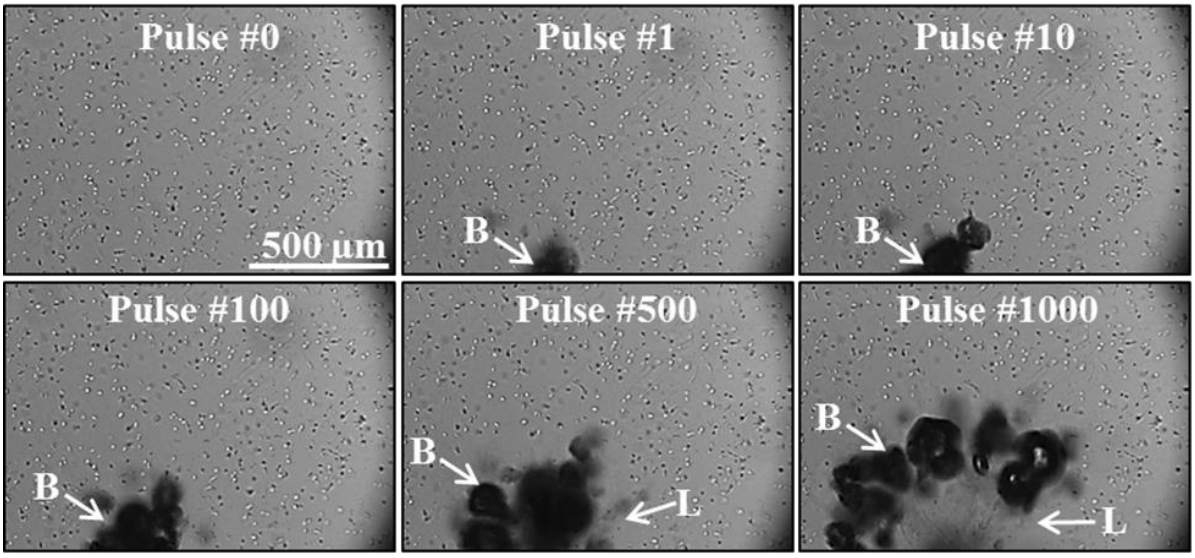

Figure 8.3. Cancer cells exposed to 1000 pulses were repeatedly deformed by bubbles (B) until cell rupture/removal was achieved, forming a well-defined lesion (L) at the focus.

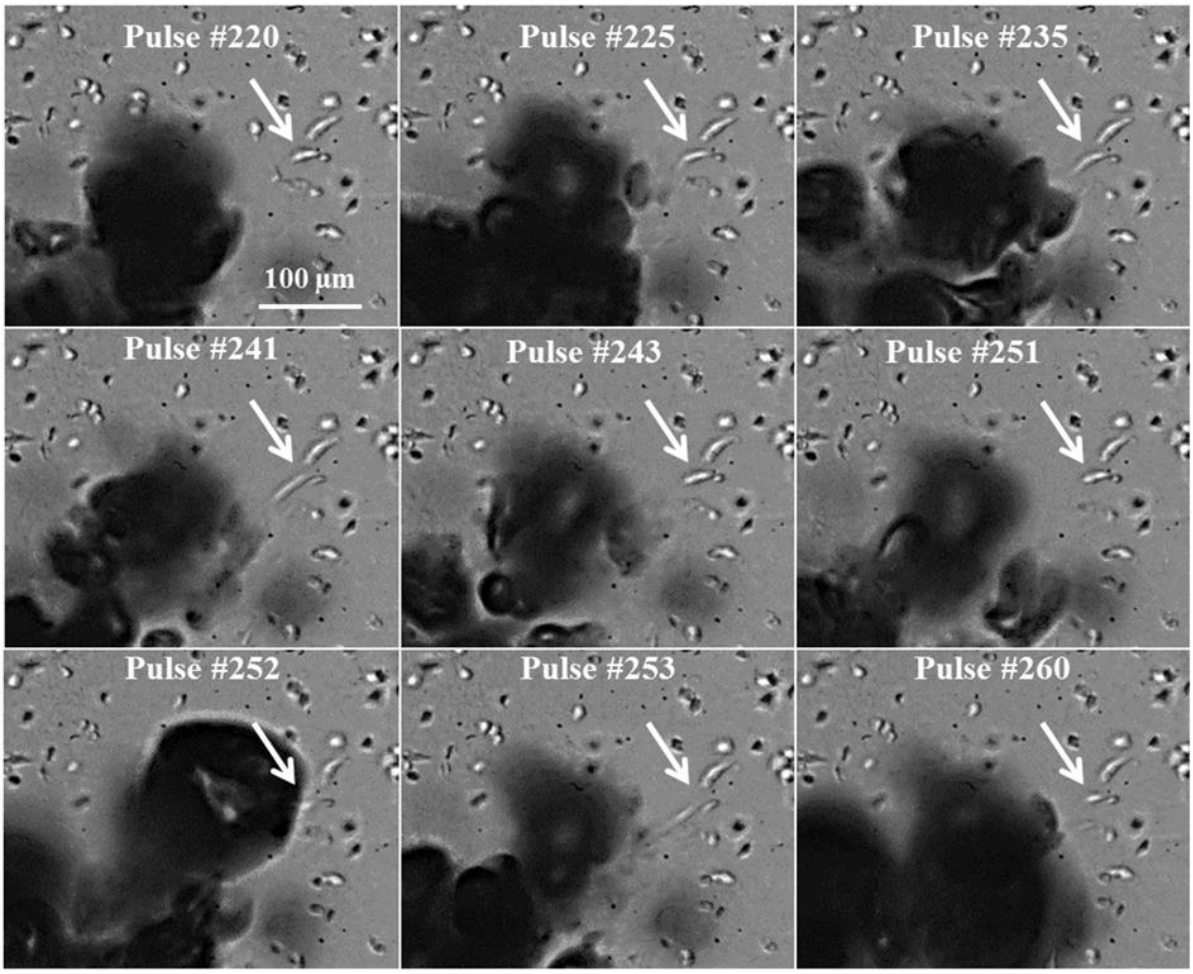

Figure 8.4. Cancer cells at the boundary of the histotripsy lesion were repeatedly deformed (pulled towards bubble) and often bisected multiple times before complete removal. Arrow indicates a breast cancer cell bisected over multiple pulses.

8.4 Discussion

In this chapter, the histotripsy tissue fractionation process was investigated on the cellular level using a custom-built histotripsy transducer incorporated into the stage of an inverted microscope, which was coupled to high-speed imaging. Histotripsy was applied to optically transparent tissue phantoms with an embedded layer of breast cancer cells to mimic real tissue with cells adherent to a three dimensional matrix, and the bubble-cell interactions produced by a single histotripsy pulse as well as over multiple histotripsy pulses were imaged. This study represents the first time the histotripsy process has been visualized on the cellular level in a relevant tissue-mimicking environment, with results supporting the hypothesis that the rapid expansion and collapse of histotripsy bubbles fractionates tissue by inducing large stress and strain on the adjacent tissue structures, resulting in precise lesions with sharp boundaries between fractionated lesion and the intact surrounding tissue.

To experimentally investigate the process of tissue fractionation on the cellular level in a relevant tissue-mimicking environment, breast cancer cells embedded inside a tissue mimicking phantom were exposed histotripsy pulses applied by a 2 MHz transducer. Results from the single pulse experiments demonstrated bubbles induced large deformations to the surrounding cells during both expansion and collapse, with the largest deformations occurring after bubble collapse to the cells immediately adjacent to the bubble. These results help to explain the formation of sharp lesions in histotripsy therapy in which the damage is localized to the regions directly exposed to the histotripsy bubbles. The results from the single pulse experiment also demonstrate that the cellular response to histotripsy is dependent on the entire tissue microenvironment, with adherent cells being deformed along with the fibrin ECM. This

observation highlights the importance of the tissue phantom used in this work. In preliminary experiments conducted without the top fibrin layer, the vast majority of cells were detached within in a single pulse (including cells further away from the bubbles), contrary to previous studies showing that histotripsy requires multiple pulses in order to fractionate a tissue [6, 8, 9, 28]. This observation makes sense based on previous work showing that histotripsy is dependent upon tissue mechanical properties [3, 4, 25, 26], which are determined by the extracellular matrix, intracellular matrix, and cell-matrix adhesions.

Results from the multi-pulse experiments demonstrated that the mechanical strain induced from the histotripsy bubbles incrementally fractionated the cells at the focus, forming a sharp lesion matching previous histological observations [6, 8-10]. As the treatment progressed, all the cells directly exposed to the histotripsy bubbles were completely fractionated, with the final region of cell damage closely corresponding to the bubble cloud area. Once the cells in the region exposed to the bubbles were removed, no further cell removal occurred during subsequent pulses. This observation shows the precision of histotripsy in creating lesions with sharply demarcated boundaries that will remain localized even if histotripsy is applied beyond the point of complete fractionation. Thus, the mechanical nature of histotripsy ensures damage will only occur in the regions in which bubbles are produced, preventing the risk of collateral damage from overtreatment as is common to other ablation methods such as thermal therapy.

Overall, the results from this chapter support our hypothesis that localized tissue fractionation is caused by the large strains induced by the expansion and collapse of the histotripsy bubbles, providing significant insight into the process of forming lesions with sharp boundaries between completely fractionated and intact tissue structures. In addition, cells at the bubble cloud boundary were deformed numerous times and often bisected multiple times before

removal, suggesting that the bisection of cells at the lesion boundary is caused by the incremental breakdown of the tissue (i.e. cells, ECM, cytoskeleton, cell-matrix adhesions). Although individual cell bisection was not observed during any of the single pulse experiments, the large deformations suggest rupture would occur if the strain was sufficiently large. Larger strains and cell bisection were observed during the multi-pulse experiments, likely due to the weakening of tissue structures from accumulating damage. These results suggest that histotripsy cell bisection is better understood by viewing cells as one component of a tissue network that includes both intracellular and extracellular structures. Cell bisection occurs as this matrix network is broken down, with cells simply being one component of the overall structure that is fractionated. This view of the histotripsy fractionation process helps to explain the previous observation that stiffer tissues are more resistant to histotripsy [25, 26], as changes and the stiffness of tissue components (i.e. cells, matrix, adhesions) would impact the strain induced by the bubbles. Future work will investigate the effects of histotripsy on a variety of cell types in phantoms with a range of ECM stiffness.

Another observation worth noting is that, for all experiments, bubbles were only generated in regions between cells, with no observed instances of cavitation forming inside of a cell. This finding suggests that the cavitation threshold is lower in the extracellular fluid space between cells than it is inside the cells. Previous work has indicated that histotripsy bubbles are formed in the water inside of the tissue [1, 3]. It is therefore possible that the ECM may have a lower cavitation threshold due to an increase in free water compared to the intercellular environment, which is densely packed and primarily contains water that is bound to proteins and ions [29, 30]. Future work will aim to aim to investigate this possibility.

8.5 Conclusion

This work represents the first time the histotripsy fractionation process has been viewed at the cellular level in a relevant tissue mimicking environment, with the results supporting our hypothesis that histotripsy tissue fractionation is caused by the large strains applied during both bubble expansion and bubble collapse. Results from single pulse experiments showed that the cell deformations produced by histotripsy occur during both bubble expansion and collapse, with the largest deformations and cell rupture observed for cells close to the bubble wall during collapse. In addition, results from multiple pulse experiments demonstrated that the mechanical strain induced from the histotripsy bubbles incrementally fractionated the cells at the focus, forming a sharp lesion matching previous histological observations. Overall, the results of this study provide an understanding of the tissue fractionation process that will help guide the future development of histotripsy.

8.6 References

[1] A. D. Maxwell, *et al.*, "Probability of cavitation for single ultrasound pulses applied to tissues and tissue-mimicking materials," *Ultrasound Med Biol*, vol. 39, pp. 449-65, Mar 2013.

[2] A. D. Maxwell, *et al.*, "Cavitation clouds created by shock scattering from bubbles during histotripsy," *J Acoust Soc Am*, vol. 130, pp. 1888-98, Oct 2011.

[3] E. Vlaisavljevich, *et al.*, "Effects of Ultrasound Frequency and Tissue Stiffness on the Histotripsy Intrinsic Threshold for Cavitation," *Ultrasound Med Biol*, 2015.

[4] E. Vlaisavljevich, *et al.*, "Histotripsy-induced cavitation cloud initiation thresholds in tissues of different mechanical properties," *IEEE Trans Ultrason Ferroelectr Freq Control*, vol. 61, pp. 341-52, Feb 2014.

[5] Z. Xu, *et al.*, "Investigation of intensity thresholds for ultrasound tissue erosion," *Ultrasound Med Biol*, vol. 31, pp. 1673-82, Dec 2005.

[6] J. E. Parsons, *et al.*, "Pulsed cavitational ultrasound therapy for controlled tissue homogenization," *Ultrasound Med Biol*, vol. 32, pp. 115-29, Jan 2006.

[7] Z. Xu, *et al.*, "Controlled ultrasound tissue erosion: the role of dynamic interaction between insonation and microbubble activity," *J Acoust Soc Am*, vol. 117, pp. 424-35, Jan 2005.

[8] T. L. Hall, *et al.*, "A real-time measure of cavitation induced tissue disruption by ultrasound imaging backscatter reduction," *IEEE Trans Ultrason Ferroelectr Freq Control*, vol. 54, pp. 569-75, Mar 2007.

[9] W. W. Roberts, *et al.*, "Pulsed cavitational ultrasound: a noninvasive technology for controlled tissue ablation (histotripsy) in the rabbit kidney," *J Urol*, vol. 175, pp. 734-8, Feb 2006.

[10] E. Vlaisavljevich, *et al.*, "Image-guided non-invasive ultrasound liver ablation using histotripsy: feasibility study in an in vivo porcine model," *Ultrasound Med Biol*, vol. 39, pp. 1398-409, Aug 2013.

[11] C. R. Hempel, *et al.*, "Histotripsy fractionation of prostate tissue: local effects and systemic response in a canine model," *J Urol*, vol. 185, pp. 1484-9, Apr 2011.

[12] A. D. Maxwell, *et al.*, "Noninvasive treatment of deep venous thrombosis using pulsed ultrasound cavitation therapy (histotripsy) in a porcine model," *J Vasc Interv Radiol*, vol. 22, pp. 369-77, Mar 2011.

[13] G. E. Owens, *et al.*, "Therapeutic ultrasound to noninvasively create intracardiac communications in an intact animal model," *Catheter Cardiovasc Interv*, vol. 77, pp. 580-8, Mar 1 2011.

[14] Z. Xu, *et al.*, "Noninvasive creation of an atrial septal defect by histotripsy in a canine model," *Circulation,* vol. 121, pp. 742-9, Feb 16 2010.

[15] N. R. Styn, *et al.*, "Histotripsy of VX-2 tumor implanted in a renal rabbit model," *J Endourol,* vol. 24, pp. 1145-50, Jul 2010.

[16] Y. Kim, *et al.*, "Developmental impact and lesion maturation of histotripsy-mediated non-invasive tissue ablation in a fetal sheep model," *Ultrasound Med Biol,* vol. 39, pp. 1047-55, Jun 2013.

[17] K. W. Lin, *et al.*, "Histotripsy beyond the intrinsic cavitation threshold using very short ultrasound pulses: microtripsy," *IEEE Trans Ultrason Ferroelectr Freq Control,* vol. 61, pp. 251-65, Feb 2014.

[18] A. D. Maxwell, *et al.*, "A tissue phantom for visualization and measurement of ultrasound-induced cavitation damage," *Ultrasound Med Biol,* vol. 36, pp. 2132-43, Dec 2010.

[19] E. Vlaisavljevich, *et al.*, "Nanodroplet-mediated histotripsy for image-guided targeted ultrasound cell ablation," *Theranostics,* vol. 3, pp. 851-64, 2013.

[20] K. A. Barbee, "Mechanical cell injury," *Ann N Y Acad Sci,* vol. 1066, pp. 67-84, Dec 2005.

[21] N. A. Hammond and R. D. Kamm, "Elastic deformation and failure in protein filament bundles: Atomistic simulations and coarse-grained modeling," *Biomaterials,* vol. 29, pp. 3152-60, Jul 2008.

[22] D. Kilinc, *et al.*, "Mechanical membrane injury induces axonal beading through localized activation of calpain," *Exp Neurol,* vol. 219, pp. 553-61, Oct 2009.

[23] G. Ofek, *et al.*, "Biomechanics of single chondrocytes under direct shear," *Biomech Model Mechanobiol,* vol. 9, pp. 153-62, Apr 2010.

[24] J. E. Parsons, *et al.*, "Cost-effective assembly of a basic fiber-optic hydrophone for measurement of high-amplitude therapeutic ultrasound fields," *J Acoust Soc Am,* vol. 119, pp. 1432-40, Mar 2006.

[25] E. Vlaisavljevich, *et al.*, "Effects of tissue mechanical properties on susceptibility to histotripsy-induced tissue damage," *Phys Med Biol,* vol. 59, pp. 253-70, Jan 20 2014.

[26] E. Vlaisavljevich, *et al.*, "Effects of Tissue Stiffness, Ultrasound Frequency, and Pressure on Histotripsy-induced Cavitation Bubble Behavior," *Phys Med Biol,* 2015.

[27] M. A. Kotlarchyk, *et al.*, "Concentration independent modulation of local micromechanics in a fibrin gel," *PLoS One,* vol. 6, p. e20201, 2011.

[28] T. Y. Wang, *et al.*, "An efficient treatment strategy for histotripsy by removing cavitation memory," *Ultrasound Med Biol*, vol. 38, pp. 753-66, May 2012.

[29] J. Fels, *et al.*, "The hydrogel nature of mammalian cytoplasm contributes to osmosensing and extracellular pH sensing," *Biophys J*, vol. 96, pp. 4276-85, May 20 2009.

[30] J. F. Leterrier, "Water and the cytoskeleton," *Cell Mol Biol (Noisy-le-grand)*, vol. 47, pp. 901-23, Jul 2001.

Chapter 9

Image-Guided Non-Invasive Liver Ablation using Histotripsy: Feasibility Study in an *in vivo* Porcine Model

A majority component of this chapter has been published in *Ultrasound in Medicine and Biology*

9.1 Introduction

Hepatocellular carcinoma (HCC) was the fastest growing cancer in the United States over the last decade with this trend expected to continue [2, 3]. While liver transplantation may be curative, only a small patient population will receive this treatment as tumors must be < 5 cm in diameter or 3 tumor nodules < 3 cm in diameter and confined to regions without major hepatic vessels. The limited donor availability also greatly constrains the number of liver transplants [2-4]. Surgical resection of liver tumors is a proven treatment option but is associated with high rates of morbidity and mortality [5]. Further, surgical resection or transplantation is not possible in many cases such as patients with decompensated cirrhosis [5, 6]. Radiofrequency ablation (RFA) is currently the standard local ablation therapy for liver cancer and has had success for selected populations in reducing mortality and morbidity when compared to surgical resection [5, 7]. Transarterial chemoembolization (TACE) and percutaneous ethanol injection (PEI) have also shown success in treating small liver tumors but are not as safe and effective as minimally invasive ablation methods [7-10].

Currently available minimally invasive ablation methods are mostly thermal based, including RFA, microwave therapy, cryoablation, and laser ablation [11-14]. While these minimally invasive therapies have shown some success, these methods share inherent limitations due to the heat sink effect originating from blood flow [15-18]. Thermal ablation is inconsistent in tissue with non-uniform heat dissipation patterns, which is common in hypervascular liver tumors [19]. In particular, for tissue near major vessels, thermal ablation often results in incomplete tumor necrosis [7, 20]. In addition, these methods are unsuitable for treating tumors larger than 3 cm or more than 3 nodules due to the excessive treatment time [15-18]. Another limitation facing these methods is the lack of imaging feedback during treatment. The treatment is evaluated before and after by computer tomography (CT) or magnetic resonance imaging (MRI) while no real-time imaging provides monitoring during treatment [12, 15, 16]. There remains an unmet clinical need for a local ablation method capable of overcoming these limitations.

High intensity focused ultrasound (HIFU) is a non-invasive thermal ablation technique [21, 22]. The current HIFU systems use MRI thermometry to provide real-time monitoring of the thermal dose during treatment [23-26]. With its non-invasiveness, real-time MRI feedback, the ability to scan the focal zone over a large tumor volume, HIFU has the promise to improve upon the current liver ablation methods [27-29]. However, as a thermal-based method, HIFU is still affected by the heat sink effect, resulting in the reduced effectiveness in ablating tissue near major blood vessels and extended treatment time for larger hypervascular liver volumes [26, 30].

Histotripsy is a non-invasive non-thermal ultrasonic ablation method that fractionates tissue through the precise control of acoustic cavitation [31-33]. Using microsecond, high-pressure pulses applied by an ultrasound transducer outside the body and focused to the target

tissue, a cluster of microbubbles are generated and the energetic expansion and collapse of the microbubbles fractionates cells at the target. With a sufficient number of pulses, the target tissue can be completely fractionated to a fluid homogenate with no recognizable cellular structures. Since histotripsy is non-thermal, it is not affected by the heat sink effect from blood vessels and does not have the limitations associated with thermal ablation methods. Histotripsy can produce consistent and fast fractionation of tissue with different heat dissipation patterns, even when the tissue is in proximity to major vessels [34-37]. The fractionation is often self-limited at the boundaries of major vessels with surrounding tissue completely homogenized. As a non-invasive ablation method, the therapy focus can be scanned to treat a large tumor volume (>3cm) and multiple nodules in a reasonably short period of time. Further, the histotripsy cavitation cloud can be visualized with ultrasound imaging, allowing precise targeting [35, 36, 38]. The change in tissue during treatment can be also be directly monitored using standard imaging modalities such as ultrasound and MRI, which allows histotripsy to be guided in real time [39, 40].

A major challenge facing the non-invasive treatment of liver cancer using ultrasound is to overcome the rib obstruction. Skin burns and subcostal edema have been reported in clinical HIFU liver ablation cases [41-43]. For transthoracic ablation of the liver using HIFU, ribs in the ultrasound pathway cause periodic blockage of ultrasound, resulting in a significantly decreased main lobe and increased grating lobes [23, 25, 44]. Moreover, due to the high ultrasound absorption coefficient of bone and reflection effects at the bone-tissue interface, overheating of ribs and surrounding tissue often results in unwanted tissue damage. Phased arrays and aberration correction algorithms have been developed to switch off the elements blocked by the ribs to reduce overheating to the ribs and associated tissue [23, 24]. Even with these improvements, grating lobes may still remain producing undesired heating and collateral damage.

Histotripsy is more resistant to the grating lobes caused by rib aberration as the cavitation cloud is only generated when the pressure exceeds a distinct threshold. By using an appropriate pressure where the main lobe is above the threshold while the grating lobes are not, a confined cloud within the main lobe and a precise lesion can be produced despite the intervening ribs [45]. Thermal damage to the overlying and surrounding tissue is also prevented by using prolonged cooling times between pulses.

In this chapter, we investigate the feasibility of developing histotripsy for non-invasive liver ablation. Previous *in vivo* animal studies have investigated histotripsy for many applications where non-invasive tissue removal is desired including treatment for benign prostatic hyperplasia [46, 47], congenital heart disease [38, 48], thrombolysis [36], renal tumor ablation [37], and fetal interventions including the treatment of fetal liver [35]. However, liver fractionation using histotripsy involves challenges not present in these previous studies, such as considerable bone obstruction and the ability to treat large lesions (>3cm) adjacent to major blood vessels. In this work, an *in vivo* porcine liver model was used due to its size and anatomic similarities to its human counterpart. First, histotripsy was used to generate consistent and complete fractionation of hepatic parenchyma through ribs and overlying tissue in various locations spanning all major regions of the liver. Second, the capability of ablating large regions in the liver was investigated. Finally, the effectiveness of tissue-selective ablation using histotripsy to fractionate the liver surrounding major blood vessels and gallbladder while preserving these critical structures was tested.

9.2 Methods

9.2.1 Porcine Surgical Procedures

A total of 8 healthy 60-90 pound mixed breed pigs were used. Each pig was pre-medicated with Telazol (6 mg/kg, Fort Dodge) and Xylazine (2.2 mg/kg, small animal AnaSed from Lloyd Labs), and an intravenous catheter was placed in the auricular ear vein. Pigs underwent endotracheal intubation with a 6-8 mm diameter endotracheal tube and were maintained under full anesthesia on isoflurane gas (1.5-2.0%, Vet One) for the duration of the surgical procedure. Vital signs monitored throughout the experiments included SpO_2, heart rate, respiration, and core body temperature with a Heska vet/ox plus 4800. Anesthetized pigs were placed in a dorsal recumbent position on the surgical table, and the skin over the targeted tissue was treated with a depilatory cream to improve ultrasound coupling. To ensure ultrasound propagation to targeted tissue, a degassed water bolus was coupled to the skin with a thin plastic membrane and ultrasound coupling gel [Fig. 9.1]. An 8 MHz phased array ultrasonic imaging probe (Model S8, used with Sonos 7500 imaging system, Philips Electronics, Andover, MA) was fixed coaxially with the histotripsy therapy transducer. The focal position of the therapy transducer in the imaging field of view was found prior to therapy by generating a bubble cloud in degassed water and identifying the location of the hyperechoic region. The location of the bubble cloud was marked on the ultrasound imager screen as an "x" to indicate the transducer focal position in free field. The therapy transducer was subsequently submerged in the water bowl for treatment. Targeting was achieved by aligning the focus marker ("x") to the selected treatment region in the liver. Histotripsy treatment was applied transcutaneously with a portion of the rib cage within the acoustic pathway. Within three hours after treatment, the pigs were euthanized without recovery with a sodium pentobarbital (140-160 mg/kg, Vet One) intravenous

injection. The treated livers were harvested for examination and tissue layers overlying the treatment target were visually inspected for signs of injury. All procedures used in this work were reviewed and approved by the University Committee on Use and Care of Animals at the University of Michigan.

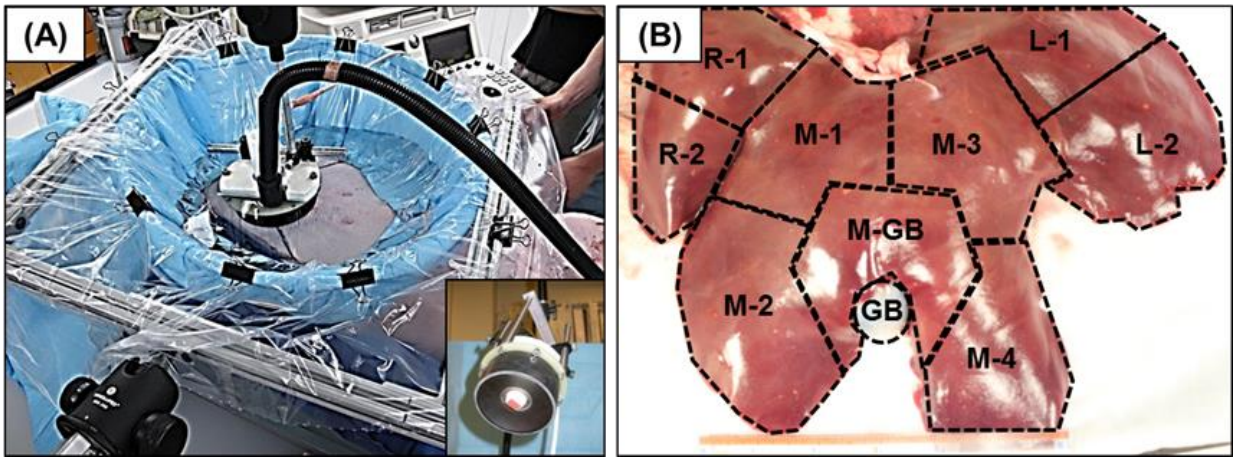

Figure 9.1. Histotripsy *in vivo* porcine liver ablation experimental setup. (A) A 1 MHz histotripsy therapy transducer with coaxially aligned ultrasound imaging probe (insert) was attached to a motorized 3D positioning system controlled using a PC console and coupled to the pig with a degassed water bolus. (B) Histotripsy was applied transcutaneously through ribs and overlying tissue with treatments targeted to all positions within the liver. Specific treatment information is listed in Table 9.1.

9.2.2 Lesion Generation through Ribs and Overlying Tissue

To demonstrate the ability of histotripsy to achieve consistent and efficient liver fractionation through overlying ribs and other intervening tissues, 12 histotripsy lesions were created in 6 pigs with treatment locations spanning various regions of the liver [Fig. 9.1(B)]. Histotripsy pulses were generated by a 1 MHz focused ultrasonic transducer (Imasonic, Besançon, France) with an aperture of 100 mm, focal length of 90 mm, and focal volume of 2.2×2.2×15 mm (defined by -6dB from the peak negative pressure). Histotripsy pulses of 10 cycles and 500 Hz pulse repetition frequency (PRF) were applied to the liver. The PRF used in

this work has previously been used to successfully treat fetal liver in an *in vivo* sheep model through overlying tissue including fetal bones [35].

Acoustic waveforms produced by the 1 MHz therapeutic transducer were measured in free field using a fiber optic hydrophone built in house [49]. Pressure wave measurements were recorded in free-field in degassed 1,3-Butanediol (Sigma-Aldrich) at room temperature. Calibration was performed in 1,3-Butanediol to prevent cavitation at the fiber tip, which allowed the measurement of the acoustic waveforms at a high-pressure level. To avoid the attenuation by Butanediol, the fiber tip was placed such that the ultrasound only travelled through 5 mm Butanediol before reaching the tip. Free field peak negative pressure values used in this work were between 23 MPa and 27 MPa. The *in situ* focal pressures could not be directly measured non-invasively. With 30-50% of the aperture covered by rib cage, 4-6 cm overlying tissue, and using 0.5 dB/cm-MHz attenuation for the overlying tissue, the *in situ* peak negative pressure was estimated to 14-17 MPa. To apply the treatment, the acoustic pressure was incrementally increased until a confined bubble cloud was visualized on ultrasound imaging. As such, a peak pressure right above the threshold to generate a bubble cloud in that treatment tissue was used for each treatment, which also allowed us to limit the cavitation cloud within the main lobe and prevent forming cavitation in the grating lobes.

After cloud initiation, histotripsy lesions were generated by mechanically scanning the therapy focus to follow a 5×5×5 mm cubic grid. Each point in the grid was treated for 8 seconds (4,000 pulses) before the focus was moved to an adjacent spot 1 mm apart. The eight-second treatment time per location was used here instead of the two seconds used in the fetal sheep liver treatment in our previous study, because the mechanical strength of the adult porcine liver is significantly higher than that of the fetal sheep liver [35]. Due to the finite size of the bubble

cloud, the effective treatment volume resulted from the scan was approximately 7.2×7.2×20 mm. The procedure was monitored in real-time with ultrasound imaging. Pre-treatment and post-treatment ultrasound images of the targeted region were collected for comparison purposes. After the pigs were euthanized, the ribs and overlying tissues were visually examined for signs of damage. The liver was harvested, imaged with MRI, and fixed in formalin for histological processing and evaluation.

9.2.3 Larger Lesion Ablation

To demonstrate the ability of histotripsy to ablate a larger region of liver tissue, two larger focal scans were performed in separate experiments covering scanned volumes of 12 cm^3 (3×2×2 cm scan) and 18 cm^3 (3×3×2 cm scan). Due to the size of the bubble cloud, the effectively treated volumes were estimated to be 3.2×2.2×3.5 cm and 3.2×3.2×3.5 cm. Histological analysis of the twelve lesions formed in the previous section was conducted before these experiments and suggested an overtreatment. Therefore, the treatment time per point was decreased to 4 seconds (2000 pulses). The spacing between points was also increased for the larger liver volume treatment, with 2 mm transverse spacing and 5 mm axial spacing. Prior to the *in vivo* experiments, these treatment parameters were validated in *ex vivo* porcine liver. The total treatment times for the two larger lesions formed here were 26.7 minutes and 60 minutes, respectively. The treatment region was examined with ultrasound imaging before, during, and after treatment including Doppler images of the blood vessels. After treatment, the livers were harvested for MRI and histological evaluation.

9.2.4 Tissue-selective Liver Ablation

To study the effectiveness of histotripsy to fractionate tissue near major vessels and the gallbladder while preserving these critical structures, treatments were selectively targeted to regions containing major vessels and gallbladder. We hypothesize that the relatively higher mechanical strength of these tissues compared to liver parenchyma will allow their preservation while the surrounding liver parenchyma with lower mechanical strength can be completely fractionated. The locations containing major hepatic blood vessels and gallbladder were identified using ultrasound imaging. The gallbladder cavity was hypoechoic compared to the surrounding liver. The major hepatic vessels were identified by detecting the blood flow using ultrasound Doppler imaging. After identifying these anatomical structures in the liver, histotripsy treatment was applied to the regions containing these structures using the acoustic parameters described above. The structures and surrounding liver tissue treated by histotripsy were evaluated by 2D ultrasound imaging during and after treatment to monitor any potential damage. Ultrasound Doppler images of blood vessels within the treated region were taken before and after treatment to determine if blood flow patterns changed after therapy. After treatment, the integrity of vital anatomical structures was assessed with MRI and histological analysis.

9.2.5 Liver MRI

MRI is the standard clinical imaging method to diagnose and evaluate tumor response to treatment. To evaluate the acute aspect of histotripsy-induced lesions in the liver by MRI, porcine liver samples were harvested and imaged *ex vivo* by a 7T small animal scanner (7.0 Tesla, 310 mm bore, Varian, Inc, Walnut Creek, CA) prior to fixing for histological evaluation. The reason why the pig liver was not imaged by MRI *in vivo* is because our small animal scanner

was not large enough to accommodate the entire pig. The samples were embedded in a gelatin mold prior to imaging. Both T1 and T2 weighted multi-slice spin-echo images of the liver were acquired along coronal and axial planes. MRI parameters were optimized for each sample but stayed within the following ranges: repetition time of 900-3000 ms, echo delay time of 13-30 ms, field of view of (50-150)×(50-150)×(1-40) mm, and acquisition times between 2-45 minutes.

9.2.6 Histological Evaluation

Treated porcine liver samples were harvested after experiments and fixed in 10% buffered formalin (Fisher Scientific). Lesion gross morphology was examined prior to histological analysis. Samples were then stained with hematoxylin and eosin (H&E) and examined under a microscope (Nikon Eclipse 50i) using 4x, 10x, 20x, and 40x objective lenses. To quantitatively assess the distribution of intermediate sized blood vessels remaining after histotripsy, the number of vessels between 50-1000 μm in diameter was counted using four H&E slides of the largest lesion, as it was the only lesion containing sufficient number of vessels for quantitative assessment. For each H&E slide, one hundred 1 mm^2 subareas (10x fields of view) within the treatment region and in the intact liver tissue outside the treatment region (control) were observed under microscope. Vessels between 50-1000 μm were counted, recorded, and organized into six groups: vessels <50 μm, 50-100 μm, 100-200 μm, 200-300 μm, 300-400 μm and 400-1000 μm. The total number of vessels over the one hundred subareas (total 100 mm^2) for each group was calculated on each slide. The mean and standard deviation of the number of vessels for each group over four slides were calculated for both treatment and control samples. To compare the treatment and control samples, a Student's t-test was conducted for each vessel

group between treatment and control samples (n=4) and p <0.01 was considered statistically significant.

9.3 Results

9.3.1 Lesion Generation through Ribs and Other Overlying Tissue

To demonstrate the ability of histotripsy to non-invasively generate precise liver lesions through ribs and overlying tissue, twelve histotripsy treatments were performed on six pigs. Therapy was targeted to locations spanning the entire liver with lesions formed in the superior and inferior regions of the left, middle, and right lobes. Treatments were performed through 3-6.5 cm of overlying tissue with rib cage covering 30-50% (including intercostal space) of the transducer aperture [Table 9.1].

Table 9.1. Histotripsy lesion generation through ribs and overlying tissue parameters. Table shows an overview of the ribcage coverage (including intercostal space), overlying tissue depth, and liver location for 12 histotripsy lesions. Treatments covered all regions of the liver and were further targeted to areas containing critical anatomical structures such as the gallbladder (GB) or major hepatic blood vessels (BV). Bubble cloud initiation was achieved for all treatments resulting in histotripsy lesions with a maximum diameter between 1 cm and 2.2 cm.

Treatment	Pig Weight	Rib Coverage	Depth	Liver Location	Proximity to Vital Structures
1	76#	30%	5 cm	L-1	Near BV
2	76#	45%	5 cm	M-2	Near BV
3	60#	45%	6 cm	M-4	Near BV
4	60#	30%	6.5 cm	M-3	Near BV
5	85#	40%	6 cm	R-1	Near BV
6	85#	30%	3 cm	L-2	Near BV
7	80#	35%	4.5 cm	R-2	Containing BV
8	80#	30%	4 cm	M-GB	Near BV and GB
9	80#	35%	6 cm	R-1	Near BV
10	80#	40%	6.5 cm	L-1	Containing BV
11	88#	50%	6.5 cm	M-1	Containing BV
12	88#	45%	6 cm	M-GB	GB Surface

A bubble cloud was successfully generated in the liver for all twelve treatments and visualized as a hyperechoic zone on ultrasound imaging allowing for real-time treatment monitoring [Fig. 9.2(A-B)]. In all treatments, the bubble cloud locations in the liver tissue (i.e. the *in situ* focal position) were within 3 mm of the marker representing the free-field focal position as shown in Figure 2. The creation of liver lesions of ~1 cm^3 from histotripsy therapy was confirmed for all twelve treatments. The treatment time for all lesions in this section was 16.7 minutes.

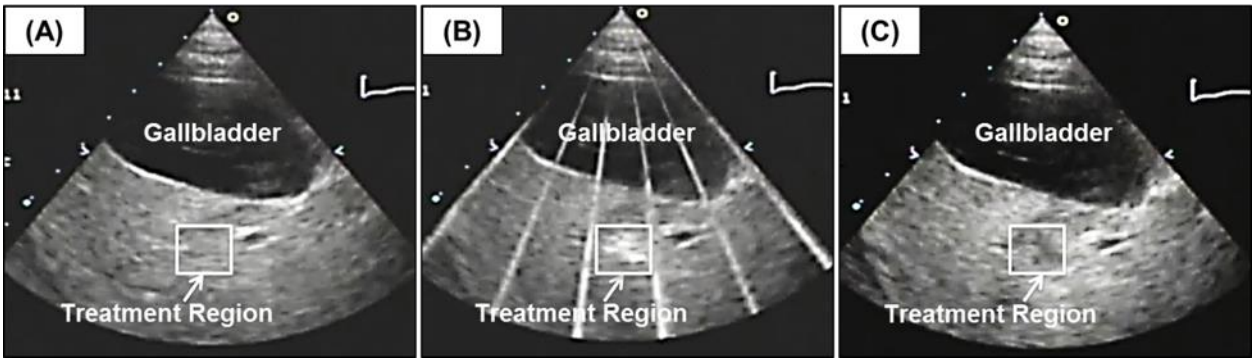

Figure 9.2. Liver ablation was guided by ultrasound imaging in real-time. Images show the histotripsy liver treatment monitored by ultrasound imaging before (A), during (B), and after (C) treatment. Prior to each treatment, the bubble cloud was generated in free water with the free-field focal location marked as an "x" on the ultrasound image (A). The histotripsy bubble cloud appears as a dynamically changing hyperechoic region on ultrasound imaging (B) while the resulting lesion appears hypoechoic (C) resulting from fractionation of liver parenchyma.

Lesions were assessed using ultrasound imaging after histotripsy. Histotripsy-induced fractionation often appears as a hypoechoic zone on ultrasound imaging due to the reduced size and density of the sound scatterers present in the fractionated zone. After each treatment, the average speckle amplitude within the treatment region was calculated and compared to that of surrounding intact liver tissue (control). In 8 of 12 lesions, there was a statistically significant decrease in average speckle amplitude (>3 dB, p-value <0.001; Student's t-test) of the treatment region compared to control. As such, the treated regions appeared as hypoechoic zones for these 8 lesions with an average decrease in backscatter intensity within the treated regions of 3.9±0.7

dB. In the remaining 4 lesions, the average speckle amplitude of the treatment region was not significantly different from control (<3 dB, p-value >0.001) with an average decrease in backscatter intensity within the treated regions of 1.2±1.6 dB. The detailed steps to calculate the average backscatter intensity in the treatment region and in the surrounding tissue have been described in a previous study [40].

After treatment, the excised liver was assessed with MRI. All twelve lesions were observed as bright, hyper-intense regions on MRI with increased T2 relaxation times for fractionated homogenate. There was a significant increase in average T2 relaxation times which was 24±1.3 ms for the histotripsy lesion compared to 17±1.8 ms for the surrounding intact liver (p=0.0015). The location and size of the lesions shown in MRI correlated well with those evaluated from gross morphology [Fig. 9.3(A)]. Additionally, dark, hypo-intense regions within the lesion were observed on MRI for certain samples corresponding to blood accumulation.

Histological evaluation of histotripsy lesions showed complete fractionation of hepatic parenchyma inside the treated volume [Fig. 9.3(B-F)]. The histotripsy lesions contained sharp boundaries with only a small area of partially ablated liver tissue <500 μm for all treatments likely caused by respiratory motion. Additionally, localized hemorrhage was often observed inside the histotripsy lesion or accumulated along the lesion boundary. No hemorrhage was observed in surrounding intact liver tissue. Overlying tissues in the acoustic path were examined after treatment for signs of potential damage. Gross morphological examination showed no signs of damage to overlying skin, muscle, or ribs. The vital signs of the pigs showed no negative responses to histotripsy. During and after treatment, the SpO_2 remained above 95%. The fluctuation of the heart rate and respiration rate was maintained within ±10% of the baseline

values observed before treatment. The core body temperature did not drop more than 1° throughout the duration of the treatment.

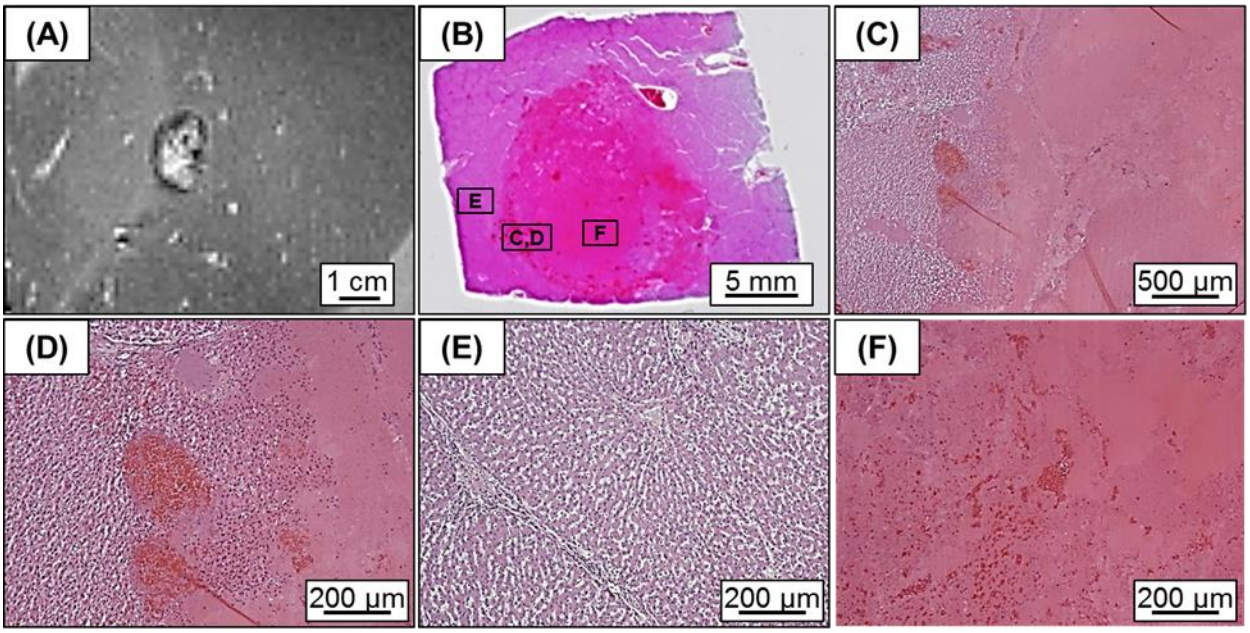

Figure 9.3. Histotripsy treatment caused complete removal of liver parenchyma. Histotripsy liver lesions appear hyper-intense on MRI imaging (A) corresponding to the fractionated liver tissue. Histological evaluation (B) demonstrates histotripsy completely fractionated liver parenchyma into acellular debris (F) without damaging surrounding liver tissue (E). Histotripsy lesions contained sharp boundaries of approximately a few hundred micrometers between homogenized and intact liver tissue (C, D).

9.3.2 Larger Lesion Ablation

To demonstrate the ability of histotripsy to ablate larger sections of liver, two larger lesions were created. MRI multi-slice analysis showed lesion volumes of approximately 2.2×2.3×3.5 cm (18 cm^3) and 5×4×3 cm (60 cm^3) [Fig. 9.4]. Treatment times were 26.7 minutes and 60 minutes for the 18 cm^3 and 60 cm^3, respectively, with no negative responses in the vital signs of the pigs observed during treatment. While the 18 cm^3 lesion was slightly smaller than the predicted scan volume plus the estimated bubble cloud size (3.2×2.2×3.5 cm), the 60 cm^3 lesion was significantly larger than the scan volume with the bubble cloud size included

(3.2×3.2×3.5 cm) as a result of substantial respiratory motion. Liver movement from breathing during the 60 cm^3 lesion treatment showed significantly larger displacement (~1 cm) compared to the 18 cm^3 lesion (~2-4 mm) and the twelve smaller lesions, which resulted in the significantly larger lesion volume than the scanned volume. Histological analysis demonstrated completely fractionated liver parenchyma throughout the treated volume with a transition zone between the fractionated tissue and intact region of <500 μm for both larger lesions.

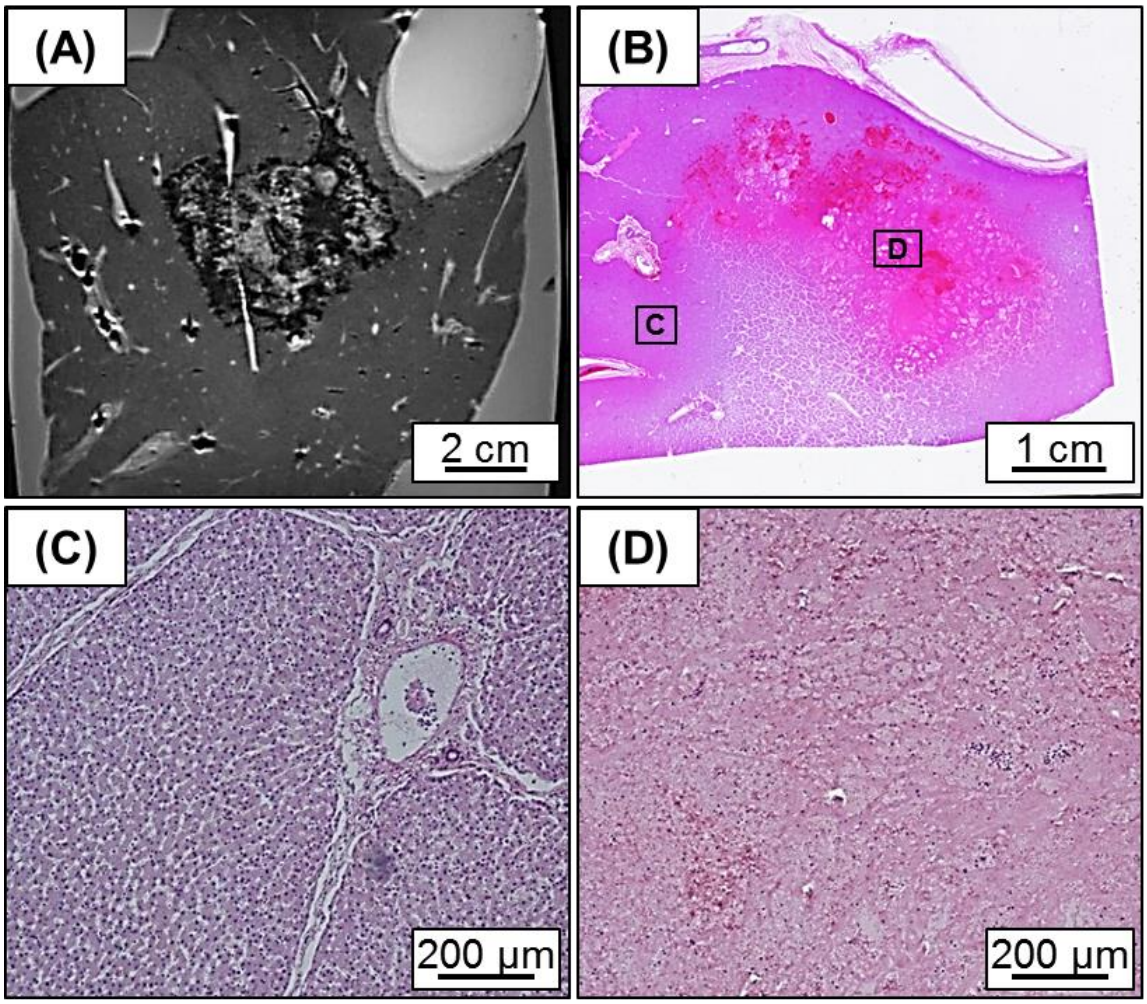

Figure 9.4. Large lesion ablation. Results show histotripsy-generated fractionation of large volumes in the liver. MRI multi-slice analysis demonstrated liver volume of approximately 5x4x3 cm (60 cm^3) (A) was ablated. Histology (B) demonstrated histotripsy caused complete ablation throughout the large focal regions (D) without causing damage to surrounding tissue (C).

9.3.3 Tissue-selective Liver Ablation

To determine the ability of histotripsy to fractionate the liver tissue near major blood vessels and gallbladder while preserving these critical structures within the treatment region, multiple histotripsy treatments were targeted to regions near or containing major hepatic vessels and gallbladder. Results demonstrated that blood vessels and gallbladder remained structurally intact inside the completely fractionated region [Fig. 9.5]. There were no vital sign alterations in any of the pigs undergoing treatments performed near critical vessels or the gallbladder.

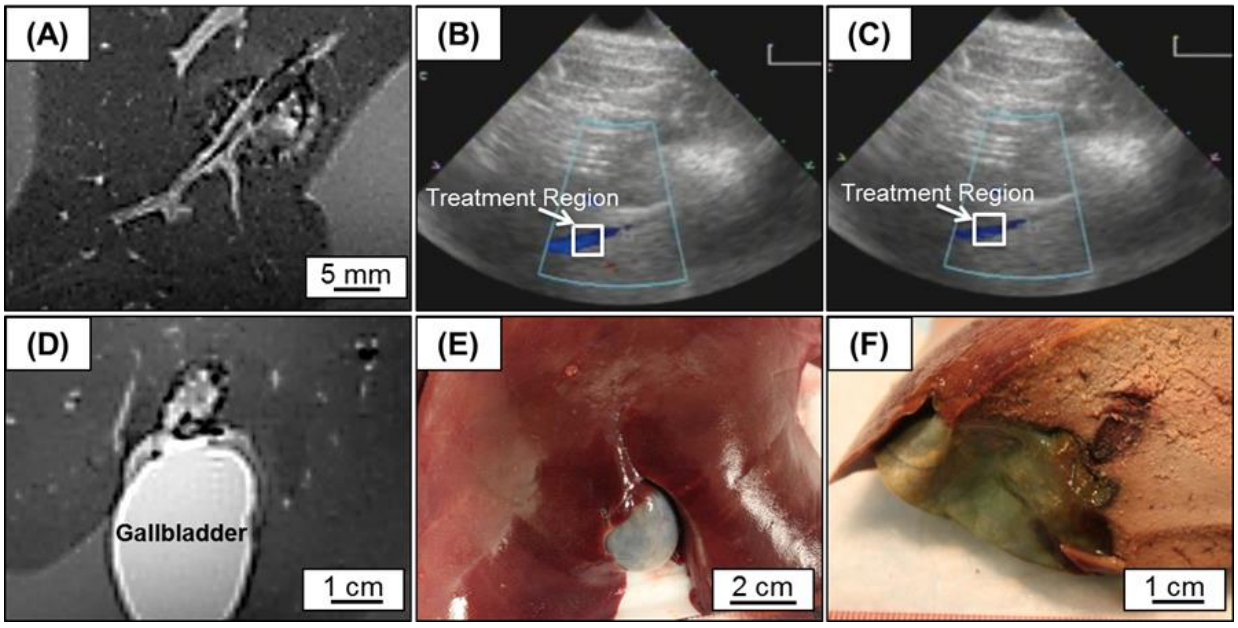

Figure 9.5. Gallbladder and hepatic vessels remained intact and functional within histotripsy treated region. MRI images demonstrate blood vessels (A) and gallbladder (D) remain structurally intact within the histotripsy focal volume while surrounding liver parenchyma was completely ablated. Doppler ultrasound images before (B) and after (C) histotripsy indicated that large vessels remained functional after treatment. Morphological observation of histotripsy lesions bordering the gallbladder (E, F) showed no signs of damage to the gallbladder itself.

Histotripsy completely fractionated hepatic parenchyma surrounding blood vessels without inducing perforation or visible damage to the vessel wall. MRI images showed that large intact blood vessels >1mm in diameter remained within the fractionated region [Fig. 9.5(A)]. Post-treatment Doppler images demonstrated that the large vessels had continued blood flow

with no observed perforation [Fig. 9.5(B-C)]. Histological evaluation showed that liver parenchyma was completely fractionated into acellular debris surrounding these vessels while no observable damage was seen in any of the large vessels inside the treated region.

Histological evaluation further demonstrated an extensive network of undamaged intermediate vessels below 1 mm diameter throughout the completely fractionated liver lesion [Fig. 9.6(A-B)]. Additionally, many smaller blood vessels and bile ducts were observed inside the lesion often accompanied by a surrounding connective tissue [Fig. 9.6(C-D)]. Six groups of vessels (<50 μm, 50-100 μm, 100-200 μm, 200-300 μm, 300-400 μm and 400-1000 μm in diameter) were counted in four H&E slides of the 60 cm^3 lesion. Figure 9.7 shows the number of vessels (mean ± standard deviation) for six vessel groups in treatment and control samples (n=4). Results demonstrated no vessels below 50 μm remained in the treatment region. For the 50-100 μm vessel group, there was a statistically significant decrease in the number of vessels ($p<0.01$). The mean number of vessels was 68.5 and 5 for the control and treatment samples, respectively, reduced by 92.7%. The mean number of vessels in 100-200 μm and 200-300 μm groups in the treatment region was decreased by 47.2% and 34.1% in comparison to the control, but these decreases were not statistically significant ($p>0.1$). The change in the mean number of vessels for 300-400 μm or 400-1000 μm vessel groups was both low, within 15% with no statistically significant difference ($p>0.3$). The small vessels (<100 um) that survived were mostly located surrounding larger hepatic structures that were protected by the extensive connective tissue. Localized hemorrhage was visible within the histotripsy lesion due to the rupture of capillaries and smaller vessels.

Results for treatments applied near the gallbladder demonstrated that histotripsy completely fractionated the liver up to the gallbladder without causing perforation even when the

bubble cloud was actively targeted to a region encompassing the gallbladder-liver interface [Fig. 9.5(D-F)]. No visible damage or perforation to the gallbladder was observed under gross inspection of harvested samples. This finding was verified with MRI showing that the histotripsy lesion extended up to gallbladder wall without perforation.

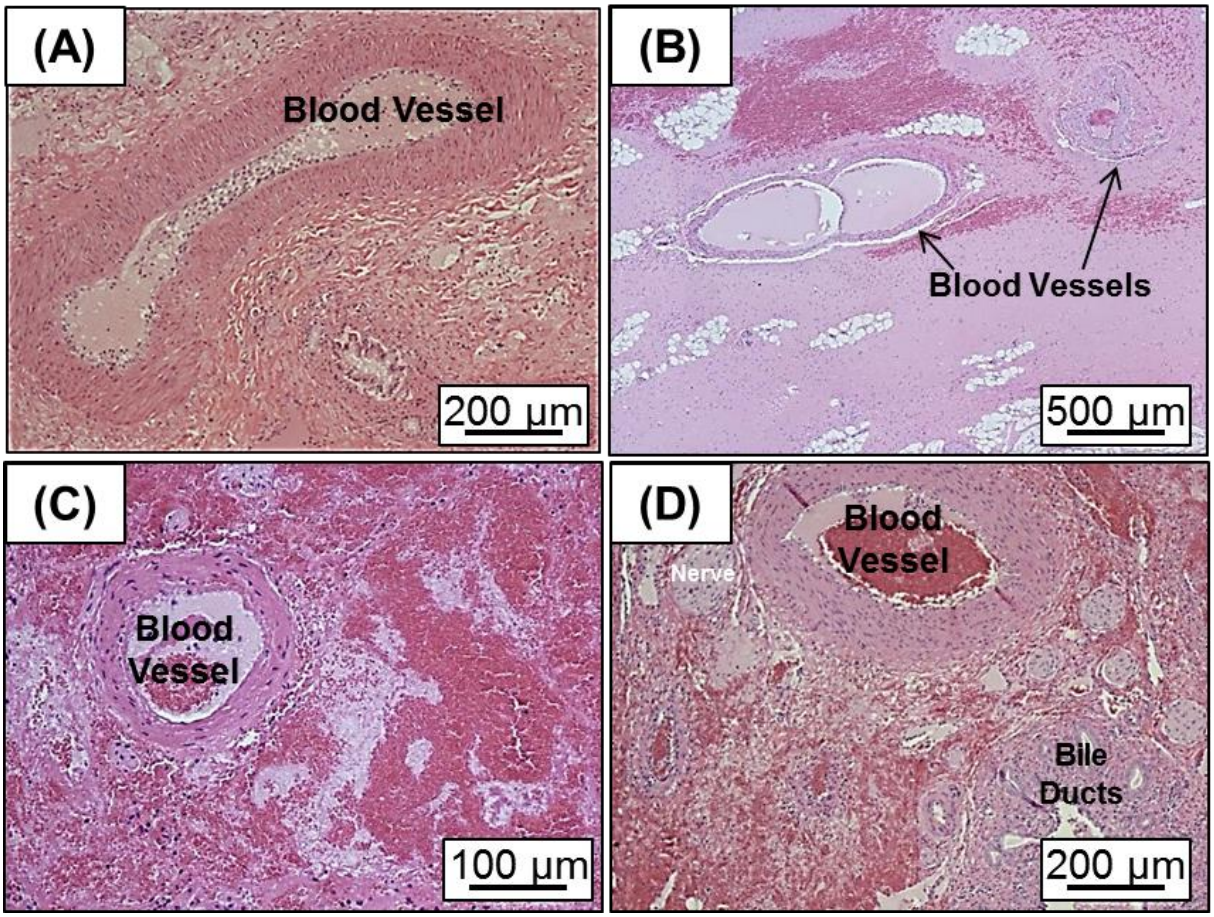

Figure 9.6. Histological evaluation of histotripsy lesions surrounding hepatic blood vessels. Results show that the tissue surrounding blood vessels was completely fractionated while blood vessels remained intact (A-D). All large and medium sized arteries (A) and veins (B) were observed to remain intact with no observed perforations. Multiple smaller blood vessels (B, C, D) and bile ducts (D) were also observed inside the histotripsy lesion. The smallest vessels observed to remain intact were approximately 50-100 µm in diameter. Localized hemorrhage within lesion resulted from rupture of capillaries and small vessels <100 µm in diameter.

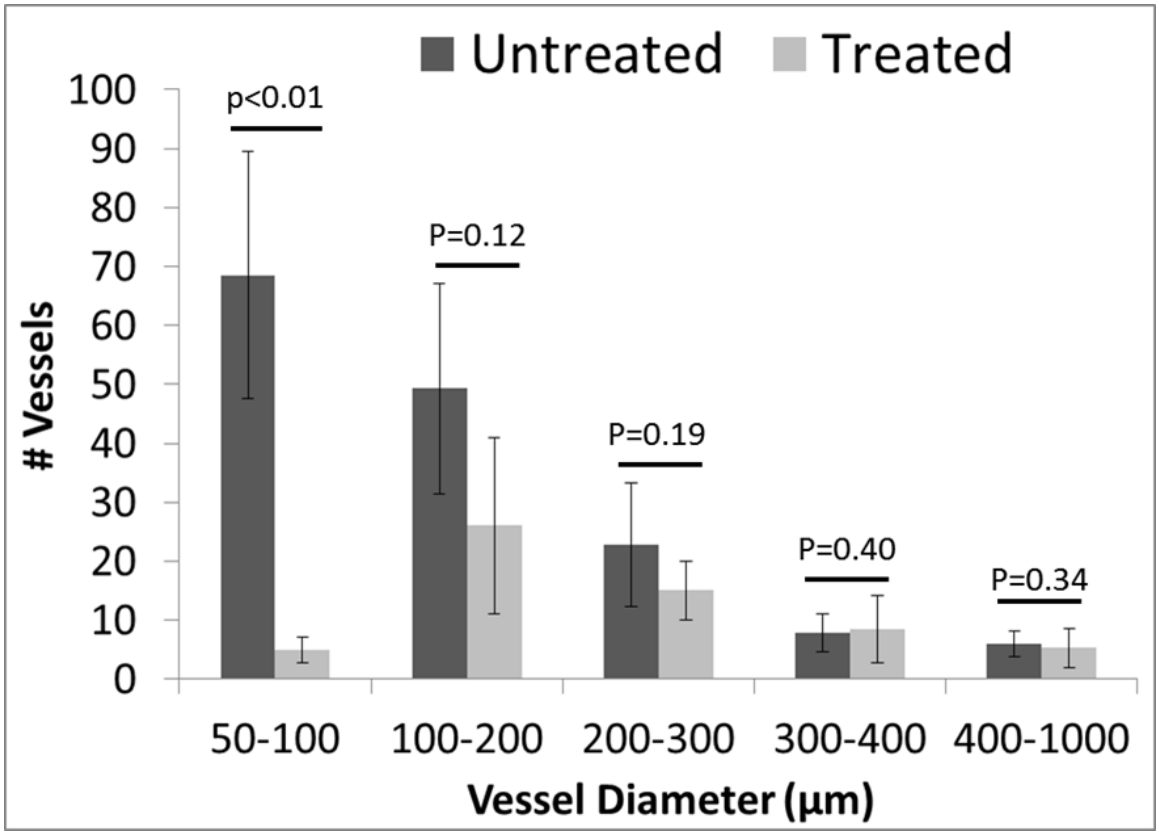

Figure 9.7. The number of vessels between 50-1000 µm were counted within a 100 mm2 region (n=4) within the histotripsy lesion and intact liver tissue. Results indicate a significant decrease in blood vessels between 50-100 µm ($p<0.01$). A decrease was observed for 100-200 µm and 200-300 µm vessels but was not significant ($p>0.1$) as a result of the high variability between samples. No significant differences in vessel count were observed between the histotripsy lesion and intact liver tissue for 300-400 µm and 400-1000 µm vessels. No blood vessels <50 µm were observed to remain within the histotripsy lesion after treatment.

9.4 Discussion

In this chapter, we investigated the feasibility of using histotripsy for non-invasive liver ablation in an *in vivo* porcine model. Results demonstrate that histotripsy created precise lesions at locations throughout the entire liver through ribs and overlying tissue without using aberration correction. Bubble clouds were successfully initiated and lesions were formed in all treatment attempts. The different heat dissipation patterns associated with regions containing different vasculatures did not affect the consistency of histotripsy liver ablation. Within the main

treatment region, the liver tissue was completely fractionated to acellular debris with only small regions of partially damaged tissue present near the lesion boundary.

Overcoming rib obstruction is a major concern for the non-invasive treatment of liver cancer using ultrasound. Recent advancement in aberration correction algorithms has allowed liver ablation using extracorporeal HIFU [50]. As the cavitation cloud is only generated when pressure exceeds a distinct threshold, histotripsy is more resistant to the increased grating lobes caused by the aberration effect from ribs in comparison to thermal therapy [45]. Previous studies have shown histotripsy ablation through neonatal porcine [38] and fetal sheep [35] ribs, but the neonatal and fetal ribs were not well calcified. This is the first time histotripsy lesions have been generated without using aberration correction through intact ribs in an adult large (porcine) animal model. In this work, the hyperechoic bubble cloud generated through the ribs and other overlying tissue was always within 3-mm of the transducer free-field focal position, as viewed on the ultrasound image. If needed, the focal position of the transducer can be adjusted to ensure the hyperechoic bubble cloud is right on the targeted tissue before treatment is applied. The ultrasound imaging pulses can be triggered by the therapy pulses, and, as such, only a few therapy pulses are sufficient to generate and view the bubble cloud for targeting before any significant damage is produced. No visual damage was observed to the ribs and overlying tissue, but a more in depth study using thermocouple measurements may be needed to investigate the potential temperature increases to the ribs and surrounding tissue. However, with the prolonged cooling time between histotripsy pulses, the temperature increase to the overlying tissue is expected to be low.

The histotripsy cavitation cloud in this work was monitored as a hyperechoic region using ultrasound imaging with treatment scans guided in real-time. Lesion assessment after

treatment indicated that damage only occurred in regions exposed to the cavitating bubble cloud. After treatment, the fractionated zone generally appears hypoechoic on ultrasound imaging, although this was not the case for 4 of the 12 initial treatments as a result of the degraded ultrasound image quality through significant overlying tissue. Current work in our laboratory is investigating methods to improve the ultrasound imaging feedback for histotripsy lesions, including ultrasound elastography-based feedback [51]. Further, results demonstrate that histotripsy lesions can be clearly visualized on spin-echo MRI for all lesions after treatment. While histotripsy lesions have been viewed extensively on ultrasound in the previous studies [32, 35, 36, 40, 47], only one study used MRI to image the histotripsy lesions generated *in vitro* [39]. This study is the first time a histotripsy-induced *in vivo* liver lesion has been visualized using MRI.

This work also studied the effectiveness of histotripsy to fractionate liver tissue near major vessels and gallbladder while preserving these critical hepatic structures. Thermal ablation methods are often ineffective in ablating tissue near major vessels or produce incomplete ablation surrounding vessels [52]. Our previous work has shown that tissues of increased mechanical strength are more resistant to histotripsy damage [47, 53]. In this work, the major hepatic vessels (>1 mm) and the gallbladder remained intact while the surrounding hepatic parenchyma was fractionated. This finding suggests that histotripsy can be effective and safe for treating tumors near major vessels and gallbladder. Leaky tumor vessels, which generally have a lower mechanical strength in comparison to normal vessels [54], are expected to be ablated along with the tumor tissue while the normal large hepatic vessels will be preserved.

In addition to large blood vessels, an extensive network of smaller vessels remained inside the treatment region. While the results of this study demonstrated all vessels <50 μm and

the majority of 50-100 μm vessels were removed, there was no significant decrease in vessels larger than 200 μm. In this study, we only performed measurement for one lesion that was large enough to contain sufficient vessel number for statistical analysis. The size distribution of remaining vessels inside a histotripsy lesion likely depends upon the acoustic parameters and treatment times. Future work will be needed to further study the effects of histotripsy on intermediate sized blood vessels. It is worth noting that, while preferable, the preservation of intermediate sized vessels (<1mm) is not a primary clinical concern for liver ablation as it is with the major vessels (>1mm).

One major concern for current liver ablation therapy, including HIFU, is the extended treatment time for large liver tumor volumes. The treatment time for recent clinical HIFU cases ranged from 2-4 hours for tumors >4cm in diameter [43] or 1-6 hours for tumors >1.7 cm in diameter [55]. When combined with TACE to inject chemotherapy agents in patients to decrease tumor blood flow, the HIFU treatment time is comparable to RFA, the current clinical standard [29]. Current research is underway to decrease HIFU treatment times by improving MRI imaging feedback during treatment or using temperature sensitive contrast agents to aid in the treatment effectiveness [56]. As histotripsy is unaffected by heat perfusion from blood flow, it has the potential to achieve fast and consistent ablation of large volumes and a greater number of tumor nodules. In this initial study, a larger porcine liver volume (60 cm^3) close to a 5 cm diameter volume (65.4 cm^3) was ablated. By optimizing the acoustic and scanning parameters, the treatment time is expected to decrease. As histotripsy pulses are only a few microseconds long separated by several milliseconds, a phased array could be utilized to electronically steer the focus to other locations in the treatment region during the time between pulses to further shorten

the treatment time. Future work will aim to optimize acoustic parameters and investigate phased array transducers to minimize the treatment time for large liver volumes.

Another concern of liver ablation is the effect of respiratory motion. The 60 cm^3 volume lesion created here was significantly larger than the treatment scan volume likely because of the large displacement (~1 cm) from respiratory motion observed during the treatment. There are multiple approaches that may be used to address this issue. To avoid the effect of motion on therapy, patients in HIFU liver tumor clinical trials were trained to hold their breath during sonication, with HIFU therapy halted during breaths. Sophisticated motion-tracking methods are being investigated for MRI guided HIFU [57-60]. Ultrasound-based tracking has also been developed using pulse-echo sequences from a subset of the therapy phased array elements to track the liver speckle [50, 61]. Our lab is investigating a histotripsy system integrated with ultrasound image-based motion tracking algorithms that can dynamically adjust the focal zone of a 2D phased-array transducer to compensate for respiratory or other motion. Our tracking algorithm uses ultrasound images but significantly accelerates the computation by limiting the search iterations for the moving target [62]. Although not used in this study, a motion tracking method will be utilized in the future to improve the precision of histotripsy for liver ablation.

9.5 Conclusion

This chapter demonstrates the feasibility of using histotripsy as a non-invasive ablation method for liver treatment. Histotripsy was capable of creating precise lesions within the liver through the intact chest without the need for aberration correction. Additionally, results show that histotripsy completely ablated a 60 cm^3 liver volume within an hour. Treatments were shown to fractionate the liver tissue surrounding major vessel and the gallbladder while the

fractionation was self-limiting at the boundaries of these critical structures. The results of this work suggest that histotripsy has potential as an innovative non-invasive liver ablation method with improvement over the current tissue ablation methods. Future work will aim to further optimize histotripsy for liver ablation and demonstrate the ability of histotripsy to treat tumors in a relevant liver cancer model.

9.6 References

[1] E. Vlaisavljevich, *et al.*, "Image-Guided Non-Invasive Ultrasound Liver Ablation Using Histotripsy: Feasibility Study in an In Vivo Porcine Model," *Ultrasound in medicine & biology,* vol. 39, pp. 1398-1409, 2013.

[2] F. X. Bosch, *et al.*, "Primary liver cancer: worldwide incidence and trends," *Gastroenterology,* vol. 127, pp. S5-S16, Nov 2004.

[3] H. B. El-Serag and A. C. Mason, "Rising incidence of hepatocellular carcinoma in the United States," *N Engl J Med,* vol. 340, pp. 745-50, Mar 11 1999.

[4] S. J. Pelletier, *et al.*, "An intention-to-treat analysis of liver transplantation for hepatocellular carcinoma using organ procurement transplant network data," *Liver Transpl,* vol. 15, pp. 859-68, Aug 2009.

[5] T. Livraghi, *et al.*, "Treatment options in hepatocellular carcinoma today," *Scand J Surg,* vol. 100, pp. 22-9, 2011.

[6] S. Parikh and D. Hyman, "Hepatocellular cancer: a guide for the internist," *Am J Med,* vol. 120, pp. 194-202, Mar 2007.

[7] M. Kudo, "Radiofrequency ablation for hepatocellular carcinoma: updated review in 2010," *Oncology,* vol. 78 Suppl 1, pp. 113-24, Jul 2010.

[8] Y. K. Cho, *et al.*, "Systematic review of randomized trials for hepatocellular carcinoma treated with percutaneous ablation therapies," *Hepatology,* vol. 49, pp. 453-9, Feb 2009.

[9] C. R. Davis, "Interventional radiological treatment of hepatocellular carcinoma," *Cancer Control,* vol. 17, pp. 87-99, Apr 2010.

[10] N. Izumi, "Recent advances of radiofrequency ablation for early hepatocellular carcinoma," *J Gastroenterol Hepatol,* vol. 26 Suppl 1, pp. 115-22, Jan 2011.

[11] R. M. Charnley, *et al.*, "Cryotherapy for liver metastases: a new approach," *Br J Surg,* vol. 76, pp. 1040-1, Oct 1989.

[12] C. Erce and R. W. Parks, "Interstitial ablative techniques for hepatic tumours," *Br J Surg,* vol. 90, pp. 272-89, Mar 2003.

[13] H. W. Head and G. D. Dodd, 3rd, "Thermal ablation for hepatocellular carcinoma," *Gastroenterology,* vol. 127, pp. S167-78, Nov 2004.

[14] E. Liapi and J. F. Geschwind, "Transcatheter and ablative therapeutic approaches for solid malignancies," *J Clin Oncol,* vol. 25, pp. 978-86, Mar 10 2007.

[15] S. A. Curley, "Radiofrequency ablation of malignant liver tumors," *Oncologist,* vol. 6, pp. 14-23, 2001.

[16] D. S. Lu, *et al.*, "Influence of large peritumoral vessels on outcome of radiofrequency ablation of liver tumors," *J Vasc Interv Radiol*, vol. 14, pp. 1267-74, Oct 2003.

[17] J. A. Marrero and S. Pelletier, "Hepatocellular carcinoma," *Clin Liver Dis*, vol. 10, pp. 339-51, ix, May 2006.

[18] E. J. Patterson, *et al.*, "Radiofrequency ablation of porcine liver in vivo: effects of blood flow and treatment time on lesion size," *Ann Surg*, vol. 227, pp. 559-65, Apr 1998.

[19] T. Livraghi, *et al.*, "Treatment of focal liver tumors with percutaneous radio-frequency ablation: complications encountered in a multicenter study," *Radiology*, vol. 226, pp. 441-51, Feb 2003.

[20] A. J. Aschoff, *et al.*, "How does alteration of hepatic blood flow affect liver perfusion and radiofrequency-induced thermal lesion size in rabbit liver?," *J Magn Reson Imaging*, vol. 13, pp. 57-63, Jan 2001.

[21] T. A. Leslie and J. E. Kennedy, "High-intensity focused ultrasound principles, current uses, and potential for the future," *Ultrasound Q*, vol. 22, pp. 263-72, Dec 2006.

[22] G. ter Haar, "High intensity ultrasound," *Semin Laparosc Surg*, vol. 8, pp. 77-89, Mar 2001.

[23] S. Bobkova, *et al.*, "Focusing of High-Intensity Ultrasound through the Rib Cage Using a Therapeutic Random Phased Array," *Ultrasound in Medicine and Biology*, vol. 36, pp. 888-906, Jun 2010.

[24] E. Cochard, *et al.*, "Ultrasonic focusing through the ribs using the DORT method," *Med Phys*, vol. 36, pp. 3495-503, Aug 2009.

[25] V. A. Khokhlova, *et al.*, "Focus Splitting Associated with Propagation of Focused Ultrasound through the Rib Cage," *Acoust Phys*, vol. 56, pp. 665-674, Sep 2010.

[26] A. Okada, *et al.*, "A case of hepatocellular carcinoma treated by MR-guided focused ultrasound ablation with respiratory gating," *Magn Reson Med Sci*, vol. 5, pp. 167-71, Oct 2006.

[27] C. X. Li, *et al.*, "[High intensity focused ultrasound for liver cancer]," *Zhonghua Zhong Liu Za Zhi*, vol. 25, pp. 94-6, Jan 2003.

[28] J. P. McWilliams, *et al.*, "Percutaneous ablation of hepatocellular carcinoma: current status," *J Vasc Interv Radiol*, vol. 21, pp. S204-13, Aug 2010.

[29] L. Zhang, *et al.*, "High-intensity focused ultrasound (HIFU): effective and safe therapy for hepatocellular carcinoma adjacent to major hepatic veins," *Eur Radiol*, vol. 19, pp. 437-45, Feb 2009.

[30] T. A. Leslie, *et al.*, "High-intensity focused ultrasound ablation of liver tumours: can radiological assessment predict the histological response?," *Br J Radiol,* vol. 81, pp. 564-71, Jul 2008.

[31] J. E. Parsons, *et al.*, "Pulsed cavitational ultrasound therapy for controlled tissue homogenization," *Ultrasound in Medicine and Biology,* vol. 32, pp. 115-29, Jan 2006.

[32] W. W. Roberts, *et al.*, "Pulsed cavitational ultrasound: a noninvasive technology for controlled tissue ablation (histotripsy) in the rabbit kidney," *J Urol,* vol. 175, pp. 734-8, Feb 2006.

[33] Z. Xu, *et al.*, "Controlled ultrasound tissue erosion," *IEEE Trans Ultrason Ferroelectr Freq Control,* vol. 51, pp. 726-36, Jun 2004.

[34] T. L. Hall, *et al.*, "Histotripsy of the prostate: dose effects in a chronic canine model," *Urology,* vol. 74, pp. 932-7, Oct 2009.

[35] Y. Kim, *et al.*, "Non-invasive pulsed cavitational ultrasound for fetal tissue ablation: feasibility study in a fetal sheep model," *Ultrasound Obstet Gynecol,* vol. 37, pp. 450-7, Apr 2011.

[36] A. D. Maxwell, *et al.*, "Noninvasive treatment of deep venous thrombosis using pulsed ultrasound cavitation therapy (histotripsy) in a porcine model," *J Vasc Interv Radiol,* vol. 22, pp. 369-77, Mar 2011.

[37] N. R. Styn, *et al.*, "Histotripsy of VX-2 tumor implanted in a renal rabbit model," *J Endourol,* vol. 24, pp. 1145-50, Jul 2010.

[38] G. E. Owens, *et al.*, "Therapeutic ultrasound to noninvasively create intracardiac communications in an intact animal model," *Catheter Cardiovasc Interv,* vol. 77, pp. 580-8, Mar 1 2011.

[39] T. L. Hall, *et al.*, "Relaxation Properties of Cavitation Induced Tissue Lesions," presented at the Joint Annual Meeting of the International Society for Magnetic Resonance in Medicine. , 2007.

[40] T. Y. Wang, *et al.*, "Quantitative ultrasound backscatter for pulsed cavitational ultrasound therapy- histotripsy," *IEEE Trans Ultrason Ferroelectr Freq Control,* vol. 56, pp. 995-1005, May 2009.

[41] R. O. Illing, *et al.*, "The safety and feasibility of extracorporeal high-intensity focused ultrasound (HIFU) for the treatment of liver and kidney tumours in a Western population," *Br J Cancer,* vol. 93, pp. 890-5, Oct 17 2005.

[42] S. E. Jung, *et al.*, "High-intensity focused ultrasound ablation in hepatic and pancreatic cancer: complications," *Abdom Imaging,* vol. 36, pp. 185-95, Apr 2011.

[43] F. Wu, *et al.*, "Extracorporeal high intensity focused ultrasound ablation in the treatment of 1038 patients with solid carcinomas in China: an overview," *Ultrason Sonochem,* vol. 11, pp. 149-54, May 2004.

[44] H. Wang, *et al.*, "Phase abberation correction and motion compensation for ultrasonic phased arrays: Experimental results.," *IEEE Trans Ultrason Ferroelectr Freq Control,* pp. 34-43, 1994.

[45] Y. Kim, *et al.*, "Lesion generation through ribs using histotripsy therapy without aberration correction," *IEEE Trans Ultrason Ferroelectr Freq Control,* vol. 58, pp. 2334-43, Nov 2011.

[46] C. R. Hempel, *et al.*, "Histotripsy fractionation of prostate tissue: local effects and systemic response in a canine model," *J Urol,* vol. 185, pp. 1484-9, Apr 2011.

[47] A. M. Lake, *et al.*, "Histotripsy: minimally invasive technology for prostatic tissue ablation in an in vivo canine model," *Urology,* vol. 72, pp. 682-6, Sep 2008.

[48] Z. Xu, *et al.*, "Noninvasive creation of an atrial septal defect by histotripsy in a canine model," *Circulation,* vol. 121, pp. 742-9, Feb 16 2010.

[49] J. E. Parsons, *et al.*, "Cost-effective assembly of a basic fiber-optic hydrophone for measurement of high-amplitude therapeutic ultrasound fields," *J Acoust Soc Am,* vol. 119, pp. 1432-40, Mar 2006.

[50] F. Marquet, *et al.*, "Optimal transcostal high-intensity focused ultrasound with combined real-time 3D movement tracking and correction," *Phys Med Biol,* vol. 56, pp. 7061-80, Nov 21 2011.

[51] T. Y. Wang, *et al.*, "Imaging Feedback of Histotripsy Treatments With Ultrasound Transient Elastography. ," in *IEEE International Ultrasonics Symposium*, Orlando, Florida, 2011.

[52] L. Chen, *et al.*, "Effect of blood perfusion on the ablation of liver parenchyma with high-intensity focused ultrasound," *Phys Med Biol,* vol. 38, pp. 1661-73, Nov 1993.

[53] E. Vlaisavljevich, *et al.*, "The Effect of Histotripsy on Tissues with Different Mechanical Properties.," in *IEEE International Ultrasonics Symposium*, Orlando, FL, 2011.

[54] R. K. Jain, "Determinants of tumor blood flow: a review," *Cancer Res,* vol. 48, pp. 2641-58, May 15 1988.

[55] M. Y. Park, *et al.*, "Preliminary experience using high intensity focused ultrasound for treating liver metastasis from colon and stomach cancer," *Int J Hyperthermia,* vol. 25, pp. 180-8, May 2009.

[56] K. Fischer, *et al.*, "Focused ultrasound as a local therapy for liver cancer," *Cancer J,* vol. 16, pp. 118-24, Mar-Apr 2010.

[57] P. Arnold, *et al.*, "3D organ motion prediction for MR-guided high intensity focused ultrasound," *Med Image Comput Comput Assist Interv*, vol. 14, pp. 623-30, 2011.

[58] B. D. de Senneville, *et al.*, "MR-guided thermotherapy of abdominal organs using a robust PCA-based motion descriptor," *IEEE Trans Med Imaging*, vol. 30, pp. 1987-95, Nov 2011.

[59] M. Pernot, *et al.*, "3-D real-time motion correction in high-intensity focused ultrasound therapy," *Ultrasound Med Biol*, vol. 30, pp. 1239-49, Sep 2004.

[60] M. Ries, *et al.*, "Real-time 3D target tracking in MRI guided focused ultrasound ablations in moving tissues," *Magn Reson Med*, vol. 64, pp. 1704-12, Dec 2010.

[61] I. A. Hein and W. R. O'Brien, "Current time-domain methods for assessing tissue motion by analysis from reflected ultrasound echoes-a review," *IEEE Trans Ultrason Ferroelectr Freq Control*, vol. 40, pp. 84-102, 1993.

[62] R. M. Miller, *et al.*, "Real-time Motion Tracking for Non-invasive Ultrasound Cardiac Therapy using Histotripsy," presented at the IEEE International Ultrasonics Symposium, Orlando, FL, 2011.

Chapter 10

Non-Invasive Ultrasound Liver Ablation using Histotripsy: Chronic Study in an *in vivo* Rodent Model

A majority component of this chapter is excerpted from a manuscript that has been submitted to *Ultrasound in Medicine and Biology*.

10.1 Introduction

Hepatocellular carcinoma (HCC) has the fastest growing incidence among solid malignancies in the United States over the last decade with this trend expected to continue [1, 2]. While liver transplantation may be curative, only a small number of patients will receive this treatment as tumors must be within early stage (single tumor 5 cm or less; 2-3 tumors 3 cm or less). The limited donor availability also greatly constrains the number of liver transplants [1, 2]. Surgical resection of liver tumors is a proven treatment option but is associated with high rates of morbidity and mortality [3]. Further, surgical resection is not possible in many cases such as patients with decompensated cirrhosis [3, 4].

One approach to address these issues is the development of local, non-invasive ablation therapies. Currently available minimally or non-invasive ablation methods are mostly thermal based, including radiofrequency ablation (RFA), microwave therapy, cryoablation, laser ablation, and high intensity focused ultrasound (HIFU) [5-10]. While these therapies have shown some success, they share inherent limitations due to the heat sink effect from blood flow [11-14] as

well as the potential for damage to adjacent structures or major biliary radicles. Thermal ablation is inconsistent in tissue with non-uniform heat dissipation patterns, which is common in hypervascular liver tumors [15]. In particular, for tissue near major vessels, thermal ablation often results in incomplete tumor necrosis [16, 17]. In addition, these methods are often unsuitable for treating tumors larger than 3 cm due to the excessive treatment time and practical probe sizes [11-14].

Recently, our group has developed histotripsy as a potential non-invasive liver cancer ablation method [18]. Histotripsy is a non-thermal ultrasonic ablation method that fractionates tissue through the precise control of acoustic cavitation [19-21]. Since histotripsy is non-thermal, it is not affected by the heat sink effect from blood vessels and does not have the limitations associated with thermal ablation methods such as damage to other structures. Further, the histotripsy cavitation cloud can be visualized with ultrasound imaging, allowing precise targeting and real-time treatment feedback [18]. The change in the tissue during treatment can also be directly monitored using standard imaging modalities such as ultrasound and MRI, which allows histotripsy to be guided by real-time imaging [22-25]. An initial study by our group demonstrated the feasibility of applying histotripsy *in vivo* for non-invasive liver ablation in a porcine model with similar size and anatomic similarities to its human counterpart [18]. Histotripsy was capable of creating precise lesions at locations throughout the entire liver through ribs and overlying tissue, with the treated liver fractionated into an acellular fluid homogenate with no recognizable cellular structures [18]. Additionally, histotripsy was shown capable of completely fractionating the liver tissue near the major hepatic blood vessels and gallbladder while preserving these critical hepatic structures, due to the resistance of stiffer tissues to histotripsy-induced tissue damage [18, 26]. Finally, a separate porcine study

demonstrated that histotripsy can generate lesions in the liver through full ribcage obstruction without inducing any substantial thermal effects or damage to overlying tissues [27].

Although previous work has demonstrated the feasibility of using histotripsy for non-invasive liver ablation, these studies have been limited to investigating the acute effects of histotripsy during and immediately following treatment [18, 27]. In this chapter, we investigate the long-term effects of histotripsy liver ablation in a in a rodent model commonly used for therapeutic development of HCC. The rat model was chosen for these studies rather than a larger animal model to allow for more animals to be treated with histotripsy at a lower cost and monitored for longer time points. Based on the previous acute studies showing histotripsy completely fractionates the liver into an acellular liquid homogenate, we hypothesize that the histotripsy lesion will be resorbed by the tissue over time, resulting in effective tissue removal. This hypothesis is supported by previous work studying the chronic response of prostate, kidney, and cardiac tissues treated with histotripsy, which showed histotripsy lesions were absorbed over time leaving only a small scar or an empty void in the treated region [28-31]. In this study, we investigate the chronic response of liver tissue to histotripsy therapy for the first time, including the use of non-invasive MRI imaging technology. Over 28 days after treatment, the histotripsy lesions were characterized using gross morphology, histological analysis, and MRI.

10.2 Methods

10.2.1 Animal Preparation

A total of 20 male Sprague Dawley rats with an average weight of 300 grams were treated with histotripsy. Before histotripsy, the rat abdomen was shaved and treated with a depilatory cream to improve ultrasound coupling. To ensure ultrasound propagation to targeted

tissue, rats were positioned and fastened onto a custom-built animal platform over a tank of degassed water [Fig. 10.1]. A temperature probe was placed into the water tank for continuous monitoring and recording of the water temperature, which was kept at a target temperature of 35-37°C. Rats were induce and then maintained on 1-5% isoflurane in 1 L/min of oxygen (SurgiVet V704001, Smiths Medical, Waukesha, Wisconsin, USA) for the duration of the histotripsy treatment [Fig. 10.1(C)]. A pulse-oximeter (SurgiVet V3395, Smiths Medical, Waukesha, Wisconsin, USA) was attached to the rat's paw for continuous monitoring and recording of the pulse and oxygenation levels throughout the procedure. In addition, a rectal thermometer was inserted into the rat to continuously measure the rectal temperature.

Prior to applying histotripsy, the desired treatment location was imaged using a 20 MHz imaging transducer (L40-8/12, Ultrasonix, Vancouver, Canada) aligned coaxially with the 1 MHz histotripsy therapy transducer [Fig. 10.1(B)]. The focal position of the therapy transducer in the imaging field of view was found prior to therapy by generating a bubble cloud in degassed water and identifying the location of the hyperechoic region. The location of the bubble cloud was marked on the ultrasound imaging screen to indicate the transducer focal position in free field. The rat was then placed above the transducer, and targeting was achieved by aligning the transducer focus to the selected treatment region in the liver. Histotripsy was applied transcutaneously with a portion of the rib cage within the acoustic pathway. After treatment, rats were either euthanized for analysis or recovered for 3, 7, 14, or 28 days (n=4 each). Recovery animals were given a Carprofen (Rimadyl, Pfizer, NY, NY, USA) analgesic (5 mg/kg) subcutaneously prior to histotripsy therapy and one day after histotripsy therapy. At the conclusion of the experiments, rats were euthanized with CO_2 administration and the target tissue

was harvested for histological evaluation. All procedures were approved by the University Committee on Use and Care of Animals at the University of Michigan.

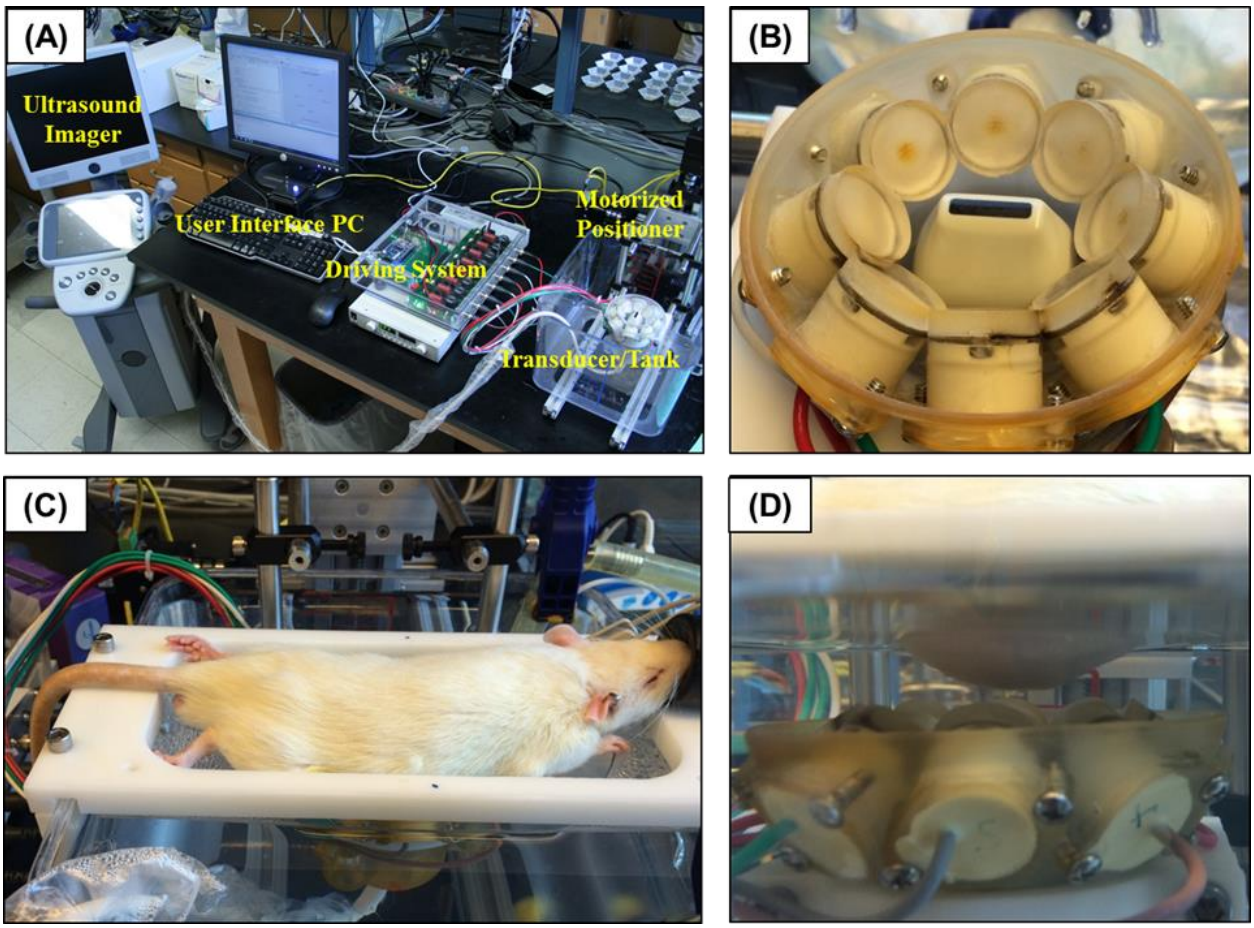

Figure 10.1. Histotripsy *in vivo* rat liver ablation experimental setup. (A,B) A 1 MHz histotripsy therapy transducer with coaxially aligned ultrasound imaging probe was attached to a motorized 3D positioning system controlled using a PC console. (C,D) The transducer was placed inside a tank of degassed water with the anesthetized rat placed above the transducer during the histotripsy liver treatments.

10.2.2 Histotripsy Lesion Generation

Histotripsy lesions were generated in the inferior regions of the liver using a custom-built 1 MHz focused ultrasonic transducer designed for small animal experiments [Fig. 10.1(B)]. To generate histotripsy pulses, a custom high-voltage pulser developed in-house was used to drive the transducers. The pulser was connected to a field-programmable gate array (FPGA)

development board (DE0-Nano Terasic Technology, HsinChu, Taiwan) specifically programmed for histotripsy therapy pulsing. This setup allowed the transducers to output short pulses consisting of less than two cycles, which have previously been shown to produce precise histotripsy bubble clouds when a distinct pressure threshold is achieved inside the tissue [32-35]. Histotripsy pulses were applied to the liver at a pulse repetition frequency (PRF) of 100 Hz and an estimated *in situ* peak negative pressure (P–) >30 MPa. The acoustic output was estimated by a summation of the output focal *p*- values from individual transducer elements as measured by a fiber-optic probe hydrophone (FOPH) built in-house [36], as outlined in previous studies [32-35].

The inferior regions of the rat liver were targeted in this study to minimize the lung tissue exposed to the acoustic field, as previous work has demonstrated that lung hemorrhage can occur at significantly lower acoustic amplitudes [37, 38]. Histotripsy lesions were generated by mechanically scanning the therapy focus to follow a 4×4 mm square grid inside the rat liver. Each point in the grid was treated for 5 seconds (500 pulses) before the focus was moved to an adjacent spot 0.5 mm apart. The procedure was monitored with ultrasound imaging [Fig. 10.2(A)], and pre-treatment and post-treatment ultrasound images of the targeted region were collected for comparison purposes. After treatment, rats were euthanized with CO_2 administration after 0, 3, 7, 14, or 28 days (n=4 each). After euthanizing, the liver and lungs were harvested for histological evaluation.

10.2.3 Magnetic Resonance Imaging (MRI)

Lesion progression of the rats euthanized after 28 days (n=4) was monitored over the course of the experiment with MRI on days 0, 3, 7, 14, and 28. MRI was performed at 7.0 T using a Direct Drive console (Agilent Technologies, Santa Clara, CA, USA). Days 0, 3, and 7

used a 60 mm inner-diameter transmit-receive radiofrequency (RF) volume coil (Morris Instruments, Ontario, Canada) while a 72 mm RF coil (Rapid Biomedical, Rimpar, Germany) was necessary on days 14 and 28 due to animal growth. Animals were anesthetized and maintained on ~2% isoflurane in 1L/min of oxygen. They were placed in the supine position for imaging. Body temperature was monitored and maintained near 37° C using a rectal temperature probe and warm air, while also monitoring respiration (SA Instruments, Stony Brook, NY; Labview, Austin, TX, USA). A high number of excitations was used to compensate for artifacts due to respiratory motion in order to provide the best contrast between normal and treated liver tissue, while maintaining a reasonable imaging time. After pilot scans to confirm positioning, a T2-weighted fast spin-echo sequence was used to visualize the liver in the coronal plane. The MRI parameters were: field of view of (60 mm)2, slice thickness of 1 mm, matrix 2562 zero-filled to 5122; repetition time of 2000 ms, echo spacing of 10 ms, echo train length of 8, effective echo time of 20 ms, 16 excitations, and an acquisition time of ~17 min. Images were analyzed using MRVision (Winchester, MA, USA). Manual tracing was used to quantify the area of the histotripsy lesion on each slice, multiplying by slice thickness to get volumetric measurements (mean ± standard deviation). When lung tissue was visible, the distance of the histotripsy lesion from the inferior lobes of the lungs was quantified using manual methods. Statistical comparisons were made using a Student's t-test. P-values<0.05 were considered significant. Error bars on graphs represent standard error of the mean (SEM). Quantification of MRI data was performed without knowledge of histological results.

10.2.4 Morphological and Histological Evaluation

Treated rat liver and overlying lung samples were harvested after experiments and fixed in 10% buffered formalin (Fisher Scientific). After fixing the tissue, lesion gross morphology was examined prior to histological analysis. Samples were then stained with hematoxylin and eosin (H&E) and examined under a microscope (Nikon Eclipse 50i) using 4x, 10x, 20x, and 40x objective lenses. The size of the histotripsy lesions in the liver was quantitatively assessed by measuring the maximum cross-sectional area of the histotripsy lesion. As the histotripsy lesions contained regions containing hematoma or granulation tissue, the size of these regions were also quantified for all liver samples, with the results compared for animals euthanized after each time point. Statistical comparisons were made using a Student's t-test. P-values<0.05 were considered significant. Error bars on graphs represent standard error of the mean (SEM).

10.3 Results

10.3.1 Histotripsy Liver Lesion Formation

Histotripsy therapy was applied to the livers of 20 rats through the intact abdomen. A bubble cloud was successfully generated in the livers of all 20 rats and visualized as a hyperechoic zone on ultrasound imaging allowing for real-time treatment monitoring [Fig. 10.2(A)]. After treatment, the fractionated tissue was observed as a hypoechoic zone on ultrasound imaging due to the reduced size and density of the sound scatterers present in the fractionated zone, as seen in previous studies [18, 24, 27]. For the acute group (n=4), the rats were euthanized within one hour after the application of histotripsy, and the liver was harvested for histological analysis. Histological evaluation of histotripsy liver lesions showed complete fractionation of hepatic parenchyma inside the treated volume, with sharp boundaries between

intact and completely fractionated tissue [Fig. 10.2(D)]. Localized hemorrhage was observed inside the acute lesions, but no hemorrhage was observed in the surrounding intact liver tissue.

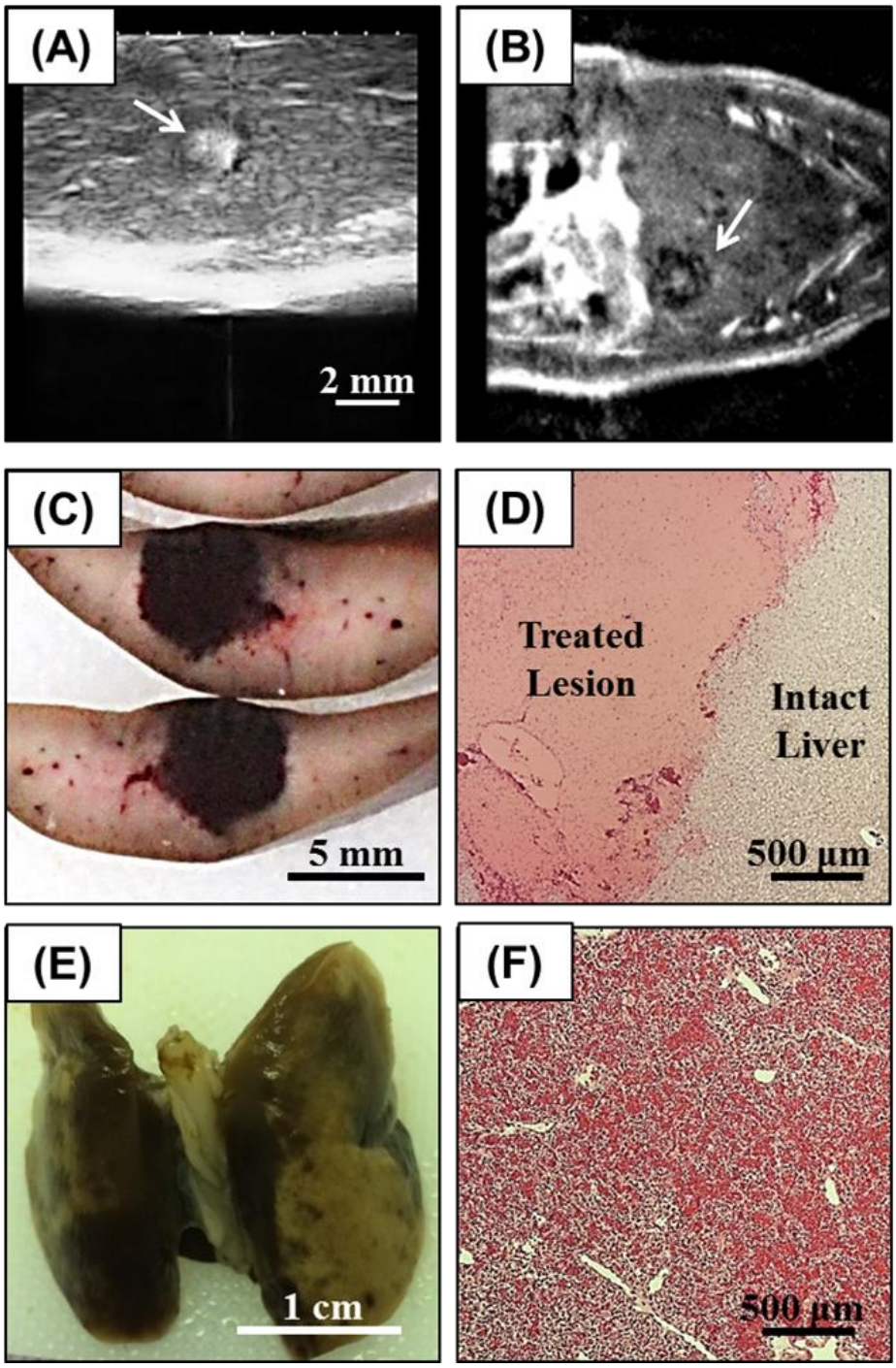

Figure 10.2. (A) Histotripsy treatments were applied to the rat liver guided by real-time ultrasound imaging. After treatment, liver lesions were assessed using (B) MRI, (C) gross morphology, and (D) histology. In addition to the liver, the inferior lobes of the lungs were harvested after treatment and assessed using (E) gross morphology and (F) histology.

Overlying tissues in the acoustic path were examined after treatment for signs of potential damage. Gross morphological examination showed no signs of damage to overlying skin, muscle, or ribs. However, localized hemorrhage was observed after treatment in the inferior regions of the lungs, which were in the acoustic path [Fig. 10.2(E,F)]. In the rats that showed the most significant lung hemorrhage, the SpO_2 was observed to decrease from >95% to ~80% during the treatment before recovering to normal levels after treatment. No hemorrhage was observed in the superior regions of the lung, likely because these regions were not exposed to the acoustic field. The fluctuation of the heart rate and respiration rate during treatment was maintained within ±10% of the baseline values observed before treatment. The core body temperature did not drop more than 1°C throughout the duration of the treatment.

10.3.2 Histotripsy Chronic Lesion Progression

The chronic response to histotripsy liver ablation was assessed for a period of 28 days. After recovery from non-invasive ultrasound surgery, rats were observed to return to normal behavior (i.e. moving around in the cage) within 30 minutes of treatment. No change in behavior was observed in the rats during the course of the 28 days. The rat urine appeared slightly pink for approximately one week after treatment, potentially a sign of acute rhabdomyolysis or hemoglobinuria, but returned to normal for the duration of the experiment. For the acute rats, histotripsy treated lesions were completely fractionated, with no recognizable cellular structures within the treatment region. The boundaries between the surrounding healthy liver tissue and the completely fractionated homogenate were sharply demarcated [Fig. 10.3(A)]. The average maximum cross-sectional area of the lesions (n=4) was 17.2±1.9 mm^2, which closely matched the 4 x 4 mm treatment grid and the finite size of the bubble cloud. Histological analysis

demonstrated that the histotripsy homogenate consisted of acellular tissue debris and dispersed red blood cells [Fig. 10.4(A)]. At later time points, morphological analysis demonstrated that the tissue homogenate (i.e. hematoma) inside the lesions was resorbed by the liver [Fig. 10.3]. The size of the hematoma was observed to significantly decrease after 3 and 7 days, with no hematoma remaining after 14 and 28 days [Fig. 10.5]. In addition to the resorption of the tissue homogenate, an acute inflammatory reaction was observed inside the histotripsy lesion after 3 days, with numerous immune cells observed throughout the lesion including various leukocytes, macrophages, and fibroblasts [Fig. 10.4]. This immune response resulted in the formation of a region of granulation tissue on the boundary of the lesion (i.e. stromal tissue surrounding a central hematoma) [Fig. 10.4]. This fibrous granulation tissue was first observed around the outside of the lesion and progressed towards the center of the lesion over time [Fig. 10.4], with the maximum volume of granulation tissue observed after 3 days [Fig. 10.5]. At later time points (7-28 days), the volume of granulation tissue decreased, corresponding to a decrease in the total lesion size [Fig. 10.5]. The decrease in lesion size corresponded with an increase in the density of the granulation tissue at the lesion boundary, with a ring of dense fibrous tissue ~50-200 μm thick encapsulating the lesion after 7 days [Fig. 10.4]. This dense fibrous tissue continued to contract over the duration of the experiment, resulting in clear indentations between the lesion and the surrounding healthy tissue [Fig. 10.3]. The lesion size continued to decrease over the course of the experiment, resulting in small lesions with an average maximum cross-sectional area of <1 mm^2 after 28 days (n=4) [Fig. 10.3(E), Fig.10.5].

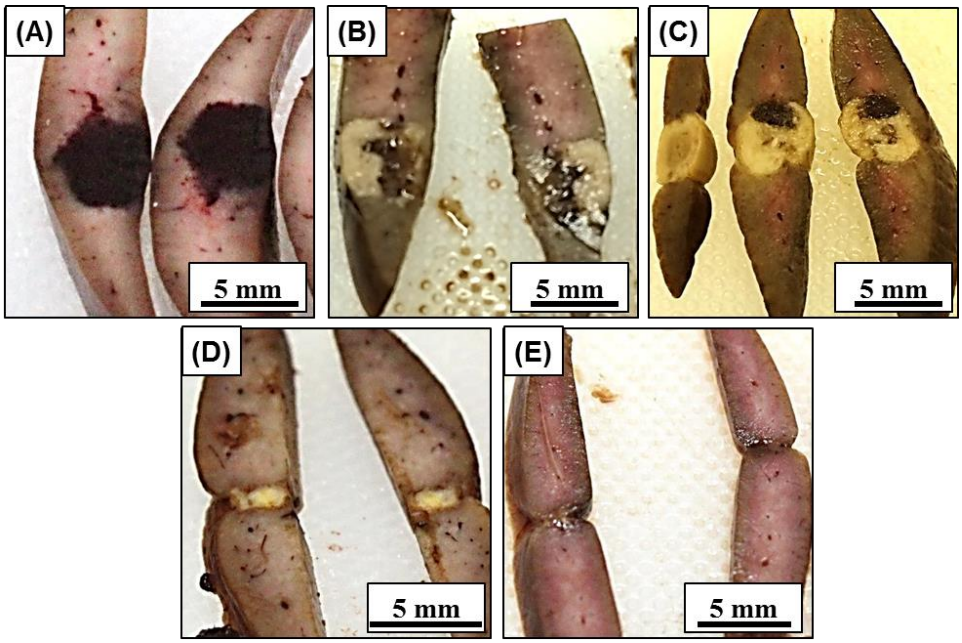

Figure 10.3. Histotripsy liver lesions were assessed for gross morphology after animals were sacrificed on days 0, 3, 7, 14, 28 (A-E). Darkly colored hematomas seen on day 0 were replaced with granulation tissue on days 3 and 7. The granulation tissue was resolved on days 14 and 28, leaving a contracted tissue with virtually no fibrotic material remaining.

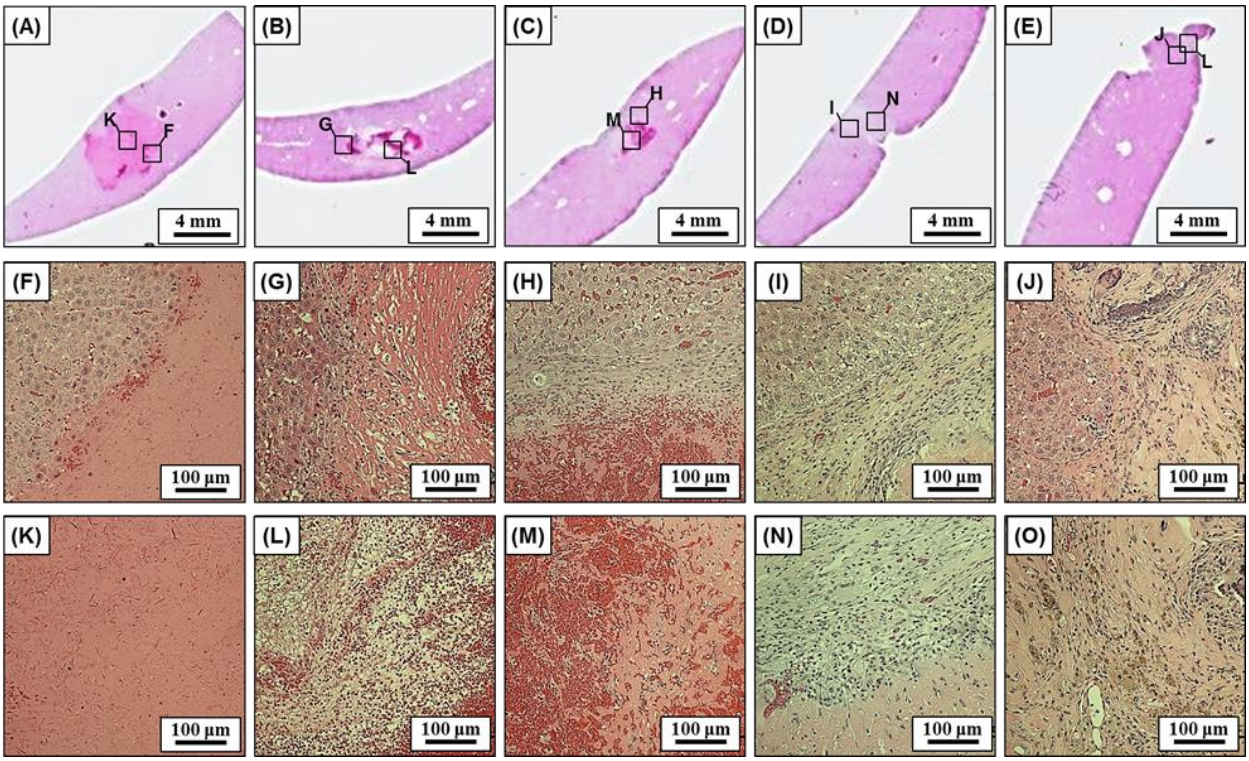

Figure 10.4. Liver lesions for animals sacrificed after day 0, 3, 7, 14, 28 (A-E). Histology images of the lesion boundary (F-J) and a central portion of the lesion (K-O) after day 0, 3, 7, 14, 28 were analyzed to characterize chronic response of the liver to histotripsy therapy.

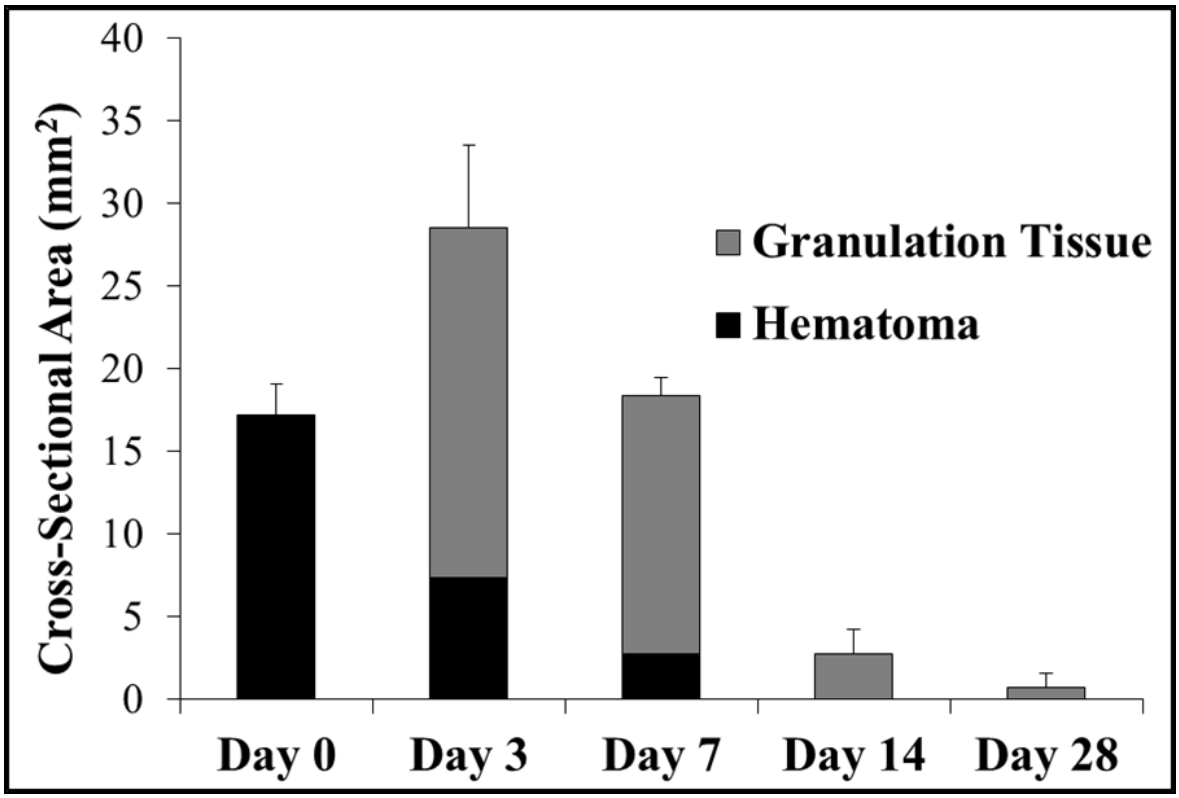

Figure 10.5. Plot shows the average maximum cross-sectional area of the histotripsy liver lesions measured over the course of the experiment. The area of the hematoma and granulation tissue components of the lesion, as well as the total lesion cross-sectional area, were compared for rats euthanized after day 0, 3, 7, 14, and 28. Following an increase in maximum cross-sectional area between day 0 and 3, there was a rapid reduction in lesion size over the remainder of the study. All differences in lesion size were significant ($p<0.05$).

10.3.3 MRI Liver Lesion Monitoring

In addition to morphological and histological analysis, lesion progression of the rats euthanized after 28 days was monitored with *in vivo* MRI over the course of the experiment. MRI was performed on days 0, 3, 7, 14, and 28. Animals tolerated MRI well at all time points, including only hours after histotripsy treatment on day 0. For time points where histotripsy lesions were visible on MRI (typically days 0, 3, and 7; only one lesion was visible at day 14), signal intensity was heterogeneous across the lesion. However, MRI consistently demonstrated primarily negative contrast on day 0 and positive contrast on day 3 [Fig. 10.6]. Such changes in signal intensity imply extracellular/extravasated blood products and edema were the dominant

influence on the MRI signal after day 0 and day 3, respectively. There was a rapid normalization of signal intensity thereafter, with no visible lesions observed at day 28. A thin dark line circumscribing the lesion along portions of its perimeter was observed in a number of images, typically days 3 and 7, implying either a higher concentration of blood products or a highly structured material. The evolution of total lesion volume by MRI demonstrated an average lesion volume of 279.2±233.2, 267.9±103.4, 71.5±60.0, 19.3±38.6, and 0±0 after days 0, 3, 7, 14, and 28, respectively [Fig. 10.7]. Although not every dataset included lungs in the same field of view as the liver lesions, for those that did, the average distance between the superior edge of the lesions and the inferior surface of the lungs was 18.0±2 mm. For a qualitative comparison of the signal intensity of the histotripsy lesions with HCC tumors, pilot data of an N1-S1 Rat Hepatoma tumor implanted in a rat liver is shown in Figure 6 (F).

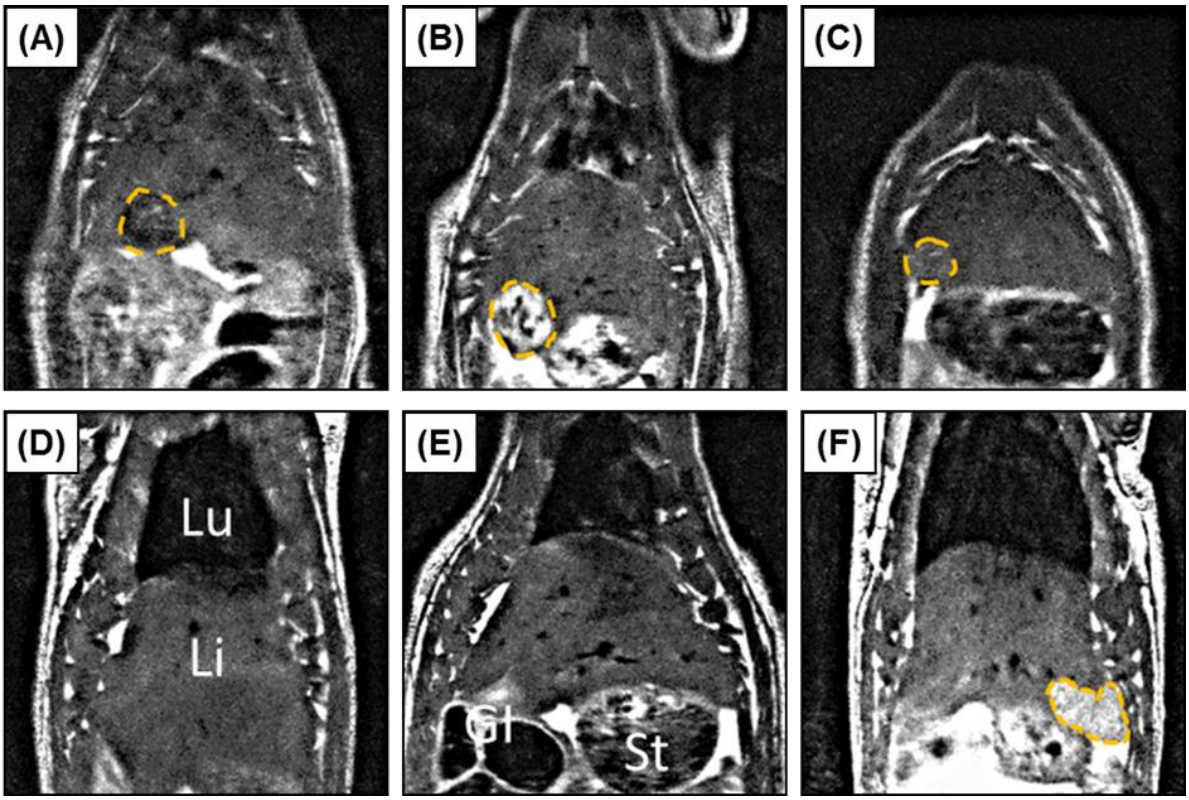

Figure 10.6. Representative MRI images for one rat acquired on days 0, 3, 7, 14, and 28 (A-E) (Lu=lungs, Li=liver, St=stomach, GI=gastrointestinal tract). (F) For a qualitative comparison of signal intensity, pilot data of an HCC tumor implanted in the rat liver is shown in Panel F.

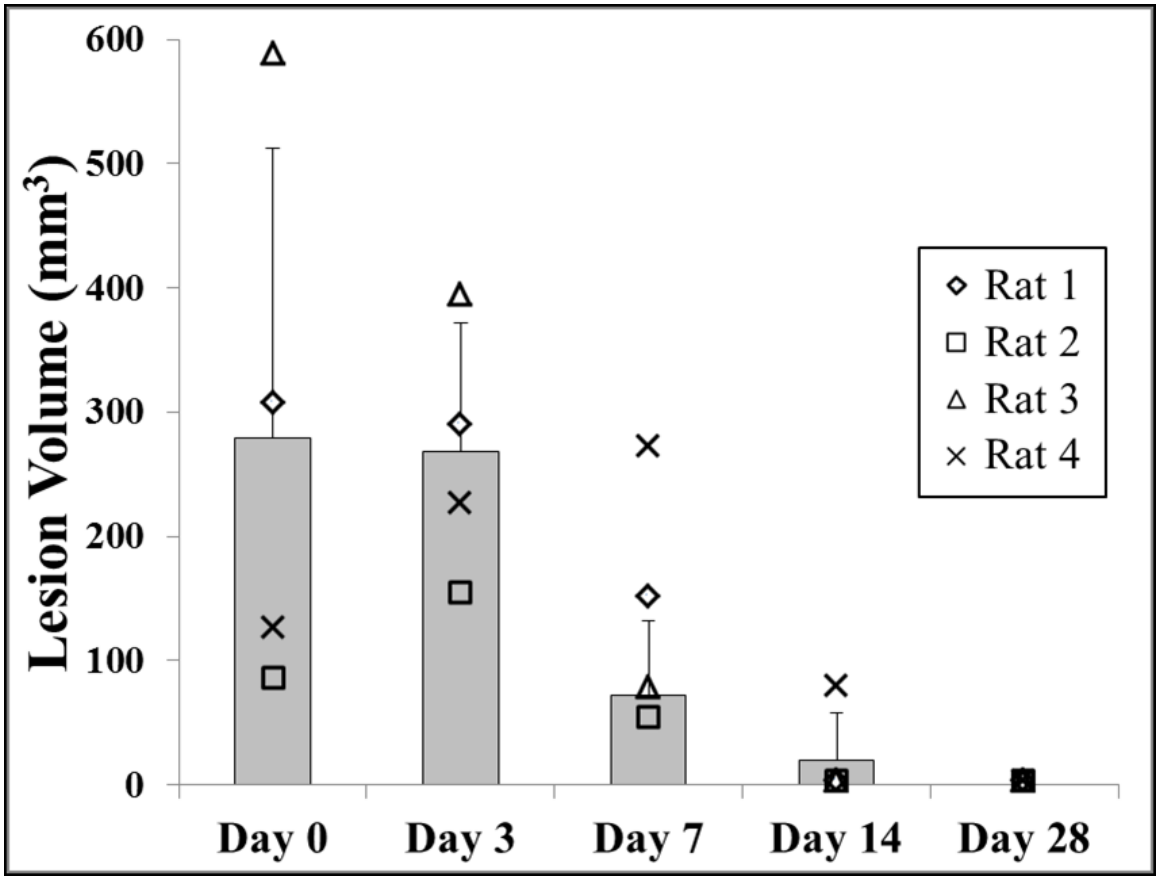

Figure 10.7. Plot shows the lesion volume measured by MRI for rats euthanized after day 28 (n=4). No significant difference in lesion size was observed between day 0 and day 3 ($p>0.05$). After day 3, there was a significant decrease in lesion volume over the remainder of the study ($p<0.05$) with no quantifiable lesions observed after day 28.

10.3.4 Lung Histological Analysis

Due to the limitations with the small animal model, the acoustic path passed though the inferior lobes of the lung, resulting in local hemorrhage in these regions following histotripsy therapy [Fig. 10.2(E)]. Histological analysis of the effected regions of the lung (i.e. regions with hemorrhage observed on gross morphology) demonstrated infiltrating red blood cells throughout the alveolar space after treatment [Fig. 10.8(A,F)]. This diffuse hemorrhage was only observed in the inferior lobes of the lung and was likely caused by cavitation damage rupturing small blood vessels, as previous work has demonstrated a significantly reduced cavitation threshold for

lung tissue due to the presence of air [37, 38]. The larger blood vessels in the effected regions of the lung were observed to remain intact, similar to previous studies demonstrating large vessels are more resistant to histotripsy damage due to the increased tissue stiffness [18, 26]. After recovery from therapy, the number of red blood cells inside the alveolar space was observed to steadily decrease, with minimal hemorrhage remaining after 28 days [Fig. 10.8]. In addition to the clearance of red blood cells, an acute immune response was observed, with local infiltration of leukocytes, macrophages, and fibroblasts observed after 3 days. The interstitial tissue surrounding the alveolar walls in the effected regions was observed to thicken over time [Fig. 10.8]. After day 28, histological analysis demonstrated nearly normal lung tissue with open alveolar space [Fig. 10.8(E)] and only a few regions of thickened alveolar walls [Fig. 10.8(J)].

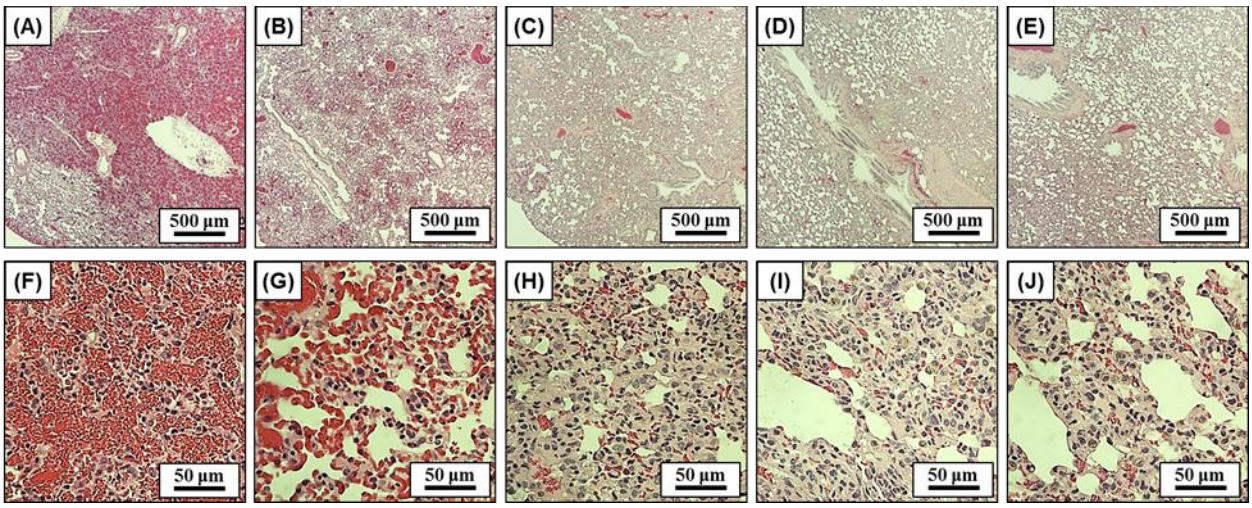

Figure 10.8. Histology images of the inferior lobes of the lung after days 0, 3, 7, 14, 28 using 4x (A-E) and 40x magnification (F-J). Results showed localized lung hemorrhage on day 0, with the number of red blood cells inside the alveolar space decreasing at later time points and minimal hemorrhage remaining after 28 days.

10.4 Discussion

In this chapter, we investigated the long-term effects of histotripsy liver ablation in a rat model. Well-confined bubble clouds were generated in the livers of all 20 rats, resulting in the

formation of precise and completely fractionated histotripsy lesions with sharply demarcated boundaries between the surrounding healthy liver tissue and the lesion. Immediately after treatment, the histotripsy lesion consisted of acellular tissue debris and red blood cells that accumulated inside the lesion due to local hemorrhage. As the animals recovered over the course of 28 days, the acellular tissue homogenate within the histotripsy lesion was resorbed and replaced by granulation tissue, characteristic of a typical wound healing response. After 28 days, the histotripsy lesions were almost completely resorbed by the tissue, with only a small fibrous lesion remaining (<1 mm^2 maximum cross-section). It is possible that this lesion would have been further resorbed over longer time points if the experiment would have been continued beyond day 28.

The results of this study are promising for the development of histotripsy as a non-invasive ablation modality for the treatment of liver cancer and demonstrate that histotripsy has the potential to safely and efficiently create precise lesions in the liver without inducing any negative long-term complications. The nearly complete resorption of the histotripsy lesions, as observed in this study after 28 days, demonstrates that histotripsy not only causes cell death to the target tissue by completely fractionating the tissue into an acellular homogenate, but also effectively removes the targeted tissue from the liver over time. If this healing response and effective tissue removal occurs in a clinical setting, then this would be a major advantage for histotripsy therapy compared to thermal ablation methods in which the tissue is destroyed by thermal necrosis, leaving behind a permanent fibrotic scar [13, 39, 40]. The fibrotic masses left behind after thermal ablation are associated with negative side effects such as pain or loss of liver function due to the displaced volume of healthy liver tissue, while also making it difficult to identify residual or recurrent tumor tissue. As such, thermal ablation methods are often used in

conjunction with surgery, with the necrotic fibrous tissue requiring subsequent removal via invasive surgery. In contrast, the results of this study suggest that histotripsy has the potential to completely ablate liver tumors into an acellular homogenate that will be resorbed by the surrounding tissue over time. It appears that the acute immune response to the histotripsy treatment contributes to the contraction of the liver around the histotripsy lesion, leaving only a very small fibrous dimple in the region of the liver previously treated with histotripsy. Furthermore, it should be noted that, although the tissue contracted around the histotripsy lesions, there was no evidence of damage to surrounding tissue due to restricted blood flow to these regions. While this study investigated the chronic effects of histotripsy liver ablation in a healthy liver model, we hypothesize that a fractionated tumor homogenate would be similarly resorbed by the tissue after treatment with histotripsy, similar to previous studies investigating histotripsy for the treatment of renal and prostate tumors [41, 42]. Future work is ongoing to investigate the long-term effects of histotripsy liver cancer ablation in a chronic liver cancer model.

In addition to the detailed assessment of lesion evolution using ultrasound imaging, gross morphology, and histology, this study used MRI to assess the progression of the histotripsy lesion over time. To our knowledge, this is the first time a histotripsy lesion has been observed on MRI in an *in vivo* setting, for either acute or chronic assessment. Given that the MRI signal is a macroscopic representation of the microscopic tissue environment, first time application of *in vivo* MRI must be validated using *ex vivo* methods such as morphology and histology. The *in vivo* MRI results were consistent with *ex vivo* endpoints in this study. The negative contrast seen on day 0 is congruent with the hematoma and extravasated blood products visualized via morphology and histology. These features are likely to contain red blood cells and hemoglobin in various oxygenated states which would reduce the T2 time constant, resulting in a lower signal

intensity [43]. Similarly, as seen on day 3, initial resorption of the hematoma temporarily increases fluid content (i.e. edema) which would lead to an increase in the T2 time constant and higher signal intensity [44]. The remaining hematoma and replacement granulation tissue, as seen on days 7-14, would lead to a residual, localized low signal intensity [45]. Finally, as the lesion is resolved, the MRI signal returns to being iso-intense. The trends in lesion size were also consistent between MRI and *ex vivo* endpoints, with the decrease in lesion volume over time measured by MRI matching the trend of decreasing cross-sectional area observed on gross morphology and histology.

The finding that MRI can be used to clearly visualize histotripsy liver lesions after treatment, acutely and chronically, using a standard MRI sequence may be a significant advantage for histotripsy, allowing for the treatment effect to be monitored immediately following therapy. The immediate histotripsy treatment feedback would be a significant improvement over thermal ablation or drug therapies, in which the effectiveness of the treatment often cannot be assessed until a few weeks or months after application [13, 39]. In addition to this immediate treatment feedback, the ability to quantify the changes in total lesion volume after recovery from treatment, as demonstrated in this study, would be a major benefit. If the large changes in T2 signal intensity and the rapid resolution of the lesion (~2 weeks) were the same in liver cancer patients, one might expect the remaining tumor to vary in intensity with respect to the healthy liver tissue, while the ablated tissue would be isointense as seen in this work, allowing for the identification of residual or untreated tumor tissue after treatment. This hypothesis is supported by comparisons of the histotripsy lesions observed in this study with images of HCC tumors implanted in rats in a pilot study [Fig.10.6]. The T2 contrast and apparent heterogeneity of the histotripsy lesion suggests that it may be possible to discriminate the

histotripsy lesion from tumor tissue in future work. However, it is also possible that the fibrous tissue circumscribing the lesion, which results in localized constriction at later time points, may be challenging to visualize in a clinical setting due to resolution limitations, respiratory motion, or surrounding tissues (such as the gastro-intestinal organs) back-filling space left by the contracted liver tissue. As a result, future work will investigate the use of alternative imaging sequences or contrast agents in order to optimally differentiate healthy liver tissue, tumor tissue, and the fractionated histotripsy tissue homogenate.

While the results of this study demonstrated that histotripsy liver ablation was well tolerated by the animals during and after treatment, the results suggest that histotripsy transducers should be designed to avoid the presence of lungs in the acoustic field in order to prevent the lung hemorrhage observed in this study. Previous work has shown a significant decrease in the cavitation threshold in lung tissue due to the gas content, which increases the likelihood of generating cavitation even at the reduce pressures outside the histotripsy focus. While it is promising that the lung damage observed in this study appeared to be reversible over time, this lung damage has the potential to be fatal during treatment if the extent of the damage is too severe as was observed in two preliminary experiments targeting the upper lobes of the liver in which the entire lungs were exposed to the acoustic field. As such, it is important to design histotripsy transducers with the proper acoustic window in order to avoid the passage of sound through the lungs. In our previous study in an *in vivo* porcine model, histotripsy was shown capable of targeting every region of the liver without inducing any lung hemorrhage [18, 27]. Due to the limitations of the small animal model used in this study, a transducer with a larger acoustic path (with respect to the animal) was required in order to generate the high pressures required for histotripsy. While the lung hemorrhage observed in this study is a limitation of the

small animal model, the results nonetheless highlight the need for histotripsy transducer designs that minimize sound propagation through the lungs.

10.5 Conclusion

This chapter demonstrates the long-term effects of histotripsy liver ablation in a rat model. Histotripsy was capable of creating precise lesions within the liver through the intact abdomen in all animals, and the lesions were observed to be resorbed by the surrounding liver tissue over the course of the 28 day experiment. The finding that histotripsy can be used to non-invasively ablate regions of the liver, resulting in the effective removal of the tissue over time, demonstrates a major advantage of histotripsy therapy compared to thermal ablation techniques that ablate the tissue by thermal necrosis, thereby leaving a chronic fibrous mass of scar tissue inside the liver. Overall, the results of this chapter suggest that histotripsy has potential as a non-invasive liver cancer ablation method for effective tissue removal.

10.6 References

[1] F. X. Bosch, *et al.*, "Primary liver cancer: worldwide incidence and trends," *Gastroenterology*, vol. 127, pp. S5-S16, Nov 2004.

[2] H. B. El-Serag and A. C. Mason, "Rising incidence of hepatocellular carcinoma in the United States," *N Engl J Med*, vol. 340, pp. 745-50, Mar 11 1999.

[3] T. Livraghi, *et al.*, "Treatment options in hepatocellular carcinoma today," *Scand J Surg*, vol. 100, pp. 22-9, 2011.

[4] S. Parikh and D. Hyman, "Hepatocellular cancer: a guide for the internist," *Am J Med*, vol. 120, pp. 194-202, Mar 2007.

[5] R. M. Charnley, *et al.*, "Cryotherapy for liver metastases: a new approach," *Br J Surg*, vol. 76, pp. 1040-1, Oct 1989.

[6] C. Erce and R. W. Parks, "Interstitial ablative techniques for hepatic tumours," *Br J Surg*, vol. 90, pp. 272-89, Mar 2003.

[7] H. W. Head and G. D. Dodd, 3rd, "Thermal ablation for hepatocellular carcinoma," *Gastroenterology*, vol. 127, pp. S167-78, Nov 2004.

[8] T. A. Leslie and J. E. Kennedy, "High-intensity focused ultrasound principles, current uses, and potential for the future," *Ultrasound Q*, vol. 22, pp. 263-72, Dec 2006.

[9] E. Liapi and J. F. Geschwind, "Transcatheter and ablative therapeutic approaches for solid malignancies," *J Clin Oncol*, vol. 25, pp. 978-86, Mar 10 2007.

[10] G. ter Haar, "High intensity ultrasound," *Semin Laparosc Surg*, vol. 8, pp. 77-89, Mar 2001.

[11] S. A. Curley, "Radiofrequency ablation of malignant liver tumors," *Oncologist*, vol. 6, pp. 14-23, 2001.

[12] D. S. Lu, *et al.*, "Influence of large peritumoral vessels on outcome of radiofrequency ablation of liver tumors," *J Vasc Interv Radiol*, vol. 14, pp. 1267-74, Oct 2003.

[13] J. A. Marrero and S. Pelletier, "Hepatocellular carcinoma," *Clin Liver Dis*, vol. 10, pp. 339-51, ix, May 2006.

[14] E. J. Patterson, *et al.*, "Radiofrequency ablation of porcine liver in vivo: effects of blood flow and treatment time on lesion size," *Ann Surg*, vol. 227, pp. 559-65, Apr 1998.

[15] T. Livraghi, *et al.*, "Treatment of focal liver tumors with percutaneous radio-frequency ablation: complications encountered in a multicenter study," *Radiology*, vol. 226, pp. 441-51, Feb 2003.

[16] A. J. Aschoff, *et al.*, "How does alteration of hepatic blood flow affect liver perfusion and radiofrequency-induced thermal lesion size in rabbit liver?," *J Magn Reson Imaging,* vol. 13, pp. 57-63, Jan 2001.

[17] M. Kudo, "Radiofrequency ablation for hepatocellular carcinoma: updated review in 2010," *Oncology,* vol. 78 Suppl 1, pp. 113-24, Jul 2010.

[18] E. Vlaisavljevich, *et al.*, "Image-guided non-invasive ultrasound liver ablation using histotripsy: feasibility study in an in vivo porcine model," *Ultrasound Med Biol,* vol. 39, pp. 1398-409, Aug 2013.

[19] J. E. Parsons, *et al.*, "Pulsed cavitational ultrasound therapy for controlled tissue homogenization," *Ultrasound in Medicine and Biology,* vol. 32, pp. 115-29, Jan 2006.

[20] W. W. Roberts, *et al.*, "Pulsed cavitational ultrasound: a noninvasive technology for controlled tissue ablation (histotripsy) in the rabbit kidney," *J Urol,* vol. 175, pp. 734-8, Feb 2006.

[21] Z. Xu, *et al.*, "Controlled ultrasound tissue erosion," *IEEE Trans Ultrason Ferroelectr Freq Control,* vol. 51, pp. 726-36, Jun 2004.

[22] S. P. Allen, *et al.*, "Controlling cavitation-based image contrast in focused ultrasound histotripsy surgery," *Magn Reson Med,* Jan 27 2014.

[23] T. L. Hall, *et al.*, "Relaxation Properties of Cavitation Induced Tissue Lesions," presented at the Joint Annual Meeting of the International Society for Magnetic Resonance in Medicine. , 2007.

[24] T. Y. Wang, *et al.*, "Quantitative ultrasound backscatter for pulsed cavitational ultrasound therapy- histotripsy," *IEEE Trans Ultrason Ferroelectr Freq Control,* vol. 56, pp. 995-1005, May 2009.

[25] X. Zhang, *et al.*, "Real-time feedback of histotripsy thrombolysis using bubble-induced color Doppler," *Ultrasound Med Biol,* vol. 41, pp. 1386-401, May 2015.

[26] E. Vlaisavljevich, *et al.*, "Effects of tissue mechanical properties on susceptibility to histotripsy-induced tissue damage," *Phys Med Biol,* vol. 59, pp. 253-70, Jan 20 2014.

[27] Y. Kim, *et al.*, "In vivo transcostal histotripsy therapy without aberration correction," *Phys Med Biol,* vol. 59, pp. 2553-68, Jun 7 2014.

[28] T. L. Hall, *et al.*, "Histotripsy of the prostate: dose effects in a chronic canine model," *Urology,* vol. 74, pp. 932-7, Oct 2009.

[29] T. L. Hall, *et al.*, "Histotripsy of rabbit renal tissue in vivo: temporal histologic trends," *Journal of Endourology,* vol. 21, pp. 1159-66, Oct 2007.

[30] Y. Kim, *et al.*, "Developmental impact and lesion maturation of histotripsy-mediated non-invasive tissue ablation in a fetal sheep model," *Ultrasound Med Biol,* vol. 39, pp. 1047-55, Jun 2013.

[31] G. E. Owens, *et al.*, "Intermediate-term effects of intracardiac communications created noninvasively by therapeutic ultrasound (histotripsy) in a porcine model," *Pediatr Cardiol,* vol. 33, pp. 83-9, Jan 2012.

[32] K. W. Lin, *et al.*, "Histotripsy beyond the intrinsic cavitation threshold using very short ultrasound pulses: microtripsy," *IEEE Trans Ultrason Ferroelectr Freq Control,* vol. 61, pp. 251-65, Feb 2014.

[33] A. D. Maxwell, *et al.*, "Probability of cavitation for single ultrasound pulses applied to tissues and tissue-mimicking materials," *Ultrasound Med Biol,* vol. 39, pp. 449-65, Mar 2013.

[34] E. Vlaisavljevich, *et al.*, "Effects of Ultrasound Frequency and Tissue Stiffness on the Histotripsy Intrinsic Threshold for Cavitation," *Ultrasound Med Biol,* Mar 9 2015.

[35] E. Vlaisavljevich, *et al.*, "Effects of tissue stiffness, ultrasound frequency, and pressure on histotripsy-induced cavitation bubble behavior," *Phys Med Biol,* vol. 60, pp. 2271-92, Mar 21 2015.

[36] J. E. Parsons, *et al.*, "Cost-effective assembly of a basic fiber-optic hydrophone for measurement of high-amplitude therapeutic ultrasound fields," *J Acoust Soc Am,* vol. 119, pp. 1432-40, Mar 2006.

[37] R. E. Apfel and C. K. Holland, "Gauging the likelihood of cavitation from short-pulse, low-duty cycle diagnostic ultrasound," *Ultrasound Med Biol,* vol. 17, pp. 179-85, 1991.

[38] C. K. Holland, *et al.*, "Direct evidence of cavitation in vivo from diagnostic ultrasound," *Ultrasound Med Biol,* vol. 22, pp. 917-25, 1996.

[39] J. E. Coad, *et al.*, "Radiofrequency ablation causes 'thermal fixation' of hepatocellular carcinoma: a post-liver transplant histopathologic study," *Clin Transplant,* vol. 17, pp. 377-84, Aug 2003.

[40] J. Ding, *et al.*, "Comparison of two different thermal techniques for the treatment of hepatocellular carcinoma," *Eur J Radiol,* vol. 82, pp. 1379-84, Sep 2013.

[41] G. R. Schade, *et al.*, "Histotripsy Focal Ablation of Implanted Prostate Tumor in an ACE-1 Canine Cancer Model," *Journal of Urology,* vol. 188, pp. 1957-1964, Nov 2012.

[42] N. R. Styn, *et al.*, "Histotripsy of VX-2 Tumor Implanted in a Renal Rabbit Model," *Journal of Endourology,* vol. 24, pp. 1145-1150, Jul 2010.

[43] M. Queiroz-Andrade, *et al.*, "MR imaging findings of iron overload," *Radiographics,* vol. 29, pp. 1575-89, Oct 2009.

[44] S. Chundru, *et al.*, "MRI of diffuse liver disease: characteristics of acute and chronic diseases," *Diagn Interv Radiol*, vol. 20, pp. 200-8, May-Jun 2014.

[45] E. Ng, *et al.*, "Characterising benign fibrous soft-tissue tumours in adults: why is it so difficult and what do we need to know?," *Clin Radiol*, Mar 14 2015.

Chapter 11
Nanodroplet-Mediated Histotripsy for Image-guided Targeted Ultrasound Cell Ablation

11.1 Introduction

Many tumor types exhibit characteristically permeable vasculature with average endothelial gaps typically between 200-600 nm and show poor lymphatic drainage, which is collectively known as the enhanced permeation and retention (EPR) effect [2-5]. To take advantage of the EPR effect, phase change nanodroplets have been shown to extravasate across tumor's leaky vasculature and enter the interstitial space to directly target cancer cells [6-12]. Nanodroplets encapsulate a perfluorocarbon (PFC) core that is stabilized by albumin, lipid, or polymer shells [6-9]. The PFC core typically has a boiling point lower than 37°C, but nanodroplets remain in the liquid form at body temperature [13-15]. After passing through the leaky microvasculature to a tumor's interstitial space, these nanodroplets can be vaporized by ultrasound to form gas bubbles through acoustic droplet vaporization (ADV) [13-15]. Attachment of optimal targeting ligands allows nanodroplets to specifically bind to cancer cells [13, 15, 16]. Research has shown the use of nanodroplets and ADV for targeted imaging [11, 15-

18], drug delivery [11, 12, 15-18], and induce cavitation to enhance ultrasound thermal therapy [19-21].

One of the biggest limitations for current nanodroplet-mediated drug delivery or ultrasound thermal therapy is that nanodroplets (100–600 nm in diameter) cannot penetrate deep into the tumor tissue to reach the core after permeating across tumor's leaky vasculature. Therefore, their therapeutic utility in facilitating drug delivery or ultrasound thermal therapy by forming gas bubbles is greatly limited. To overcome this major limitation, we started working on combining PFC-encapsulated nanodroplets with histotripsy, which is a new, non-invasive, image-guided, ultrasound ablation method [22-26]. Histotripsy uses extremely high pressure, microseconds long pulses to generate a cluster of microbubbles (bubble cloud) from pre-existing gas pockets in the tissue where the rapid expansion and collapse of the microbubbles disrupts cells [23, 24, 26]. We hypothesize that combining histotripsy with PFC-encapsulated nanodroplets will cause the ultrasound pulses to vaporize the nanodroplets delivered to the surface of the tumor nodules and form gas bubbles. Using the resulting gas bubbles as cavitation nuclei will significantly reduce the pressure threshold needed to generate and maintain the cavitation bubble cloud, which will fractionate the tumor nodules layer by layer until the entire tumor is destroyed whereas, the surrounding normal tissue without the nanodroplets will have a higher threshold and will be preserved from the histotripsy-induced fractionation. As such, even with nanodroplets diffusing only to regions next to tumor vasculature, targeted histotripsy will destroy the tumor core, overcoming the limitation caused by the shallow penetration depth of nanodroplets. This hypothesis is supported by our previous studies showing that once the cavitation bubble cloud is initiated, the histotripsy process can be maintained at a much lower pressure than that needed for initiation [25]. The ability of histotripsy alone to erode a tissue

layer by layer has been demonstrated in excised tissue samples [27] and *in vivo* large animal models [28, 29]. Further, the resulting gas bubbles can function as ultrasound contrast agents, which will allow the tumor sites to be seen on ultrasound imaging and allow the histotripsy treatment to be guided and monitored in real-time by ultrasound imaging. By employing an ultrasound transducer with a large focal zone, this technique could also achieve efficient treatment of tumors with multiple nodules.

Before a nanodroplet-mediated histotripsy approach can be investigated *in vivo*, nanodroplets must be synthesized with an optimum size (< 500 nm) that allows them to diffuse through the tumor vasculature cancer [6-12]. Furthermore, these nanodroplets must be capable of reducing the pressure threshold to generate histotripsy bubbles and fractionate tissue. The goal of this study is to demonstrate the initial feasibility of nanodroplet-mediated histotripsy to set the foundation for future studies aimed at extending this technology to tumor ablation *in vivo*. We have synthesized an amphiphilic tri-block copolymer that encapsulates PFC forming nanodroplets with an average diameter of ~200 nm. This ABC tri-block copolymer is composed of a hydrophilic poly(ethylene glycol) (PEG) block, a central poly(acrylic acid) (PAA) block, and a random copolymer of heptadecafluorodecyl methacrylate (HDFMA) and methyl methacrylate (MMA) as the hydrophobic block. Nanodroplets are formulated using the PEG_{45}-*b*-PAA_{10}-*b*-P($HDFMA_8$-*co*-MMA_{21}) copolymer that encapsulates perfluoropentane (PFP, boiling temperature 29°C) in the droplet's core. The PAA block is chemically cross-linked to "stitch" adjacent polymer chains forming a flexible polymer shell, which increases the stability of the formed nanodroplets. We hypothesized that our nanodroplets will remain stable at body temperature (37 ºC) in the presence of serum proteins without an increase in their diameter above

the size cutoff of tumor vasculature, which will allow them to extravasate into the tumor tissue *in vivo*.

In this chapter, we describe initial studies examining the ability to combine our nanodroplets with histotripsy to achieve efficient cell ablation in tissue-mimicking phantoms. We first simulated the peak negative pressure threshold needed to form a gas microbubble of 50 μm in diameter using an initial bubble nucleus of 5-500 nm in diameter and a single 2-cycle pulse with different frequencies. In previous histotripsy studies, microbubbles were generated and expanded to >50μm in diameter to produce cell disruption. This microbubble dynamic is different from other nanodroplet studies for targeted imaging and drug delivery, and therefore requires substantially different acoustic parameters. Based on the simulation results, a 500 kHz focused transducer was used to apply a single 2-cycle ultrasound pulse, and the pressure threshold to acoustically vaporize the PFP encapsulated in the nanodroplet core and expand the resulting gas bubble to >50 μm was measured. We also examined the feasibility of using this technique to produce cavitation in selected regions and image the resulting bubbles with ultrasound imaging. Finally, we evaluated the ability of nanodroplets to fractionate red blood cells embedded in tissue-mimicking agarose gels when combined with a histotripsy pulse.

11.2 Methods

11.2.1 Formulation and Characterization of Nanodroplets

We synthesized an ABC triblock copolymer composed of a hydrophilic poly(ethylene glycol) (PEG) block, a central poly(acrylic acid) (PAA) block, and a random copolymer of heptadecafluorodecyl methacrylate (HDFMA) and methyl methacrylate (MMA) as the hydrophobic block via a one-pot "click" reaction [30-32]. PEG_{45}-*b*-PAA_{10}-*b*-P($HDFMA_8$-*co*-

MMA_{21}) copolymers were used to prepare PFP-loaded nanodroplets following the procedure shown in Figure 11.1. Briefly, PEG_{45}-*b*-PAA_{10}-*b*-P($HDFMA_8$-*co*-MMA_{21}) copolymers were dissolved in tetrahydrofuran (THF) (0.2% w/v) and cooled down to 0^{o}C before the addition of PFP (2% v/v) while vigorously stirring the reaction mixture. An equal amount of water was slowly added to this solution mixture to trigger micelle formation and the mixture was stirred for 1h in an ice bath. The micelles solution was transferred into a dialysis bag (MWCO of 1 KDa) and dialyzed against ice-cold 2-(*N*-morpholino) ethanesulfonic acid (MES) solution or water to remove the THF. After 12 hours of dialysis, a slightly milky solution of PFP-loaded nanodroplets was observed. The PAA block was chemically cross-linked using 2,2`-(ethylenedioxy)-bis(ethylamine) as a cross-linker via NHS/EDC coupling chemistry [33-35] to form a flexible polymer shell that stabilizes the nanodroplets but allows acoustic droplet vaporization to form microbubbles. Selection of ideal polymer composition and PFP content used in this study has been optimized in a separate investigation [31, 32].

Nanodroplet concentration and size distribution were characterized using Nanoparticle Tracking Analysis (NTA). Measurements were obtained using a NanoSight NS500 (NanoSight Ltd., Amesbury, United Kingdom), equipped with an LM14 (405 nm laser), high sensitivity EMCCD Andor Luca camera and a syringe pump. Upon dilution to the appropriate NTA concentration with DI Water (MilliQ, 18MΩ), both capture and analysis were carried out using the NTA software (Version 2.3, Build 0027) at 22^{o}C and 37^{o}C. The samples were measured by capturing 60 s videos (6 videos per each sample). The error bars represent the standard deviation of the repeat measurements of each sample. The mean size and standard deviation values obtained by the NTA software correspond to arithmetic values calculated with the sizes of all particles analyzed for each sample (n = 6).

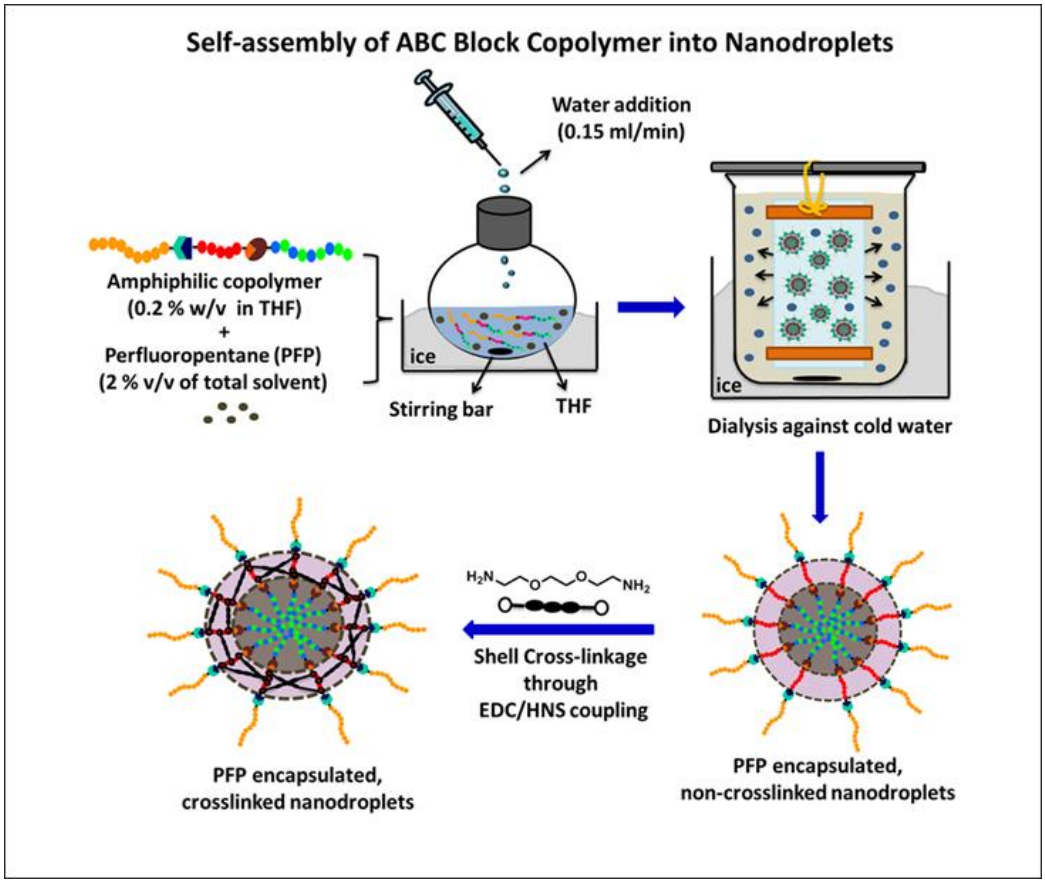

Figure 11.1. Formulation of PFP-loaded nanodroplets by self-assembly of amphiphilic triblock PEG45-b-PAA10-b-P(HDFMA8-co-MMA21) copolymer around the PFP core followed by shell cross-linkage via EDC/HNS coupling reactions.

11.2.2 Biocompatibility of Nanodroplets

Toxicity of the PEG_{45}-*b*-PAA_{10}-*b*-P($HDFMA_8$-*co*-MMA_{21}) copolymer used to formulate the nanodroplets was investigated as a function of polymer concentration using the MTT assay (EMD Millipore, Billerica, MA). Briefly, human prostate cancer cells (PC-3) were seeded at a seeding density of 1×10^5 cells/well in 96-well plates and allowed to adhere overnight before replacing the culture medium with phenol red-free RPMI 1640 medium solution containing 0.3, 1.5, 15, 30 and 75 μg/mL of the PEG_{45}-*b*-PAA_{10}-*b*-P($HDFMA_8$-*co*-MMA_{21}) copolymer formulated into PFP-loaded nanodroplets with an average diameter of ~200 nm, which

corresponds to droplets concentrations of $2.06x10^8$, $1.03x10^9$, $1.03x10^{10}$, $2.06x10^{10}$, $5.15x10^{10}$ particles/mL, respectively. The nanodroplets solution was aspirated after incubating for 24 hours under normal culture conditions followed by adding 10 μL of the MTT reagent to each well and incubating for 2 hours according the manufacturer's guidelines to allow enough time for the formation of the purple formazan precipitate. A 100 μL of the detergent solution was added to each well and incubated for 3 hours in the dark at room temperature before measuring the UV absorbance at 570 nm using a Multiskan microplate reader (Thermo Fisher Scientific Inc., Waltham, MA). PC-3 cells incubated with blank RPMI1640 culture medium and 5% v/v Triton X-100 solution were used as negative and positive controls, respectively. The statistical difference in UV absorbance between RPMI1640-treated cells (negative control) and those incubated with different concentrations of the copolymer was evaluated using student's *t*-test where $p < 0.05$ indicated a statistically significant difference in cell viability.

11.2.3 Threshold Simulation for Nanodroplet-Mediated Cavitation

A numerical simulation based on a modified Keller-Miksis equation for soft-tissue bubble dynamics [36, 37], was performed to estimate the relationship between frequency and bubble expansion for nanodroplet-mediated histotripsy with nanodroplets of 5-500 nm diameter. The peak negative pressure to expand initial bubbles of 5-500 nm diameters into 50 μm diameter bubbles was determined. Vaporization was not accounted for in this simulation, but the P- thresholds to achieve this bubble expansion are expected to be sufficiently high to vaporize the nanodroplets based on the literature [13, 38].

The simulation computed the bubble radius vs. time in response to a driving pressure waveform by

$$\left(1-\frac{\dot{R}}{c}\right)R\ddot{R}+\left(1-\frac{\dot{R}}{3c}\right)\frac{3}{2}\dot{R}^2=\left(1+\frac{\dot{R}}{c}\right)\frac{p_w(\dot{R},R,t)}{\rho}+\frac{R}{\rho c}\frac{\partial p_w}{\partial t}, \textbf{(E11.1)}$$

where R is the bubble radius, the dot indicates a derivative with respect to time, c is the sound speed, ρ is the medium density, and p_w is the pressure at the bubble wall in the medium surrounding the bubble, defined as

$$p_w\left(\dot{R},R,t\right)=\left(p_0-p_v+\frac{2\sigma}{R_0}\right)\left(\frac{R_0}{R}\right)^{3\kappa}-p_0-\frac{2\sigma}{R}-\frac{4G}{3R^3}\left(R^3-R_0{}^3\right)-\frac{4\mu\dot{R}}{R}-p_a(t) \textbf{(E11.2)}.$$

In Eq. 2, p_0 and p_v are the ambient and vapor pressure, respectively, σ is surface tension, R_0 is the initial bubble radius, κ is the polytropic index, G is the shear modulus, μ is the dynamic viscosity, and $p_a(t)$ is the acoustic driving pressure. The tissue Young's modulus ($E \sim 3G$) and μ were chosen to match the agarose tissue phantom properties used in this study (E = 38 kPa and μ = 0.05 Pa-s), which were within the property range of hepatocellular carcinoma (E = 20.4–75 kPa), metastatic liver tumors (E = 23.6–75 kPa), and prostate cancer tissue (E = 24 kPa) [39, 40]. The surface tension (σ) was estimated for soft tissue as σ = 54 mN/m [41]. Other properties were selected to match values for water at 20^{o}C.

The pressure waveform for the simulation employed an analytical pulse model [42] to create a 2-cycle, asymmetric pulse with a similar P_+/P_- to that in Figure 2. The pressure is given as

$$p_a(t)=p_f\sum_{k=1}^{\infty}\left[\frac{\sin\left(k\omega\left(t-\tau\right)+\phi\right)}{k}\right]\cdot\exp\left[-\left(\frac{t-\delta}{\xi}\right)^2\right] \textbf{(E11.3)},$$

where p_f is the fundamental pressure amplitude, ω is the radial frequency, τ is the starting phase, ϕ is a phase shift to create waveform asymmetry, δ is the time delay to the center of the pulse, and ξ defines pulse duration. The waveform at 0.5 MHz, $\omega = 3.14 \times 10^6$ rad/s, $\tau = 1.25\ \pi$ /

ω, $\phi = -\pi/4$, $\delta = 6.3$ μs, and $\xi = 2.6$ μs. The simulation was also performed at $f = 0.2$ and 1.1 MHz, scaling the above parameters to maintain the same waveform shape.

11.2.4 Ultrasound Setup

Ultrasound pulses were generated by two 500 kHz focused ultrasound transducers built in house. The two transducers were fabricated using rapid prototyping technology and contained 32 and 7 elements, respectively. Each module consists of a 2 inch (50.8 mm) diameter lead zirconate titanate (PZT) disc element coupled to an elliptical acoustic lens through a quarter wavelength matching layer. Transducer shells contained threaded receptacles populated with individual element modules. The 32 element transducer had an aperture diameter of 300 mm, a focal distance of 150 mm, and a focal zone (Measured -6 dB Pressure) of 1.8 x 3.9 mm. The 7 element transducer had an aperture diameter of 200 mm, a focal distance of 150 mm, and a focal zone (Measured 6 dB Pressure) of 3.4 x 20.7 mm. A field-programmable gate array (FPGA) was used as a custom pulse generator to electronically control each channel (Altera Corp., San Jose, CA). The FPGA was connected to a 32-channel bank of high voltage pulsers developed in-house. Acoustic waveforms produced by the 500 KHz therapeutic transducer [Fig. 11.2(B-C)] were obtained using a fiber optic probe hydrophone built in house [43]. Pressure wave measurements were recorded in free-field in degassed water at room temperature. At higher pressures above the histotripsy cavitation threshold, pressure could not be accurately measured due to instantaneous cavitation at the fiber tip. These higher pressure levels were estimated as a summation of the pressures generated by the individual elements, which were sparsely distributed without a significantly overlapping beam and closely matched the predicted values using a linear extrapolation of the lower pressure values measured with all elements. The 7 element transducer

was used for the selective cavitation generation experiment, because the larger focal region of this transducer was needed for that experiment set. The 32 element transducer was used for all other experiments, as it is capable of generating high pressure beyond the intrinsic threshold. Cavitation bubbles were optically imaged using a high-speed, 1 megapixel CCD camera, (Phantom V210 - Vision Research, Wayne, New Jersey, USA) [Fig. 11.2(A)]. The camera was focused through a macro lens (Tominon 105 mm f/4.5 Kyocera Corp., Japan) and folding optical bellows (Nikon Corp., Japan).

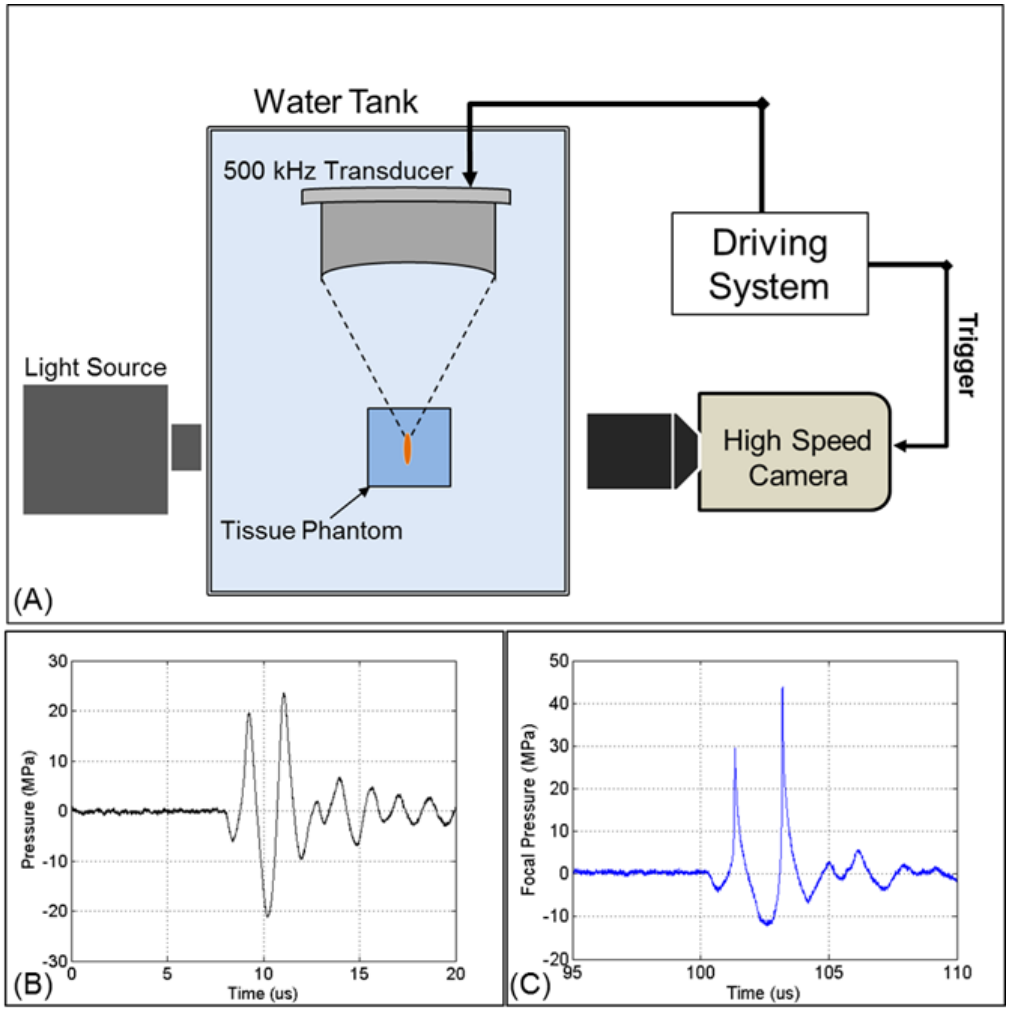

Figure 11.2. Acoustic waveform and experimental setup. (A) The focus of one of the 500 kHz transducers was aligned inside tissue phantoms containing nanodroplets. Cavitation was monitored using high speed optical imaging. Example of a 2-cycle histotripsy pulse generated by the (B) 32 element and (C) 7 element transducers.

11.2.5 Preparation of Tissue Phantoms

Agarose phantoms were used to provide a well-controlled viscoelastic medium for this study, as histotripsy-induced damage is highly dependent on the tissue mechanical properties. Tissue phantoms containing 1% agarose w/v were prepared by slowly mixing agarose powder (Agarose Type VII, Sigma-Aldrich, St. Louis, MO) into s saline solution (0.9% sodium chloride, Hospira) heated to above 70°C while stirring until the gel became completely transparent. Agarose solutions were degassed under a partial vacuum of 20.5 mmHg for 30 minutes before allowing the agarose solutions to cool down to 37°C. Phantoms containing nanodroplets were prepared by slowly adding the nanodoplets ($2.36x10^8$ particles/mL) into the agarose solution while stirring. The agarose mixtures were poured into rectangular polycarbonate holders and placed in a refrigerator at 4°C to allow the solution to solidify forming tissue phantoms with embedded nandroplets (test) or without nanodroplets (control). The Young's modulus of the tissue phantom was 38kPa [44], which is within the range of the Young's modulus of hepatocellular carcinoma tumors (20.4–75 kPa), metastatic liver tumors (23.6–75 kPa), and prostate tumors (24 kPa) [39, 40]. Tissue phantoms were warmed prior to use and maintained at 37°C for the duration of all experiments performed in this work.

For cell fractionation experiments, tissue phantoms with a red blood cell (RBC) layer were prepared using canine RBCs in 0.9% isotonic saline and 1% agarose solutions with and without nanodroplets. Fresh canine blood was obtained from adult research subjects in an unrelated study and added to an anticoagulant solution of citratephosphate-dextrose (CPD) (Sigma-Aldrich Co., St. Louis, MO) with a CPD-to-blood ratio of 1:9 mL. Whole blood was separated in a centrifuge at 3000 rpm for 10 min. The plasma and white buffy coat were removed,

and the RBCs were saved for addition to the phantom. To prepare the RBC phantom, an initial layer of 1% agarose mixture (with and without nanodroplets) was poured into a rectangular polycarbonate housing to fill half of it at 37°C. The housing was placed in a refrigerator at 4°C to allow the agarose to cool and solidify. The remaining solution was kept at 37°C. A small amount of agarose solution was mixed with the RBCs (5% RBCs v/v). The frame with solidified agarose was removed from refrigeration, and a thin layer of the RBC-agarose solution was poured onto the gel surface to allow the entire surface to coat in a thin layer. After 5 min, the RBC-agarose layer was solidified, and the remaining agarose solution without RBCs was poured to completely fill the frame. This procedure created a thin layer of RBCs suspended in the center of the agarose phantom.

11.2.6 Measurement of Histotripsy Threshold in Agarose Tissue Phantoms

The pressure threshold to form and expand microbubble to >50 μm diameter using a single 2-cycle ultrasound pulse was recorded in agarose tissue phantoms with and without nanodroplets. To determine the cavitation threshold, the ultrasound pulse was applied to the center of tissue phantoms with and without nanodroplets using the 32 element 500 kHz transducer at pressures ranging from 2–40 MPa. The sample size was 100 pulses for each pressure level by applying 100 pulses separated by 10 sec between pulses (i.e., pulse repetition frequency (PRF) of 0.1 Hz), to provide adequate time for any residual nuclei from the bubble collapse by the previous pulse to dissolve. In this way, each of the 100 pulses was expected to generate cavitation independently without influence from the previous pulses. To evaluate the threshold variation using different nanodroplet formulations in different phantoms, this process

was repeated using nanodroplets synthesized on 3 different occasions each evaluated using two tissue phantoms (total n=6) using 100 pulses at each pressure level.

Cavitation was monitored using high-speed optical imaging [Fig. 11.2]. A high-speed V210 camera (Vision Research, Wayne, NJ) was used to capture images of the focal zone directly after the propagation of each pulse through the focus in the phantoms. The camera was focused with a macro-bellows lens (Tominon, Kyocera, Kyoto, Japan) through the optical window of the chamber to observe the focal region. The camera was backlit by a continuous light source to produce shadowgraphic images of cavitation bubbles. The camera was triggered to record one image for each pulse applied, 10–40 μs after the beginning of the pulse reached the focal center. The timing was actively adjusted at each pressure level to coincide with the maximal bubble expansion occurrence. This process ensured that the pressure pulse had passed over the entire focal volume at the time of capture and the bubbles were imaged at the point of maximal expansion. The camera exposure time was 2 μs for all images. After acquisition, images were converted from grayscale to binary by an intensity threshold determined based on the background intensity of the shadowgraphs in image-processing software (Matlab; The Math-Works, Natick, MA, USA). The events when a bubble was expanded to >50μm within the focus were analyzed and recorded for each pressure level because such bubble expansion was shown in histotripsy to achieve tissue fractionation. The number of pulses (out of 100) in which one or more such cavitation events was observed to occur was recorded for each sample as the cavitation probability (P_{cav}). The average cavitation probability at each pressure level for the six samples was plotted for tissue phantoms containing nanodroplets as well as control phantoms without nanodroplets with the error bars representing the standard deviation. An interpolation fit was performed on the plot in Matlab to calculate the P- threshold, which was considered to be

the point at which 50% of the pulses generated cavitation bubbles >50 um (i.e. P_{cav}=0.50). The P-threshold was calculated for each sample (n=6) and reported as the mean ± the standard deviation. The minimum pressure level at which any cavitation bubbles >50 μm were observed was similarly analyzed and reported as the mean ± the standard deviation. Finally, the difference between P_{cav}=0.15 and P_{cav}=0.85, a relative measure of the steepness of the transition from P_{cav}=0 to P_{cav}=1 was calculated and reported as the mean ± the standard deviation for phantoms containing nanodroplets as well as histotripsy only controls.

11.2.7 Selective Cavitation in Composite Agarose Phantom

Using a focal zone covering multiple sub-regions loaded with the nanodroplets adjacent to other sub-regions without the nanodroplets, we hypothesized that cavitation can be selectively generated only in the sub-regions containing the nanodroplets by applying ultrasound at an acoustic pressure that is above the cavitation threshold with nanodroplets but below the cavitation threshold using histotripsy alone. To test this hypothesis, we prepared agarose phantoms containing hexagonal inclusions that were the only regions within the gel loaded with the nanodroplets. Briefly, composite tissue phantoms were prepared by pouring 1% agarose solution into a rectangular polycarbonate housing before submerging and fixing eight 6.5 mm thick hexagonal inclusions inside the phantom. The phantom with the inclusions was placed in a refrigerator at 4°C to allow the agarose to solidify. After the agarose solution solidified, the hexagon inclusions were removed from the tissue phantom leaving hexagonal voids that were then filled with 1% agarose solution containing the nanodroplets at a concentration of $3.0x10^8$ particles/mL. This procedure created a tissue phantom with hexagonal “islands” containing nanodroplets surrounded by an agarose gel without nanodroplets. Subsequently, the focus of the

7 element transducer was aligned to cover two of the nanodroplets-containing hexagons and the agarose gel without nanodroplets between them. Histotripsy pulses were applied to the focus at a PRF of 10 Hz at a peak negative pressure of 17.3 MPa. The resulting cavitation bubbles were monitored by high-speed optical imaging. Additionally, cavitation bubble generation was monitored by a clinical ultrasound imaging system (HDI 5000 Ultrasound system).

11.2.8 Bubble Behavior

To determine if nanodroplet-mediated cavitation bubbles exhibited similar expansion and collapse behavior to histotripsy bubbles, optical images of the growth and collapse of bubbles were recorded by the high-speed camera. Nanodroplet-mediated cavitation bubbles were generated by the 32 element 500 kHz transducer at a peak negative pressure of 15.6 MPa. This pressure level was selected because it is lowest pressure at which a cavitation cloud was always generated using a 2-cycle ultrasound pulse in tissue phantoms with nanodroplets. The expansion and collapse behavior of bubbles was reconstructed from a series of bubble clouds imaged at different time delays after the pulse. Ten pulses were applied to agarose tissue phantoms containing nanodroplets at each time delay at a PRF of 1 Hz. The focus was then moved to a different location within the tissue phantom and camera delay was increased 3 μs. Delay intervals of 0–60 μs were used to reconstruct a sequence of bubble images covering the entire period of bubble expansion and collapse. Shadowgraph images were converted from grayscale to binary by an intensity threshold determined by the background intensity using image processing software (Matlab, The Mathworks). Bubbles were indicated by black regions >5 pixels. The minimum resolvable diameter of a bubble using this minimum 5-pixel area was approximately 15 μm. The average diameter of 10 bubbles visible within the focus was measured for each pulse

at each time delay. A sample size of 10 pulses was used for each time delay and the average bubble size ± the standard deviation was plotted as a function of time.

11.2.9 Ablation of Red Blood Cells in Tissue Phantom

Agarose gel phantoms with an embedded RBC layer were used to characterize cell fractionation induced by nanodroplet-mediated histotripsy. Fractionation of the RBCs turns the color of the embedded cell layer from opaque red to translucent as the RBCs were lysed, which allows direct visualization of the histotripsy-induced fractionation process [45]. Previous studies have also shown that the lesion visualized in RBC phantoms is similar to the lesion generated in tissue identified by histology [45]. The focus of the 32 element 500 kHz transducer was aligned with the center of the red blood cell phantom layer and 2000 histotripsy pulses were applied at a PRF of 10 Hz at peak negative pressures of 6.2 MPa, 11.0 MPa, 15.9 MPa, and 20.7 MPa with and without nanodroplets (n=6). The bubble cloud and resulting cell fractionation was recorded by high-speed optical imaging after each pulse [Fig. 11.2]. The high-speed camera (Phantom V211, Vision Research) was focused to the red blood cell layer and backlit by a continuous light source. The camera was triggered to record two images for each applied pulse, one 10 μs after the pulse reached the focus to visualize the bubble activity and another frame between pulses, 50 ms after each pulse, to assess tissue damage. The camera exposure time was 10 μs. The bubbles appeared as black regions in the shadowgraphic image and RBC fractionation was visualized as RBCs turn transparent after fractionation. Cell fraction was compared between RBC phantoms with nanodroplets and control RBC phantoms without nanodroplets. Shadowgraph images were converted from grayscale to binary by an intensity threshold determined by the background

intensity using image processing software (MATLAB, The Mathworks) and the lesion area after 2000 pulses was calculated by summing the pixels within the fractionated region.

11.3 Results

11.3.1 Nanodroplets Formulation and Biocompatibility

Results show that PEG_{45}-*b*-PAA_{10}-*b*-P($HDFMA_8$-*co*-MMA_{21}) copolymer successfully encapsulated PFP (2% v/v) forming nanodroplets with an average diameter of 192±4.6 nm and 204±4.7 nm at 22°C and 37°C, respectively. Figure 11.3(A) is a representative image showing the size distribution for a single sample of nanodroplets in the range of 100–400 nm with >99% of the nanodroplets smaller than 400 nm and <0.01% larger than 600 nm. The peak of the size distribution is 128.5 ± 9.1 nm and 138.5 ± 8.0 nm at 22°C and 37°C, respectively. The similar size distribution at 22°C and 37°C indicates that the encapsulated PFP core remained as a liquid at the body temperature (37°C) and did not change into a gas, which is consistent with previous studies [13-15]. The observed control over the size and shape of the formed nanodroplets is a result of the fine control over the length, molecular weight, and composition of the amphiphilic polymer used to formulate these nanodroplets [46, 47]. Specifically, the PAA and P(HDFMA-*co*-MMA) blocks in the amphiphilic PEG_{45}-*b*-PAA_{10}-*b*-P($HDFMA_8$-*co*-MMA_{21}) copolymer were synthesized via atom transfer radical polymerization (ATRP), which allows fine control over the length, composition, and functionality of the formed blocks [46] [48].

Research showed that self-assembled polymeric micelles tend to disassemble at higher temperatures and upon dilution to concentrations below their critical micelle concentration [46]. Nanodroplets with polymer, lipid, and protein shells have also been shown to coalesce forming larger microbubbles, which limits their ability to diffuse across tumor vasculature *in vivo* [49].

Therefore, we relied on covalent chemical cross-linkage of the polymer shell to increase nanodroplets stability against physiological shear stress *in vivo* and maintain the size, shape and concentration of the nanodroplets. Our results show that nanodroplets' concentration at 22^{o}C (3.07 x 10^{10} particles/mL) did not change upon increasing the solution temperature to 37^{o}C (3.00 x 10^{10} particles/mL) [Fig. 11.3(A)], which is critical for the success of the envisioned ablation approach as the number of cavitation nuclei is directly proportional to the number of stable nanodroplets present at tumor site. The initial testing of stability and biocompatibility of these nanodroplets is promising. Further, the size range of our nanodroplets should allow them to preferentially diffuse through the leaky tumor vasculature while preventing diffusion through normal blood vessels [2-5]. In addition, this nanodroplet design allows the covalent attachment of different targeting ligands to the free end of the PEG block allowing the incorporation of a "tunable" number of targeting motifs on the droplets surface. These targeted nanodroplets will allow selective binding to cancer cells, which should increase droplets concentration and retention in the tumor tissue.

Research shows that 90% of the PFP concentration in the blood can be eliminated from the body within 10 minutes after their administration, which diminishes the risk of toxicity [50]. Therefore, we investigated the toxicity of the PEG_{45}-*b*-PAA_{10}-*b*-P($HDFMA_8$-*co*-MMA_{21}) polymer used to formulate the nanodroplets as a function of polymer concentration using the MTT assay. Results show that there was no change in the number of viable PC-3 cells upon incubation with the PFP-loaded nanodroplets for 24 hours up to a polymer concentration of 75 μg/mL ($5.15x10^{10}$ droplets/mL) compared to the negative control ($p>0.05$) [Fig. 11.3(B)]. This is a significant finding given that the highest reported nontoxic concentration of nanodroplets that were formulated using PEG-lipid conjugates is $2.5x10^8$ droplets/mL[51], which is 200-fold

lower than the nanodroplets concentration used in our study. These results collectively indicate the ability to reproducibly formulate stable nanodroplets that are nontoxic to mammalian epithelial cells at high concentrations up to $5.15x10^{10}$ particles/mL.

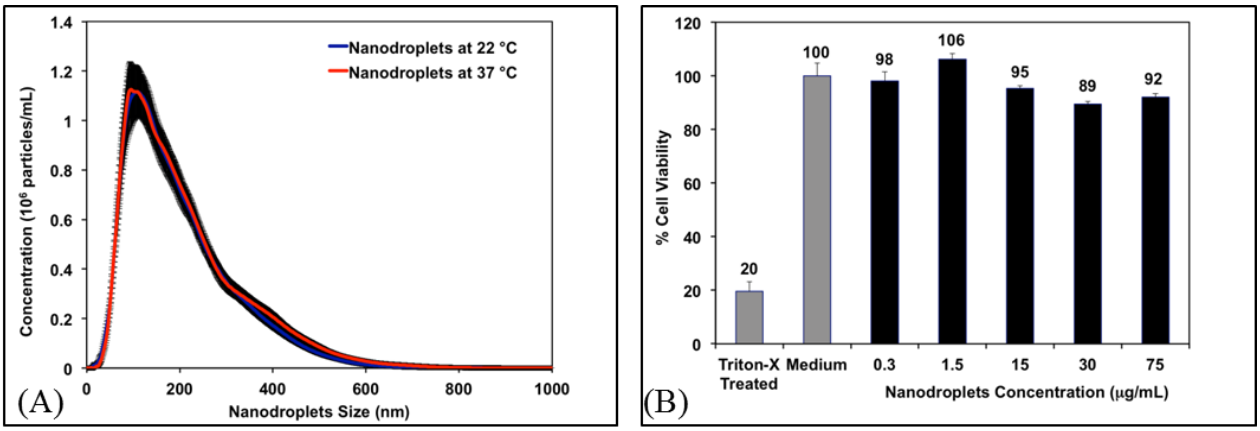

Figure 11.3. (A) A representative image showing the size distribution of PFP-loaded nanodroplets. Results show an average nanodroplet size of approximately 200 nm with the peak of the size distribution at 128.5 ± 9.1 nm and 138.5 ± 8.0 nm at 22°C and 37°C, respectively. (B) MTT results show no significant change in the viability of PC-3 cells incubated with 0.3, 1. 5, 15, 30 and 75 µg/mL of the triblock copolymer used to formulate the PFP-loaded nanodroplets compared to PC-3 cells incubated with blank culture medium.

11.3.2 Threshold Simulation for Nanodroplet-Mediated Cavitation

In a previous histotripsy study, the threshold to generate cavitation using a single, µs-length pulse in multiple tissues and tissue-mimicking media was measured to be 26–30 MPa peak negative pressure [37]. At the high pressure above 26 MPa, cavitation bubbles are generated from pre-existing gas pockets in the tissue <10 nm in size and expanded to >50 µm followed by energetic collapse, all within a hundred µs. This energetic bubble activity disrupts adjacent cells and eventually produces complete fractionation of cells in the target tissue into a liquefied homogenate. To determine the effects of nanodroplets on reducing the peak negative pressure (P-) threshold to generate and expand microbubbles to >50 µm, a numerical simulation based on a modified Keller-Miksis equation for soft-tissue bubble dynamics as outlined in a

previous study [37] was performed using initial gas bubbles 5–500 nm in diameter. We will refer to this threshold as the "histotripsy threshold" in this paper to distinguish from cavitation threshold commonly referred in the literature, which is often observed to be at much lower pressure levels with the presence of nuclei on the order of microns and/or using much longer pulses [52, 53]. The simulation used a 2-cycle pulse and compared frequencies of 0.2, 0.5, and 1.1MHz. The simulation showed that the histotripsy threshold increased substantially with increasing frequency [Fig. 11.4]. For example, the histotripsy threshold using an initial 200 nm bubble was 1.7, 6.3, and 21.3 MPa at 0.2, 0.5, and 1.1 MHz, respectively. Using an initial gas bubble at a diameter of 200 nm and above, there was no significant change in the threshold for the same frequency, whereas using a 100 nm initial nucleus, the histotripsy threshold was higher. The initial bubble size mattered little in the 200–500 nm range because the pressure amplitude to achieve 50 μm max radius is much larger than the inertial cavitation threshold for bubbles this size. In this case the bubble motion is dominated by inertia, which leads to bubbles expanding to approximately the same size regardless of initial radius. Nanodroplet vaporization was not accounted for in this simulation, but P- thresholds are expected to be sufficiently high to vaporize the nanodroplets based on the literature [13, 38].

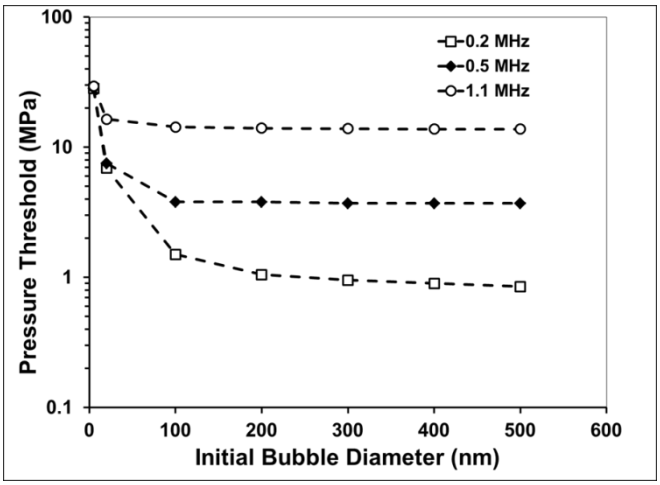

Figure 11.4. A plot showing the simulated peak negative pressure (P-) threshold to expand a bubble from an initial diameter of 5–500 nm to 50 μm in tissue.

11.3.3 Measurement of Histotripsy Threshold in Agarose Tissue Phantoms

In order to validate the simulation results, the pressure threshold to vaporize the nanodroplets and expand the resulting bubbles >50 μm was measured in tissue-mimicking agarose phantoms with and without nanodroplets. Based on the analysis of high-speed images, results demonstrated a significant decrease in the histotripsy threshold with nanodroplets compared to histotripsy only controls. The minimum pressure level at which cavitation bubbles >50 μm was observed by high speed images to be 3.02±2.49 MPa for phantoms containing nanodroplets and 15.60±2.35 MPa for histotripsy only controls without nanodroplets [Fig. 11.5]. The pressure level at which 50% of the 100 pulses generated cavitation bubbles >50 μm, P_{cav} = 0.50, was found to be 10.77±0.32 MPa with nanodroplets compared to 28.79±0.47 MPa without nanodroplets (n=6). The difference between P_{cav}=0.15 and P_{cav}=0.85 was found to be 3.17±0.65 MPa and 2.14±0.41 MPa for phantoms with and without nanodroplets, respectively. At pressures ≥15.9 MPa, cavitation microbubbles were always observed (P_{cav} = 1). At pressure greater than 11MPa, the area of the bubble cloud increased with increasing pressure [Fig. 11.6]. For example, the lateral width of the bubble cloud was 1.1 mm, 2.0 mm, and 2.4 mm at peak negative pressures of 13.9 MPa, 15.9 MPa, and 20.7 MPa, respectively. These widths match closely with the lateral width of the focal zone where the pressure was above 11 MPa.

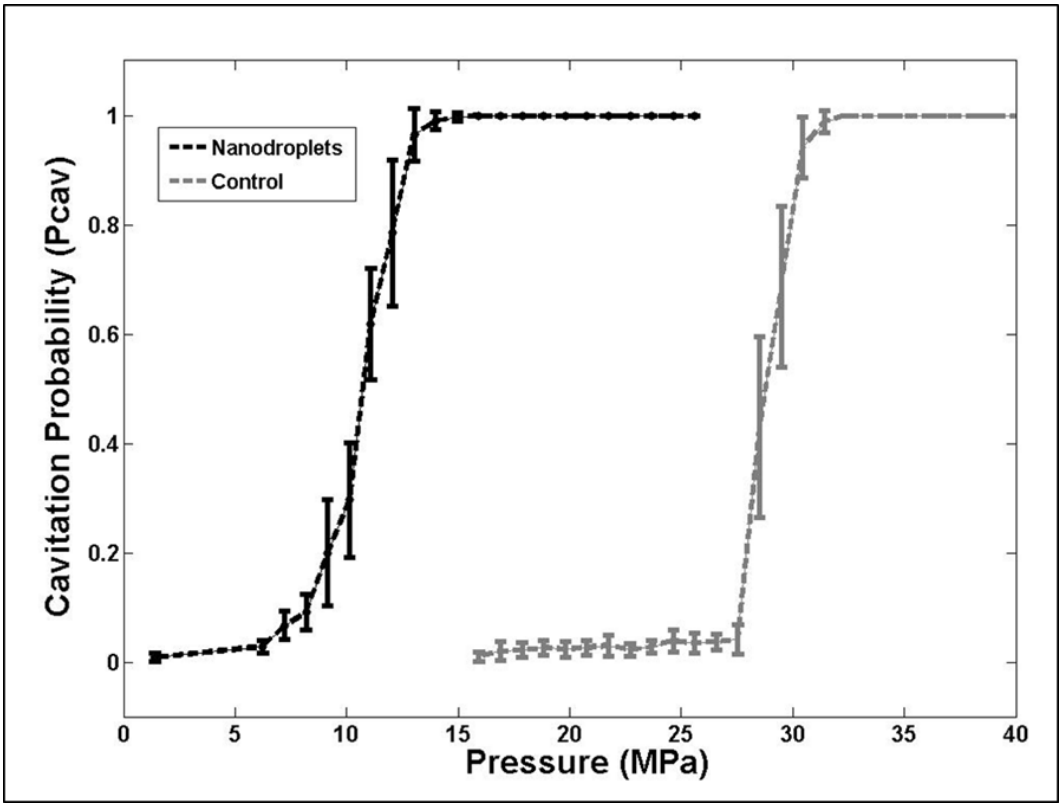

Figure 11.5. A plot showing the histotripsy threshold in agarose tissue phantoms with and without nanodroplets. Results demonstrated a significant decrease in the pressure threshold to generate cavitation bubbles >50 μm with nanodroplets compared to control conditions (histotripsy only).

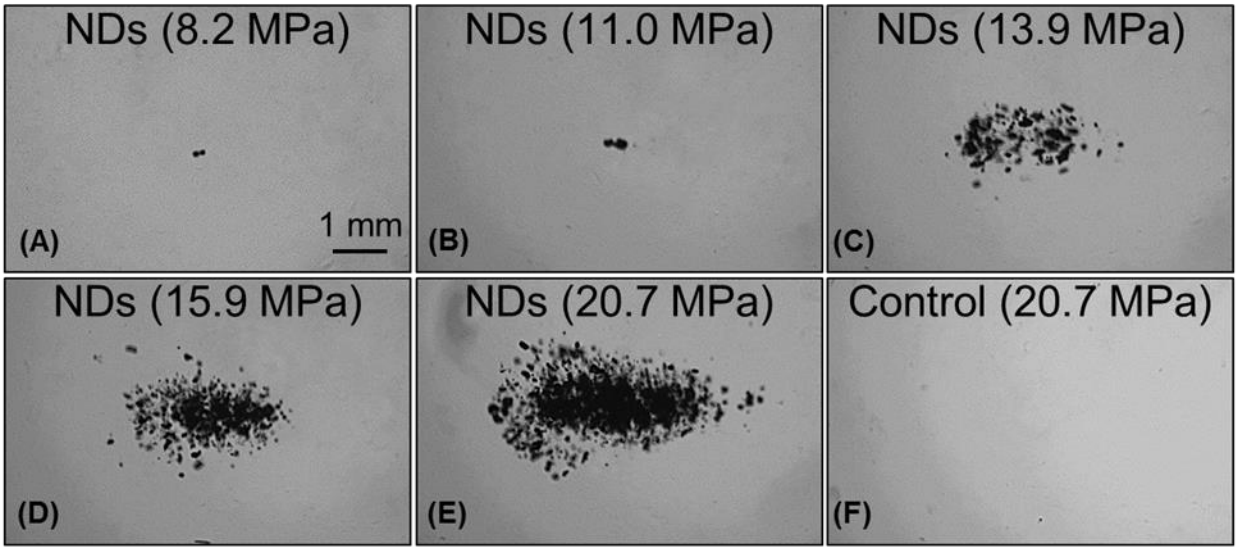

Figure 11.6. Images of nanodroplet-mediated cavitation in agarose tissue phantoms at increasing acoustic pressures. Images of cavitating bubble clouds (dark) generated using agarose phantoms containing nanodroplets at the pressure of 8.2–20.7 MPa (A–E). With increasing pressure, the area of the bubble cloud increased. In comparison, cavitation wasn't observed in control samples in this pressure range MPa (F).

11.3.4 Selective Cavitation in Composite Agarose Phantom

Based on the reduced histotripsy threshold using nanodroplets, cavitation should be selectively generated in multi-tumor nodules with nanodroplets inside the focal zone, whereas no cavitation should be formed at normal tissue without nanodroplets. The feasibility of using nanodroplets to generate selective cavitation was investigated using a composite agarose tissue phantom. Histotripsy pulses were applied inside the composite agarose tissue phantom containing inclusions with nanodroplets. Using 2-cycle pulses at a peak negative pressure of 17.3 MPa, which is above the histotripsy threshold using nanodroplets and below the intrinsic threshold using histotripsy alone, cavitation bubble clouds were formed only in the inclusions containing nanodroplets located within the focal volume of the 500 kHz transducer [Fig. 11.7(A)]. Optical images indicated two separate dense cavitation clouds inside the nanodroplet-containing inclusions inside the focal region throughout the 2000 pulses while no bubbles were observed outside the inclusions within the focal region [Fig. 11.7(B)]. Correspondingly, ultrasound imaging showed two dynamically changing hyperechoic zones inside the hexagon inclusions, while no bubbles were observed elsewhere [Fig. 11.7(C)]. As these cavitation bubbles generated in the process are viewed clearly on ultrasound imaging, the histotripsy therapy process can be monitored and guided by ultrasound imaging in real-time.

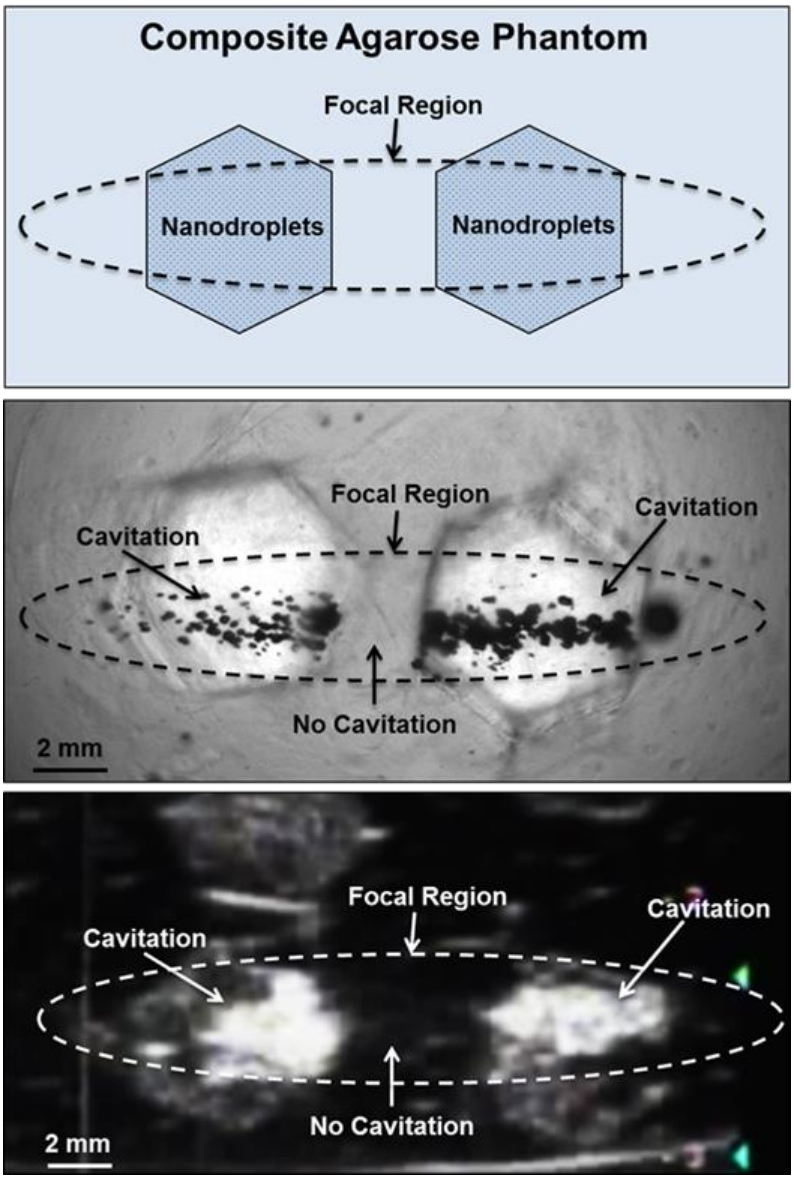

Figure 11.7. Selective cavitation in a composite agarose tissue phantom. Optical images (middle) of agarose phantoms with hexagon shaped inclusions containing nanodroplets (top) showed cavitation within the focal area only occurred in locations containing nanodroplets while no cavitation was observed in regions without nanodroplets. Ultrasound imaging (bottom) demonstrated nanodroplet guided cavitation treatment can be monitored in real-time with bubbles appearing as dynamically changing hyperechoic regions.

11.3.5 Bubble Behavior

The bubble expansion and collapse observed in histotripsy is substantially more energetic than traditionally defined inertial cavitation where the maximal bubble diameter becomes equal or greater than twice the initial bubble size [54]. In histotripsy, microbubbles formed from

preexisting nuclei <10nm grow to over 50 μm before violently collapsing, all occurring within 100 μs. This bubble behavior is critical to achieve cell disruption. To study the behavior of cavitation bubbles generated by nanodroplet-mediated histotripsy, optical images of bubbles were recorded by the high-speed camera at different time delays after the arrival of the histotripsy pulse. The peak negative pressure of 15.6 MPa was used, because it is the lowest pressure at which a cavitation cloud was always generated (P_{cav}=1) using nanodroplets. In agarose gel, the bubble diameter increased to the maximum diameter of 311.2±49.9 μm at 21 μs [Fig. 11.8]. The average bubble lifespan from the arrival of the histotripsy pulse to when the bubble became too small to be observed on the optical image was measured to be ~60 μs. This level of bubble expansion and collapse is similar to the behavior of bubbles formed using histotripsy alone at higher pressures and is anticipated to create cell disruption.

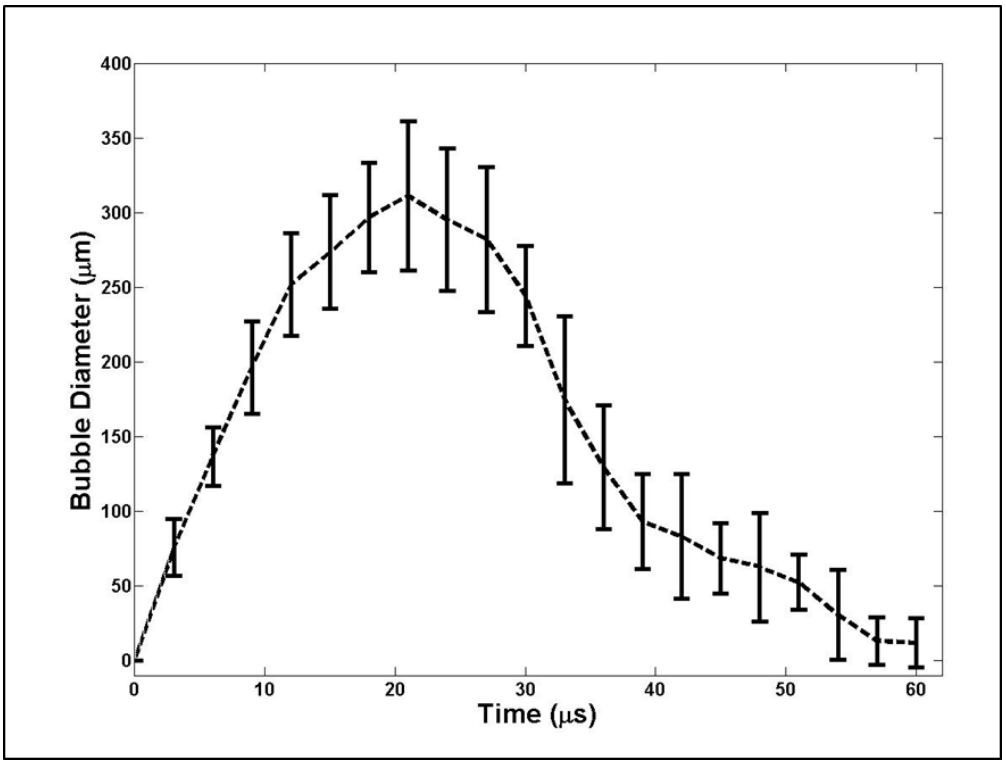

Figure 11.8. A plot of bubble behavior in agarose tissue phantoms. The diameter of bubble generated using a 2-cycle 500kHz pulse at 15MPa as a function of time. At each time point, the average bubble diameter and standard deviation are plotted.

11.3.6 Ablation of Red Blood Cells in Tissue Phantom

Agarose tissue phantoms embedded with RBC layers were used to evaluate the ability of nanodroplet-mediated histotripsy to create cell fractionation, as lesions visualized in RBC phantoms have been shown to be similar to those generated in tissue identified by histology [45]. Nanodroplet-mediated histotripsy resulted in consistent, well-defined lesions in RBC phantoms, similar to those observed for histotripsy therapy, but at pressure levels well below the histotripsy intrinsic threshold. At peak negative pressure below 10 MPa, no microbubbles were observed and no lesions were visualized. At peak negative pressure of 11.0 MPa and greater, when cavitation bubbles were generated, well-defined lesions were formed in the RBC phantoms using nanodroplets combined with histotripsy [Fig.11.9]. Nanodroplet-mediated histotripsy fractionated the RBC phantom with similar efficiency to histotripsy at higher pressure with all RBCs within the focal volume completely fractionated within 2,000 pulses, resulting in transparent lesions with no intact RBCs remaining. The lesion area was analyzed following the procedure described in the Experimental Section demonstrating the area of lesion in the RBC layer increased with increasing pressure. For example, the lesion areas for RBC phantoms containing nanodroplets (n=6) were 0.77±0.09 mm^2, 3.92±0.41 mm^2, and 6.27±0.86 mm^2 for peak negative pressures of 11.0 MPa, 15.9 MPa, and 20.7 MPa, respectively [Fig. 11.9]. Furthermore, lesion area was plotted as a function of pulse number demonstrating >75% of the focal region was fractionated within the first 1,000 pulses and >95% of the focal region fractioned after 1,500 pulses at all pressure levels treated [Fig. 11.10]. In comparison, in control gels without nanodroplets, no lesions were formed at any treatments in this pressure range. These results are important to show that nanodroplet-mediated cavitation can indeed create cell disruption with the same effectiveness (i.e., the same number of pulses) as using histotripsy

alone but at a significantly lower pressure. This is an important validation of our hypothesis confirming that the cavitating microbubbles generated via nanodroplets are destructive to use for ablation.

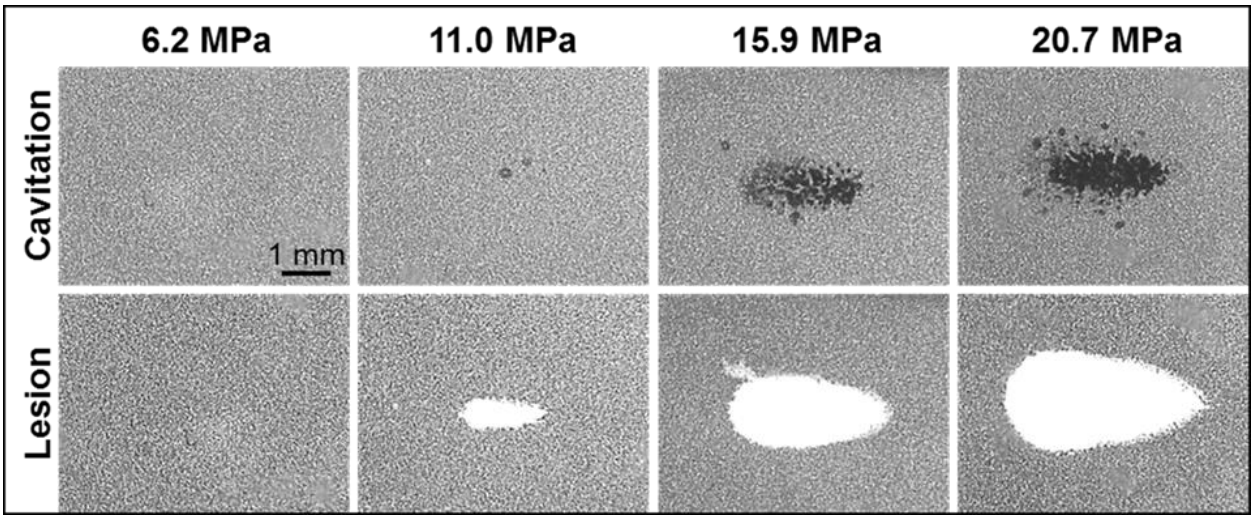

Figure 11.9. Optical images of nanodroplet-mediated cell fractionation. Images of cavitation bubble cloud (dark) and lesions (white) generated in the RBC agarose gel (grey) using nanodroplet-mediated histotripsy at different pressure levels. A total of 2000 2-cycle pulses at 10 Hz PRF were used for each treatment.

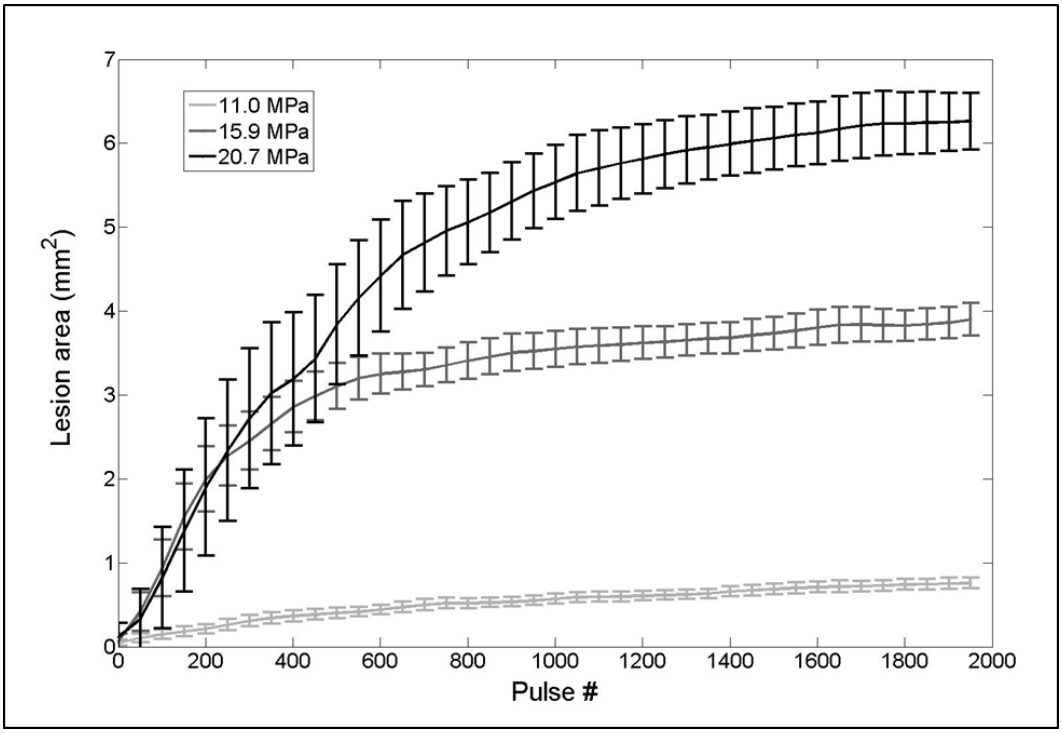

Figure 11.10. Nanodroplet-mediated lesion formation. The lesion area formed in the RBC agarose gel as a function of pulse number for treatments at 11.0, 15.9, and 20.7 MPa. No damage was formed for treatments at 6.2 MPa.

11.4 Discussion

In this chapter, the feasibility of using nanodroplets for enhanced histotripsy ablation was investigated. Polymer encapsulated perfluoropentane (PFP) nanodroplets were synthesized with an average size of ~100–400 nm, which should allow them to preferentially diffuse through the leaky tumor vasculature while preventing diffusion through normal blood vessels. Furthermore, biocompatibility experiments demonstrated no signs of toxicity even at high concentrations of nanodroplets. The ability of these nanodroplets to reduce the histotripsy cavitation threshold was investigated both theoretically and experimentally, with results supporting our hypothesis that the nanodroplets result in a significant decrease in the cavitation threshold.

In the first part of this chapter, a single bubble model was used to investigate the effects of frequency on the cavitation threshold using a 200 nm sized initial bubble. The results of the single bubble simulations suggested that lower frequency (≤500kH) would be better suited to use for nanodroplet-mediated histotripsy, as it results in a significantly lower histotripsy threshold. This dependence is opposite to a previous study by Kripfgans et al. using micron-sized droplets, where they found the pressure threshold to vaporize the droplets decreased with increasing frequency [14]. In comparison, we used much smaller droplets and measured the threshold to expand the bubbles resulting from vaporized droplets to >50μm. It is likely that a different mechanism is responsible for our study. The trend of decreasing threshold with decreasing frequency is consistent with the frequency dependency in inertial cavitation, which we plan to investigate as a potential mechanism for nanodroplet-mediated histotripsy. Using a lower frequency offers multiple advantages for ablation therapy. First, as the transducer focal zone scales with the wavelength, a low frequency transducer will yield a large focal zone, allowing histotripsy to be applied simultaneously to cover multi-nodule tumors seeded with our

nanodroplets, thus increasing the treatment efficiency for multiple tumor nodules. With the reduced threshold at the tumor nodules with nanodroplets, only tumors will be treated while preserving surrounding normal tissue. Lower frequency is also more resistant to acoustic aberration and attenuation from bone obstruction and long overlying tissue, resulting in deeper penetration depth.

In the second part of this chapter, the effects of nanodroplet on the histotripsy cavitation threshold were investigated experimentally at 500 kHz. The experimental results further support our hypothesis that histotripsy-induced cavitation bubble cloud can be formed at a significantly reduced pressure using nanodroplets, which is the basis to achieve selective tumor ablation using nanodroplet-mediated histotripsy. These experimental results also match well with the simulation. The simulation results showed a 200 nm initial nucleus and a single 500 kHz ultrasound pulse results in a histotripsy threshold of 6.3 MPa. Measured with the 500 kHz transducer and 200 nm nanodroplets, the histotripsy threshold was 9.01±0.62 MPa at P_{cav} = 0.15 and 10.8±0.3 MPa at P_{cav} = 0.5. The measured threshold was higher likely because droplet vaporization and the effects of the cross-linked polymer shell were not included in the simulation. Although the vaporization threshold wasn't measured in this work, the pressures used here are higher than the ADV threshold using similar sized nanodroplets reported in the literature [13-15]. While the pressure required to generate histotripsy bubbles using these nanodroplets was significantly lower than histotripsy alone, it is possible that the histotripsy threshold could be further reduced by using a lower boiling temperature PFC core, such as decafluorobutane (boiling temperature -1°C), which have been shown to vaporize at significantly lower pressure [15].

In the final part of this chapter, nanodroplet-mediated histotripsy bubbles were shown to expand to >50 μm and induce tissue fractionation in an RBC tissue phantom similar to

histotripsy therapy but at a significantly reduced pressure. Additionally, the feasibility of using nanodroplets for selective ablation was demonstrated in composite tissue phantoms containing nanodroplet inclusions. Overall, the findings in this work demonstrated a proof of concept for selective cavitational ablation by combining histotripsy with nanodroplets. Our nanodroplets are in the size range required to penetrate through the leaky tumor vasculature and have been shown to decrease the pressure threshold required for histotripsy. These initial experiments demonstrate the potential of selectively applying histotripsy to cancer cells by using an appropriate pressure level. Furthermore, by using a low frequency transducer with a large focal zone, it is possible to apply histotripsy simultaneously to a large focal volume with cavitation occurring only at locations containing nanodroplets. As such, the treatment time for a larger volume of tissue would be shortened while still maintaining high treatment selectivity to cancer cells through the targeted nanodroplets.

11.5 Conclusion

In this chapter, the feasibility of using PFP encapsulated nanodroplets for enhanced histotripsy ablation was investigated. Results support our hypothesis that nanodroplets significantly decrease the histotripsy threshold to form a cavitation bubble cloud while maintaining the effectiveness of histotripsy tissue ablation. Nanodroplet-mediated histotripsy was shown capable of creating microbubble expansion and collapse as well as well-defined ablation similar to histotripsy but at significantly lower pressure. To build upon this initial study, future work will aim to test the hypothesis that our nanodroplets can be functionalized to bind to cancer cells *in vitro* and demonstrate that nanodroplet-mediated histotripsy can selectively fractionate cancer cells. We will also investigate that using nanodroplets delivered to the capsule

of tumor nodules, the tumor nodule can be fractionated from outside to the inner core. Furthermore, future experiments will aim to show that nanodroplets can be delivered and accumulated at a tumor site for the selective histotripsy ablation of cancer cells in a relevant *in vivo* cancer model.

11.6 References

[1] E. Vlaisavljevich, *et al.*, "Nanodroplet-mediated histotripsy for image-guided targeted ultrasound cell ablation," *Theranostics,* vol. 3, pp. 851-64, 2013.

[2] R. B. Campbell, "Tumor physiology and delivery of nanopharmaceuticals," *Anticancer Agents Med Chem,* vol. 6, pp. 503-12, Nov 2006.

[3] S. K. Hobbs, *et al.*, "Regulation of transport pathways in tumor vessels: role of tumor type and microenvironment," *Proc Natl Acad Sci U S A,* vol. 95, pp. 4607-12, Apr 14 1998.

[4] V. Torchilin, "Tumor delivery of macromolecular drugs based on the EPR effect," *Adv Drug Deliv Rev,* vol. 63, pp. 131-5, Mar 18 2011.

[5] J. Fang, *et al.*, "The EPR effect: Unique features of tumor blood vessels for drug delivery, factors involved, and limitations and augmentation of the effect," *Adv. Drug Deliv. Rev.,* vol. 63, pp. 136-151, 2011.

[6] Z. Gao, *et al.*, "Drug-loaded nano/microbubbles for combining ultrasonography and targeted chemotherapy," *Ultrasonics.*, vol. 48, pp. 260-70. Epub 2007 Nov 19., Aug 2008.

[7] K. i. Kawabata, *et al.*, "Sustaining Microbubbles Derived from Phase Change Nanodroplet by Low-Amplitude Ultrasound Exposure," *Japanese Journal of Applied Physics,* vol. 49, p. 07HF20 (4 pp.), 2010.

[8] P. S. Sheeran, *et al.*, "Formulation and acoustic studies of a new phase-shift agent for diagnostic and therapeutic ultrasound," *Langmuir : the ACS journal of surfaces and colloids,* vol. 27, pp. 10412-20, Sep 6 2011.

[9] P. S. Sheeran, *et al.*, "Decafluorobutane as a Phase-Change Contrast Agent for Low-Energy Extravascular Ultrasonic Imaging," *Ultrasound in Medicine and Biology,* vol. 37, pp. 1518-1530, 2011.

[10] L. Du, *et al.*, "Ultrasound-Triggered Drug Release and Enhanced Anticancer Effect of Doxorubicin-Loaded Poly(D,L-Lactide-Co-Glycolide)-Methoxy-Poly(Ethylene Glycol) Nanodroplets," *Ultrasound Med Biol,* vol. 37, pp. 1252-58, 2011.

[11] N. Rapoport, *et al.*, "Ultrasound-mediated tumor imaging and nanotherapy using drug loaded, block copolymer stabilized perfluorocarbon nanoemulsions," *J Control Release,* vol. 153, pp. 4-15, Jul 15 2011.

[12] N. Y. Rapoport, *et al.*, "Application of Ultrasound for Targeted Nanotherapy of Malignant Tumors," *Acoust Phys,* vol. 55, pp. 594-601, Oct 1 2009.

[13] Z. Gao, *et al.*, "Drug-loaded nano/microbubbles for combining ultrasonography and targeted chemotherapy," *Ultrasonics,* vol. 48, pp. 260-70, Aug 2008.

[14] O. D. Kripfgans, *et al.*, "Acoustic droplet vaporization for therapeutic and diagnostic applications," *Ultrasound Med Biol,* vol. 26, pp. 1177-89, Sep 2000.

[15] P. S. Sheeran, *et al.*, "Decafluorobutane as a phase-change contrast agent for low-energy extravascular ultrasonic imaging," *Ultrasound Med Biol,* vol. 37, pp. 1518-30, Sep 2011.

[16] K. Kawabata, *et al.*, "Acoustic response of microbubbles derived from phase-change nanodroplet.," *Japanese Journal of Applied Physics,* vol. 49, p. 07HF18, 2010.

[17] P. S. Sheeran, *et al.*, "Formulation and acoustic studies of a new phase-shift agent for diagnostic and therapeutic ultrasound," *Langmuir,* vol. 27, pp. 10412-20, Sep 6 2011.

[18] K. Wilson, *et al.*, "Biomedical photoacoustics beyond thermal expansion using triggered nanodroplet vaporization for contrast-enhanced imaging," *Nat Commun,* vol. 3, p. 618, 2012.

[19] K. i. Kawabata, *et al.*, "Cavitation assisted HIFU with phase-change nano droplet," *2008 IEEE International Ultrasonics Symposium, 2-5 Nov. 2008,* pp. 780-3, 2008.

[20] J. A. Kopechek, *et al.*, "Synthesis of phase-shift nanoemulsions with narrow size distributions for acoustic droplet vaporization and bubble-enhanced ultrasound-mediated ablation," *J Vis Exp,* p. e4308, 2012.

[21] M. Zhang, *et al.*, "Acoustic droplet vaporization for enhancement of thermal ablation by high intensity focused ultrasound," *Acad Radiol,* vol. 18, pp. 1123-32, Sep 2011.

[22] K. Kieran, *et al.*, "Refining histotripsy: defining the parameter space for the creation of nonthermal lesions with high intensity, pulsed focused ultrasound of the in vitro kidney," *J Urol,* vol. 178, pp. 672-6, Aug 2007.

[23] F. Winterroth, *et al.*, "Examining and analyzing subcellular morphology of renal tissue treated by histotripsy," *Ultrasound Med Biol,* vol. 37, pp. 78-86, Jan 2011.

[24] Z. Xu, *et al.*, "Size measurement of tissue debris particles generated from pulsed ultrasound cavitational therapy-histotripsy," *Ultrasound Med Biol,* vol. 35, pp. 245-55, Feb 2009.

[25] Z. Xu, *et al.*, "A new strategy to enhance cavitational tissue erosion using a high-intensity, Initiating sequence," *IEEE Trans Ultrason Ferroelectr Freq Control,* vol. 53, pp. 1412-24, Aug 2006.

[26] Z. Xu, *et al.*, "Controlled ultrasound tissue erosion: the role of dynamic interaction between insonation and microbubble activity," *J Acoust Soc Am,* vol. 117, pp. 424-35, Jan 2005.

[27] Z. Xu, *et al.*, "Controlled ultrasound tissue erosion," *IEEE Trans Ultrason Ferroelectr Freq Control,* vol. 51, pp. 726-36, Jun 2004.

[28] A. D. Maxwell, *et al.*, "Noninvasive treatment of deep venous thrombosis using pulsed ultrasound cavitation therapy (histotripsy) in a porcine model," *J Vasc Interv Radiol,* vol. 22, pp. 369-77, Mar 2011.

[29] Z. Xu, *et al.*, "Noninvasive creation of an atrial septal defect by histotripsy in a canine model," *Circulation,* vol. 121, pp. 742-9, Feb 16 2010.

[30] H. Durmaz, *et al.*, "One-pot synthesis of ABC type triblock copolymers via in situ click 3+2 and Diels-Alder 4+2 reactions.," *Macromolecules. ,* vol. 40, pp. 191-198, 2007.

[31] Y. Y. Durmaz, *et al.*, "Development of targeted nano-bubbles for ultrasound imaging and ablation of prostate cancer," *35th Annual Symposium of Macromolecular Science & Engineering,* vol. October 27, Ann Arbor, Michigan., 2011.

[32] Y. Y. Durmaz, *et al.*, "Development of nanodroplets for targeted ultrasound-mediated ablation of cancer," *Engineering Graduate Symposium,* vol. November 2, Ann Arbor, Michigan, 2011.

[33] D. Bartczak and A. G. Kanaras, "Preparation of peptide-functionalized gold nanoparticles using one pot EDC/sulfo-NHS coupling," *Langmuir,* vol. 27, pp. 10119-23, Aug 16 2011.

[34] K. Nam, *et al.*, "Controlling coupling reaction of EDC and NHS for preparation of collagen gels using ethanol/water co-solvents," *Macromol Biosci,* vol. 8, pp. 32-7, Jan 9 2008.

[35] L. Wildling, *et al.*, "Linking of sensor molecules with amino groups to amino-functionalized AFM tips," *Bioconjug Chem,* vol. 22, pp. 1239-48, Jun 15 2011.

[36] X. Yang and C. C. Church, "A model for the dynamics of gas bubbles in soft tissue," *J Acoust Soc Am,* vol. 118, pp. 3595-606, Dec 2005.

[37] A. D. Maxwell, *et al.*, "Probability of cavitation for single ultrasound pulses applied to tissues and tissue-mimicking materials," *Ultrasound Med Biol,* vol. 39, pp. 449-65, Mar 2013.

[38] P. S. Sheeran and P. A. Dayton, "Phase-change contrast agents for imaging and therapy," *Curr Pharm Des,* vol. 18, pp. 2152-65, 2012.

[39] R. Masuzaki, *et al.*, "Assessing liver tumor stiffness by transient elastography," *Hepatol Int,* vol. 1, pp. 394-7, Sep 2007.

[40] M. Zhang, *et al.*, "Quantitative characterization of viscoelastic properties of human prostate correlated with histology," *Ultrasound Med Biol,* vol. 34, pp. 1033-42, Jul 2008.

[41] M. Friedman, *et al.*, "Two-dimensional Rayleigh model for bubble evolution in soft tissue," *Phys Fluids,* vol. 14, pp. 1768-1780., 2002.

[42] E. J. Ayme and E. L. Carstensen, "Cavitation induced by asymmetric distorted pulses of ultrasound: theoretical predictions," *IEEE Trans Ultrason Ferroelectr Freq Control,* vol. 36, pp. 32-40, 1989.

[43] J. E. Parsons, *et al.*, "Cost-effective assembly of a basic fiber-optic hydrophone for measurement of high-amplitude therapeutic ultrasound fields," *J Acoust Soc Am,* vol. 119, pp. 1432-40, Mar 2006.

[44] V. Normand, *et al.*, "New insight into agarose gel mechanical properties," *Biomacromolecules,* vol. 1, pp. 730-8, Winter 2000.

[45] A. D. Maxwell, *et al.*, "A tissue phantom for visualization and measurement of ultrasound-induced cavitation damage," *Ultrasound Med Biol,* vol. 36, pp. 2132-43, Dec 2010.

[46] R. K. O'Reilly, "Spherical polymer micelles: nanosized reaction vessels?," *Philosophical Transactions of the Royal Society A: Mathematical, Physical and Engineering Sciences,* vol. 365, pp. 2863-2878, December 15, 2007 2007.

[47] E. B. Zhulina, *et al.*, "Diblock Copolymer Micelles in a Dilute Solution," *Macromolecules,* vol. 38, pp. 5330-5351, 2005/06/01 2005.

[48] K. Matyjaszewski and J. Xia, "Atom Transfer Radical Polymerization," *Chemical Reviews,* vol. 101, pp. 2921-2990, 2001/09/01 2001.

[49] Z. Gao, *et al.*, "Drug-loaded nano/microbubbles for combining ultrasonography and targeted chemotherapy," *Ultrasonics,* vol. 48, pp. 260-270, 2008.

[50] K. Shiraishi, *et al.*, "A facile preparation method of a PFC-containing nano-sized emulsion for theranostics of solid tumors," *International Journal of Pharmaceutics,* vol. 421, pp. 379-387, 2011.

[51] C.-H. Wang, *et al.*, "Aptamer-conjugated and drug-loaded acoustic droplets for ultrasound theranosis," *Biomaterials,* vol. 33, pp. 1939-1947, 2012.

[52] R. E. Apfel and C. K. Holland, "Gauging the likelihood of cavitation from short-pulse, low-duty cycle diagnostic ultrasound," *Ultrasound Med Biol,* vol. 17, pp. 179-85, 1991.

[53] E. L. Carstensen, *et al.*, "The search for cavitation in vivo," *Ultrasound Med Biol,* vol. 26, pp. 1377-85, Nov 2000.

[54] T. G. Leighton, *The Acoustic Bubble*: Academic Press 1994.

Chapter 12
Effects of Ultrasound Frequency on Nanodroplet-Mediated Histotripsy

A majority component of this chapter has been published in *Ultrasound in Medicine and Biology*

12.1 Introduction

Histotripsy is a noninvasive, image-guided tissue ablation method that controllably fractionates soft tissue through cavitation generated by high pressure, short duration ultrasound pulses [2-5]. Histotripsy depends on the initiation and maintenance of a dense cavitation bubble cloud to produce mechanical tissue fractionation [4, 6]. Previous work has shown that, using a 1-2 cycle pulse with a single dominant negative pressure phase, histotripsy bubbles can be reproducibly generated in tissue when the peak negative pressure is raised above the histotripsy intrinsic threshold of ~25-30 MPa [7, 8]. In order to effectively fractionate tissue into acellular debris, histotripsy requires bubbles to rapidly expand into large cavitation bubbles, often greater than ~50μm in diameter [2, 9-11]. Using a pressure high enough to initiate a bubble cloud, histotripsy has been shown capable of completely fractionating soft tissue into a liquid tissue homogenate with no cellular structures remaining [3, 5, 12]. Histotripsy is currently being studied for many clinical applications in which non-invasive tissue removal is desired including

benign prostatic hyperplasia [13], deep vein thrombosis [14], congenital heart disease [15, 16], and cancer ablation [17, 18].

Although histotripsy has shown promise for many clinical applications including tumor ablation, this approach is limited to applications in which the target tissue can be identified and imaged prior to treatment, which is often not feasible in cancer patients with many small tumor nodules and micro-metastases. As a result, our team has developed a new targeted ablation approach combining perfluoropentane (PFP) encapsulated nanodroplets with histotripsy [9, 19]. This nanodroplet-mediated histotripsy (NMH) approach takes advantage of the significantly reduced cavitation threshold of the nanodroplets, allowing for cavitation to be selectively generated only in regions containing the nanodroplets [9]. Preparing nanodroplets in the size range of ~100-400 nm allows them to diffuse across the leaky tumor vasculature and preferentially accumulate in the tumor, which allows NMH to potentially achieve selective ablation of tumors [9, 19]. In a previous study [9], the initial feasibility of this approach was demonstrated, with results supporting our hypothesis that nanodroplets significantly decrease the histotripsy threshold to form a cavitation bubble cloud while maintaining the effectiveness of histotripsy tissue ablation. NMH was shown capable of creating microbubble expansion and collapse as well as well-defined ablation similar to histotripsy but at significantly lower pressure [9]. Furthermore, the potential to use this approach for simultaneous multi-focal ablation was demonstrated [9].

To build upon our initial study, this work aims to investigate the effects of ultrasound frequency on NMH. We hypothesize that lower frequency will offer multiple advantages for NMH therapy. First, as the transducer focal zone scales with the wavelength, a low frequency transducer will yield a large focal zone, allowing histotripsy to be applied simultaneously to

cover large and/or multi-nodule tumors seeded with our nanodroplets, thus increasing the treatment efficiency for such tumors. Lower frequency is also more resistant to acoustic aberration and attenuation from bone obstruction and long overlying tissue, resulting in deeper penetration depth. The use of nanodroplets targeted for tumor uptake will allow selective ablation of such tumors without need to otherwise identify the treatment location, keeping the selectivity of targeting the tumor despite the larger focal zones. Additionally, we hypothesize that lower frequency will decrease the cavitation threshold using nanodroplets while facilitating greater bubble expansion compared to higher frequency. This hypothesis is based on previous work showing that lower frequency decreases the histotripsy intrinsic threshold (without droplets) and increases bubble expansion [8, 10]. While previous work studying acoustic droplet vaporization (ADV) has shown the ADV threshold decreases with increasing frequency due to superharmonic focusing, these effects are expected to be negligible for the frequency range (345 kHz-3 MHz) and droplet size (<500 nm in diameter) used in this study [20, 21]. Therefore, we hypothesize that lower frequency will reduce the NMH threshold for the conditions used in this work. In this study, we tested this hypothesis by exposing tissue phantoms with and without nanodroplets to histotripsy pulses produced by 345 kHz, 500 kHz, 1.5 MHz, and 3 MHz histotripsy transducers. First, the probability of generating inertial cavitation from a single 1-2 cycle histotripsy pulse was measured for each frequency, with the cavitation threshold defined as the peak negative pressure at which the probability of generating cavitation, p_{cav}, from a single histotripsy pulse was 0.5 (i.e. $p_{cav} = 0.5$). Next, the effect of frequency on the size of NMH bubbles was compared using high speed optical imaging. Finally, the ability of PFP-encapsulated nanodroplets to act as sustainable cavitation nuclei over multiple pulses was investigated, as multiple pulses (often>50 pulses) are needed to completely destroy all the cells within the

treatment volume. Overall, these results will improve our understanding of the NMH process and help guide parameter optimization for multi-focal tumor ablation using NMH.

12.2 Methods

12.2.1 Formulation and Characterization of Nanodroplets

The ideal polymer composition and PFP content of the nanodroplets used in this study were identified in our previous study [19]. A poly(ethylene glycol)-*b*- poly(acrylic acid)-*b*-poly(heptadecafluorodecyl methacrylate-*co*-methyl methacrylate) triblock copolymer was synthesized using a combination of atom transfer radical polymerization (ATRP) and "click" coupling techniques to prepare PFP-loaded nanodroplets [19]. Briefly, the copolymers were dissolved in tetrahydrofuran anhydrous (THF, >99.9 %, Sigma-Aldrich, St. Louis, MO, USA) (0.2% w/v) and cooled down to 0^{o}C before the addition of perfluoropentane (PFP, 97% ca. 85% n-isomer, Alfa Aesar, Ward Hill, Massachusetts, USA) (2% v/v) while vigorously stirring the reaction mixture. An equal amount of water was slowly added to this solution mixture to trigger micelle formation and the mixture was stirred for 1h in an ice bath. The micelles solution was transferred into a dialysis bag (MWCO of 1 KDa, Spectrum, Rancho Dominguez, CA, US) and dialyzed against ice-cold 2-(*N*-morpholino) ethanesulfonic acid monohydrate solution (MES, 99 %, Acros Organics, Geel, Belgium) of pH 5.5 for 12 hours to remove the THF and get a milky solution of non- cross-linked PFP-loaded nanodroplets. This milky solution was transferred to a round bottom flask and mixed with the 2,2`-(ethylenedioxy)-bis(ethylamine) cross-linker (98% 2,2`-(ethylenedioxy)-bis(ethylamine), Sigma-Aldrich, St. Louis, MO, USA) which reacts with the central PAA block in the polymer backbone via NHS/EDC coupling chemistry (97% N-hydroxy succinimide; 98% N-(3-Dimethylaminopropyl)-N′-ethylcarbodiimide hydrochloride,

Sigma-Aldrich, St. Louis, MO, USA) forming cross-linked nanodroplets with a flexible polymer shell. Shell cross-linked nanodroplets were dialyzed against ice-cold water for 12 hours to remove the byproducts of the cross-linkage reaction.

Concentration and size distribution of the nanodroplets were measured using Nanoparticle Tracking Analysis (NTA). Briefly, the NanoSight™ LM10 (Malvern Instruments, Amesbury, UK), equipped with a temperature-controlled 405 nm laser module, high sensitivity Scientific Complementary Metal–Oxide–Semiconductor (sCMOS) camera (Hamamatsu, Orca, Hamamatsu City, Japan), and a syringe pump was used for the collection of NTA data. Upon diluting the nanodroplet solution to the appropriate particle concentration with deionized (DI) water (Thermo Scientific, GenPure, Waltham, MA, US), image capture and analysis was carried out using the NTA software (Version 3.0, Build 0066, Malvern Instruments, Amesbury, UK) at 37°C. The samples were measured by capturing 60s videos (5 videos per each sample). Figure 12.1 is a representative plot showing the size distribution for a single sample of nanodroplets. The error bars represent the standard deviation of the repeat measurements of each sample. The mean size and standard deviation values obtained by the NTA software correspond to arithmetic values calculated with the sizes of all particles analyzed for each sample (n=5). Results from all samples demonstrated that the average size of the nanodroplets (NDs) was 177.9±1.9 nm with 10% of NDs have a diameter ≤ 111±1.4 nm, 50% of the NDs have a diameter ≤ 155.7±2.1 nm, 90% of the NDs have a diameter ≤ 268.5±6.7 nm, and >99% of the NDs smaller than 400 nm and <0.01% larger than 600 nm. These results clearly show that the average size of the NDs is much smaller than the size cutoff (~500 nm) of the tumor vasculature [22, 23].

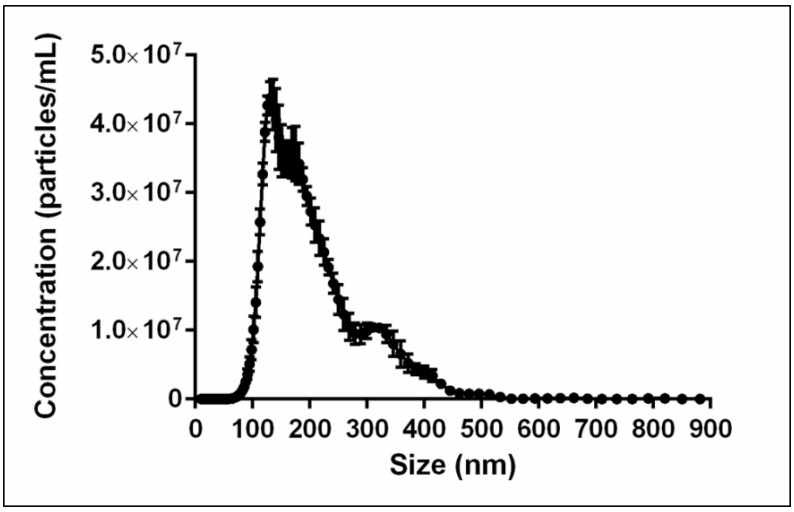

Figure 12.1. Size distribution results show an average nanodroplet size of 177.9±1.9 nm.

12.2.2 Preparation of Tissue Phantoms

Agarose phantoms were used to provide a well-controlled viscoelastic medium for this study, as histotripsy bubble behavior is highly dependent on the tissue mechanical properties [24-26]. The Young's modulus of the agarose tissue phantom was 38kPa, which is within the range of the Young's modulus of hepatocellular carcinoma tumors (20.4–75 kPa), metastatic liver tumors (23.6–75 kPa), and prostate tumors (24 kPa) [27-29]. Tissue phantoms containing 1% agarose w/v were prepared by slowly mixing agarose powder (Agarose Type VII; Sigma-Aldrich, St. Louis, MO, USA) into saline solution (0.9% sodium chloride; Hospira, Lake Forest, Illinois, USA) heated to boiling temperature. The solution was stirred on a hot plate until the gel turned completely transparent and then allowed to boil for ten minutes. After boiling, solutions were allowed to cool and were degassed under a partial vacuum (~20 kPa, absolute) for 30 minutes. After degassing, phantoms containing nanodroplets were prepared by slowly adding the nanodroplets ($2.0x10^8$ particles/mL) into the agarose solution while stirring. The agarose mixtures were poured into rectangular polycarbonate holders with acoustic windows and placed in a refrigerator at 4°C to allow the solution to solidify, forming tissue phantoms with embedded

nanodroplets (test) or without nanodroplets (control). A nanodroplet concentration of $2.0x10^8$ particles/mL was used for all samples, as preliminary experiments demonstrated that lower concentrations (i.e. ~10^6-10^7 particles/mL) did not significantly reduce the cavitation threshold in comparison to control conditions.

12.2.3 Histotripsy Pulse Generation

Histotripsy pulses were generated at four ultrasound frequencies (345 kHz, 500 kHz, 1.5 MHz, and 3 MHz) using three custom-built histotripsy transducers. The 345 kHz pulses were generated by a twenty-element array transducer with a geometric focus of 150 mm, an aperture size of 272 mm, and an effective f-number of 0.55. The 1.5 MHz pulses were generated by a six-element array transducer with a geometric focus of 55 mm, an aperture of 79 mm in the elevational direction and 69 mm in the lateral direction, and effective f-numbers of 0.7 and 0.8 in the elevational and lateral directions, respectively. The 500 kHz and 3 MHz pulses were generated by a dual frequency array transducer that consisted of twelve 500-kHz elements and seven 3-MHz elements. For the 500 kHz elements, the geometric focus was 40 mm, the aperture size was 71 mm, and the effective f-number was 0.56. For the 3 MHz elements, the geometric focus was 40 mm, the aperture size was 80 mm, and the effective f-number was 0.5. The design of this dual frequency transducer has been described in detail in a previous study [30].

To compare the NMH cavitation threshold with the histotripsy intrinsic threshold, short pulses with a single dominant negative pressure half-cycle were applied to the tissue phantoms with and without nanodroplets. To generate a short therapy pulse, a custom high-voltage pulser developed in-house was used to drive the transducers. The pulser was connected to a field-programmable gate array (FPGA) board (Altera DE1 Terasic Technology, Dover, DE, USA)

specifically programmed for histotripsy therapy pulsing. This setup allowed the transducers to output short pulses of less than two cycles. A fiber-optic probe hydrophone built in-house [31] was used to measure the acoustic output pressure of the transducers. At higher pressure levels (*p*- > 23 MPa), the acoustic output could not be directly measured due to cavitation at the fiber tip. These pressures were estimated by a summation of the output focal peak negative pressure (*p*-) values from individual transducer elements. This approximation assumes minimal nonlinear distortion of the waveform occurs within the focal region. In a previous study [7], this estimated *p*- was found to be accurate within 15% compared to direct focal pressure measurements in water and in a medium (1,3 butanediol) with a higher cavitation threshold. Sample acoustic waveforms produced by the four frequency transducers are shown in Figure 12.2.

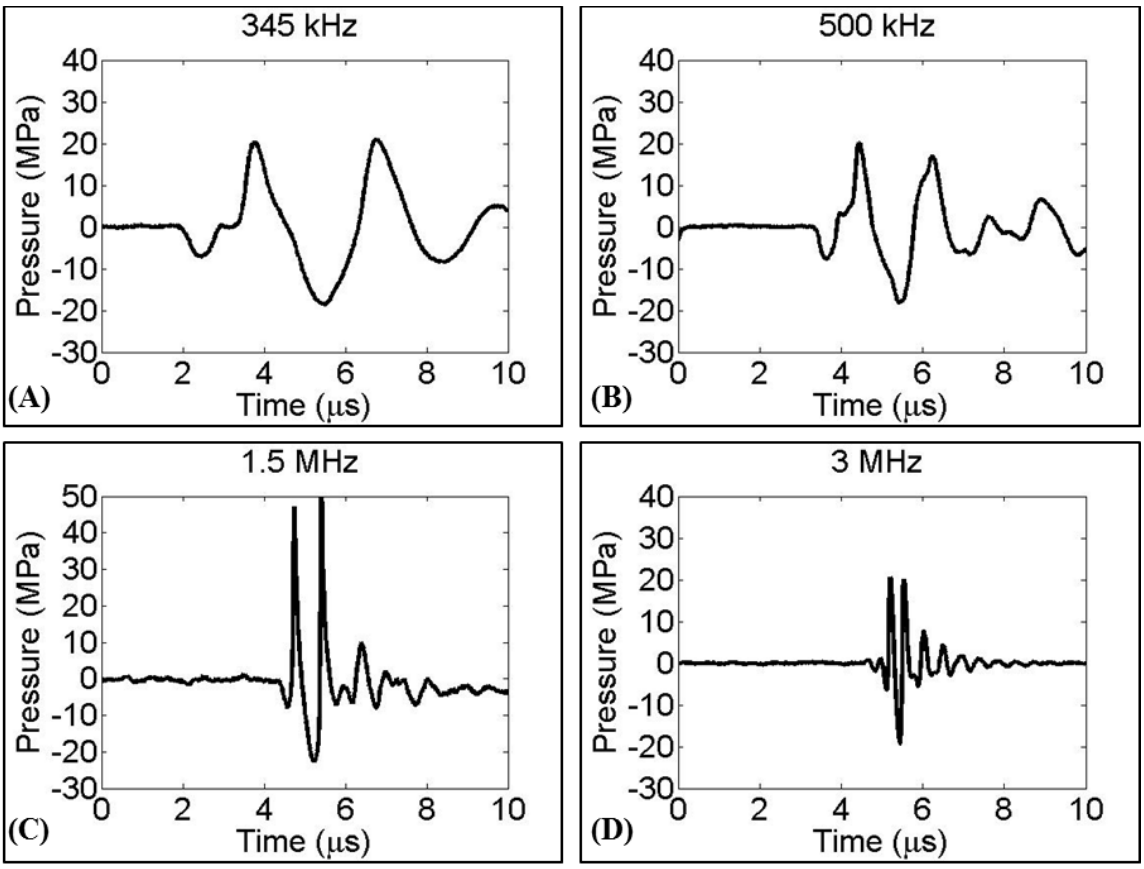

Figure 12.2. Acoustic waveforms. Example of a 2-cycle histotripsy pulses generated by the 345 kHz, 500 kHz, 1.5 MHz, and 3 MHz histotripsy transducers.

12.2.4 Optical Imaging and Image Processing

High speed optical imaging was used to capture images of the focal zone after the propagation of each pulse through the focus for water and agarose tissue phantoms using two high speed cameras [Fig. 12.3]. The optics were varied for the different transducers to provide the highest resolution based on the geometric constraints of the transducers and the available optical windows. For experiments with the 345 kHz and 1.5 MHz transducers, a high-speed, 1 megapixel CCD camera (Phantom V210, Vision Research, Wayne, NJ, USA) was aligned with the transducer and backlit by a continuous white-light source. The camera was focused using a macro-bellows lens (Tominon 1:4.5, F=105 mm; Kyocera, Kyoto, Japan), giving the captured images a resolution of approximately 5.9 μm per pixel and 3.4 μm per pixel for 345 kHz and 1.5 MHz, respectively. For experiments with the 500 kHz and 3 MHz dual frequency transducer, a digital, 1.3-megapixel CCD camera (PN: FL3-U3-13Y3M-C, Flea® 3, PointGrey, Richmond, BC, Canada) was positioned perpendicularly to the dual-frequency array transducer facing one of the transducer's optical windows. A Nikon 4X objective was attached to the camera with extension tubes to magnify the image plane, giving the captured images a resolution of approximately 2.5 μm per pixel. A pulsed white-light LED was placed on the diametrically-opposed optical window of the dual-frequency array transducer, which provided back-lit illumination. The cameras were triggered to record one image for each applied pulse. After acquisition, shadowgraph images were converted from grayscale to binary by an intensity threshold determined by the background intensity using image processing software (MATLAB, The Mathworks, Natick, MA, USA), as described in a previous study [7]. Bubbles were indicated as any black regions greater than 5 pixels in diameter. By this criterion, the minimum

resolvable bubble radius was 14.75 µm, 6.25 µm, 8.5 µm, and 6.25 µm for the 345 kHz, 500 kHz, 1.5 MHz, and 3 MHz transducers, respectively.

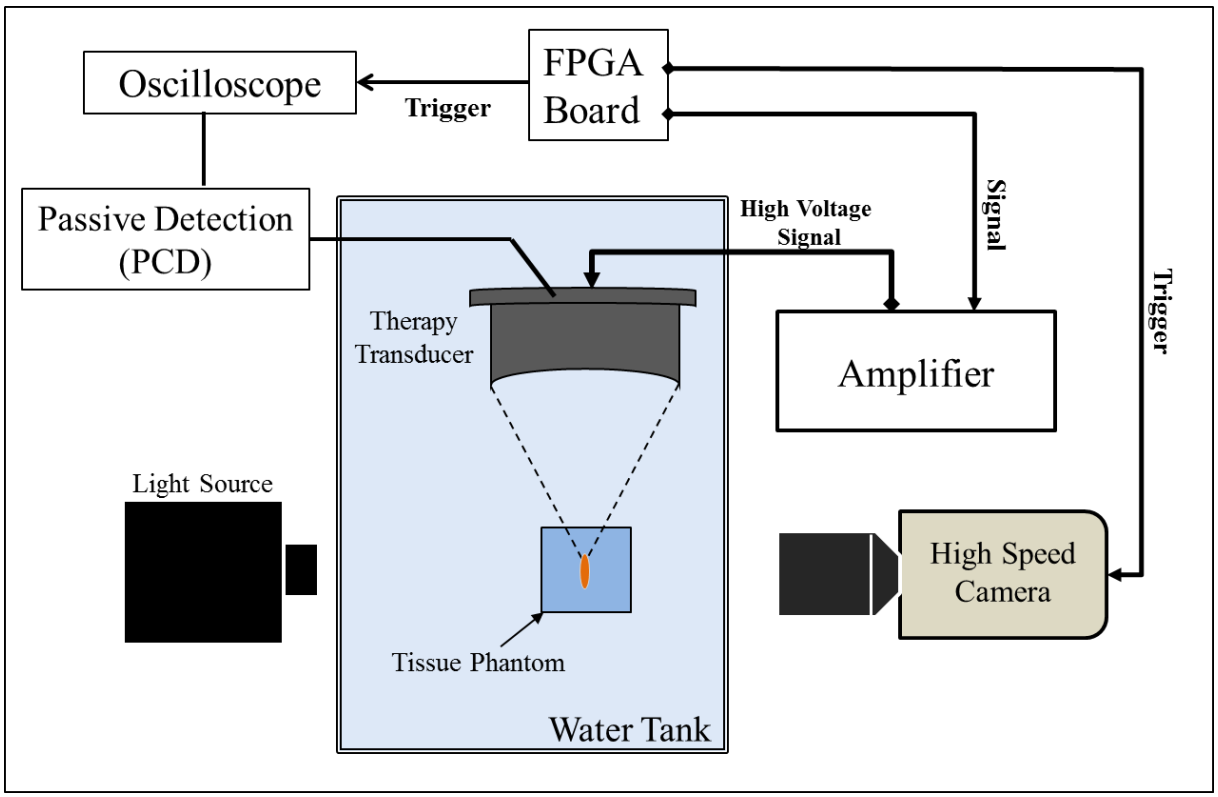

Figure 12.3. Experimental set-up. The focus of the histotripsy transducer was aligned inside tissue phantoms with and without nanodroplets. Cavitation was monitored using high speed optical imaging and passive cavitation detection using one of the therapy elements.

12.2.5 Passive Cavitation Detection (PCD)

In addition to high speed imaging, an acoustic method was used to identify cavitation in the focal zone for cavitation threshold experiments. For each experiment, one of the transducer's therapy elements was also used for passive cavitation detection (PCD) to detect the presence of cavitation in the focal region [Fig. 12.3]. The PCD signal was connected to an oscilloscope (LT372; Lecroy, Chestnut Ridge, NY, USA) with the time window selected to record the backscattering of the therapy pulse from cavitation bubbles [7, 8, 25]. To determine whether cavitation occurred during a pulse, the signal generated by backscattering of the incident pulse

from the focus was analyzed following the method used in previous studies [7, 8]. A significant fraction of the incident wave energy is scattered when a cavitation bubble expands, greatly increasing the backscattered pressure amplitude received by the PCD. This signal appeared on the PCD at the time point corresponding to two times the time of flight for the focal length of the respective transducers. The integrated frequency power spectrum (S_{PCD}) of the backscatter signal was used as a measure of whether cavitation occurred according to the method previously described by Maxwell *et al* [7].

12.2.6 NMH Cavitation Threshold

For cavitation threshold experiments, 100 pulses were applied inside each sample at each pressure level at a pulse repetition frequency (PRF) of 0.5 Hz. The PRF was kept low to minimize the possibility that cavitation from one pulse would change the probability of cavitation on a subsequent pulse. In a previous study, it was demonstrated that cavitation during a pulse increased the likelihood of cavitation on a following pulse for PRFs > 1 Hz, but this effect was not observed for PRFs below 1 Hz [7]. In addition to this low PRF, the focus was translated for each pulse by 1 mm transverse to the acoustic propagation direction in a 10 × 10 grid in order to minimize the effects of cavitation damage to the nanodroplets or tissue phantom sample from altering the probability of cavitation. For each pulse, cavitation was monitored using both high speed imaging and PCD, and the fraction of total pulses (out of 100) for which cavitation was detected was determined as the cavitation probability.

The probability of observing cavitation followed a sigmoid function, given by

$$P(p_-) = \frac{1}{2} + erf\left(\frac{p_- - p_t}{\sqrt{2\sigma^2}}\right) \quad (\mathbf{E12.1})$$

where *erf* is the error function, p_t is the negative pressure at which the probability p_{cav}=0.5, σ is a variable related to the width of the transition between p_{cav}=0 and p_{cav}=1, with ± σ giving the difference in pressure from about p_{cav}=0.15 to p_{cav}=0.85 for the fit [7]. The cavitation threshold for each sample, p_t, is defined as the p- corresponding to p_{cav}=0.5 as calculated by the curve fit. Curve fitting for all data sets was performed using an OriginLab curve fitting program (OriginPro 9.1; OriginLab Corporation, Northampton, MA, USA). The fit curves for all samples were analyzed statistically to determine whether the differences in the values of p_t were significantly different from each other. The standard errors for p_t were estimated by a covariance matrix using the delta method [32]. The curves were compared using a two-sample t-test with statistic $t\left(p_{int1}-p_{int2},\sqrt{SE_1^2+SE_2^2}\right)$ at a 95% confidence interval. Results were considered statistically significant for p<0.05. Note that the standard error does not include the uncertainty in absolute pressure from the hydrophone measurement, only the uncertainty in the fit, because the values p_t are relative. A sample size of 3 tissue phantoms was used for each experimental condition.

12.2.7 NMH Bubble Size

To determine if nanodroplet-mediated cavitation bubbles were expanded similarly to histotripsy bubbles at higher pressure, optical images of the growth and collapse of bubbles were recorded by the high-speed camera. Nanodroplet-mediated cavitation bubbles were generated by the 345 kHz, 500 kHz, 1.5 MHz, and 3 MHz transducers at peak negative pressures slightly above the nanodroplet cavitation threshold at each frequency. More specifically, the peak negative pressure was 10.8 MPa (345 kHz), 10.3 MPa (500 kHz), 12.9 MPa (1.5 MHz), and 14.7 MPa (3 MHz). For comparison, bubbles were produced in tissue phantoms without nanodroplets

at estimated peak negative pressures of 26.4 MPa (345 kHz), 26.3 MPa (500 kHz), 26.8 MPa (1.5 MHz), and 28.8 MPa (3 MHz), which is slightly above the intrinsic threshold without nanodroplets. The maximum radius of bubbles was compared by reconstructing the average expansion and collapse behavior using a series of time-delayed images of the bubbles produced by identical histotripsy pulses. The specific delay times were varied based on the frequency and sample in order to reconstruct a sequence of bubble images and determine the time point corresponding to the maximum bubble radius, R_{max}. The R_{max} was compared between samples by analyzing results from 20 identical histotripsy pulses recorded at the time of maximum expansion, with each pulse applied to a different point in the sample (2 mm spacing) to prevent the effects of cavitation damage from altering the tissue phantom and nanodroplet properties. The size of single bubbles was measured for all twenty pulses to determine the bubble radius, and the mean and standard deviation in bubble radius were calculated. A sample size of 6 tissue phantoms was used for each experimental condition.

12.2.8 NMH Multi-pulse Sustainability

To determine if nanodroplets are sustainable cavitation nuclei over multiple pulses, 1000 ultrasound pulses were applied to a single focal region in tissue phantoms containing nanodroplets at a PRF of 1 Hz and peak negative pressures of 10.8 MPa (345 kHz), 10.3 MPa (500 kHz), 12.9 MPa (1.5 MHz), and 14.7 MPa (3 MHz). In a previous study, nanodroplet-mediated histotripsy created consistent, well-defined fractionation in tissue phantoms at 10 Hz PRF by maintaining cavitation at over multiple pulses [9]. However, it is unclear whether the nanodroplets themselves or the residual nuclei from previous pulses are responsible for seeding cavitation after the first few pulses. As a result, the PRF in this study was kept low (1 Hz) to

minimize the contributions of residual nuclei from a previous pulse from effecting cavitation generation on a subsequent pulse in order to determine if nanodroplets continue to function as viable cavitation nuclei after the first few pulses or if the nanodroplets are destroyed in the cavitation process. Cavitation was monitored using high speed optical imaging, and the number of bubbles produced by each pulse was compared for 1000 histotripsy pulses in each sample. In order to quantify the ability of nanodroplets to sustain a cavitation bubble cloud over multiple pulses, the number of pulses before cloud extinction, $P\#_{Ext}$, was plotted as a function of frequency. A sample size of 6 tissue phantoms was used for each experimental condition.

12.3 Results

12.3.1 NMH Cavitation Threshold

To investigate the effects of ultrasound frequency on the NMH threshold, histotripsy pulses were applied to tissue-mimicking agarose phantoms with and without nanodroplets using the 345 kHz, 500 kHz, 1.5 MHz, and 3 MHz histotripsy transducers. For all frequencies, cavitation bubbles were observed on the high-speed camera when a certain negative pressure was exceeded, with close agreement between optical imaging and PCD detection methods [Fig. 12.4], as seen in previous studies [7, 8]. Results from phantoms without nanodroplets show that the histotripsy intrinsic threshold, p_{t_int}, was p_{t_int} =24.8±1.1 MPa, with σ_{mean} = 2.0 MPa for 345 kHz; p_{t_int} = 25.5±1.7 MPa, with σ_{mean} = 1.8 MPa for 500 kHz; p_{t_int} = 26.7±0.4 MPa, with σ_{mean} = 1.0 MPa for 1.5 MHz; and p_{t_int} = 26.8±0.5 MPa, with σ_{mean} = 0.9 MPa for 3 MHz [Fig. 12.5]. Note that at lower amplitudes, cavitation was occasionally observed that deviated from the curve function, especially at lower frequency. These cavitation events were probably caused by contamination of the sample by heterogeneities in the liquid that could not be entirely avoided

throughout the experiment. The effects of nanodroplets on the cavitation threshold demonstrated a significant decrease in the cavitation threshold compared to the histotripsy intrinsic threshold [Fig. 12.5]. The NMH threshold for phantoms containing PFP nanodroplets, p_{t_PFP}, was p_{t_PFP} =7.4±0.1 MPa, with σ_{mean} = 1.4 MPa for 345 kHz; p_{t_PFP} = 9.2±0.9 MPa, with σ_{mean} = 0.8 MPa for 500 kHz; p_{t_PFP} = 10.5±0.2 MPa, with σ_{mean} = 0.4 MPa for 1.5 MHz; and p_{t_PFP} = 13.2±0.4 MPa, with σ_{mean} = 0.6 MPa for 3 MHz [Fig. 12.5]. The results of the cavitation threshold for all frequencies are plotted in Figure 12.6. Comparing the results for the NMH threshold and histotripsy intrinsic threshold demonstrated a significant decrease in the cavitation threshold and a significant increase in the steepness of the S-curve (σ) for samples containing nanodroplets at all frequencies. Additionally, it was observed that the NMH threshold was significantly decreased at lower frequency [Fig. 12.6].

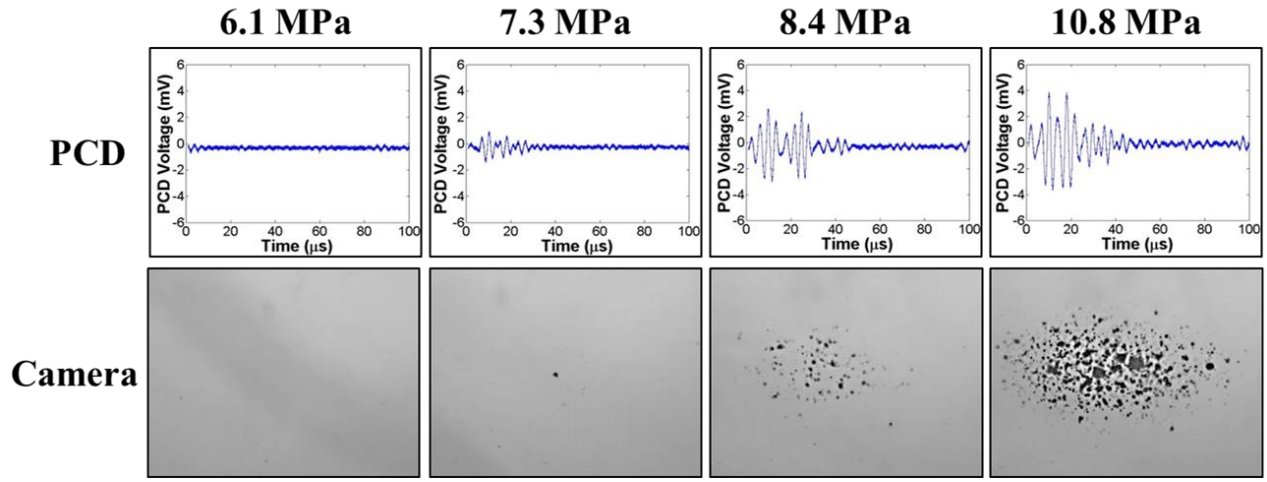

Figure 12.4. Cavitation detection. Sample passive cavitation detection (PCD) signals (top) and high speed optical images (bottom) used for cavitation detection. Results showed good agreement between the two methods. Representative images shown above are from 345 kHz histotripsy pulses applied to tissue phantoms containing nanodroplets.

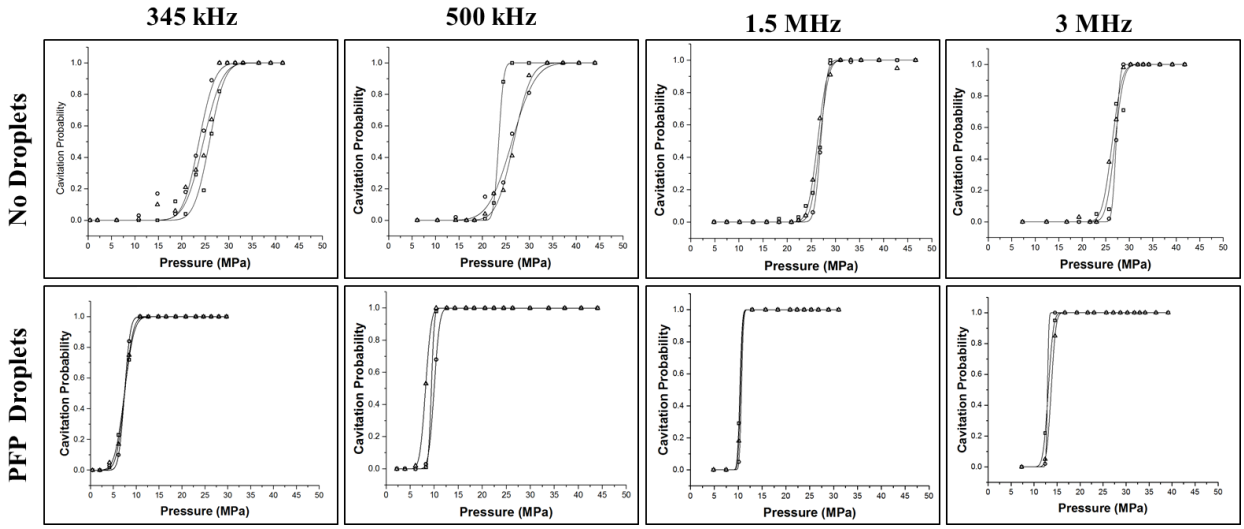

Figure 12.5. Cavitation threshold curves. Probability curves for tissue phantoms with and without nanodroplets. Results showed a significant decrease in the cavitation threshold with nanodroplets compared to controls. Results also showed a significant increase in the nanodroplet cavitation threshold with increasing frequency.

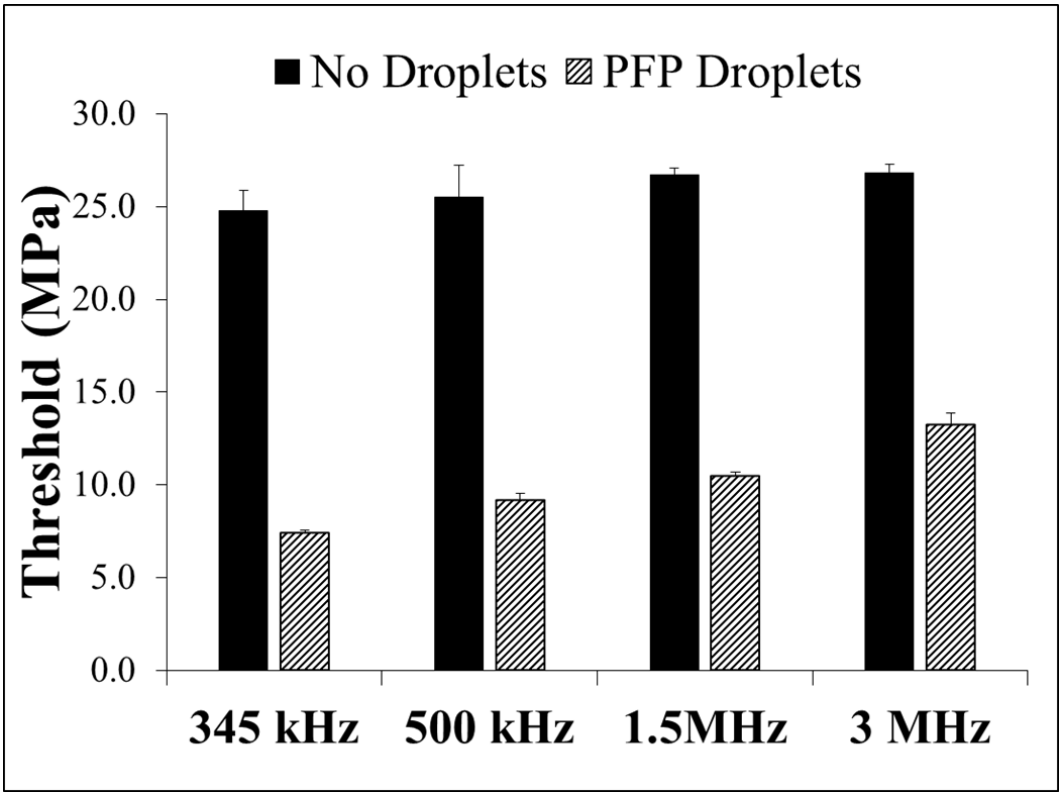

Figure 12.6. Cavitation threshold results. Bar plots show the cavitation threshold results for tissue phantoms with and without perfluoropentane (PFP) nanodroplets at all frequencies studied in this work.

12.3.2 NMH Bubble Size

To study the effects of ultrasound frequency on the expansion of NMH bubbles, the maximum bubble radius, R_{max}, produced by 345 kHz, 500 kHz, 1.5 MHz, and 3 MHz histotripsy pulses was measured in phantoms with and without nanodroplets. The peak negative pressure used for each frequency was chosen to be slightly above the cavitation threshold at each frequency so that cavitation was always generated (P_{cav}=1). Optical imaging results demonstrated that NMH bubbles were significantly smaller than histotripsy bubbles generated above the intrinsic threshold [Fig. 12.7]. Note that different image magnifications were used for each frequency for the images shown in Figure 12.7, to provide a better image of the bubbles produced at each frequency. At all frequencies, results showed that the R_{max} for NMH bubbles was between 30%-40% of the R_{max} measured for histotripsy bubbles produced above the intrinsic threshold [Fig. 12.8]. Results further showed that larger bubbles were observed at lower frequency for both the histotripsy only and NMH conditions [Fig. 12.8]. For example, R_{max} for NMH bubbles was shown to decrease from 126.7±47.5 µm at 345 kHz to 106.5±17.6 µm, 34.7±13.4 µm, and 12.9±5.3 µm at 500 kHz, 1.5 MHz, and 3 MHz, respectively [Table 12.1]. Comparing R_{max} for NMH and histotripsy bubbles showed that, although NMH bubbles were significantly smaller than histotripsy bubbles for all frequencies, NMH bubbles produced at the lower two frequencies (345 kHz, 500 kHz) grew larger than histotripsy bubbles produced at the two higher frequencies (1.5 MHz, 3 MHz). For example, the R_{max} of NMH bubbles produced at 345 kHz and 500 kHz (126.7±47.5 µm and 106.5±17.6 µm) were significantly larger than the R_{max} of histotripsy bubbles generated above the intrinsic threshold at 1.5 MHz and 3 MHz (79.5±11.5µm and 34.3±8.5) [Fig. 12.8]. The complete list of R_{max} results are listed in Table 12.1 along with the peak negative pressure applied for each condition.

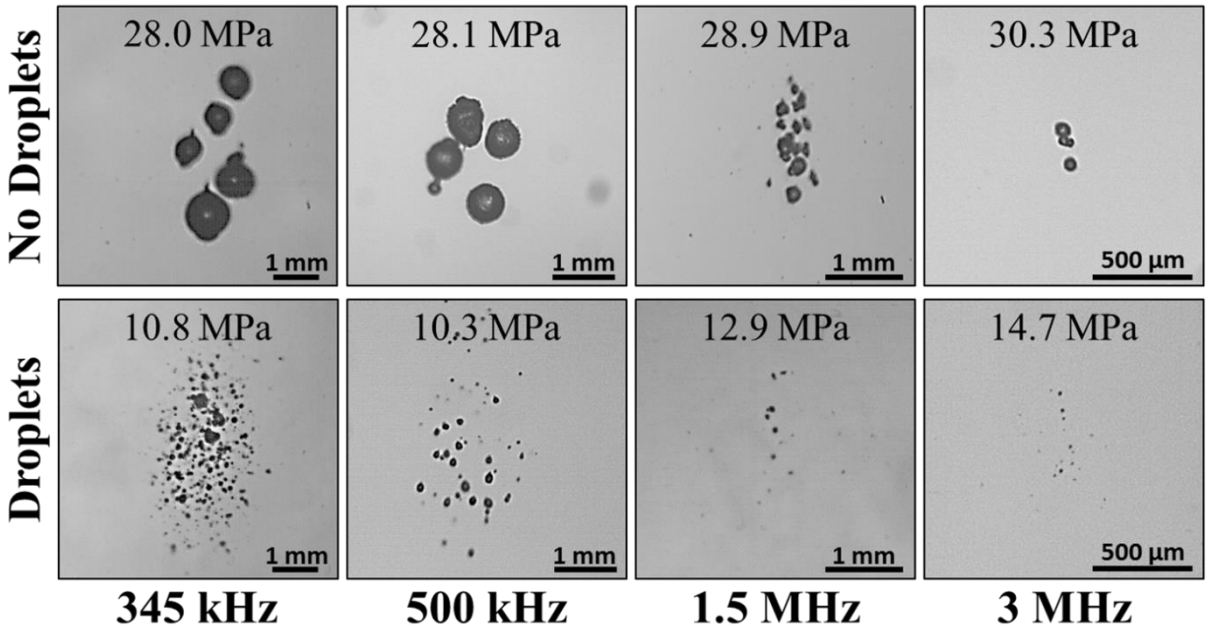

Figure 12.7. Optical imaging results show a decrease in NMH bubble size compared with control bubbles produced at the same frequency at higher pressure. Results further show a significant decrease in bubble size with increasing frequency. Note: Different image magnifications were used for the above images to better image the bubbles at each frequency.

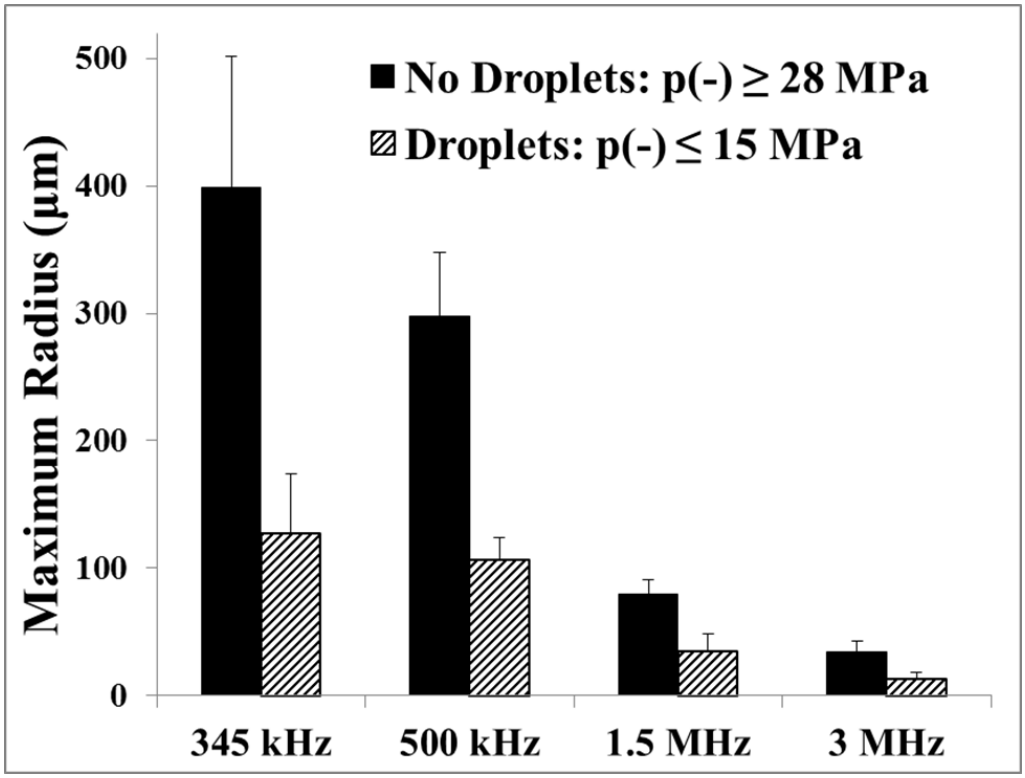

Figure 12.8. Plot shows a comparison of the maximum bubble radius produced in tissue phantoms with and without nanodroplets by 345 kHz, 500 kHz, 1.5 MHz, and 3 MHz histotripsy pulses. The peak negative pressures (p-) applied for each condition are listed in Table 12.1.

Table 12.1 Table shows the maximum bubble radius produced in tissue phantoms with and without nanodroplets, along with the peak negative pressure (*p*-) applied for each condition. The *p*- for each condition was chosen to be slightly above the nanodroplet-mediated histotripsy (NMH) and intrinsic cavitation thresholds of the sample at each frequency.

Frequency	Sample	P- (MPa)	Max Radius (μm)
345 kHz			
	No Droplets	28	398.8±102.5
	Droplets	10.8	126.7±47.5
500 kHz			
	No Droplets	28.1	297.4±50.5
	Droplets	10.3	106.5±17.6
1.5 MHz			
	No Droplets	28.9	79.5±11.5
	Droplets	12.9	34.7±13.4
3 MHz			
	No Droplets	30.3	34.3±8.5
	Droplets	14.7	12.9±5.3

12.3.3 NMH Multi-pulse Sustainability

To determine if nanodroplets are sustainable cavitation nuclei over multiple pulses, 1000 histotripsy pulses were applied to a single focal region in phantoms containing nanodroplets at a PRF of 1 Hz. Results demonstrated that a bubble cloud consisting of many bubbles was observed after the first pulse [Fig. 12.9]. However, the number of bubbles observed inside the cloud significantly decreased with increasing number of pulses [Fig. 12.9]. For example, for the 3 MHz sample shown in Figure 12.9, only one bubble was observed after 5 pulses with no bubbles remaining after 10 pulses. At lower frequency, bubbles were generated for more pulses than at higher frequency, but still showed the same trend of decreasing number of bubbles with increasing pulse number [Fig. 12.9]. It is likely that bubbles lasted for more pulses at lower frequency due to enhanced bubble expansion resulting in a larger population of residual nuclei

and a corresponding increase in dissolution time. Figure 12.10 shows the number of pulses before cloud extinction, $P\#_{Ext}$, as a function of frequency (n=6). Results demonstrated a significant decrease ($p<0.05$) in $P\#_{Ext}$ at higher frequencies, with $P\#_{Ext}$ observed to decrease from 80.5±10.3 pulses at 345 kHz to 51.7±7.3 pulses, 15.7±4.8 pulses, and 5.5±1.9 pulses at 500 kHz, 1.5 MHz, and 3 MHz, respectively [Fig. 12.10]. For all frequencies, no bubbles were observed after 100 pulses were applied to the samples.

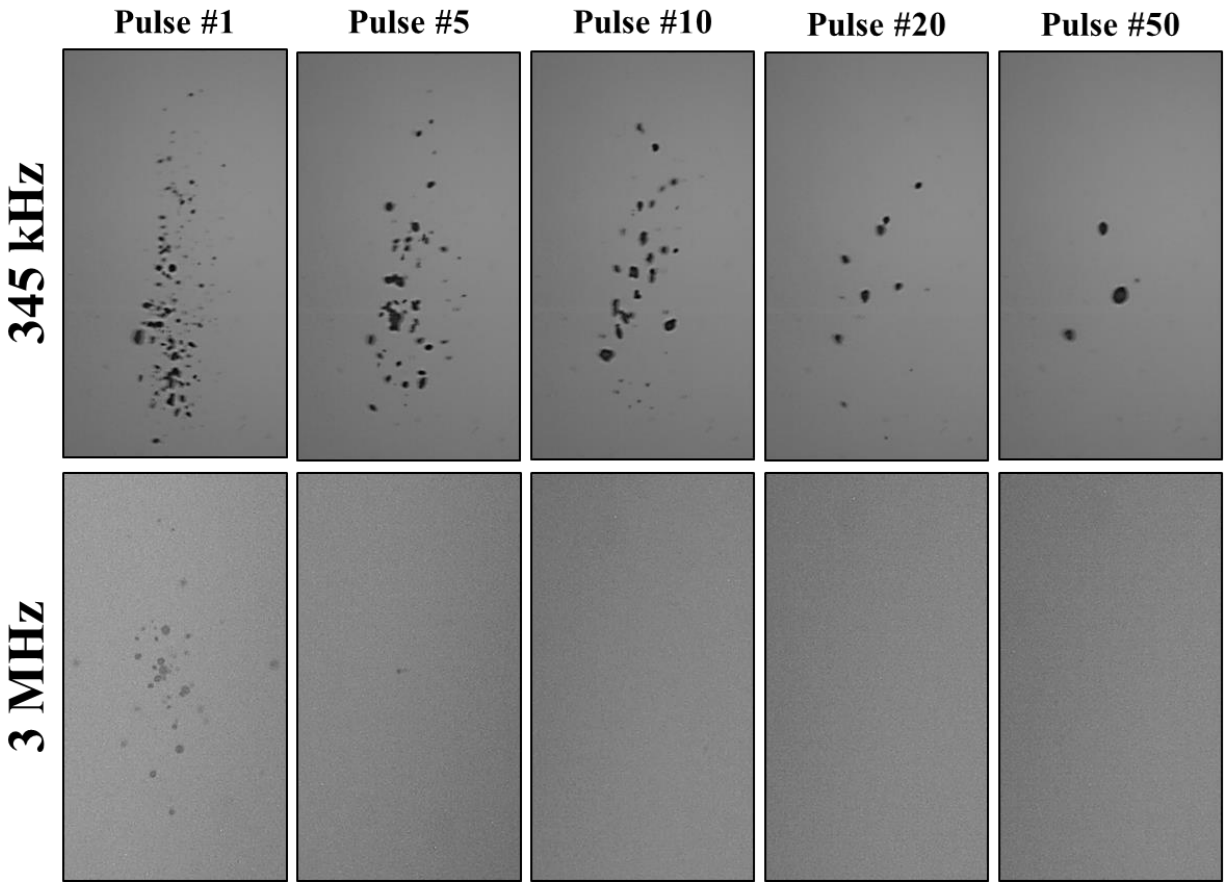

Figure 12.9. Optical images show NMH bubbles produced by 345 kHz (p-=10.8 MPa) and 3 MHz (p-=14.7 MPa) at a single focal point in tissue phantoms containing nanodroplets at a pulse repetition frequency (PRF) of 1 Hz. Results showed a decrease in the number of bubbles observed at the focus with increasing pulse number.

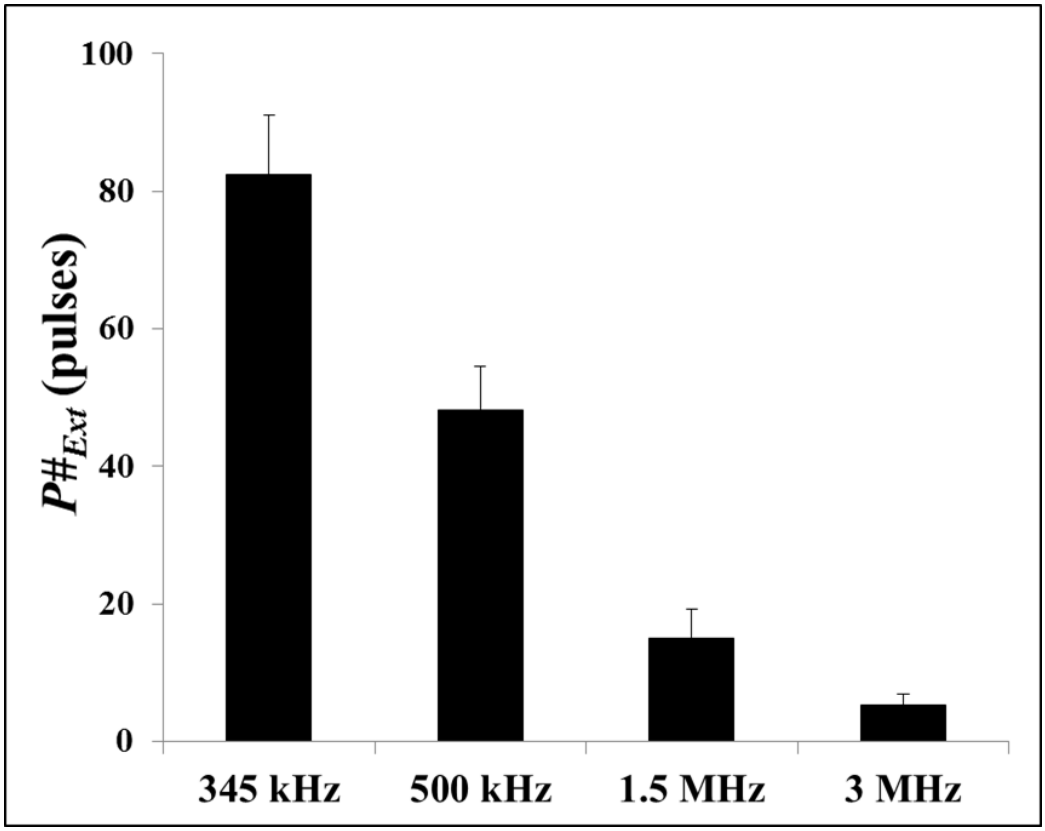

Figure 12.10. Plot shows a significant decrease ($p<0.05$) in P#Ext with increasing frequency. A sample size of 6 tissue phantoms was used for each experimental condition.

12.4 Discussion

In this chapter, we investigated the effects of frequency on nanodroplet-mediated histotripsy (NMH) using our polymer encapsulated PFP nanodroplets [19]. This work builds upon two previous studies which demonstrated that NMH has the potential to be used for targeted tissue ablation by decreasing the pressure threshold required to generate histotripsy bubbles [9, 19]. In this chapter, we investigated the effects of frequency in order to optimize the acoustic parameters used for NMH therapy. Since one of the goals of NMH therapy is to efficiently treat large and/or multi-focal tumor nodules, NMH parameters should be optimized to increase the size of the focal zone, decrease the NMH cavitation threshold, and increase NMH bubble expansion, all of which were improved at lower frequencies as shown in this study.

In the first part of this chapter, the effects of frequency on the NMH cavitation threshold were investigated, with results demonstrating that PFP nanodroplets significantly reduced the cavitation threshold compared to the histotripsy intrinsic threshold. At all frequencies tested, the NMH threshold was significantly lower than the histotripsy intrinsic threshold, while maintaining a steep threshold behavior. This distinct threshold behavior is promising for the development of NMH therapy, in which the applied pressure must be chosen in the region above the NMH threshold but below the histotripsy intrinsic threshold to ensure cavitation is only generated in regions containing nanodroplets. The results of this study show that all the frequencies investigated (345kHz-3MHz) could be used for NMH, with lower frequencies offering the largest drop in threshold compared to the histotripsy intrinsic threshold while maintaining the distinct threshold behavior. These results suggest that lower frequencies will be more efficient for NMH applications in which large volume or multi-focal ablation is desired. However, it should be noted that lower frequencies may reduce the treatment precision due to the larger focal volume, which would increase the likelihood of generating collateral damage outside of the desired treatment region. As such, higher frequencies may be preferred for NMH applications in which very high precision is required.

The frequency dependence of the NMH cavitation threshold observed in this study is opposite to that reported in previous work on acoustic droplet vaporization (ADV) which showed that the ADV threshold decreases with increasing frequency [33-35]. However, those studies used larger droplets, higher frequency ranges, and/or longer duration exposures. Recent work has revealed that the decrease in the ADV threshold at higher frequencies is due to superharmonic focusing inside the droplet, which is significantly enhanced at higher frequencies and in larger droplets [20, 21]. These previous studies help to explain why the cavitation thresholds in this

study do not follow the trends observed for ADV, since the extent of superharmonic focusing is negligible for the droplet size (<400 nm) and frequencies (≤3MHz) used in this study [20]. In contrast to those previous studies, the results of this work suggest that NMH bubbles are generated inside the droplets directly from the incident *p*- (tensile portion of the incident wave), similar to histotripsy bubbles generated above the intrinsic threshold [8]. This hypothesis is supported by the trends in the cavitation threshold with lower frequencies resulting in a lower cavitation threshold, likely due to the longer duration of the applied *p*- and the larger focal zone at lower frequencies, which increases the volume of PFP exposed to the *p*- and therefore increases the probability of nucleating cavitation inside the PFP nanodroplets. This would also imply that the NMH threshold will be affected by nanodroplet concentration, since a higher concentration of nanodroplets would result in a larger volume of PFP being exposed to the applied *p*-. This would explain why a concentration of 2.0×10^8 particles/mL was required in order to reduce the cavitation threshold in this study while concentrations $<\sim 10^6$-10^7 particles/mL did not significantly reduce the cavitation threshold compared to the histotripsy intrinsic threshold. This threshold behavior suggests that the nanodroplets decrease the cavitation threshold by carrying a lower threshold media (PFP) rather than by acting as discrete nuclei as would be the case for gas-filled contrast agents. Future work will further investigate the role of droplet concentration on NMH therapy.

In the second part of this chapter, the effects of frequency on NMH bubble expansion were investigated, with results showing that lower frequencies facilitated larger bubble expansion. While it is likely that NMH will be able to fractionate tissue even at higher frequencies, the results of this study suggest that NMH will be more efficient at lower frequencies due to enhanced bubble expansion. A previous study investigating the effects of

frequency on histotripsy bubble expansion demonstrated that the increase in bubble expansion at lower frequencies is due the increased duration of the applied rarefactional pressure [10]. This same effect likely explains the results of this study in which NMH bubbles at lower frequencies grew larger than bubbles produced by histotripsy without nanodroplets at higher frequencies, despite a >18 MPa decrease in the peak negative pressure of the applied pulses. For example, NMH bubbles produced at 345 kHz and 500 kHz grew larger than bubbles produced by histotripsy without nanodroplets at 1.5 MHz and 3 MHz, which have previously been shown capable of achieving tissue fractionation [26, 30]. This finding supports our hypothesis that NMH can be used to efficiently create histotripsy lesions when using lower frequencies.

In the final part of this chapter, the ability of PFP nanodroplets to act as sustainable cavitation nuclei over multiple pulses was investigated. In a previous study, nanodroplet-mediated histotripsy created consistent, well-defined fractionation at pressure levels (11-20 MPa) significantly below the histotripsy intrinsic threshold (~26-30 MPa) in tissue phantoms at a PRF of 10 Hz by maintaining cavitation at over multiple pulses [9]. However, it is unclear whether the nanodroplets themselves or residual nuclei from previous pulses were responsible for seeding cavitation after the first few pulses. In this study, the PRF was kept low (1 Hz) to minimize the contributions of residual nuclei from a previous pulse, with results showing a significant reduction in the number of bubbles generated by NMH with increasing number of pulses. For all frequencies, no bubbles were observed in tissue phantoms after 100 pulses. These results suggest that the nanodroplets are destroyed by the cavitation process and only function as cavitation nuclei for the first few pulses, potentially due to the PFP being dissolved after undergoing the NMH cavitation process. This finding indicates that NMH will need to be applied at a higher PRF in order sustain cavitation for the duration of the treatment, since previous work has shown

that multiple pulses (often>50 pulses) are needed to completely destroy all the cells within the treatment volume. It is also possible that nanodroplets containing a higher boiling point perfluorocarbon, such as perfluorohexane, would re-condense into a liquid and remain sustainable nuclei over multiple pulses, which would be a major benefit for NMH therapy, as previous work has shown a decrease in ablation efficiency for higher PRF treatments that rely on residual nuclei from previous pulses to maintain the cavitation bubble cloud [36]. However, higher boiling point droplets may also require a higher pressure in order to generate cavitation, which would not be desired for NMH therapy. Future work will investigate the possibility of using nanodroplets containing a higher boiling point perfluorocarbon for NMH therapy.

12.5 Conclusion

In this chapter, the effects of ultrasound frequency on nanodroplet-mediated histotripsy were investigated, with results supporting our hypothesis that using a lower frequency will improve NMH therapy. The results demonstrated that the NMH threshold was significantly reduced at lower frequencies, ranging from 7.4 MPa at 345 kHz to 13.2 MPa at 3 MHz. Furthermore, the results demonstrated that NMH bubble expansion was enhanced at lower frequency, generating bubbles with a maximum radius >100 μm despite the reduced pressure applied. Finally, multi-pulse experiments demonstrated that nanodroplets are destroyed during the first few pulses at 1Hz PRF. Overall, the results of this chapter provide significant insight in the role of ultrasound parameters in NMH therapy and will provide a rational basis to specifically tailor acoustic parameters in order to improve NMH tissue fractionation.

12.6 References

[1] E. Vlaisavljevich, *et al.*, "The Effects of Ultrasound Frequency on Nanodroplet-Mediated Histotripsy," *Ultrasound Med Biol*, 2015.

[2] J. E. Parsons, *et al.*, "Pulsed cavitational ultrasound therapy for controlled tissue homogenization," *Ultrasound Med Biol*, vol. 32, pp. 115-29, Jan 2006.

[3] W. W. Roberts, *et al.*, "Pulsed cavitational ultrasound: a noninvasive technology for controlled tissue ablation (histotripsy) in the rabbit kidney," *J Urol*, vol. 175, pp. 734-8, Feb 2006.

[4] Z. Xu, *et al.*, "Investigation of intensity thresholds for ultrasound tissue erosion," *Ultrasound Med Biol*, vol. 31, pp. 1673-82, Dec 2005.

[5] Z. Xu, *et al.*, "Controlled ultrasound tissue erosion: the role of dynamic interaction between insonation and microbubble activity," *J Acoust Soc Am*, vol. 117, pp. 424-35, Jan 2005.

[6] J. E. Parsons, *et al.*, "Spatial variability in acoustic backscatter as an indicator of tissue homogenate production in pulsed cavitational ultrasound therapy," *IEEE Trans Ultrason Ferroelectr Freq Control*, vol. 54, pp. 576-90, Mar 2007.

[7] A. D. Maxwell, *et al.*, "Probability of cavitation for single ultrasound pulses applied to tissues and tissue-mimicking materials," *Ultrasound Med Biol*, vol. 39, pp. 449-65, Mar 2013.

[8] E. Vlaisavljevich, *et al.*, "Effects of Ultrasound Frequency and Tissue Stiffness on the Histotripsy Intrinsic Threshold for Cavitation," *Ultrasound Med Biol*, Mar 9 2015.

[9] E. Vlaisavljevich, *et al.*, "Nanodroplet-mediated histotripsy for image-guided targeted ultrasound cell ablation," *Theranostics*, vol. 3, pp. 851-64, 2013.

[10] E. Vlaisavljevich, *et al.*, "Effects of tissue stiffness, ultrasound frequency, and pressure on histotripsy-induced cavitation bubble behavior," *Phys Med Biol*, vol. 60, pp. 2271-92, Mar 21 2015.

[11] Z. Xu, *et al.*, "High speed imaging of bubble clouds generated in pulsed ultrasound cavitational therapy--histotripsy," *IEEE Trans Ultrason Ferroelectr Freq Control*, vol. 54, pp. 2091-101, Oct 2007.

[12] T. L. Hall, *et al.*, "Histotripsy of rabbit renal tissue in vivo: temporal histologic trends," *J Endourol*, vol. 21, pp. 1159-66, Oct 2007.

[13] C. R. Hempel, *et al.*, "Histotripsy fractionation of prostate tissue: local effects and systemic response in a canine model," *J Urol*, vol. 185, pp. 1484-9, Apr 2011.

[14] A. D. Maxwell, *et al.*, "Noninvasive treatment of deep venous thrombosis using pulsed ultrasound cavitation therapy (histotripsy) in a porcine model," *J Vasc Interv Radiol,* vol. 22, pp. 369-77, Mar 2011.

[15] G. E. Owens, *et al.*, "Therapeutic ultrasound to noninvasively create intracardiac communications in an intact animal model," *Catheter Cardiovasc Interv,* vol. 77, pp. 580-8, Mar 1 2011.

[16] Z. Xu, *et al.*, "Noninvasive creation of an atrial septal defect by histotripsy in a canine model," *Circulation,* vol. 121, pp. 742-9, Feb 16 2010.

[17] N. R. Styn, *et al.*, "Histotripsy of VX-2 tumor implanted in a renal rabbit model," *J Endourol,* vol. 24, pp. 1145-50, Jul 2010.

[18] E. Vlaisavljevich, *et al.*, "Image-Guided Non-Invasive Ultrasound Liver Ablation Using Histotripsy: Feasibility Study in an In Vivo Porcine Model," *Ultrasound in medicine & biology,* vol. 39, pp. 1398-1409, 2013.

[19] Y. Yuksel Durmaz, *et al.*, "Development of nanodroplets for histotripsy-mediated cell ablation," *Mol Pharm,* vol. 11, pp. 3684-95, Oct 6 2014.

[20] O. Shpak, *et al.*, "Acoustic droplet vaporization is initiated by superharmonic focusing," *Proc Natl Acad Sci U S A,* vol. 111, pp. 1697-702, Feb 4 2014.

[21] D. S. Li, *et al.*, "Initial nucleation site formation due to acoustic droplet vaporization," *Appl Phys Lett,* vol. 104, p. 063703, Feb 10 2014.

[22] Z. Gao, *et al.*, "Drug-loaded nano/microbubbles for combining ultrasonography and targeted chemotherapy," *Ultrasonics,* vol. 48, pp. 260-70, Aug 2008.

[23] P. S. Sheeran, *et al.*, "Formulation and Acoustic Studies of a New Phase-Shift Agent for Diagnostic and Therapeutic Ultrasound," *Langmuir,* vol. 27, pp. 10412-10420, Sep 6 2011.

[24] E. Vlaisavljevich, *et al.*, "Effects of tissue mechanical properties on susceptibility to histotripsy-induced tissue damage," *Phys Med Biol,* vol. 59, pp. 253-70, Jan 20 2014.

[25] E. Vlaisavljevich, *et al.*, "Histotripsy-induced cavitation cloud initiation thresholds in tissues of different mechanical properties," *IEEE Trans Ultrason Ferroelectr Freq Control,* vol. 61, pp. 341-52, Feb 2014.

[26] E. Vlaisavljevich, *et al.*, "Investigation of the role of tissue stiffness and ultrasound frequency in histotripsy-induced cavitation. ," *Symposium on Therapeutic Ultrasound,* 2014.

[27] R. Masuzaki, *et al.*, "Assessing liver tumor stiffness by transient elastography," *Hepatol Int,* vol. 1, pp. 394-7, Sep 2007.

[28] V. Normand, *et al.*, "New insight into agarose gel mechanical properties," *Biomacromolecules,* vol. 1, pp. 730-8, Winter 2000.

[29] M. Zhang, *et al.*, "Quantitative characterization of viscoelastic properties of human prostate correlated with histology," *Ultrasound Med Biol,* vol. 34, pp. 1033-42, Jul 2008.

[30] K. W. Lin, *et al.*, "Dual-beam histotripsy: a low-frequency pump enabling a high-frequency probe for precise lesion formation," *IEEE Trans Ultrason Ferroelectr Freq Control,* vol. 61, pp. 325-40, Feb 2014.

[31] J. E. Parsons, *et al.*, "Cost-effective assembly of a basic fiber-optic hydrophone for measurement of high-amplitude therapeutic ultrasound fields," *J Acoust Soc Am,* vol. 119, pp. 1432-40, Mar 2006.

[32] D. W. Hosmer and S. Lemeshow, "Confidence interval estimation of interaction," *Epidemiology,* vol. 3, pp. 452-6, Sep 1992.

[33] O. D. Kripfgans, *et al.*, "Acoustic droplet vaporization for therapeutic and diagnostic applications," *Ultrasound Med Biol,* vol. 26, pp. 1177-89, Sep 2000.

[34] K. C. Schad and K. Hynynen, "In vitro characterization of perfluorocarbon droplets for focused ultrasound therapy," *Phys Med Biol,* vol. 55, pp. 4933-47, Sep 7 2010.

[35] R. Williams, *et al.*, "Characterization of submicron phase-change perfluorocarbon droplets for extravascular ultrasound imaging of cancer," *Ultrasound Med Biol,* vol. 39, pp. 475-89, Mar 2013.

[36] T. Y. Wang, *et al.*, "Imaging feedback of histotripsy treatments using ultrasound shear wave elastography," *Ultrasonics, Ferroelectrics and Frequency Control, IEEE Transactions on,* vol. 59, pp. 1167-1181, 2012.

Chapter 13

Effects of Droplet Composition on Nanodroplet-Mediated Histotripsy

A majority component of this chapter is excerpted from a manuscript that has been submitted to *Theranostics.*

13.1 Introduction

Histotripsy is a noninvasive tissue ablation method that controllably fractionates soft tissue through cavitation generated by high pressure, short duration ultrasound pulses [1-3]. Histotripsy depends on the initiation and maintenance of a dense cavitation bubble cloud to produce mechanical tissue fractionation [4, 5]. Previous work has shown that, using a 1-2 cycle pulse with a single dominant negative pressure phase, cavitation bubbles can be reproducibly generated in tissue when the peak negative pressure (*p*-) is raised above the histotripsy intrinsic threshold of ~25-30 MPa [6, 7]. In order to effectively fractionate tissue into acellular debris, histotripsy requires a dense cavitation bubble cloud to be initiated and maintained over multiple pulses (often >100) until the tissue is completely fractionated into a liquid-appearing homogenate with no cellular structures remaining [2, 3, 8]. Histotripsy is currently being studied for many clinical applications where non-invasive tissue removal is desired including benign prostatic hyperplasia [9], deep vein thrombosis [10], congenital heart disease [11, 12], and cancer [13, 14].

Although histotripsy has shown promise for many clinical applications including tumor ablation, this approach is limited to applications in which the target tissue can be identified and imaged prior to treatment, which is often not feasible in cancer patients with many small tumor nodules and micro-metastases. As a result, our group has developed a targeted ablation approach combining polymer encapsulated nanodroplets with histotripsy [15-17]. This nanodroplet-mediate histotripsy (NMH) approach takes advantage of the significantly reduced cavitation threshold of the nanodroplets, allowing for cavitation to be selectively generated only in regions containing nanodroplets [16]. By synthesizing nanodroplets in a size range (~100-400 nm) in which they can diffuse through the leaky tumor vasculature and preferentially accumulate in the tumor, NMH has the potential for selective ablation of tumors [16, 17]. Previous work has demonstrated that NMH can be used to create well-defined ablation similar to histotripsy but at significantly lower pressure and has demonstrated the potential to use NMH for simultaneous multi-focal ablation [16]. Furthermore, a previous study by Yuksel Durmaz *et al* investigated the optimal characteristics of polymer encapsulated perfluoropentane (PFP) nanodroplets, with results showing optimal NMH ablation for nanodroplets with a shell-cross-linked triblock amphiphilic copolymer composed of a poly(ethylene glycol) (PEG) block as a biocompatible corona, a poly(acrylic acid) (PAA) middle block reacting with the cross-linker to form a shell, and a poly(heptadecafluorodecyl methacrylate-*co*-methyl methacrylate) (P(HDFMA-co-MMA)) fluorinated hydrophobic block encapsulating 2% v/v PFP [17]. However, although this previous study determined the optimal conditions for PFP nanodroplets, the effects of perfluorocarbon boiling temperature on NMH therapy have not been previously investigated.

In this chapter, we compare perfluoropentane (PFP, boiling point ~29°C) and perfluorohexane (PFH, boiling point ~56°C) nanodroplets for NMH therapy. Based on previous

work comparing PFP and PFH droplets for acoustic droplet vaporization [18, 19], we hypothesize that PFH nanodroplets will have a slightly higher cavitation threshold than PFP droplets, but that the cavitation threshold of both droplets will be significantly lower than the histotripsy intrinsic threshold. To test this hypothesis, tissue phantoms containing PFP nanodroplets, PFH nanodroplets, and no nanodroplets were exposed to histotripsy pulses produced by 345 kHz, 500 kHz, 1.5 MHz, and 3 MHz custom-built histotripsy transducers. The probability of generating inertial cavitation from a single 1-2 cycle histotripsy pulse was measured, with the cavitation threshold defined as the peak negative pressure at which the probability of generating cavitation, p_{cav}, from a single histotripsy pulse was p_{cav}=0.5. In addition to the effects of droplet composition on the cavitation threshold, we also investigate the effects of droplet composition on cavitation sustainability over multiple histotripsy pulses. In a previous studies, PFP nanodroplets were used to created consistent, well-defined fractionation at pressure levels (11-20 MPa) significantly below the histotripsy intrinsic threshold (~26-30 MPa) in tissue phantoms at a pulse repetition frequency (PRF) of 10 Hz by maintaining cavitation over multiple pulses [16, 17]. However, it was also observed that cavitation was not maintained over multiple pulses when ultrasound was applied at a lower PRF (1 Hz) [15-17]. A low PRF (1 Hz) has been shown to produce more efficient tissue fractionation and is not affected by the cavitation memory effect, in which residual gas bubbles from previous cavitation events function as nuclei for generating cavitation on a subsequent pulse [20]. This result suggests that PFP nanodroplets are destroyed during the first few pulses, requiring cavitation on subsequent pulses to be generated from residual nuclei remaining from previous pulses. We hypothesize that, due to their higher boiling point, PFH nanodroplets will re-condense into a liquid after cavitation and remain sustainable nuclei over multiple (>100) pulses, allowing cavitation to be maintained over

multiple pulses even at low PRF. To test this hypothesis, 1000 histotripsy pulses were applied to a single focal zone tissue in phantoms containing PFP and PFH nanodroplets, and the number of NMH bubbles generated was compared after each pulse. Overall, these results will improve our understanding of the NMH process and help to determine the optimal nanodroplet characteristics for NMH therapy.

13.2 Methods

13.2.1 Materials

Methyl methacrylate (MMA, Sigma-Aldrich, 99 %), 3,3,4,4,5,5,6,6,7,7,8,8,9,9,10,10,10 heptadecafluorodecyl methacrylate (HDFMA, Sigma-Aldrich, 97 %), *tert*-butyl acrylate (*t*BA, Sigma-Aldrich, 98 %) and *N, N, N', N'', N''*-pentamethyldiethylenetriamine (PMDETA, Sigma-Aldrich, 99 %) were passed through a basic alumina column to remove the inhibitor. Copper (I) bromide (CuBr, Sigma-Aldrich, 99.9 %), 2-bromoisobutyryl bromide (Fluka, >97 %), tetrahydrofuran anhydrous (THF, Sigma-Aldrich, >99.9 %), *N,N'*-Dicyclohexylcarbodiimide (DCC, Sigma-Aldrich, 99 %), dimethylaminopyridine (DMAP, Acros, 99 %), 4-pentynoic acid (Sigma-Aldrich, 99 %), furan (Sigma-Aldrich, ≥99 %), maleic anhydride (Fluka, ≥99 %), 9-anthracene methanol (Aldrich, ≥ 99%), perfluoropentane (PFP, Alfa Aesar, 97% ca. 85% n-isomer), perfluorohexane (PFH, SynQuest Lab, > 98%) *N*-hydroxy succinimide (NHS, Fluka, 97 %), *N*-(3-Dimethylaminopropyl)-*N* ethylcarbodiimide hydrochloride (EDC, Fluka >98 %), poly(ethylene glycol) monomethylether (Me-PEG, M_n : 2000 g/mol, Sigma-Aldrich), sodium azide (NaN_3, Acros, 99 %), 2-(*N*-morpholino)ethanesulfonic acid monohydrate (MES, Acros, 99 %), triethylamine (TEA, Sigma-Aldrich, ≥ 99%), trifluoroacetic acid (TFA, Acros, 99 %), ethylene carbonate (Sigma-Aldrich, 98 %), 2,2`- (ethylenedioxy)-bis(ethylamine) (Sigma-

Aldrich, 98%) agarose powder (Type VII, Sigma-Aldrich), citratephosphate-dextrose (CPD, Sigma-Aldrich), heptane fraction (Sigma-Aldrich, > 99%), dicholoromethane (DCM or CH_2Cl_2, Sigma-Aldrich, >99.5%) were used as received.

13.2.2 Nanodroplet Formulation and Characterization

A well-defined, triblock amphiphilic copolymer containing a hydrophilic poly(ethylene glycol) (PEG) block, a middle block poly(acrylic acid) (PAA) block, and a hydrophobic random copolymer of heptadecafluorodecyl methacrylate (HDFMA) and methyl methacrylate (MMA) was engineered using a combination of atom transfer radical polymerization (ATRP) and "click" coupling techniques as previously described [Fig. 13.1] [17]. The synthesis of the P(HDFMA-*co*-MMA)-*b*-PAA-*b*-PEG triblock copolymer is shown in Figure 13.1, and described in detail in our previous study [17]. The synthesized P($HDFMA_8$-*co*-MMA_{20})-*b*-PAA_{12}-*b*-PEG_{45} triblock amphiphilic copolymer was used to prepare PFP- and PFH-loaded nanodroplets. Briefly, the copolymers were dissolved in tetrahydrofuran (THF) (0.2% w/v) and cooled down to 0 $^{\circ}$C before the addition of PFP (2% v/v) or PFH (2% v/v) while vigorously stirring in the copolymer-perfluorocarbon mixture. An equal amount of purified water was drop-wise added to this solution mixture to initiate micelle formation and the mixture was stirred for 1h in an ice bath. The micelles solution was transferred into a dialysis bag (MWCO of 1 KDa, Spectrum, Rancho Dominguez, CA, US) and dialyzed against ice-cold MES solution of pH 5.5 during overnight to remove the THF and get a milky solution of non-cross-linked PFP-loaded nanodroplets and non-cross-linked PFH-loaded nanodroplets. Each nanodroplet in the milky solution was transferred to a round bottom flask and mixed with the 2,2`-(ethylenedioxy)-bis(ethylamine) cross-linker, which reacts with the carboxyl groups of the central PAA block in the copolymer via NHS/EDC

coupling chemistry forming cross-linked nanodroplets with a flexible polymer shell. Shell cross-linked nanodroplets were dialyzed against ice-cold water for 12 hours to remove unreacted cross-linker debris with byproducts of the reaction.

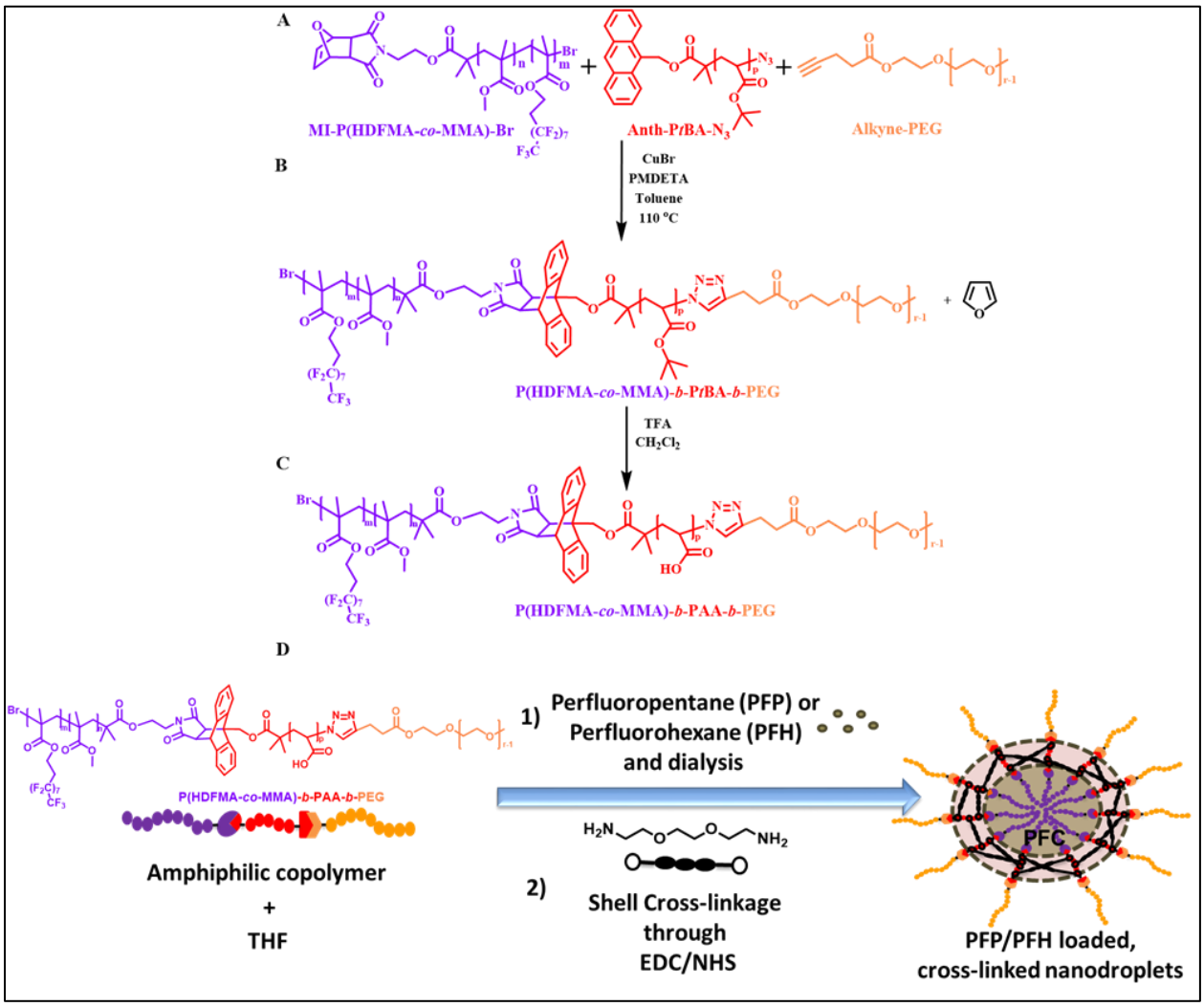

Figure 13.1. Formulation of the triblock fluorinated amphiphilic copolymer and nanodroplet preparation [17]. **(A)** Chemical structure of each block in the triblock copolymer. **(B)** One-pot "click" reaction forms P(HDFMA-*co*-MMA)-*b*-P*t*BA-*b*-PEG. **(C)** Hydrolysis of the copolymer gives P(HDFMA-*co*-MMA)-*b*-PAA-*b*-PEG. **(D)** The process of PFC encapsulation into nanodroplets.

Concentration and size distribution of the nanodroplets were measured using Nanoparticle Tracking Analysis (NTA). Briefly, the NanoSight™ LM10 (Malvern Instruments, Amesbury, UK), equipped with a temperature-controlled 405 nm laser module, high sensitivity

scientific Complementary Metal–Oxide–Semiconductor (sCMOS) camera (Hamamatsu, Orca, Hamamatsu City, Japan), and a syringe pump was used for the collection of NTA data. Upon diluting the nanodroplet solution to the appropriate particle concentration with deionized water (Thermo Scientific, GenPure, Waltham, MA, US), image capture and analysis was carried out using the NTA software (Version 3.0, Build 0066) at 37 °C. The samples were measured by capturing 60s videos (5 videos per each sample). Based on these videos, nanodroplet concentration was plotted as a function of droplet size, with the error bars representing the standard deviation of the repeat measurements of each sample. The mean size and standard deviation values obtained by the NTA software correspond to arithmetic values calculated with the sizes of all particles analyzed for each sample (n=5).

13.2.3 Preparation of Tissue Phantoms

Agarose phantoms were used to provide a well-controlled viscoelastic medium for this study. Tissue phantoms containing 1% agarose w/v were prepared by slowly mixing agarose powder (Agarose Type VII; Sigma-Aldrich, St. Louis, MO, USA) into saline solution (0.9% sodium chloride; Hospira, Lake Forest, Illinois, USA) heated to boiling temperature. The solution was stirred on a hot plate until the gel turned completely transparent and then allowed to boil for ten minutes. After boiling, solutions were allowed to cool and were degassed under a partial vacuum (~20 kPa, absolute) for 30 minutes. After degassing, phantoms containing nanodroplets were prepared by slowly adding the nanodroplets (2.0×10^8 particles/ml) into the agarose solution while stirring (). The agarose mixtures were poured into rectangular polycarbonate holders with acoustic windows and placed in a refrigerator at 4°C to allow the

solution to solidify, forming tissue phantoms with embedded PFP nanodroplets, PFH nanodroplets, and without nanodroplets (control).

13.2.4 Histotripsy Pulse Generation

Histotripsy pulses were generated at four ultrasound frequencies (345 kHz, 500 kHz, 1.5 MHz, and 3 MHz) using three custom-built histotripsy transducers. The 345 kHz pulses were generated by a twenty-element array transducer with a geometric focus of 150 mm, an aperture size of 272 mm, and an effective f-number of 0.55. The 1.5 MHz pulses were generated by a six-element array transducer with a geometric focus of 55 mm, an aperture of 79 mm in the elevational direction and 69 mm in the lateral direction, and effective f-numbers of 0.7 and 0.8 in the elevational and lateral directions, respectively. The 500 kHz and 3 MHz pulses were generated by a dual frequency array transducer that consisted of twelve 500-kHz elements and seven 3-MHz elements. For the 500 kHz elements, the geometric focus was 40 mm, the aperture size was 71 mm, and the effective f-number was 0.56. For the 3 MHz elements, the geometric focus was 40 mm, the aperture size was 80 mm, and the effective f-number was 0.5. The design of the dual frequency transducer has been described in detail in a previous study [21].

To compare the NMH cavitation threshold with the histotripsy intrinsic threshold, short pulses with a single dominant negative pressure half-cycle were applied to the tissue phantoms with and without nanodroplets. To generate a short therapy pulse, a custom high-voltage pulser developed in-house was used to drive the transducers. The pulser was connected to a field-programmable gate array (FPGA) board (Altera DE0-Nano Terasic Technology, Dover, DE, USA) specifically programmed for histotripsy therapy pulsing. This setup allowed the transducers to output short pulses of less than two cycles. A fiber-optic probe hydrophone built

in-house [22] was used to measure the acoustic output pressure of the transducers. At higher pressure levels (p- > 23 MPa), the acoustic output could not be directly measured due to cavitation at the fiber tip. These pressures were estimated by a summation of the output focal p-values from individual transducer elements. This approximation assumes minimal nonlinear distortion of the waveform occurs within the focal region. In a previous study [6], this estimated p- was found to be accurate within 15% compared to direct focal pressure measurements in water and in a medium (1,3 butanediol) with a higher cavitation threshold. Sample acoustic waveforms produced by the four frequency transducers are shown in Figure13.2(A).

13.2.5 Optical Imaging and Image Processing

High speed optical imaging was used to capture images of the focal zone after the propagation of each pulse through the focus using two high speed cameras [Fig.13.2(B)]. For experiments with the 345 kHz and 1.5 MHz transducers, a high-speed, 1 megapixel CCD camera (Phantom V210, Vision Research, Wayne, NJ, USA) was aligned with the transducer and backlit by a continuous white-light source. The camera was focused using a macro-bellows lens (Tominon, Kyocera), giving the captured images a resolution of approximately 5.9 μm per pixel and 3.4 μm per pixel for 345 kHz and 1.5 MHz, respectively. For experiments with the 500 kHz and 3 MHz dual frequency transducer, a digital, 1.3-megapixel CCD camera (PN: FL3-U3-13Y3M-C, Flea® 3, PointGrey, Richmond, BC, Canada) was positioned perpendicularly to the dual-frequency array transducer facing one of the transducer's optical windows. A Nikon 4X objective was attached to the camera with extension tubes to magnify the image plane, giving the captured images a resolution of approximately 2.5 μm per pixel. A pulsed white-light LED was placed on the diametrically-opposed optical window of the dual-frequency array transducer,

which provided back-lit illumination. The cameras were triggered to record one image for each applied pulse. After acquisition, shadowgraph images were converted from grayscale to binary by an intensity threshold determined by the background intensity using image processing software (MATLAB, The Mathworks, Natick, MA, USA), as described in a previous study [6]. Bubbles were indicated as any black regions >5 pixels. By this criterion, the minimum resolvable bubble radius was 14.75 μm, 6.25 μm, 8.5 μm, and 6.25 μm for the 345 kHz, 500 kHz, 1.5 MHz, and 3 MHz transducers, respectively.

13.2.6 Passive Cavitation Detection (PCD)

In addition to high speed imaging, an acoustic method was used to identify cavitation in the focal zone for cavitation threshold experiments. For each experiment, one of the transducer's therapy elements was also used for PCD to detect the presence of cavitation in the focal region [Fig.13.2(B)]. The PCD signal was connected to an oscilloscope (LT372; Lecroy, Chestnut Ridge, NY, USA) with the time window selected to record the backscattering of the therapy pulse from cavitation bubbles [6, 7, 21]. To determine whether cavitation occurred during a pulse, the signal generated by backscattering of the incident pulse from the focus was analyzed following the method used in previous studies [6, 7]. A significant fraction of the incident wave energy is scattered when a cavitation bubble expands, greatly increasing the backscattered pressure amplitude received by the PCD. This signal appeared on the PCD at the time point corresponding to two times the time of flight for the focal length of the respective transducers. The integrated frequency power spectrum (S_{PCD}) of the backscatter signal was used as a measure of whether cavitation occurred according to the method previously described by Maxwell *et al* [6].

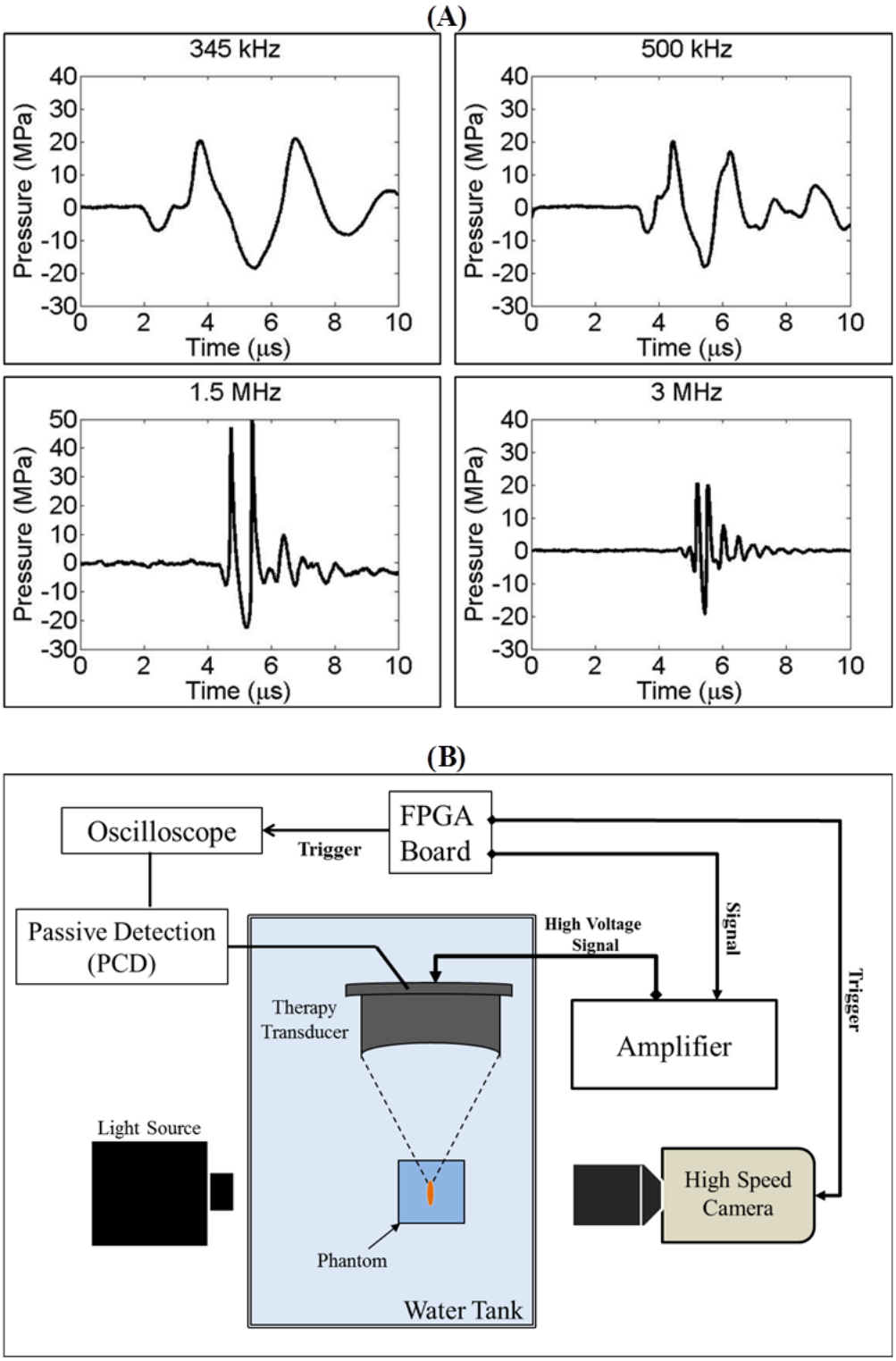

Figure 13.2. (A) Example waveforms for 2-cycle histotripsy pulses generated by custom-built 345 kHz, 500 kHz, 1.5 MHz, and 3 MHz transducers. (B) Experimental set-up showing the focus of the histotripsy transducers aligned inside tissue phantoms containing PFP, PFH, or no nanodroplets. Cavitation was monitored using high speed optical imaging and passive cavitation detection using one of the therapy elements.

13.2.7 NMH Cavitation Threshold

For cavitation threshold experiments, 100 pulses were applied inside each sample at each pressure level at a pulse repetition frequency (PRF) of 0.5 Hz. The PRF was kept low to minimize the possibility that cavitation from one pulse would change the probability of cavitation on a subsequent pulse. In a previous study, it was demonstrated that cavitation during a pulse increased the likelihood of cavitation on a following pulse for PRFs > 1 Hz, but this effect was not observed for PRFs < 1 Hz [6]. In addition to this low PRF, the focus was translated for each pulse by 1 mm transverse to the acoustic propagation direction in a 10 × 10 grid in order to minimize the effects of cavitation damage to the nanodroplets or tissue phantoms from altering the probability of cavitation. For each pulse, cavitation was monitored using both high speed imaging and PCD, and the fraction of total pulses (out of 100) for which cavitation was detected was determined as the cavitation probability.

The probability of observing cavitation followed a sigmoid function, given by

$$P(p_-) = \frac{1}{2} + erf\left(\frac{p_- - p_t}{\sqrt{2\sigma^2}}\right) \quad (\mathbf{E13.1})$$

where *erf* is the error function, p_t is the negative pressure at which the probability p_{cav}=0.5, σ is a variable related to the width of the transition between p_{cav}=0 and p_{cav}=1, with ± σ giving the difference in pressure from about p_{cav}=0.15 to p_{cav}=0.85 for the fit [6]. The cavitation threshold for each sample, p_t, is defined as the p- corresponding to p_{cav}=0.5 as calculated by the curve fit. Curve fitting for all data sets was performed using an OriginLab curve fitting program (OriginPro 9.1; OriginLab Corporation, Northampton, MA, USA). The fit curves for all samples were analyzed statistically to determine whether the differences in the values of p_t were significantly different from each other. The standard errors for p_t were estimated by a covariance

matrix using the delta method [22]. The curves were compared using a two-sample t-test with statistic $t\left(p_{int1}-p_{int2},\sqrt{SE_1^2+SE_2^2}\right)$ at a 95% confidence interval. Results were considered statistically significant for $p<0.05$. Note that the standard error does not include the uncertainty in absolute pressure from the hydrophone measurement, only the uncertainty in the fit, because the values p_t are relative. A sample size of 3 tissue phantoms was used for each experimental condition (i.e. PFP nanodroplets, PFH nanodroplets, or no nanodroplets).

13.2.8 NMH Multi-pulse Sustainability

To test the hypothesis that PFH nanodroplets will remain sustainable cavitation nuclei over multiple pulses while PFP nanodroplets will be destroyed during the first few pulses, 1000 ultrasound pulses were applied to a single focal region in tissue phantoms containing PFP and PFH nanodroplets at a PRF of 1 Hz and peak negative pressures of 11.8 MPa (345 kHz), 12.6 MPa (500 kHz), 14.3 MPa (1.5 MHz), and 15.6 MPa (3 MHz). The PRF in this study was kept low (1 Hz) to minimize the contributions of residual nuclei from a previous pulse from effecting cavitation generation on a subsequent pulse in order to determine if PFP and PFH nanodroplets continue to function as viable cavitation nuclei after the first few pulses or if the nanodroplets are destroyed in the cavitation process. Furthermore, a PRF of 1 Hz was also chosen as previous work has shown an increase in ablation efficiency for 1 Hz treatments in comparison to higher PRF treatments that rely on residual nuclei from previous pulses to maintain the cavitation bubble cloud [20, 23]. Cavitation was monitored using high speed optical imaging, and the number of bubbles produced by each pulse was compared for 1000 histotripsy pulses in each sample.

13.3 Results

13.3.1 Nanodroplet Characterization

In this study, we aimed to encapsulate PFH into a P(HDFMA-*co*-MMA)-*b*-PAA-*b*-PEG fluorinated copolymer synthesized in-house in order to compare the cavitation ability of PFH-loaded nanodroplets with PFP-loaded nanodroplets. In our previous study, we demonstrated that PFP can be encapsulated in the fluorinated copolymer, forming nanodroplets containing an elastic shell with an average size of ~100-400 nm [17]. In contrast to PFP, the solubility of PFH is limited in most common polar solvents as well as water. Moreover, when PFH is added to any of these solvents, it is not dissolved and leads to phase-separation from the solvent. In this study, we hypothesized that PFH could be homed with the same fluorinated copolymer formulation of P(HDFMA-*co*-MMA)-*b*-P*t*BA-*b*-PEG in order to form nanodroplets with similar size and characteristics to the PFP droplets synthesized in our previous study [17]. Results demonstrated that both PFP and PFH encapsulated into stable nanodroplets in the desired size range (100-600 nm). NTA size analysis showed similar characteristics for the PFP and PFH droplets [Fig.13.3]. PFP-loaded nanodroplets size ranged from 100-450 nm with the major peak <300 nm. The size distribution of PFH-loaded nanodroplets was slightly larger than the PFP-loaded ones, ranging from 00-600 nm. Three additional high-intense peaks in the range of 200-300 nm, 300-450 nm, and 450-600 nm were observed in the large size portion of the PFH nanodroplet size plot [Fig.13.3]. The larger size of the PFH-loaded nanodroplets is possibly due to the miscibility character differences between PFP and PFH in the THF/copolymer mixture. For example, PFP was observed to homogenously dispense in the THF/copolymer mixture in the beginning of particle preparation, whereas PFH remained separate from the mixture on the bottom of the round-bottom flask. This energetically favorable phase separation was broken by adding water in

drop-wise to trigger the micellization process of the amphiphilic copolymer under vigorous stirring. This strategy allowed for the unmixed PFH in the mixture to be made miscible in the aqua system due to the fluorinated-hydrophobic and hydrophilic polymer contents of the amphiphilic copolymer. Both types of droplets were dispersed throughout the medium, and neither droplet type was observed to aggregate together due to the amphiphilic character of the triblock copolymer that stabilized the perfluorocarbons in the core of the nanodroplets as well as enhanced the solubility of the particles with the contribution of hydrophilic PEG corona. Nanodroplet concentration and size characterization demonstrated similar size distributions for the PFP and PFH nanodroplets [Fig.13.3]. The error bars on the size distribution plots represent the standard deviation of the repeat measurements of each sample. The mean size and standard deviation values obtained by the NTA software correspond to arithmetic values calculated with the sizes of all particles analyzed for each sample (n=5). Results from all samples demonstrated an average size of 177.9±1.9 nm and 233.9±3.9 nm for PFP and PFH nanodroplets, respectively.

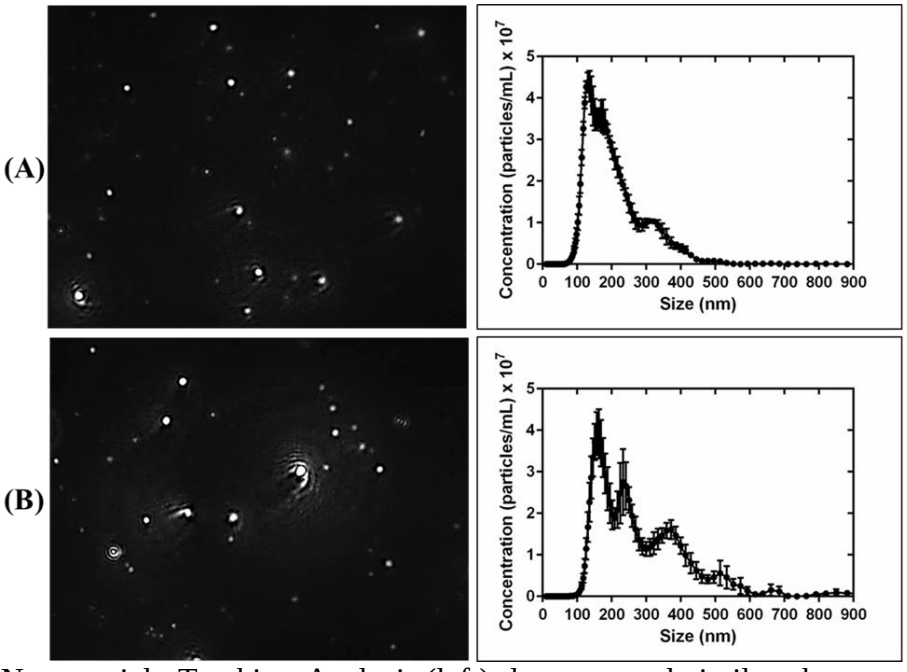

Figure 13.3. Nanoparticle Tracking Analysis (left) demonstrated similar characteristics for (A) PFP and (B) PFH nanodroplets. Size distribution plots (right) show the average size of the droplets was 177.9±1.9 nm and 233.9±3.9 nm for PFP and PFH, respectively.

13.3.2 NMH Cavitation Threshold

To investigate the effects of nanodroplet composition on the NMH threshold, histotripsy pulses were applied to tissue-mimicking agarose phantoms with PFP nanodroplets, PFH nanodroplets, and no nanodroplets using the 345 kHz, 500 kHz, 1.5 MHz, and 3 MHz histotripsy transducers. For all experimental conditions, cavitation bubbles were observed on the high-speed camera in an increasingly larger area with increasing pressure once a certain negative pressure was exceeded, with close agreement between optical imaging and PCD detection methods [Fig.13.4], as seen in previous studies [6, 7]. Plotting the probability of cavitation as a function of peak negative pressure demonstrated a significant decrease in the cavitation threshold with both PFP and PFH nanodroplets compared to controls at all frequencies [Fig.13.5]. Additionally, results showed a slight increase in the nanodroplet cavitation threshold for PFH nanodroplets compared to PFP nanodroplets [Fig.13.5]. Cavitation threshold results for all experimental conditions are listed in Table 13.1. Comparing the threshold results for phantoms containing PFH nanodroplets with control phantoms demonstrated that the cavitation threshold was decreased by 14.4 MPa, 15 MPa, 13.7 MPa, and 11.9 MPa at 345 kHz, 500 kHz, 1.5 MHz, and 3 MHz, respectively [Fig.13.6]. When comparing phantoms containing PFP and PFH nanodroplets [Fig.13.6], a decrease of 3 MPa, 1.3 MPa, 2.5 MPa, and 1.7 MPa was observed for PFP phantoms at 345 kHz, 500 kHz, 1.5 MHz, and 3 MHz, respectively [Fig.13.6]. For all experimental conditions, the cavitation threshold was observed to decrease at lower frequency, as has been observed in previous studies [Fig.13.6] [7, 16].

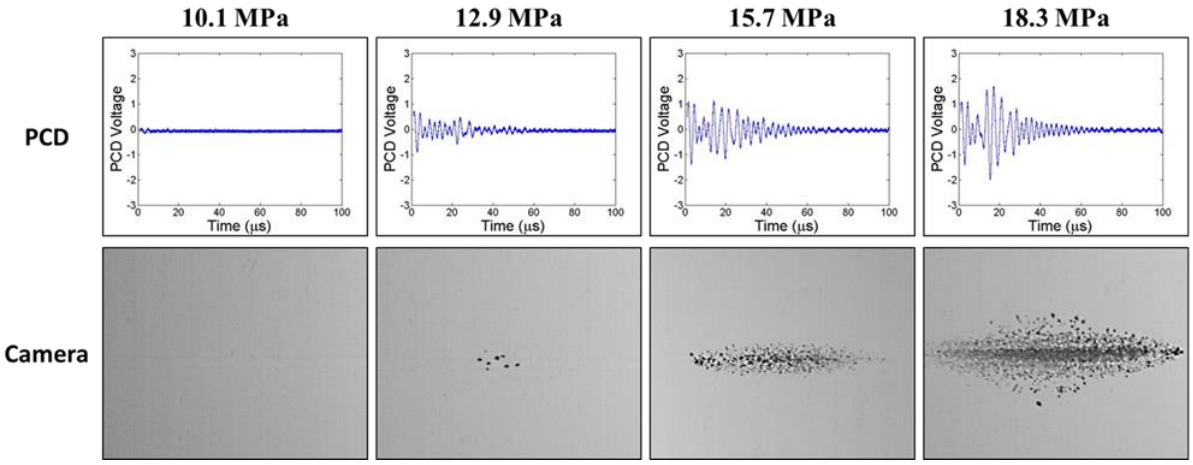

Figure 13.4. Sample PCD signals (top) and high speed optical imaging (bottom) were used for cavitation detection for cavitation threshold experiments. Results showed good agreement between the two methods. Representative images shown above are from 1.5 MHz histotripsy pulses applied to tissue phantoms containing PFH nanodroplets.

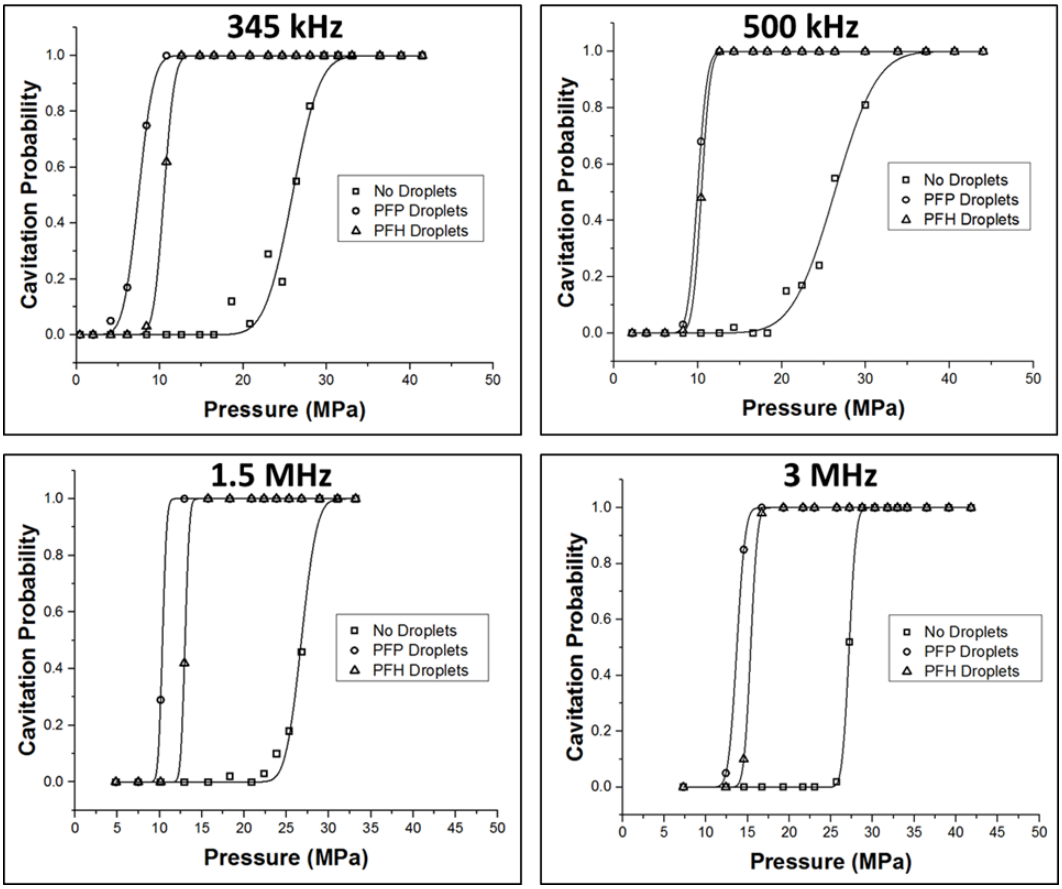

Figure 13.5. Plots show sample probability curves for tissue phantoms containing PFP nanodroplets, PFH nanodroplets, and no nanodroplets at 345 kHz, 500 kHz, 1.5 MHz, and 3 MHz. At all frequencies, results showed a significant decrease in the cavitation threshold with both PFP and PFH nanodroplets compared to controls. Results also showed a slight increase in the nanodroplet cavitation threshold for PFH nanodroplets compared to PFP nanodroplets.

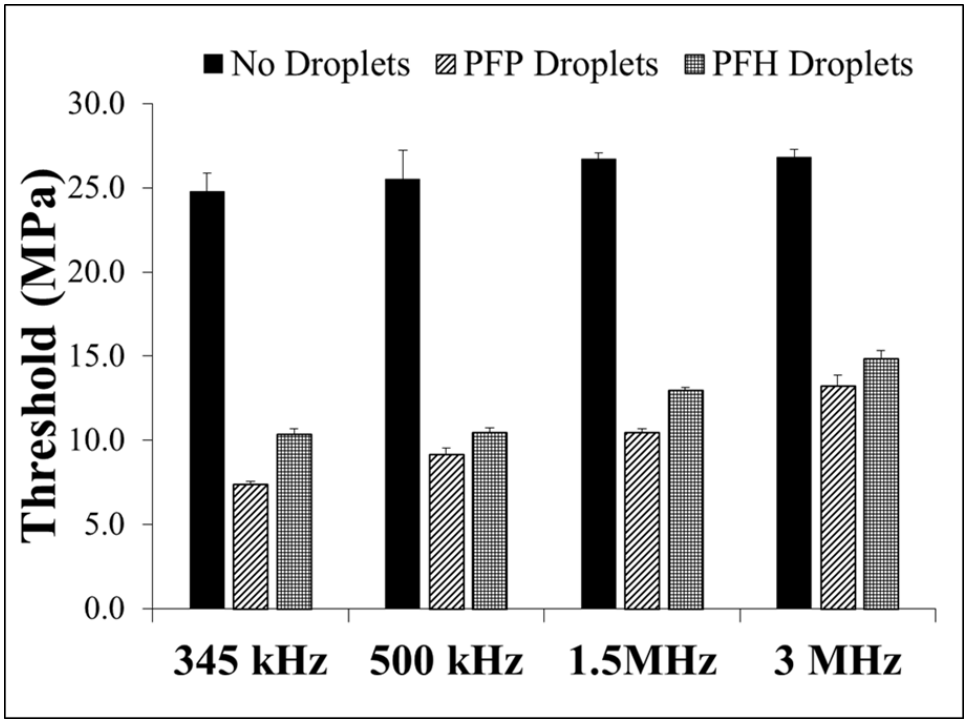

Figure 13.6. Bar plots show the complete cavitation threshold results for tissue phantoms containing PFP nanodroplets, PFH nanodroplets, and no nanodroplets. All differences in the cavitation threshold between samples were statistically significant ($p<0.05$).

Table 13.1 Table shows the values for the peak negative pressure, p_t, at which the fit curve set $P_{cav} = 0.5$ for each sample as well as the mean values for p_t and σ. A Student's t-test showed all differences in p_{t_mean} between samples were statistically significant ($p<0.05$).

Frequency	Material	P_t (1)	P_t (2)	P_t (3)	P_t (mean)	σ(mean)
345 kHz	No Droplets	25.9	23.7	24.7	24.8	2.0
	PFP Droplets	7.3	7.4	7.4	7.4	1.4
	PFH Droplets	10.5	10.1	10.6	10.4	0.9
500 kHz	No Droplets	23.5	26.3	26.7	25.5	1.8
	PFP Droplets	9.4	10.0	8.2	9.2	0.8
	PFH Droplets	10.4	10.8	10.3	10.5	0.8
1.5 kHz	No Droplets	26.8	27.0	26.3	26.7	1.0
	PFP Droplets	10.3	10.7	10.5	10.5	0.4
	PFH Droplets	12.8	13.0	13.1	13.0	0.3
3 MHz	No Droplets	26.9	27.2	26.3	26.8	0.9
	PFP Droplets	13.1	12.9	13.7	13.2	0.6
	PFH Droplets	14.6	14.6	15.4	14.9	0.4

13.3.3 NMH Multi-pulse Sustainability

To compare the ability of nanodroplets to act as sustainable cavitation nuclei over multiple pulses, 1000 histotripsy pulses were applied to a single focal region in phantoms containing PFP and PFH nanodroplets at a PRF of 1 Hz. Results demonstrated that a bubble cloud consisting of many bubbles was observed after the first pulse for both types of droplets [Fig. 13.7]. However, the bubble cloud generated in PFH phantoms was a more well-defined bubble cloud, similar to those previously observed for histotripsy above the intrinsic threshold [7, 24]. At all frequencies, over all 1,000 pulses, a dense bubble cloud was produced in PFH phantoms, with the bubbles more tightly confined inside the focal region and no significant change in the number of bubbles inside the cloud [Fig. 13.7, Fig.13.8]. In comparison, after the first pulse, the bubble cloud generated in the PFP phantom is sparsely populated [Fig. 13.7, Fig.13.8]. At all frequencies, the number of bubbles observed inside PFP phantoms significantly decreased with increasing number of pulses, and bubbles distinguished after ~5-50 pulses. At a higher frequency, the bubble cloud distinguished with fewer number of pulses. For example, no bubbles were observed after ~50 pulses in PFP phantoms exposed to 500 kHz (p-=12.6 MPa) pulses and after ~5 pulses exposed to 3 MHz (p-=15.6 MPa) pulses.

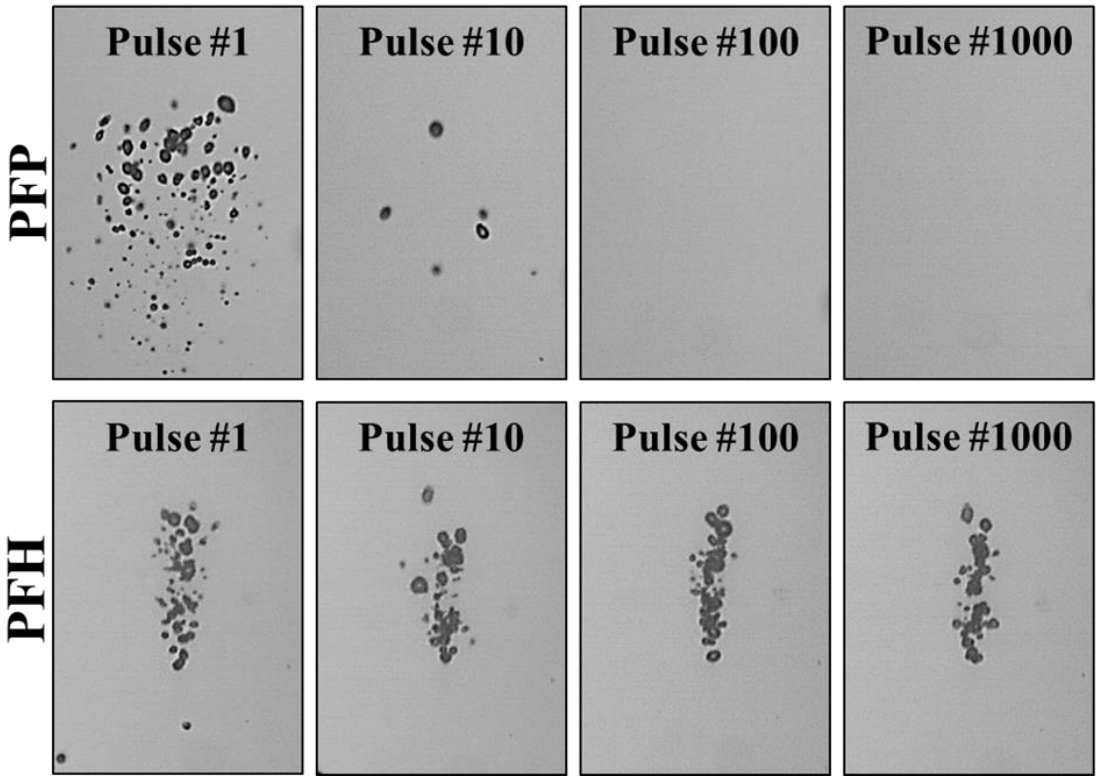

Figure 13.7. Optical images show NMH bubbles produced by 500 kHz (p-=12.6 MPa) pulses at a single focal point in tissue phantoms containing PFP and PFH nanodroplets at a PRF of 1 Hz.

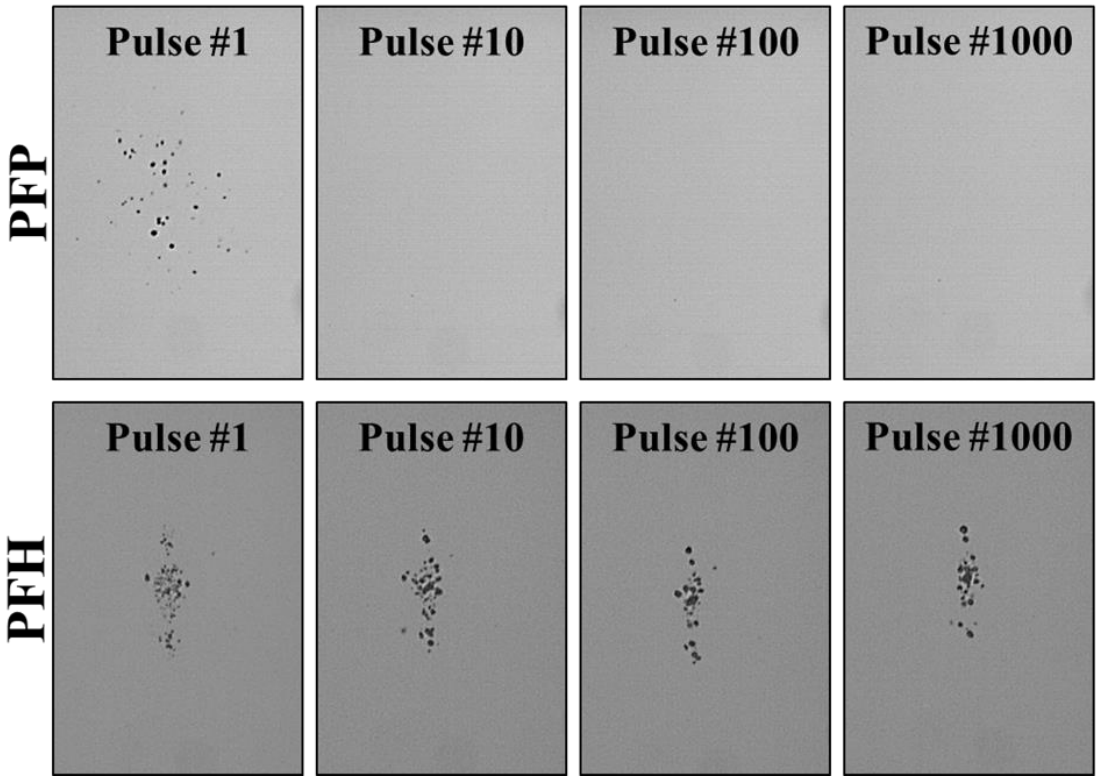

Figure 13.8. Optical images show NMH bubbles produced by 3 MHz (p-=15.6 MPa) pulses at a single focal point in tissue phantoms containing PFP and PFH nanodroplets at a PRF of 1 Hz.

13.4 Discussion

In this chapter, the effects of droplet composition on NMH therapy were investigated using perfluoropentane (boiling point~29°C, surface tension~9.5 mN/m) and perfluorohexane (boiling point~56°, surface tension~1.2 mN/m) droplets. In the first part of this chapter, PFP and PFH droplets were synthesized using a previous developed method [17]. The results from the nanodroplet characterization suggest that the droplet preparation method described by Yuksel Durmaz *et al* can be used to create nanodroplets with similar surface characteristics within the media while the composition of the encapsulated perfluorocarbon can be modulated as desired [17]. The design of the triblock amphiphilic copolymer acts to increase the particle's solubility in aqueous environments due the hydrophilic character of the outer PEG block while also improving hemocompatibility (i.e. no protein adsorption on the particles, no macrophage recognition, and minimum interaction with blood cells during blood circulation) [17, 25, 26]. The results of this study suggest that the PFC inside the nanodroplets can be easily modified to take advantage of different boiling point perfluorocarbons without losing the benefits of the functionalized polymer shell. Being able to independently alter the droplet parameters without affecting the engineered nanodroplet particle offers significant advantages for optimizing NMH therapy, allowing for the development of droplets with varying boiling points that maintain the same targeting behavior for NMH tumor therapy. This desired targeting behavior includes having nanodroplets in the optimal size range for passive targeting through the leaky tumor vasculature (100-800 nm) as well as having the functionalized particles for active targeting to tumor cells or other diseased lesions using targeting ligands [27, 28].

In the second part of this chapter, the effects droplet composition on the histotripsy cavitation threshold were investigated, with resulting showing a significant decrease in the cavitation threshold for both types of nanodroplets compared to controls, with a slightly lower threshold observed for PFP phantoms, likely due to the decrease in surface tension for PFP. These results support our hypothesis that both PFP and PFH nanodroplets can be used to significantly reduce the pressure required to generate histotripsy bubbles for NMH therapy. At all frequencies tested, the NMH threshold for both types of droplets was significantly lower (>10 MPa decrease) than the histotripsy intrinsic threshold, while maintaining a steep threshold behavior. In fact, the σ_{mean} values calculated by the curve fit decreased (i.e. sharper threshold curve) for phantoms containing nanodroplets, with the lowest σ_{mean} values observed for phantoms containing PFH droplets [Table 13.1]. This distinct threshold behavior is promising for the development of NMH therapy in which the applied pressure must be chosen in the region above the NMH threshold but below the histotripsy intrinsic threshold to ensure cavitation is only generated in regions containing nanodroplets. The results of these threshold experiments suggest that both PFP and PFH nanodroplets could be used for NMH, with PFP droplets offering a slightly lower threshold (~1-3 MPa decrease). With everything else equal, one might expect a lower cavitation threshold for the larger PFH droplets (233.9±3.9 nm) compared to PFP droplets (177.9±1.9 nm). It is possible that the slight decrease in threshold for PFP droplets is due to the lower surface tension of PFP (9.5 mN/m) compared to PFH (1.2 mN/m), as previous work has demonstrated that the cavitation threshold is highly dependent upon the surface tension of the media when using the 1-2 cycle pulses used in this study [6, 7]. These results suggest that the nanodroplets may actually decrease the cavitation threshold by carrying a lower threshold medium, rather than each droplet acting as single cavitation nuclei as would be the case for an air

contrast agent. Based on this finding, the results of this work suggest that the NMH threshold can be selectively modulated by changing the droplet composition, with lower surface tension resulting in a decreased cavitation threshold. The finding that the NMH threshold can be finely tuned by changing droplet composition while maintaining the distinct threshold behavior is a significant benefit for the development of NMH therapy as well as for other nanodroplet applications such as selective drug delivery [29].

In the final part of this chapter, the effects of droplet composition on cavitation sustainability were investigated, with results showing that PFH nanodroplets were sustainable cavitation nuclei over multiple pulses, while PFP nanodroplets were destroyed during the initial pulses. This effect is most likely due to the re-condensing of PFH droplets into a liquid after the cavitation event occurs, due to the higher boiling point of the PFH droplets. The finding that PFH nanodroplets act as sustainable cavitation nuclei over multiple pulses, while PFP droplets are destroyed during the initial pulses, supports our hypothesis that using droplets with a higher boiling point is advantageous for NMH therapy. Results suggest that PFH droplets may re-condense into a liquid after the collapse of the cavitation bubble while the PFP bubbles are destroyed by the cavitation process (i.e. do not return to liquid form). These results suggest that higher boiling point droplets can be used to significantly reduce the nucleation threshold for generating cavitation bubbles over multiple pulses, allowing NMH therapy to be applied for multiple pulses until the targeted tissue is completely fractionated, even at low PRF. These results suggest that, due to the lower boiling point, PFP nanodroplets are only capable of reducing the cavitation threshold on the initial pulses, requiring cavitation on subsequent pulses to be generated from residual nuclei remaining in the focal region from previous pulses. The finding that higher boiling point droplets can serve as functional cavitation nuclei over multiple

pulses is therefore a major benefit for NMH therapy, as previous work has shown a decrease in ablation efficiency for higher PRF treatments that rely on residual nuclei from previous pulses to maintain the cavitation bubble cloud [20].

In addition to the finding that PFH droplets acted as sustainable cavitation nuclei over multiple pulses, it was also observed that the NMH bubble clouds produced from PFH droplets were more well-defined and densely populated compared to the sparse bubble clouds produced by the PFP droplets, even when comparing bubble clouds produced on the first pulse. The well confined, dense bubble clouds produced inside the PFH phantoms closely match the behavior of bubble clouds previously observed for histotripsy treatments above the intrinsic threshold, which have been shown to be efficient and precise at fractionating the target tissue [6, 7, 23, 24]. In contrast, the more sparse bubble clouds produced inside the PFP phantoms resemble bubble clouds generated at higher PRF or bubble clouds that rely upon residual nuclei in order to maintain cavitation, which have been shown to be less efficient at fractionating tissue while increasing collateral damage to surrounding tissue [20]. This observation suggests that NMH bubble clouds produced using PFH droplets will be more efficient at fractionating tissue and provide less collateral damage to surrounding tissue compared to NMH using PFP droplets.

13.5 Conclusion

In this chapter, the effects of droplet composition on NMH therapy were investigated using perfluoropentane (boiling point~29°C, surface tension~9.5 mN/m) and perfluorohexane (boiling point~56°, surface tension~1.2 mN/m) droplets. The results demonstrated a significant decrease in the cavitation threshold for both types of nanodroplets compared to controls, with a slightly lower threshold observed for PFP phantoms, likely due to the decrease in surface tension

for PFP. Results further demonstrated that PFH nanodroplets were sustainable cavitation nuclei over multiple pulses, while PFP nanodroplets were destroyed during the initial pulses. This effect is most likely due to the re-condensing of PFH droplets into a liquid after the cavitation event occurs, due to the higher boiling point of the PFH droplets. The results of this study suggest that NMH therapy can be significantly enhanced by modulating droplet composition in order to optimize the cavitation threshold (decrease droplet surface tension) and increase the multi-pulse sustainability (increase droplet boiling point). Overall, the results of this chapter provide significant insight in the role of droplet composition in NMH therapy and will provide a rational basis to specifically tailor droplet parameters in order to improve NMH tissue fractionation.

13.6 References

[1] J. E. Parsons, *et al.*, "Pulsed cavitational ultrasound therapy for controlled tissue homogenization," *Ultrasound Med Biol,* vol. 32, pp. 115-29, Jan 2006.

[2] W. W. Roberts, *et al.*, "Pulsed cavitational ultrasound: a noninvasive technology for controlled tissue ablation (histotripsy) in the rabbit kidney," *J Urol,* vol. 175, pp. 734-8, Feb 2006.

[3] Z. Xu, *et al.*, "Controlled ultrasound tissue erosion: the role of dynamic interaction between insonation and microbubble activity," *J Acoust Soc Am,* vol. 117, pp. 424-35, Jan 2005.

[4] J. E. Parsons, *et al.*, "Spatial variability in acoustic backscatter as an indicator of tissue homogenate production in pulsed cavitational ultrasound therapy," *IEEE Trans Ultrason Ferroelectr Freq Control,* vol. 54, pp. 576-90, Mar 2007.

[5] Z. Xu, *et al.*, "Investigation of intensity thresholds for ultrasound tissue erosion," *Ultrasound Med Biol,* vol. 31, pp. 1673-82, Dec 2005.

[6] A. D. Maxwell, *et al.*, "Probability of cavitation for single ultrasound pulses applied to tissues and tissue-mimicking materials," *Ultrasound Med Biol,* vol. 39, pp. 449-65, Mar 2013.

[7] E. Vlaisavljevich, *et al.*, "Effects of Ultrasound Frequency and Tissue Stiffness on the Histotripsy Intrinsic Threshold for Cavitation," *Ultrasound Med Biol,* 2015.

[8] T. L. Hall, *et al.*, "Histotripsy of rabbit renal tissue in vivo: temporal histologic trends," *J Endourol,* vol. 21, pp. 1159-66, Oct 2007.

[9] C. R. Hempel, *et al.*, "Histotripsy fractionation of prostate tissue: local effects and systemic response in a canine model," *J Urol,* vol. 185, pp. 1484-9, Apr 2011.

[10] A. D. Maxwell, *et al.*, "Noninvasive treatment of deep venous thrombosis using pulsed ultrasound cavitation therapy (histotripsy) in a porcine model," *J Vasc Interv Radiol,* vol. 22, pp. 369-77, Mar 2011.

[11] G. E. Owens, *et al.*, "Therapeutic ultrasound to noninvasively create intracardiac communications in an intact animal model," *Catheter Cardiovasc Interv,* vol. 77, pp. 580-8, Mar 1 2011.

[12] Z. Xu, *et al.*, "Noninvasive creation of an atrial septal defect by histotripsy in a canine model," *Circulation,* vol. 121, pp. 742-9, Feb 16 2010.

[13] N. R. Styn, *et al.*, "Histotripsy of VX-2 tumor implanted in a renal rabbit model," *J Endourol,* vol. 24, pp. 1145-50, Jul 2010.

[14] E. Vlaisavljevich, *et al.*, "Image-Guided Non-Invasive Ultrasound Liver Ablation Using Histotripsy: Feasibility Study in an In Vivo Porcine Model," *Ultrasound in medicine & biology,* vol. 39, pp. 1398-1409, 2013.

[15] E. Vlaisavljevich, *et al.*, "The Effects of Ultrasound Frequency on Nanodroplet-Mediated Histotripsy," *Ultrasound Med Biol,* 2015.

[16] E. Vlaisavljevich, *et al.*, "Nanodroplet-mediated histotripsy for image-guided targeted ultrasound cell ablation," *Theranostics,* vol. 3, pp. 851-64, 2013.

[17] Y. Yuksel Durmaz, *et al.*, "Development of nanodroplets for histotripsy-mediated cell ablation," *Mol Pharm,* vol. 11, pp. 3684-95, Oct 6 2014.

[18] M. L. Fabiilli, *et al.*, "The role of inertial cavitation in acoustic droplet vaporization," *IEEE Trans Ultrason Ferroelectr Freq Control,* vol. 56, pp. 1006-17, May 2009.

[19] T. Giesecke and K. Hynynen, "Ultrasound-mediated cavitation thresholds of liquid perfluorocarbon droplets in vitro," *Ultrasound Med Biol,* vol. 29, pp. 1359-65, Sep 2003.

[20] T. Y. Wang, *et al.*, "Imaging feedback of histotripsy treatments using ultrasound shear wave elastography," *Ultrasonics, Ferroelectrics and Frequency Control, IEEE Transactions on,* vol. 59, pp. 1167-1181, 2012.

[21] E. Vlaisavljevich, *et al.*, "Histotripsy-induced cavitation cloud initiation thresholds in tissues of different mechanical properties," *IEEE Trans Ultrason Ferroelectr Freq Control,* vol. 61, pp. 341-52, Feb 2014.

[22] D. W. Hosmer and S. Lemeshow, "Confidence interval estimation of interaction," *Epidemiology,* vol. 3, pp. 452-6, Sep 1992.

[23] K. W. Lin, *et al.*, "Histotripsy beyond the intrinsic cavitation threshold using very short ultrasound pulses: microtripsy," *IEEE Trans Ultrason Ferroelectr Freq Control,* vol. 61, pp. 251-65, Feb 2014.

[24] E. Vlaisavljevich, *et al.*, "Effects of Tissue Stiffness, Ultrasound Frequency, and Pressure on Histotripsy-induced Cavitation Bubble Behavior," *Phys Med Biol,* 2015.

[25] M. A. Dobrovolskaia, *et al.*, "Preclinical studies to understand nanoparticle interaction with the immune system and its potential effects on nanoparticle biodistribution," *Mol Pharm,* vol. 5, pp. 487-95, Jul-Aug 2008.

[26] D. Kim, *et al.*, "Interaction of PLGA nanoparticles with human blood constituents," *Colloids Surf B Biointerfaces,* vol. 40, pp. 83-91, Feb 10 2005.

[27] V. Torchilin, "Tumor delivery of macromolecular drugs based on the EPR effect," *Adv Drug Deliv Rev,* vol. 63, pp. 131-5, Mar 18 2011.

[28] L. L. Kusnetzky, *et al.*, "Acute mortality in hospitalized patients undergoing echocardiography with and without an ultrasound contrast agent: results in 18,671 consecutive studies," *J Am Coll Cardiol,* vol. 51, pp. 1704-6, Apr 29 2008.

[29] M. L. Fabiilli, *et al.*, "Acoustic droplet-hydrogel composites for spatial and temporal control of growth factor delivery and scaffold stiffness," *Acta Biomater,* vol. 9, pp. 7399-409, Jul 2013.

Chapter 14

The Role of Positive and Negative Pressure on Cavitation Nucleation in Nanodroplet-Mediated Histotripsy

A majority component of this chapter is excerpted from a manuscript that has been submitted to *Physics in Medicine and Biology*.

14.1 Introduction

Histotripsy is a noninvasive tissue ablation method that controllably fractionates soft tissue through cavitation generated by high pressure, short duration ultrasound pulses [1-3]. Histotripsy is currently being studied for many clinical applications where non-invasive tissue removal is desired including benign prostatic hyperplasia [4, 5], deep vein thrombosis [6, 7], congenital heart disease [8, 9], fetal interventions [10, 11], and cancer [12, 13]. Although histotripsy has shown promise for many clinical applications including tumor ablation, this approach is limited to applications in which the target tissue can be identified and imaged prior to treatment, which is often not feasible in cancer patients with many small tumor nodules and micro-metastases. Histotripsy also requires very high pressure (P–>20MPa), which may not achievable in some target tissue with limited acoustic access. Due to these limitations, our group has recently developed a targeted ablation approach combing polymer encapsulated nanodroplets with histotripsy [14, 15]. Nanodroplet-mediated histotripsy (NMH) takes advantage of the significantly reduced cavitation threshold of the nanodroplets, allowing for cavitation to be

selectively generated only in regions containing nanodroplets [14]. By synthesizing nanodroplets in a size range (~100-400 nm) in which they can diffuse through the leaky tumor vasculature and preferentially accumulate in the tumor, NMH has the potential for selective ablation of tumors [14, 15]. Previous work has demonstrated that NMH can be used to create well-defined ablation similar to histotripsy but at significantly lower pressure and has the potential to be used for simultaneous multi-focal ablation [14].

Understanding the physical mechanisms underlying the NMH cavitation process is essential for the development of NMH therapy. Previous studies on acoustic droplet vaporization (ADV) have shown that the ADV vaporization thresholds do not appear to follow the trends predicted by classical nucleation theory (CNT), which predicts that cavitation will be nucleated inside the droplets directly from the applied negative pressure (*p*-) [16-25]. These studies have led to the hypothesis that nanodroplet nucleation in ADV is caused by a different mechanism than what is predicted by CNT, such as droplet deformation, hydrodynamic cavitation, or acoustic heating [20, 21, 23]. However, these ADV studies used larger droplets, higher frequency ranges, and pulses with more acoustic cycles than those used in NMH therapy [14, 15, 20-23, 25-27]. In NMH, cavitation bubbles are generated from nanodroplets <600 nm in diameter using single-cycle ultrasound pulses at frequencies in the hundreds of kHz to low MHz range [14, 15, 26, 27]. The NMH cavitation thresholds measured in previous studies are significantly higher than the vaporization thresholds previously measured for ADV, with the trends appearing the follow the predictions of CNT [16-19, 24]. For example, previous work has demonstrated a significant reduction in the histotripsy cavitation threshold for both perfluoropentane (PFP) and perfluorohexane (PFH) nanodroplets exposed to single cycle histotripsy pulses [24, 26-28]. The NMH cavitation threshold decreases at lower frequencies [26, 27], in contrast to the increasing

ADV threshold with higher frequency observed using micron sized droplets [20-22, 25]. The NMH frequency dependence appears to agree with CNT, which predicts that lower frequency will decrease the cavitation threshold due to the longer duration of the applied *p*- and the larger focal zone at lower frequencies [16-19, 24, 26, 27]. Furthermore, a slight increase in the NMH cavitation threshold has been observed for PFH nanodroplets compared to PFP droplets due to the increase in the surface tension and boiling point of PFH, which also agrees with the predictions of CNT [16-19, 24, 26, 27].

Based on these previous studies, we hypothesize that NMH bubbles are generated after cavitation is nucleated inside the droplets directly from the incident *p*- (tensile portion of the incident wave), similar to histotripsy bubbles generated without nanodroplets when the negative pressure directly exceeds the intrinsic threshold [24, 28, 29]. In order to test this hypothesis, in this chapter we separate the effects of negative and positive pressure on NMH cavitation nucleation using near half-cycle ultrasound pulses with dominant negative (negative-polarity pulses) or positive (positive-polarity pulses) pressure phases. This paper reports the first study that separately investigates the effects of negative and positive pressure on the NMH cavitation process. The generation of near monopolar pulses was made possible by using a frequency compounding transducer recently developed in our lab, which aligns the positive or negative phases of multiple-frequency components while destructive interference occurs elsewhere in space and time, leading to pulses with a single dominant negative or positive pressure phase [29]. Tissue phantoms containing PFH nanodroplets and control phantoms without droplets were exposed to negative-polarity and positive-polarity pulses, and the NMH cavitation threshold was measured as a function of peak negative (P–) and peak positive (P+) pressure. Overall, the results

of this chapter will improve our understanding of the physical mechanisms underlying the NMH cavitation process, which is essential for the development of NMH therapy.

14.2 Methods

14.2.1 Nanodroplet Formulation and Characterization

Polymer encapsulated perfluorohexane (PFH) nanodroplets were used for this study based on recent work demonstrating that PFH droplets have many benefits for NMH therapy [27]. A PEG_{45}-*b*-PAA_{12}-*b*-P($HDFMA_8$-*co*-MMA_{20}) triblock copolymer was synthesized using a combination of atom transfer radical polymerization (ATRP) and "click" coupling techniques to prepare PFH-loaded nanodroplets, as described in detail in our previous study [15]. The copolymers were dissolved in tetrahydrofuran (THF) (0.2% w/v) and cooled down to 0^oC before the addition of PFH (2% v/v) while vigorously stirring the reaction mixture. An equal amount of water was slowly added to this solution mixture to trigger micelle formation and the mixture was stirred for 1h in an ice bath. The micelles solution was transferred into a dialysis bag (MWCO of 1 KDa) and dialyzed against ice-cold 2-(*N*-morpholino) ethanesulfonic acid (MES) solution of pH 5.5 for 12 hours to remove the THF and get a milky solution of non- cross-linked PFP-loaded nanodroplets. This milky solution was transferred to a round bottom flask and mixed with the 2,2`-(ethylenedioxy)-bis(ethylamine) cross-linker, which reacts with the central PAA block in the polymer backbone via NHS/EDC coupling chemistry forming cross-linked nanodroplets with a flexible polymer shell. Shell cross-linked nanodroplets were dialyzed against ice-cold water for 12 hours to remove the byproducts of the cross-linkage reaction.

Concentration and size distribution of the nanodroplets were measured using Nanoparticle Tracking Analysis (NTA). Briefly, the NanoSight™ LM10 (Malvern Instruments,

Amesbury, UK), equipped with a temperature-controlled 405 nm laser module, high sensitivity Scientific Complementary Metal–Oxide–Semiconductor (sCMOS) camera (Hamamatsu, Orca, Hamamatsu City, Japan), and a syringe pump was used for the collection of NTA data. Upon diluting the nanodroplet solution to the appropriate particle concentration with deionized (DI) water (Thermo Scientific, GenPure, Waltham, MA, US), image capture and analysis was carried out using the NTA software (Version 3.0, Build 0066, Malvern Instruments, Amesbury, UK) at 37°C. The samples were measured by capturing 60s videos (5 videos per each sample). Figure 14.1 is a representative plot showing the size distribution of the PFH nanodroplets. The error bars represent the standard deviation of the repeat measurements of each sample. The mean size and standard deviation values obtained by the NTA software correspond to arithmetic values calculated with the sizes of all particles analyzed for each sample (n=5). Results from all samples demonstrated that the average size of the nanodroplets (NDs) was 233±3.9 nm with 10% of NDs have a diameter ≤ 135.3±2.6 nm, 50% of the NDs have a diameter ≤ 192.7±5.3 nm, 90% of the NDs have a diameter ≤ 373.7±7.2 nm, and >99% of the NDs are ≤ 600 nm.

14.2.2 Preparation of Tissue Phantoms

Agarose phantoms were used to provide a well-controlled viscoelastic medium for this study. Tissue phantoms containing 1% agarose w/v were prepared by slowly mixing agarose powder (Agarose Type VII; Sigma-Aldrich, St. Louis, MO, USA) into saline solution (0.9% sodium chloride; Hospira, Lake Forest, Illinois, USA) heated to boiling temperature. The solution was stirred on a hot plate until the gel turned completely transparent and then allowed to boil for ten minutes. After boiling, solutions were allowed to cool and were degassed under a partial vacuum (~20 kPa, absolute) for 30 minutes. After degassing, phantoms containing

nanodroplets were prepared by slowly adding the nanodroplets (2.0×10^8 particles/ml) into the agarose solution while stirring. The agarose mixtures were poured into polycarbonate holders and placed in a refrigerator at 4°C to allow the solution to solidify, forming tissue phantoms with embedded PFH nanodroplets and without nanodroplets (control).

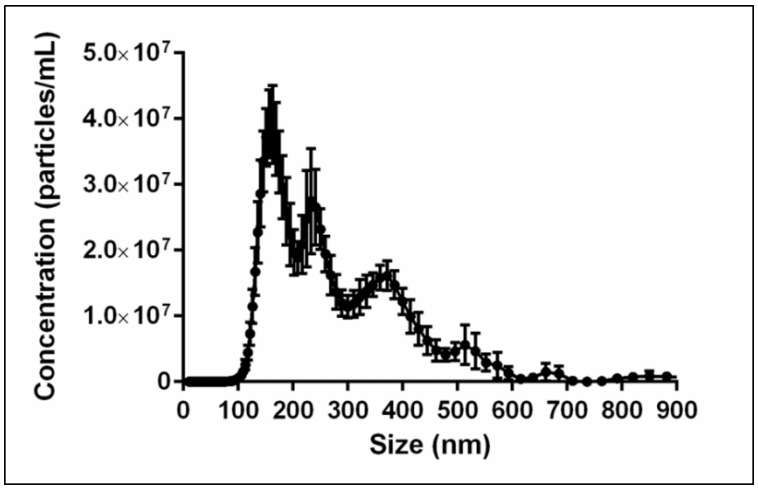

Figure 14.1. Nanoparticle Tracking Analysis demonstrated PFH nanodroplets had an average size of 233.9±3.9 nm.

14.2.3 Histotripsy Pulse Generation

Histotripsy pulses with dominant negative (negative-polarity pulse) and positive (positive-polarity pulse) pressure phases were generated used a frequency compounding transducer, adapted from a previous study [29]. The frequency-compounding transducer was composed of 12 elements (20 mm in diameter) with various resonant frequencies: 500 kHz (three elements), 1 MHz (two elements), 1.5 MHz (two elements), 2 MHz (two elements), and 3 MHz (three elements) [29]. The elements had a common geometric focus at 40 mm and were populated in a scaffold in a specific order to ensure that adjacent elements did not have the same frequency. This was done to reduce nonlinear propagation effects that occur when acoustic waves of the same frequency propagate closely in space and interfere constructively. Additionally, the frequency-compounding transducer has two diametrically opposed optical

windows to allow for optical imaging at the geometric focus. The design of the frequency compounding transducer has been described in detail in a previous study [29].

A custom high voltage pulser with 12 parallel channels was used to drive the frequency-compounding transducer. The pulser was connected to a field-programmable gated array (FPGA) development board (Altera DE1, Terasic Technology, Dover, DE, USA) specifically programmed for frequency compounding pulse generation. This setup allowed each element to individually output short pulses with only one large negative or positive pressure phase. The generation of negative-polarity pulses was achieved by adjusting the arrival times of individual frequency components to allow their principal negative phase peaks to arrive at the focus of the transducer concurrently [Fig. 14.2(A)]. In this situation, destructive interference occurs elsewhere in space and time, leading to a diminution of the peak positive pressure of the combined ultrasound pulse [Fig. 14.2(A)]. For the generation of positive-polarity pulses, the driver pulses for the individual elements were inverted, resulting in ultrasound pulses with a single principal positive phase from each element. The arrival times of individual frequency components were then adjusted to allow their principal positive phase peaks to arrive at the focus concurrently [Fig. 14.2(B)].

A fiber-optic probe hydrophone (FOPH) built in-house [30] was used to calibrate and measure the acoustic output of the frequency-compounding transducer, with example waveforms shown in Figure 14.2. For threshold experiments, the probability of cavitation was plotted as a function of both the peak negative (P–) and peak positive (P+) pressure as measured by the FOPH. In order to determine the peak pressure values for the negative and positive polarity pulses, 2D spatial pressure fields were directly measured using the FOPH in order to identify the locations corresponding to the P– and P+ in the focal region. The ratio of P– to P+ measured for

the negative-polarity pulses in this location was between 2.9-3.7 for the pressure ranges used in this study. For the positive-polarity pulses, the 2D spatial pressure fields measured by the FOPH demonstrated the location of the P– in the focal region occurred ~0.5 mm away from the geometric focus, while the location of the P+ remained near the geometric focus [Fig. 14.3]. This effect is due to the temporal alignment of the principle peak positive peaks of the individual frequency components at the geometric focus, which resulted in a near monopolar positive pulse at the geometric focus with two low-negative-pressure lobes outside of the focal region. The ratio of P+ to P– for the positive-polarity pulses was measured to be between 3.2-3.9 for the pressure ranges used in this study using the P+ and P– measured at the maximum locations in the field.

14.2.4 Optical Imaging and Image Processing

High speed optical imaging was used to capture images of the focal zone after the propagation of each pulse through the focus. A digital, 1.3-megapixel CCD camera (PN: FL3-U3-13Y3M-C, Flea® 3, PointGrey, Richmond, BC, Canada) was positioned perpendicularly to the frequency compounding transducer facing one of the transducer's optical windows [Fig. 14.4]. A Nikon 4X objective was attached to the camera with extension tubes to magnify the image plane, giving the captured images a resolution of approximately 3.6 μm per pixel. A pulsed white-light LED was placed on the diametrically-opposed optical window of the dual-frequency array transducer, which provided back-lit illumination. The cameras were triggered to record one image after the passage of each pulse at a time point approximately corresponding to the maximum bubble expansion. This time point was determined for the negative-polarity and positive-polarity pulses prior to experiments by changing the delay time on the camera to

identify the time corresponding to maximum bubble expansion, as described in previous studies [24, 26, 31]. After acquisition, shadowgraph images were converted from grayscale to binary by an intensity threshold determined by the background intensity using image processing software (MATLAB, The Mathworks, Natick, MA, USA), as described in a previous study [28]. Bubbles were indicated as any black regions greater than 5 pixels in diameter. By this criterion, the minimum resolvable bubble radius was 9 μm.

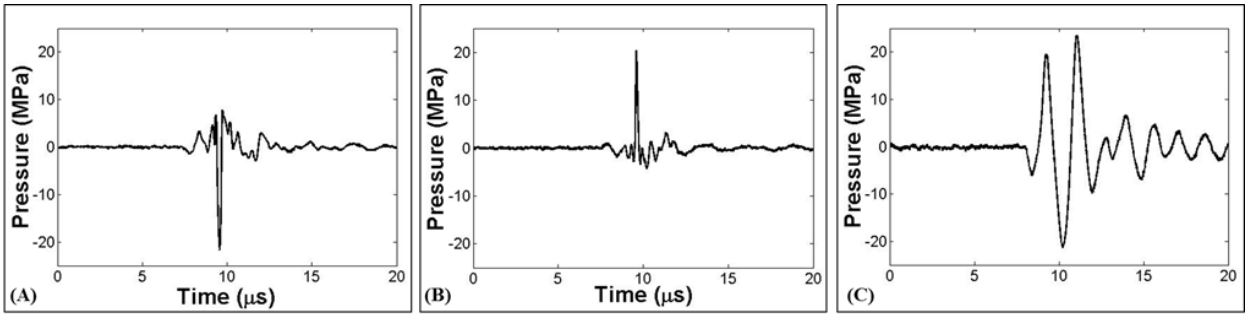

Figure 14.2. Example of (A) negative-polarity and (B) positive-polarity pulses produced by the frequency compounding transducer compared with a (C) dual-polarity pulse (500 kHz).

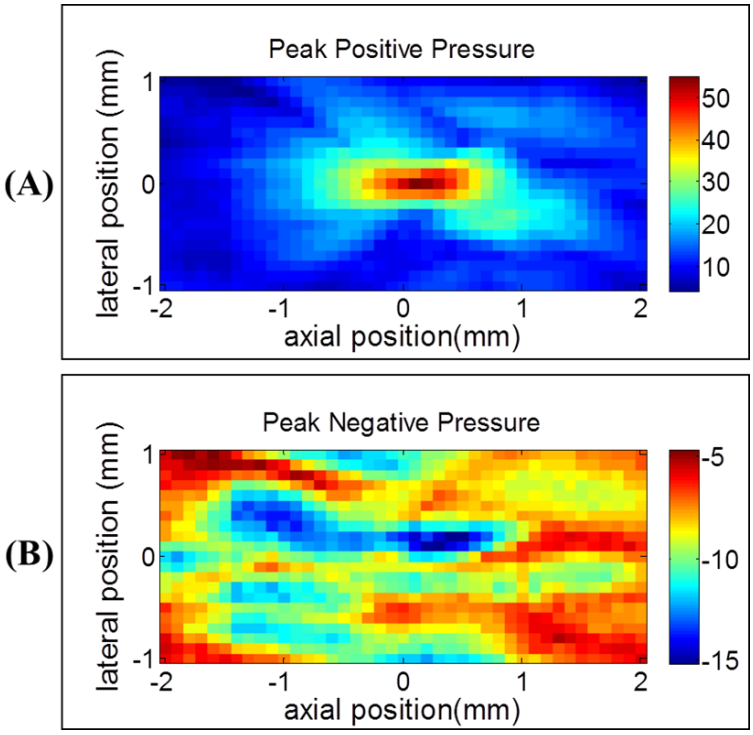

Figure 14.3. 2D spatial pressure fields were measured by the FOPH for a positive-polarity pulse. (A) Results demonstrated the location corresponding to the highest positive pressure was near the geometric focus. (B) The location corresponding to the highest negative pressure was ~0.5 mm away from the geometric focus in the axial direction.

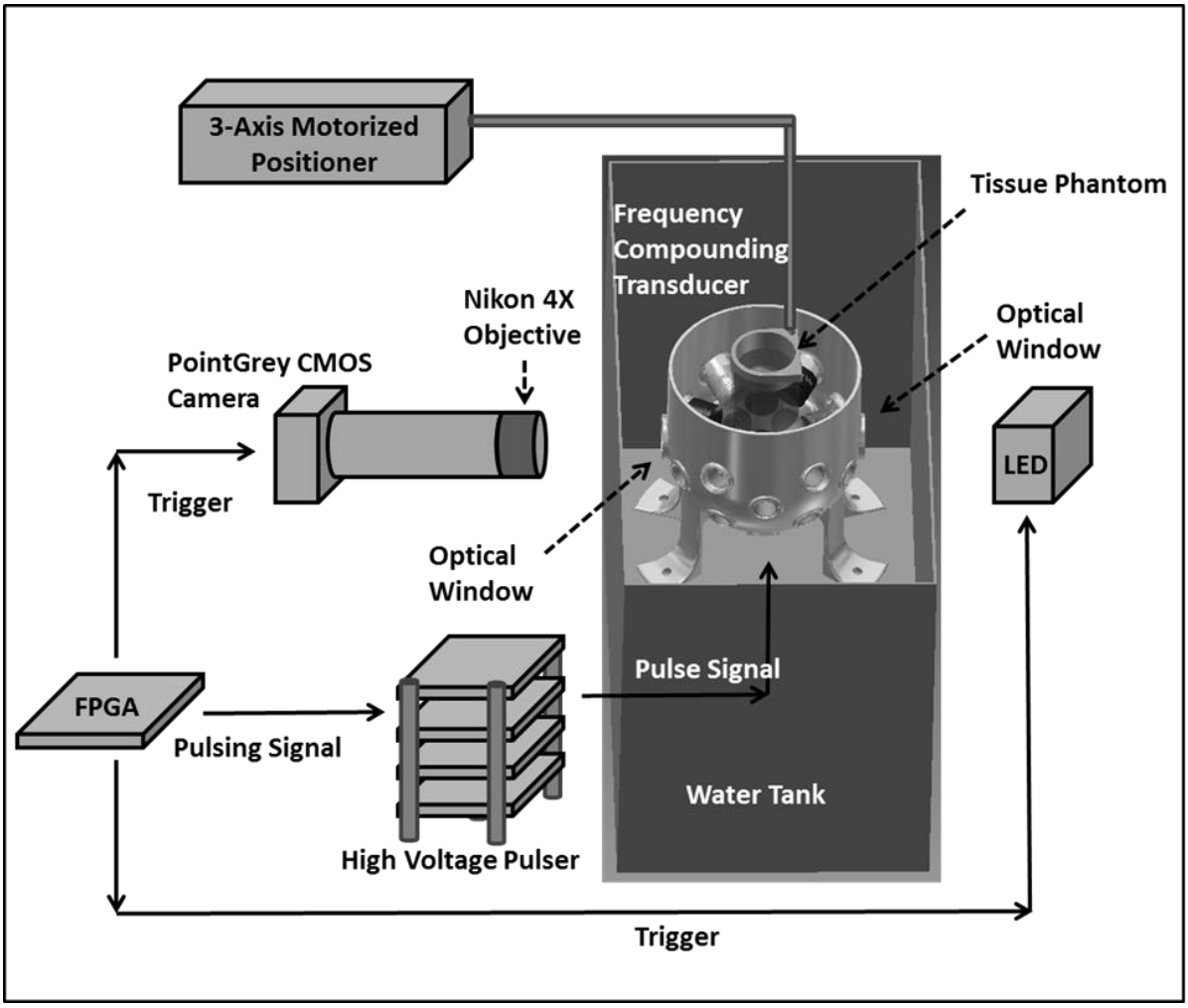

Figure 14.4. Tissue phantoms with and without PFH nanodroplets were placed at the focus of the frequency-compounding transducer [29] for cavitation threshold experiments. Cavitation was monitored using high-speed optical imaging through the transducer's optical windows.

14.2.5 NMH Cavitation Threshold

For cavitation threshold experiments, 100 pulses were applied inside each sample at each pressure level at a pulse repetition frequency (PRF) of 0.5 Hz. The PRF was kept low to minimize the possibility that cavitation from one pulse would change the probability of cavitation on a subsequent pulse. In a previous study, it was demonstrated that cavitation during a pulse increased the likelihood of cavitation on a following pulse for PRFs > 1 Hz, but this effect was not observed for PRFs < 1 Hz [28]. In addition to this low PRF, the focus was

translated for each pulse by 1 mm transverse to the acoustic propagation direction in a 10 × 10 grid in order to minimize the effects of cavitation damage to the nanodroplets or tissue phantoms from altering the probability of cavitation. For each pulse, cavitation was monitored using high speed imaging, and the fraction of total pulses (out of 100) for which cavitation was detected was determined as the cavitation probability.

The probability of observing cavitation followed a sigmoid function, given by

$$P(p) = \frac{1}{2} + erf\left(\frac{p - p_t}{\sqrt{2\sigma^2}}\right) \quad (\mathbf{E14.1})$$

where *erf* is the error function, p_t is the pressure at which the probability p_{cav}=0.5, σ is a variable related to the width of the transition between p_{cav}=0 and p_{cav}=1, with ± σ giving the difference in pressure from about p_{cav}=0.15 to p_{cav}=0.85 for the fit [28]. The cavitation threshold for each sample, p_t, is defined as the pressure, p, corresponding to p_{cav}=0.5 as calculated by the curve fit. Curve fitting for all data sets was performed using an OriginLab curve fitting program (OriginPro 9.1; OriginLab Corporation, Northampton, MA, USA). The fit curves for all samples were analyzed statistically to determine whether the differences in the values of p_t were significantly different from each other. The standard errors for p_t were estimated by a covariance matrix using the delta method [32]. The curves were compared using a two-sample t-test with statistic $t\left(p_{int1} - p_{int2}, \sqrt{SE_1^2 + SE_2^2}\right)$ at a 95% confidence interval. Results were considered statistically significant for $p<0.05$. Note that the standard error does not include the uncertainty in absolute pressure from the hydrophone measurement, only the uncertainty in the fit, because the values p_t are relative. For each sample, the curves were analyzed as a function of both positive and negative pressure, with the corresponding cavitation threshold values calculated as $p_t(+)$ and $p_t(-)$, respectively. A sample size of 3 tissue phantoms was used for each experimental

condition (i.e. phantoms containing PFH nanodroplets or no nanodroplets exposed to negative-polarity or positive-polarity pulses).

14.3 Results

14.3.1 NMH Cavitation Threshold: Negative-Polarity Pulse

In the first set of experiments, the histotripsy cavitation threshold was measured for agarose tissue phantoms with and without PFH nanodroplets exposed to negative-polarity pulses [Fig. 14.2(A)]. For both types of phantoms, cavitation bubbles were only observed on the high-speed camera once a certain pressure threshold was exceeded [Fig. 14.5], as seen in previous studies [24, 26-28]. As the pressure was further raised above this threshold value, cavitation was observed in an increasingly larger region of the focal area, forming well-defined histotripsy bubble clouds similar to those observed in previous work using dual-polarity pulses at various frequencies [24, 26-28, 31]. Plotting the probability of cavitation as a function of P– demonstrated a significant decrease in p_t(–) for tissue phantoms containing nanodroplets compared to control phantoms [Fig. 14.6(A,B)], with the P– threshold measured to be $p_{t\_}$(–) = 29.8±0.3 MPa, with σ_{mean} = 0.7 MPa for control phantoms without nanodroplets and p_t(–) = 11.7±0.2 MPa, with σ_{mean} = 0.4 MPa for PFH phantoms. These results closely matched the P– thresholds measured in previous studies using single-cycle dual-polarity pulses with center frequencies ranging from 345kHz to 3MHz [Table 14.1]. The single-cycle dual-polarity pulses commonly used in histotripsy studies contain both high amplitude positive and negative pressure phases [Fig. 14.2(C)]. The P– thresholds for generating cavitation previously measured with the dual-polarity pulse were 24-27 MPa without nanodroplets and 10-15 MPa with PFH nanodroplets [Table 14.1] [24, 26, 27]. Plotting the probability of cavitation for the negative-

polarity pulses as a function of P+ demonstrated a significant decrease in $p_t(+)$ for tissue phantoms containing nanodroplets compared to control phantoms [Fig. 14.7(A,B)], with the P+ threshold measured to be $p_{t\_}(+)$ = 9.9±0.1 MPa, with σ_{mean} = 0.2 MPa for control phantoms and $p_t(+)$ = 4.0±0.1 MPa, with σ_{mean} = 0.2 MPa for PFH phantoms. The P+ threshold results measured for the negative-polarity pulses were significantly lower than the P+ thresholds measured in previous studies using dual-polarity pulses, which ranged from $p_t(+)$ = 28.1-51.2 MPa and $p_t(+)$ = 10.2-15.8 MPa for control and PFH phantoms, respectively [Table 14.1].

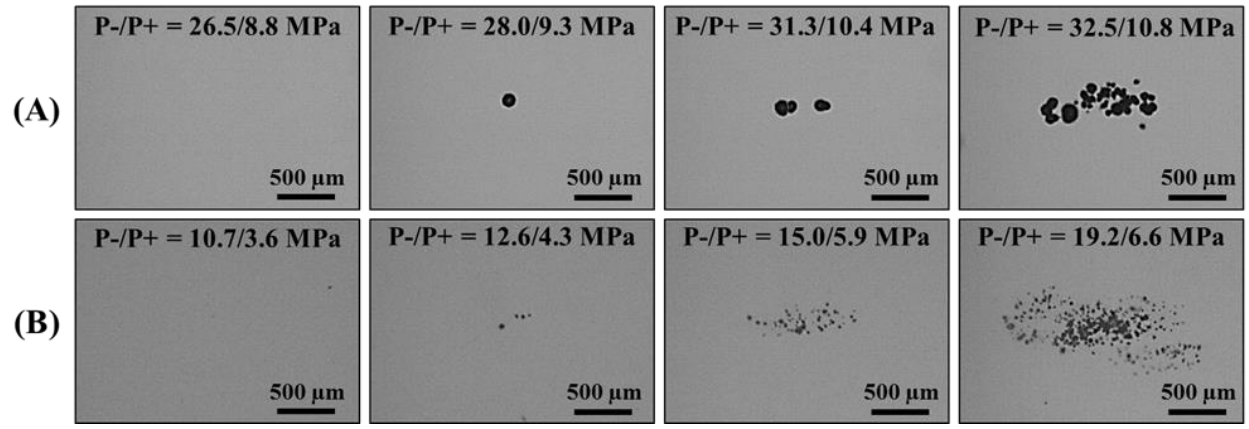

Figure 14.5. Optical Images of cavitation bubbles generated from negative-polarity pulses inside (A) control phantoms and (B) PFH phantoms.

Table 14.1 Table shows the values for the P– and P+ thresholds measured for control and PFH phantoms exposed to the negative-polarity and positive-polarity pulses along with previously measured thresholds using dual-polarity pulses [24, 26, 27].

Sample	Pulse Characteristics	P- Threshold (MPa)	P+ Threshold (MPa)
No Droplets	Dual-Polarity: 345 kHz	24.8±1.1	31.4±1.5
	Dual-Polarity: 500 kHz	25.5±1.7	28.1±1.9
	Dual-Polarity: 1.5 MHz	26.7±0.4	51.2±2.3
	Dual-Polarity: 3 MHz	26.8±0.5	29.4±0.7
	Negative-Polarity	29.8±0.3	9.9±0.1
	Positive-Polarity	>18.4	>61.1
PFH Droplets	Dual-Polarity: 345 kHz	10.4±0.3	10.2±0.2
	Dual-Polarity: 500 kHz	10.5±0.2	10.7±0.2
	Dual-Polarity: 1.5 MHz	13.0±0.1	14.1±0.2
	Dual-Polarity: 3 MHz	14.9±0.4	15.8±0.4
	Negative-Polarity	11.7±0.2	4.0±0.1
	Positive-Polarity	11.4±0.1	42.6±0.2

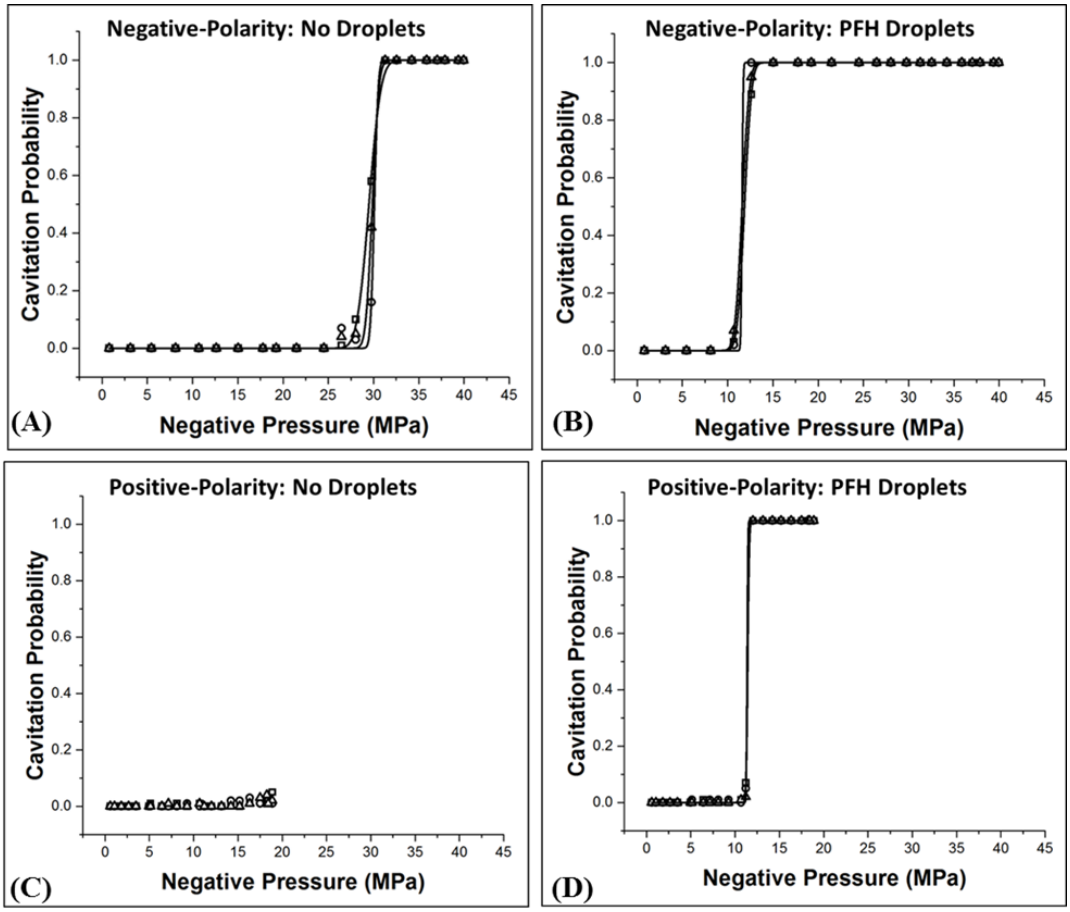

Figure 14.6. Plots show the cavitation probability as a function of negative pressure for (A,C) control and (B,D) PFH phantoms exposed to (A,B) negative-polarity pulses and (C,D) positive-polarity pulses. Cavitation couldn't be generated in control phantoms exposed to positive-polarity pulses (Max P–=18.4 MPa).

14.3.2 NMH Cavitation Threshold: Positive-Polarity Pulse

In the second set of experiments, the histotripsy cavitation threshold was measured for tissue phantoms with and without PFH nanodroplets exposed to positive-polarity pulses [Fig. 14.2(B)]. For control phantoms without nanodroplets, cavitation bubbles were not consistently observed in the focal region at any of the pressure levels tested [Fig. 14.8]. Plotting the probability of cavitation as a function of P– [Fig. 14.6(C)] and P+ [Fig. 14.7(C)] for control phantoms without nanodroplets demonstrated that the cavitation threshold was not reached even when the frequency compounding transducer was driven at its maximum output pressure for the

positive-polarity pulses (P–/P+=18.4/61.1 MPa). This finding matched previous work studying the histotripsy intrinsic threshold which has shown that cavitation is only generated when the P– is raised above the intrinsic threshold (~25-30 MPa) [24, 28, 29, 33].

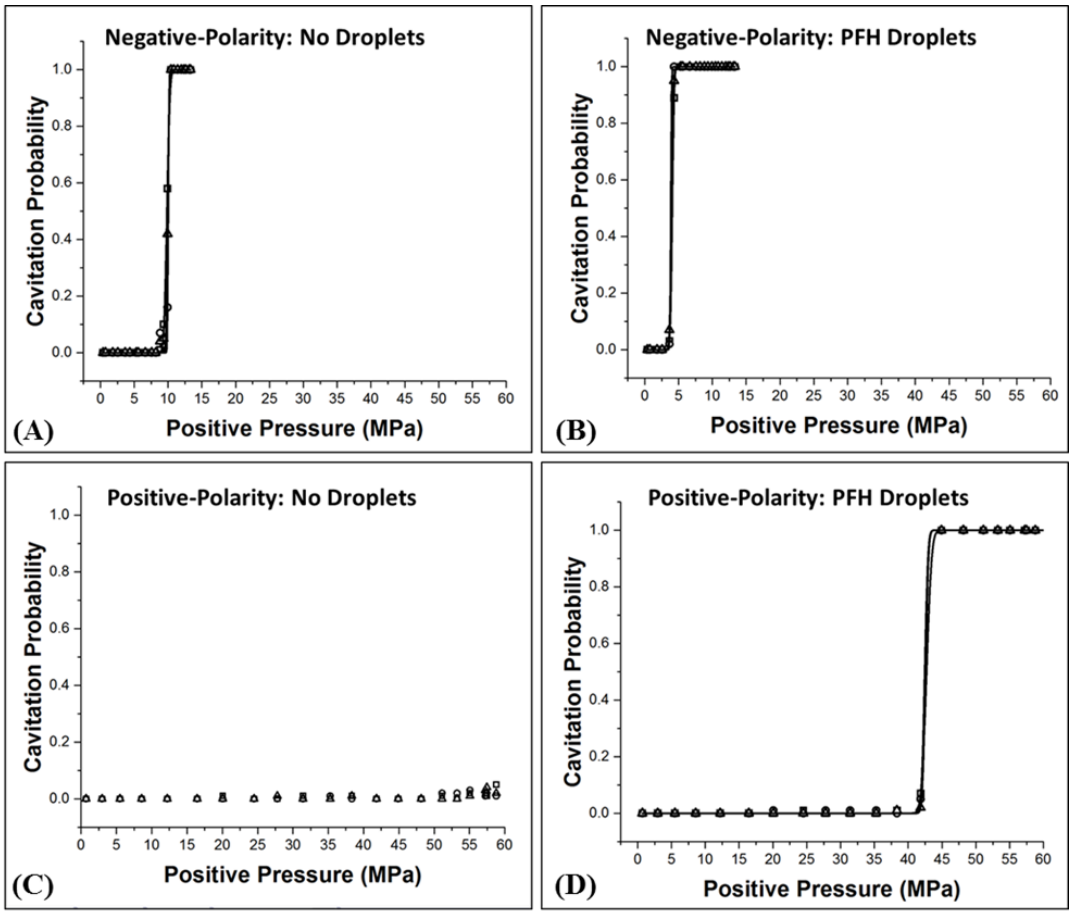

Figure 14.7. Plots show the cavitation probability as a function of positive pressure for (A,C) control and (B,D) PFH phantoms exposed to (A,B) negative-polarity pulses and (C,D) positive-polarity pulses. A significant increase in the P+ threshold was observed for both control and PFH phantoms exposed to the positive-positive polarity pulses.

For PFH phantoms exposed to the positive-polarity pulses, cavitation was observed once a certain pressure threshold was exceeded [Fig. 14.8]. However, cavitation did not occur at the center of the geometric focus of the transducer. Instead, the location of the cavitation was ~0.5 mm from the geometric focus, closely matching the location in the field with the highest P– [Fig. 14.3]. As the pressure was further increased above the NMH cavitation threshold, two separate

regions containing cavitation were observed in the PFH phantoms [Fig. 14.7], with these locations closely corresponding to the two regions of highest P– as measured by the FOPH [Fig. 14.3]. The probability of cavitation for PFH phantoms exposed to positive-polarity pulses was plotted as a function of P– (measured at the location corresponding to the highest P–), with the results demonstrating $p_t(-)$ = 11.4±0.1 MPa, with σ_{mean} = 0.1 MPa [Fig. 14.5(D)]. This P– threshold closely matched the P– threshold for the negative-polarity pulses as well as the P– thresholds previously measured using dual-polarity pulses [Table 14.1]. Plotting the probability of cavitation for PFH phantoms exposed to positive-polarity pulses as a function of P+ resulted in a P+ threshold of $p_t(+)$ = 42.6±0.2 MPa, with σ_{mean} = 0.4 MPa [Fig. 14.6(D)]. This P+ threshold was significantly higher than the P+ thresholds measured for the negative-polarity pulses as well as the P+ thresholds previously measured for dual-polarity pulses [Table 14.1]. Figure 14.9 shows a comparison of the P– and P+ thresholds measured for PFH phantoms exposed to the positive-polarity and negative polarity pulses generated in this study as well as dual-polarity pulses at various frequencies (345 kHz-3MHz) measured in a previous study [27], with results suggesting that the NMH threshold is a function of the applied P–.

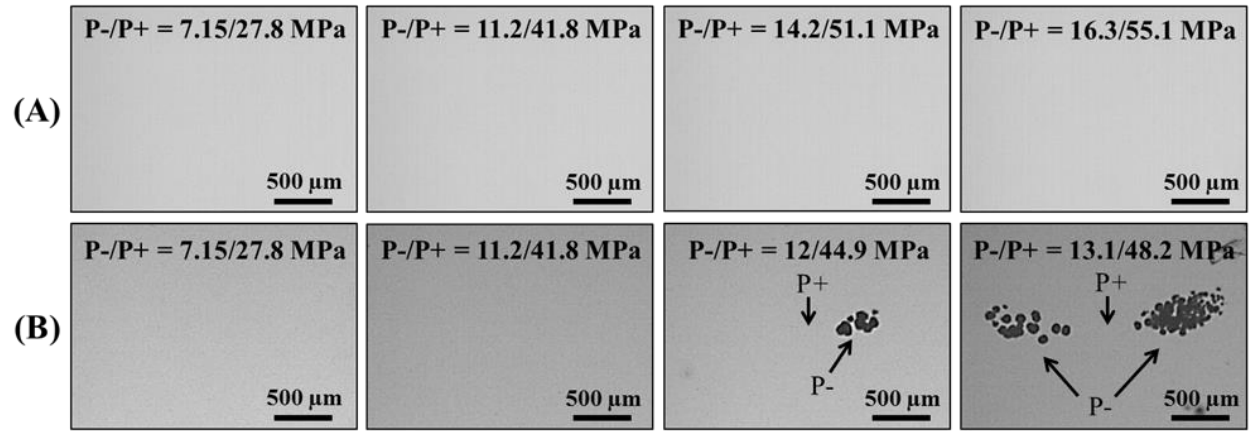

Figure 14.8. Optical Images of cavitation bubbles generated from positive-polarity pulses inside (A) control phantoms and (B) PFH phantoms. Arrows on the plot indicate the locations in the focal region corresponding to the highest positive (P+) and negative (P–) pressures as measured by the FOPH [Fig. 14.3].

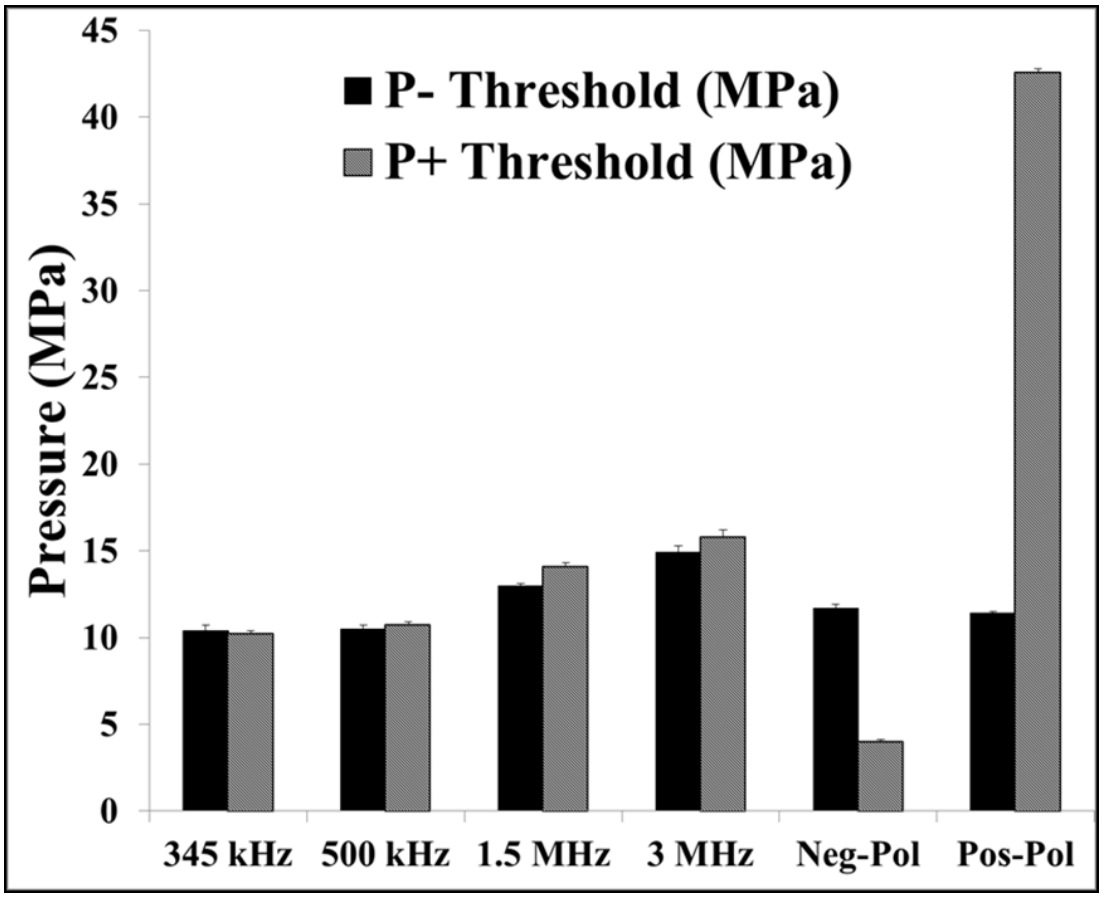

Figure 14.9. Plot compares the P– and P+ thresholds measured for PFH phantoms in this study (negative-polarity and positive-polarity pulses) with the thresholds previously measured using dual-polarity pulses (f=345kHz, 500kHz, 1.5MHz, 3 MHz) [27]. Results suggest NMH cavitation is generated directly from the *p*-of the incident wave.

14.4 Discussion

In this chapter, we were able to generate pulses with dominant negative and positive pressure phases, which allowed us to investigate the effects of positive and negative pressure on the NMH cavitation threshold separately. The results supported our hypothesis that NMH bubbles are generated after cavitation is nucleated inside the droplets directly from the incident *p*- (tensile portion of the incident wave), similar to histotripsy bubbles generated without nanodroplets when the *p*- directly exceeds the intrinsic threshold of the target media. Results showed close agreement in the P– threshold for PFH phantoms exposed to negative-polarity

(11.4±0.1 MPa), positive-polarity (11.7±0.2 MPa), and dual-polarity (10-15 MPa) pulses. The P+ thresholds, in contrast, were measured to be significantly different for PFH phantoms exposed to negative-polarity (4.0±0.1 MPa), positive-polarity (42.6±0.2 MPa), and dual-polarity (10-16 MPa) pulses. These results support our hypothesis that NMH cavitation is purely dependent upon the applied *p*-. This hypothesis was further supported by the observation that exposing PFH phantoms to positive-polarity pulses resulted in cavitation only being generated in the regions with the highest P– [Fig. 14.8], as measured by the FOPH [Fig. 14.3].

The results of this chapter provide significant insight into the nanodroplet nucleation process. Our previous results showing NMH threshold decreases with frequency and the results from this study both support the hypothesis that the nanodroplet nucleation in NMH can be explained by classical nucleation theory (CNT). The ADV literature has hypothesized that droplet nucleation in ADV is caused by a different mechanism than what is predicted by classical nucleation theory (CNT), based on previous studies showing that the ADV threshold decreases with increasing frequency [20-23, 25]. Many alternative mechanisms have been proposed to explain the discrepancy between the trends predicted by CNT and the experimental trends observed for ADV including droplet deformation, hydrodynamic cavitation, or acoustic heating [20, 21, 23]. The results of this study, however, suggest that the nucleation process involved in NMH does in fact follow the mechanism described by CNT, which predicts that cavitation is nucleated inside the droplets directly from the applied *p*-. These results suggest that nanodroplets reduce the cavitation threshold by carrying a lower threshold medium, with the probability of nucleation being a function of the *p*- exposed to the PFC. We think this theory can also be extended to explain the nucleation mechanism for ADV using multi-cycle pulses and various droplet sizes, as recent work has revealed that the decrease in the ADV threshold at higher

frequencies is due to superharmonic focusing, which significantly increases the amplitude of the *p*- inside the droplet and is enhanced at higher frequencies and in larger droplets [34, 35]. It is likely that the probability of nucleation in ADV will still follow the trends predicted by CNT once the pressure focusing effects are accounted for.

Although the results of this chapter and previous ADV studies suggest that the same nucleation process may be responsible in ADV and NMH, it is important to note that the resulting bubble dynamics are significantly different in these two cases. For example, stable bubbles are formed in ADV [20, 21, 36-40] while NMH produces cavitation bubbles that rapidly expand and then violently collapse [14, 15, 26]. There are many factors determining the resulting bubble behavior after nucleation, including the ultrasound pulse parameters, initial droplet characteristics, and the properties of the surrounding microenvironment. For example, the higher frequencies and multi-cycle pulses commonly used in ADV result in oscillatory bubble growth, which allows ADV bubbles to stabilize [36, 38]. In contrast, NMH bubbles are exposed to a single large *p*- at lower frequencies, producing bubbles that rapidly expand to sizes much larger (R_{max}~10-150 μm) than those observed for nanodroplet ADV (R_{max}~1-10 μm), followed by the violent collapse of the NMH bubbles [14, 15, 26, 36, 41]. In addition to the effects of ultrasound parameters, the resulting bubble behavior is dependent upon the droplet properties (i.e. size, concentration, total volume, and PFC boiling point) [36-38]. Finally, the bubble behavior will also be highly dependent upon the properties of the surrounding media including the temperature, Young's modulus, viscosity, surface tension, and gas concentration [14, 26, 31, 36-38]. It is therefore important to understand the impact of these properties on the resulting bubble dynamics of ADV or NMH therapies, even though the underlying nucleation process is likely the same for these two approaches.

The finding that the nanodroplet nucleation thresholds are determined by the applied *p*- and exhibit a distinct threshold behavior is promising for the development of NMH. This distinct P- threshold is dependent upon the droplet properties and can be changed by modulating droplet composition (i.e. changing droplet surface tension to modulate the nucleation threshold) [27]. With knowledge of the applied pressure fields and droplet characteristics (i.e. size, composition, concentration), predictable and reliable NMH therapy strategies can be developed. For example, the applied P– in NMH therapy must be chosen in the region above the NMH threshold but below the histotripsy intrinsic threshold to ensure cavitation is only generated in regions containing nanodroplets. This approach also suggests that NMH therapy will share the same advantages of histotripsy treatments performed above the intrinsic threshold, such as the generation of precise lesions matching the portion of the beam profile above the P– threshold as well as the ability to manipulate bubble dynamics by changing the pulse parameters [24, 28, 31, 33]. Furthermore, the sharp P– threshold behavior observed in this study suggests that generating cavitation from nanodroplets is more predictable and reproducible than generating cavitation from micron-sized air contrast agents, which do not require nucleation (i.e. phase transition) in order to initiate the cavitation process and therefore do not show the same distinct threshold behavior [24, 42, 43]. Overall, the results of this chapter improve our understanding of the physical mechanisms underlying the nanodroplet nucleation process, which will help to guide the development of NMH therapy.

14.5 Conclusion

In this chapter, the effects of positive and negative pressure on the NMH cavitation threshold were investigated separately, with results supporting our hypothesis that the NMH

cavitation threshold is determined by the incident *p*-. Close agreement was observed for the P– thresholds measured for PFH tissue phantoms exposed to negative-polarity (11.4±0.1 MPa) and positive-polarity (11.7±0.2 MPa) pulses. The P+ thresholds, in contrast, were significantly different for the negative-polarity (4.0±0.1 MPa) and positive-polarity (42.6±0.2 MPa) pulses. Furthermore, the positive-polarity pulse experiments demonstrated that cavitation was preferentially generated in the regions with the highest P–. Overall, the results of this chapter support our hypothesis that nanodroplet nucleation is determined by the applied *p*- and provide significant insight into the physical mechanisms underlying the NMH process.

14.6 References

[1] J. E. Parsons, *et al.*, "Pulsed cavitational ultrasound therapy for controlled tissue homogenization," *Ultrasound Med Biol*, vol. 32, pp. 115-29, Jan 2006.

[2] W. W. Roberts, *et al.*, "Pulsed cavitational ultrasound: a noninvasive technology for controlled tissue ablation (histotripsy) in the rabbit kidney," *J Urol*, vol. 175, pp. 734-8, Feb 2006.

[3] Z. Xu, *et al.*, "Controlled ultrasound tissue erosion: the role of dynamic interaction between insonation and microbubble activity," *J Acoust Soc Am*, vol. 117, pp. 424-35, Jan 2005.

[4] C. R. Hempel, *et al.*, "Histotripsy fractionation of prostate tissue: local effects and systemic response in a canine model," *J Urol*, vol. 185, pp. 1484-9, Apr 2011.

[5] T. L. Hall, *et al.*, "Histotripsy of the prostate: dose effects in a chronic canine model," *Urology*, vol. 74, pp. 932-7, Oct 2009.

[6] A. D. Maxwell, *et al.*, "Noninvasive treatment of deep venous thrombosis using pulsed ultrasound cavitation therapy (histotripsy) in a porcine model," *J Vasc Interv Radiol*, vol. 22, pp. 369-77, Mar 2011.

[7] A. D. Maxwell, *et al.*, "Noninvasive thrombolysis using pulsed ultrasound cavitation therapy - histotripsy," *Ultrasound Med Biol*, vol. 35, pp. 1982-94, Dec 2009.

[8] G. E. Owens, *et al.*, "Therapeutic ultrasound to noninvasively create intracardiac communications in an intact animal model," *Catheter Cardiovasc Interv*, vol. 77, pp. 580-8, Mar 1 2011.

[9] Z. Xu, *et al.*, "Noninvasive creation of an atrial septal defect by histotripsy in a canine model," *Circulation*, vol. 121, pp. 742-9, Feb 16 2010.

[10] Y. Kim, *et al.*, "Non-invasive pulsed cavitational ultrasound for fetal tissue ablation: feasibility study in a fetal sheep model," *Ultrasound in Obstetrics & Gynecology*, vol. 37, pp. 450-457, Apr 2011.

[11] Y. H. Kim, *et al.*, "Developmental Impact and Lesion Maturation of Histotripsy-Mediated Non-Invasive Tissue Ablation in a Fetal Sheep Model," *Ultrasound in Medicine and Biology*, vol. 39, pp. 1047-1055, Jun 2013.

[12] N. R. Styn, *et al.*, "Histotripsy of VX-2 tumor implanted in a renal rabbit model," *J Endourol*, vol. 24, pp. 1145-50, Jul 2010.

[13] E. Vlaisavljevich, *et al.*, "Image-Guided Non-Invasive Ultrasound Liver Ablation Using Histotripsy: Feasibility Study in an In Vivo Porcine Model," *Ultrasound in medicine & biology*, vol. 39, pp. 1398-1409, 2013.

[14] E. Vlaisavljevich, *et al.*, "Nanodroplet-mediated histotripsy for image-guided targeted ultrasound cell ablation," *Theranostics,* vol. 3, pp. 851-64, 2013.

[15] Y. Yuksel Durmaz, *et al.*, "Development of nanodroplets for histotripsy-mediated cell ablation," *Mol Pharm,* vol. 11, pp. 3684-95, Oct 6 2014.

[16] A. Arvengas, *et al.*, "Fiber optic probe hydrophone for the study of acoustic cavitation in water," *Rev Sci Instrum,* vol. 82, p. 034904, Mar 2011.

[17] F. Caupin and E. Herbert, "Cavitation in water: a review," *Comptes Rendus Physique,* vol. 7, pp. 1000-1017, Nov-Dec 2006.

[18] J. C. Fisher, "The Fracture of Liquids," *Journal of Applied Physics,* vol. 19, pp. 1062-1067, 1948.

[19] E. Herbert, *et al.*, "Cavitation pressure in water," *Phys Rev E Stat Nonlin Soft Matter Phys,* vol. 74, p. 041603, Oct 2006.

[20] O. D. Kripfgans, *et al.*, "On the acoustic vaporization of micrometer-sized droplets," *J Acoust Soc Am,* vol. 116, pp. 272-81, Jul 2004.

[21] O. D. Kripfgans, *et al.*, "Acoustic droplet vaporization for therapeutic and diagnostic applications," *Ultrasound Med Biol,* vol. 26, pp. 1177-89, Sep 2000.

[22] K. C. Schad and K. Hynynen, "In vitro characterization of perfluorocarbon droplets for focused ultrasound therapy," *Phys Med Biol,* vol. 55, pp. 4933-47, Sep 7 2010.

[23] P. S. Sheeran and P. A. Dayton, "Phase-change contrast agents for imaging and therapy," *Curr Pharm Des,* vol. 18, pp. 2152-65, 2012.

[24] E. Vlaisavljevich, *et al.*, "Effects of Ultrasound Frequency and Tissue Stiffness on the Histotripsy Intrinsic Threshold for Cavitation," *Ultrasound Med Biol,* 2015.

[25] R. Williams, *et al.*, "Characterization of submicron phase-change perfluorocarbon droplets for extravascular ultrasound imaging of cancer," *Ultrasound Med Biol,* vol. 39, pp. 475-89, Mar 2013.

[26] E. Vlaisavljevich, *et al.*, "The Effects of Ultrasound Frequency on Nanodroplet-Mediated Histotripsy," *Ultrasound Med Biol,* 2015.

[27] E. Vlaisavljevich, *et al.*, "Investigation of the Role of Ultrasound Frequency and Droplet Composition in Nanodroplet-mediated Histotripsy," presented at the International Society for Therapeutic Ultrasound, Utrecht, Netherlands, 2015.

[28] A. D. Maxwell, *et al.*, "Probability of cavitation for single ultrasound pulses applied to tissues and tissue-mimicking materials," *Ultrasound Med Biol,* vol. 39, pp. 449-65, Mar 2013.

[29] K. W. Lin, *et al.*, "Synthesis of monopolar ultrasound pulses for therapy: the frequency-compounding transducer," *IEEE Trans Ultrason Ferroelectr Freq Control,* vol. 61, pp. 1123-36, Jul 2014.

[30] J. E. Parsons, *et al.*, "Cost-effective assembly of a basic fiber-optic hydrophone for measurement of high-amplitude therapeutic ultrasound fields," *J Acoust Soc Am,* vol. 119, pp. 1432-40, Mar 2006.

[31] E. Vlaisavljevich, *et al.*, "Effects of Tissue Stiffness, Ultrasound Frequency, and Pressure on Histotripsy-induced Cavitation Bubble Behavior," *Phys Med Biol,* 2015.

[32] D. W. Hosmer and S. Lemeshow, "Confidence interval estimation of interaction," *Epidemiology,* vol. 3, pp. 452-6, Sep 1992.

[33] K. W. Lin, *et al.*, "Histotripsy beyond the intrinsic cavitation threshold using very short ultrasound pulses: microtripsy," *IEEE Trans Ultrason Ferroelectr Freq Control,* vol. 61, pp. 251-65, Feb 2014.

[34] D. S. Li, *et al.*, "Initial nucleation site formation due to acoustic droplet vaporization," *Appl Phys Lett,* vol. 104, p. 063703, Feb 10 2014.

[35] O. Shpak, *et al.*, "Acoustic droplet vaporization is initiated by superharmonic focusing," *Proc Natl Acad Sci U S A,* vol. 111, pp. 1697-702, Feb 4 2014.

[36] N. Reznik, *et al.*, "The efficiency and stability of bubble formation by acoustic vaporization of submicron perfluorocarbon droplets," *Ultrasonics,* vol. 53, pp. 1368-1376, Sep 2013.

[37] N. Reznik, *et al.*, "Investigation of Vaporized Submicron Perfluorocarbon Droplets as an Ultrasound Contrast Agent," *Ultrasound in Medicine and Biology,* vol. 37, pp. 1271-1279, Aug 2011.

[38] A. A. Doinikov, *et al.*, "Vaporization dynamics of volatile perfluorocarbon droplets: a theoretical model and in vitro validation," *Med Phys,* vol. 41, p. 102901, Oct 2014.

[39] N. Rapoport, *et al.*, "Ultrasound-mediated tumor imaging and nanotherapy using drug loaded, block copolymer stabilized perfluorocarbon nanoemulsions," *Journal of Controlled Release,* vol. 153, pp. 4-15, 2011.

[40] O. Shpak, *et al.*, "Ultrafast dynamics of the acoustic vaporization of phase-change microdroplets," *J Acoust Soc Am,* vol. 134, pp. 1610-21, Aug 2013.

[41] S. Xu, *et al.*, "Bubble size distribution in acoustic droplet vaporization via dissolution using an ultrasound wide-beam method," *Ultrason Sonochem,* vol. 21, pp. 975-83, May 2014.

[42] C. K. Holland and R. E. Apfel, "Thresholds for transient cavitation produced by pulsed ultrasound in a controlled nuclei environment," *J Acoust Soc Am*, vol. 88, pp. 2059-69, Nov 1990.

[43] D. L. Miller and R. M. Thomas, "Ultrasound contrast agents nucleate inertial cavitation in vitro," *Ultrasound Med Biol*, vol. 21, pp. 1059-65, 1995.

Chapter 15
Summary and Future Work

15.1 Summary

This dissertation investigated the effects of tissue properties on pulsed ultrasound cavitation ablation, or histotripsy, in order to develop optimal strategies for targeted tissue ablation using histotripsy. More specifically, this research 1) Investigated the effects of tissue properties (i.e. tissue stiffness, temperature) on histotripsy therapy, 2) Performed *in vivo* studies to demonstrate the feasibility and safety of histotripsy liver ablation, and 3) Developed nanodroplet-mediated histotripsy for targeted cancer cell ablation.

In the first part of this dissertation, the effects of tissue properties on histotripsy therapy were investigated. Results demonstrated that the pressure threshold for generating dense histotripsy bubble clouds using the shock scattering method increases in stiffer tissues due to the impeded expansion of initial bubbles expanded in the focus (Chapter 2), while the intrinsic threshold is independent of tissue stiffness for water-based soft tissues since the intrinsic threshold method of cloud initiation does not depend on the expansion of initial bubbles (Chapter 3). Further investigations of the intrinsic threshold demonstrated a slight decrease in the intrinsic threshold at lower frequency due to the larger focal zone and longer duration of the applied *p*- (Chapter 3) and a significant decrease in the intrinsic threshold with increasing temperature, which was primarily due to the decreased surface tension of water at higher temperatures (Chapter 4). In addition to cavitation initiation, the effects of tissue properties on susceptibility to

histotripsy-induced tissue damage were also investigated, demonstrating that stiffer tissue are more resistant to histotripsy (Chapter 5), potentially due to the higher ultimate stress and strain as well reduced bubble expansion, which was observed in tissue phantoms with increased stiffness (Chapter 7). Based on these results, two strategies were investigated for increasing the effectiveness of using histotripsy for the treatment of stiffer tissues. First, the effects of thermal preconditioning on tissue susceptibility to histotripsy was investigated, with results showing that prolonged heating of tissues at ~60°C caused tissue softening via collagen denaturing, thereby increasing tissue susceptibility to histotripsy, while prolonged heating of tissues at ~90°C caused tissue stiffening via collagen contraction which decreased tissue susceptibility to histotripsy unless collagen hydrolysis into gelatin was achieved (Chapter 6). In addition, investigations of pulsing parameters suggested that using lower frequency may increase the efficiency of histotripsy tissue ablation by increasing bubble expansion (Chapter 7). These results were supported by high-speed observations of cell-bubble interactions which demonstrated that histotripsy tissue ablation is due to the stress and strain directly applied to the cells by the rapid expansion and collapse of the histotripsy cavitation bubbles (Chapter 8).

In the second part of this dissertation, the feasibility of using histotripsy for targeted liver ablation was investigated in two *in vivo* studies. First, the feasibility of applying histotripsy *in vivo* for non-invasive liver ablation was investigated using a porcine model with similar size and anatomic similarities to its human counterpart, with results demonstrating that histotripsy was capable of creating precise lesions throughout the entire liver through the intact chest without the need for aberration correction (Chapter 9). Additionally, the hypothesis that differences in tissue stiffness could be utilized to develop a tissue selective ablation approach, which was suggested based on the results of Chapter 5, was tested *in vivo*, with results showing that histotripsy was

capable of completely fractionating the liver tissue surrounding the major hepatic vessels and the gallbladder while the fractionation was self-limiting at the boundaries of these critical structures (Chapter 9). In addition to this initial feasibility study, the long-term effects of histotripsy liver ablation were investigated in an *in vivo* rodent model, with results demonstrating that the completely fractionated tissue homogenate was resorbed by the tissue over the course of 28 days (Chapters 10).

In the final part of this dissertation, a novel ablation method combining histotripsy with acoustically sensitive nanodroplets was developed for targeted cancer cell ablation, with results demonstrating perfluoropentane nanodroplets can be used to significantly reduce the histotripsy cavitation threshold, demonstrating the potential of using nanodroplet-mediated histotripsy (NMH) for targeted, multi-focal tissue ablation (Chapter 11). Further studies demonstrated that lower frequency may improve NMH therapy by increasing the size of the focal zone, decreasing the NMH cavitation threshold, and increasing bubble expansion (Chapter 12). In addition, a study investigating the effects of droplet composition on NMH therapy demonstrated that perfluorohexane droplets may improve NMH therapy by providing sustainable cavitation nuclei over multiple pulses (Chapter 13). Finally, the role of positive and negative pressure on cavitation nucleation in NMH therapy was investigated using a frequency compounding transducer capable of generating near monopolar pulses with either a dominant positive or negative pressure phase. Results demonstrated that NMH cavitation nucleation is caused directly from the peak negative pressure of the incident wave, similar to histotripsy bubbles generated above the intrinsic threshold (Chapter 14).

Overall, the results of this dissertation provide significant insight into the physical processes underlying histotripsy tissue ablation and will help to guide the future development of

histotripsy therapy for clinical applications such as the treatment of liver cancer. Future work will aim to build upon the studies detailed in this dissertation in order to further our understanding of the physical processes involved in histotripsy tissue ablation and to promote the clinical translation of histotripsy.

15.2 Future Work

15.2.1 Investigation of Cavitation Nuclei in tissue

A significant portion of this dissertation was dedicated to investigating the process of generating cavitation in histotripsy therapy. More specifically, this work investigated the effects of tissue properties on the histotripsy cavitation thresholds using both the shock scattering and intrinsic threshold methods of cloud initiation (Chapters 2-4, 11-14). While these studies provide significant insight into the physical processes that determine the pressure required to generate histotripsy bubble clouds, they do not conclusively determine the nature of the initial cavitation nuclei population. Future work should build upon the results of this study to determine the cavitation nuclei involved in intrinsic threshold histotripsy, shock scattering histotripsy, and boiling histotripsy.

In order to gain a better understanding of the cavitation nuclei population in tissue and their role in the histotripsy process, future work should be conducted in studies that manipulate the nuclei environment in order to determine the potential nuclei characteristics. For example, one strategy currently being pursued in our lab is investigating the cavitation thresholds in experiments using bubble deletion pulses that have recently been developed for the removal of stable residual bubbles after the application of histotripsy pulses [1]. These bubble deletion pulses should allow for the removal of large stable bubbles which have been proposed to be

necessary for generating cavitation below the intrinsic threshold (i.e. incidental cavitation threshold) as well as for generating the initial bubbles in the focus during shock scattering histotripsy. Studies of the shock scattering threshold using the bubble deletion pulses should help to validate the hypothesis that the shock scattering process is initiation when large stable bubble nuclei are expanded in the focus.

In addition to shock scattering histotripsy, experiments utilizing these bubble deletion pulses may shed some insight on the "intrinsic nuclei" responsible for intrinsic threshold histotripsy. Previous work has suggested that the histotripsy intrinsic threshold relies upon cavitation nuclei that are intrinsic to the media [2, 3]. By intrinsic, we mean that the nuclei appear to be associated with the properties of the medium itself rather than impurities. Although it is possible that these nuclei too are related to impurities, it seems unlikely, as several groups using different sample processing methods have measured approximately the same threshold for inertial cavitation associated with these nuclei in the range of 24 to 33 MPa in distilled water [2-7]. Previous work has suggested that the "intrinsic nuclei" may consist of either semi-permanent stabilized gas nuclei [6, 8-10] or spontaneous nuclei that form bubbles in a medium by energy-density fluctuations described by classical nucleation theory (CNT) [11-14]. By using the bubble deletion pulses, it may be possible to determine if the initial bubbles are in fact stable bubbles or spontaneous nuclei. However, it remains unclear if the bubble deletion pulses would be capable of removing very small stable bubbles such as the nanometer sized bubble proposed to be responsible for the histotripsy intrinsic threshold. As such, future work will aim to develop more advanced microscopic models in order to fully describe the characteristics of the intrinsic nuclei population.

15.2.2 Intrinsic Threshold *In Vivo*

The results of this work suggest that the intrinsic threshold of water-based soft tissues is an intrinsic property of the water inside of the tissue. As a result, generating cavitation should be reliable and reproducible *in vivo*, likely at a peak negative pressure ~21-24 MPa based on the frequency and the local temperature at the focus. While preliminary *in vivo* studies support this hypothesis, future work should be conducted to carefully measure the *in vivo* intrinsic thresholds using the same pulsing methods and PCD detection scheme used in *ex vivo* experiments in order to validate this hypothesis.

15.2.3 Effects of Temperature on the Shock Scattering Threshold

In Chapter 4, the effects of temperature on the histotripsy intrinsic threshold were investigated, with results demonstrating a significant decrease in the intrinsic threshold with increasing temperature due to the decrease in the surface tension of water at higher temperatures. This work further suggested that the shock scattering threshold may not be significantly affected by changes in temperature since the shock scattering threshold likely depends on the formation of initial bubbles from larger sparse cavitation nuclei whose behavior is not dominated by the surface tension of the media. However, as the dense bubble cloud in shock scattering is formed when the scattered shockwave constructively interferes with the incident negative pressure phase of the following cycles in order to overcome the intrinsic threshold of the media, it is possible that the shock scattering threshold will be impacted by changes in the intrinsic threshold rather than being affected by changes in the initial bubble generation or expansion as seen in stiffer tissues in Chapter 2. As a result, future work is needed to fully investigate the role of temperature in the shock scattering process.

15.2.4 *In vivo* Tumor Ablation

Chapters 9 and 10 demonstrated the initial feasibility and term safety of using histotripsy for targeted liver ablation. These studies suggest that histotripsy will offer many advantages for the treatment of liver cancer compared to alternative thermal ablation approaches. In order to build upon this work, future studies will be conducted using relevant liver cancer tumor models to demonstrate that histotripsy can completely fractionate a tumor into acellular debris without inducing metastasis or causing tumor recurrence after healing. These studies will be essential to setting the foundation for the clinical translation of histotripsy as a method for non-invasive liver cancer surgery.

15.2.5 Dual-modality Therapy Approaches

The results of this study demonstrate that histotripsy therapy is highly dependent upon the properties of the local tissue environment. More specifically, stiffer tissues have been shown to be resistant to histotripsy-induced tissue damage. This finding is a significant advantage for histotripsy therapy and has led to the development of a tissue selective ablation approach in which stiff tissues such as blood vessels are preserved inside the focus while the target tissue is destroyed. Future work should take advantage of this feature of histotripsy therapy and develop novel approaches to modulate the local tissue environment prior to treatment in order to enhance these effects. One potential method of using this dual modality approach that was outlined in Chapter 6 is using local heating to alter the tissue properties prior applying histotripsy. Future work will aim to extend this approach to include other dual-modality strategies such as locally administering a drug or enzyme that disrupts tissue collagen prior to histotripsy treatment. It is

possible that this “tissue marinating” pretreatment approach may be more feasible than the “tissue cooking” approach in certain clinical applications in which thermal ablation is impractical, such as the treatment of large volumes or in regions containing large blood vessels [15, 16]. Future work will further aim to develop these strategies for specific clinical applications which may require this dual-modality approach, such as the treatment of very stiff tissues that are resistant to conventional histotripsy methods.

15.2.6 Nanodroplet-mediated Histotripsy *In Vivo* Validation

The final part of this dissertation developed a novel ablation method combining histotripsy with acoustically sensitive nanodroplets for targeted cancer cell ablation. While this work provides significant insight into the physical processes involved in nanodroplet-mediated histotripsy (NMH), future work will aim to extend NMH to the *in vivo* setting. First, *in vivo* studies must be conducted to demonstrate the ability of using nanodroplets to precisely target the tumor tissue inside the body. These bio-distribution studies are extremely important in order to establish the feasibility of using NMH for targeted tumor ablation, as the nanodroplets must preferentially accumulate in the tumor tissue in order to NMH therapy to be successful. Further *in vivo* studies should also be conducted in a relevant multi-focal tumor model to demonstrate the ability of using NMH for targeted tumor ablation *in vivo*.

15.3 References

[1] A. P. Duryea, *et al.*, "Acoustic bubble removal to enhance SWL efficacy at high shock rate: an in vitro study," *Journal of Endourology,* vol. 28, pp. 90-5, Jan 2014.

[2] A. D. Maxwell, *et al.*, "Probability of cavitation for single ultrasound pulses applied to tissues and tissue-mimicking materials," *Ultrasound Med Biol,* vol. 39, pp. 449-65, Mar 2013.

[3] E. Vlaisavljevich, *et al.*, "Effects of Ultrasound Frequency and Tissue Stiffness on the Histotripsy Intrinsic Threshold for Cavitation," *Ultrasound Med Biol,* 2015.

[4] L. J. Briggs, "The Limiting Negative Pressure of Water between 0-Degrees-C and 50-Degrees-C," *Science,* vol. 111, pp. 461-461, 1950.

[5] M. Greenspan and C. E. Tschiegg, "Radiation-Induced Acoustic Cavitation - Threshold Versus Temperature for Some Liquids," *Journal of the Acoustical Society of America,* vol. 72, pp. 1327-1331, 1982.

[6] G. N. Sankin and V. S. Teslenko, "Two-threshold cavitation regime," *Doklady Physics,* vol. 48, pp. 665-668, Dec 2003.

[7] E. Herbert, *et al.*, "Cavitation pressure in water," *Physical Review E,* vol. 74, Oct 2006.

[8] N. F. Bunkin, *et al.*, "Cluster structure of stable dissolved gas nanobubbles in highly purified water," *Journal of Experimental and Theoretical Physics,* vol. 108, pp. 800-816, May 2009.

[9] E. N. Harvey, *et al.*, "Bubble formation in animals I. Physical factors," *Journal of Cellular and Comparative Physiology,* vol. 24, pp. 1-22, Aug 1944.

[10] D. E. Yount, "Skins of Varying Permeability - Stabilization Mechanism for Gas Cavitation Nuclei," *Journal of the Acoustical Society of America,* vol. 65, pp. 1429-1439, 1979.

[11] A. Arvengas, *et al.*, "Fiber optic probe hydrophone for the study of acoustic cavitation in water," *Rev Sci Instrum,* vol. 82, p. 034904, Mar 2011.

[12] A. Arvengas, *et al.*, "Cavitation in heavy water and other liquids," *J Phys Chem B,* vol. 115, pp. 14240-5, Dec 8 2011.

[13] J. C. Fisher, "The Fracture of Liquids," *Journal of Applied Physics,* vol. 19, pp. 1062-1067, 1948.

[14] M. S. Pettersen, *et al.*, "Experimental investigation of cavitation in superfluid 4He," *Phys Rev B Condens Matter,* vol. 49, pp. 12062-12070, May 1 1994.

[15] T. A. Leslie, *et al.*, "High-intensity focused ultrasound ablation of liver tumours: can radiological assessment predict the histological response?," *Br J Radiol,* vol. 81, pp. 564-71, Jul 2008.

[16] A. Okada, *et al.*, "A case of hepatocellular carcinoma treated by MR-guided focused ultrasound ablation with respiratory gating," *Magn Reson Med Sci,* vol. 5, pp. 167-71, Oct 2006.